Conference Proceedings of the Society for Experimental Mechanics Series

Sven Bossuyt · Gary Schajer
Alberto Carpinteri *Editors*

Residual Stress, Thermomechanics & Infrared Imaging, Hybrid Techniques and Inverse Problems, Volume 9

Proceedings of the 2015 Annual Conference on Experimental and Applied Mechanics

Springer

Conference Proceedings of the Society for Experimental Mechanics Series

Series Editor

Kristin B. Zimmerman, Ph.D.
Society for Experimental Mechanics
Bethel, CT, USA

More information about this series at http://www.springer.com/series/8922

Sven Bossuyt • Gary Schajer • Alberto Carpinteri
Editors

Residual Stress, Thermomechanics & Infrared Imaging, Hybrid Techniques and Inverse Problems, Volume 9

Proceedings of the 2015 Annual Conference on Experimental and Applied Mechanics

Springer

Editors
Sven Bossuyt
Aalto University
Helsinki, Finland

Gary Schajer
Univ of British Columbia
Vancouver, British Columbia, Canada

Alberto Carpinteri
Politecnico di Torino
Torino, Italy

ISSN 2191-5644 ISSN 2191-5652 (electronic)
Conference Proceedings of the Society for Experimental Mechanics Series
ISBN 978-3-319-21764-2 ISBN 978-3-319-21765-9 (eBook)
DOI 10.1007/978-3-319-21765-9

Library of Congress Control Number: 2015949812

Springer Cham Heidelberg New York Dordrecht London

Printed on acid-free paper

Springer International Publishing AG Switzerland is part of Springer Science+Business Media (www.springer.com)

Preface

Residual Stress, Thermomechanics & Infrared Imaging, Hybrid Techniques and Inverse Problems represents one of nine volumes of technical papers presented at the 2015 SEM Annual Conference & Exposition on Experimental and Applied Mechanics organized by the Society for Experimental Mechanics and held in Costa Mesa, CA, June 8–11, 2015. The complete Proceedings also include volumes on: *Dynamic Behavior of Materials; Challenges in Mechanics of TimeDependent Materials; Advancement of Optical Methods in Experimental Mechanics; Experimental and Applied Mechanics; MEMS and Nanotechnology; Mechanics of Biological Systems and Materials; Mechanics of Composite & Multifunctional Materials; and Fracture, Fatigue, Failure and Damage Evolution*.

Each collection presents early findings from experimental and computational investigations on an important area within Experimental Mechanics, Residual Stress, Thermomechanics and Infrared Imaging, Hybrid Techniques and Inverse Problems being three of these areas.

Residual stresses have a great deal of importance in engineering systems and design. The hidden character of residual stresses often causes them to be underrated or overlooked. However, they profoundly influence structural design and substantially affect strength, fatigue life and dimensional stability. Since residual stresses are induced during almost all materials processing procedures, for example, welding/joining, casting, thermal conditioning and forming, they must be taken seriously and included in practical applications.

In recent years, the applications of infrared imaging techniques to the mechanics of materials and structures have grown considerably. The expansion is marked by the increased spatial and temporal resolution of the infrared detectors, faster processing times and much greater temperature resolution. The improved sensitivity and more reliable temperature calibrations of the devices have meant that more accurate data can be obtained than were previously available.

Advances in inverse identification have been coupled with optical methods that provide surface deformation measurements and volumetric measurements of materials. In particular, inverse methodology was developed to more fully use the dense spatial data provided by optical methods to identify mechanical constitutive parameters of materials. Since its beginnings during the 1980s, creativity in inverse methods has led to applications in a wide range of materials, with many different constitutive relationships, across material heterogeneous interfaces. Complex test fixtures have been implemented to produce the necessary strain fields for identification. Force reconstruction has been developed for high strain rate testing. As developments in optical methods improve for both very large and very small length scales, applications of inverse identification have expanded to include geological and atomistic events.

Helsinki, Finland — Sven Bossuyt
Vancouver, British Columbia, Canada — Gary Schajer
Torino, Italy — Alberto Carpinteri

Contents

Chapter 1
Reconstruction of Spatially Varying Random Material Properties by Self-Optimizing Inverse Method

Joshua M. Weaver and Gunjin J. Yun

Abstract In this paper, a new methodology for reconstructing spatially varying random material properties is presented by combining stochastic finite element (SFE) models with Self-Optimizing Inverse Method (Self-OPTIM). The Self-OPTIM can identify model parameters based on partial boundary force and displacement data from experimental tests. Statistical information (i.e. spatial mean, variance, correlation length and Gaussian normal random variables) of spatially varying random fields (RFs) are parameterized by Karhunen-Loève (KL) expansion method and integrated into SFE models. In addition, a new software framework is also presented that can simultaneously utilize any number of remote computers in a network domain for the Self-OPTIM simulation. This can result in a significant decrease of computational times required for the optimization task. Two important issues in the inverse reconstruction problem are addressed in this paper: (1) effects of the number of internal measurements and (2) non-uniform reaction forces along the boundary on the reconstruction accuracy. The proposed method is partially proven to offer new capabilities of reconstructing spatially inhomogeneous material properties and estimating their statistical parameters from incomplete experimental measurements.

Keywords Inverse analysis • Inverse reconstruction • Self-optimizing inverse method • Parameter estimation • Parallel computations

1.1 Introduction

Understanding and characterizing behavior of the materials we use is one of the fundamental aspects of engineering design. Constitutive models are often used to predict the response of such materials under various loadings. Theses constitutive models can contain various parameters that are used to approximate their mechanical response of materials. With increasing complexity of the constitutive models, it becomes very difficult to determine all material parameters with one simple experimental test. This causes the parameter identification procedure to become costly and time comprehensive. The parameter identification of material constitutive models has been studied by many researchers within the same inverse problem setting: naming a few representative researches, Mahnken, et al. [1–5], Saleeb, et al. [6–9], Geriach et al. [10, 11], Akerstrom et al. [12] and Castello, et al. [13]. Various methods for parameter estimation of the constitutive models have been researched including the finite element model updating method (FEMU) [14], the constitutive equation gap method (CEGM) [15, 16], the virtual fields method (VFM) [17, 18], the equilibrium gap method (EGM) [19] and the reciprocity gap method (RGM) [20]. All of these methods require full-field measurements of displacements. Recently, Yun et al. developed Self-Optimizing Inverse Method called Self-OPTIM [21]. The Self-OPTIM was used to identify the constitutive material parameters of an elasto-plasticity model based upon one experimental material test [22]. The Self-OPTIM is suitable for parameter estimations using a large-scale finite element model under general loading conditions since its algorithm is designed to minimize errors of full-field and inhomogeneous stresses and strains computed from two parallel finite element simulations subjected to experimentally measured boundary force and displacement data, respectively, rather than a least squares functional between experimental response (e.g. displacements) along limited boundaries and corresponding model-based predictions. For example, a comparison with a least-square functional between experimental and FE-simulated displacements showed that Self-OPTIM can offer better convexity of the optimization problem [23]. A group of German mathematicians provided a strong mathematical basis proving the existence of a global minimum of the Self-OPTIM's objective function for the case of linear non-homogeneous and non-isotropic elasticity in the stationary case [24]. Self-OPTIM was also successfully applied to identification of damping of highway bridge embankments from real earthquake acceleration response [23].

J.M. Weaver • G.J. Yun (✉)
Department of Civil Engineering, The University of Akron, 244 Sumner St. ASEC 210, Akron, OH 44325-3905, USA
e-mail: gy3@uakron.edu

S. Bossuyt et al. (eds.), *Residual Stress, Thermomechanics & Infrared Imaging, Hybrid Techniques and Inverse Problems, Volume 9*, Conference Proceedings of the Society for Experimental Mechanics Series, DOI 10.1007/978-3-319-21765-9_1

Many times a material is modeled as a homogenous material across the entirety of the model. However, in reality this is not the case. Uncertainties in raw materials, geometric heterogeneity of constituents in composite materials, manufacturing process, long-term operation under uncertain environmental and loading conditions cause a non-uniform distribution of material properties. Therefore, reconstruction of heterogeneous material properties is important for condition assessments. Several approaches used for parameter estimation have been applied for damage identification problems. The EGM method was used for identifying heterogeneous map of elastic moduli [19]. Heterogeneous elasto-plastic properties could be identified based on full-field measurements by the CEGM method [25]. Generally, distributions of damage over the structures are inhomogeneous and the number of parameters thus increases in proportional to the size of the finite element model. Therefore, compared to parameter estimation problems for constitutive models, updating a set of damage parameters defined at a large number of degrees of freedom and/or elements yields a much more challenging inverse problem. To reduce the number of updating parameters, the concept of damage function like finite element shape functions were used in dynamic modal based FE modeling [26–28]. However, in their studies, spatial correlation between identified local properties could not be taken into account. Recently, Adhikari and Friswell applied Karhunen-Loève expansion (KLE) method to modal-based model updating for identifying distributed properties (i.e. mass and stiffness) of beam structures [29]. In their study, statistical properties (i.e. spatial mean, variance and correlation length) are assumed to be *a priori* known properties. The KLE method have also been applied to model updating for identifying distributions and statistical parameters of spatially correlated random variables in 2D and 3D complex structures [30–32] whereby stochastic finite element with spatial varying material properties was integrated with Self-OPTIM [30]. In spite of these efforts, stochastic inverse material parameter characterization and/or damage detection still requires identifying a large number of updating parameters from incomplete measurements. Global optimization methods (e.g. evolutionary algorithms) are considered suitable for the large number of unknown parameters. However, they usually entail a large number of runs of finite element analyses.

This paper present a new methodology for reconstructing spatially varying random material properties by combining stochastic finite element (SFE) models with Self-Optimizing Inverse Method (Self-OPTIM) and a new software framework that can simultaneously utilize any number of remote computers in a network domain for the Self-OPTIM simulation. This software framework offers efficiency of optimization as well as the ability for Self-OPTIM to easily interact with finite element analysis program. Because the optimization of complex models can be time comprehensive, a parallelization method will be created and used to dramatically reduce the time required for optimization. Two important issues in the inverse reconstruction problem are addressed in this paper: (1) effects of the number of internal measurements and (2) non-uniform reaction forces along the boundary on the reconstruction accuracy. The proposed method is partially proven to offer new capabilities of reconstructing spatially inhomogeneous material properties and estimating their statistical parameters from incomplete experimental measurements.

1.2 Random Field Modeling and Self-OPTIM Methodology

In this paper, Self-OPTIM was integrated with stochastic finite element models for the purpose of characterizing the random distribution of material properties. For this method, the Karhunen-Loève expansion (KLE) method was used to discretize the spatially varying random fields. This method produces two dimensional (2D) random fields with non-zero mean values. The 2D random field is broken down into deterministic and stochastic parts as follows:

$$E(\boldsymbol{x},\ \theta) = \ \overline{E}(\boldsymbol{x}) + \sum_{i=1}^{M} \sqrt{\lambda_i} \varphi_i(\boldsymbol{x}) \xi_i(\theta) \tag{1.1}$$

where M is the truncation number of KLE terms; $\boldsymbol{x}$ is the position vector over the domain; θ is the primitive randomness; $\bar{E}$ is the mean value of the random variable; λ_i and φ_i are the eigenvalue and eigenfunction of an assumed covariance kernel (e.g. an exponential covariance kernel); and ξ_i is the statistically uncorrelated normal variable. Assuming that the random field is second-order homogeneous, $\bar{E}(\boldsymbol{x})$ is constant and therefore can be simplified as the mean value $\bar{E}$. The Galerkin finite element approach is used to approximate the covariance kernel by the eigensolutions by discretizing the problem domain. Details on its formulation can be referred to [33]. This paper used the exponential covariance kernel expressed as

$$C_i(\mathbf{x}_1, \mathbf{x}_2) = \sigma_i^2 \exp\left(-\frac{|x_1 - x_2|}{l_x} - \frac{|y_1 - y_2|}{l_y}\right) \tag{1.2}$$

where l_x and l_y are the correlation length parameters in x and y directions, respectively; and ${\sigma_i}^2$ is the variance. Stochastic finite element models with spatial variations of material parameters are used in Self-OPTIM analysis. In Self-OPTIM, $\mathbf{x}=[\overline{E}, l_x, l_y, \sigma^2, \ <\xi_i>_i=1,..,k]$ will be a set of unknown statistical parameters to be identified. Self-OPTIM runs two parallel finite element simulations under experimentally measured boundary forces and displacements, respectively. The variation of the full-field stress and strain values between the two simulations exhibit errors in the material parameters and are used in the objective function to determine the correct material parameters of the constitutive model. The problem in Self-OPTIM is a nonlinear unconstrained optimization problem as follows

$$\text{Minimize } \mathbf{\Pi}(\mathrm{x}) = \sum_{i=1}^{n} \frac{RMSE_i^{\varepsilon}(F,D) + MAE_i^{\varepsilon}(F,D)}{R_i^{\varepsilon}2(F,D) + 1} + \sum_{i=1}^{n} \frac{RMSE_i^{\sigma}(F,D) + MAE_i^{\sigma}(F,D)}{R_i^{\sigma}2(F,D) + 1} \tag{1.3}$$

$$\text{where } R(A,B) = \frac{\sum_n (A_n - \overline{A})(B_n - \overline{B})}{\sqrt{\left(\sum_n (A_n - \overline{A})^2\right)\left(\sum_n (B_n - \overline{B})^2\right)}} \tag{1.4}$$

$$RMSE(A,B) = \sqrt{\frac{\sum_n (A_n - B_n)^2}{n}} \tag{1.5}$$

$$MAE(A,B) = \frac{\sum_n |A_n - B_n|}{n} \tag{1.6}$$

The unconstrained nonlinear optimization problem of Self-OPTIM uses the implicit objective function in (1.3), which utilizes the stress and strain values obtained from finite element simulations of the two models; force driven and displacement driven analyses. The root mean square error (RMSE), mean absolute error (MAE) and correlation (R) between the stress and strains of the two models make up the objective function and are calculated as by (1.4–1.6). The stress and strains of the two models must be normalized before the statistical measures are calculated for the objective function. This allows the strain values to become equally valuable in the determination of the objective function. Normalization is done by determining the maximum and minimum values of the force and displacement based simulations for each component of stress and strain and then applying (1.7) to each component using those maximum and minimum values. This is done for each simulation of the force and displacement based models. Equation (1.7) also allows the normalization process to identify the high stress regions; whether they are positive or negative. The low stress regions can then be removed from the objective function calculation by using a cutoff value. For example, if a cutoff value of 0.2 is used, any stress value less than twenty percent of the maximum stress is removed from the calculation of the objective function.

$$\overline{\sigma}_{ij} = \frac{|\sigma_{ij}|}{max\left(|\sigma_{ij\_max}|, \ |\sigma_{ij\_min}|\right)} \tag{1.7}$$

In addition to (1.3), Self-OPTIM has the ability to incorporate displacements at internal degrees of freedom from sources such as Digital Image Correlation (DIC) in the objective function as expressed in (1.8). The additional objective functional is the statistical measure between the displacement of the force driven finite element simulation and the internal displacements from the experimental tests. This provides Self-OPTIM with the ability to optimize the material parameters more accurately.

$$\text{Minimize } \mathbf{\Pi}_{DIC}(\mathbf{x}) = \sum_{i=1}^{n} \frac{RMSE_i^{\varepsilon}(F,D) + MAE_i^{\varepsilon}(F,D)}{R_i^{\varepsilon}2(F,D)+1} + \sum_{i=1}^{n} \frac{RMSE_i^{\sigma}(F,D) + MAE_i^{\sigma}(F,D)}{R_i^{\sigma}2(F,D)+1} + \sum_{i=1}^{n} \frac{RMSE_i^{U}(F,DIC) + MAE_i^{U}(F,DIC)}{R_i^{U}2(F,DIC)+1} \tag{1.8}$$

In this paper, firefly algorithm is used to identify unknown parameters [34].

1.3 Development of Self-OPTIM Software Framework

The Self-OPTIM framework was created in the C# programming language and utilizes various components of the .NET framework to expedite the optimization process. The use of multiple threads and the ability to create asynchronous TCP/IP sockets to connect to remote clients prove invaluable to the optimization speed of Self-OPTIM. Another benefit to using the C# programming language is the ability to create a graphical user interface (GUI) which allows the user to effectively create any optimization run in a time efficient manner.

The development of the Self-OPTIM framework was made in such a way that additional modules could easily be created to implement the Self-OPTIM procedure. Any module that implements the abstract base class of the Self-OPTIM framework shown in Fig. 1.1 can be used in the optimization process. For example, the primary FEA tool utilized by the Self-OPTIM framework at this time is ABAQUS. However, other third party FEA tools could also be implemented if desired. For this implementation several sub-modules have been created that utilize ABAQUS. The two primary ones are the Standard module, which utilize the input file, and the UMAT module, which uses a Fortran file for user defined materials. The final module that we will use in this paper is the Stochastic module which is a derivative of the UMAT module. The diagram in Fig. 1.1 shows the modules utilized in Self-OPTIM and provides an idea of how additional modules can be created. Note that a module needs to implement the abstract methods identified in the abstract Self-OPTIM class in order for it to be used in the framework.

1.3.1 Parallelization of Self-OPTIM Simulations

Depending upon the scale of the model, a single analysis in ABAQUS can be quite demanding on a computer's resources and can be time comprehensive. Since each firefly has a unique solution, every firefly must be analyzed using ABAQUS. The total number of times of ABAQUS analyses on the model is N_r=2 × N_F × N_{Iter} where N_F and N_{Iter} indicate the number of

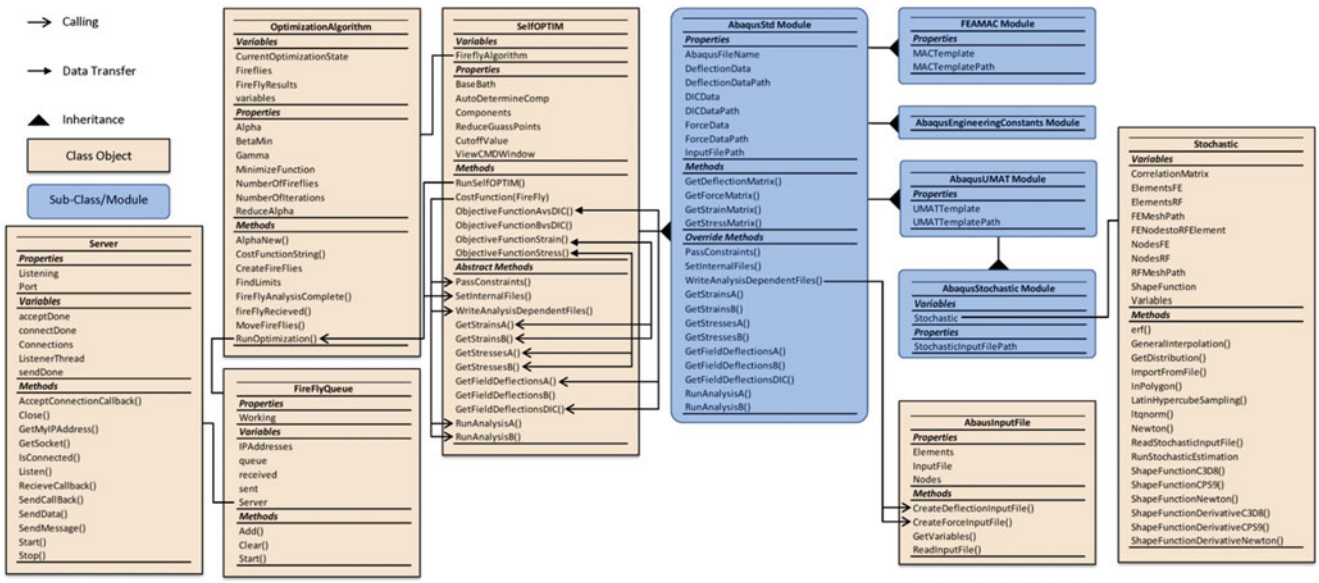

Fig. 1.1 Self-OPTIM module diagram

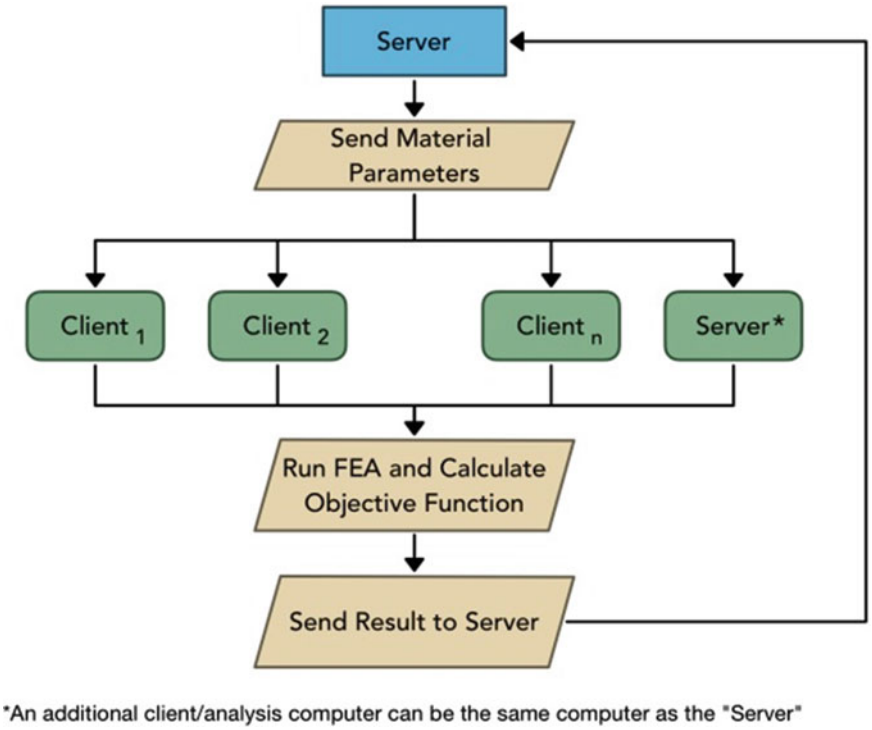

Fig. 1.2 Diagram of server–client interaction

fireflies and iterations set by the user. As a result of the number of runs that need to be implemented, the total time required to run an optimization using Self-OPTIM can be very large. Therefore, the implementation of multiple computers to run simulations was determined as a reasonable method to reduce the time requirements for optimization.

A single computer could be considered the server as illustrated in Fig. 1.1 Self-OPTIM Module Diagram Fig. 1.2. Any additional computer that has Self-OPTIM installed on it can then connect to the server, establishing a connection that can be used to send the fireflies out from the server and receive the objective function value back from the client; each firefly contains a unique solution to the optimization problem. Any number of client computers can be connected to the server. Also, the server itself can also act like a client and receive fireflies and send back results using an IP loopback. The fireflies are sent asynchronously to the clients; meaning that as soon as a client is done with an analysis it will receive a new firefly to analyze. Depending upon the performance of the individual computers, the time required to optimize the material parameters can be reduced dramatically with additional computers.

1.3.2 Optimization Algorithm

The firefly algorithm is used by Self-OPTIM as the optimization algorithm to determine the constitutive material parameters. The algorithm is based upon the characteristics of fireflies in the night sky. The light intensity of a flash of a specific firefly is directly related to the objective function that is to be optimized. The fireflies in the solution domain move with some randomness in the direction of the nearest firefly with a light intensity greater then itself. The fireflies will move around the domain until a local or global minimum is acquired [34]. The number of fireflies dictates how many unique solutions will be analyzed per iteration. The more fireflies that there are, the greater the possibility of determining the global optimum, or in this case the correct material parameters. The number of iterations determines how many times each firefly will be analyzed. The Alpha parameter dictates the randomness of the firefly's movements. The value of Alpha must be between 0 and 1. Beta is another value that determines the characteristics of the firefly's movements. Lastly, the light absorption coefficient Gamma characterizes the variation of the attractiveness of the fireflies through the sky. Essentially, this allows the light intensity of a firefly to decrease relative to another firefly based upon the distance they are from one another. This parameter is important in determining the speed at which the convergence of the optimization will take place. However, the faster the optimization takes place, the less likely that the global optimum is the returned solution.

1.4 Reconstruction of Random Fields by Self-OPTIM

1.4.1 Effects of the Number of DIC Measurements

To determine the effect of the number of DIC (Digital Image Correlation) points on the ability of Self-OPTIM to estimate the random field of the material strength parameter, a series of tests with varying number of DIC points was conducted. An 8×4 rectangular model was used with pinned restraints on the left edge of the model and the uniaxial loading applied on the right edge. The synthetic model was created using a fixed displacement and a synthetic reference random field distribution with a normalized median of 1, log normal variance of 0.05, and a correlation length of 5. The resulting forces were then used to create the corresponding force driven model for Self-OPTIM. For this specific test, the forces were taken at the nodal points and used to calculate a uniformly distributed load on the specimen. This will show that the Self-OPTIM can determine distribution of random fields even when more realistic boundary conditions are used.

Using a series of DIC points ranging from 0 to 15, the effect of the ability of Self-OPTIM to obtain the correct random distribution could be obtained. The 15 DIC points that were used in this test can be seen in Fig. 1.3a. For a specific test, the DIC points used are equivalent to the number of points desired and all numbers below. For example, if 8 nodes are used in the experiment then nodes 1–8 are used. Five KLE terms (ξ_i, i=1, .., 5) were included as unknown parameters. Using a series of DIC points ranging from 0 to 15, the effect of the ability of Self-OPTIM to obtain the correct random distribution could be obtained. In order to measure the errors in each of the tests, the Self-OPTIM objective function, as shown in (1.3), was used to calculate the errors between the simulated test and the identification model at each Gaussian point. In this way, the error in the random field could be quantified. It can be seen from Fig. 1.3b that a minimum of two DIC points is sufficient in this test for a semi-accurate result from Self-OPTIM. Using five or more DIC points resulted in the least amount of error between the reference and identification simulations. An error of 0.0132 was obtained when 5 DIC points were used. This indicates that Self-OPTIM can identify distributions of random fields from incomplete measurements.

1.4.2 Effect of Non-uniform Reaction Forces on Reconstruction of Random Fields

In case of reconstruction of spatially inhomogeneous random fields, it is difficult to measure inhomogeneous reaction forces along the boundary. Simplification of non-uniform distribution of reaction forces to uniform distribution in the identification model needs to be addressed for practical applications of Self-OPTIM. It is worth noting that there will be negative effects on the identification results from uniform distribution of reaction forces with varying degrees of extent. However, negative

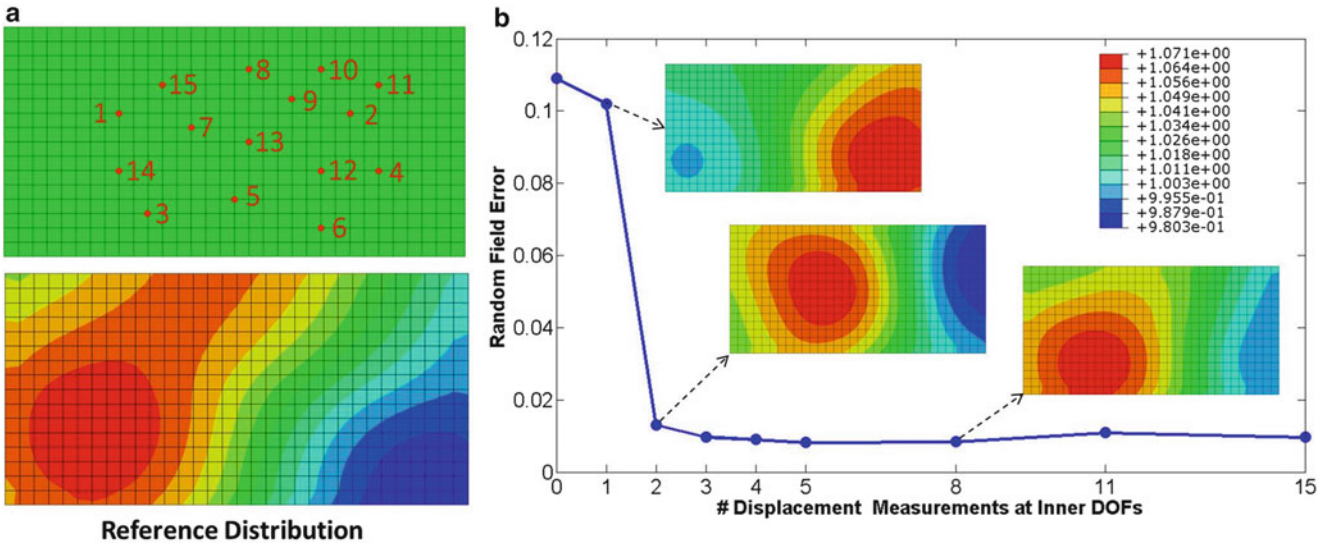

Fig. 1.3 (**a**) Location of DIC points and reference distribution of elastic modulus (**b**) changes of random field error ($=\left[\boldsymbol{RMSE}\left(\boldsymbol{r}_{id}, \boldsymbol{r}_{ref}\right) + \boldsymbol{MAE}\left(\boldsymbol{r}_{id}, \boldsymbol{r}_{ref}\right)\right] / \left[1 + \boldsymbol{R}\left(\boldsymbol{r}_{id}, \boldsymbol{r}_{ref}\right)\right]$ vs. the number of DIC points

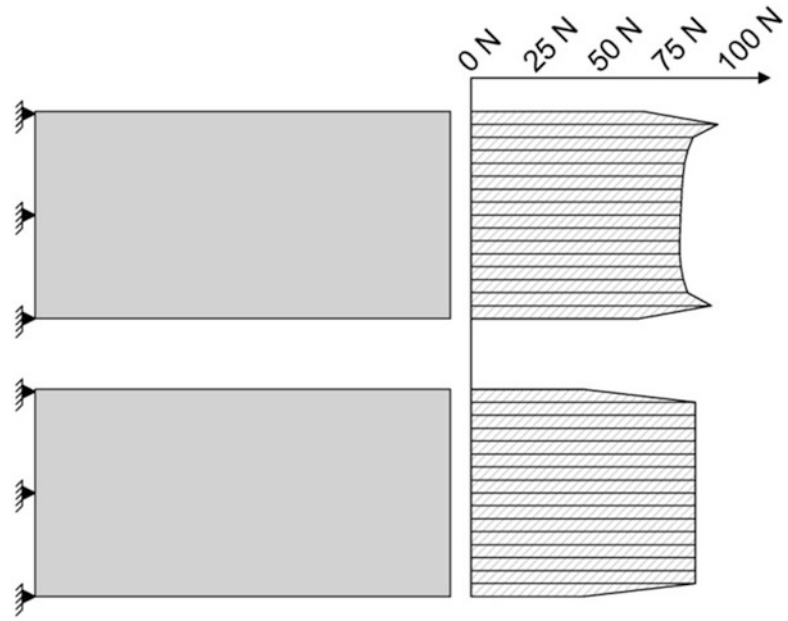

Fig. 1.4 Uniform and non-uniform force distribution along right edge of specimen

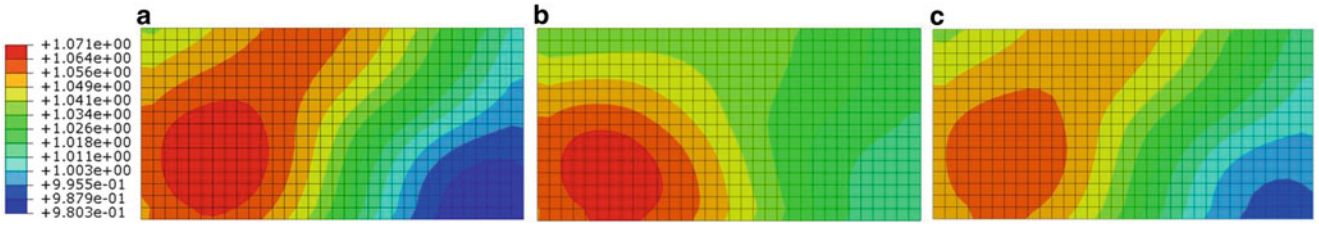

Fig. 1.5 Effect of non-uniform reaction forces on reconstruction of elastic modulus by Self-OPTIM, (**a**) reference distribution, (**b**) reconstruction of elastic modulus with 15 DIC points and uniform reaction forces, (**c**) with 15 DIC points and non-uniform reaction forces

effects of discrepancies between FE model boundary and real-life boundary can be reduced by avoiding extraction of stress and strain fields away from the boundary.

In addition to the above results with a varying number of DIC points, an additional test with the non-uniform reaction force obtained from the synthetic model and 15 DIC points was conducted. A plot of the uniform and non-uniform force distributions along the right edge of the model can be seen in Fig. 1.4. The purpose of this test is to show that with the synthetic force data a more accurate random field realization can be obtained even though convergence of the random field has already been established at five DIC points per Fig. 1.3b. Also, this shows that the results in Fig. 1.3b are truly optimized for real life situations.

The resulting random field distribution can be seen in Fig. 1.5c and when compared to the reference distribution in Fig. 1.5a, it can be seen that the results are very accurate. The error produced between the test and reference random fields was calculated to be 0.0000569, which is significantly lower than the error of 0.00962 obtained when a uniform force distribution was used.

1.5 Conclusions

In this paper, a networked parallel software framework was presented for the purpose of characterizing and reconstructing spatially varying random fields by Self-OPTIM methodology with incomplete measurements. The proposed software framework has benefits of significantly reducing computational times by using remote client computers connected through a local network. A global optimization algorithm called firefly algorithm was used. Spatially varying random fields were modeled by Karhunen-Loève (KL) expansion method and used in the identification model within Self-OPTIM analysis.

Using the proposed software framework, two critical aspects in the inverse reconstruction problems were addressed. According to Self-OPTIM analysis results presented in this paper, the Self-OPTIM methodology could potentially reconstruct inhomogeneous distributions of material properties with incomplete full-field measurements and partial boundary force and displacement. It was shown that simplification of non-uniform distributions of the boundary forces can induce errors in the reconstruction results. The proposed method is partially proven to offer new capabilities of reconstructing spatially inhomogeneous material properties and estimating their statistical parameters from incomplete experimental measurements.

References

1. R. Mahnken, A comprehensive study of a multiplicative elastoplasticity model coupled to damage including parameter identification. Comput. Struct. **74**(2), 179–200 (2000)
2. R. Mahnken, An inverse finite-element algorithm for parameter identification of thermoelastic damage models. Int. J. Numer. Methods Eng. **48**(7), 1015–1036 (2000)
3. R. Mahnken, Identification of material parameters for constitutive equations. Encyclopedia Comput. Mech. **2**, 637–655 (2004)
4. R. Mahnken, M. Johansson, K. Runesson, Parameter estimation for a viscoplastic damage model using a gradient-based optimization algorithm. Eng. Comput. **15**(6–7), 925 (1998)
5. R. Mahnken, E. Stein, A unified approach for parameter identification of inelastic material models in the frame of the finite element method. Comput. Methods Appl. Mech. Eng. **136**(3-4), 225–258 (1996)
6. A.F. Saleeb, A.S. Gendy, T.E. Wilt, Parameter-estimation algorithms for characterizing a class of isotropic and anisotropic viscoplastic material models. Mech. Time-Depend. Mater. **6**(4), 323–362 (2002)
7. A.F. Saleeb et al., Interactive software for material parameter characterization of advanced engineering constitutive models. Adv. Eng. Softw. **35**(6), 383–398 (2004)
8. A.F. Saleeb et al., Effective strategy for automated characterization in complex viscoelastoplastic and damage modeling for isotropic/anisotropic aerospace materials (vol 15, pg 84, 2002). J. Aerosp. Eng. **15**(4), 166–166 (2002)
9. A.F. Saleeb et al., An anisotropic viscoelastoplastic model for composites—sensitivity analysis and parameter estimation. Composites Part B Engineering **34**(1), 21–39 (2003)
10. S. Gerlach, A. Matzenmiller, On parameter identification for material and microstructural properties. GAMM-Mitteilungen **30**(2), 481–505 (2007)
11. A. Matzenmiller, S. Gerlach, Parameter identification of elastic interphase properties in fiber composites. Composites Part B Engineering **37**(2-3), 117–126 (2006)
12. P. Akerstrom, B. Wikman, M. Oldenburg, Material parameter estimation for boron steel from simultaneous cooling and compression experiments. Model. Simul. Mater. Sci. Eng. **13**(8), 1291–1308 (2005)
13. D.A. Castello et al., Constitutive parameter estimation of a viscoelastic model with internal variables. Mech. Syst. Signal Process **22**(8), 1840–1857 (2008)
14. E. Pagnacco, et al. Inverse strategy from displacement field measurement and distributed forces using FEA. SEM Annual Conference and Exposition on Experimental and Applied Mechanics, Poland, 2005
15. A. Constantinescu, On the identification of elastic moduli from displacement-force boundary measurements. Inverse Prob. Eng. **1**(4), 293–313 (1995)
16. G. Geymonat, S. Pagano, Identification of mechanical properties by displacement field measurement: a variational approach. Meccanica **38**(5), 535–545 (2003)
17. M. Grediac, F. Pierron, Applying the virtual fields method to the identification of elasto-plastic constitutive parameters. Int. J. Plast. **22**(4), 602–627 (2006)
18. M. Grediac et al., The virtual fields method for extracting constitutive parameters from full-field measurements: a review. Strain **42**(4), 233–253 (2006)
19. D. Claire, F. Hild, S. Roux, A finite element formulation to identify damage fields: the equilibrium gap method. Int. J. Numer. Methods Eng. **61**(2), 189–208 (2004)
20. A. Ben Abda, H. Ben Ameur, M. Jaoua, Identification of 2D cracks by elastic boundary measurements. Inverse Prob. **15**(1), 67–77 (1999)
21. G.J. Yun, S. Shang, A self-optimizing inverse analysis method for estimation of cyclic elasto-plasticity model parameters. Int. J Plast. **27**, 576–595 (2011)
22. S. Shang, G.J. Yun, Identification of elasto-plastic constitutive parameters by self-optimizing inverse method: experimental verifications. Comput. Mater. Continua **635**(1), 1–18 (2012)
23. M.R. Rahimi, G.J. Yun, S. Shen, Inverse estimation of dynamic stiffness of highway bridge embankment from earthquake records. J. Bridge Eng. **19**(SPECIAL ISSUE: Recent Advances in Seismic Design, Analysis, and Protection of Highway Bridges): p. A4014005 (2014)
24. M. Wolff, M. Böhm, Zu einem neuen Ansatz zur Parameterbestimmung in der Mechanik der Festkörper, (University of Bremen, Bremen, 2013)
25. F. Latourte et al., Elastoplastic behavior identification for heterogeneous loadings and materials. Exp. Mech. **48**(4), 435–449 (2008)
26. A. Teughels, J. Maeck, G. De Roeck, Damage assessment by FE model updating using damage functions. Comput. Struct. **80**(25), 1869–1879 (2002)
27. A. Teughels, G. De Roeck, Structural damage identification of the highway bridge Z24 by FE model updating. J. Sound Vib. **278**(3), 589–610 (2004)

28. M.M.A. Wahab, G. De Roeck, B. Peeters, Parameterization of damage in reinforced concrete structures using model updating. J. Sound Vib. **228**(4), 717–730 (1999)
29. S. Adhikari, M.I. Friswell, Distributed parameter model updating using the karhunen-loeve expansion. Mech. Syst. Signal Process **24**(2), 326–339 (2010)
30. S. Shang, Stochastic material characterization of heterogeneous media with randomly distributed material properties. Department of Civil Engineering 2012, The University of Akron: Doctoral Dissertation
31. G.J. Yun, L. Zhao, E. Iarve, Probabilistic mesh-independent discrete damage analyses of laminate composites. Comp. Sci. Tech. (2015)
32. S. Shang, G.J. Yun, Stochastic material characterization for spatially varying random macroscopic material properties by stochastic self-optimizng inverse method. Probab. Eng. Mech. (2014)
33. S. Shang, G.J. Yun, Stochastic finite element with material uncertainties: implementation in a general-purpose simulation program. Finite Elem. Anal. Des. **64**, 65–78 (2013)
34. X.S. Yang, Firefly algorithms for multimodal optimization. Stochastic Algorithms Foundations Appl. Proc. **5792**, 169–178 (2009)

Chapter 2
Performance Assessment of Integrated Digital Image Correlation Versus FEM Updating

A.P. Ruybalid, J.P.M. Hoefnagels, O. van der Sluis, and M.G.D. Geers

Abstract Full-field identification methods can adequately identify constitutive material parameters, by combining Digital Image Correlation (DIC) with Finite Element (FE) simulation. It is known that interpolation within the DIC procedure is an important error source for DIC-results. In this study, the influence of these errors on the eventual identification results is investigated.

Virtual experiments are conducted from which constitutive parameters are identified by two approaches: the commonly used method of Finite Element Model Updating (FEMU) and the more recent method of Integrated Digital Image Correlation (IDIC), in which the utilized interpolation functions are varied, and the influence on the identified parameters is investigated.

It was found that image-interpolation has a significant effect on the accuracy of both methods. However, the observed differences in results between the two methods of FEMU and IDIC cannot be explained by interpolation errors.

Keywords Digital Image Correlation (DIC) • Inverse parameter identification • Finite Element Method (FEM) • Interpolation errors • Integrated DIC • FEMU

2.1 Introduction

To properly describe the mechanical behavior of materials, constitutive parameters must be identified, which is best done by using *full-field* kinematic data in the form of (microscopic) images of the deformation process, and combining simulation with in-situ experimentation. This is particularly interesting for the solid sate lighting industry where, ideally, dense, complex material stacks must be characterized from one test.

The most intuitive and widely used full-field identification method is that of Finite Element Model Updating (FEMU) [1]. In this technique, parameters are optimized by comparing displacement fields from finite element (FE) simulation with measured displacement fields acquired through (subset-based) Digital Image Correlation (DIC) on experimental images containing speckle-patterns.

A more recently developed method [2], termed *Integrated Digital Image Correlation (IDIC)*, intimately integrates mechanical descriptions of a material with full-field measurements to identify model parameters. The method eliminates the need for calculating displacements from images before parameter identification can be realized. Instead, digital images are directly correlated by optimizing the mechanical parameters that govern the deformation of the imaged material. Mechanical knowledge drives the correlation procedure, and can be introduced to the problem through FE-simulation. In essence, the correlation procedure and identification procedure are integrated into a *one-step* approach, making it distinct from FEMU, which is a *two-step* approach in which post-processing of experimental images precedes the identification procedure. Overviews of both methods are shown in Figs. 2.1 and 2.2.

2.2 Systematic Error

The dense material stacks in microelectronics only exhibit small displacements upon material or interface failure. Such fine kinematics make full-field, DIC-based identification methods prone to systematic errors that result in biased solutions. An important systematic error source results from inevitable interpolation steps needed in (1) the DIC procedure to correlate

A.P. Ruybalid • J.P.M. Hoefnagels (✉) • O. van der Sluis • M.G.D. Geers
Department of Mechanical Engineering, Eindhoven University of Technology, P.O. Box 513, Eindhoven 5600, The Netherlands
e-mail: j.p.m.hoefnagels@tue.nl

S. Bossuyt et al. (eds.), *Residual Stress, Thermomechanics & Infrared Imaging, Hybrid Techniques and Inverse Problems, Volume 9*, Conference Proceedings of the Society for Experimental Mechanics Series, DOI 10.1007/978-3-319-21765-9_2

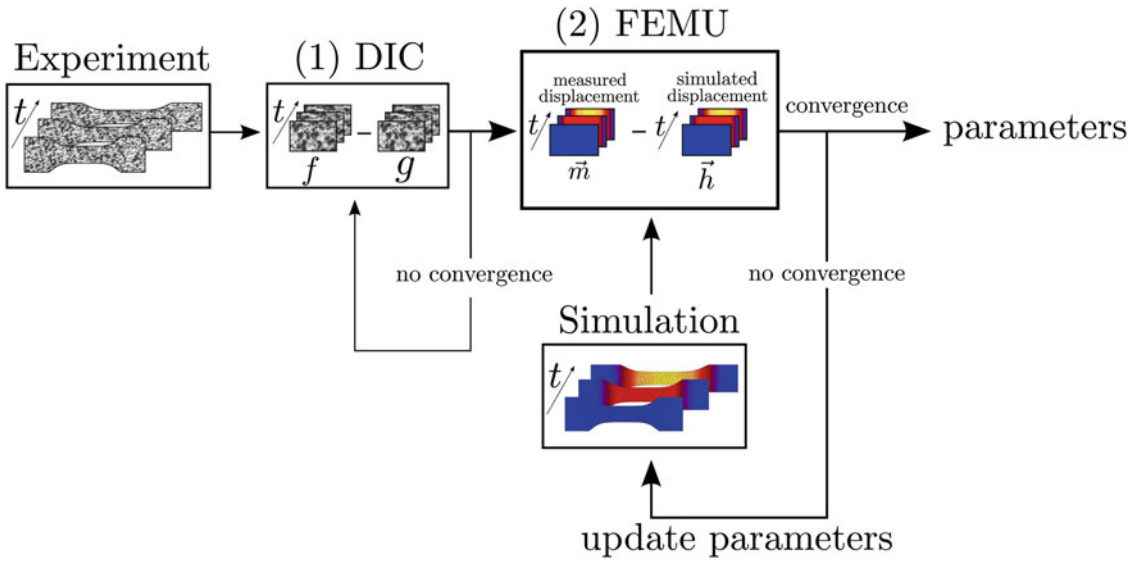

Fig. 2.1 Overview of the two-step method of FEMU, which consists of two iteration loops for (1) DIC and (2) identification of parameters

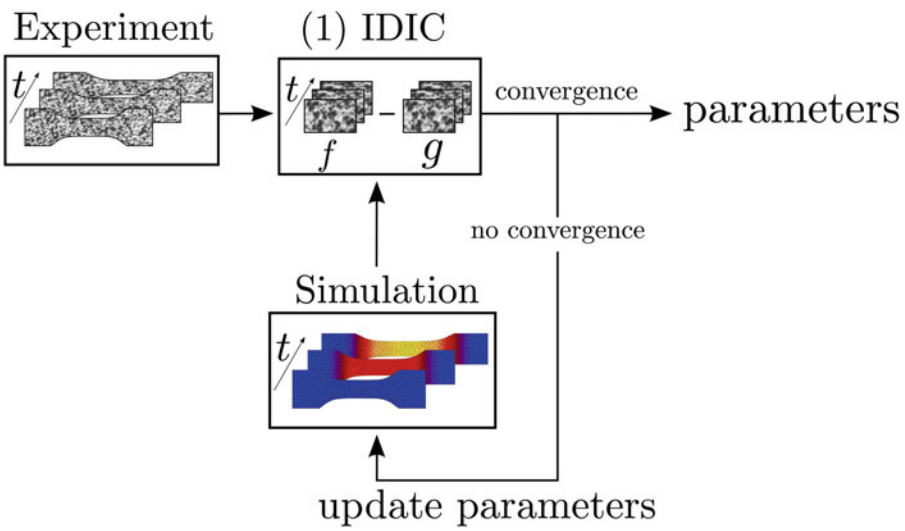

Fig. 2.2 Overview of the one-step method of IDIC, which integrates DIC and the identification of parameters, resulting in one iteration loop

images, and (2) transposing displacement fields from the FE-discretized space to the image pixel space (in case of IDIC) or the subset space of the measured displacement field (in case of FEMU).

To illustrate this issue, a virtual tensile test, described later in the subsequent section, on a linear elastic, cubic orthotropic material, described by three known parameters, E_x, ν_{xy}, and G_{xy}, reveals the sensitivity of IDIC and FEMU to systematic errors, when initialized with the known, reference parameters, as shown in Fig. 2.3. The goal of this study is to further explore the influence of these systematic errors on the accuracy of the identification results of FEMU and IDIC.

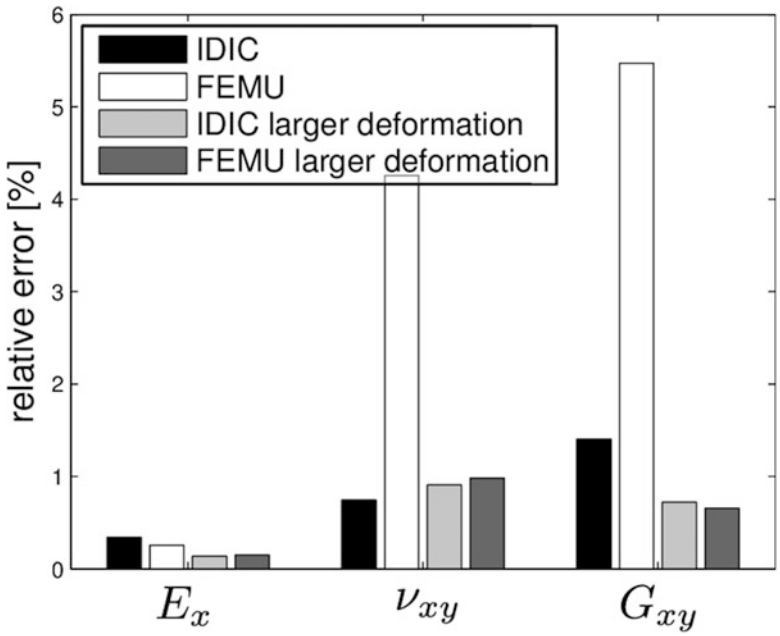

Fig. 2.3 The relative errors of the identified parameters for the IDIC and FEMU methods, initialized with perfect initial guesses for the parameters. When larger deformations are imposed during the virtual test, the relative parameter errors decrease, showing that systematic errors become especially influential in case of small displacements

2.3 Virtual Experimentation

In order to quantitatively assess the parameter errors caused by interpolation in IDIC and FEMU and exclude effects of errors that cannot be quantified, virtual experiments were conducted. In such an experiment, an artificial speckle pattern in reference image $f\left(\vec{x}, t_0\right)$, is deformed by numerically simulated displacements, to produce subsequent images $g\left(\vec{x}, t\right)$. The altering speckle pattern represents a virtual material that mechanically deforms over time. The finite element method was used in this study to simulate the displacement fields by which the speckle patterns were deformed to generate images. The acquired images were subsequently used in IDIC and FEMU, with which the mechanical parameters that govern the virtual material's deformation, were identified. Since the reference parameters used for virtual experimentation are known, the accuracy of parameters, identified by IDIC and FEMU, can be quantitatively assessed.

Uniaxial tensile tests (2D plane stress simulations) were performed on a virtual tensile bar of $30 \times 46 \times 0.9$ mm^3, with two circular notches with a radius of 11 mm, of which an illustration is shown in Fig. 2.4. The artificial speckle pattern was stored in an 8-bit, gray-valued image of 2048×1536 pixels, corresponding to an imaged region of 27×20 mm^2. The pattern is built from random gray values drawn from three standard normal distributions with different widths that are superposed, establishing a combination of pattern features of 2, 18, and 150 pixels in width.

The test-case corresponds to a cubic orthotropic, linear elastic material, which is described by three independent model parameters [3]; Young's modulus $E_x = 130$ GPa, Poisson's ratio $\nu_{xy} = 0.28$, and the shear modulus $G_{xy} = 79.6$ GPa. The virtual tensile bar is loaded in x -direction by an applied horizontal tensile force of 2500 N. This results in sub-pixel displacements throughout the specimen with an average value of 0.64 pixel, and a maximum strain of 0.25 % in the center of the specimen (where the strain is largest due to the presence of the notches). Such small deformations, which are realistic in materials, such as silicon, used in the microelectronics industry, are challenging for the identification methods, since it puts high demands on the required resolution of the DIC method, which must be capable of capturing these fine kinematics.

To focus the study on the influence of interpolation errors on the relative parameter errors for IDIC and FEMU, the iterative identification procedures are initialized with perfect initial guesses for these parameters, and noiseless images are used. Different choices are thereby used for image-interpolation and displacement field interpolation. For the former, *cubic spline* and *linear* functions are investigated, and for the latter, *cubic* and *linear* functions are tested.

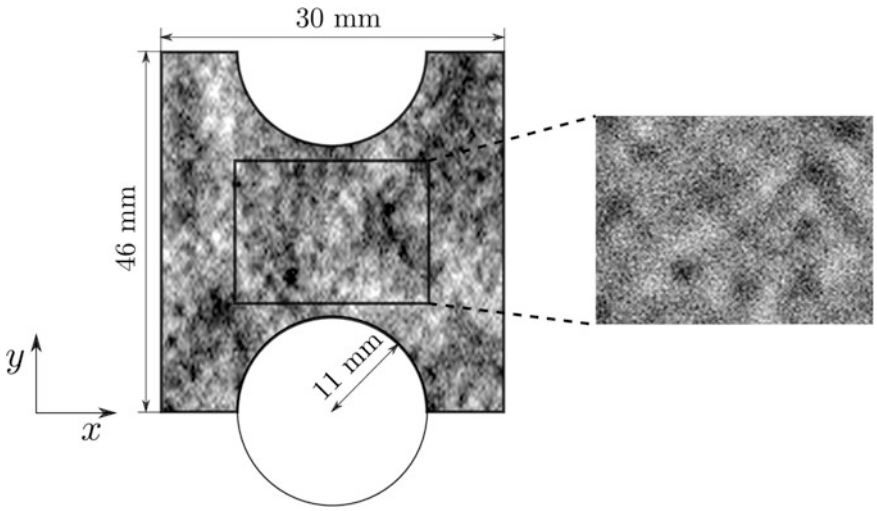

Fig. 2.4 Schematic of a tensile bar with circular notches, used in virtual uniaxial tensile tests, in which loading is applied in the x-direction. The indicated imaged region of the tensile specimen is used in the identification routines

2.4 Results and Discussion

The results for IDIC and FEMU, in terms of the relative errors on the three cubic orthotropic elastic parameters are shown in Fig. 2.5. The choices for image and displacement field interpolation are listed, in that order, in the legends. For example: "spline linear" indicates that cubic spline functions were used for image-interpolation and linear functions were used for the displacement field interpolation.

The first conclusion is that, for both IDIC and FEMU, different choices for displacement field interpolation do not affect the solution at all. Since the element shape functions used in the FE-simulation are linear, it is concluded that both linear and cubic interpolation functions are accurate for transposing the displacement fields from the FE-discretization space to the image and subset space, for IDIC and FEMU, respectively. When higher order element shape functions are used with the FE-scheme (e.g., bicubic elements), a more pronounced influence on the parameter accuracy is expected. The interpolation functions must at least match the order of the element shape functions.

Secondly, both methods are significantly affected by the image-interpolation functions, since when spline interpolation functions are used, more accurate results are obtained. This is in accordance with the conclusions of Schreier et al., who showed that higher order interpolation functions lead to more accurate DIC-results [4]. Only the FEMU result for Poisson's ratio ν_{xy} is an exception and could be further investigated.

Thirdly, when making a comparison between the results of IDIC and FEMU for the cases when the most appropriate image-interpolation functions are used (higher order splines as proposed by Schreier et al.; indicated by "spline linear" and "spline cubic" in the legends), it is observed that IDIC produces less erroneous results than FEMU. This difference is not explained by interpolation errors but is believed to arise from extra regularization choices in the separate DIC-algorithm used within the two-step FEMU routine. The one-step IDIC method is, by nature and automatically, very much regularized by a small number of mechanical parameters, while regularization choices must be made in the case of FEMU, in which the DIC-process is performed separately from the identification routine. The separate DIC-algorithm typically requires a much higher degree of regularization, depending on, e.g., the number of local subsets, the degree of global polynomial shape functions, or the number of connected finite elements. It is known that the choice of regularization is important in DIC and directly affects the accuracy of the DIC-results [5, 6]. Errors made in the separate DIC-routine within FEMU propagate into the identification results and therefore govern the difference in performance between IDIC and FEMU.

2.5 Conclusions

It was observed that displacement field interpolation does not affect the accuracy of either IDIC of FEMU. It is expected that when the interpolation functions undermatch the order of the shape functions used with the FE-scheme, the accuracy will be affected. Although it was observed that image-interpolation has a significant effect on the accuracy of either methods, it is also concluded that interpolation errors do not explain the observed differences in performance between IDIC and FEMU.

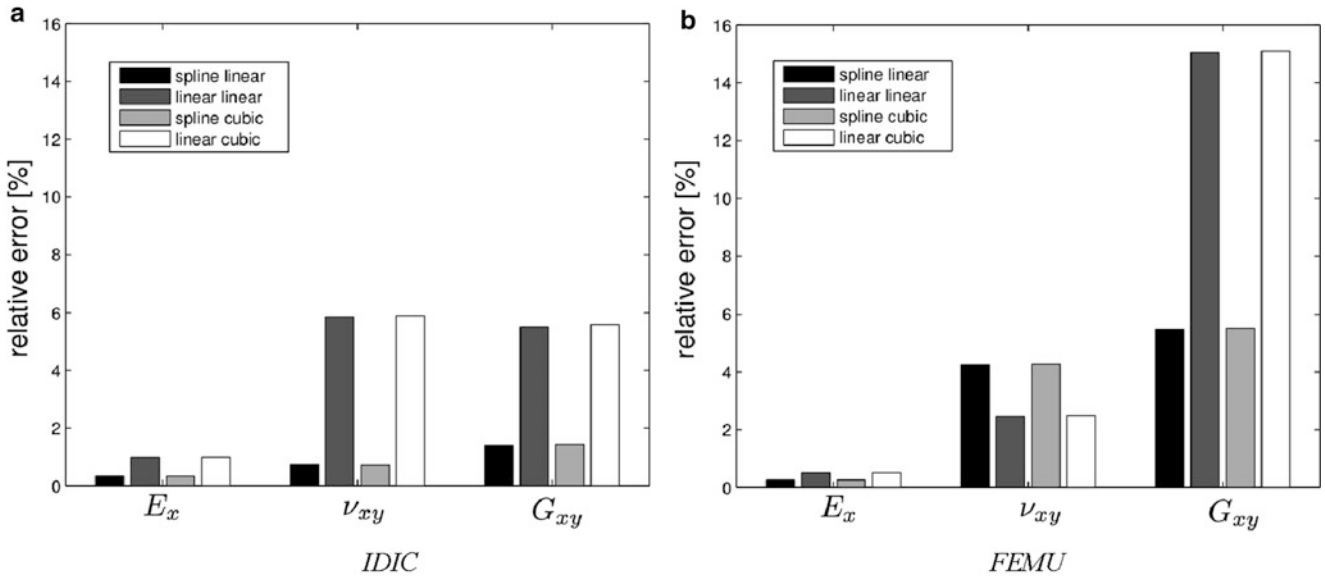

Fig. 2.5 Relative errors of parameters identified by IDIC (**a**) and FEMU with optimized DIC-settings (**b**) for different choices for image-interpolation and displacement field interpolation

Another factor that plays an important role, which was not thoroughly investigated here, is the degree of regularization of the DIC-problem. Although it is known that these regularization choices affect the DIC-results, the exact influence on the identification results is not known and could be further explored by using virtual experimentation and varying the regularization scheme within the DIC-routine.

References

1. J. Kajberg, G. Lindkvist, Characterisation of materials subjected to large strains by inverse modelling based on in-plane displacement fields. Int. J. Solids Struct. **41**(13), 3439–3459 (2004)
2. J. Réthoré, S. Roux, F. Hild, An extended and integrated digital image correlation technique applied to the analysis of fractured samples. Eur. J. Comput. Mech. **18**, 285–306 (2009)
3. M.A. Hopcroft, W.D. Nix, T.W. Kenny, What is the Young's modulus of silicon? J. Microelectromech. Syst. **19**(2), 229–238 (2010)
4. H.W. Schreier, J.R. Braasch, M.A. Sutton, Systematic errors in digital image correlation caused by intensity interpolation. Opt. Eng. **39**(11), 2915–2921 (2000)
5. P. Lava, S. Cooreman, S. Coppieters, M. De Strycker, D. Debruyne, Assessment of measuring errors in DIC using deformation fields generated by plastic FEA. Opt. Lasers Eng. **47**(7–8), 747–753 (2009)
6. H.W. Schreier, M.A. Sutton, Systematic errors in digital image correlation due to undermatched subset shape functions. Exp. Mech. **42**(3), 303–310 (2002)

Chapter 3
IGMU: A Geometrically Consistent Framework for Identification from Full Field Measurement

J.-E. Dufour, J. Schneider, F. Hild, and S. Roux

Abstract DIC can be coupled with computational tools in order to characterize materials by using identification techniques such as finite element model updating or integrated approaches. In this study a framework using CAD-based stereo-DIC coupled with Isogeometric Analyses is followed to implement such identification procedures. Using both techniques allows us to be consistent with the designed geometry and its kinematics as the NURBS formalism is kept during the whole process and fewer degrees of freedom are needed (for the displacement field and the geometric representation of the surfaces) than in classical (finite element) approaches. This technique can be adapted to be written within an integrated framework (whose sensitivity fields are given by an isogeometric code).

Keywords CAD representation • DIC • Global approach • Identification • Stereo-correlation

3.1 Introduction

Identification from full-field measurement is widely used in the experimental mechanics field to calibrate material parameters. Techniques such as Finite Element Model Updating (FEMU) [1] or Integrated Digital Image Correlation (I-DIC) [2] can be used to extract these parameters from the coupling of numerical and experimental results.

The present work is dedicated to the development of an identification method coupling CAD-Based Stereo-DIC [3] and Isogeometric Analyses [4] in a framework similar to FEMU to identify material parameters. These techniques provide a geometrically consistent framework and a reduced kinematic basis as Non-Uniform Rational B-Splines (NURBS [5]) are used during the whole process. Such type of approach will also be extended into an integrated DIC framework.

The outline of the paper is as follows. First, a virtual experiment is created. Second, the principle of the so-called IsoGeometric Model Updating (IGMU) framework is introduced. Last, the concept of Integrated CAD-based Stereo-DIC is explained and the same experiment is used to show the feasibility of such an approach.

3.2 Virtual Experiment for Identification Porpuses

In order to test the developed identification procedure, a simple virtual case is designed. Using an isogeometric analysis code [6], a tensile test is simulated on a virtual beam sample (Fig. 3.1a). Pictures for the correlation analyses are then created (Fig. 3.1b) by projecting two faces of the beam onto 2D image planes using known projection matrices [7] and virtually applying a gray level pattern on the considered surfaces. In the present setting, four pictures are computed for each considered loading step of this virtual experiment.

J.-E. Dufour (✉)
LMT Cachan, ENS Cachan/CNRS UMR 8535/University Paris Saclay, 61 Avenue du Président Wilson, Cachan 94235, France

SAFRAN Snecma Villaroche, Rond-point René Ravaud, Réau 77550, France
e-mail: dufour@lmt.ens-cachan.fr

J. Schneider
SAFRAN Snecma Villaroche, Rond-point René Ravaud, Réau 77550, France

F. Hild • S. Roux
LMT Cachan, ENS Cachan/CNRS UMR 8535/University Paris Saclay, 61 Avenue du Président Wilson, Cachan 94235, France

S. Bossuyt et al. (eds.), *Residual Stress, Thermomechanics & Infrared Imaging, Hybrid Techniques and Inverse Problems, Volume 9*, Conference Proceedings of the Society for Experimental Mechanics Series, DOI 10.1007/978-3-319-21765-9_3

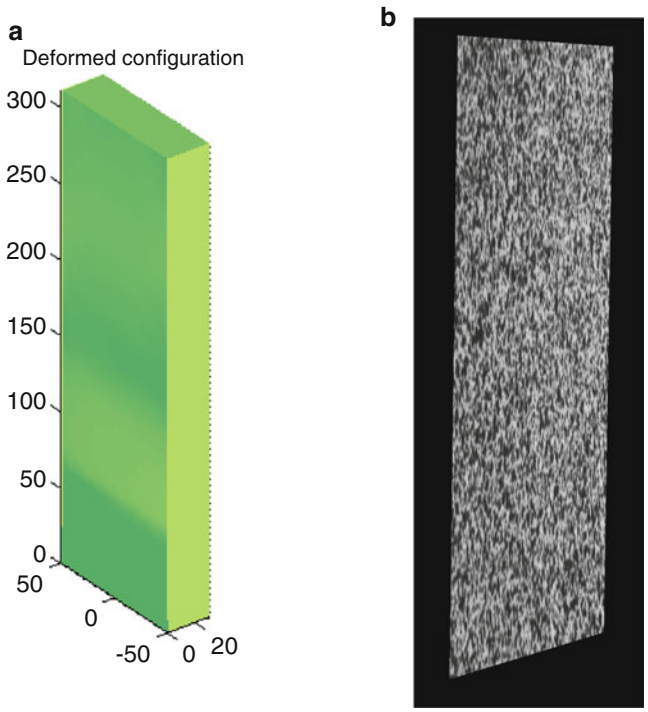

Fig. 3.1 Deformed model used in the simulation (**a**). Example of gray level image created from the deformed surface (**b**)

3.3 Iso-Geometric Model Updating (IGMU) Framework

An isogeometric model updating method is similar to FEMU in its principle, but uses Iso-Geometric Analyses (IGA) instead of finite element simulations (Fig. 3.2). The measured (Dirichlet) boundary conditions (computed via Stereo-DIC) are prescribed to the IGA model. As in FEMU, the simulations provide sensitivity fields (i.e., displacement field and load variations with respect to the chosen parameters) using finite differences, to be considered in a functional to be minimized via, for example, a Newton–Raphson algorithm.

Using this procedure on the virtual experiment, leads to identified values of Young's modulus and Poisson's ratio. Figure 3.3a illustrates the change of Young's modulus during the iterations of the identification procedure. The residual error at convergence is 3.5 % of the reference value.

The change of Poisson's ratio is shown in Fig. 3.3b. The error between the prescribed value and the identified parameter is 3.3 %. In both cases, acceptable error levels are reached.

The root mean square error between the simulated and measured displacement fields is shown in Fig. 3.4. At convergence, the level (44 μm) is very small, thereby validating the proposed framework.

3.4 Integrated CAD-based Stereo-DIC

An integrated approach can be derived from the IGMU framework. In such formalism, the kinematic basis used during the correlation process is replaced by the sensitivity fields with respect to the chosen parameters [8]. Thus the generalized degrees of freedom become the material parameters themselves. The principle of integrated CAD-based Stereo-DIC is illustrated in Fig. 3.5. In this approach, the kinematic basis is supplied as the sensitivity fields computed from the IGA code.

The virtual experiment is analyzed again using this integrated approach and Fig. 3.6 shows the change of the Poisson's ratio during iterations of the integrated code. The residual error in this case is 0.1 % of the reference value, which is significantly lower than that observed with the IGMU approach.

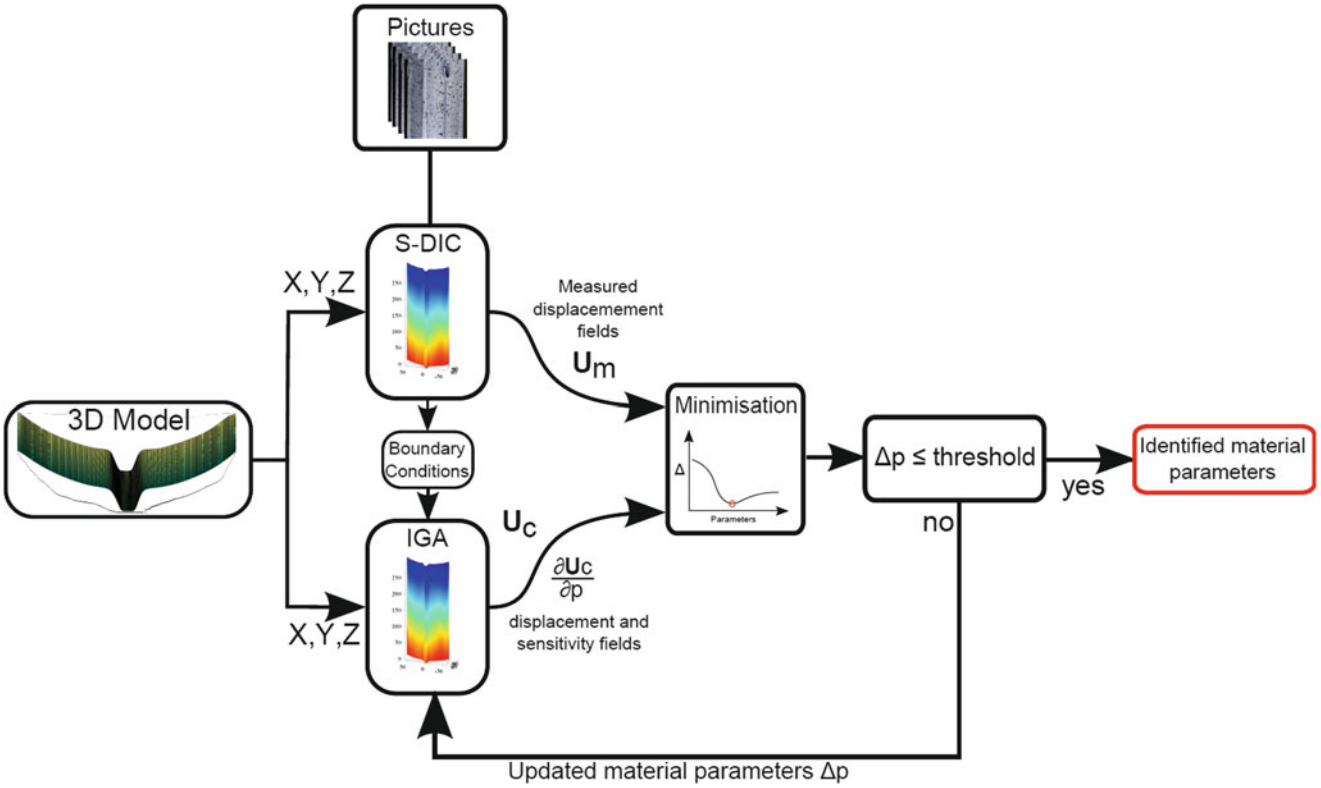

Fig. 3.2 Principle of the identification procedure using IGMU

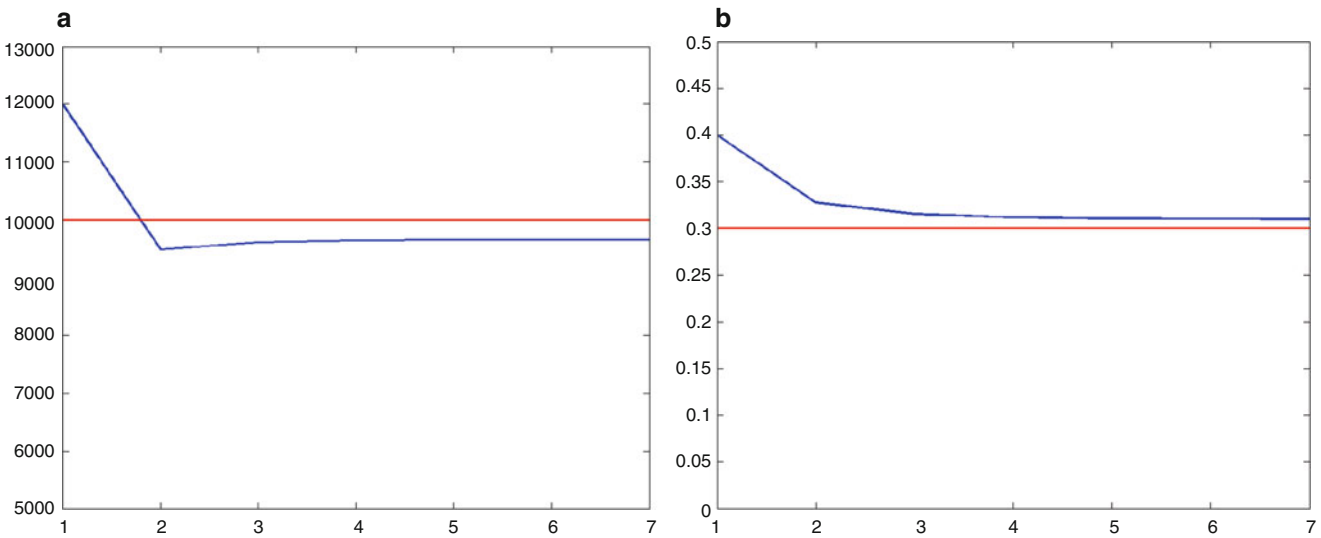

Fig. 3.3 (**a**) Change of Young's modulus at each iteration (*blue*) compared to the prescribed level (*red*) using IGMU; (**b**) Change of Poisson's ratio at each iteration (*blue*) compared to the prescribed level (*red*) using IGMU

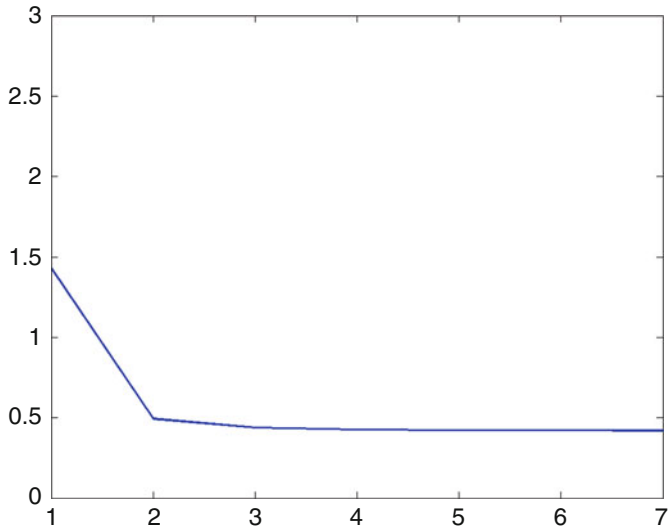

Fig. 3.4 Value of the root mean square (RMS) error expressed in mm between the measured and simulated displacement fields as a function of the iteration number

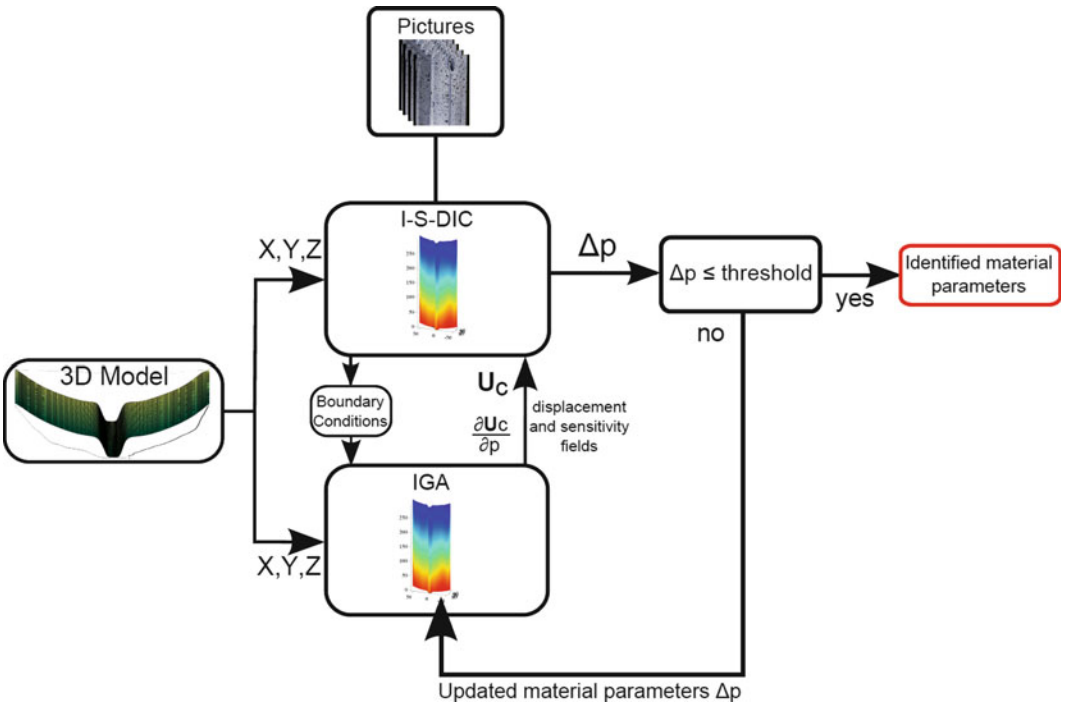

Fig. 3.5 Principle of integrated CAD-based stereo-DIC

3.5 Conclusions

A geometrically consistent framework has been developed in which the identification is carried out by comparing experimental and simulated displacement fields. As the present technique is using NURBS as generalized shape functions for the geometric representation and displacement discretization, the number of degrees of freedom is decreased compared to classical approaches (such as standard finite element methods). It is possible to build an integrated approach using the same type of formalism, which improves very significantly the performance of the method when applied to a virtual experiment.

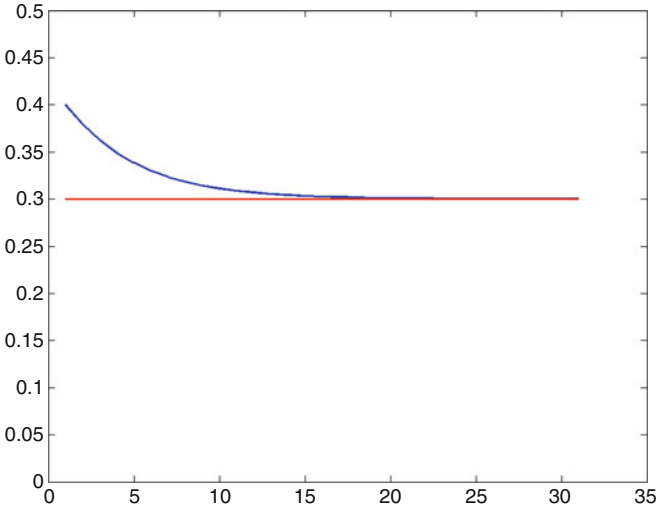

Fig. 3.6 Change of Poisson's ratio at each iteration (*blue*) compared to the prescribed level (*red*) with an integrated approach

Acknowledgements The authors would like to acknowledge Snecma for supporting this research. This work is part of the "PRC Composite" research project supported by DGAC, and involving the Safran group, the Onera, and the CNRS.

References

1. T. Kavanagh, R.W. Clough, Finite element applications in the characterization of elastic solids. Int. J. Solids Struct. **7**, 11–23 (1971)
2. S. Roux, F. Hild, Stress intensity factor measurements from digital image correlation: post-processing and integrated approaches. Int. J. Fract. **142**, 51–67 (2006)
3. J.A. Cottrell, T.J.R. Hughes, Y. Bazilevs, *Toward Integration of CAD and FEA. Isogeometric Analysis* (Wiley, Chichester, 2009)
4. B. Beaubier, J.-E. Dufour, F. Hild, S. Roux, S. Lavernhe, K. Lavernhe-Taillard, CAD-based calibration and shape measurement with stereoDIC: Principle and application on test and industrial parts. Exp. Mech. **54**(3), 329–341 (2014)
5. L.A. Piegl, W. Tiller, *The NURBS Book* (Springer, New York, 1995)
6. C. de Falco, A. Reali, R. Vázquez, GeoPDEs. A research tool for Isogeometric Analysis of PDEs. Adv. Eng. Softw. **42**(12), 1020–1034 (2011)
7. O. Faugeras, *Three-Dimensional Computer Vision: A Geometric Viewpoint* (MIT Press, Cambridge, 1993)
8. F. Mathieu, H. Leclerc, F. Hild, S. Roux, Estimation of Elastoplastic Parameters via Weighted FEMU and Integrated-DIC. Exp. Mech. **55**(1), 105–119 (2015)

Chapter 4
Characterization of the Dynamic Strain Hardening Behavior from Full-field Measurements

J.-H. Kim, M.-G. Lee, F. Barlat, and F. Pierron

Abstract The purpose of the present study is to provide a procedure for identifying dynamic strain hardening parameters using an inverse method to determine more accurate hardening properties at high strain rates for automotive crash analysis simulations. In order to validate the procedure, an approprate elasto-plastic constitutive model was chosen and simulated measurements were retrieved using a finite element (FE) analysis program. The same identification procedure as that which will be implemented in the experiments was applied. The virtual fields method (VFM) was used as an inverse analytical tool to identify the constitutive parameters. Because accurate measurement of the applied load is not easy at high strain rates due to the inertial effect, the identification was conducted using the acceleration fields without utilizing load information. The identified parameters using the VFM were compared with the reference ones, which were fed into the FE simulations. Very promising results were acquired using the VFM.

Keywords Full-field measurements • Virtual fields method • Plasticity • Dynamic hardening • Advanced high strength steel

4.1 Introduction

Crash analysis using finite element (FE) simulation is now indispensable in the automotive industry to assess automobile crashworthiness. In order to guarantee reliable simulation results, accurate material behaviors in the range of intermediate or high strain rates should be given into the FE simulation. However, the dynamic strain hardening behavior of materials at high strain rates is not readily achieved since precise measurement of load is difficult because of the inertial effect [1]. In this paper, the dynamic strain hardening behavior of thin steel sheet specimens is characterized using the virtual fields method (VFM) [2] without using the load information. Also, the VFM can retrive the plastic material parameters from the heterogeneous stress state, enabling to acquire the true stress–strain curve at large strains after the uniform elongation region. Generally, conventional measuring techniques and analytical formulas are only applicable up to the maximum uniform elongation point to obtain the true stress–strain relationship due to the assumption of uniform deformation. In this study, the methodology is introduced and a validation of the proposed identification procedure against simulated data is given.

4.2 Identification Procedure

In the experiments, high speed tensile tests on sheet metal specimens will be conducted and full-field displacement fields will be measured by a digital image correlation (DIC) technique [3] using a high-speed camera. In this study, virtual dynamic tensile tests were carried out using the FE software ABAQUS/Explicit.

J.-H. Kim (✉) • F. Barlat
GIFT, POSTECH, 77 Cheongam-Ro, Nam-Gu, Pohang, Gyeongbuk 790-784, South Korea
e-mail: jinkim@postech.ac.kr

M.-G. Lee
Department of Materials Science and Engineering, Korea University, 145, Anam-ro, Seongbuk-gu, Seoul 136-701, South Korea

F. Pierron
Faculty of Engineering and the Environment, University of Southampton, Highfield, Southampton SO17 1BJ, UK

S. Bossuyt et al. (eds.), *Residual Stress, Thermomechanics & Infrared Imaging, Hybrid Techniques and Inverse Problems, Volume 9*, Conference Proceedings of the Society for Experimental Mechanics Series, DOI 10.1007/978-3-319-21765-9_4

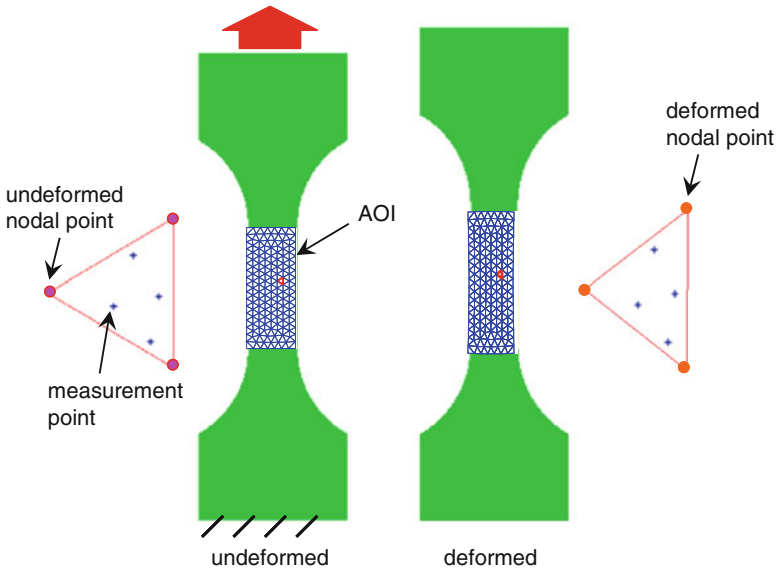

Fig. 4.1 Test configuration used in the FE simulation

4.2.1 Logarithmic (True) Strain

In order to simulate the measurement points from DIC, fine mesh size was employed first. Three nodes triangular shell elements were used. Reference (undeformed) and deformed coordinates of measurement points were recorded and the whole area of interest (AOI) was meshed using triangular elements as shown in Fig. 4.1.

The deformation gradient F for each triangle was calculated from the undeformed and deformed coordinates of measurement points using the analytical approach adopted in [4] and the theory of finite deformation [5]. A plane stress state and incompressibility ($\det(F) = 1$) in plasticity were assumed. Then the logarithmic strain tensor ε_{ln} was obtained from the deformation gradient F through the left stretch tensor V ($V^2 = F^{\mathrm{T}}F$) as in (4.1).

$$\varepsilon_{\ln} = \sum_{i=1}^{3} \ln(\lambda_i) r_i \otimes r_i \tag{4.1}$$

where λ_{i} and r_{i} are the eigenvalues and eigenvectors of the left stretch tensor V respectively.

4.2.2 Constitutive Model

Choosing a constitutive model which can describe the dynamic strain hardening behavior properly is important. In this study, von Mises yield criterion for isotropic material and Swift model for a rate independent hardening law were chosen as an initial study. The associated flow rule was assumed.
Swift model:

$$\sigma_s = K\left(\varepsilon_o + \varepsilon_p\right)^n \tag{4.2}$$

where σ_{s} is the current yield stress and ε_{p} the equivalent plastic strain. K, ε_0 and n are the material parameters to be identified.

4.2.3 The Virtual Fields Method

In this study, the virtual fields method (VFM) was used for an inverse method to retrieve the constitutive parameters from the measured deformation fields. The VFM makes use of the principle of virtual work which describes the condition of global equilibrium. The equilibrium equation in the case of elasto-plasticity for dynamic loading, and in absence of body forces, can be written as follows:

$$-\int_V \left[\int_0^t \dot{\sigma}_{ij} dt\right] \varepsilon^*_{ij} dV + \int_{S_f} T_i u^*_i dS = \int_V \rho a_i u^*_i dV \tag{4.3}$$

where $\dot{\sigma}$ is the stress rate which is a function of $\dot{\varepsilon}$ (actual strain rate), σ (actual stress) and unknown constitutive parameters, V the measurement volume, T the distribution of applied forces acting on S_f, ε^* the virtual strain field derived from u^* (the virtual displacement field), ρ the density and a the acceleration.

Material parameters can be determined from the acceleration fields by choosing proper virtual fields which can get rid of the external virtual work (EVW) term including the loads. For an elasto-plasticity problem, the identification is carried out using an iterative procedure [6] to minimize the quadratic gap between the internal virtual work (IVW) and the acceleration term (the right hand side of (4.3)). Since the constitutive parameters are unknown, initial guesses are required to initiate the iteration. Then, the stress components are recalculated until the equilibrium equation is satisfied by updating the parameters. Nelder-Mead algorithm was used for the minimization. In this study, simple virtual fields were applied to find the material parameters as in (4.4).

$$u^*_x = 0, \quad u^*_y = (y - y_{\min})(y - y_{\max}) \tag{4.4}$$

where y is the vertical coordinate of the measurement points in the current (deformed) configuration. The chosen virtual fields cancels out the EVW term. The parameters were determined in less than 5 min.

4.2.4 Speed and Acceleration

The speed fields can be obtained from the measured displacement fields using simpe finite difference.

$$v_i\left(t + \frac{\Delta t}{2}\right) = \frac{u_i(t + \Delta t) - u_i(t)}{\Delta t} \tag{4.5}$$

where i can be either x or y and t is time.

The acceleration fields can be computed from the displacement fields by double temporal differentiation as in (4.6). Due to the nature of the quantities, the speed is defined at time $t + \Delta t/2$ and the acceleration is at time t.

$$a_i(t) = \frac{u_i(t + \Delta t) + u_i(t - \Delta t) - 2u_i(t)}{\Delta t^2} \tag{4.6}$$

4.3 Results

4.3.1 FE Model

A specimen geometry was chosen as in Fig. 4.1. The dimensions of the specimen were 80 mm (height) × 30 mm (width) × 1 mm (thickness). The width for the AOI was 10 mm. In ABAQUS/Explicit, input parameters for Swift hardening law were; K: 1300 MPa, ε_0: 0.0024, n: 0.16. Those parameters were obtained from a static uniaxial tensile test on a dual phase (DP) 780 steel specimen. Dynamic tensile tests were simulated by constraining the lower edge and by applying vertical load at the upper edge. During the deformation, the deformed coordinates of each measurement point were saved at evenly spaced

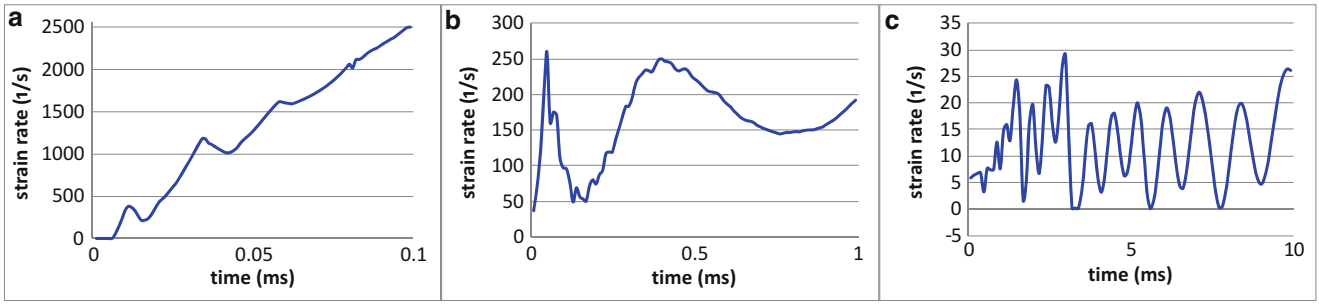

Fig. 4.2 Average strain rates in the loading direction (**a**) case A: high strain rate (**b**) case B: intermediate strain rate (**c**) case C: low strain rate

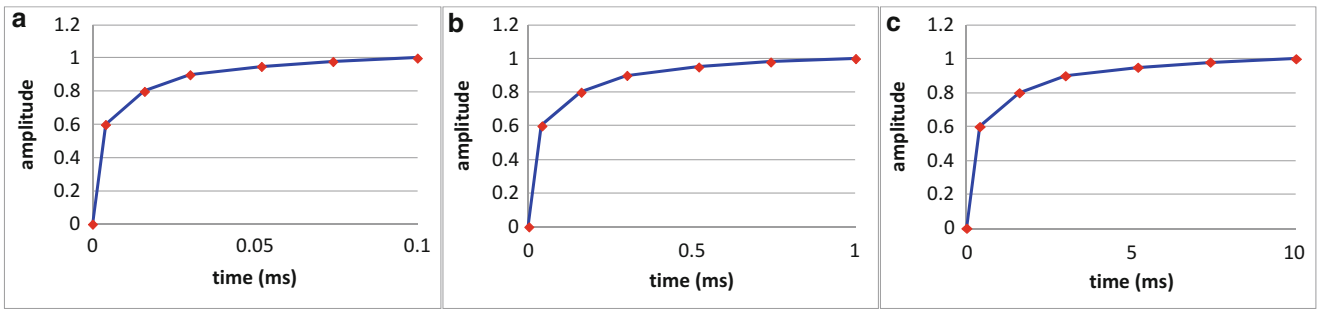

Fig. 4.3 Force amplitudes (**a**) case A: high strain rate (**b**) case B: intermediate strain rate (**c**) case C: low strain rate

time intervals (100 loading steps). Then, the logarithmic strain fields of the AOI were calculated using the procedure described in Sect. 4.2.1.

Three different strain rates were simulated in ABAQUS/Explicit as shown in Fig. 4.2. Case A is the high strain rate, case B the intermediate strain rate and case C the low strain rate. The time period was 0.0001 s (0.1 ms) for case A, 0.001 s (1 ms) for case B and 0.01 s (10 ms) for case C. The magnitude of applied load was adjusted to induce the maximum strain of around 20 % in the loading direction at the central area of the AOI for all the cases. The force amplitudes as a function of time are given in Fig. 4.3.

4.3.2 Effect of Strain Rates

The first condition investigated in this study was the effect of strain rates on the identification. Three different strain rates were considered as shown in Fig. 4.2. For a fair comparison, the identification was conducted for all the cases when the maximum ε_{yy} in the loading direction was around 20 % at the central area. The material parameters were extracted from the central AOI. As can be seen in Table 4.1, the parameters of Swift hardening law were correctly retrieved for the cases of high and intermediate strain rates, but the identification is unsatisfactory for the case of low strain rate. The relative error for ε_0 is relatively large. It is the most difficult term to identify accurately because the influence of ε_0 on the cost function is negligible [4].

In order to check the temporal variation of speed and acceleration, the averages of speed and acceleration fields in the loading direction are plotted in Figs. 4.4 and 4.5. The average acceleration is significantly low for case C compared to that of cases A and B. It is considered that the acceleration information is insufficient for the identification with the VFM for case C, low strain rate. In this case, the material parameters should be obtained using the external virtual work term including loads instead of the acceleration term in (4.3).

Table 4.1 Comparison between target and identified parameters (case A: high strain rate, case B: intermediate strain rate, case C: low strain rate, *R.E.* relative error)

	K	ε_0	n
Target	1300	0.0024	0.16
Identified (case A)	1305	0.00262	0.162
R.E. (case A)	−0.41 %	−9.33 %	−1.11 %
Identified (case B)	1299	0.00244	0.159
R.E. (case B)	0.11 %	−1.51 %	0.11 %
Identified (case C)	1111	0.00247	0.291
R.E. (case C)	14.5 %	−3.17 %	−81.6 %

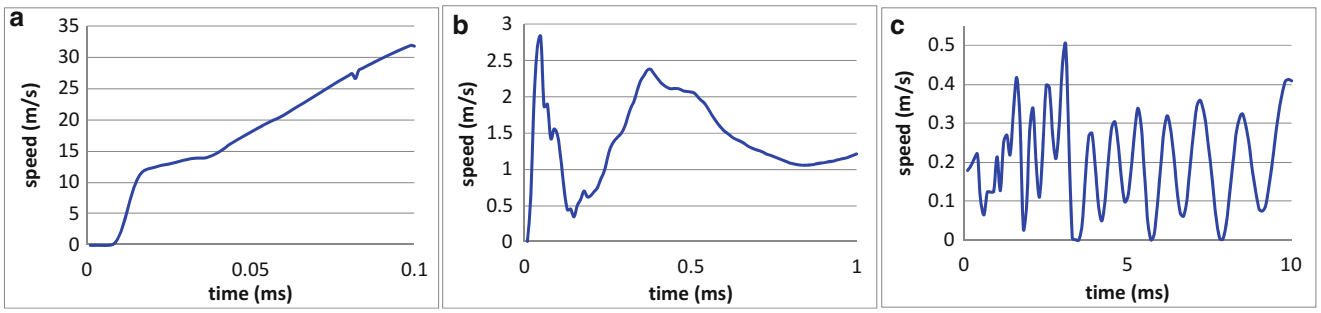

Fig. 4.4 Average speed in the loading direction (**a**) case A: high strain rate (**b**) case B: intermediate strain rate (**c**) case C: low strain rate

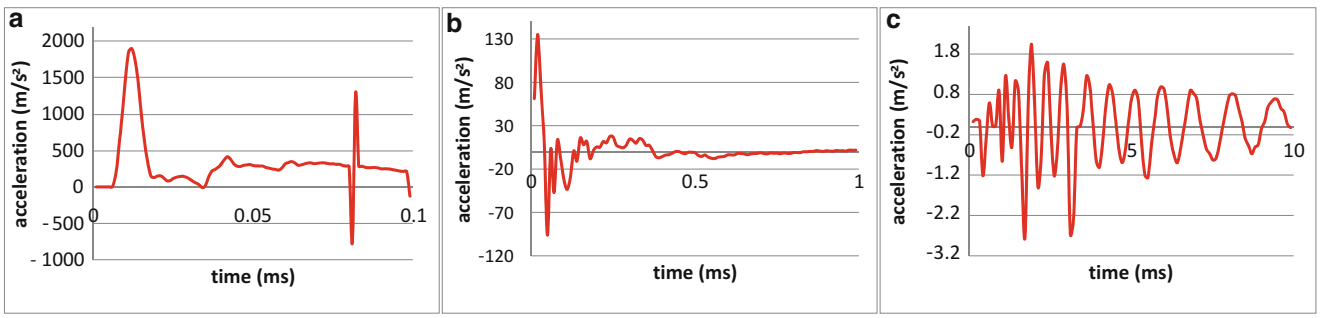

Fig. 4.5 Average acceleration in the loading direction (**a**) case A: high strain rate (**b**) case B: intermediate strain rate (**c**) case C: low strain rate

4.4 Conclusion

In this study, a new methodology has been applied to determine the dynamic true stress–strain curve of sheet metals using the virtual fields method (VFM) without measuring loads. In the FE simulation, parameters of the Swift hardening law were retrieved successfully from the acceleration fields by introducing appropriate virtual fields which can remove the virtual work term including the external loads. In the future, high speed tensile tests will be carried out on sheet metal specimens using a high-speed camera and the validation against experimental measurements will be performed. The identification results with the Swift model at various strain rates will be compared with those from the conventional identification procedure using a load-cell.

References

1. F. Pierron, M.A. Sutton, V. Tiwari, Ultra high speed DIC and virtual fields method analysis of a three point bending impact test on an aluminium bar. Exp. Mech. **51**(4), 537–563 (2011)
2. F. Pierron, M. Grédiac, *The Virtual Fields Method* (Springer, New York, 2012)
3. M.A. Sutton, J.J. Orteu, H. Schreier, *Image Correlation for Shape, Motion and Deformation Measurements: Basic Concepts, Theory and Applications* (Springer, New York, 2009)
4. J.H. Kim, A. Serpantié, F. Barlat, F. Pierron, M.G. Lee, Characterization of the post-necking strain hardening behavior using the virtual fields method. Int. J. Solids. Struct. **50**(24), 3829–3842 (2013)
5. F. Dunne, P. Nik, *Introduction to Computational Plasticity* (Oxford University Press, New York, 2005)
6. M. Grédiac, F. Pierron, Applying the virtual fields method to the identification of elasto-plastic constitutive parameters. Int. J. Plasticity **22**(4), 602–627 (2006)

Chapter 5
Bridging Kinematic Measurements and Crystal Plasticity Models in Austenitic Stainless Steels

A. Guery, F. Latourte, F. Hild, and S. Roux

Abstract A digital image correlation procedure is developed to perform kinematic measurements on the surface of 316LN austenitic steel polycrystals. A sequence of images is acquired using a Scanning Electron Microscope (SEM) during *in situ* tensile tests for various mean grain sizes. To enable digital image correlation, a speckle pattern adapted to the microscopic scale is deposited onto the specimen surface by microlithography. The knowledge of the microstructure at the surface allows for kinematic measurements to be performed using an unstructured finite element mesh consistent with the grain boundaries. The same mesh is then used for the simulation of each tensile test on the experimental microstructure with the measured nodal displacements prescribed as boundary conditions. A crystal plasticity law is considered to simulate the observed strain heterogeneities. An inverse identification method is proposed for the determination of the sought constitutive parameters based on both the local displacement fields and the material homogenized behavior. The parameters associated with isotropic hardening at the grain level are thus identified.

Keywords Austenitic steel • Crystal plasticity • Digital image correlation • Identification • SEM

5.1 Introduction

The mechanical behavior of austenitic stainless steel needs to be well known since this material is used in Pressurized Water Reactor (PWR) internals. In particular, to ensure the in-service strength of components, predictive constitutive models are established in micromechanical frameworks and are designed to account for material ageing due to irradiation [1]. Experimentally, the characteristic dimensions of the polycrystalline microstructure are well adapted to study crack initiation, transgranular fracture or cleavage often leading to the material failure. Thus, numerous crystal plasticity models have been developed to allow for accurate descriptions of intragranular plastic strains [2]. However the identification of their constitutive parameters remains challenging [3]. Full-field measurements can be performed at the microstructure scale by using a Scanning Electron Microscope (SEM) [4]. It provides spatially dense experimental information that is well suited for the validation of microstructural calculations and the identification of constitutive law parameters [5, 6]. In this paper, an inverse method for the identification of crystal plasticity parameters is presented, which is based on *both* the local displacement fields and the material homogenized behavior.

5.2 Kinematic Measurements Using Digital Image Correlation

Kinematic measurements are performed by Digital Image Correlation (DIC) on the surface of a polycrystal of 316LN austenitic steel. For that purpose, a sequence of SEM images has been acquired during *in situ* tensile tests, using an FEI Quanta FEG 600 SEM. DIC requires a gray level texture with a dynamic range as large as possible with local contrast

A. Guery (✉)
EDF R&D, Site des Renardières, Avenue des Renardières—Ecuelles, Moret-sur-Loing 77818, France

LMT-Cachan, ENS Cachan/CNRS, University Paris Saclay, 61 Avenue du Président Wilson, Cachan Cedex 94235, France
e-mail: adrien.guery@edf.fr

F. Latourte
EDF R&D, Site des Renardières, Avenue des Renardières—Ecuelles, Moret-sur-Loing 77818, France

F. Hild • S. Roux
LMT-Cachan, ENS Cachan/CNRS, University Paris Saclay, 61 Avenue du Président Wilson, Cachan Cedex 94235, France

S. Bossuyt et al. (eds.), *Residual Stress, Thermomechanics & Infrared Imaging, Hybrid Techniques and Inverse Problems, Volume 9*, Conference Proceedings of the Society for Experimental Mechanics Series, DOI 10.1007/978-3-319-21765-9_5

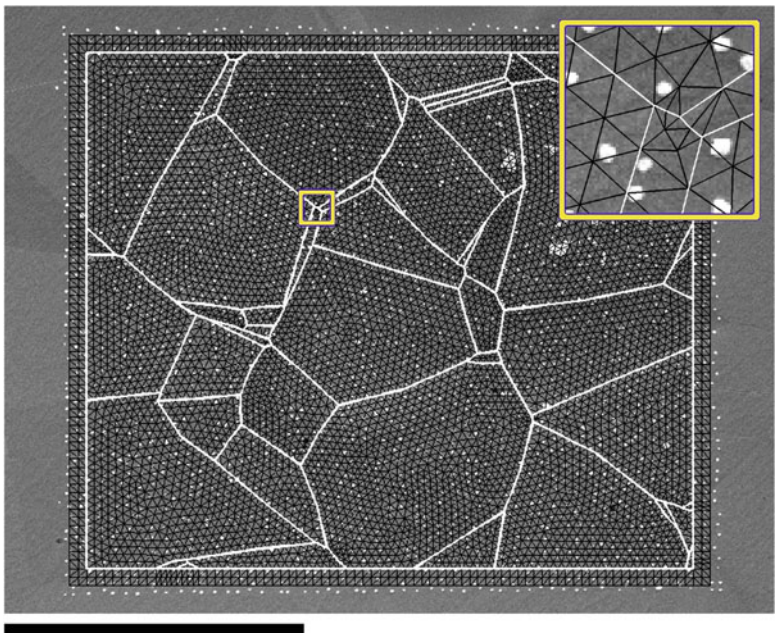

Fig. 5.1 Unstructured finite element mesh compatible with the underlying microstructure (shown as *white lines*) for DIC measurements. The scale bar is 100 µm

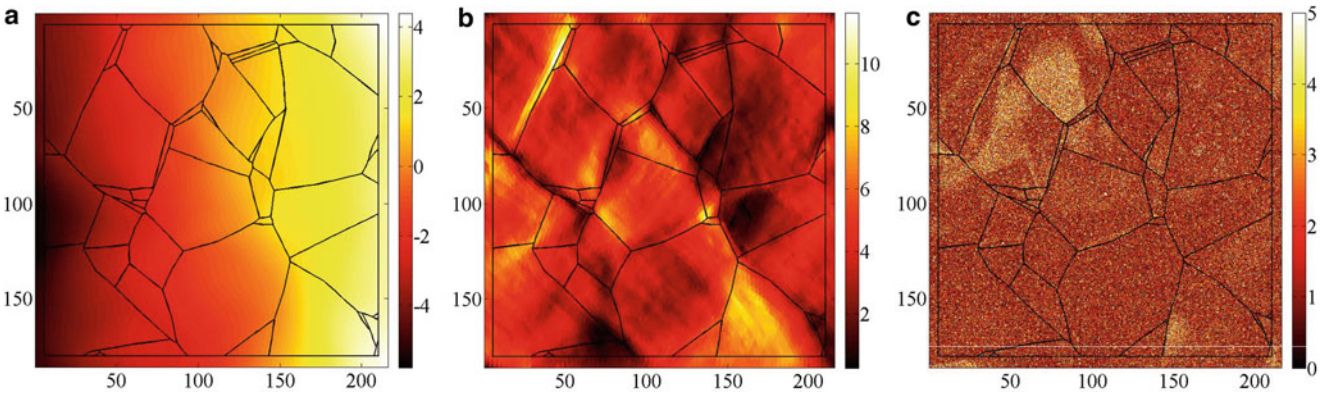

Fig. 5.2 Displacement field expressed in micrometers (**a**) and strain field in percents (**b**) along the horizontal loading direction measured by DIC for a macroscopic strain of 5 %. Corresponding correlation residuals expressed in percentage of the picture dynamic range (**c**). The axes are in micrometers. The microstructure boundaries are shown as black lines

variations. In the present case, because the natural texture of the material does not provide enough contrast, a computer-generated random pattern is deposited onto the surface by microlithography [7]. The displacement fields are measured between two consecutive images with a continuous finite element based DIC procedure [8, 9]. Thanks to a prior Electron Back-Scattered Diffraction (EBSD) acquisition providing grain boundaries and orientations, the displacement discretization is performed using an unstructured mesh taking as support the microstructure interfaces and overlaid on the first image of the sequence [10] as shown in Fig. 5.1. It is composed of 3-noded triangular elements whose characteristic length is about 20 pixels (or 3 µm). The Region Of Interest (ROI) covers a 200 µm side square surface that corresponds to 1500 pixels.

The noise of SEM imaging is relatively high, namely about 2 % of the dynamic range of the image. In addition, the mesh is fine, so that plastic strain localizations may be captured in details. For those reasons, DIC calculations are assisted with mechanics [9] with a regularization length four times greater than the characteristic length of the mesh. The adopted DIC technique leads to a displacement uncertainty, as a Root Mean Square (RMS) value, of 0.029 pixel (or 4.3 nm). Figure 5.2a shows the displacement field along the loading direction (horizontal) measured when the macroscopic strain is about 5 %. The corresponding strain field is shown in Fig. 5.2b. Strain localizations are successfully captured at some microstructure boundaries and inside some grains, whose local level reaches about 12 %, which is more than twice the macroscopic applied strain. The gray level residuals at this step of the loading are shown in Fig. 5.2c, proving the quality of the DIC measurement.

In this figure, one may observe areas with higher values of the residual field that correspond to a change of the gray level in some grains over time that is likely to be induced by electron channeling contrast [11].

5.3 Simulation Using a Crystal Plasticity Model

The simulation of the experimental tensile test is performed using the finite element software Code_Aster. The phenomenological crystal plasticity law proposed by Méric and Cailletaud [12] has been chosen in this study. It implies plastic flows (5.1 and 5.2), isotropic (5.3) and kinematic (5.4) hardening relationships expressed for each of the 12 octahedral slip systems s

$$\dot{\gamma}_s = \dot{p}_s \frac{\tau_s - c\alpha_s}{|\tau_s - c\alpha_s|} \tag{5.1}$$

$$\dot{p}_s = \left\langle \frac{|\tau_s - c\alpha_s| - r_s(p_s)}{k} \right\rangle_+^n \tag{5.2}$$

$$r_s = r_0 + q\left(\sum_{r=1}^{12} h_{sr}\left(1 - e^{-b\,p_r}\right)\right) \tag{5.3}$$

$$\dot{\alpha}_s = \dot{\gamma}_s - d\alpha_s \dot{p}_s \tag{5.4}$$

where c, k, n, r_0, q, b, d are constitutive parameters, and h_{sr} the coefficients of the interaction matrix between slip systems. The brackets $<.>_+$ denote the positive part of their argument. The three parameters associated with isotropic hardening are identified by homogenization using the model of Berveiller and Zaoui [13] and the experimental macroscopic stress–strain curve. The other parameters are set to previously identified values [14].

EBSD acquisitions do not provide a characterization of the microstructure in the bulk in a non-destructive way. As a consequence, a 2D modeling of the experimental aggregate is chosen in this study. The finite element calculation uses the same 2D mesh as that employed for the DIC measurements. This direct link between DIC and simulations allows the experimentally measured boundary conditions with their time evolution to be prescribed without interpolation or extrapolation. In addition, the assumption of plane stress condition is made, so that the 3D strain and stress tensors expected by the crystal plasticity law can be built.

Figure 5.3 shows the gap between the displacement fields along the loading direction for a macroscopic strain of about 5 %, when measured by DIC and simulated using the initial set of parameters. This difference is rather low with an RMS value of 0.3 µm when compared to the dynamic of the displacement field of 9.3 µm. However, when compared to the standard measurement uncertainty (4.3 nm), the modeling error appears significant. The gap between displacement fields is to be minimized at each time step in order to identify parameters of the crystal plasticity law.

5.4 Parameter Identification

A weighted Finite Element Model Updating (FEMU) procedure is proposed in this study in order to identify some parameters of the crystal plasticity law. It is based on the minimization of the combination of two least squares criteria. One is dealing with the displacement fields at the microstructural scale, denoted by χ_u, the other one with the load level at the macroscopic scale, denoted χ_F, such as the total cost function χ_T reads

$$\chi_T^2(\mathbf{p}) = (1 - w)\chi_u^2 + w\chi_F^2 \tag{5.5}$$

where w is a weight to be chosen between 0 and 1 [15], and

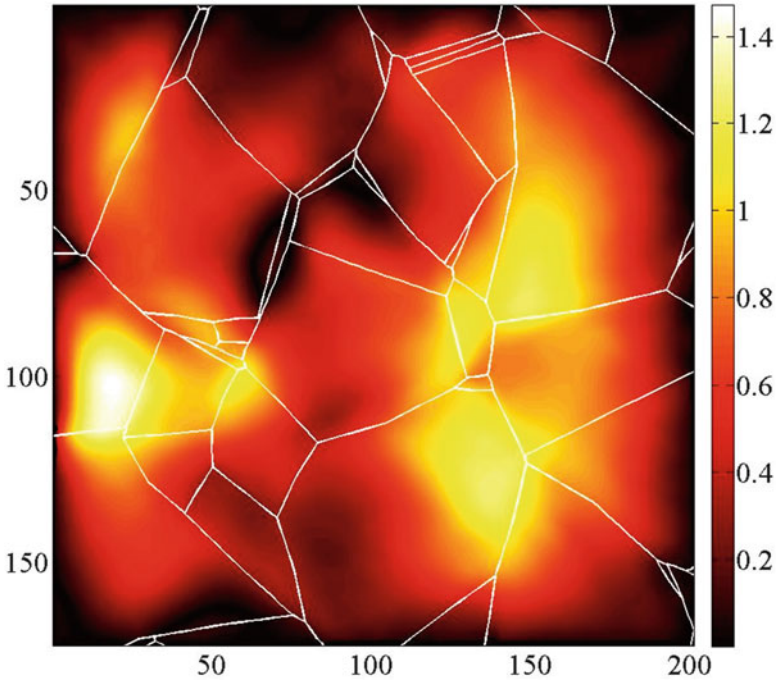

Fig. 5.3 Absolute value of the difference between measured and simulated displacement fields along the horizontal direction for a macroscopic strain of 5 %. The field and the axes are expressed in micrometers. The microstructure boundaries are shown as *white lines*

$$\chi_T^2(\mathbf{p}) = (1-w)\frac{1}{2\eta_f^2 N_{dof} N_t}\sum_t \{\mathbf{\Delta u_t}\}^T[\mathbf{M}]\{\mathbf{\Delta u_t}\} + w\frac{1}{\eta_F^2 N_t}\{\mathbf{\Delta F}\}^T\{\mathbf{\Delta F}\} \tag{5.6}$$

where $\mathbf{p}$ is the set of parameters to identify, $\{\mathbf{\Delta u_t}\}$ the column vector of the difference at each degree of freedom at the time step t between measured and simulated displacements, $\{\mathbf{\Delta F}\}$ the column vector of the difference at each time step between the experimental load and that obtained by homogenization with the current value of $\mathbf{p}$. N_{dof} and N_t are respectively the number of degrees of freedom of the mesh and the number of time steps. $[\mathbf{M}]$ is the DIC matrix introduced with the standard deviation of noise of SEM images η_f in order to weight the least squares criterion since these quantities are related to the covariance matrix $[\mathbf{C}]$ of the measured kinematic degrees of freedom [16]

$$[\mathbf{C}] = 2\eta_f^2[\mathbf{M}]^{-1} \tag{5.7}$$

Similarly, the standard deviation of the load resolution η_F is introduced to normalize χ_F. The minimization of χ_T with respect to the parameters is performed iteratively via a Gauss-Newton algorithm.

It is now applied to the identification of the parameters associated with the isotropic hardening of Méric-Cailletaud's law, focusing on the case of the experimental microstructure presented before. Figure 5.4a shows the identified values of the parameters r_0 and b according to the chosen value of the weight w. This range of values is bounded by the extrema obtained on the one hand by considering only the macroscopic load level (*i.e.*, for $w = 1$), on the other hand by considering only the macroscopic displacement fields (*i.e.*, for $w = 0$). One may notice that with an equal weight (i.e., $w = 0.5$), the identification procedure is essentially driven by the minimization of χ_F, which is equivalent to not considering displacement measurements. Therefore, a lower weight should be used in order to favor the decrease of the displacements gap more than the global equilibrium gap. However, it is observed in Fig. 5.4b that decreasing w increases the gap between the simulated homogenized behavior and experimental data. For this reason the cost function on the displacement fields needs to be combined with the one dealing with the load level in the identification procedure to keep a realistic prediction of the effective behavior. If the simulated stress–strain curves obtained with $w = 0.01$ or $w = 0.001$ do not appear realistic, the gap between the experimental curve and the simulated one with $w = 0.1$ remains subjectively acceptable. In terms of displacement fields, the decrease of χ_u is moderate, from 21.80 when $w =$ 1–20.95 when $w = 1$. It is worth noting that χ_u would reach unity if the model were perfect and only measurement uncertainty due to imaging noise were involved in the displacements gap.

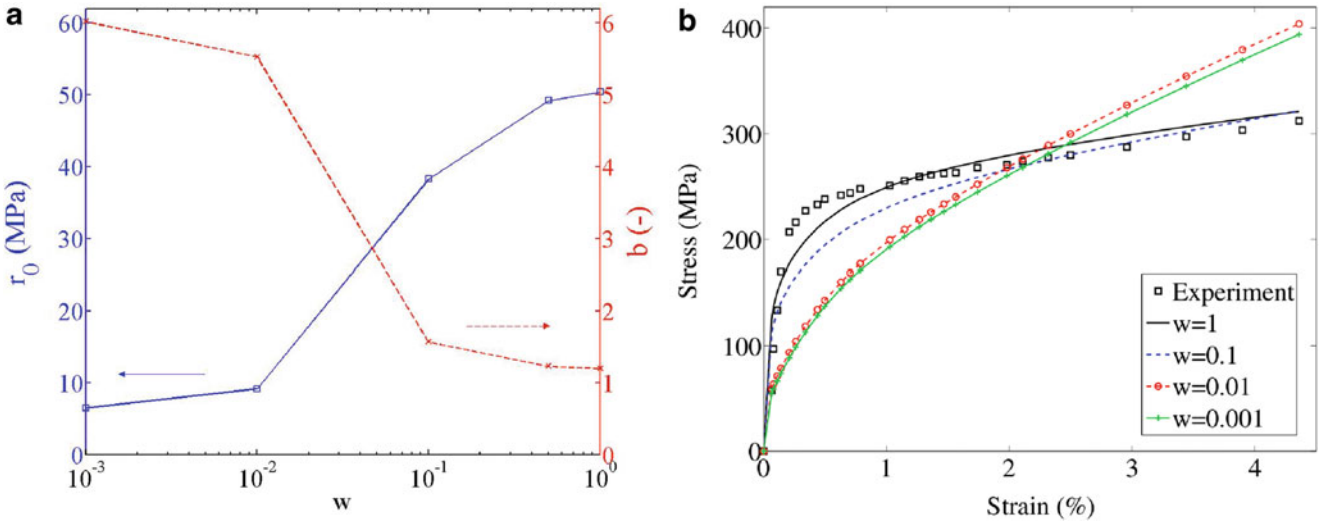

Fig. 5.4 Values of the identified parameters r_0 and b as functions of w (**a**). Stress–strain curves obtained by homogenization at convergence of the identification performed with different values of w, compared to the experimental curve (**b**)

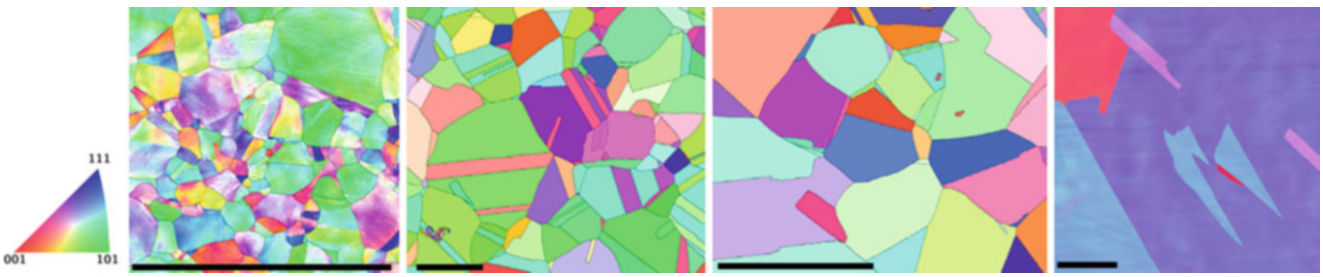

Fig. 5.5 EBSD inverse pole figures and grain boundary map of different microstructures over four ROI considered in this study. The scale bar is 100 µm

An assessment of the effect of the mean grain size on the identification of the parameters is now presented. Four experimental microstructures are considered, which are obtained by different rolling and heat treatments from the same 316LN plate. The microstructures over the ROI in which the DIC measurements are performed during *in situ* tensile tests are shown in Fig. 5.5. From left to right in this figure, the measured mean grain size is respectively 10 µm, 50 µm, 70 µm and millimetric.

From the identified values of r_0 when the identification procedure is performed as previously but for each microstructure, one may identify the Hall–Petch relationship at the slip system scale. Usually, this equation is derived at the macroscopic scale from the yield stress dependence on the mean grain size. Herein, a similar dependence is sought between the critical resolved shear stress r_0 and the mean grain size d such that

$$r_0 = c_1 + \frac{c_2}{\sqrt{d}} \tag{5.8}$$

where c_1 and c_2 are two constants. The result of the least squares fit is shown in Fig. 5.6 when $w = 1$ and $w = 0.1$. We can see that the choice $w = 0.1$ leads to a better fit of Hall-Petch's law with a correlation coefficient of 0.99 against 0.91 when $w = 1$. This improvement tends to validate the choice of $w = 0.1$ to optimize the simulated displacement fields.

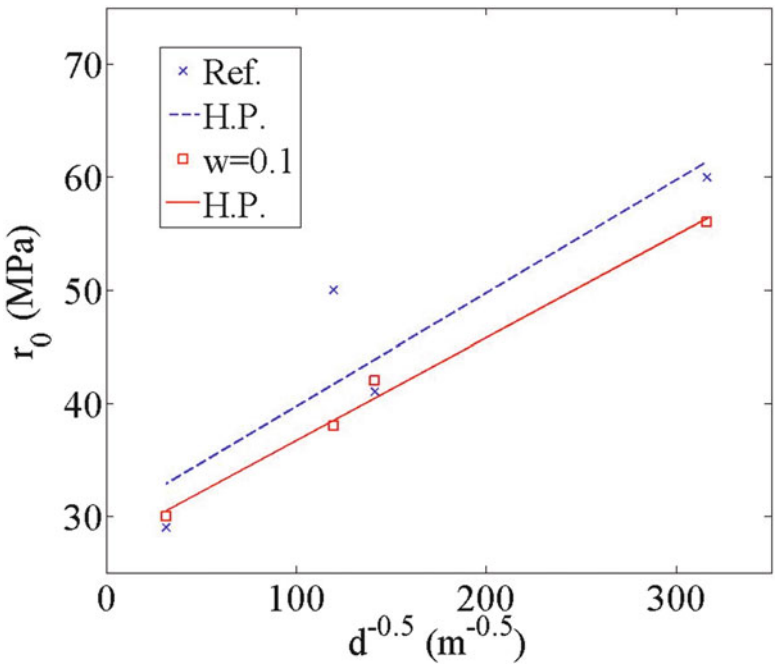

Fig. 5.6 Identification of the Hall–Petch (H.P.) law from the initial values of r_0 identified by homogenization ($w = 1$) and from those identified with $w = 0.1$

5.5 Conclusions

It was proposed in this study to bridge kinematic measurements in austenitic stainless steel polycrystals and crystal plasticity calculations. On the one hand, displacement fields have been measured on the surface of an *in situ* tested specimen via digital image correlation based on a finite-element mesh that is itself tailored to the specimen microstructure as observed via EBSD. On the other hand, finite element simulations of the same experiment have been performed using the same mesh and the crystal plasticity law proposed by Méric and Cailletaud. The comparison between measured and simulated fields has led to the inverse identification of parameters of the law. It consists of a weighted finite element model updating technique using both displacement fields and load levels. It has been applied to the identification of the parameters associated with isotropic hardening. It has been shown that the identified values depend of the relative weight given to the displacement fields or the load levels. A weighting has been selected and has led to a very good fit of a Hall–Petch trend at the slip system scale when four different microstructures are considered. Identification residuals remain high, which is an indication that the assumed model is not fully consistent with the experimental observation. As a consequence, other crystal plasticity laws may be tested. Moreover, experimental approaches for characterizing the true 3D microstructure, which was one key information missing in the present study, may be considered in the future.

References

1. S. Leclercq, D. Lidbury, S. Van Dyck, D. Moinereau, A. Alamo, M.A. Al, PERFORM 60—prediction of the effects of radiation for reactor pressure vessel and in-core materials using multi-scale modelling—60 years foreseen plant lifetime. J. Nuclear Mater. **406**(1), 193–203 (2010)
2. F. Roters, P. Eisenlohr, L. Hantcherli, D.D. Tjahjanto, T.R. Bieler, D. Raabe, Overview of constitutive laws, kinematics, homogenization and multiscale methods in crystal plasticity finite-element modeling: theroy, experiments, applications. Acta Materialia **58**, 1152–1211 (2010)
3. T. Hoc, J. Crépin, L. Gélébart, A. Zaoui, A procedure for identifying the plastic behavior of single crystals from the local response of polycrystals. Acta Materialia **51**(18), 5477–5488 (2003)
4. M.A. Sutton, N. Li, D.C. Joy, A.P. Reynolds, X. Li, Scanning electron microscopy for quantitative small and large deformation measurements part I: Sem imaging at magnifications from 200 to 10.000. Exp. Mech. **47**(6), 775–787 (2007)
5. E. Héripré, M. Dexet, J. Crépin, L. Gélébart, A. Roos, M. Bornert, D. Caldemaison, Coupling between experimental measurements and polycrystal finite element calculations for micromechanical study of metallic materials. Int. J. Plast. **23**(9), 1512–1539 (2007)
6. H. Lim, J.D. Carroll, C.C. Battaile, B.L. Boyce, C.R. Weinberger, Quantitative comparison between experimental measurements and CP-FEM predictions of plastic deformation in a tantalum oligocrystal. Int. J. Mech. Sci. **92**, 98–108 (2015)

7. A. Guery, F. Latourte, F. Hild, S. Roux, Characterization of SEM speckle pattern marking and imaging distortion by digital image correlation. Meas. Sci. Technol. **25**, 015401 (2014)
8. H. Leclerc, J.-N. Périé, S. Roux, F. Hild, Integrated digital image correlation for the identification of mechanical properties, *MIRAGE 2009*. LNCS **5496**, 161–171 (2009)
9. Z. Tomičević, F. Hild, S. Roux, Mechanics-aided digital image correlation. J. Strain Anal. Eng. Des. **48**, 330–343 (2013)
10. A. Guery, F. Hild, F. Latourte, S. Roux, Slip activities in FCC polycrystals determined by coupling DIC and crystal plasticity calculations. (2014)
11. S. Zaefferer, N.-N. Elhami, Theory and application of electron channelling contrast imaging under controlled diffraction conditions. Acta Materialia **75**, 20–50 (2014)
12. L. Méric, P. Poubanne, G. Cailletaud, Single crystal modeling for structural calculations: part 1—model presentation. J. Eng. Mater. Tech. **113**, 162–170 (1991)
13. M. Berveiller, A. Zaoui, An extension of the self-consistent scheme to plastically-flowing polycrystals. J. Mech. Phys. Solids **26**, 325–344 (1979)
14. Y. Guilhem, S. Basseville, F. Curtit, J.-M. Stéphan, G. Cailletaud, Investigation of the effect of gran clusters on fatigue crack initiation in polycrystals. Int. J. Fatigue **32**, 1748–1763 (2010)
15. F. Mathieu, H. Leclerc, F. Hild, S. Roux, Estimation of elastoplastic parameters via weighted FEMU and integrated-DIC. Exp. Mech. (2014). doi: 10.1007/s11340-014-9888-9
16. G. Besnard, F. Hild, S. Roux, "Finite-Element" displacement fields analysis from digital images: application to portevin-le chatelier bands. Exp. Mech. **46**(6), 789–803 (2006)

Chapter 6
Inverse Identification of Plastic Material Behavior Using Multi-Scale Virtual Experiments

D. Debruyne, S. Coppieters, Y. Wang, P. Eyckens, T. Kuwabara, A. Van Bael, and P. Van Houtte

Abstract Mixed numerical-experimental techniques used to identify plastic material properties of sheet metal are conventionally based on experimental data (e.g. full-field data) acquired during mechanical experiments. Although those techniques definitely enable to reduce the experimental effort for identifying plastic material properties, accurate identification of advanced phenomenological plasticity models still requires a significant amount of experimental effort. In this paper, we explore the opportunity to further reduce this experimental effort by replacing the mechanical experiments by virtual experiments using a physics-based multi-scale model. To this purpose, the Alamel polycrystal plasticity model, which solely requires the input of the initial crystallographic texture and a single tensile curve, is used to generate virtual plastic work contours in the first quadrant of stress space. The generated virtual experimental data is then used to inversely identify a phenomenological yield function. Finally, the predictive accuracy of the proposed method is investigated by using a finite element code to simulate the hydraulic bulge test.

Keywords Multi-scale virtual experiments • Anisotropic yield function • Differential work hardening • Bulge test • Sheet metal

6.1 Introduction

This paper deals with phenomenological material models which are widely adopted for numerical analysis and optimization of sheet metal forming operations. The industrial application of advanced phenomenological material models, however, highly depends on the experimental effort to calibrate the governing parameters. Conventionally, these experiments involve proportional loading of the test material with different true stress ratios (σ_x:σ_y). Accurate testing under a fixed stress ratio (σ_x:σ_y) over the large strain range requires the combination of different experiments. Cruciform specimens [1, 2] can be used for moderately small plastic strains. Larger strains can be probed using the tube expansion test [3]. The experimental effort required for constructing the plastic work contours consists of a number of stress-controlled material tests. Obviously, the accuracy of the identified plastic work contour increases with the number of stress ratios probed. Figure 6.1 shows an accurate measurement (nine stress ratios in the first quadrant of the stress space are probed) of stress points forming normalized contours of plastic work of mild steel sheet. The experimental effort associated with Fig. 6.1 consists of the following material tests: two tensile tests (σ_x:σ_y = 1:0; 0:1), seven biaxial tests using cruciform specimens ($\varepsilon_{eq}^{pl} \approx 0.05$ and σ_x:σ_y = 2:1; 1:1;3:4;4:3 and 1:2), seven tube expansion tests ($\varepsilon_{eq}^{pl} > 0.05$ and σ_x:σ_y = 2:1; 1:1;3:4;4:3 and 1:2) and one bulge test (σ_x:σ_y = 1:1). As such, 17 state-of-the-art material tests are required resulting in a quite extensive experimental campaign. Mixed numerical-experimental techniques [4] can be devised to reduce the experimental effort for identifying plastic material properties, however, accurate identification of advanced phenomenological plasticity models still requires a significant amount of experimental effort. In this paper, we explore the opportunity to reduce the experimental effort by replacing the mechanical experiments by virtual experiments using a physics-based multi-scale model. To this purpose, the Alamel polycrystal plasticity model [5], which solely requires the input of the initial crystallographic texture measurement and a single uniaxiale tensile test in one direction, is used to generate virtual plastic work contours in the first quadrant of

D. Debruyne (✉) • S. Coppieters • Y. Wang
Department of Materials Engineering, KU Leuven Technology Campus Ghent, Gebroeders de Smetstraat 1, Ghent 9000, Belgium
e-mail: dimitri.debruyne@kuleuven.be

P. Eyckens • A.V. Bael • P.V. Houtte
Department of Materials Engineering, KU Leuven, Kasteelpark Arenberg 44, Leuven 3001, Belgium

T. Kuwabara
Division of Advanced Mechanical Systems Engineering, Tokyo University of Agriculture and Technology, 2-24-16 Nakacho, Koganei-shi, Tokyo 184-8588, Japan

S. Bossuyt et al. (eds.), *Residual Stress, Thermomechanics & Infrared Imaging, Hybrid Techniques and Inverse Problems, Volume 9*, Conference Proceedings of the Society for Experimental Mechanics Series, DOI 10.1007/978-3-319-21765-9_6

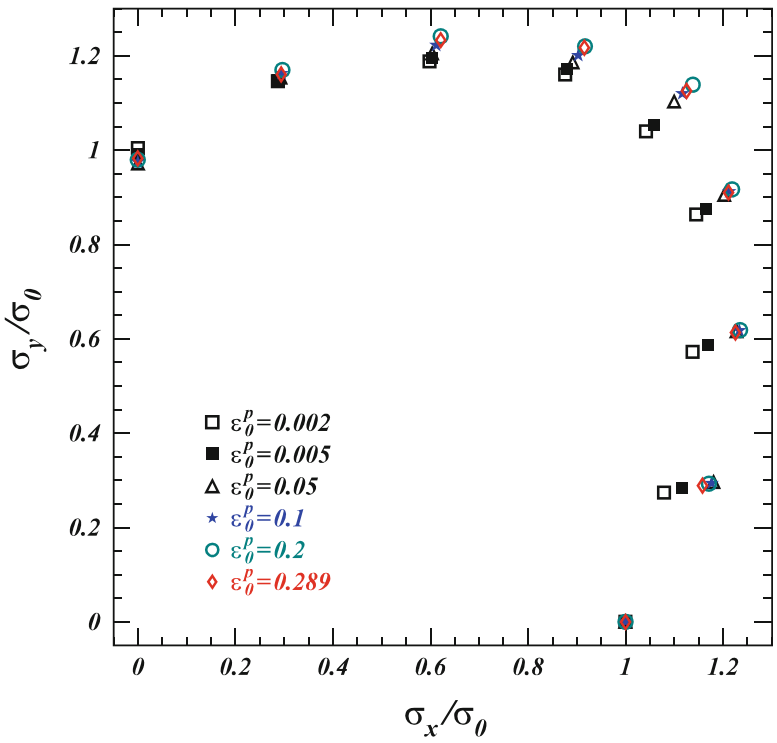

Fig. 6.1 Measured stress points forming normalized contours of plastic work [7]

stress space. Indeed, the multi-scale plasticity model can be efficiently employed to generate material response to monotonic loadings under different stress ratios. The model can be used to generate the virtual stress points which can be used to identify phenomenological yield functions. In this contribution, we scrutinize the quality of the contours of plastic work predicted by the multi-scale plasticity model. Additionally, the virtual work contours are used to calibrate the Yld2000-2d yield function [6]. Finally, the identified yield loci are implemented in a finite element code which is used to simulate the hydraulic bulge test.

6.2 Material

In the present study a cold rolled interstitial-free steel sheet with an initial sheet thickness of 0.65 mm is used. This material was characterized in advance using two types of biaxial tensile tests. The cruciform specimen proposed by Kuwabara et al. [1, 2] was used to measure the plastic material response in biaxial tension in the moderately small strain range, i.e. equivalent plastic strains up to 0.05. In order to probe larger plastic strains the Multi-axial Tube Expansion Test (MTET) [3] was used. It must be noted that for the stress ratio σ_x:σ_y = 1:1 (equibiaxial stress state) fracture occurred at the weld line of the tubular specimen. To cope with this, the work hardening behavior for strains larger than 0.13 was identified using the hydraulic bulge test. Figure 6.1 shows the normalized plastic work contours associated with different values of the reference true plastic strain $\varepsilon_0{}^{\mathrm{p}}$. It can be inferred from this figure that in the majority of the stress states the contours of plastic work expand with increase of $\varepsilon_0{}^{\mathrm{p}}$. Moreover, expansion of the work contours seems to be confined to the initial deformation up to $\varepsilon_0^{\mathrm{p}}$=0.2. The shape of the work contours remains almost constant for $0.2 < \varepsilon_0^{\mathrm{p}} < 0.289$. Standard tensile tests (JIS 13 type-B) were conducted to determine the work hardening properties in the rolling direction of the sheet. The Swift hardening law, which reads as:

$$\sigma_{eq} = K\left(\varepsilon_0 + \varepsilon_{eq}^{pl}\right)^n \tag{6.1}$$

was fitted to the available pre-necking data and the parameters can be found in Table 6.1. In all experiments the von Mises equivalent plastic strain rate was kept constant at approximately $5 \times 10^{-4} \frac{1}{s}$.

Table 6.1 Swift's hardening law fitted to the pre-necking data obtained through a tensile test in the rolling direction

Parameter	Value
K [MPa]	541
$\boldsymbol{\varepsilon}_0$	0.0036
n	0.249

Table 6.2 Calibrated parameters of the mirco-Swift's hardening law using the Alamel model

Parameter	Value
k [MPa]	541
$\boldsymbol{\Gamma}_0$	0.00859
n	0.243

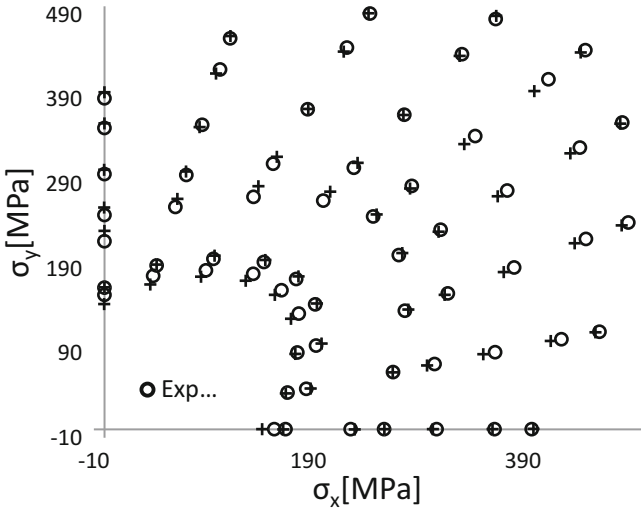

Fig. 6.2 Experimentally and virtually obtained plastic work contours for different values of $\boldsymbol{\varepsilon}_0^{pl}$=0.002; 0.03; 0.1 and $\boldsymbol{\varepsilon}_0^{pl}$=0.289

6.3 Virtual Material Tests

The Alamel polycrystal plasticity model [5] is used in this section to generate virtual plastic work contours in the first quadrant of stress space. Those calculations are based on a XRD texture measurement of the initial crystallographic texture of the test material. Additionally, the input of a single uniaxial tensile test in one direction is required to tune the micro-Swift hardening law within the multi-scale plasticity model:

$$\tau = k(\Gamma_0 + \Gamma)^n \tag{6.2}$$

where τ and Γ are the critical resolved shear stress of all slip systems and the accumulated slip in a grain, respectively. The parameters of the calibrated micro-Swift hardening law can be found in Table 6.2.

The Alamel model is then employed to generate material response to monotonic loadings under the same nine different stress ratios as shown in Fig. 6.1. As such, nine virtual experiments are conducted to generate the virtual stress points. Next, the latter data is used to construct the virtual contours of plastic work. To this purpose, the same approach is followed as used to construct the experimentally obtained work contours shown in Fig. 6.1. The true stress-true strain curve in the RD was used a reference datum for work hardening. This means that the curve was used to determine the virtual uniaxial true stress σ_0 and the virtual plastic work per unit volume W_0 corresponding to particular values of the reference plastic strain $\varepsilon_0{}^{pl}$. The uniaxial true stress σ_{90} and the biaxial true stress components $(\sigma_x : \sigma_y)$ obtained from the virtual experiments were then determined at the same plastic work W_0. Finally, the virtual stress points $(\sigma_0 : 0)$, $(0 : \sigma_{y90})$ and $(\sigma_x : \sigma_y)$ can be plotted in the principal stress space corresponding to a certain value of the reference plastic strain $\varepsilon_0{}^{pl}$. The experimentally obtained plastic work contours along with the virtually obtained plastic work contours at selected values of $\varepsilon_0{}^{pl}$ are shown in Fig. 6.2. In order to quantitatively compare the difference between the shapes of the virtual work contours and the experimentally measured work contours, the following error metric is used:

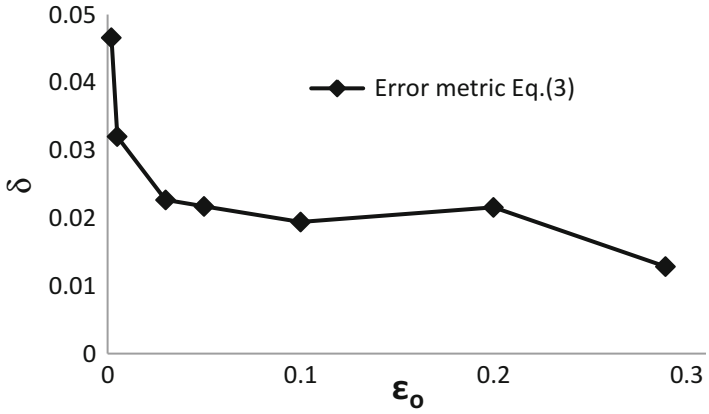

Fig. 6.3 Quantitative comparison of the shapes of the virtual work contours and the measured work contours

$$\delta = \sqrt{\frac{\left[\sum_{i=1}^{N}\left(\delta_{i,\ vir} - \delta_{i,\ exp}\right)^2\right]}{N-1}} \tag{6.3}$$

Where $\delta_{i,\ vir}$ and $\delta_{i,\ exp}$ are the distances between the origin of the principal stress space and the ith virtual stress point and experimental stress point, respectively. Figure 6.3 shows the error metric δ as a function of the reference plastic strain. It can be inferred from this figure that the error metric is larger at the initial deformation, i.e. the first 5 %. In other words, at larger plastic strains the shape of the virtual work contours is in closer agreement with the experimentally measured work contours. Although the Alamel model predicts sufficiently accurate stress levels (see Fig. 6.2), a weaker differential work hardening is predicted than experimentally observed, especially in the first 5 % plastic strain. Finally, it can be observed from Fig. 6.2 that the Swift law (6.1) cannot accurately reproduce the initial yield stress.

6.4 Finite Element Simulation

The plastic work contours from the previous section can be used to identify the parameters of advanced phenomenological yield functions. In this work the Yld2000-2d yield function [6] is adopted and the governing parameters are identified by stress state fitting at different reference plastic strains ε_0^{pl}. Figure 6.4 shows the virtual stress points along with the fitted Yld2000-2d yield function at different values of ε_0^{pl}.

The ultimate goal of this research is to limit the amount of experimental work associated with the identification of advanced phenomenological yield functions. Clearly, the presented approach can only be of interest if equivalent simulation qualities are achieved, i.e. compared to experimentally calibrated yield functions. To this purpose, the Yld2000-2d yield function was calibrated using experimental data and virtual data predicted by the texture-based Alamel model. Hydraulic bulge tests were performed to quantitatively evaluate the effect of the material models on the predictive accuracy of sheet metal forming simulations.

The test material was characterized up to an equivalent plastic strain of about 0.3. In order to avoid any extrapolation of the acquired material data, the hydraulic bulge test was limited to an equivalent plastic strain of 0.3 at the top of the dome. Potential differential work hardening was ignored and the yield loci were calibrated for a reference plastic strain of ε_0^{pl}=0.1. The latter value is more or less the average plastic deformation which can be expected at the top of the dome. The diameter of the die opening was 150 mm with a die radius of 8 mm. The blank diameter was 220 mm and material flow-in was prevented by a draw-bead with a diameter of 190 mm. The hydraulic pressure P was controlled so that the equivalent plastic strain rate was constant at $10^{-4}\frac{1}{s}$. The surface strain at the top of the dome was measured using MatchID-3D [8]. Abaqus/Standard was used to simulate the hydraulic bulge test. The FE model contained a blank with a diameter of 190 mm of which the nodal displacements along the edge were assumed to be zero to represent the draw bead. Quadrilateral four-node shell elements, S4R, were used. The blank holder force of 60 kN was ignored and a coulomb friction coefficient of 0.3 was assumed between the sheet and the blank holder.

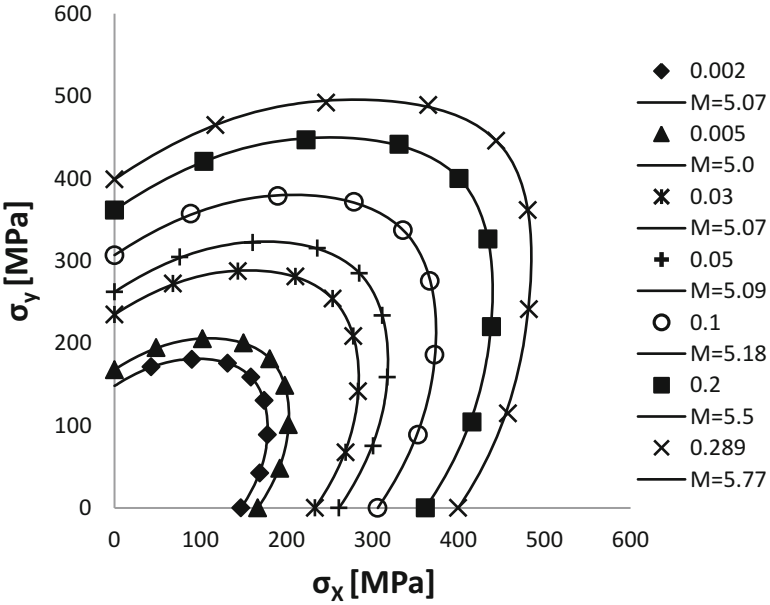

Fig. 6.4 Virtual contours of plastic work for different values of the reference plastic strain (ε_0^{pl}=0.002; 0.005; 0.03; 0.05; 0.1; 0.2; and 0.289). M is the exponent of the fitted Yld2000-2d yield function

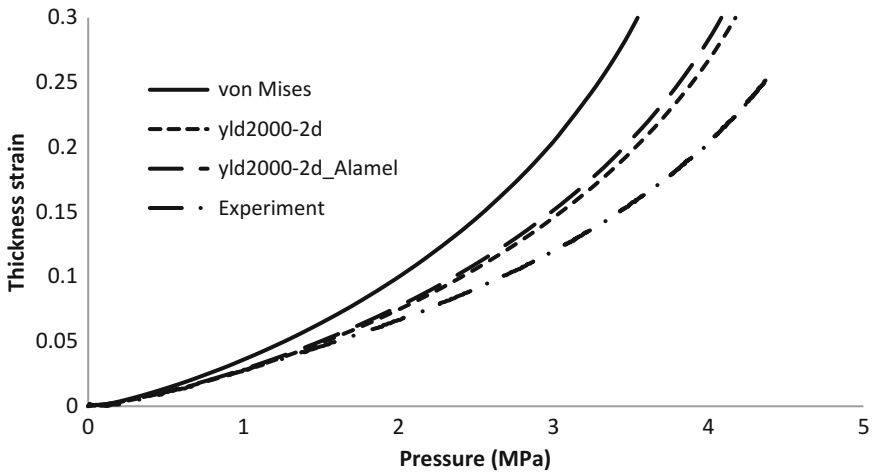

Fig. 6.5 Experimentally measured true thickness strain-pressure curve along simulation results

Figure 6.5 shows the experimentally measured true thickness strain-pressure curve along with the simulations. It can be observed that all simulations underestimate the maximum pressure. The Yld2000-2d yield function calibrated using experimental data (labeled as *yld2000-2d*) shows the closest agreement with the experiment. The difference, however, with the Yld2000-2d yield function calibrated using virtual plastic work contours (labeled as *yld2000-2d_Alamel*) is small. The latter suggests an equivalent predictive accuracy of both simulations. Figure 6.5 also shows the results obtained with the von Mises yield criterion. Although the results can be significantly improved by taking in-plane anisotropy into account, the simulations using anisotropic yield functions cannot perfectly reproduce the experimental observations. The result shown in Fig. 6.5 can be only slighty improved by taking differental work hardening into account [9].

6.5 Conclusions

In this paper, the opportunity to reduce the experimental effort to identify advanced phenomenological yield functions by replacing the mechanical experiments by virtual experiments using a physics-based multi-scale model is explored. The quality of the contours of plastic work predicted by the multi-scale plasticity model is scrutinized. The predicted virtual work

contours are used to calibrate the Yld2000-2d yield function. Hydraulic bulge tests and finite simulations were performed to quantitatively evaluate the predictive accuracy of the proposed method. It has been shown that an equivalent predictive accuracy can be achieved compared to a calibration based on experimentally aqcuired data.

References

1. T. Kuwabara, S. Ikeda, T. Kuroda, Measurement and analysis of differential work hardening in cold-rolled steel sheet under biaxial tension. J. Mater. Process Tech. **80–81**, 517–523 (1998)
2. Y. Hanabusa, H. Takizawa, T. Kuwabara, Numerical verification of a biaxial tensile test method using a cruciform specimen. J. Mater. Process Tech. **213**, 961–970 (2013)
3. T. Kuwabara, F. Sugawara, Multiaxial tube expansion test method for measurement of sheet metal deformation behavior under biaxial tension for large strain range. Int. J. Plast. **45**, 103–118 (2013)
4. S. Cooreman, D. Lecompte, H. Sol, J. Vantomme, D. Debruyne, Identification of mechanical material behavior through inverse modeling and DIC. Exp. Mech. **48**(4), 421–433 (2008)
5. P. Van Houtte, S. Li, M. Seefeldt, L. Delannay, Deformation texture prediction: from the Taylor model to the advanced Lamel model. Int. J. Plast. **21**, 589–624 (2005)
6. F. Barlat, J.C. Brem, J.W. Yoon, K. Chung, R.E. Dick, D.J. Lege, F. Pourboghrat, S.H. Choi, E. Chu, Plane stress yield function for aluminum alloy sheets: part 1—theory. Int. J. Plast. **19**, 1297–1319 (2003)
7. S. Coppieters, T. Kuwabara, Identification of post-necking hardening phenomena in ductile sheet metal. Exp. Mech. **54**(8), 1355–1371 (2014)
8. MatchID 3D, http://www.matchidmbc.be/
9. K. Ichikawa, T. Kuwabara, S. Coppieters, Forming simulation considering the differential work hardening behavior of a cold rolled interstitial-free steel sheet. Key Eng. Mater. **611–612**, 56–61 (2014)

Chapter 7
An Effective Experimental-Numerical Procedure for Damage Assessment of Ti6Al4V

L. Cortese, F. Nalli, G.B. Broggiato, and T. Coppola

Abstract A numerical model relying on triaxial and deviatoric levels of stress is used to describe ductile damage accumulation in the Ti6Al4V alloy. To this purpose, an experimental campaign is carried out on a reasonably limited set of tests: tensile tests on smooth and notched cylindrical bars, plane strain tensile tests on flat specimens, and torsion tests. For all of them, FEA analysis is used to get information about the states of stress and strain anywhere in the critical section. Moreover, the comparison between experimental evidence and numerical simulation provides the strain to fracture for each test. The geometries of the specimens are studied, to reduce the number of different tests needed for an effective tuning of the model. Outcomes of this optimization are detailed in the paper. Tuning of material constitutive law, and of damage model, is achieved by means of inverse techniques, starting from global load-deflection experimental data. The damage model is implemented in a commercial FEM code as user subroutine. Eventually, the accuracy of the elasto-plastic description and damage prediction of the adopted formulation is investigated.

Keywords Multiaxial tests • Inverse calibration • Ti6Al4V • Damage accumulation • Large strains

7.1 Introduction

In this paper a damage model based on the stress state triaxiality as well as on a deviatoric parameter related to the Lode angle is tuned on a Ti6A4V alloy. This goal has been achieved using a limited but effective number of multiaxial experimental tests, relying on simple geometries and conventional facilities. Sample shapes were previously optimized to sweep the entire domain of the damage governing parameters, and the same tests have been also used for the identification of the material constitutive behavior. Alongside the experimental campaign, numerical models reproducing all tests have been setup. In particular, stress–strain curves have been obtained up to large strain both from axisymmetric and torsion tests. For the former, an inverse procedure using FE analysis was needed, while for the latter a direct post-processing has been used. To avoid excessive complexity in the methodology, the *J2* isotropic plasticity model has been chosen to describe material elasto-plastic behavior, being available in all finite element codes. It must be pointed out that this formulation demonstrated to be not completely accurate for several classes of ductile materials whenever medium to large strains are involved [1–7]. Particularly, there is evidence of a Lode parameter influence on plasticity, which suggests the introduction of the *J3* invariant in the theoretical framework [8–10]. This has been also observed in this work. Improvements have been attempted in [11, 12].

Provided the constitutive law, again exploiting numerical simulation, the histories of triaxiality and deviatoric parameters with deformation have been collected for all tests, along with the value of the strain to fracture exhibited in the critical point of the specimen. This information allowed the calibration of a damage model whose formulation has been proposed in [13]. Moreover a custom subroutine calculating the damage has been implemented in the FEM code allowing the post-processing and visualization of all damage related quantities. A critical discussion of the results will be presented, showing how the

L. Cortese (✉)
Faculty of Science and Technology, Free University of Bozen, Piazza Università 5, Bolzano 39100, Italy
e-mail: luca.cortese@unibz.it

F. Nalli
Sapienza Università di Roma, Via Eudossiana, 18, Rome 00184, Italy

G.B. Broggiato
Mechanical and Aerospace Engineering Department, Sapienza Università di Roma, Via Eudossiana, 18, Rome 00184, Italy

T. Coppola
Centro Sviluppo Materiali S.p.A. (CSM), Via di Castel Romano, 100, Rome 00128, Italy

S. Bossuyt et al. (eds.), *Residual Stress, Thermomechanics & Infrared Imaging, Hybrid Techniques and Inverse Problems, Volume 9*, Conference Proceedings of the Society for Experimental Mechanics Series, DOI 10.1007/978-3-319-21765-9_7

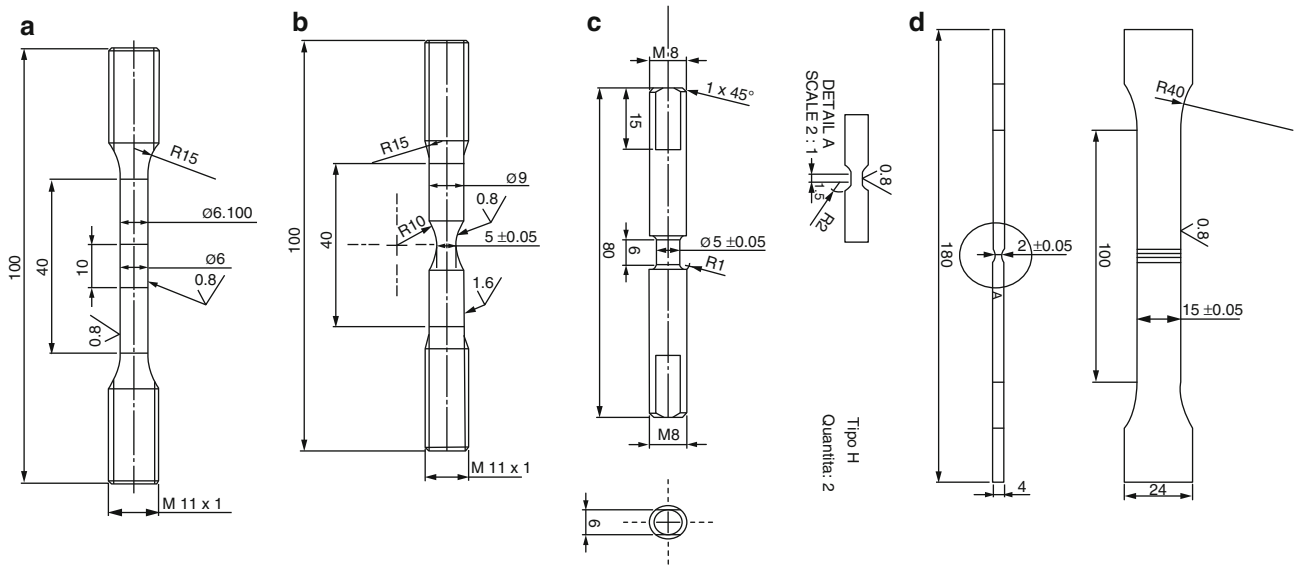

Fig. 7.1 Specimen geometries: (**a**) standard tensile test; (**b**) tensile test on round notch bar ($r = 10$ mm); (**c**) torsion test; (**d**) plane strain test

proposed method can lead to a successful tuning of numerical models to be used effectively in real industrial applications. In this regard the subroutine will eventually represent an easy damage evaluation tool for any end user, once the model is calibrated.

7.2 Experimental Campaign

A Ti6Al4V alloy has been investigated in the paper. Raw material was supplied in the form of a round cylindrical bar, with cross-section diameter of 30 mm. All specimens have been extracted along the bar longitudinal direction. Their dimensions have been chosen in order to match the testing machine range, at the same time attempting to exploit the available material to the utmost. Different kinds of tests, both uniaxial and multiaxial, have been executed. More in details: tensile tests on smooth round bars, tensile tests on notched cylindrical bars, with moderate notch radius ($r = 10$ mm), torsion tests on cylindrical specimens, and finally plane strain tensile tests on large flat specimens have been run. For all tensile tests a 250 kN servo-hydraulic MTS machine has been used; torsion tests, instead, have been performed on a dedicated tension-torsion equipment devised by some of the authors. Ti6Al4V stress–strain curve has been retrieved up to large strain, disjointedly using tensile and torsion tests. Damage model has been calibrated, on the other hand, using all four available tests. More details on these procedures are provided in the next section. Figure 7.1 reports specimen geometries and dimensions for all tests.

In particular, a novel geometry (Fig. 7.1, d) has been chosen to reproduce plane strain conditions: traditionally, to obtain this state of stress, large specimens with a transverse severe groove are adopted. In this work, to avoid unwanted stress concentrations the groove has been replaced by a constant rectangular large section with limited axial extension. Each test has been run under quasi-static loading conditions. For all tensile tests axial load and specimen gauge elongation have been acquired. From the strain measurement, the corresponding specimen elongation has been computed. The elongation is referred to an initial gauge length of 25 mm. Three repetitions for each test ensured the necessary confidence in the results, given the high qualitative standard of Ti6Al4V manufacturing process.

7.3 Numerical Models Formulation and Calibration Procedure

As stated in the introduction, the von Mises plasticity has been adopted. Concerning the damage model, widely described in [13, 14], it can be formulated as:

$$D = \int_0^{\varepsilon_f} \frac{f(T)}{G(X)^{\frac{1}{n}}} d\varepsilon_p \tag{7.1}$$

where:

$$f(T) = C_1 e^{C_2 T} \quad G(X) = \frac{\alpha_d}{\cos\left[\frac{\pi}{6}\beta - \frac{1}{3}\arccos(\gamma X)\right]} \tag{7.2}$$

T and X are the well known triaxiality and deviatoric parameters (the latter related to the Lode angle θ) which are defined as functions of the deviatoric stress invariants:

$$T = \frac{p}{\sqrt{J_2}} \quad X = \cos(3\theta) = \frac{3\sqrt{3}}{2}\frac{J_3}{J_2^{3/2}} \tag{7.3}$$

p being the hydrostatic pressure. Whenever D equals 1, fracture occurs. Damage driving parameters (7.3) are the same of the models proposed in [15, 16]. Material parameters C_1, C_2, β, γ must be tuned from experiments. In the model, n is the exponent of a power law able to fit the tensile stress strain curve. α_d is a constant which can be calculated from the others parameters. The form of the triaxiality function in (7.2) is widely described in many works in the literature. The deviatoric function G(X) comes from a specialization of what proposed in [17]. It can be proved that $X = 1$ in tests (a) and (b), and $X = 0$ in tests (c) and (d) (see again Fig. 7.1). The deviatoric parameters X and T can be averaged over the strain path, and regarded as constant along the tests with acceptable approximation. This is a reasonable postulate for the specific tests performed here; they have been actually devised in order to fulfill proportional loading conditions. Given that, (7.1) can be rewritten as a function of the strain to fracture ε_f:

$$\varepsilon_f = \frac{1}{C_1} e^{-C_2 T} \left(\frac{G(X,\beta,\gamma)}{G(X=1,\beta,\gamma)}\right)^{\frac{1}{n}} \tag{7.4}$$

To calibrate both the plasticity and damage models the following procedure has been followed. The stress strain curve has been identified up to large strain using an inverse method, by matching experimental and numerical global quantities relative to the tensile tests on smooth and notched geometries concurrently. This has been obtained using a dedicated C++ routine and MSC Marc 2005 R2 code. The analytical expression used for the fitting of the work hardening has an exponential form:

$$\sigma = \sigma_0 + A\left(1 - e^{-B\varepsilon}\right) + C\varepsilon \tag{7.5}$$

Where σ_0 represents the yield stress, and A, B, C are material parameters to be identified. Additionally, the stress–strain relation has been also built from torsion test data, using Nadai's expression [18] which relates torque and rotation to shear stresses and strains through:

$$\tau(\gamma_0) = \frac{1}{2\pi r_0^3}\left(\vartheta_N \frac{dM}{d\vartheta_N} + 3M\right) \quad \gamma_0 = \gamma(r_0), \quad \theta_N = \frac{d\theta}{dz} \tag{7.6}$$

where the quantities are referred to the outer specimen surface. The transformation from $\tau - \gamma$ to $\sigma - \varepsilon$ is made assuming again the J_2 plasticity hypothesis:

$$\sigma = \sqrt{3}\tau \quad \varepsilon = \frac{\gamma}{\sqrt{3}} \tag{7.7}$$

A comparison of the two curves is presented and critically discussed in the next section. The stress–strain curve from tension is used in the following for all tests but the torsion one. For plain strain the use of a curve from tensile test is justified, given that though the critical point has $X = 0$, the great part of the volume exhibits X values close to unity.

Regarding the damage model, first guess parameters C_1, C_2 in (7.4) have been tuned from tests a) and b) in Fig. 7.1, for which holds $X = 1$; finite element analysis is used to retrieve the average T, as well as ε_f at failure. Then, β, γ first guesses have been found using tests (c) and (d) for which $X = 0$. Again T, ε_f are retrieved exploiting numerical simulation. Finally all four parameters have been further varied together through a first order optimization algorithm to achieve the best fit.

7.4 Results and Discussion

Material constitutive relation, in the analytical form expressed by (7.5), has been identified successfully from asymmetrical tests. Best fit parameters are reported in Table 7.1.

The same relation has been obtained from torsion test using (7.6) and (7.7), and fitted again by an exponential expression. Both curves are reported in Fig. 7.2.

Different constitutive curves are justified, since dissimilarities in the elasto-plastic behavior are expected for tests at different lode parameter X. This non unicity could be addressed by a more sophisticated plasticity model [8].

Figures 7.3, 7.4, 7.5 and 7.6 show the outcome of the experimental campaign for the four kinds of tests performed, along with the prediction from numerical simulation using the constitutive law tuned as described above. Data from the three repetitions have been averaged for the sake of clarity. The matching is very good, suggesting that FE analysis can be regarded as reliable. This is crucial since from them local quantities at the critical points will be estimated for all test to calibrate the damage model.

Table 7.1 Best fit parameters for stress–strain curve from axisymmetric tests

σ_0 [MPa]	A [MPa]	B [−]	C [MPa]
930	130	50	300

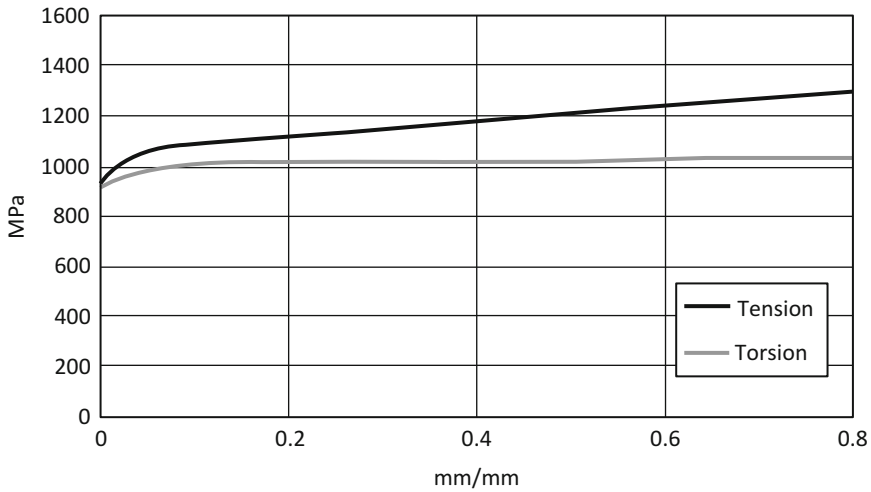

Fig. 7.2 Stress–strain curve for Ti6Al4V from tensile tests and torsion test

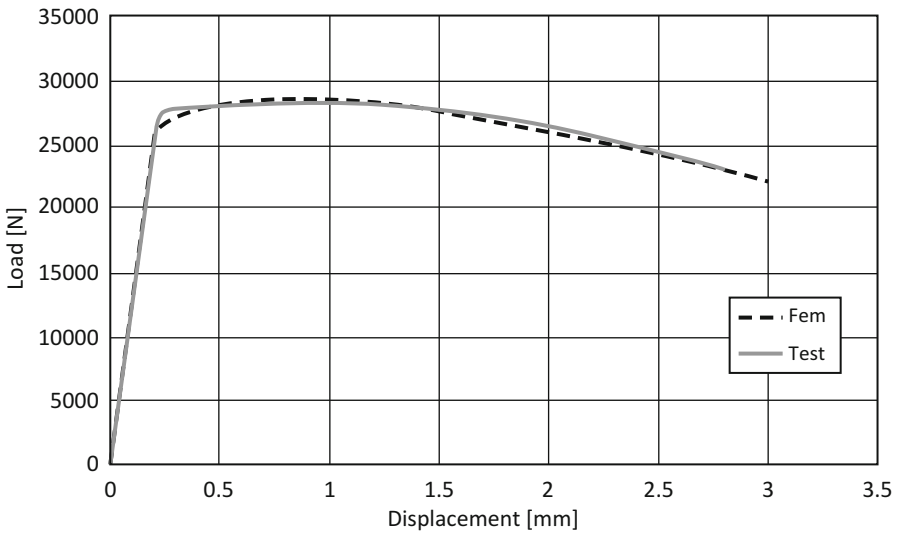

Fig. 7.3 Tensile test: load–displacement curve from experiment and numerical simulation

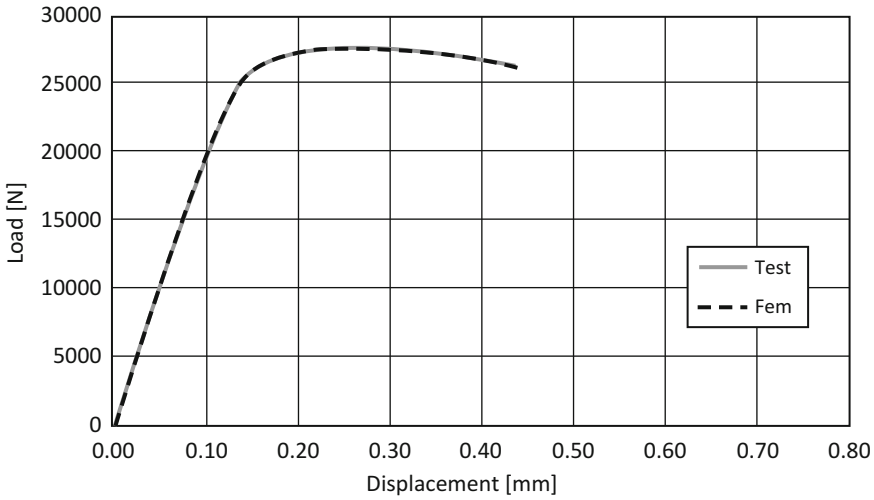

Fig. 7.4 Round notch bar test: load–displacement curve from experiment and FEA

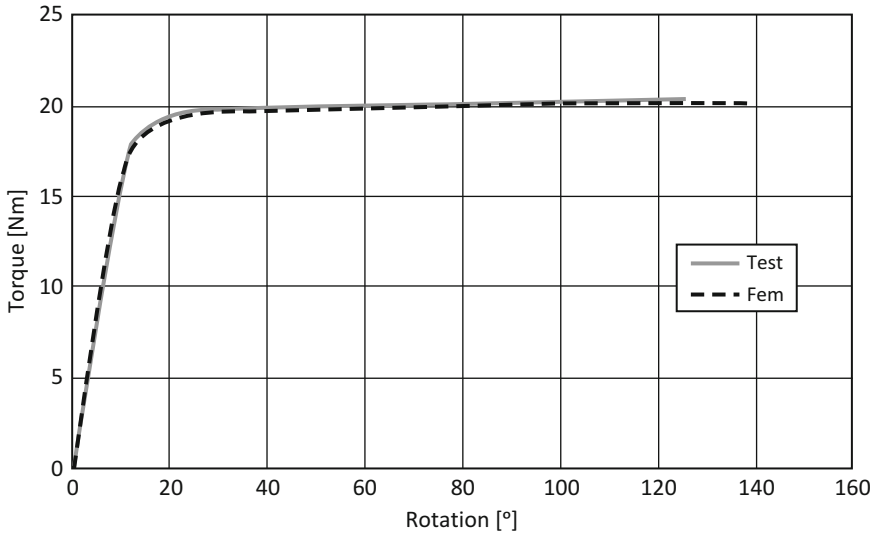

Fig. 7.5 Torsion test: torque-rotation curve from experiment and FEA

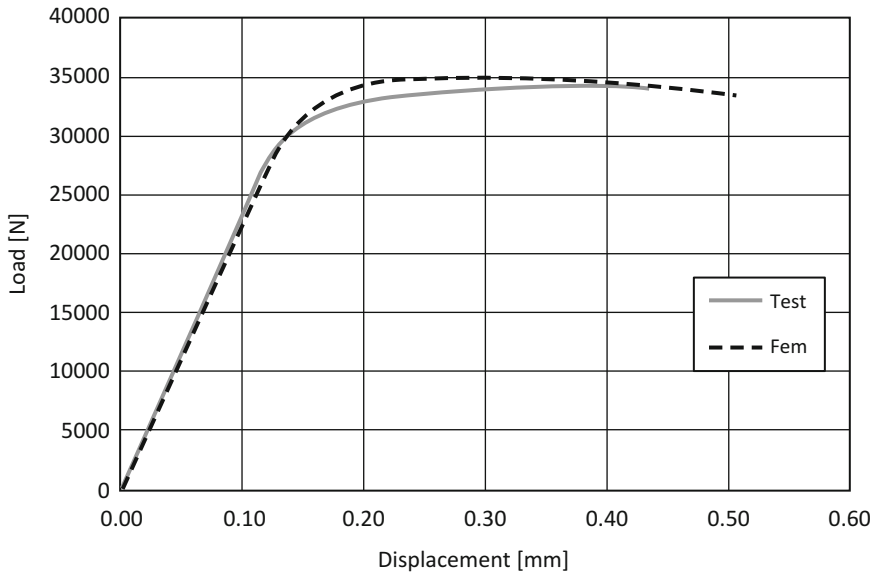

Fig. 7.6 Plane strain test: load–displacement curve from experiment and FEA

Table 7.2 Damage model calibration: best fit parameters based on four tests

C1	*C2*	β	γ	*n*
0.85	1.5	1.3	0.999	0.32

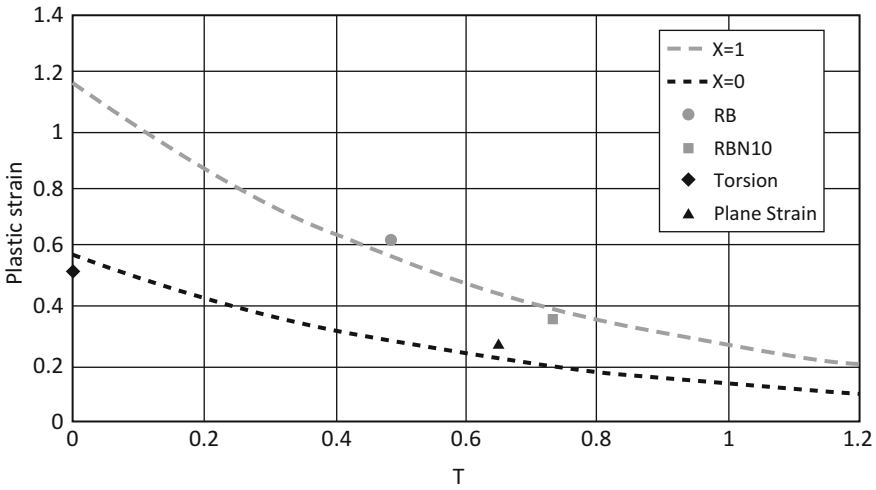

Fig. 7.7 Damage model calibration: upper ($X = 1$) and lower ($X = 0$) limiting bounds after calibration

Damage model calibration has been carried out through the procedure described in the previous section. Best fit parameters are summarized in Table 7.2. The adopted model, already successfully used for steel applications [10] demonstrated to be capable to capture fracture of Ti6A4V alloy with fairly good accuracy, also. This is testified in Fig. 7.7, where the model estimation is plotted against experimental data used for calibration. In the figure, sections of the fracture surface at $X = 1$ and $X = 0$ are shown, for a wide range of the triaxiality parameter T. It is worth noting that this has been obtained using only four tests, from simple geometries and equipment.

7.5 Conclusion and Further Development

With the proposed approach, the authors suggest that a fast calibration of damage models based on triaxiality and deviatoric parameters is possible, using only four proper tests, without the need for special equipment or complex sample geometries. Significant improvements in the methodology could come from a more accurate elasto-plastic prediction, as well as relying on a higher number of tests, for calibration. Further validation tests should also be run, to assess the transferability of the adopted model when used for failure prediction of Ti6Al4V components.

References

1. W. Lode, Versuche über den einfluß der mittleren hauptspannung auf das fließen der metalle eisen kupfer und nickel. Zeitschrift für Physik **36**(11–12), 913–939 (1926)
2. C.D. Wilson, A critical reexamination of classical metal plasticity. J. Appl. Mech. Trans. ASME **69**(1), 63–68 (2002)
3. L. Malcher, F.M. Andrade Pires, J.M.A. César de Sà, An assessment of isotropic constitutive models for ductile fracture under high and low stress triaxiality. Int. J. Plast. **30–31**, 81–115 (2012)
4. F. Yang, Q. Sun, W. Hu, Yield criterions of metal plasticity in different stress states. Acta Metallurgica Sinica **22**(2), 123–130 (2009)
5. X. Gao, T. Zhang, J. Zhou, S.M. Graham, M. Hayden, C. Roe, On stress-state dependent plasticity modeling: Significance of the hydrostatic stress, the third invariant of stress deviator and the non-associated flow rule. Int. J. Plast. **27**(2), 217–231 (2011)
6. X. Gao, T. Zhang, M. Hayden, C. Roe, Effects of the stress state on plasticity and ductile failure of an aluminum 5083 alloy. Int. J. Plast. **25**, 2366–2382 (2009)
7. W. Hu, Z.R. Wang, Multiple-factor dependence of the yielding behavior to isotropic ductile materials. Comput. Mater. Sci. **32**(1), 31–46 (2005)
8. W. Prager, Strain hardening under combined stresses. J. Appl. Phys. **16**(12), 837–840 (1945)

9. M.P. Miller, D.L. McDowell, Modeling large strain multiaxial effects in FCC polycrystals. Int. J. Plast. **12**(7), 875–902 (1992)
10. Y. Ohashi, M. Tokuda, Precise measurement of plastic behaviour of mild steel tubular specimens subjected to combined torsion and axial force. J. Mech. Phys. Solids **21**(4), 241–261 (1973)
11. T. Coppola, L. Cortese, F. Campanelli, Implementation of a Lode angle sensitive yield criterion for numerical modelling of ductile materials in the large strain range. ed. by E. Oñate, D.R.J. Owen, D. Peric, B. Suárez. XII International conference on computational plasticity. Fundamentals and applications. COMPLAS XII, Barcelona, 3–5 Sept 2013
12. L. Cortese, G.B. Broggiato, T. Coppola, F. Campanelli, An enhanced plasticity model for material characterization at large strain. Conf. Proc. Soc. Exp. Mech. Series **8**, 287–294 (2014)
13. T. Coppola, L. Cortese, P. Folgarait, The effect of stress invariants on ductile fracture limit in steels. Eng. Fract. Mech. **76**, 1288–1302 (2009)
14. L. Cortese, T. Coppola, F. Campanelli, F. Campana, M. Sasso, Prediction of ductile failure in materials for onshore and offshore pipeline applications. Int. J. Damage Mech. **23**, 104–123 (2014)
15. Y. Bai, T. Wierzbicki, A new model of metal plasticity and fracture with pressure and Lode dependence. Int. J. Plast. **24**(6), 1071–1096 (2008)
16. Y. Bai, T. Wierzbicki, Application of extended Mohr-Coulomb criterion to ductile fracture. Int. J. Fract. **161**, 1–20 (2010)
17. D. Bigoni, A. Piccolroaz, Yield criteria for quasibrittle and frictional materials. Int. J. Solids Struct. **41**, 2855–2878 (2004)
18. A. Nadai, *Theory of Flow and Fracture Solids*, vol. 2 (McGraw Hill, New York, 1963)

Chapter 8
Identification of the YLD2000-2D Model with the Virtual Fields Method

Marco Rossi, Frédéric Barlat, Fabrice Pierron, Marco Sasso, and Attilio Lattanzi

Abstract In this paper an inverse method, the virtual fields method (VFM), is used to identify the parameters of an anisotropic plasticity model, the Yld2000-2D yielding criterion. Digital image correlation (DIC) is used to measure the strain field over the specimen surface. In particular, the developed experiments are intended to investigate a region of the yielding surface close to the plane strain condition. As first step, the YLD2000-2D yielding criterion is implemented in the VFM framework for large strain plasticity. Afterwards, experiments are performed on steel sheet coupons and the proposed method is used to identify the constitutive parameters. The specimens are designed in order to guarantee a good compromise between the aspect ratio and the spatial resolution of the DIC measurement. In order to look at the anisotropic behaviour, the specimens are cut in different orientations with respect to the rolling direction. The results achieved with the VFM using Yld2000-2D are compared with the identification performed using the Hill48 model. The identified results are also compared with reference values obtained from standard tensile tests.

Keywords Anisotropic plasticity • Virtual fields method • Inverse identification • Digital image correlation • Large strains

8.1 Introduction

Sheet metals under plastic deformation often exhibit an anisotropic behaviour. This is due to the texture of the metal that has preferential orientations because of the rolling process. Anisotropy plays an important role in metal forming and other industrial applications. Nowadays, being able to correctly simulate the behaviour of sheet metals by FE models is fundamental for the industry. For this reason, during the years, several constitutive models have been developed to describe the plastic behaviour in case of anisotropy. One of the first, and still widely used model, is Hill48 [1], which is a simple modification of the standard von Mises plasticity. However, this model is rather basic and, often, is not able reproducing the behaviour of actual materials. A more flexible and adaptable model is the Yld2000-2D model [2, 3], which overtakes the main limitations of Hill48.

This model requires the identification of a set of constitutive parameters. The correct identification of such parameters is fundamental to predict the behaviour of the material successfully. Usually, the identification is performed using standard laboratory tests (i.e. uniaxial tension), however in the last years the use of inverse methods and full-field measurement is opening new possibilities [4].

A first approach is to employ finite element model updating (FEMU), as described in [5]. Other examples of methods that use full-field measurements can be found in [6–8]. In the present paper, the virtual fields method (VFM) [9] is used to this purpose. The VFM has been already applied to plasticity, for instance in [10, 11]. Kim et al. [12] used the VFM to identify the post-necking behaviour. Furthermore, applications of VFM to anisotropic plasticity are in [13, 14].

In this paper, the Yld2000-2D is implemented in the framework of the non-linear VFM at large strain, then notched specimens are used to identify the constitutive parameters of a stainless steel sheet metal.

M. Rossi (✉) • M. Sasso • A. Lattanzi
Università Politecnica delle Marche, via brecce bianche, Ancona 60100, Italy
e-mail: m.rossi@univpm.it; m.sasso@univpm.it; a.lattanzi@pm.univpm.it

F. Barlat
Materials Mechanics Laboratory, GIFT-POSTECH, 77 Cheongam-ro, Nam-gu, Pohang, Gyeongbuk 790-784, Republic of Korea
e-mail: f.barlat@postech.ac.kr

F. Pierron
Faculty of Engineering and the Environment, University of Southampton, Southampton SO17 1BJ, UK
e-mail: f.pierron@soton.ac.uk

S. Bossuyt et al. (eds.), *Residual Stress, Thermomechanics & Infrared Imaging, Hybrid Techniques and Inverse Problems, Volume 9*, Conference Proceedings of the Society for Experimental Mechanics Series, DOI 10.1007/978-3-319-21765-9_8

8.2 Theory

The used identification method is the non-linear VFM for large strains. More details about the procedure are given in [13], where the theoretical framework is presented for a general three-dimensional case. Here, the procedure is applied to plane stress, using Yld2000-2D as constitutive model. According to VFM, the model's constitutive parameters are identified minimizing a cost function defined according to the principle of virtual work, written for large deformations [11]:

$$\Psi(\boldsymbol{\xi}) = \sum_{i=1}^{N_{vf}} \sum_{j=1}^{N_{step}} \left| \int_V \mathbf{T}_j^{1PK} : \delta \mathbf{F}_i^{\bullet} \, dv - \int_{\partial V} \left(\mathbf{T}_j^{1PK} \mathbf{n} \right) \cdot \delta \mathbf{v}_i \, dS \right| \tag{8.1}$$

$\mathbf{T}^{1PK}$ is the 1st Piola-Kirchhoff stress tensor, $\delta\mathbf{v}$ is a virtual displacement field defined by the user, $\delta\mathbf{F}^{\bullet}$ is the corresponding virtual displacement gradient tensor, V is the volume of the inspected solid, ∂V is the boundary surface and $\mathbf{n}$ the surface normal in the undeformed configuration. The principal of virtual work is represented by the equation within the absolute value. The first integral can be viewed as the virtual work of the internal forces and the second one as the virtual work of the external forces. In condition of equilibrium, this absolute value should be zero. The cost function is computed for each measurement step and defined virtual field, where N_{step} and N_{vf} are the total number of measurement steps and adopted virtual fields, respectively.

The stress field, in (8.1), is computed using the constitutive model, which, in turn, depends on a series of constitutive parameters. Let us denote the constitutive parameters in terms of a vector $\boldsymbol{\xi} = [\xi_1, \xi_{2,\ldots}, \xi_N]$. According to non-linear VFM, an optimization algorithm iteratively varies the vector ξ, in order to find out the set of parameters that minimize the cost function of (8.1). The obtained parameters are the ones that best satisfy the equilibrium equation, written in terms of the principle of virtual work.

In this work, we used three sets of virtual fields in the cost function:

$$\delta\mathbf{v}_1 = \begin{cases} \delta v_x = 0 \\ \delta v_y = y/L \end{cases} \quad \delta\mathbf{v}_3 = \begin{cases} \delta v_x = \dfrac{x}{W} \dfrac{(|y| - L)}{L} \\ \delta v_y = 0 \end{cases} \quad \delta\mathbf{v}_3 = \begin{cases} \delta v_x = \sin\left(\pi \dfrac{x}{W}\right) \cos\left(\pi \dfrac{x}{H}\right) \\ \delta v_y = \sin\left(\pi \dfrac{x}{W}\right) \cos\left(\pi \dfrac{x}{H}\right) \end{cases} \tag{8.2}$$

L is the semi-length of the inspected area and W is the semi-width of the middle section. The origin of the coordinate system is situated at the centre of the specimen. With this assumption, the virtual work of the external forces, for the first virtual field, becomes:

$$\int_{\partial V} \left(\mathbf{T}_j^{1PK} \mathbf{n} \right) \cdot \delta\mathbf{v}_1 \, dS = 2 f_j \tag{8.3}$$

where f_j is the force measured by the load cell at the time increment j. The virtual work of the external force, for the second and the third virtual fields of (8.2), is equal to zero.

The Yld2000-2D plane stress yield function is employed to describe the anisotropic behaviour of stainless steel sheet. Under the assumption of orthotropic material behaviour, which implies symmetry along the sheet rolling, transverse and normal directions, this function introduces anisotropic material characteristics through two linear transformations on the Cauchy's stress tensor, as reported below:

$$\begin{bmatrix} X'_{xx} \\ X'_{yy} \\ X'_{xy} \end{bmatrix} = \begin{bmatrix} L'_{11} & L'_{12} & 0 \\ L'_{21} & L'_{22} & 0 \\ 0 & 0 & L'_{66} \end{bmatrix} \begin{bmatrix} \sigma_{xx} \\ \sigma_{yy} \\ \sigma_{xy} \end{bmatrix} \tag{8.4}$$

$$\begin{bmatrix} X''_{xx} \\ X''_{yy} \\ X''_{xy} \end{bmatrix} = \begin{bmatrix} L''_{11} & L''_{12} & 0 \\ L''_{21} & L''_{22} & 0 \\ 0 & 0 & L''_{66} \end{bmatrix} \begin{bmatrix} \sigma_{xx} \\ \sigma_{yy} \\ \sigma_{xy} \end{bmatrix}, \tag{8.5}$$

where x and y subscripts indicate the rolling and transverse direction of the sheet, respectively, and the components of $\mathbf{L}'$ and $\mathbf{L}''$ matrices are represented as functions of 8 independent parameters α_j:

$$\begin{aligned} L'_{11} &= \frac{2\alpha_1}{3} & L''_{11} &= \frac{8\alpha_5 - 2\alpha_3 - 2\alpha_6 + 2\alpha_4}{9} \\ L'_{12} &= -\frac{\alpha_1}{3} & L''_{12} &= \frac{4\alpha_6 - 4\alpha_4 - 4\alpha_5 + \alpha_3}{9} \\ L'_{21} &= -\frac{\alpha_2}{3} & L''_{21} &= \frac{4\alpha_3 - 4\alpha_5 - 4\alpha_4 + \alpha_6}{9} \\ L'_{22} &= -\frac{2\alpha_2}{3} & L''_{22} &= \frac{8\alpha_4 - 2\alpha_6 - 2\alpha_3 + 2\alpha_5}{9} \\ L'_{66} &= \alpha_7 & L''_{66} &= \alpha_8 \end{aligned} \tag{8.6}$$

Hence, indicating with X'_i and X''_i (with $i = 1,2$) the principal values of linear transformations of Cauchy's stress tensor components, the yield function Yld2000-2D is defined as follows:

$$\Phi = \varphi' + \varphi'' = 2\overline{\sigma}^a \tag{8.7}$$

where $\overline{\sigma}$ is the equivalent stress, a represents a material coefficient depending on the crystal structure (six for BCC and eight for FCC reticulum), φ' and φ'' are functions defined as follow:

$$\varphi' = \left|X'_1 - X'_2\right|^a \tag{8.8}$$

$$\varphi'' = \left|2X''_2 + X''_1\right|^a + \left|2X''_1 + X''_2\right|^a \tag{8.9}$$

According to the associated flow rule, the direction of the plastic flow is normal to the yield surface at the yielding point, and can be expressed as:

$$\frac{\partial \overline{\sigma}}{\partial \sigma_k} = \left\{2a\overline{\sigma}^{(a-1)}\right\}^{-1} \frac{\partial \Phi}{\partial \sigma_k} \tag{8.10}$$

The steps to compute the gradient of (8.7) are given in [3]. The hardening law is described using the following equation (Swift's law):

$$\sigma_{eq} = K(p + \varepsilon_0)^N \tag{8.11}$$

The hardening curve is not very sensitive to parameter ε_0 [12], therefore its value was set equal to 0.01 in the following computation. Summarizing, using the hardening law of (8.11) and the Yld2000-2D criterion, there is a total of ten independent parameters that have to be identified, i.e. $\boldsymbol{\xi} = [K, N, \alpha_1, \alpha_2, \alpha_3, \alpha_4, \alpha_5, \alpha_6, \alpha_7, \alpha_8]$.

Following the steps described in [13], the strain field measured with a full-field optical technique is used to evaluate the stress field corresponding to a given set of constitutive parameters $\boldsymbol{\xi}$. This stress field, written in terms of the first Piola-Kirchhoff tensor, is then used in (8.1) for the non-linear VFM.

8.3 Experiments

The tests were conducted on three notched specimen cut in three different directions, namely 0°, 45° and 90° respect to the rolling one. Figure 8.1 illustrates the shape of the specimen as well as the experimental set-up. An INSTRON 880 tensile machine with hydraulic grips was used to perform the tests. The displacement field was measured by stereo-DIC [15] using a couple of CCD cameras, able to acquire 2048 × 2048 pixels with 10-bit dynamic range.

The DIC was performed using the commercial software Vic-3D, employing a correlation window of 27 pixels and a step of 5 pixels. A typical displacement map is shown in Fig. 8.2, the red line highlights the measurement zone used in the identification with VFM.

Figure 8.3 shows an example of strain maps obtained from the measurement. The strain field is heterogeneous with a strain concentration close to the notches. With the adopted DIC settings, each strain map has 201 × 101 points. For each specimen configuration, 48 time steps were used in the identification.

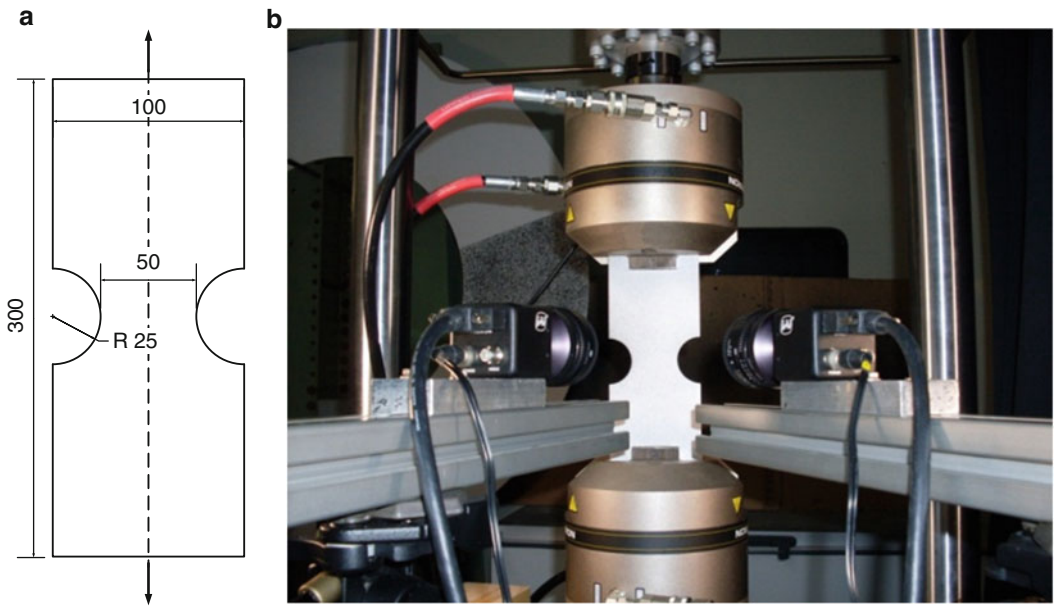

Fig. 8.1 Specimen shape and adopted experimental set-up

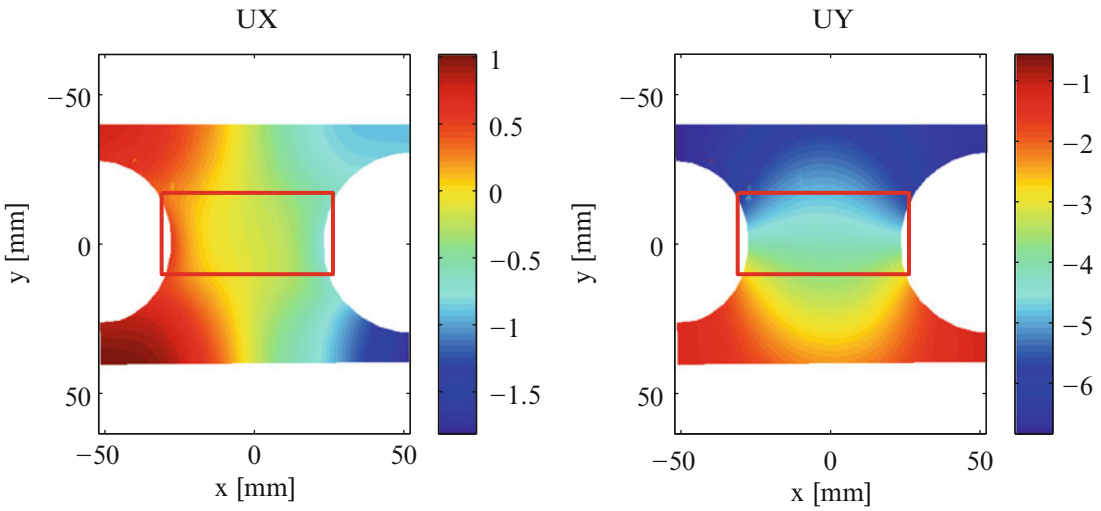

Fig. 8.2 Measured displacement fields and area of the specimen used to perform the identification

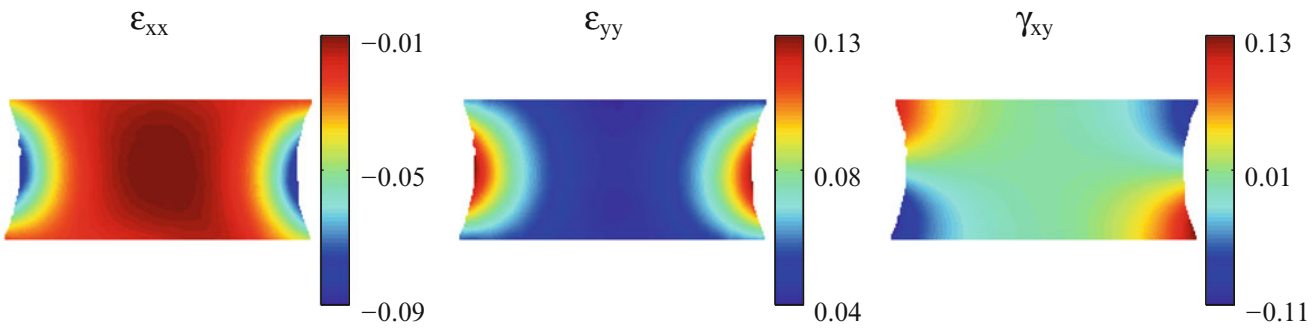

Fig. 8.3 Example of strain maps used for the identification

Table 8.1 Identified parameters for Yld2000-2D

Hardening	Yld2000-2D parameters								
K [MPa]	N	α_1	α_2	α_3	α_4	α_5	α_6	α_7	α_8
852	0.41	1.11	1.35	1.21	1.11	1.07	0.96	1.21	1.15

Table 8.2 Identified parameters for Hill48

Hardening		Hill48 parameters			
K [MPa]	N	f	g	h	n
735	0.41	0.49	0.45	0.55	3.56

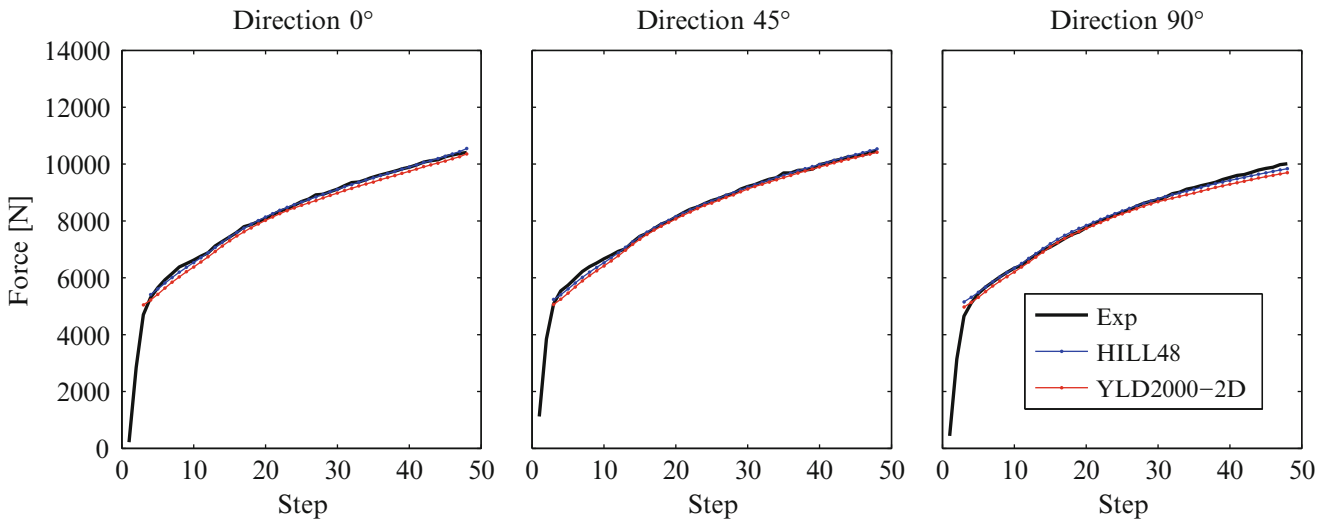

Fig. 8.4 Comparison of the experimental force and the computed one from the strain field with Hill48 and Yld2000-2D

8.4 Results and Discussion

The non-linear VFM was applied to the DIC strain measurement. The optimization was performed using the optimization toolbox in Matlab®. Table 8.1 lists the identified parameters. Table 8.2 lists the parameters identified on the same data using Hill48 as constitutive model, (see for instance [16]).

As first check, the identified parameters are used to evaluate the force measured during the experiments. This can be easily done exploiting (8.2). In this way, the force is computed starting from the measured strain data and the identified parameters. The results are presented in Fig. 8.4, both Hill48 and Yld2000-2D allow to correctly reproduce the test in term of measured force.

Table 8.3 Comparison of the identified Lankford parameters

Model	R_0	R_{45}	R_{90}
Hill48	1.21	1.32	1.12
Yld2000-2D°	2.00	1.63	2.07
Reference	1.8	1.5	2.1

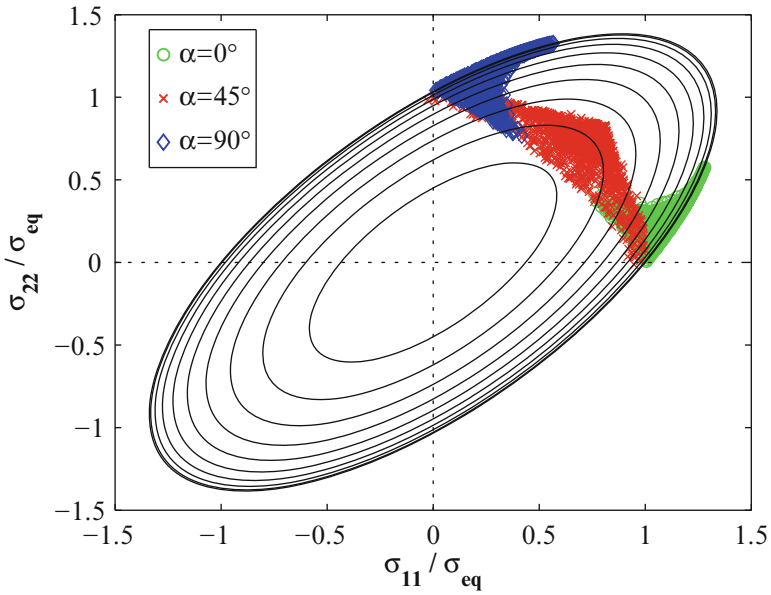

Fig. 8.5 Stress distribution obtained from the experimental tests

Table 8.3 shows a comparison of the two models in terms of the Lankford parameter R, which is the ratio of the transverse to the through-thickness strain. The Lankford parameters characterizes the plastic flow in different anisotropic directions.

In this case, Hill48 is not able to reproduce the actual behaviour, while a reasonably good agreement is found using Yld2000-2D. The reference values were obtained from simple uniaxial tests in different directions.

The inverse identification with VFM and notched tests, allows the calculation of the Yld2000-2D parameters that are consistent with the material properties. However, this type of test only allows the investigation of a small portion of the yield surface. In Fig. 8.5, the stress states obtained with the notched specimens in the three directions are plotted over the normalized yield surface. Only a small portion is covered and it is not possible to investigate the biaxial or pure shear conditions. In the future, other specimen geometries should be designed so that a larger part of the yield surface can be investigated.

8.5 Conclusion

In this paper, the non-linear VFM is used to identify the parameters of the Yld2000-2D yield function, coupled with a Swift's hardening law. Experimental tests were conducted on notched specimens, cut on three different directions (0°, 45° and 90°). The strain field was measured by DIC and used to perform an inverse identification with VFM. The identified parameters are in good agreement with the reference value for the used material, especially when compared with the results achieved using the Hill48 model. In future, simulated experiments will be used to validate the proposed approach and quantify the identification error and the accuracy of the technique.

References

1. R. Hill, A theory of yielding and plastic flow of anisotropic metals. Proc. R. Soc. Lond. A Math. Phys. Sci. **193**, 281–297 (1948)
2. F. Barlat, J. Brem, J. Yoon, K. Chung, R. Dick, D. Lege, F. Pourboghrat, S.-H. Choi, E. Chu, Plane stress yield function for aluminium alloy sheets: part 1—theory. Int. J. Plast. **19**(9), 1297–1319 (2003)

3. J.-W. Yoon, F. Barlat, R. Dick, K. Chung, T. Kang, Plane stress yield function for aluminum alloy sheets—part II: FE formulation and its implementation. Int. J. Plast. **20**(3), 495–522 (2004)
4. M. Grédiac, F. Hild, A. Pineau, *Full-Field Measurements and Identification in Solid Mechanics* (John Wiley & Sons, Hoboken, 2012)
5. A. Güner, C. Soyarslan, A. Brosius, A. Tekkaya, Characterization of anisotropy of sheet metals employing inhomogeneous strain fields for yld2000-2d yield function. Int. J. Solids Struct. **49**(25), 3517–3527 (2012)
6. M. Rossi, G.B. Broggiato, S. Papalini, Application of digital image correlation to the study of planar anisotropy of sheet metals at large strains. Meccanica **43**, 185–199 (2008)
7. S. Coppieters, S. Cooreman, H. Sol, P. Van Houtte, D. Debruyne, Identification of the post-necking hardening behaviour of sheet metal by comparison of the internal and external work in the necking zone. J. Mater. Process. Technol. **211**(3), 545–552 (2012)
8. S. Coppieters, T. Kuwabara, Identification of post-necking hardening phenomena in ductile sheet metal. Exp. Mech. **54**(8), 1355–1371 (2014)
9. F. Pierron, M. Grédiac, *The Virtual Fields Method* (Springer, New York, 2012)
10. M. Grédiac, F. Pierron, Applying the virtual fields method to the identification of elasto-plastic constitutive parameters. Int J Plast. **22**, 602–627 (2006)
11. F. Pierron, S. Avril, T.V. The, Extension of the virtual fields method to elasto-plastic material identification with cyclic loads and kinematic hardening. Int. J. Solids Struct. **47**, 2993–3010 (2010)
12. J.-H. Kim, A. Serpanti, F. Barlat, F. Pierron, M.-G. Lee, Characterization of the post-necking strain hardening behavior using the virtual fields method. Int. J. Solids Struct. **50**(24), 3829–3842 (2013)
13. M. Rossi, F. Pierron, Identification of plastic constitutive parameters at large deformations from three dimensional displacement fields. Comput. Mech. **49**, 53–71 (2012)
14. J.-H. Kim, F. Barlat, F. Pierron, M.-G. Lee, Determination of anisotropic plastic constitutive parameters using the virtual fields method. Exp. Mech. **54**, 1189–1204 (2014)
15. M.A. Sutton, J.J. Orteu, H.W. Schreier, *Image Correlation for Shape, Motion and Deformation Measurements* (Springer, New York, 2009)
16. M. Rossi, F. Pierron, M. Stamborska, F. Simcak, Identification of the anisotropic plastic behaviour of sheet metals at large strains. Conf. Proc. Soc. Exp. Mech. Ser. **4**, 229–235 (2013)

Chapter 9
Identification of Post-necking Strain Hardening Behavior of Pure Titanium Sheet

S. Coppieters, S. Sumita, D. Yanaga, K. Denys, D. Debruyne, and T. Kuwabara

Abstract This paper deals with the identification of the post-necking strain hardening behavior of pure titanium sheet. Biaxial tensile tests using a servo-controlled multi-axial tube expansion testing machine revealed that commercial pure titanium sheet exhibits significant differential work hardening (DWH). The latter phenomenon implies that the shapes of the work contours significantly change during plastic deformation which is accurately measured in the first quadrant of the stress space up to an equivalent plastic strain of approximately 0.3. In this paper we focus on the plastic material behavior beyond the point of maximum uniform strain in a quasi-static tensile test. To this purpose, the material is subjected to a post-necking tensile experiment during which the strain field in the diffuse necking zone is measured using a dedicated Digital Image Correlation (DIC) system. The key point in the identification of the post-necking strain hardening is the minimization of the discrepancy between the external work and internal work in the necking zone. In this study, we scrutinize the influence of DWH in the pre-necking regime on the identification of the post-necking strain hardening behavior of pure titanium sheet. Finally, a strain hardening model which enables disentangling pre- and post-necking hardening behavior is presented.

Keywords Post-necking strain hardening • Tensile test • Differential work hardening • Pure titanium • DIC

9.1 Introduction

Pioneering work of Bridgman [1] resulted in a solution for the problem of diffuse necking in a tensile specimen. Bridgman considered his method as a second level of approximation because the method is only concerned with the distribution of stress and strain across the diffuse neck. He also envisioned a third level of approximation, also referred to as the "complete solution" of the general problem, which takes the material state and the shape of the whole deforming specimen into account. Several researchers arrived at such complete solutions using finite-element based inverse methods. From a practical point of view, however, the coupling between the experimentally measured quantities and the numerically computed response can be a burden. Moreover, the iterative FE simulations to predict the plastic instability are usually very time-consuming. In order to avoid the shortcomings of the FE-based inverse method, a new method based on the complete solution to retrieve the strain hardening behavior hidden in the diffuse necking regime was presented in [2]. The key point in this method is that the strain hardening behavior can be identified by minimizing the discrepancy between the internal and the external work in the region where the diffuse neck develops. The method was experimentally validated [3] beyond the point of maximum uniform strain using the tube expansion test [4]. Kim et al. [5] presented a similar approach to identify post-necking strain hardening behavior of sheet metal using the Virtual Fields Method (VFM). Clearly, both methods [2, 5] rely on the computation of (actual and virtual, respectively) internal work, and, consequently, need access to the stresses associated with the experimentally measured strains. The later requires a phenomenological material model and an appropriate stress updating algorithm. Unlike the work of Kim et al. [5], Coppieters and co-workers [2, 3] incorporated in-plane plastic anisotropy in their identification procedure. The assumption made in [2] that an increase of the cost function caused by an error in the work hardening law is significantly larger than an increase caused by an error in the anisotropic yield criterion

S. Coppieters • K. Denys • D. Debruyne
Department of Materials Engineering, KU Leuven, Campus Ghent, Gebroeders de Smetstraat 1, Ghent 9000, Belgium
e-mail: sam.coppieters@kuleuven.be

S. Sumita (✉) • D. Yanaga
Graduate School of Engineering, Tokyo University of Agriculture and Technology, 2-24-16 Nakacho, Koganei-shi, Tokyo 184-8588, Japan

T. Kuwabara
Division of Advanced Mechanical Systems Engineering, Tokyo University of Agriculture and Technology, 2-24-16 Nakacho, Koganei-shi, Tokyo 184-8588, Japan

S. Bossuyt et al. (eds.), *Residual Stress, Thermomechanics & Infrared Imaging, Hybrid Techniques and Inverse Problems, Volume 9*, Conference Proceedings of the Society for Experimental Mechanics Series, DOI 10.1007/978-3-319-21765-9_9

was scrutinized in [3, 6]. The key point to guarantee a sufficient accurate identification is that the adopted yield function enables to describe the material response within the diffuse neck. Theoretically, the stress state in the diffuse neck approaches plane strain which implies that a fairly large portion of the yield surface will be used in the identification of the post-necking hardening behavior. Although, in practice plane strain is not reached during diffuse necking, the accuracy of the yield function gains importance when biaxial stress states are probed in materials which exhibit strong plastic anisotropy. The identified post-necking hardening behavior in the rolling direction (RD) of the materials investigated in [2, 3] did not strongly depend on the selected yield loci. This work is an attempt to extend the method to materials which exhibit strong in-plane anisotropy and differential work hardening.

9.2 Material

To this purpose, a commercially pure titanium sheet with an initial thickness of 0.52 mm is studied in the present work. This material exhibits complex texture-induced anisotropy along with differential work hardening. Sumita and Kuwabara [7] identified the differential work hardening behavior of a pure titanium sheet up to an equivalent plastic strain of 0.3 using the servo-controlled combined tension-internal pressure testing machine developed by Kuwabara and Sugawara [4]. Figure 9.1 shows the measured stress points forming the contours of plastic work for different levels of ε_0^{pl}. It can be inferred that the work contours shows significant asymmetry with respect to the equibiaxial stress state, i.e., σ_x=σ_y. Moreover, the asymmetry of successive work contours decreases with an increase in ε_0^{pl} exemplifying the so-called differential work hardening. This material behavior is quantitatively in line with other investigations on pure titanium, e.g., [8].

Standard uniaxial tensile tests (JIS 13 B-type) were conducted to determine work hardening properties and the r-values. The pre-necking strain hardening curve the rolling direction can be found in Fig. 9.2. This figure also shows the fitted Swift hardening law which reads as:

$$\sigma_{eq} = K\left(\varepsilon_0 + \varepsilon_{eq}^{pl}\right) \tag{9.1}$$

It must be noted that the Swift law cannot perfectly describe the strain hardening behavior in the pre-necking region. Indeed, the Swift law cannot accurately reproduce the initial yield stress and the yield stress at maximum uniform strain. The r-values can be found in Table 9.1. It can be inferred from Fig. 9.2 that the Swift law cannot perfectly describe the material behavior. To be specific, the initial yield stress and the yield stress at maximum uniform strain $\varepsilon_{max} \approx 0.27$ cannot be accurately predicted by the Swift law. Figure 9.2 also shows the hardening behavior of the test material in the transverse

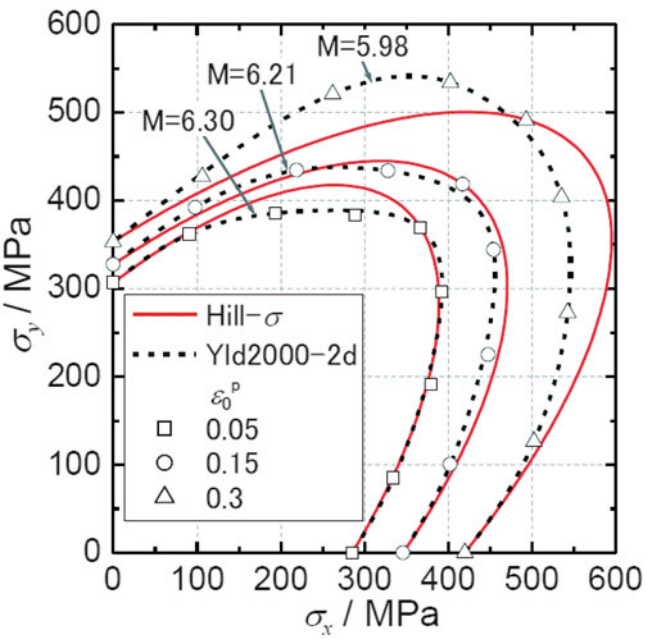

Fig. 9.1 Stress points forming contours of plastic work compared with the theoretical yield loci calculated using the Yld2000-2d and Hill48 yield functions [7]

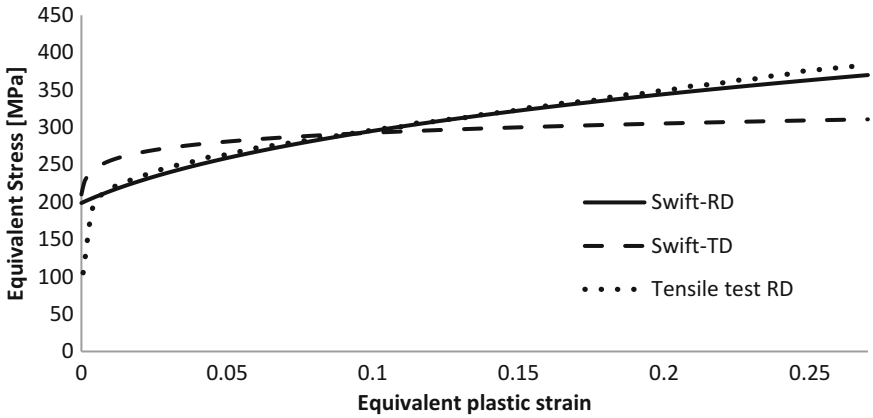

Fig. 9.2 Pre-necking hardening behavior of pure titanium (strain rate $\approx 4 \times 10^{-4}\frac{1}{s}$). The Swift law in the TD was extrapolated beyond the point of maximum uniform strain $\varepsilon_{max} \approx 0.05$

Table 9.1 r-values of pure titanium measured at an engineering strain of 0.15

Direction	r-value
RD	1.39
45	2.74
TD	3.91

direction (TD). It must be noted that the latter curve is extrapolated since the maximum uniform strain ε_{max} in the TD is limited to $\varepsilon_{max} \approx 0.05$. Clearly, the strain hardening behavior in the TD significantly differs from the behavior in the RD. Figure 9.1 also shows selected yield loci associated with specific values of reference strain ε_0^{pl}. The stress based Hill48 yield function yields satisfactory results up to ε_0^{pl}=0.15. Beyond this point, however, Hill48-σ tends to overestimate the work contours in certain stress states. The yld2000-2d yield function enables to accurately describe the work contours provided that the variations in r_0, r_{90} and r_b with respect to ε_0^{pl} are taken into account in the parameter determination. Such material behavior requires the development of new constitutive material models. Yanaga et al. [9] proposed to reproduce DWH based on the Yld2000-2d yield function with the exponent and material parameters changing as functions of the amount of plastic work. Implementation of such advanced yield functions within finite element codes enables to optimize sheet metal forming processes [10]. It must be noted that accurate determination of differential work hardening requires a significant amount of experimental effort. In this contribution, we scrutinize the necessity of incorporating DWH into the material model when identifying the post-necking hardening through a tensile test as proposed by Coppieters et al. [2] and Coppieters and Kuwabara [3].

9.3 Method

The method presented in Coppieters et al. [2] was originally conceived from the observation that in a quasi-static tensile test the internal work equals the external work. As such, the key point in the method is the minimization of the discrepancy between the internal and the external work in the necking zone during a tensile test. Computation of the internal work requires access to the experimental strain field and the associated stress field. The experimental strain field is derived from the experimentally measured displacement field using stereo-DIC. To do so, an element mesh is fitted to the measured displacement field. The monitored zone in which the diffuse neck develops spanned a region of 12.5 mm $\times$ 40 mm. This mesh contained 250 square elements (4 node bilinear elements) with an element size of 1.5 mm. The test material was subjected to the Post-Necking Tensile Experiment (PNTE) in the RD using a standard tensile specimen (JIS 13 type-B) and a regular tensile machine (Zwick/Roell) with a load capacity of 10 kN. The experiment was displacement controlled using a constant cross-head speed of $0.05\frac{mm}{s}$. The tensile machine was equipped with a stereo-DIC system to capture the displacement fields at the surface of the specimen. Both cameras (8-bit AVT STINGGRAY F-201B 1/1.8) with a resolution of 1624 $\times$ 1232 pixels^2 were equipped with a Schneider 23 mm lens. The image resolution was approximately 0.08 mm/px. The images were synchronized with the tensile force and consequently each set of pictures corresponds to a different load step. All images were post-processed using MatchID-3D [11] via the so called subset-based method. During the PNTE full field information was captured in 95 load steps.

9.4 Validation: Pre-necking Hardening Behaviour

The aim of this paper is to identify the post-necking hardening behavior of pure titanium using the method presented in [2, 3]. Before embarking on this, it should be noted that the pre-necking hardening behavior can be directly determined solely based on the measured force and the measured elongation using simple analytical formulas. Therefore, in a first step, the identification procedure is validated by identifying the pre-necking hardening behavior. Additionally, this step enables to tune the element mesh required to compute the strain fields from the measured displacement fields. In this section the experimentally acquired pre-necking data (55 load steps, i.e., the load step in which the maximum uniform strain ε_{eq}^{pl}=0.27 is reached) are used to identify the Swift hardening law (9.1). Since the pre-necking hardening behavior is readily available from the tensile test, the accuracy of the identification procedure can be directly assessed. First, the potential in-plane anisotropy and DWH is ignored and the von Mises yield criterion is adopted to identify the pre-necking hardening behavior. Figure 9.3 shows the identified pre-necking hardening behavior using the von Mises yield criterion (labeled as *PNTE Swift-von Mises (1)*) along with the Swift law fitted to the pre-necking data.

It can be observed that the pre-necking strain hardening behavior is not perfectly retrieved. It was found that this error originates from an inaccurate computation of the external work. Figure 9.4 shows the load-elongation curve of the tensile test in the RD. Although, the stereo-DIC system was synchronized with the tensile test machine, a deviation between the experimentally measured tensile forces occurred. The identification could be improved by using the corrected tensile force and the result (labeled as *PNTE Swift-von Mises (2)*) is shown in Fig. 9.3. Second, the in-plane anisotropy of the titanium sheet was included by using the r-based Hill48 yield criterion. It can be seen in Fig. 9.3 that this yields identical results as those obtained using von Mises yield criterion. Consequently, the identification procedure along with the adopted yield loci is validated in the pre-necking region.

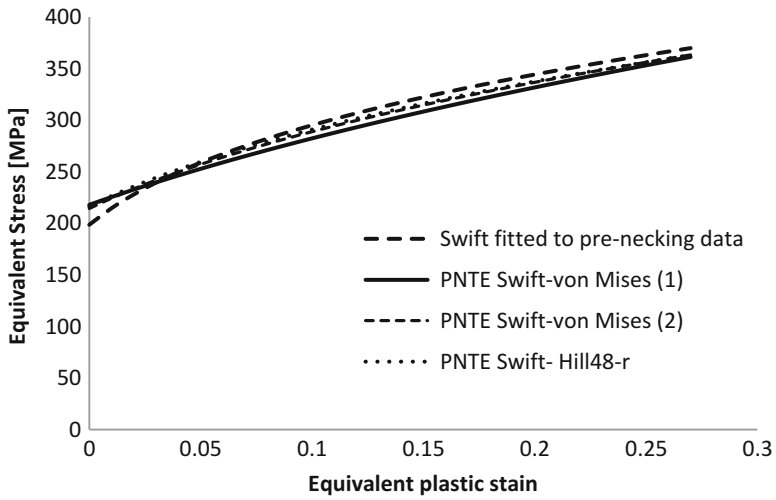

Fig. 9.3 Identified pre-necking hardening behavior of pure titanium sheet in the RD

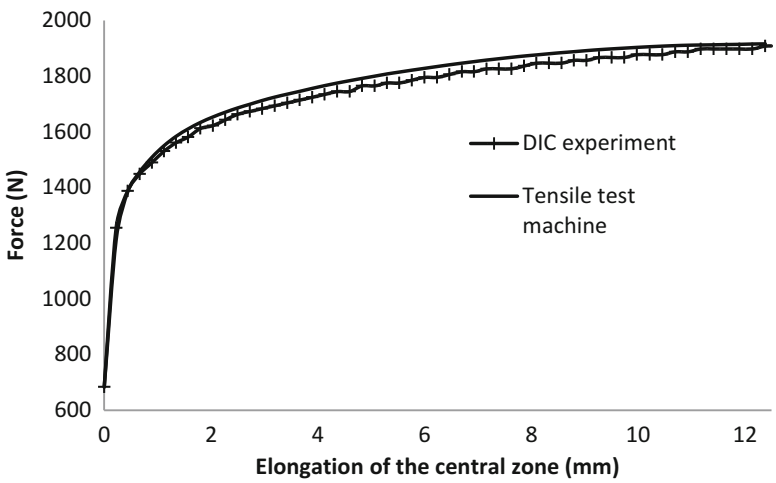

Fig. 9.4 Force-elongation curve (pre-necking region, RD, initial length central zone = 40 mm)

9.5 Results: Post-necking Hardening Behaviour

In this section we embark on the post-necking strain hardening behavior of pure titanium. 95 load steps were used to identify the complete hardening behavior. The maximum equivalent strain probed in the experiment was $\varepsilon_{eq}^{pl} \approx 0.8$. Only diffuse necking is taken into account. Figure 9.5 shows the results. The black solid curve (labeled *EM Swift*) represents the extrapolated Swift law fitted to the pre-necking data. The same Swift law was also identified using the PNTE (labeled *PNTE Swift-von Mises*) and this yield a similar behavior as predicted by the extrapolation method (EM). The latter suggests that the Swift law is an appropriate hardening law to describe the hardening behavior of pure titanium in the RD. In order to disentangle pre- and post-necking hardening behavior the so-called p-model [3], which is based on successive phenomenological equations, can be used:

$$\sigma_{eq} = \begin{cases} K\left(\varepsilon_0 + \varepsilon_{eq}^{pl}\right)^n, & \varepsilon_{eq}^{pl} \leq \varepsilon_{max} \\ K(\varepsilon_0 + \varepsilon_{max})^n + Q\left[1 - e^{-p\left(\varepsilon_{eq}^{pl} - \varepsilon_{max}\right)}\right], & \varepsilon_{eq}^{pl} > \varepsilon_{max} \end{cases} \tag{9.2}$$

In this phenomenological hardening model, the parameters K, ε_0 and n are identified through the available pre-necking data. ε_{max} is the maximum uniform strain in the tensile test. In the post-necking regime the model switches to a post-necking hardening description. To guarantee a smooth transition a simple relation between p and Q can be found [3]. As a result, the only unknown in the post-necking regime is the post-necking hardening parameter p. In the case a von Mises material is assumed, the p-model (labeled *PNTE p-model—von Mises*) is in very good agreement with the extrapolated Swift law. If the p-model, however, is identified using the r-based Hill48 yield criterion then the post-necking parameter increases resulting in a slightly decreased strain hardening rate deep into the diffuse neck. Figure 9.6 shows the adopted yield loci used to identify the hardening behavior. Clearly, both yield loci cannot accurately describe the material response of pure titanium in the first quadrant of the stress space. However, they enable to describe the material response of titanium in the vicinity of uniaxial tension in the RD, i.e., the stress ratio $(\sigma_x : \sigma_y)$=1 : 0.

The later means that the yield loci can be adopted to retrieve the hardening behavior when the stress ratio in the diffuse neck remains close to $(\sigma_x : \sigma_y)$=1 : 0. However, the deviation in the post-necking regime between the results obtained by the different yield loci indicates that the stress ratio deviates from $(\sigma_x : \sigma_y)$=1 : 0. Indeed, in the diffuse neck transverse stresses develop, and, consequently, biaxial stress states are probed. It is inferable from Fig. 9.6 that the adopted yield loci differ significantly hence resulting in a different identified post-necking hardening behavior. Finally, it must be noted that the present work did not include the strain rate sensitivity of the material. Indeed, the strain rate in the diffuse neck increases when uniform straining ceases and deformation becomes concentrated in the necking zone. It was experimentally observed that some material points in the diffuse neck reach a strain rate of $\dot{\varepsilon}_{eq}^{pl} \approx 0.01\frac{1}{s}$. Given the fact that very few material point reach this value, however, it is currently assumed that the impact on the global identified hardening behavior will be small.

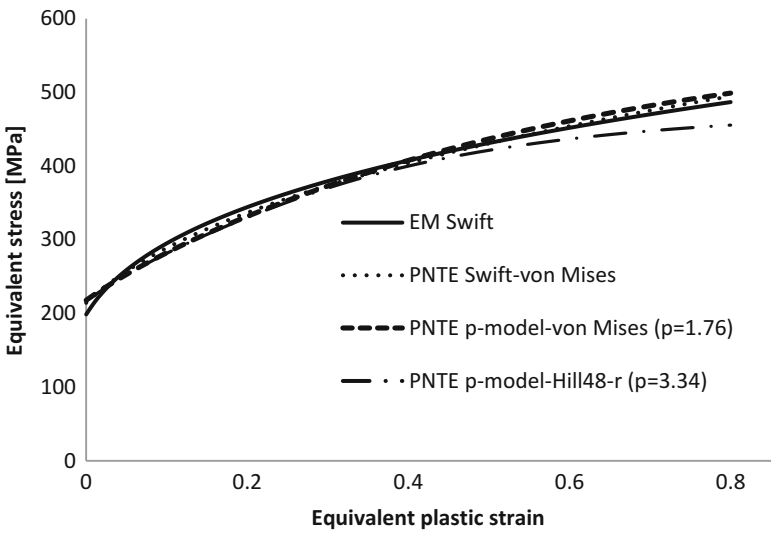

Fig. 9.5 Identified pre- and post-necking hardening behavior of pure titanium in the RD

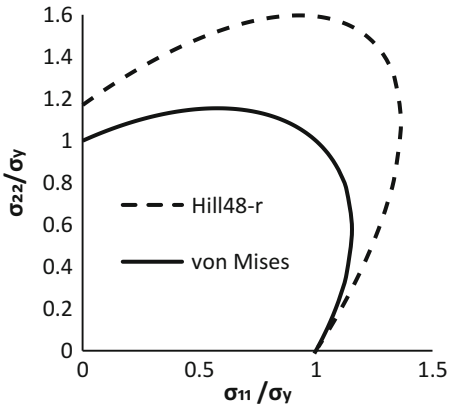

Fig. 9.6 Adopted yield loci to identify the post-necking hardening behavior of pure titanium in the RD

Nevertheless, since pure titanium exhibits a significant strain-rate sensitivity [7], future work should try to include the strain rate as a state variable in the hardening law.

9.6 Conclusions

This work is an attempt to identify the post-necking hardening behavior of pure titanium sheet through a tensile test in the rolling direction. To this purpose, an alternative method is used which is based on the minimization of the external and internal work in the diffuse neck of a standard tensile specimen. It is well-known that the accuracy of this identification method depends on the adopted phenomenological yield function. Clearly, the yield function gains importance when the material exhibits strong in-plane anisotropy and biaxial stress states are probed in the diffuse neck. In this paper, the post-necking strain hardening behavior of pure titanium, which exhibits strong texture-induced anisotropy and differential work hardening, is under investigation. The aim of this paper was to scrutinize the necessity of using an advanced phenomenological yield function, which enables to describe such complex material behavior, to identify the post-necking hardening behavior. While inconclusive, the obtained results suggest that the post-necking hardening behavior of pure titanium can be determined without incorporating a highly advanced yield function provided that the post-necking tensile experiment is conducted in the rolling direction. A more profound analysis requires the implementation of an advanced material model which enables to describe differential work hardening. Additionally, strain rate should be included as a state variable in the hardening law. Research along these lines is currently conducted and will be published in a forthcoming paper.

References

1. P.W. Bridgman, *Studies in Large Plastic Flow and Fracture* (McGraw-Hill, New York, 1952)
2. S. Coppieters, S. Cooreman, H. Sol, P. Van Houtte, D. Debruyne, Identification of the post-necking hardening behavior of sheet metal by comparison of the internal and external work in the necking zone. J. Mater. Process. Technol. **211**(3), 545–552 (2011)
3. S. Coppieters, T. Kuwabara, Identification of post-necking hardening phenomena in ductile sheet metal. Exp. Mech. **54**(8), 1355–1371 (2014)
4. T. Kuwabara, F. Sugawara, Multiaxial tube expansion test method for measurement of sheet metal deformation behavior under biaxial tension for large strain range. Int. J. Plasticity **45**, 103–118 (2013)
5. J.-H. Kim, A. Serpantié, F. Barlat, F. Pierron, M.-G. Lee, Characterization of the post-necking hardening behaviour using the virtual fields method. Int. J. Solids Struct. **50**, 3829–3842 (2013)
6. S. Coppieters, K. Ichikawa, D. Debruyne, T. Kuwabara, Identification of post-necking hardening behaviour of sheet metal: influence of the yield function. International conference on experimental mechanics. Cambridge (UK), 7–11 July 2014
7. T. Sumita, T. Kuwabara, Measurement and material modeling of biaxial work-hardening behavior for pure titanium sheet. Proc. NUMISHEET **2014**(1567), 516–519 (2014). doi:10.1063/1.4850025
8. M. Ishiki, T. Kuwabara, Y. Hayashida, Measurement and analysis of differential work hardening behavior of pure titanium sheet using spline function. Int. J. Mater. Form. **4–2**(1), 93–204 (2011). doi:10.1007/s12289-010-1024-5
9. D. Yanaga, H. Takizawa, T. Kuwabara, Formulation of differential work hardening of 6000 series aluminum alloy sheet and application to finite element analysis. J. Jpn. Soc. Technol. Plasticity **55**(636), 55–61 (2014)
10. K. Ichikawa, T. Kuwabara, S. Coppieters, Forming simulation considering the differential work hardening behavior of a cold rolled interstitial-free steel sheet. Key Eng. Mater. **611–612**, 56–61 (2014). doi:10.4028/www.scientific.net/KEM.611-612.56
11. MatchID 3D, http://www.matchidmbc.be/

Chapter 10
Challenges for High-Pressure High-Temperature Applications of Rubber Materials in the Oil and Gas Industry

Allan Zhong

Abstract As deeper and deeper wells are drilled offshore, the well temperatures are hotter, and the downhole pressures are higher. The higher pressures and temperatures in these deepwater wells pose significant challenges for both metallic and nonmetallic materials. These challenges are especially serious for rubber and other polymer-based materials due to significant degradation of material properties that these extreme conditions cause. In this paper, a broad overview of the challenges for applications of rubber and other polymer-based materials in downhole tools under high pressure, high temperature environments will be presented along with current approaches taken by the industry to address these challenges. The need for new material development as well as fundamental understanding of rubber mechanics under HPHT conditions also will be discussed.

Keywords High-pressure • High-temperature • Modulus • Material degradation • Rubber mechanics

10.1 Introduction

Due to its elasticity and resilience, rubber has wide applications in the oil/gas industry, primarily as sealing components. However, rubber properties are highly sensitive to temperature. The mechanical properties of rubbers which include modulus, elongation at break, compression set, and fracture toughness, can degrade rapidly when their maximum temperature ranges are approached.

For example, tensile tests of size-325 Aflas O-rings (Fig. 10.1), showed that the modulus of the rubber decreases with increasing temperature and stabilizes around 200 °F (93 °C) in air and that the elongation at break decreases monotonically with any temperature increase from room temperature. These characteristics of rubber pose significant challenges for downhole tool designers and material scientists in applications subjected to high temperatures.

In order to extract more oil and gas from underground, past history has shown that the depth of the higher producing wells has been greater, and thus, depths will continue to increase steadily; consequently, downhole temperatures will also increase. This is especially true for offshore wells. For example, the maximum depth of wells drilled from 1966 to 2003 has almost doubled (see Fig. 10.2) [2].

Not only are the temperatures in these deepwater wells much higher than in shallower wells, the bottomhole pressures are significantly higher as well. Thus, sealing requirements in the HPHT downhole environment poses challenges for applications of elastomer and non-elastomer materials. In the following sections, an overview of applications of rubber and polymeric materials in the upstream sector of the oil/gas industry is given first. The next section focuses on HPHT related topics, where and when HPHT environments occur, and what the definition is for HPHT in the oil/gas industry. Challenges for HPHT applications of rubber materials will be summarized along with examples concerning how the industry addresses some of these challenges.

10.2 Applications of Rubber Materials in the Oil and Gas Industry

The main application for which rubber materials are used in the industry is static and dynamic sealing between mechanical components. Unlike applications in most other industries, typical downhole pressures can range from 1000 to 10,000 psi. Based on applications and sizes, sealing elements can be categorized into two groups. The measured radial clearance or

A. Zhong (✉)
R&D and Engineering Simulations-Halliburton Company, 819052Dallas, TX 75381, USA
e-mail: allan.zhong@halliburton.com

S. Bossuyt et al. (eds.), *Residual Stress, Thermomechanics & Infrared Imaging, Hybrid Techniques and Inverse Problems, Volume 9*, Conference Proceedings of the Society for Experimental Mechanics Series, DOI 10.1007/978-3-319-21765-9_10

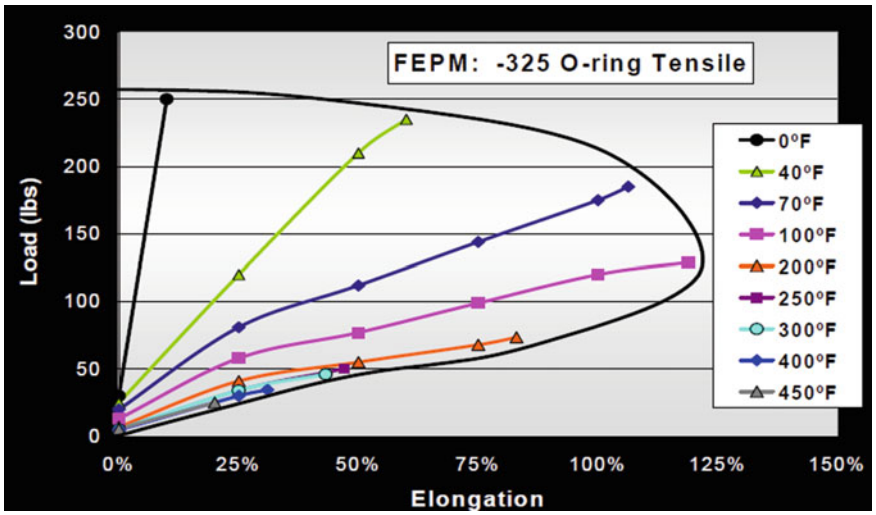

Fig. 10.1 Change of rubber stress strain curve with temperature increase [1]

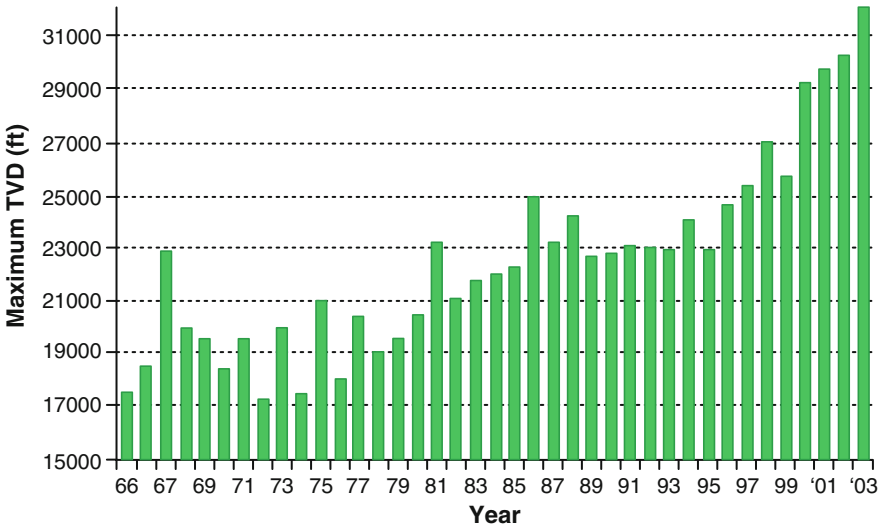

Fig. 10.2 Well maximum total depths in Gulf of Mexico, 1966–2003 [2]

"sealing gap" across a fluid or gas passageway for which the seal must isolate and contain differential pressure is a primary factor the seal designer must consider when selecting an appropriate sealing system. Seals are typically installed into cavities or seal glands which are tightly controlled-tolerance machined features in metal tool components. For small sealing gaps, the seals are typically O-rings and their variations, which can be V-ring packing stacks, bonded seals, etc. O-ring glands are typically characterized as a machined groove feature, while other seal types utilize longer seal gland features. O-rings rely on resiliency properties to allow contact stress in the gland for initial sealing, and to return to their original shape when pressure is removed for proper sealing. For large sealing gaps, thicker cross-section pressure isolating seals called packer elements are used on production packers and on well intervention bridge plugs, and must be mechanically loaded to deploy them into the required sealing configuration.

In the case of small sealing gaps for relatively low differential pressures typically hundreds to several thousand psi, a properly sized O-ring is sufficient. When pressure increases to a certain magnitude, the O-ring starts to extrude through the annulus (Fig. 10.3, Reference [3]), hence the sealing gap is typically called the extrusion gap. A common approach is to add a backup seal ring that typically is made of a thermo-plastic material; e.g., PEEK, which is much harder than O-ring rubber to contain the O-ring and to improve the sealing performance. An extension of an O-ring with a backup design is the typically referred to as a Vee-packing seal; it is a more complex design with a multiple layer of seal components along the length of

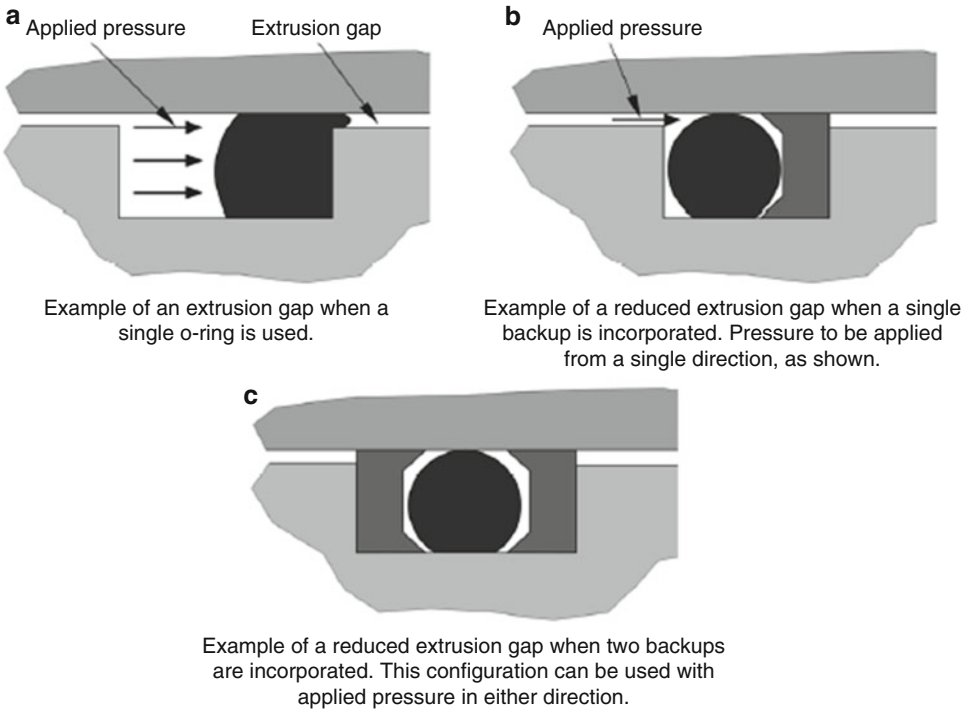

Fig. 10.3 Examples of O-ring seals with and without backup rings [3]

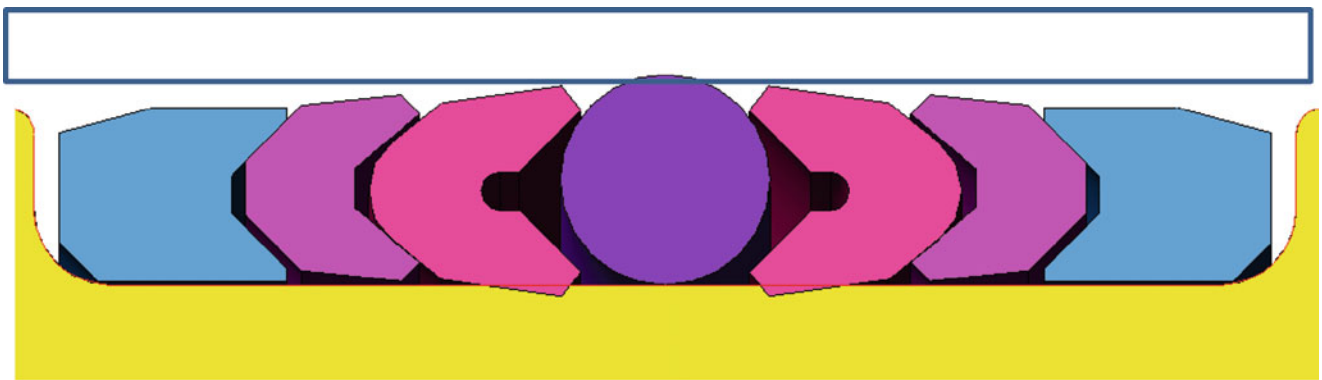

Fig. 10.4 Schematics of a V-packing seal structure

the sealing gland. When used in the Vee-packing stack, the O-ring serves the purpose of "energizing" the vee rings for optimum sealing when differential pressure is applied. Each layer may be of a different material and/or geometry, which has a metal backup at the ends, plastic backups in between metal backups, and a rubber O-ring. A typical Vee-pack seal design is shown in Fig. 10.4.

The bonded seal (or molded seal) design as shown in Fig. 10.5 provides an integrated metal backup to the elastomeric seal, which enables control of rubber deformation and displacement in the sealing gland under differential pressure, and is readily used in dynamic sealing applications.

For large sealing gaps e.g., the radial clearance between the production tubing and casing, which is typically a pipe cemented into the wellbore, the chosen seal system is not usually O-ring type seals; these seals are now called packers, and are a standard sealing component of completion tools used in oil/gas applications. Production packers are a mechanical assemblies which provide zonal isolation in the annulus between the outside of the production tubing and the inside of the casing or liner. Based on the application, production packers are classified into two types i.e., permanent packers and

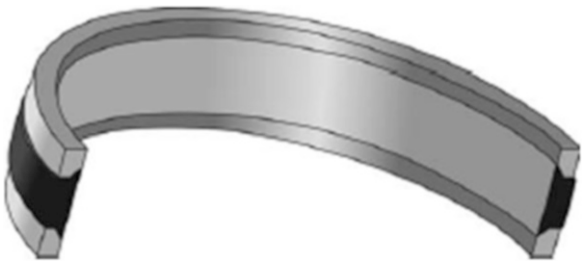

Fig. 10.5 Example of molded and bonded seal [3]

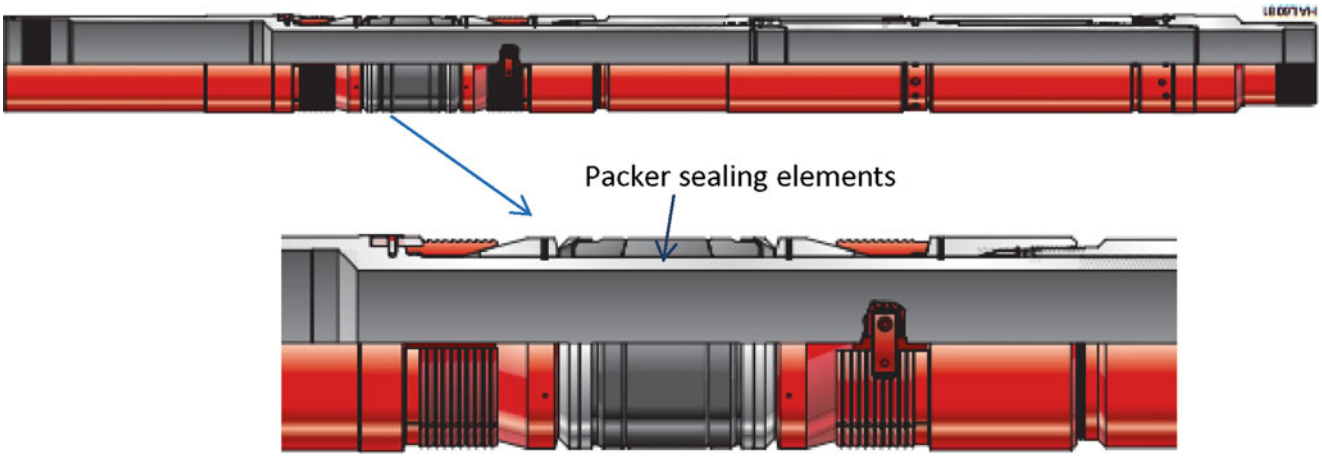

Fig. 10.6 Example of a hydrostatic set permanent packer [4]

retrievable packers. Once set in the wellbore, permanent production packers are intended to remain in the well during well production for the life of the completion and are typically removed by milling operations. Retrievable production packers have an integral releasing mechanism and may be retrieved by service tools and workstring tubing manipulation. Service tool retrievable packers are used only for a short period of time during well intervention services, such as well testing, cement squeezing, well stimulation, casing perforation, etc. After service operations are complete, these packers are mechanically retrieved or milled in place for removal.

One significant difference between packer-type seals and O-ring-type seals is that packer seal elements are not in a sealing position when a completion tool string is initially installed in the well bore. They must be squeezed into a sealing configuration or "set" after being placed into the designated position in the well. In order to keep packer elements in the sealing (set) position, the packer must have an anchoring mechanism such as slips and related locking components that can hold the packer in the set position after the setting force is removed. A typical packer system is shown in Fig. 10.6, reference [4]; this packer has three elastomeric sealing elements, one pair of metallic backup shoes, one pair of wedges that facilitate the engagement and "biting" of the slips into the casing ID, and a pair of slips for securely anchoring the tool into the well casing, along with other components that work together during the setting process. For proper sealing to occur, the packer element must maintain sufficient sealing stress along the length of the packer seal gland. This means that the contact force between the element ID and the packer mandrel OD, and between the element OD and the ID of the casing must be sufficient to seal against pressure differential.

Different service companies provide different packer offerings (see Figs. 10.7 and 10.8) (references [5, 6]), but they are similar in that they all have sealing elements, backups for the sealing elements, wedges, and slips.

In addition to being used as sealing components, rubber and polymeric materials are also used for other functions, such as a cement wiping plug (see Fig. 10.9, Reference [7]) for cleaning tubing IDs after the cement is pumped through them; an expandable liner hanger (Fig. 10.10, Reference [8]) is an anchoring and sealing system that provides load-carrying capacity beyond the cased hole to areas where there may be no casing. Another application of polymeric materials in downhole tools is plastic electronic components (Reference [9]).

As discussed previously, rubber and other polymeric materials have wide applications in downhole operations. However, their main application is for sealing. In sealing applications, rubber components are used to isolate different zones and are

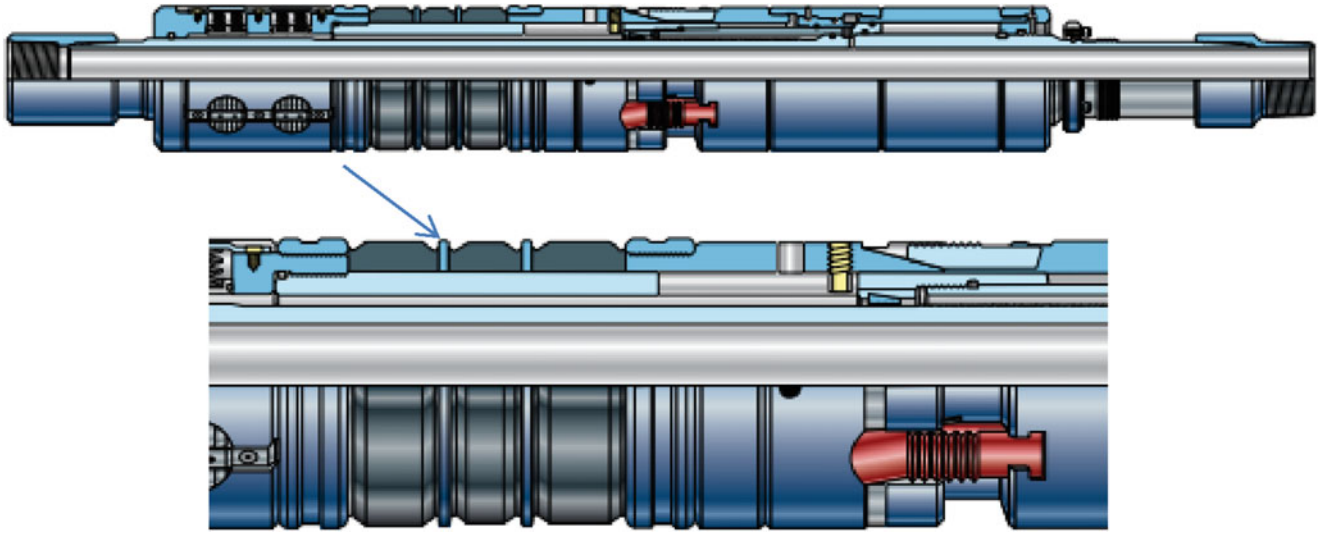

Fig. 10.7 An alternate design of packer [5]

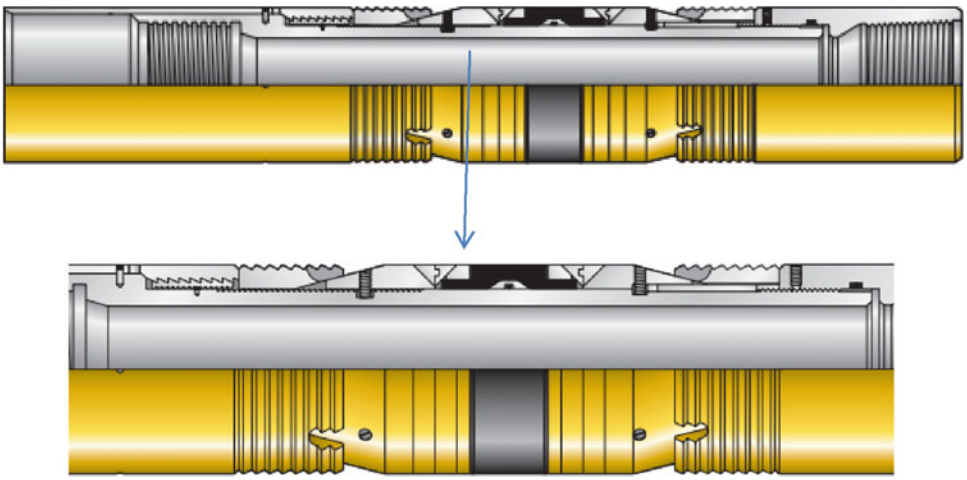

Fig. 10.8 Another alternate design of packers [6]

Fig. 10.9 Cement wiper plug [7]

subject to differential pressures. The common service requirements on rubber include resistance to extrusion, resistance to fracture, and performance at low or high temperature (relative to room temperature). The common parameters are hardness, modulus, compression set, tear strength, tensile strength, elongation at break, and fracture toughness. Other important parameters that are considered for determining rubber applications in oil/gas wells include compatibility with fluids, time to exposure to the fluid, time to exposure to the temperature, and explosive decompression (in gas wells).

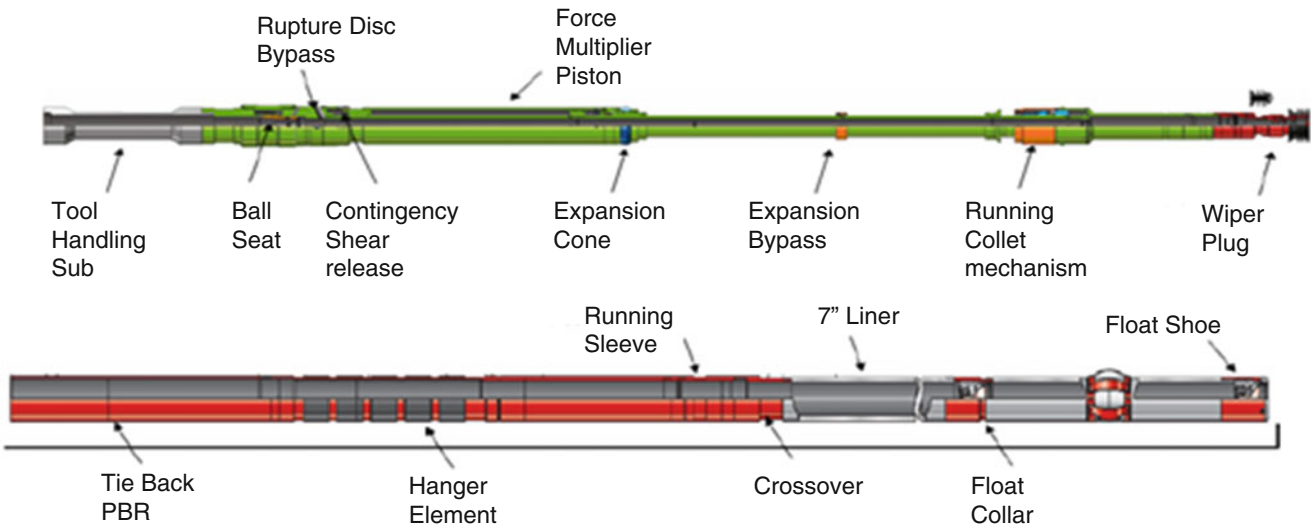

Fig. 10.10 Expandable liner hanger [8]

10.3 High Temperature/High Pressure Environments

As depths of wells drilled offshore increase, the well temperature gets hotter, and downhole pressure becomes higher. This has been the case over the past 25 years. The term high pressure / high temperature (HPHT) was first coined around 1990 (References [10, 11]). However, the wells that are HPHT were drilled much earlier, and the first HPHT test well was drilled onshore in 1965 in Mississippi (Reference [9]), with well depths reaching 19,700–22,250 ft, reservoir pressure between 17,500 and 22,000 psi, and bottomhole temperatures between 365 and 385 °F. A well was drilled offshore Alabama in 1981 (Reference [12]) to reach a formation that was ~20,000-ft deep with reservoir pressure between 10,000 and 20,000 psi, and reservoir temperature exceeding 400 °F. Fluids produced from this well contained up to 10 % H_2S, 4 % CO_2, as well as sulphur. Many North-Sea deepwater formations were discovered and explored between 1981 and 1995 (Reference [13–16]), with depths ranging from 17,000 to 20,000 ft, formation pressures of 12,000–17,000 psi, and formation temperatures of 300–423 °F. Some started production in the early 2000 s. The development of the Gulf of Mexico (GOM) Deepwater wells (Reference [17]) started in the late 1990s through the early 2000s, with fields such as Thunderhorse, Cascade, Chinook, and Tahiti. The reservoirs in these fields exhibited reservoir pressures from 18,000 to 19,950 psi, but the temperatures were not as high as those mentioned earlier, as they were only up to 270 °F.

The development of deepwater wells in the GOM continues with well depths now reaching beyond 30,000 ft. The Shenandoah-2 well drilled by Anadarko Petroleum Corporation in early 2013, which was located in Walker Ridge Block 51, was drilled to a total depth of 31,405 ft in approximately 5800 ft of water (www.anadarko.com). The deepest well drilled by Cobalt International Energy in the GOM reached a depth of 36,552 ft (www.ft.com), but no commercial quantities of oil or gas were found.

The chart in Fig. 10.11 gives the bottomhole temperature and pressure distribution of HPHT wells drilled between 2007 and 2010 (Reference [18]). Now, deep water exploration and production has expanded from the North Sea and GOM to Southeast Asia, Africa, and South America and is continuing to expand. Figure 10.12 shows locations of HPHT projects around the world as of 2008; Reference [19].

The harsh environments these wells have high temperatures or high pressures or both. Different operators have had different definitions as to what constitutes an HPHT environment. A widely accepted industry definition of HPHT conditions is given in Fig. 10.13. However, the American Petroleum Institute; i.e., API, an oil/gas industry code organization officially defines HPHT as conditions with pressure above 15,000 psi and temperature above 350 °F. This appears in code *API PER 15 K*. So, the official HPHT definition falls into the extreme HPHT category when comparing it to what the industry considers the prevailing HPHT definition.

HPHT wells typically are deep wells that are onshore or offshore. There are other wells such as steam injection or steam-assisted gravity-drainage (SAGD) wells for heavy (high viscosity) oil production that may not be very deep but can still have

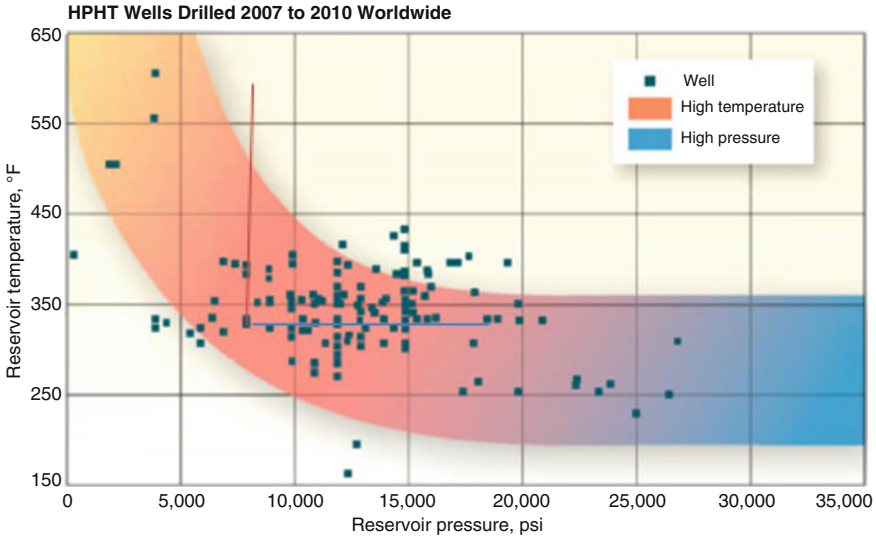

Fig. 10.11 HPHT wells drilled 2007–2010 worldwide [18]

^ HPHT projects around the world. During the past decade the number of HPHT projects has increased significantly; nevertheless, these projects represent only about 1% of producing reservoirs worldwide. The principal HPHT areas are found in the United States (deepwater Gulf of Mexico and deep, hot onshore wells), North Sea, Norwegian Sea, Thailand and Indonesia. In addition, thermal-recovery projects to extract heavy oil are located in Canada, California, Venezuela and eastern Europe.

Fig. 10.12 HPHT projects around the world [19]

very high temperatures in their operations. In these wells, steam may be used to reduce heavy oil viscosity. Geothermal wells are another type of well that can have extremely high temperatures. There are also wells that do not have very high temperatures but have very high pressures, such as the wells drilled in low-temperature high-pressure salt zones in the GOM.

Rubber materials and high performance plastics are reaching their performance limits under the current HPHT environments, and the aggressive chemicals used in the HPHT environment are further exacerbating the situation.

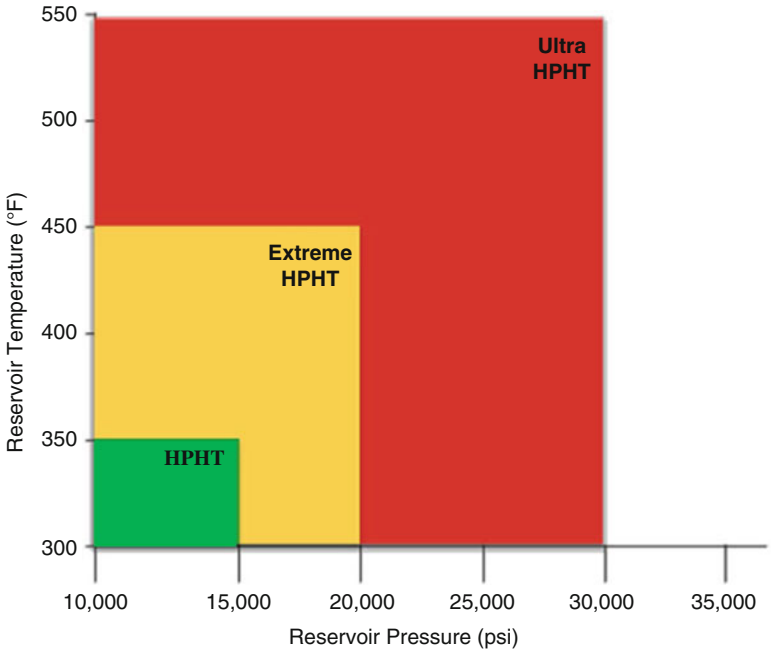

Fig. 10.13 HPHT designations defined by reservoir pressure and temperature [9]

10.4 Challenges for Rubber Materials in HPHT Applications

In a recent case history, a packer was used in extreme conditions—25,000 psi pressure and 500 ˚F temperature (Reference [20]). HPHT environment leads to significant degradation of material properties for both metallic and nonmetallic materials, and particularly to rubber and polymeric materials; thus, the available materials and designs that could meet the demanding harsh conditions in the wells were limited. It should be noted that the industry as a whole considers *seal performance* as the area in which the industry's number one technology gap exists (Reference [21]).

One main factor that limits the application of rubber and many polymeric materials to HPHT environments is the *significant degradation of their mechanical strength*, which include modulus, elongation at break, and fracture toughness. Figure 10.14 "Temperature effect on Rubber elongation at break," is derived from Fig. 10.1, and reveals the implicit relation between elongation to break and temperature. The elongation at break is reduced to ~35 % at 350 ˚F from 110 % at 70 ˚F. Similar dramatic decreases in modulus and fracture toughness are also observed. A lesser known parameter that can impact rubber applications under HPHT environment is that their bulk modulus can decrease substantially (see Fig. 10.15), which shows the temperature effect on rubber bulk modulus (References [22, 23]). The reduction of bulk modulus can substantially increase rubber/polymer compressibility and reduce seal capability, which in turn, will impact the capability of the packer element to seal, even if the seals could maintain integrity in the HPHT conditions.

These degradations lead to rubber deformation too easily, and the rubber becomes prone to fracture and extrusion during the setting process as well as when subjected to high differential pressure. As mentioned earlier, plastic or metallic backups are usually used to help contain rubber seals or rubber packer elements to improve their sealing performance. Under extreme HPHT conditions, metals and plastics lose substantial mechanical strength as well. Furthermore, rubber and polymeric materials may lose their thermal stability and chemical resistance, rendering them useless.

Some rubber and polymeric materials may function for a short time under HPHT conditions; however their material service longevity and reliability is in doubt for permanent packers and seals. Obviously, the demand for developing high performance rubber and polymeric materials for HPHT applications is high.

On the other hand, the limitations of acceptable rubber or polymeric materials at temperatures above 350 ˚F are partly due to the fact that their performance limits are determined by tests conducted in air. The test results from in-air tests are especially skewed for aging tests at temperature due to oxidation, which is usually not representative of downhole conditions. In an anaerobic environment, it is expected that rubber and polymeric material performance limits could be higher. *Developing test methods and related test standards for in-situ conditions for testing is needed*. For example, how to evaluate seals and packer service life in an accelerated laboratory test that can be representative of their downhole service life is needed. Lack of material data at HPHT conditions can reduce substantially the confidence level for HPHT tool designs.

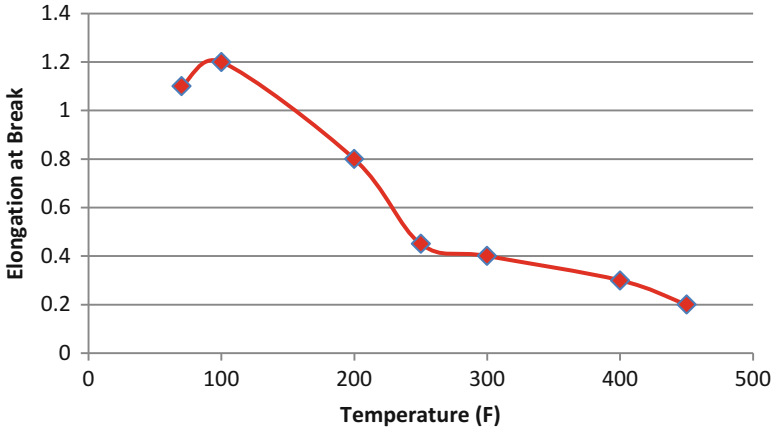

Fig. 10.14 Temperature dependency of elongation and break strength

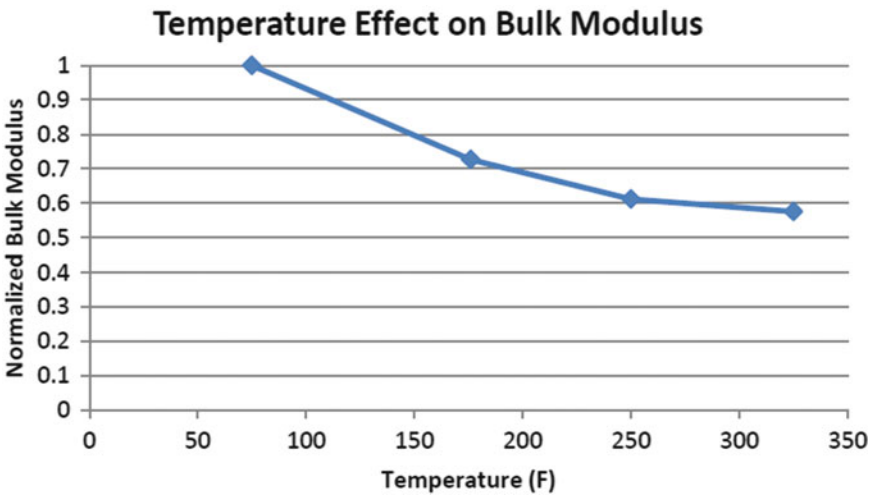

Fig. 10.15 Temperature effect on bulk modulus [22]

Physical tests of tools for HPHT applications are expensive and time consuming. Numerical simulations of tool performance at HPHT conditions should help to reduce dramatically the number of physical tests needed, and thus, could shorten product development time and reduce product development costs. In order to have high fidelity simulations of physical tests, material behaviors at HPHT conditions should be adequately characterized and modeled. During the life of permanent packers, they are subjected to load cycle from temperature changes and the rising and falling of pressure. Compression set, microdamage, and local fracture from one load cycle can influence the packer's performance in the next load cycle. *There is no material model that can accurately capture rubber and polymer behaviors at HPHT conditions*, such as compression set, damage accumulations, and change of stress–strain relation with the change of temperature. Because of the high pressure, tool components are subject to loading deflection which changes the radial clearances and extrusion gaps of sealing systems, and such dimensional changes must be considered in design process.

API is developing codes for HPHT equipment designs. The methods of accounting for uncertainty while not having a "huge" safety factor or load factor in the design and design-verification process is a major undertaking for the industry. See reference [24] for general discussions on the subject.

10.5 Some Current Approaches for HPHT Applications

Despite all the challenges for HPHT applications of rubber materials for sealing discussed in the previous section, the industry has been moving forward with many successes through development of new materials and new design concepts.

10.5.1 Nano Material Reinforced Rubber

One way to improve sealing components for downhole application under HPHT conditions is to improve sealing component material property using nano materials. There have been numerous attempts in this regard (see examples in [25–27] and references cited therein). However, substantial difficulty existed in making nanomaterial-reinforced rubber perform as expected in actual conditions. For example, in the case of nano carbon tuber (NCT)-reinforced rubber, the poor dispersion of NCT and poor bonding between NCT and rubber matrix led to nonuniformity in material performance and low fracture toughness.

It is reported in [28] that a multiwall carbon nanotube (MWNT) nanocomposite via "cellulation" to disperse MWNT homogeneously and a specialized "treatment process" to optimize the surface conditions of MWNT for optimum bonding with matrix was successfully developed in 2012. O rings made from this nano composite were reportedly capable of sealing at 45,000 psi and 500 °F (260 °C). In [29], a different approach; i.e., application of nano thin film to commercial rubbers, was taken to improve rubber's fluid compatibility, resistance to swell, and resistance to downhole chemicals.

10.5.2 Improved PEEK for HPHT Backup

Rubber materials suitable for HT applications (Reference [9]) include fluroelastomers such as Viton, and Aflas and FFKM materials such as Kalrez. They have good thermal stability and meet chemical resistance requirements. However, since they are rubber materials, their moduli are lowered at higher temperatures and are susceptible to extrusion through the annulus they are supposed to seal off. As discussed earlier, metallic or plastic backups are used typically to contain seal or packer elements by reducing extrusion gaps, preventing extreme deformation, and thus, improving their sealing capacity. PEEK is a commonly used thermoplastic material for plastic backup. Under HPHT conditions, plastic backups themselves frequently fail due to fracture or extrusion. So another approach to improve HPHT seal performance is to improve the design of backups through development of better thermoplastics and better geometry of the backups. One effort is to enhance PEEK's HPHT performance (Reference [10]). This enhanced PEEK was demonstrated to have the usual excellent resistances to downhole chemicals, with substantially increased high-temperature strength, stiffness, and creep resistance (see Fig. 10.16), which shows change in break strength at 450 °F in ISO fluids, Fig. 10.17, which shows the change in shear strength at 450 °F in ISO fluid, and Fig. 10.18, which shows the change in creep resistance.

The improved PEEK performance is also demonstrated in seal HPHT tests with FKM-O rings, which are concave design backup rings, made of the enhanced PEEK. The tests were conducted in a pressure vessel (shown in Fig. 10.19) with water-based control-line fluid (HT2), 40,000 psi pressure and 450 °F temperature for 48 h. The enhanced PEEK has been shown to dramatically lower the magnitude of extrusion, when compared to standard PEEK (see Fig. 10.20, which compares extrusion test results).

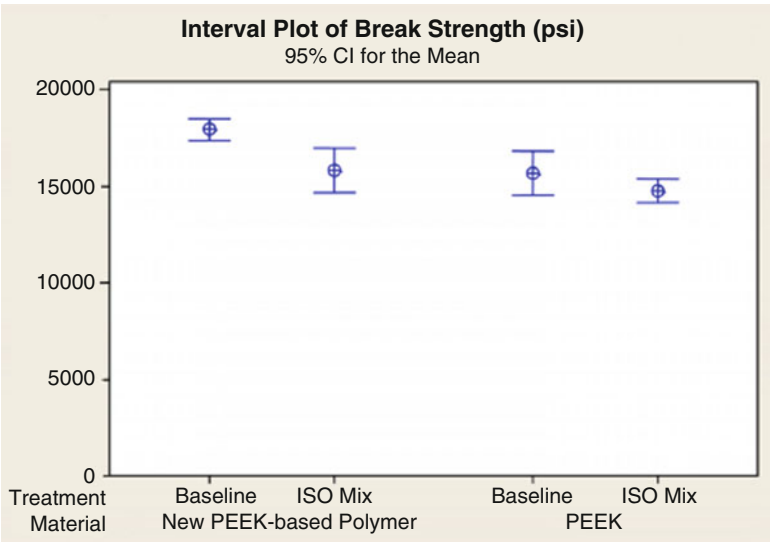

Fig. 10.16 Interval plot of break strength [10]

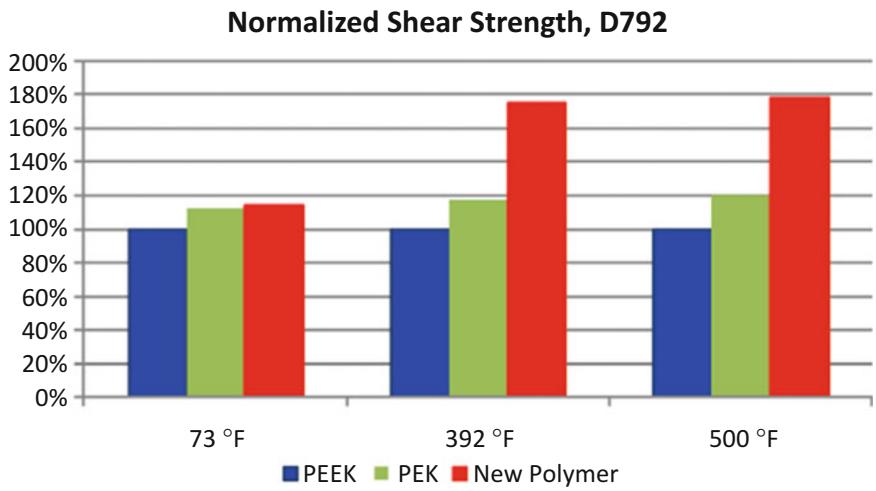

Fig. 10.17 Properties of thermoplastic materials [10]

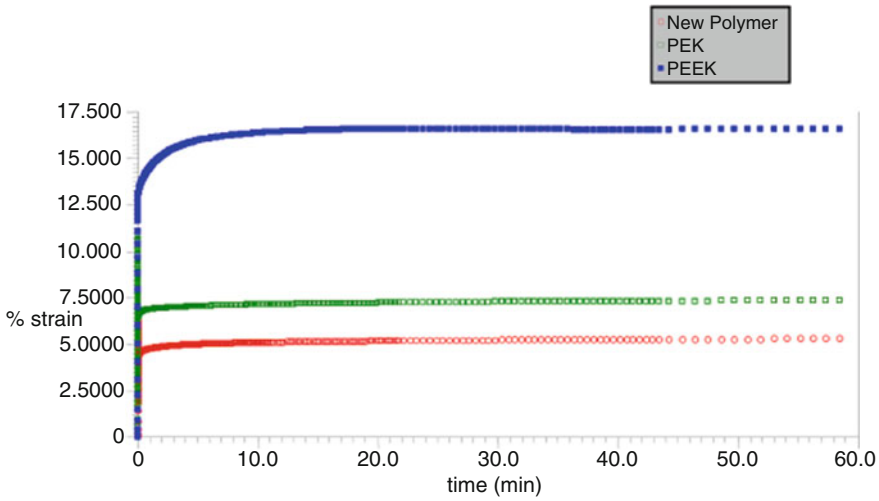

Fig. 10.18 Creep resistance of materials shown in Fig. 10.17 [10]

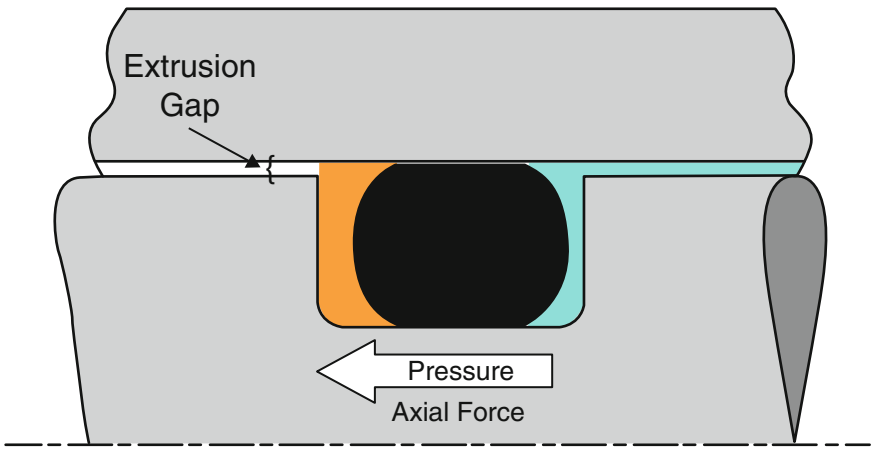

Fig. 10.19 O-ring test fixture used to evaluate concave backup ring [10]

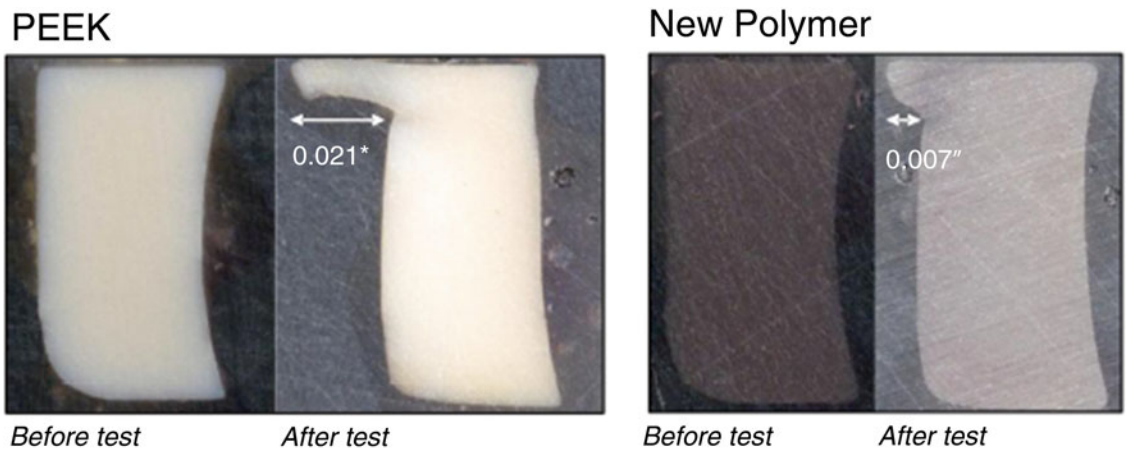

Fig. 10.20 Cross-section view of concave design back-up rings before and after testing [10]

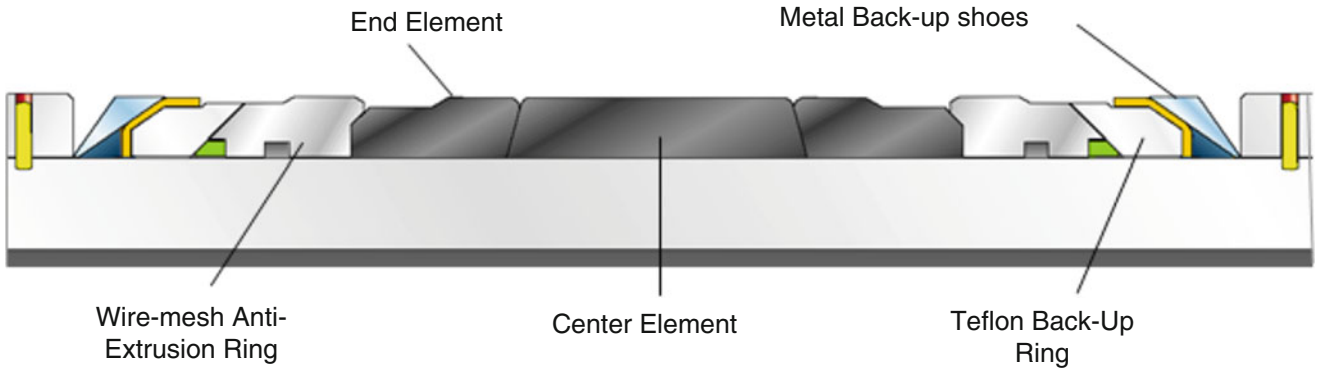

Fig. 10.21 HPHT packer element system [21]

10.5.3 Improved Packer Designs for HPHT Applications

The improvements in packer design for HPHT applications are similar to those made for seals; i.e., improvements in rubber materials, backup materials, and in geometric designs.

One example of a successful packer HPHT application was discussed in [30]. An HPHT element package for a 9-7/8-in. packer was designed (See Fig. 10.21 to see this successful HPHT packer element design), which included three Aflas elements, and an HPHT backup system. The backup system consists of two wire mesh anti-extrusion rings, two Teflon anti-extrusion rings, and two pairs of metal back-up shoes—one pair was made of brass, and another pair was made of low-alloy steel. This backup system allows for gradual stiffness change from elastomeric elements to steel backup shoes, and thus, it is compliant to component deformation. It provides full 360˚ support for Aflas elements and enables the elements to have the necessary HPHT sealing capability. The packer was tested at 450 ˚F and maximum differential pressure of 15,000 psi through temperature and pressure cycles. It was qualified for a 450 ˚F/15,000 psi rating and was successfully deployed in a North Sea HPHT well.

There are many ways to improve packer element design, and a different HPHT element design was proposed in SPE-159182 [31]. This element design is shown in Fig. 10.22 and resembles that of a molded seal with and integrated backup and element. The element is set via expansion of the element mandrel on a ramp. The rubber for the packer seal was perflouroelastomer (FFKM), which has good thermal stability and chemical resistance. Nickel alloy C-276 was chosen as the seal material carrier (element mandrel), because it has excellent ductility, corrosion, and fracture resistance.

This second packer element design was reportedly tested to seal 25,000 psi differentials from above and below at both 250 and 500 ˚F.

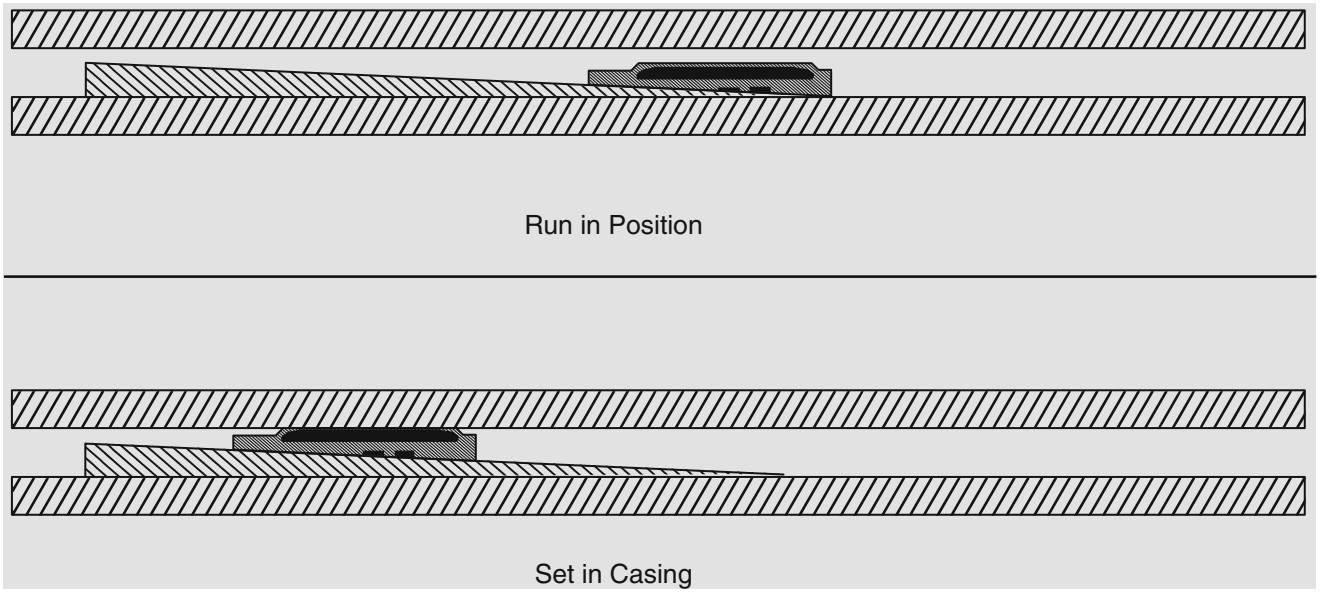

Fig. 10.22 Expanding packer sealing system [31]

10.5.4 Alternate Seal Design Concepts

So far, the main focus to improve seal designs for oil/gas well completion and production has been to develop high-performance rubber and thermoplastics for HPHT environments. The efforts in this regards have achieved many successes as illustrated in the previous sections.

However, some feels that a total shift of paradigm may be more effective and efficient, and that is to switch from rubber/metal seals to metal-to-metal seals. In this way the drastic degradation of material properties and low stiffness … at HPHT conditions can be alleviated significantly or eliminated. There are applications of metal-to-metal seals in many projects, but metal-to-metal seals have not been widely used for primary zonal isolation—a function that packers with rubber elements still dominate. Metal-to-metal sealing capability relies primarily on plastic deformation between the mating surfaces. There are some good reasons for the low acceptance of metal-to-metal seals, and these reasons include problems such as their effectiveness in the presence of debris, and their sealing capacity when there are grooves or scratches on one of the metal sealing surfaces; e.g., casing inside surface.

One patent pending technology [32] for expandable liner hanger without elastomer or with minimum rubber was proposed and was physically tested successfully. It was shown that metal-to-metal seal at packer element scale can be achieved, which is significantly less sensitive to high temperature when compared to rubber and polymeric seals. This resulted in a new product offering [33], VersaFlex XtremeGrip Expandable Liner Hanger System.

10.6 Concluding Remarks

To make robust, long service life downhole seals and packers under high pressure high temperature (HPHT) conditions, it is of high priority to develop new thermally stable rubbers for sealing elements and high strength thermoplastics for intermediate backups. In addition to material development, it is necessary to develop new test methods that can assess rubber and polymeric material behavior in realistic downhole HPHT conditions. It is also necessary to improve the material constitutive models that can capture rubber and polymer HPHT behavior accurately so that designs, design verification, and numerical simulations of product performance can be carried out with high confidence.

It is noted that challenges HPHT impose on oil/gas industry are many, and are not limited to nonmetallic material performance.

Despite tremendous challenges, the oil/gas industry has made steady progress in HPHT sealing technology through new material development and new concept designs.

Acknowledgement The author wishes to thank the organizers at 2015 Annual conference of Society of Experimental Mechanics for their invitation to the author to present at the conference. The author also wishes to thank Halliburton Management for permission to presentation this work.

Aflas is a registered trademark of the Asahi Glass Corporation.

References

1. B. Slay, S. Streich, W. Webber, Extreme oil field seal applications. HPE & Polymer for Oil Applications 2012, 17–18 April, 2012. (Aberdeen, Scotland, 2012)
2. D. Tapriyal, R. Enick, M. McHugh, et al., High pressure, high temperature equation of state density correlations and viscosity correlations. NETL-TRS-1-2012. (National Energy Technology Laboratory, 2012), p. 114
3. S. Streich, E. Webb, H. Roger, Successful applications of conventional elastomers in HPHT environments. Deep Gulf 2010, Galveston, Texas, 8–10 Dec 2010
4. Halliburton Company, www.halliburton.com
5. Schlumberger Limited, www.slb.com
6. Baker Hughes Incorporated, http://www.bakerhughes.com
7. H. Syed, Best practice in designing HP/HT cement plug, SPE 116698. 2008 SPE Annual Technical Conference and Exhibition, Denver, 21–24 Sept 2008
8. S.K. Lee, Y.S. Kim, et al., Lessons learned from highly deviated open hole completions in two HP/HT retrograde gas–condensate field using expandable liner hangers, external sleeve inflatable packer collars and swellable packers for zonal isolation, IADC/SPE114789. IADC/SPE Asia Pacific Drilling Technology Conference and Exhibit, Jakarta, Indonesia, 25–27 Aug 2008
9. D. Lehr, S.D. Collins, The HPHT completion landscape—Yesterday, Today and Tomorrow, SPE-170919. SPE Annual Technical Conference and Exhibition, Amsterdam, The Netherland, 27–29 Oct 2014
10. K. Drake, R. Callaway, New polymeric materials development for extreme environments. OTC-25304, Offshore Technology Conference, Houston, 5–8, 2014
11. S.M. Wilson, Feeling the heat, Can't stand the pressure? First Break **24**(5), 37–41 (2006)
12. J. R. McDermott, D. L. Martin, Completion design for deep, sour norphlet gas wells offshore, SPE 24772. SPE Annual Technical Conference and Exhibition, Washington, DC, 4–7 Oct 1992
13. R.M. Shivers, J.P. Brubaker, Development planning for the HPHT Erskine Field, SPE30370. Offshore European Conference, Aberdeen, Scotland, UK, 5–8 Sept 1995
14. K. Ravi, M. Bosma, L. Hunter, Optimizing the cement sheath design in HPHT shearwater field, SPE/IDAC79905. SPE/IDAC Drilling Conference, Amsterdam, The Netherland, 19–21, February 2003
15. I.A.C. Palmer, Jade North Sea HPHT development: innovative well design generates best in class performance. SPE/IDAC Drilling Conference, Amsterdam, The Netherland, 23–25, February 2005
16. A. Brown, C. Farrow, J. Cowie, The Rhum field: a successful HP/HT Gas subsea development (case history), SPE 108942. Offshore European Conference, Aberdeen, Scotland, UK, 4–7, September 2007
17. C.L. Palagi, et al., The development and production of Cascade and Chinook fields in Gulf of Mexico—an overview, OTC24156. Offshore Technology Conference, Houston, 6–9, 2013
18. C. Avant, B.K. Behera et al., Testing the limits in extreme well conditions. Oilfield Rev. **24**, 4–19 (2012)
19. G. DeBruijn et al., High pressure—high temperature technologies. Oilfield Rev. **20**(3), 4–17 (2008)
20. J. Doane, et al., A completion technology milestone—the first 25000 psi, 500 F packer Seal system, SPE 159182. SPE Annual Technical Conference and Exhibition, San Antonio, 8–10, October 2012
21. A. Shadravan, M. Amani, HPHT101—what petroleum engineers and geoscientists should know about high pressure high temperature wells environment. Energy Sci. Technol. **2012**(4), 36–60 (2012)
22. A. Zhong, et al., Performance evaluation of a large bore expandable liner hanger for field operations in the Gulf of Mexico, OTC 25995, the Offshore Technology Conference, Houston, Texas, USA, 4–7, May 2015 (accepted)
23. W.K. Moonan, N.W. Tschoegl, Effect of pressure on the mechanical properties of polymers. 2. Expansivity and compressibility measurements. Macromolecules **16**(1), 55–59 (1983)
24. H.B. Skeels, What well completions can learn from drilling in HPHT environments. 2010 IADC Well control Europe Conference, Aberdeen, 13–14, April 2010
25. US patent 8283402
26. P. Pourafshary, et al., Priority assessment in development of nanotechnology in upstream petroleum industry, SPE126101. SPE Saudi Arabia Section Technical Symposium and Exhibit, AlKhobar, Saudi Arabia, 9–11, May 2009
27. S. Kapusta, L. Balzano, P. Riele, Nanotechnology applications in oil and gas exploration and production, IPTC 15152. International Petroleum Technology Conference, Bangkok, Thailand, 7–9, February 2012

28. M. Ito, et al., Game changing technology with MWNT nanocomposites for HPHT and hostile environment sealing in enhancing oil recovery, SPE 156347. SPE International Oilfield Nanotechnology Conference, Noordwijik, The Netherland, 12–14, June 2012
29. J.C. Welch, et al., Nano-enhancement of elastomers for improved downhole barrier, SPE 147409. SPE Deepwater Drilling and Completions Conference, Galveston, 20–21, 2012
30. R. Innes, et al., New 9 7/8" HPHT permanent packer with new backup system provides North Sea operator with an effective solution for worn casing, OTC 21066. Offshore Technology Conference, Houston, 3–6 May 2010
31. J. Doane, G. Deng, S. Collins, A completion technology milestone—the first 25000 psi 500 F Packer Seal system, SPE 159182. SPE Annual Technical Conference and Exhibition, San Antonio, 8–10 October 2012
32. A. Zhong, D. Moller, Improved Hanger, PCT/US2012/071171 (2012)
33. Halliburton Company, http://www.halliburton.com/en-US/ps/completions/well-completions/liner-hangers/VersaFlex-XtremeGrip.page?node-id=hfqel9w0#

Chapter 11
Full-Field Strain Imaging of Ultrasonic Waves in Solids

C. Devivier, F. Pierron, P. Glynne-Jones, and M. Hill

Abstract Lamb waves are well-known guided waves propagating in thin plates. They are often considered as a convenient tool for non-destructive testing but one of the major challenges consists in measuring them [1]. Several techniques allow one to do this. First, ultrasonic transducers provide point measurement of the vibration amplitude. However, this is only a point measurement and does not provide very much spatial resolution even if several transducers are used simultaneously. Shearography on the other hand does provide a map of surface slopes that can for instance be related to the presence of a delamination. However, this technique does easily not allow for time-resolved measurements. Finally, the most versatile is certainly scanning laser Doppler vibrometry (SLDV) which provides excellent temporal resolution. The spatial resolution arises from the scanning of the surface. This takes time and requires periodic loading with stable excitation over the duration of the scan. More details about these techniques can be found in [1].

Keywords Lamb waves • Deflectometry • High speed imaging • Ultrasonic testing • Vibrations

11.1 Introduction

Lamb waves are well-known guided waves propagating in thin plates. They are often considered as a convenient tool for non-destructive testing but one of the major challenges consists in measuring them [1]. Several techniques allow one to do this. First, ultrasonic transducers provide point measurement of the vibration amplitude. However, this is only a point measurement and does not provide very much spatial resolution even if several transducers are used simultaneously. Shearography on the other hand does provide a map of surface slopes that can for instance be related to the presence of a delamination. However, this technique does easily not allow for time-resolved measurements. Finally, the most versatile is certainly scanning laser Doppler vibrometry (SLDV) which provides excellent temporal resolution. The spatial resolution arises from the scanning of the surface. This takes time and requires periodic loading with stable excitation over the duration of the scan. More details about these techniques can be found in [1].

This article proposes an alternative based on deflectometry, a full-field slope measurement method.

11.2 Experimental Set-Up

Deflectometry relies on the principle of deforming mirrors. If a grid pattern is reflected off a flat shiny surface, any variation of the local slope of this mirror-like surface, caused for instance by bending loads or flexural waves, will cause a local shift in the grid image. By calculating the full-field displacement of the grid image using spatial phase-shifting algorithms (here, a windowed discrete Fourier transform with triangular weighting), the two components of the slope field of the mirror-like test specimen can be imaged. More details can be found in [2]. It has been shown that this technique could resolve micro-radians. From the slopes, numerical integration provides the deflection and numerical differentiation leads to the curvatures. Here, the curvatures have been multiplied by half the plate thickness to obtain surface strains according to thin plate theory.

The experimental set-up is shown in Fig. 11.1. The specimen is a piece of flat mirror glass lightly fixed into a vice, to hold it but not clamp it. A piezoelectric transducer is bonded on its back face to provide excitation at 43.3 kHz. This frequency was selected as it provided a larger response of the plate (close to a resonance). A 2 mm pitch cross-hatched grid was printed on a piece of A3 paper, bonded onto a metallic plate and positioned opposite the tested specimen. An ultra-high speed

C. Devivier • F. Pierron (✉) • P. Glynne-Jones • M. Hill
Engineering and the Environment, University of Southampton, Southampton, UK
e-mail: f.pierron@soton.ac.uk

S. Bossuyt et al. (eds.), *Residual Stress, Thermomechanics & Infrared Imaging, Hybrid Techniques and Inverse Problems, Volume 9*, Conference Proceedings of the Society for Experimental Mechanics Series, DOI 10.1007/978-3-319-21765-9_11

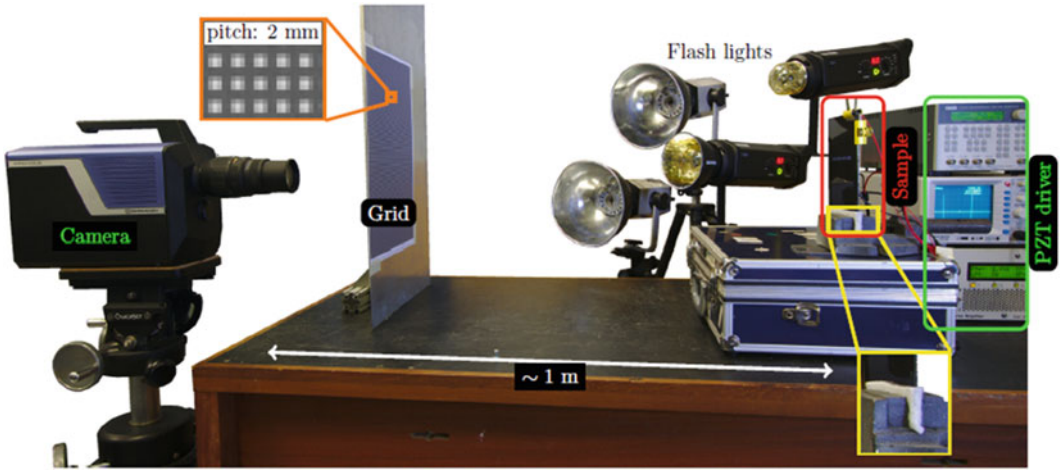

Fig. 11.1 Schematic of the inertial impact test

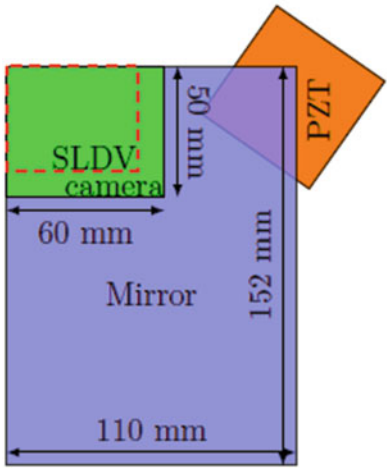

Fig. 11.2 Dimensions of the specimen (thickness: 1.9 mm), field of view and schematic of excitation

Shimadzu HPV-2 camera was used to record images at 1 μs interframe time and flash lights were used to illuminate the grid during the short acquisition time. The camera has a spatial resolution of 312 × 260 pixels^2. Each period of the grid is sampled by 5 pixels providing a field of view of 60 × 50 mm^2, as shown in Fig. 11.2.

To provide a check of the results, scanning laser Doppler vibrometry (SLDV) was used over a grid of 15 × 17 points, which were then linearly interpolated to a grid of 40 × 50 points similar to what deflectometry provides. The deflection was then differentiated once to provide slopes, and twice to derive curvatures, hence surface strains.

11.3 Results

Figure 11.3 shows the two components of the slope field obtained through deflectometry, scanning laser Doppler vibrometry and finite element modelling. There is an excellent correlation between the two measurement techniques, both in terms of spatial wavelengths and amplitudes of the waves, though it is clear that the spatial resolution of deflectometry is far superior to that of SLDV. The simulation provides very similar spatial wavelengths but far larger amplitudes but this is not so surprising as material properties input into the model were only approximate, in particular damping. In any case, the objective here was not to develop an accurate FE model but just to provide an additional sanity check.

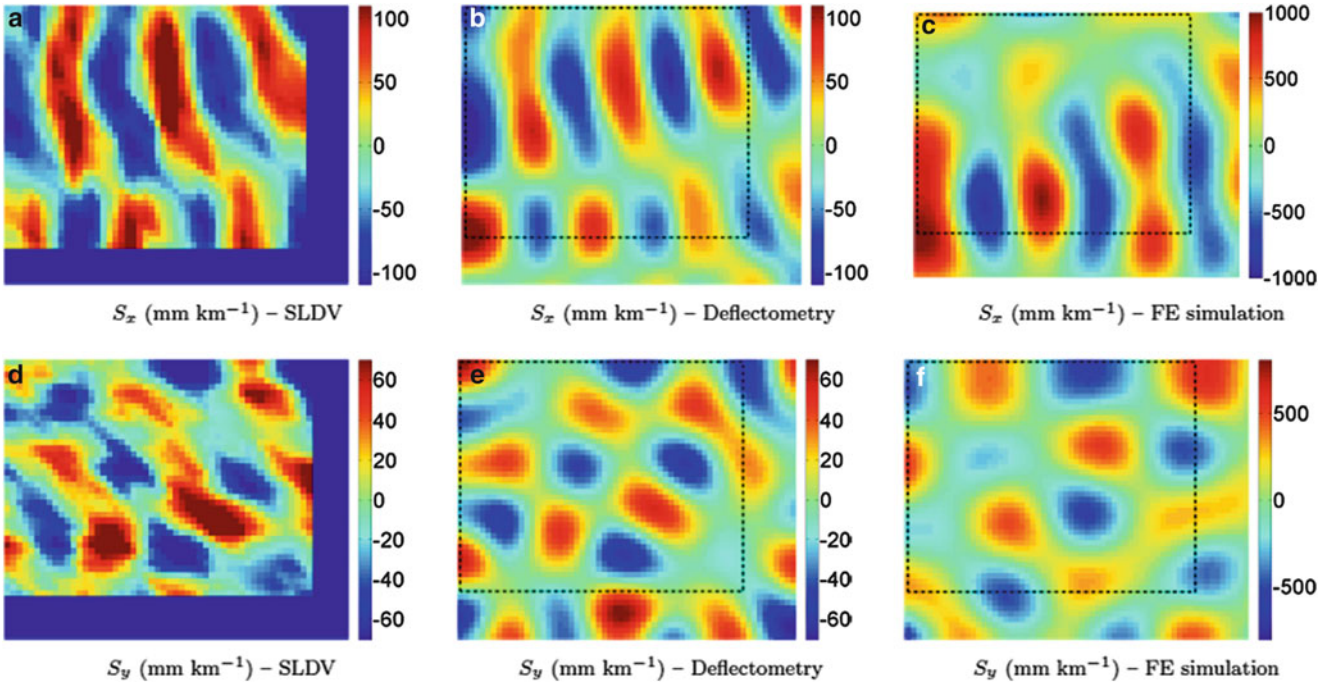

Fig. 11.3 Comparison of the horizontal and vertical slopes between scanning laser Doppler vibrometry, deflectometry and finite element simulation for the mirror sample excited at 43.3 kHz

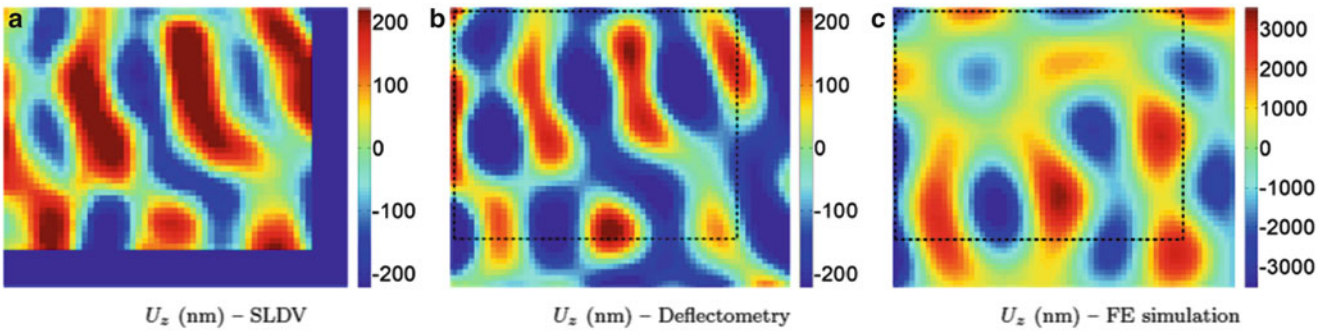

Fig. 11.4 Comparison of the out-of-plane displacements between scanning laser Doppler vibrometry, deflectometry and finite element simulation for the mirror sample excited at 43.3 kHz

Figure 11.4 shows the deflection derived from the measured slopes for deflectometry, directly measured from SLDV and output from FE results. Again, an excellent match is found between the two techniques, with the same distance to the FE model. It is worth noticing here the very small amplitude of these vibrations, about 400 nm peak to peak. A noise floor study has shown that the limit of resolution of deflectometry in the present configuration was about 0.5 nm, so much smaller amplitudes could be measured (higher excitation frequencies, or smaller excitation currents).

Finally, surface strains are provided in Fig. 11.5. This is where the superiority of deflectometry is obvious. The SLDV map is degraded by double spatial differentiation and though the orders of magnitude of the strains are the same, the spatial resolution is really degraded. Much larger scan grids could have been used but the current measurement of $15 \times 17 = 255$ data points already takes 5 min, so a 40×50 grid of 2000 points would take nearly an hour. And the double spatial differentiation would still amplify measurement noise.

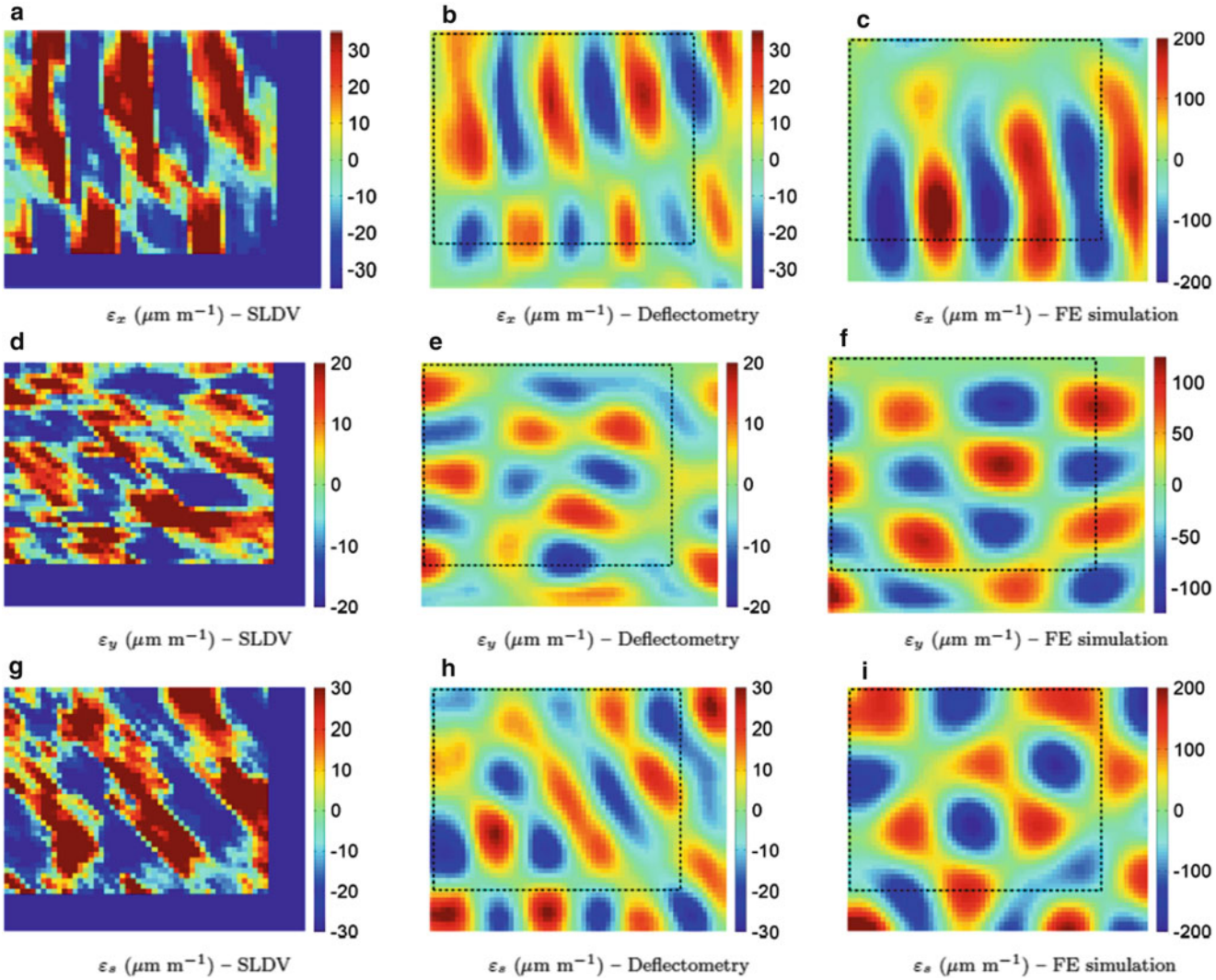

Fig. 11.5 Comparison of the horizontal, vertical and shear strains between scanning laser Doppler vibrometry, deflectometry and finite element simulation for the mirror sample excited at 43.3 kHz

11.4 Conclusion

The present paper reports for the first time the use of deflectometry to image Lamb waves at the surface of a plate. This technique relies of specular reflection of a grid pattern onto the smooth and shiny surface of a test panel. This technique was shown to provide higher quality data than scanning laser Doppler vibrometry in a much shorter time as it is a one shot full-field technique, so no scanning is required. Coupled to ultra-high speed imaging, the technique provides the unique capability of simultaneous temporal and spatial resolution, allowing to follow transient waves for instance. The main current limitation of deflectometry is that it requires a specularly reflective surface and that it is for the moment limited to flat panels. Work is underway to address these limitations. The next step is to couple these measurements with recently published procedures to either identify pressure distributions from plate surface response [3] (for aero-elastic problems for instance) or detect defects [4].

References

1. W. Ostachowicz, M. Radzieński, P. Kudela, 50th anniversary article: comparison studies of full wavefield signal processing for crack detection. Strain **50**(4), 275–291 (2014)
2. C. Devivier, F. Pierron, M. Wisnom, Damage detection in composite materials using full-field slope measurements. Compos. A: Appl. Sci. Manuf. **43**(10), 1650–1666 (2012)
3. A. Berry, O. Robin, F. Pierron, Identification of dynamic loading on a bending plate using the virtual fields method. J Sound Vib. **333**(26), 7151–7164 (2014)
4. C. Devivier, F. Pierron, M.R. Wisnom, Impact damage detection in composite plates using deflectometry and the virtual fields method. Compos. A: Appl. Sci. Manuf. **48**, 201–218 (2013)

Chapter 12
Acoustic Emission Analysis in Titanium Grade 5 Samples During Fatigue Test

C. Barile, C. Casavola, G. Pappalettera, and C. Pappalettere

Abstract In this paper fatigue test results are presented for titanium grade 5 specimens subjected to uniaxial sinusoidal loading. Specimen were previously machined in order to obtain notches of known size and geometry. The sample was equipped by a couple of strain gages to monitor the deformation of the sample during the test. At the same time also a couple of piezoelectric sensors were attached on the surface of the sample in order to allow detection of acoustic signals generated inside the material during the whole test and obtain linear localization of the emission source. A data acquisition system allowed to record, during the whole test, information about the acoustic activity in terms of cumulative hits number recorded by each sensor, localization of the acoustic event, energy of the event and the associated waveform. Results of the fatigue behaviour of the analyzed material beside the acoustic emission track are presented and discussed.

Keywords Titanium grade 5 • Acoustic emission • Crack propagation • Fatigue

12.1 Introduction

Nowadays Titanium grade 5 (Ti6Al4V) is a material of great interest in many fields. It has a very good strength-to-density ratio and a very high resistance to corrosion. Due to these reasons it is very appealing for the aircraft industry which is spending many efforts on the introduction of new materials that can allow to get lighter structural elements. This would lead in fact to a reduction in fuel consumption and, as a consequence, to costs and greenhouse emissions reduction [1–3]. Titanium grade 5 is also highly compatible from a biological point of view and this occurrence enlarges its applications also to other fields like biomechanical ones where it can be successfully used for manufacturing prostheses. However still few data on fatigue characterization of titanium alloy are presented in literature [4–7] and much more insight is required to fully understand fracture mechanisms in this material. Having this in mind, in this paper, results in terms of acoustic emission (AE) recorded during sinusoidal uniaxial fatigue testing of Ti grade 5 are presented. Acoustic Emission (AE) is a phenomenon which takes place when a sample or a structure is subjected to an external stimulus: mechanical, thermal, thermo-mechanical etc. A release of energy follows the structural modifications occurring inside solid materials that appears in form of a stress wave. These acoustic signals can be related to several sources i.e., motion of dislocations, crack nucleation, crack propagation etc. The acoustic emissions technique detects stress waves produced during the transient release of energy in materials subjected to heat treatments such as local annealing [8–11] or mechanical stresses [12–14], it is a non-invasive technique that can act both in active and in passive way. AE are detected in the ultrasonic range of frequencies by using high sensitivity piezoelectric sensors having the resonance frequency close to the frequency of the ultrasound signal to be monitored. In this work, in fact, a live monitoring of acoustic emission behavior during the whole fatigue test was performed.

12.2 Materials and Methods

Experimental tests were carried out on eight Ti grade 5 samples with rectangular cross section 40×4 mm^2 and 200 mm long. Two notches were cut in the middle of the samples, symmetrically with respect to the median line, in order to identify a precise location for monitoring both crack nucleation and propagation. Notches were obtained by means of laser cutting and had a radius of curvature $r = 5$ mm.

C. Barile • C. Casavola (✉) • G. Pappalettera • C. Pappalettere
Dipartimento di Meccanica, Matematica e Management, Politecnico di Bari, Viale Japigia 182, Bari 70126, Italy
e-mail: katia.casavola@poliba.it

S. Bossuyt et al. (eds.), *Residual Stress, Thermomechanics & Infrared Imaging, Hybrid Techniques and Inverse Problems, Volume 9*, Conference Proceedings of the Society for Experimental Mechanics Series, DOI 10.1007/978-3-319-21765-9_12

Fatigue tests were carried out using a Instron servo-hydraulic machine equipped with a 200 kN loading cell. A sinusoidal loading was applied to the samples having a loading ratio $R = -1$. The loading frequency was set to 3 Hz. Two strain gages with a 3 mm base length were placed near the notches and their signals were acquired by the StrainSmart 5000 acquisition system. The acquisition frequency was set to 10 Hz. Also two piezoelectric sensors were placed symmetrically to the transverse median line crossing the two notches (Fig. 12.1). Acoustic emission events are identified by a set of shots (*hits*) [15]. The hits represent the number of times the voltage generated from the PZT sensor overcomes a given threshold. In this work the threshold voltage was fixed, after preliminary test to $V_{th} = 45$ dB. This value was good to eliminate most of the noise and at the same time to detect the acoustic events of interest. Every shot is characterized by an intensity value proportional to the energy of the detected event. Two Mistras Pico-sensors (Table 12.1 [16]) were placed on the surface of the specimen; the two sensors were about 80 mm far apart one from each other (Fig. 12.1) and at the same distance from the notches. The difference in the time of arrival recorded at the two sensors allow to calculate the longitudinal position of the acoustic event that is to say to get the d_{1y} and d_{2y} distances of the event from the two sensors. Figure 12.2 shows a detail of the instrumented specimen.

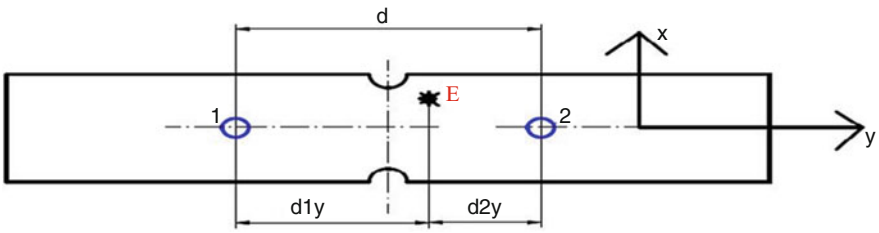

Fig. 12.1 Schematic of acoustic sensor locations on the specimen

Table 12.1 Main characteristics of the Pico Sensor

Peak sensitivity	54 dB
Operating frequency range	200–750 kHz
Resonant frequency	250 KHz
Temperature range	−65 to 177 °C
Size	5 × 4 mm

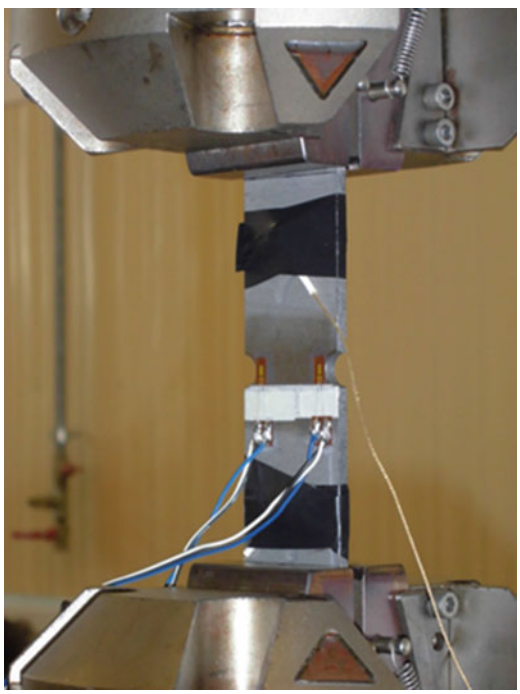

Fig. 12.2 Ti grade 5 specimen equipped with strain gages and PZT acoustic emission detectors

The experimental plan is defined so that three specimen were tested at ±18 kN corresponding to a maximum nominal stress $\Delta\sigma_0 = 300$ MPa. Three specimen were tested at ±15 kN corresponding to a maximum nominal stress $\Delta\sigma_0 = 250$ MPa. One specimen was tested at ±11 kN corresponding to a maximum nominal stress $\Delta\sigma_0 = 183.4$ MPa.

12.3 Results and Discussion

In Table 12.2 are summarized the main working parameters and the results obtained during the fatigue tests. Also indication about the occurrence of rupture of the specimen after the reported number of cycles is indicated. In Fig. 12.3 is reported the Wöhler diagram corresponding to the tested specimens.

In Fig. 12.4 the typical behavior observed for the cumulative number of hits is displayed. Data are referred to the specimen number 4 subjected to ±15 kN, however analogous trends were observed for all the tested samples. Both sensors display almost the same trend. The cumulate number of hits increases almost constantly in the first part of the test while it tends to a constant by going on with the experiment. Figure 12.5 displays the 3D histogram plot representing the Hits distribution as a function of the time and of the linear y position of the detected events. The graph is referred to the sample 4, however, similar features were found in all the other samples. As it can be inferred by looking at the graph there is a position where acoustic events appear to be concentrated. This position corresponds to the location where notches are presents. In this region the motion of the dislocations is higher due to the higher stress concentration and this leads to higher acoustic activity. Activity appears to be concentrated in the first part of the test while it is strongly reduced starting from about $16{\cdot}10^4$ s from the beginning of the test (about 50,000 cycles). Acoustic activity keeps low for about the same amount of time and then it starts to increase again, once more in correspondence of the region where notches are present. Final rupture occurs a few cycles after

Table 12.2 Working parameter and results obtained in fatigue tests on Ti grade 5 samples

Specimen #	Load (kN)	Number of cycles	R	Applied stress $\Delta\sigma_0$ (MPa)	$\Delta\varepsilon$ (με)	Frequency (Hz)	Broken samples
1	±18	518,367	−1	300	1550	3	Yes
2	±18	538,476	−1	300	1500	3	Yes
3	±11	5,221,715	−1	183,4	860	3	No
4	±15	1,079,732	−1	250	1220	3	Yes
5	±15	5,228,503	−1	250	1200	3	No
6	±18	723,921	−1	300	1490	3	Yes
7	±15	4,345,696	−1	250	1280	3	Yes

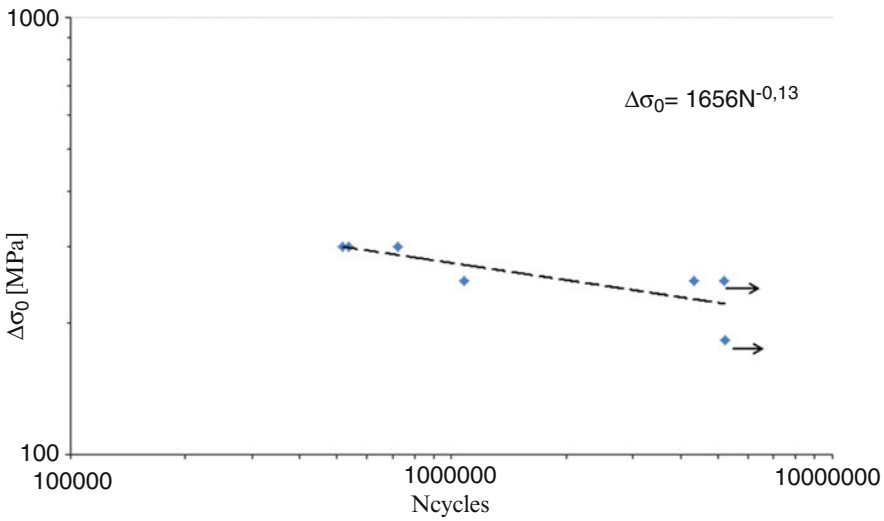

Fig. 12.3 $\Delta\sigma_0$ vs. N_{cycles} diagram obtained by testing Ti grade 5 specimen subjected to uniaxial sinusoidal loading

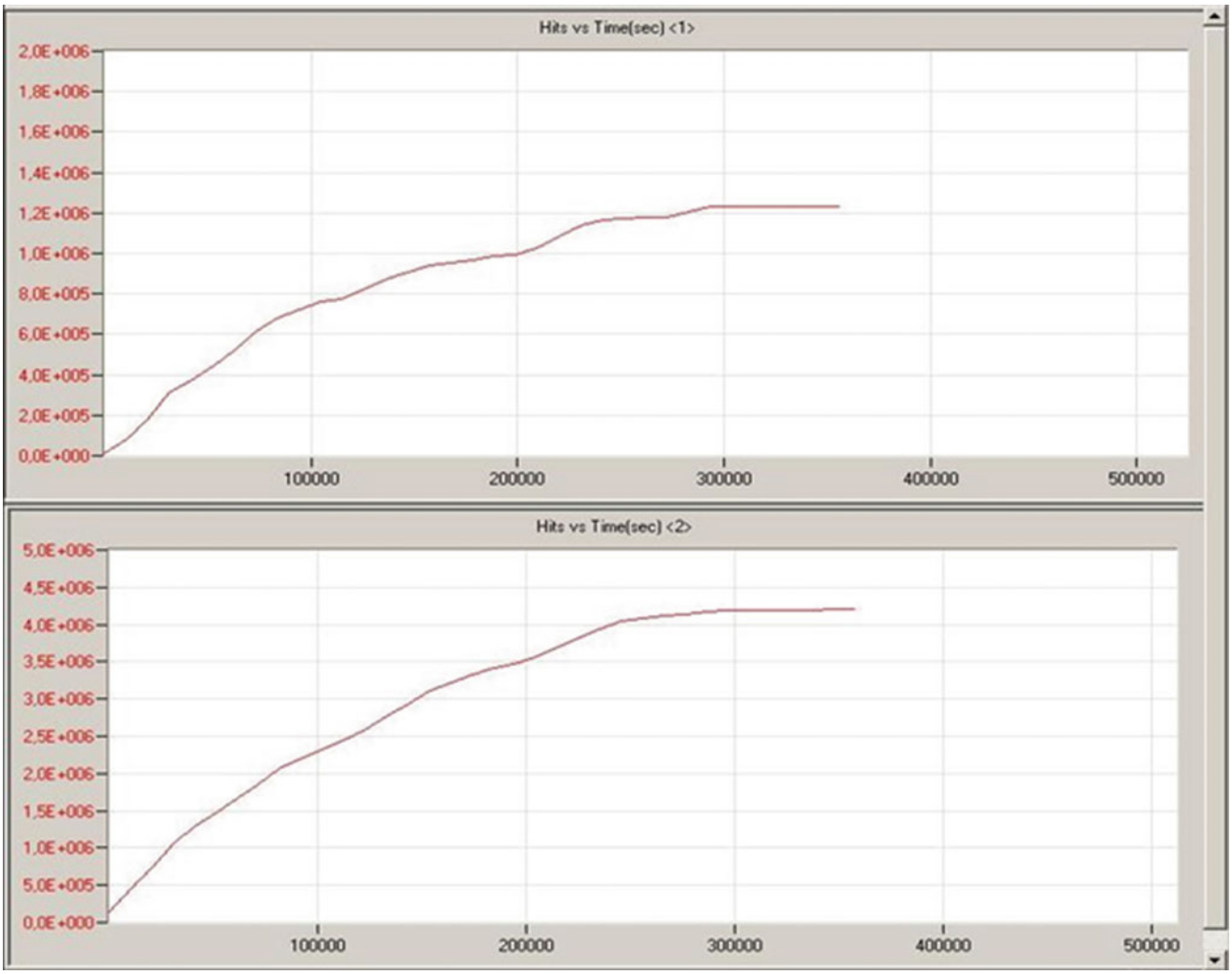

Fig. 12.4 AE activity recorded by the two sensors placed on the specimen: (*up*) Hits VS. Test time, sensor 1; (*down*) Hits vs. Time, sensor 2

Fig. 12.5 3D histogram plot Hits vs. Test Time vs. Y position recorded for one of the tested specimens

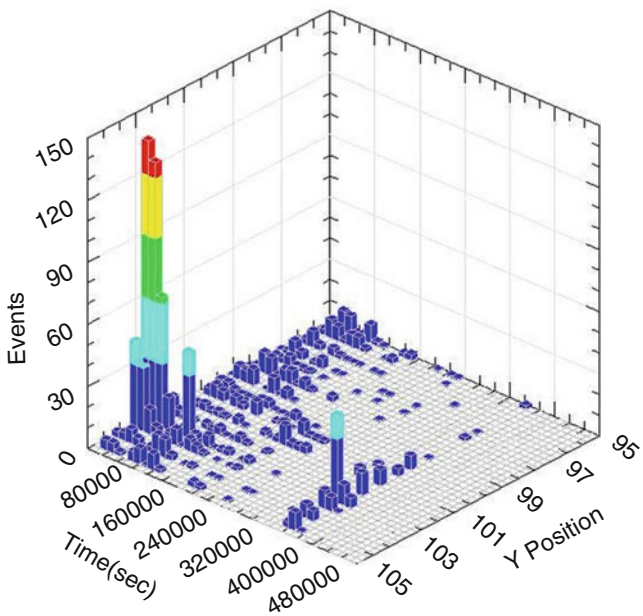

the restart of the acoustic activity. In view of this observation the AE technique appears to be reliable in detecting the position of the cracks and in providing some information about motion dislocations and crack propagation in Ti grade 5 [17–20].

12.4 Conclusions

In this paper crack propagation during fatigue tests was analyzed. The samples subjected to uniaxial loading fatigue tests all displayed a well detectable acoustic activity. Most of the acoustic events are concentrated in the region of higher stress i.e., next to the notches. Data recorded provide precise information about the crack localization, the direction of propagation, also some indication about the motion of the dislocations and crack propagation are inferable.

References

1. C. Casavola, L. Lamberti, C. Pappalettere, F. Tattoli, A comprehensive numerical stress—strain analysis of laser beam butt-welded titanium compared with austenitic steel joints. J. Strain Anal. Eng. Design **45**(7), 535–554 (2010)
2. C. Casavola, C. Pappalettere, G. Pluvinage, Fatigue resistance of titanium laser and hybrid welded joints. Mater. Design **32**(5), 3127–3135 (2011)
3. C. Casavola, C. Pappalettere, F. Tursi, Residual stress on Ti6Al4V hybrid and laser welded joints. Conference proceedings of the society for experimental mechanics series, vol. 8, pp. 111–118, 2011
4. C. Casavola, F. Tattoli, C. Pappalettere, Static and fatigue characterization of titanium alloy welded joints. Proceedings of the SEM annual conference and exposition on experimental and applied mechanics 2007, vol. 3, pp. 1400–1411 (2007)
5. C. Casavola, C. Pappalettere, Discussion on local approaches for the fatigue design of welded joints. Int. J. Fatigue **31**(1), 41–49 (2009)
6. C. Casavola, C. Pappalettere, F. Tattoli, Experimental and numerical study of static and fatigue properties of titanium alloy welded joints. Mech. Mater. **41**(3), 231–243 (2009)
7. C. Casavola, R. Nobile, C. Pappalettere, A local strain method for the evaluation of welded joints fatigue resistance: the case of thin main-plates thickness. Fatigue Fract. Eng. Mater. Struct. **28**(9), 759–767 (2005)
8. C. Barile, C. Casavola, G. Pappalettera, C. Pappalettere, Feasibility of local stress relaxation by laser annealing and x-ray measurement. Strain **49**, 393–398 (2013)
9. C. Barile, C. Casavola, G. Pappalettera, C. Pappalettere, Preliminary analysis for a new approach to relieve residual stresses by laser heating. Conference proceedings of 11th YSESM youth symposium experimental solid mechanics, Brasov, Romania, May 30th–June 2nd, 2012
10. C. Barile, C. Casavola, G. Pappalettera, C. Pappalettere, Discussion on the thermal field produced by laser annealing for the residual stress relaxation. Conference proceedings of new trends in fatigue and fracture, pp. 22–30, Moscow, Russia, May 13th–16th, 2013
11. R.K. Miller, P. McIntire, *Acoustic emission testing,* Nondestructive Testing Handbook Ed., 2nd ed., American Society for Nondestructive Testing, vol. 5, pp. 275–310, 1987
12. T.F. Drouillard, T.G. Glenn, Production acoustic emission testing of braze joint. J. Acoust. Emiss. **1**(2), 81–85 (1985)
13. C. Barile, C. Casavola, G. Pappalettera, C. Pappalettere, Acoustic emission analysis of aluminum specimen subjected to laser annealing. Residual Stress, Thermomechanics & Infrared Imaging, Hybrid Techniques and Inverse Problems **8**, 309–315 (2014)
14. Y.H. Pao, *Theory of acoustic emission*. Elastic waves and non-destructive testing of materials, AMD20, American Society of Mechanical Engineers, pp. 107–128, 1978
15. M. Enoki, T. Kishi, S. Kohara, *Determination of microcracking moment tensor of quasi-cleavage facet by AE source characterization*. Progress in acoustic emission III. Proceedings of the eighth international acoustic emission symposium. The Japanese Society for Non-Destructive Inspection, pp. 763–770, 1983
16. www.mistrasgroup.com
17. K. Ono, Trends of recent acoustic emission literature. J. Acoust. Emiss. **12**, 177–198 (1994)
18. D.A. Dornfeld, Application of acoustic emission techniques in manufacturing. NDT Int. **25**, 259–269 (1992)
19. C. Barile, C. Casavola, G. Pappalettera, C. Pappalettere, *Hybrid thermography and acoustic emission testing of fatigue crack propagation in Aluminum Samples*. Conference proceedings of the society for experimental mechanics series, **66**(5), 247–252 (2015)
20. C. Barile, C. Casavola, G. Pappalettera, C. Pappalettere, *Consideration on Acoustic Emissions in Ti Grade 5 During Fatigue Test*. Proc. Eng. **109**, 320–326 (2015)

Chapter 13
Analysis of High-Frequency Vibrational Modes Through Laser Pulses

G. Lacidogna, S. Invernizzi, B. Montrucchio, O. Borla, and A. Carpinteri

Abstract The authors are currently doing fatigue tests, by using sonotrodes working at 20 kHz, and compression tests on solid samples of rock materials. The specimens are monitored by laser sources focused on spots of the external surface. The main purpose is to identify in the crystal lattice mechanical oscillations in a frequency range higher than the Acoustic Emission (kHz) and comprised between MHz and THz. Such vibrational modes in the THz regime will be the signature of developing anomalies in piezoelectric or piezomagnetic materials, such as neutron and/or alpha particle emissions, and compositional changes. Moreover, it is also known that laser current pulses should be effective in exciting vibrational modes in the high-frequency range in conductive samples.

A photodetector connected to an usual oscilloscope, measuring the intensity of reflected light, detects vibrations in the range from MHz up to few GHz. To reduce the limitations in the ability to acquire high frequency signals, additional experiments are planned exploiting the Raman effect. Through the scattered light spectrum analysis, capable of detecting radiation in the visible light field, it should be obtained information on the intermolecular interactions that during solicitations induce resonant vibrations in the field of THz.

Keywords Raman spectroscopy • Electromagnetic emission • Neutron emission • Ultrasonic vibrations • Laser measurements

13.1 Introduction

This paper presents the results obtained through different experimental tests which are aimed to examine the structural, chemical and thermal behavior of particular rock specimens. These tests are linked to previous experimental analyses, in which energy emissions in brittle material samples under mechanical loading were evaluated in detail. Indeed, when catastrophic failures develop in quasi-brittle materials such as granitic rocks, acoustic emissions (AE) [1–9] and electromagnetic radiation (EM) [10–19] together with bursts of neutron emission (NE) arise.

If the first two effects are well-known, specifically in Geophysics with regard to rock fractures, volcanic eruptions and earthquakes, neutron emissions are quite unexpected, at least until some years ago when the first studies started to describe them [20–24]. Such emissions are due to piezonuclear reactions depending on the modality of energy release. For specimens characterized by a large size and/or slenderness, the high probability of neutron emission at the failure time is directly connected to the relatively high energy release. Therefore, being NE clearly connected to fracture, they can be considered, as AE and EM, an important precursor of critical events [18, 19].

The production of neutrons could be caused by resonance phenomena of nuclei occurring when the state of the matter is excited by EM waves whose frequency ranges between Hz and MHz, up to microwave frequencies. As remarked also by Widom et al. [25, 26], subsequently to micro-cracking, the elastic energy release involves ultrasonic vibrations, measurable with AE instrumentation, which are converted into electromagnetic oscillations; the latter are able to accelerate the condensed matter allowing the emission of neutrons and neutrinos.

In this paper the authors describe the experimental results obtained by examining different rock specimens under various loading conditions, in order to analyze the matter vibration in a very high frequencies field, up to THz. In particular, two analyses are performed: with respect to calcite and quartz crystal. During compression tests, variations of crystal lattice

G. Lacidogna (✉) • S. Invernizzi • O. Borla • A. Carpinteri
Department of Structural, Geotechnical and Building Engineering, Politecnico di Torino,
Corso Duca degli Abruzzi 24, Torino 10129, Italy
e-mail: giuseppe.lacidogna@polito.it

B. Montrucchio
Department of Control and Computer Engineering, Politecnico di Torino, Corso Duca degli Abruzzi 24, Torino 10129, Italy

S. Bossuyt et al. (eds.), *Residual Stress, Thermomechanics & Infrared Imaging, Hybrid Techniques and Inverse Problems, Volume 9*, Conference Proceedings of the Society for Experimental Mechanics Series, DOI 10.1007/978-3-319-21765-9_13

structure are evaluated by means of Raman spectroscopy. The specimens, which are represented as small bricks with a volume of about 4–10 cm^3, are investigated exploiting a system of measurement mainly composed by an oscilloscope, a photodiode, a monochromator, and a laser ray.

On the other hand, with respect to cylindrical "Luserna Stone" samples ($\phi = 50$ mm; $H = 93$ mm), a sonotrode is used to transfer mechanical vibrations with a frequency of 20 kHz. In this case, the purpose is twofold: on one hand, to assess the heat produced in the rock during the test through a thermographic camera; on the other hand, to examine how much energy emission—AE, EM, NE—occurs as a consequence of a micro or macro cracking. More detailed information on the presented experimental procedures are reported in the following sections.

13.2 Compression Tests on Calcite Samples by the MTS Machine

Preliminary tests on prismatic specimens are performed to evaluate the structural behavior of pure calcite. The aim of the tests is twofold: on one hand, the acquisition of the load–displacement curve from which information regarding the stiffness, the peak load and the post-peak behaviour up to the complete fragmentation of the specimens, are acquired; on the other hand, to perform a Raman spectroscopy of the fragments to evaluate possible variations from the original crystalline structure. Such tests are executed at the Materials & Structures Laboratory of the Politecnico di Torino, whereas the Raman spectroscopy at the "G. Scansetti" Laboratory of the University of Turin.

The specimens are prisms of calcite having an average area of about 4.4 cm^2 and a height of about 1.4 cm. Such rocks are subjected to uniaxial compression test to assess information regarding their ultimate strength and post-peak behaviour (Fig. 13.1). To this aim, a MTS servo-hydraulic press having a maximum capacity of 500 kN is used. The specimens are arranged with their top and bottom surfaces in contact with two rigid plates, by means of which the press transmits the load. The machine is also equipped with control electronics to perform tests in displacement control.

In particular, two different types of test are developed: the first one (Test N. 1) is aimed to evaluate the peak load and the post-peak behaviour as the specimen is gradually pulverized.

In this case, a preload with a velocity of 0.1 mm/s is set up, until a total final load of 1 kN is reached. After that, the test is carried on with a velocity equal to 0.001 mm/s. Once obtained the full stress–strain curve, during which the specimen has been crushed down to a heap of fragments (Fig. 13.2a), the load is increased once again (Fig. 13.2b). Finally, the test is stopped when a load about sixteen times higher than the peak load is reached (Fig. 13.2b). In the diagram of Fig. 13.2b the slope of the load versus displacement curve coincides with the testing machine stiffness.

In the second case (Test N. 2), defined by the same preload, the test is driven with a velocity of 0.02 mm/s. The press is stopped when in the post-peak branch the load tends to zero, getting only the specimen fragmentation and not its pulverization. Detailed information regarding these tests are reported in Fig. 13.3.

From the load vs. displacement diagrams represented in Figs. 13.2a and 13.3, a sufficiently ductile behavior of these small specimens can be seen. The maximum loads to which the material can be subjected are 28.8 kN and 6.4 kN, respectively in the first and in the second case. Therefore, it is also interesting to note the wide dispersion of the compressive strength values of the calcite, ranging from about 65 MPa in the first case to about 14 MPa in the second one.

Fig. 13.1 Calcite rock sample subjected to compression under monotonic displacement control

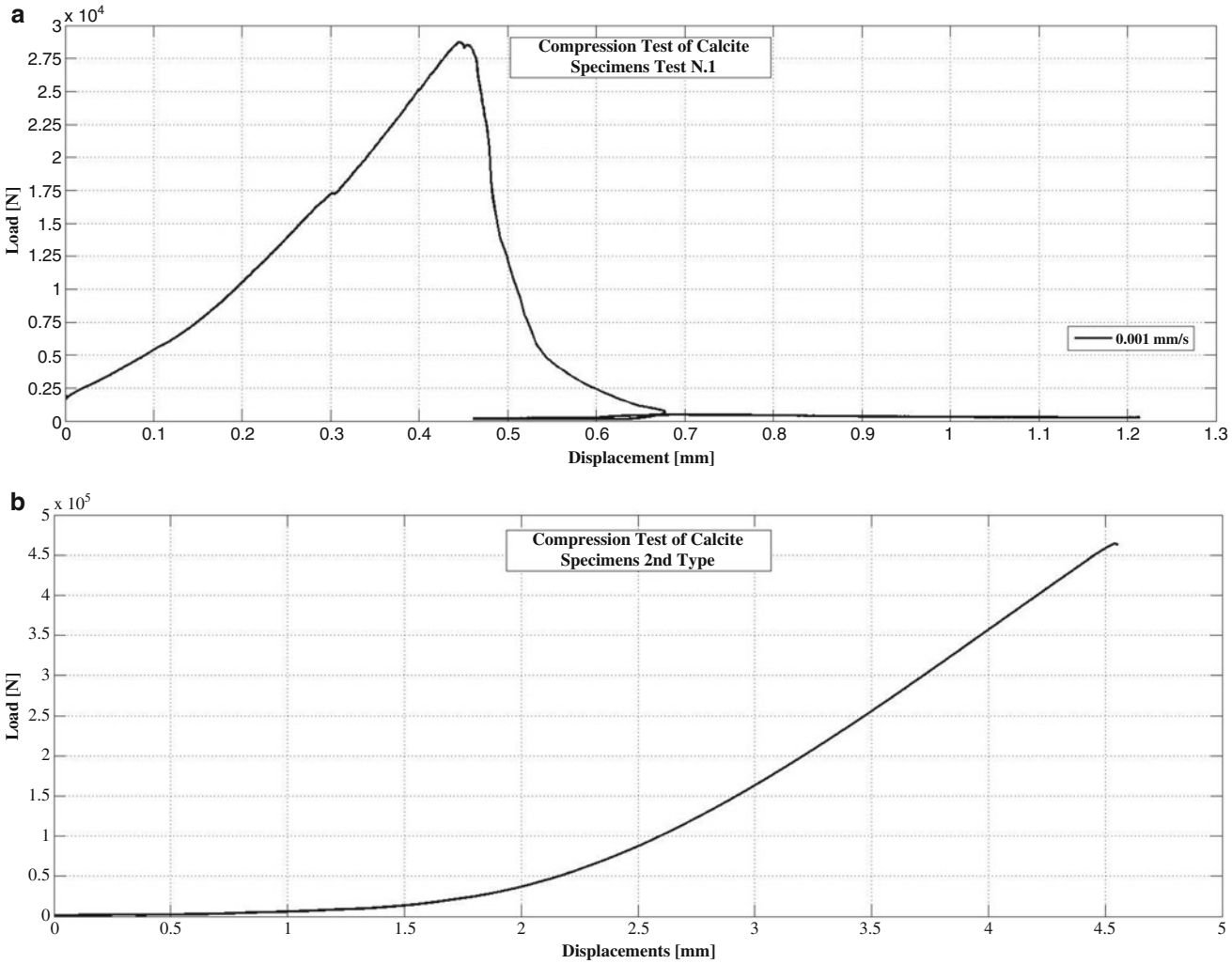

Fig. 13.2 Load–displacement diagram of calcite specimen, Test N. 1. Load–displacement curve during fragmentation (**a**). Load–displacement curve during pulverization (**b**)

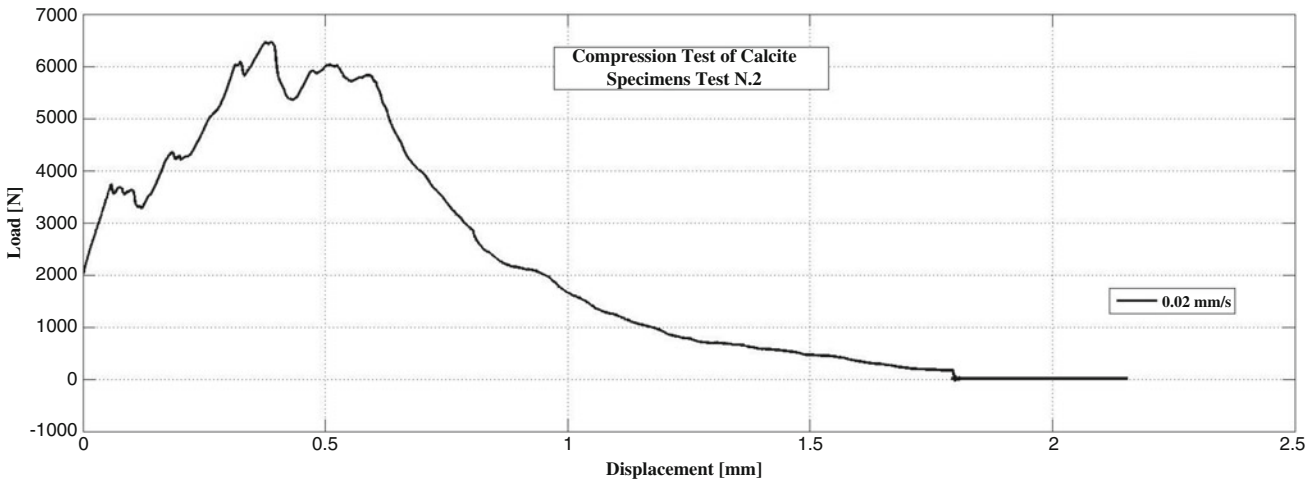

Fig. 13.3 Load–displacement diagram of calcite specimen, Test N. 2. Load–displacement curve during fragmentation

13.3 Raman Spectroscopy

Raman spectroscopy is based on inelastic scattering of light by matter. Monochromatic light scattered by matter contains radiations with frequencies different from the exciting light. This effect, predicted by Smekal (1923), was demonstrated by Raman (1928) and named after him [27].

A Raman spectrum is the plot of light intensity expressed as arbitrary units, or counts, versus the frequency of scattered light (i.e., Raman vibrational modes) expressed in frequency units (wave-numbers $\tilde{\nu} = \nu/c = 1/\lambda$ in cm^{-1}, where c is the velocity of light).

The Rayleigh scattered frequency (i.e., light-source wave-number) lies at 0 cm^{-1}, whereas Raman frequencies are expressed as relative wave numbers, or Raman shifts (Fig. 13.4).

In Raman technique, spectra frequencies correspond to the energy levels of different molecular vibrations and are independent from the wavelength of the laser beam. A spectrum comprises one or more bands which correspond to the vibration energies of the molecules of the analyzed sample; these in turn are related to the nature of the bonding. The most important molecular vibrations include stretching and bending modes, stretching frequencies being generally higher than bending frequencies.

In order to obtain precise references for the test in compression on calcite specimens, some measurements with Raman spectroscopy before and after their fracture are carried out. The analyses are performed at the Interdepartmental Center "G. Scansetti" of Università di Torino where a Micro-Raman device is installed.

The equipment is composed by an optical petrographic microscope (Olympus BX41), a motorized table sample holder, a spectrometer (Horiba Jobin Yvon HR800), a CCD detector, two polarized lasers (HeNe red—$\lambda = 633$ nm, 20 mW; Nd solid state green—$\lambda = 532$ nm, 250 mW) together with a set of interference filters, a console managing the laser and a PC workstation equipped with Labspec 5 software.

In order to ensure the repeatability in the measurements pre and post fracture, on the three orthogonal faces of the specimens parallel lines of different colors (red, blue and black) are drawn (Fig. 13.5a). In total on a single intact sample thirty Raman spectra are acquired (Fig. 13.5b). No differences in terms of frequency shift between the Raman spectra on the three analyzed

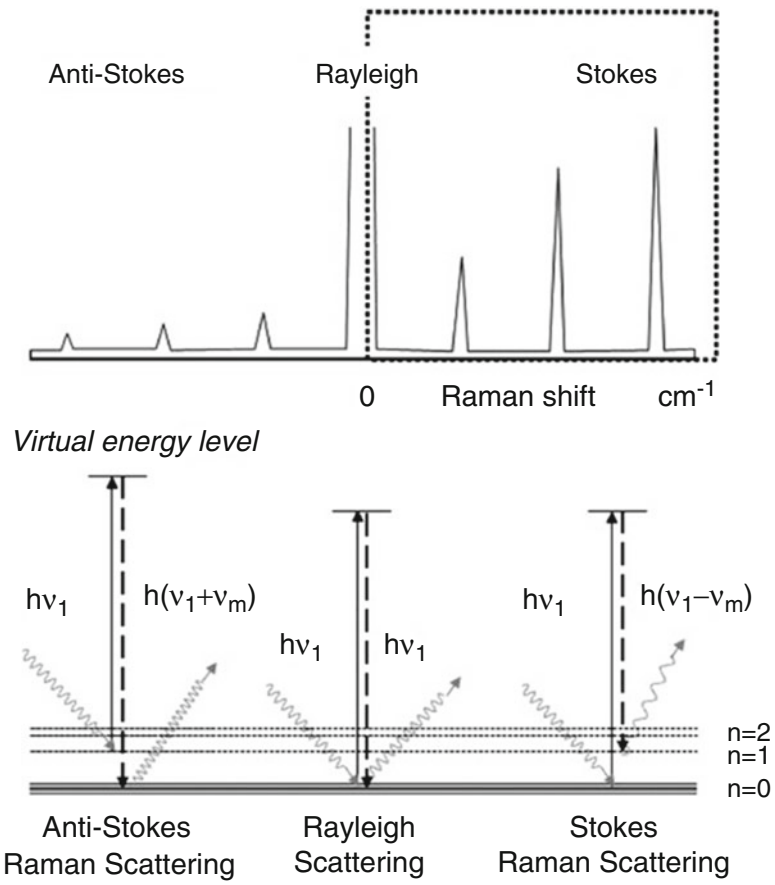

Fig. 13.4 Raman spectra frequencies and energy levels corresponding to different molecular vibrations

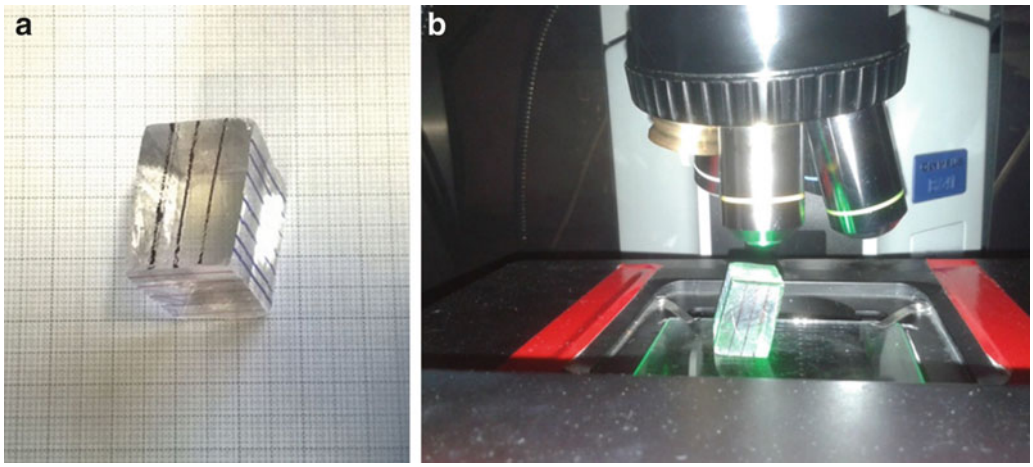

Fig. 13.5 Calcite specimen with the orthogonal faces painted by different colors lines (**a**). Raman spectroscopy on the same calcite sample (**b**)

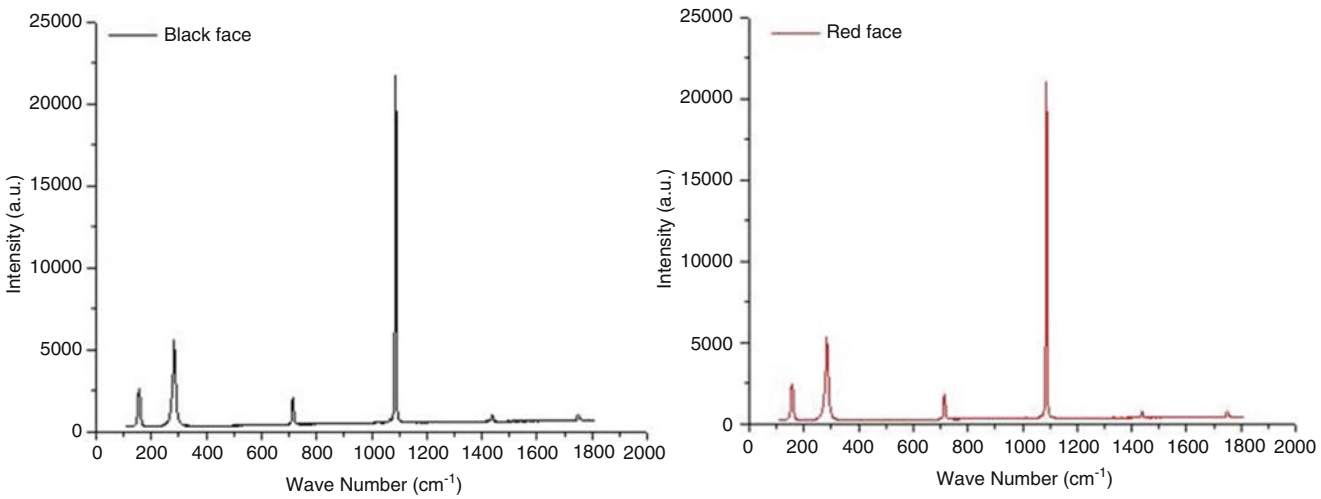

Fig. 13.6 Average Raman spectrum of two perpendicular faces (*black* and *red*) of calcite specimen

faces are found, while differences with regard to the intensity of individual peaks can be observed. Four main Stokes peaks of the Raman spectrum of calcite, located approximately at 156, 283, 715 and 1087 cm^{-1} can be clearly identified (Fig. 13.6).

After the previously described fragmentation tests, new analyses aimed to find any variance in the Raman spectra are developed.

As it was previously mentioned, at the end of the compression Test N. 2, the sample is divided into numerous small fragments; only pieces attributable to the red and black faces can be efficiently examined. On the black face, perpendicular to the direction of the mechanical stress, the intensity of the main peak decreases of about 21.6 % compared to the initial value, as demonstrated by Fig. 13.7. Whereas, considering the red face, parallel to the direction of the mechanical stress, the peak value increases of about 14.1 % (see Fig. 13.7). As the peaks are related to a very specific vibration mode of the considered chemical species, such modes proves to be inhibited by the pressure on a face (black) and amplified on the other (red). As regards the analysis on the powders coming from the specimen of the compression Test N. 1, in general a reduction of the peaks of about 20 % is found.

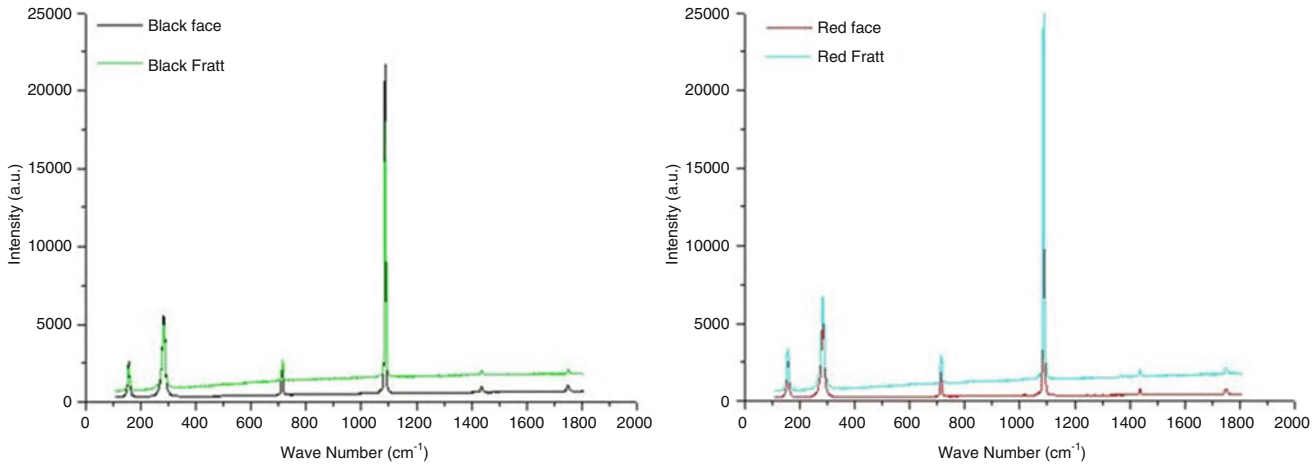

Fig. 13.7 Comparison of average Raman spectra for the *black* and *red* face, before and after the failure test

13.4 Compression Tests on Crystal Samples by a Manual Press Machine

Further tests on calcite and quartz rocks are planned in order to verify the properties of the materials during a monotonic compression test. In this case, the procedure considers a specimen subjected to an increasing load, applied gradually by means of a manual hydraulic press machine. During the loading steps the sample is monitored by an apparatus specially designed to perform Raman analysis.

In each different test stages, developed in a completely dark environment, the transparent crystal sample is crossed by a conveniently filtered laser ray which is originally pointed towards a monochromator able to stop all the electromagnetic waves, with the exception of the one characterized by a specific wave length. Such wave is, finally, caught by a photodiode and processed by a connected oscilloscope (Figs. 13.8 and 13.9). The monochromator is designed so that its properties can be easily modified to allow the transit of waves having different frequencies. In this way, the entire system functions as an adjustable wave receiver.

Initially, the measurement devise is set up so that only the laser red ray, defined by a wave length of about 636 nm, can be observed by the instrumentation. Subsequently, its properties are modified in order to find the frequency of further waves generated as a consequence of the interaction between the laser and the sample (*Raman Scattering*).

In the case of calcite rock, when the external load is zero, the oscilloscope allows to identify a maximum signal corresponding to a wave length of about 652.2 nm. Such value unequivocally describes the characteristics of the inspected material, as demonstrated by Raman himself [28, 29]. Starting from this configuration, the uniaxial compression test is executed. With the increase of the load, the scattered light is described by an intensity different from the original and, in particular, it decreases after each load step, as shown in Fig. 13.10.

In the case of quartz rock, the oscilloscope identifies a maximum signal when the reference wave length of the monochromator is equal to about 650 nm. Also in this case, such signal decreases as the external load increases; then, when the action is suddenly removed, the initial signal is restored after a few seconds (Figs. 13.11a and 13.12). On the contrary, if the reference wave length of the monochromator is set up higher, e.g., 652 nm, without external load the measured amplitude is clearly lower than the previous case. Nevertheless, after the loading process, an increase of the amplitude can be observed (Fig. 13.11b).

The observed phenomena can be easily explained by considering the scheme of Fig. 13.13: two curves describe the same sample in the unloaded and loaded condition. Let us suppose to fix on the monochromator the value λ_1 which determines the maximum amplitude of the signal when the sample is unloaded (point *a* on the first curve); by applying the load, the second curve is considered and, therefore, the amplitude suddenly decreases (point *b* on the second curve). On the contrary, let us suppose to fix the value $\lambda_2 > \lambda_1$ for which, in the unloaded case, the amplitude proves to be smaller than the previous case (point *c* compared to point *a* on the first curve). In this case, when the load is applied, the amplitude increases (point d on the second curve).

Therefore, starting from the experimental results, such simple scheme suggests that the frequency (wave length), which unequivocally describes in the unloaded case the material as demonstrated by Raman spectroscopy, undergoes a downward (upward) shift after the application of a compression load.

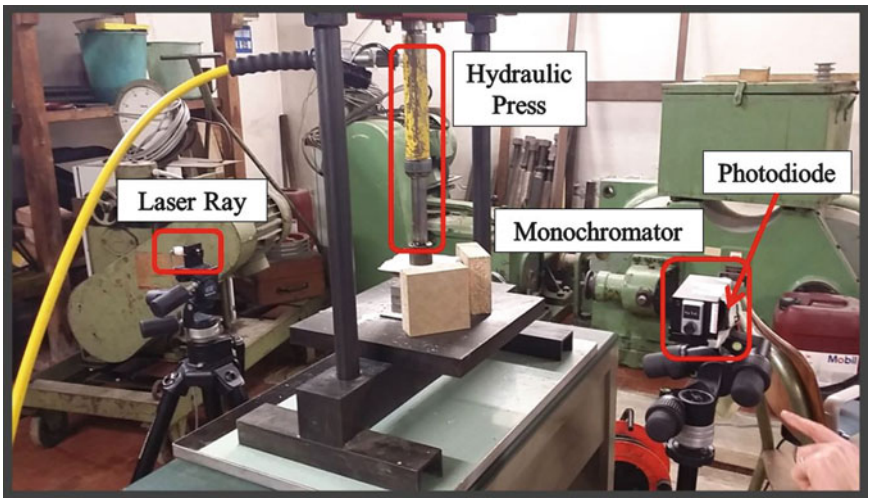

Fig. 13.8 Picture of the experimental test

Fig. 13.9 Calcite specimen between steel plates and crossed by a laser ray

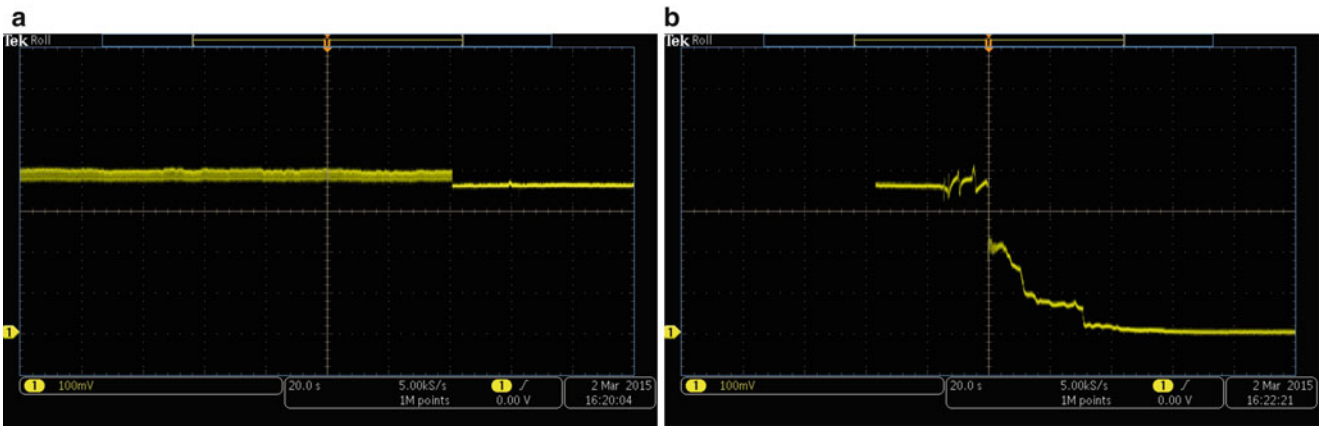

Fig. 13.10 Calcite sample. Unloaded condition (**a**). During the loading process, each step corresponds to a negative jump of the signal amplitude (**b**)

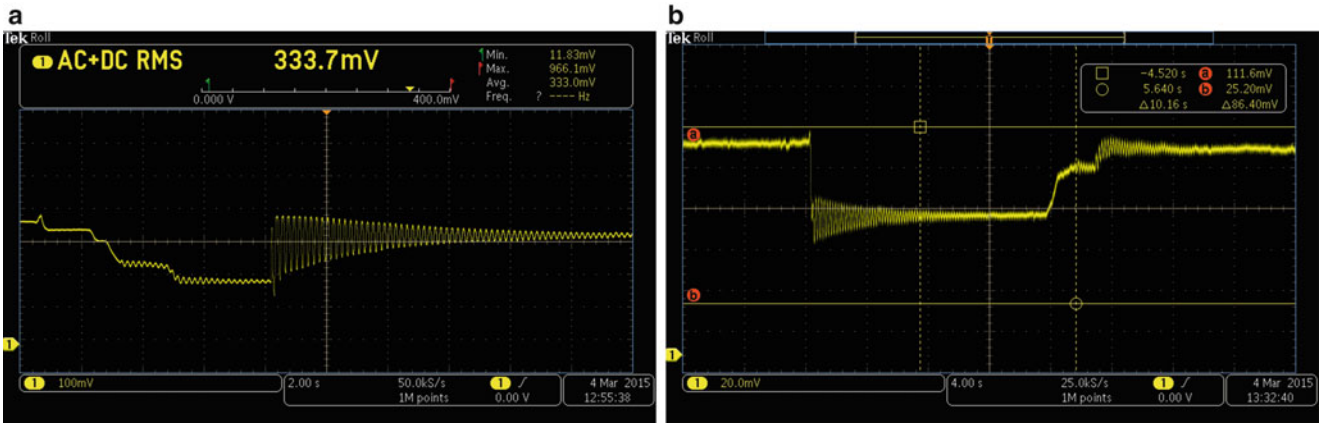

Fig. 13.11 Quartz sample. After the loading process, the initial condition is restored as the load is removed ($\lambda = 650$ nm) (**a**). After the unloading process, the initial condition is restored by some load steps ($\lambda = 652$ nm) (**b**)

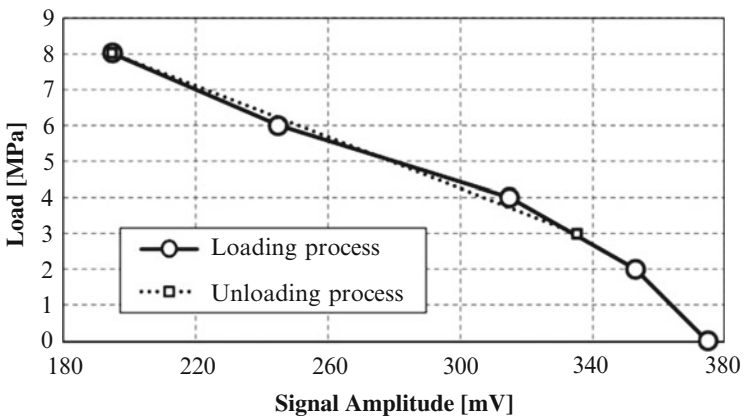

Fig. 13.12 Quartz sample. Decrease of the signal amplitude with the increase of the external pressure ($\lambda = 650$ nm)

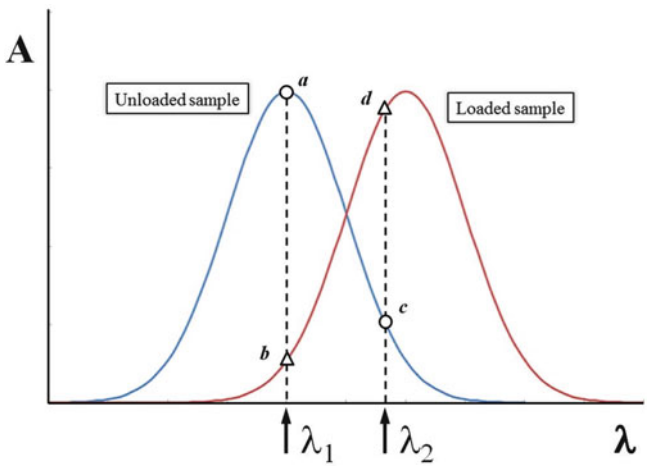

Fig. 13.13 Frequency shift in a rock specimen subjected to compression and examined by Raman spectroscopy

This phenomenon of reducing frequencies by increasing the compressive applied stress is already known in the structural mechanics [30]. This deduction shows as the matter is subject to the same mechanical laws both at the nanoscale, as well as the scale of the structures.

13.5 Ultrasonic Tests Performed by a Sonotrode

Preliminary tests are devised to validate the instrumentation and the experimental procedure which is aimed to excite rock specimens with a specific high frequency and examine if micro or macro cracks arise in the material, combined with emission of neutrons.

With this aim, the evaluation of the ultrasonic vibration of rock specimens, which are rigidly connected to an high intensity ultrasonic horn, is performed at LADISPE Laboratory of Politecnico di Torino.

The ultrasonic horn (Bandelin HD 2200, Figure N) is a sonotrode working at 20 kHz, able to guarantee a constant amplitude whose range is comprised between 10 and 100 %. It is composed by an inner generator which converts electrical energy to 20 kHz ultrasounds and by a transducer able to commute the energy into mechanical vibrations defined by the same frequency. As the rock specimens are fixed to the horn, such frequency is supposed to be transmitted to the same sample without significant variations.

The oscillations of the specimens are caught by using a Lasiris 635 nm—10 mW, class III, laser ray and a Tektronix oscilloscope, that delivers powerful features as maximum sample rate equal to 10 GSa/s, coupled with a photodiode. This latter component works as an optical sensor able to recognize a specific electromagnetic wave length, and to change it into an electric signal, which is processed by the oscilloscope. The electromagnetic wave intercepted by the photodiode is represented by the laser ray reflected on the sample surface. Therefore, during the ultrasonic test, the specimen vibrations are measured by the oscilloscope which analyzes the variation of the electric signals produced by the photodiode (Fig. 13.14).

In this case, the investigated sample is a cylindrical body made of “Luserna Stone” (Gneiss), having a circular section of about 50 mm and a total height of 93 mm. Such element is designed so that its shape allows the resonance exactly in the frequency range of the sonotrode, based on measured density and speed of sound propagation.

The output data provided by the oscilloscope are reported in Fig. 13.15. In the first, the laser ray is switched off and the obtained information are referred to a background level; the second image describes the ongoing test and the other main

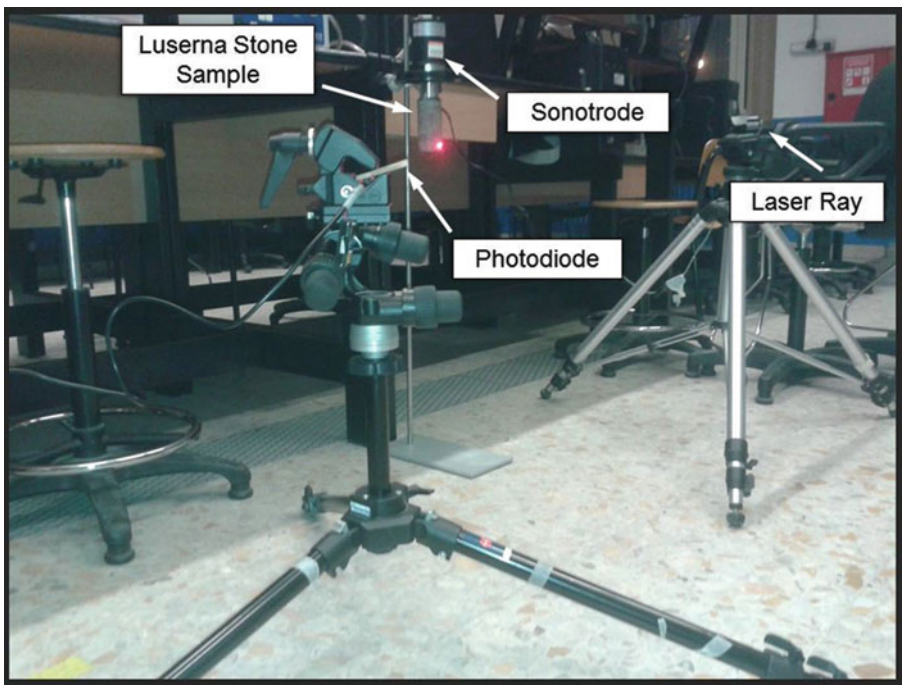

Fig. 13.14 Experimental set-up. The “Luserna Stone” specimen connected to the sonotrode and the laser-photodiode analyzer

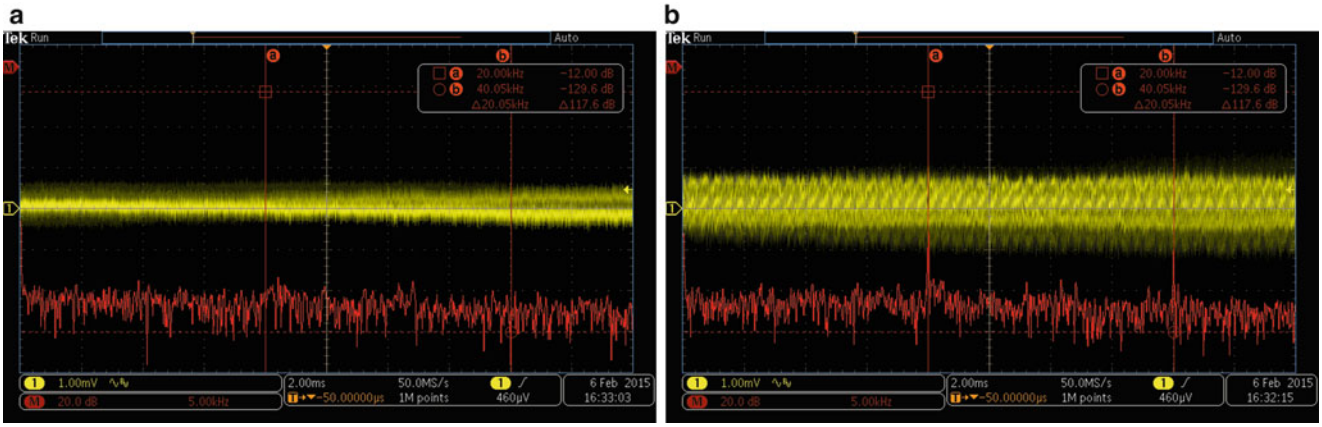

Fig. 13.15 Output data provided by the oscilloscope when the laser ray is switched off (**a**) and during the test (**b**)

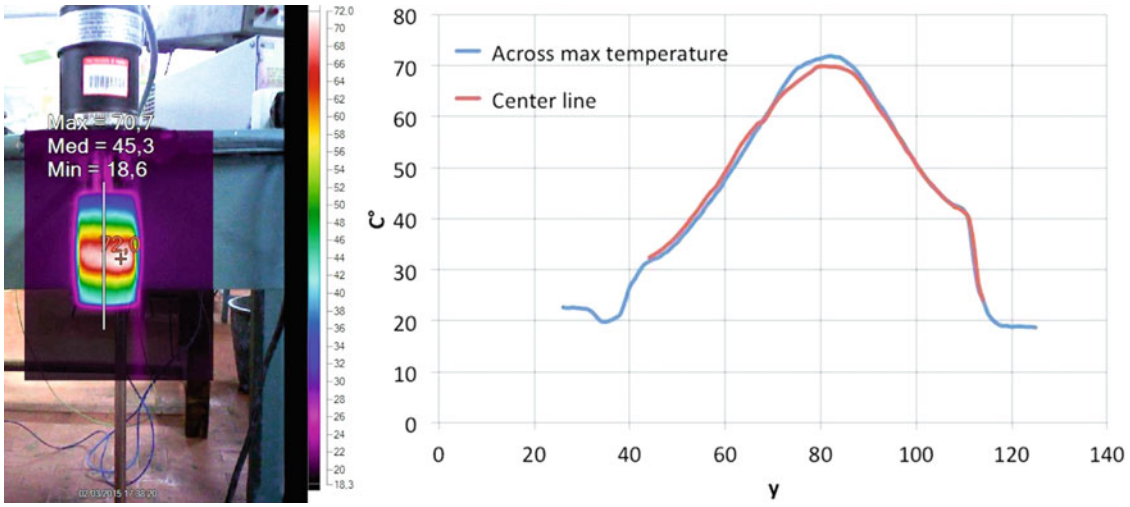

Fig. 13.16 Output data provided by the thermographic camera. Diagrams of Celsius temperatures across the center line and across the maximum temperature point

frequencies of the ultrasonic devise can be clearly observed, in particular the peaks at 20 kHz (point a) and 40 kHz (point b). Such comparison demonstrates the effectiveness of the instrumentation and of the experimental procedure in the evaluation of the correct frequencies of the vibrating system.

However, considering a more wide range of frequencies other peaks, although with decreasing amplitude, up to few tens of MHz are noticed. This does assume that the specimens response to the mechanical wave generated by the sonotrode is not only represented by a sinusoid with an exactly frequency of 20 kHz. It would be a periodic function with higher order harmonics at very high frequency. In other words, the corresponding Fourier spectrum, with its different harmonic, could present components on the THz frequencies, with amplitudes significantly reduced, but still able to excite the matter and obtain neutron and/or alpha particle emissions, as already demonstrated in [22–24].

Finally, in parallel to the previous analyses, a thermal estimation is conducted on the same specimen by using a thermographic camera. As can be seen from Fig. 13.16, the sample becomes warmer and warmer, already after a few minutes from the initial condition; in particular, it is evident that most of the heat is concentrated in the middle of its height, where a peak of about 72.0° Celsius after 5 min is reached.

13.6 Conclusions

Calcite and quartz rock specimens are evaluated by means of Raman spectroscopy [27]. Calcite crystal samples are analyzed before and after fracture tests. In addition, other experiments on calcite and quartz crystal samples are carried out precisely during compression tests. During the loading steps the samples are monitored by an apparatus to perform Raman analysis. The purpose is to analyze, during solicitation, the vibrational energy levels of the matter portions in a very high frequencies range, up to the THz regime.

In both cases, variations in energy levels and crystal lattice structure are evaluated. In general, the main original observation is that the signal intensity, on the typical Raman frequencies of calcite and quartz crystals, decreases with increasing pressure. In addition, it is also experimentally found that a reduction in the frequency takes place by increasing the compressive applied stress. This phenomenon, that is already known in macroscopic structural mechanics [30], shows how the matter is subject to the same laws also at the nanoscale.

Even in the tests conducted with the sonotrode, it is observed how the specimens response to the generated mechanical wave is not only represented by a sinusoid with a frequency of exactly of 20 kHz. It would be a periodic function with higher order harmonics at very high frequency. Moreover, from the thermal estimation, conducted by using a thermographic camera, it can be seen how during the solicitation the sample becomes warmer and warmer in few minutes.

This information on the molecular interactions may be important in an attempt to induce, in subsequent experiments, resonant vibrations of matter in the range of THz. On the basis of the encouraging results obtained in this preliminary analysis and from previous experiments conducted with the sonotrode [22–24], this objective could be achieved by applying dynamic solicitations, rather than static loads, to the matter.

Since the piezonuclear phenomena are induced by pressure waves at THz frequencies [31] a promising way for observing them is that of selectively producing highly excited vibrations in condensed matter. Such vibrational modes in the TeraHertz regime will be exceptionally effective for developing anomalies, such as neutron and/or alpha particle emissions, and compositional changes. To directly trigger the piezonuclear phenomena, without the intervention of fracture, laser sources working in the tens of TeraHertz range will be used. It is well-known, in fact, that high energy short laser pulse pulses are effective in exciting conductive materials [32]. Our purpose will be that of triggering heat generation from piezoelectric and piezomagnetic materials.

Acknowledgements The authors are grateful to Dr Sandro Cammarano and Eng. Andrea Bassani of Politecnico di Torino, Department of Structural, Geotechnical and Building Engineering, for their needful cooperation in carrying out Raman and compression tests. Special thanks are also due to Prof. Piergiorgio Rossetti, Dr Roberto Cossio and Dr Simona Ferrando of Università di Torino, Department of Earth Sciences. The Micro-Raman data have been obtained with the equipment acquired by the Interdepartmental Center "G. Scansetti" of Università di Torino for Studies on Asbestos and Other Toxic Particulates, with a grant from Compagnia di San Paolo,Torino.

References

1. D.A. Lockner, J.D. Byerlee, V. Kuksenko, A. Ponomarev, A. Sidorin, Quasi static fault growth and shear fracture energy in granite. Nature **350**, 39–42 (1991)
2. M. Ohtsu, The history and development of acoustic emission in concrete engineering. Mag. Concr. Res. **48**, 321–330 (1996)
3. J.B. Rundle, D.L. Turcotte, R. Shcherbakov, W. Klein, C. Sammis, Statistical physics approach to understanding the multiscale dynamics of earthquake fault systems. Rev. Geophys. **41**, 1019–1049 (2003)
4. G. Niccolini, A. Schiavi, P. Tarizzo, A. Carpinteri, G. Lacidogna, A. Manuello, Scaling in temporal occurrence of quasi-rigid-body vibration pulses due to macrofractures. Phys. Rev. E **82**, 46115 (2010) (1-5)
5. A. Carpinteri, G. Lacidogna, Damage monitoring of an historical masonry building by the acoustic emission technique. Mater. Struct. **39**, 161–167 (2006)
6. A. Carpinteri, G. Lacidogna, Structural monitoring and integrity assessment of medieval towers. J. Struct. Eng. (ASCE) **132**, 1681–1690 (2006)
7. A. Carpinteri, G. Lacidogna, Damage evaluation of three masonry towers by acoustic emission. Eng. Struct. **29**, 1569–1579 (2007)
8. A. Carpinteri, G. Lacidogna, G. Niccolini, Critical behaviour in concrete structures and damage localization by acoustic emission. Key Eng. Mater. **312**, 305–310 (2006)
9. A. Carpinteri, G. Lacidogna, N. Pugno, Structural damage diagnosis and life-time assessment by acoustic emission monitoring. Eng. Fract. Mech. **74**, 273–289 (2007)
10. G. Lacidogna, A. Carpinteri, A. Manuello, G. Durin, A. Schiavi, G. Niccolini, A. Agosto, Acoustic and electromagnetic emissions as precursor phenomena in failure processes. Strain **47**(2), 144–152 (2010)
11. A. Carpinteri, G. Lacidogna, A. Manuello, A. Niccolini, A. Schiavi, A. Agosto, Mechanical and electromagnetic emissions related to stress-induced cracks. Exp. Tech. **36**, 53–64 (2010)

12. A. Misra, Theoretical study of the fracture-induced magnetic effect in ferromagnetic materials. Phys. Lett. A **62**, 234–236 (1977)
13. V. Frid, A. Rabinovitch, D. Bahat, Fracture induced electromagnetic radiation. J. Phys. D **36**, 1620–1628 (2003)
14. A. Rabinovitch, V. Frid, D. Bahat, Surface oscillations. A possible source of fracture induced electromagnetic oscillations. Tectonophysics **431**, 15–21 (2007)
15. V. Hadjicontis, C. Mavromatou, D. Nonos, Stress induced polarization currents and electromagnetic emission from rocks and ionic crystals, accompanying their deformation. Nat. Hazards Earth Syst. Sci. **4**, 633–639 (2004)
16. J.W. Warwick, C. Stoker, T.R. Meyer, Radio emission associated with rock fracture: possible application to the great Chilean earthquake of May 22, 1960. J. Geophys. Res. **87**, 2851–2859 (1982)
17. T. Nagao, Y. Enomoto, Y. Fujinawa et al., Electromagnetic anomalies associated with 1995 Kobe earthquake. J. Geodyn. **33**, 401–411 (2002)
18. O. Borla, G. Lacidogna, E. Di Battista, G. Niccolini, A. Carpinteri, Multiparameter approach for seismic risk evaluation through environmental monitoring. Atti del 21 Congresso Nazionale di Meccanica Teorica ed Applicata (AIMETA) (Torino, Italy, 2013) CD-ROM
19. O. Borla, G. Lacidogna, E. Di Battista, G. Niccolini, A. Carpinteri, Electromagnetic emission as failure precursor phenomenon for seismic activity monitoring. Fracture, Fatigue, Failure, and Damage Evolution, Chap. 29, Vol. 5:221–229 (2014). Proc. of the 2014 Annual Conference on Experimental and Applied Mechanics
20. A. Carpinteri, F. Cardone, G. Lacidogna, Piezonuclear neutrons from brittle fracture: early results of mechanical compression tests. Strain **45**, 332–339 (2009)
21. F. Cardone, A. Carpinteri, G. Lacidogna, Piezonuclear neutrons from fracturing of inert solids. Phys. Lett. A **373**, 4158–4163 (2009)
22. A. Carpinteri, O. Borla, G. Lacidogna, A. Manuello, Neutron emissions in brittle rocks during compression tests: monotonic vs cyclic loading. Phys. Mesomech. **13**, 268–274 (2010)
23. A. Carpinteri, G. Lacidogna, A. Manuello, O. Borla, Energy emissions from brittle fracture: neutron measurements and geological evidences of piezonuclear reactions. Strength Fract. Comp. **7**, 13–31 (2011)
24. A. Carpinteri, G. Lacidogna, A. Manuello, O. Borla, Piezonuclear fission reactions from earthquakes and brittle rocks failure: evidence of neutron emission and non-radioactive product elements. Exp. Mech. **53**, 345–365 (2013)
25. A. Widom, J. Swain, Y.N. Srivastava, Neutron production from the fracture of piezoelectric rocks. J. Phys. G: Nucl. Part. Phys. **40**, 15006 (2013) (1-8)
26. A. Widom, J. Swain, Y.N. Srivastava, Photo-disintegration of the iron nucleus in fractured magnetite rocks with magnetostriction. Meccanica (2014) DOI:10.1007/s11012-014-0007-x
27. J.R. Ferraro, K. Nakamoto, C.W. Brown, *Introductory Raman spectroscopy*, 2nd edn. (Academic, Amsterdam, 2003)
28. P. Gillet, J. Badro, P. McMillan, A. Grzechnik, J. Schott, Thermodynamic properties and isotopic fractionation of calcite from vibrational spectroscopy of O-substituted calcite. Geochim. Cosmochim. Ac. **60**, 3471–3485 (1996)
29. M.L. Frezzotti, F. Tecce, A. Casagli, Raman spectroscopy for fluid inclusion analysis. J. Geochem. Explor. **112**, 1–20 (2012)
30. A. Carpinteri, R. Malvano, A. Manuello, G. Piana, Fundamental frequency evolution in slender beams subjected to imposed axial displacements. J. Sound Vib. **333**, 2390–240 (2014)
31. A. Carpinteri, TeraHertz phonons and piezonuclear reactions from nano-scale mechanical instabilities. Chap. 1. In: "Acoustic, Electromagnetic, Neutron Emissions from Fracture and Earthquakes", Springer (2015) (in print)
32. P.L. Hagelstein, D. Letts, D. Cravens, Terahertz difference frequency response of PdD in two-laser experiments. J. Cond. Mat. Nucl. Sci. **3**, 59–76 (2010)

Chapter 14
Acquisition of Audio Information from Silent High Speed Video

Jason Quisberth, Zhaoyang Wang, and Hieu Nguyen

Abstract A method to construct audio information from silent high speed video is presented. While an audio sample is played, an object's small vibrations generated by the sound waves are recorded by a single high-speed camera at high frame rates. Images are then analyzed using a Digital Image Correlation (DIC) scheme, where subsets of pixels are observed for displacement in two dimensions. The displacement data can be mapped to audio signals over time. Prior DIC analysis applications rely on artificial speckle patterns for observations, whereas the proposed method can employ natural patterns on objects, such as those on a piece of newspaper or a myriad of other common objects. Thin, flexible, and lightweight objects were found to output audio signals with less audible noise than other objects. Experiments have concluded that this method is a rapid and effective dynamic measurement process that results in acquisition of audio information that was not captured during high-speed recording.

Keywords Digital image correlation • Image matching • Vibration • Audio extraction • High speed video

14.1 Introduction

Image matching techniques have been an important topic in a variety of fields. With the exponential growth of digital technology, the devices used to capture images have increased in detail, file size, and accuracy. This has allowed the emergence of high-speed camera imaging a practical approach in many fields of metrology. A popular image matching technique called Digital Image Correlation (DIC) has been used extensively in the field of experimental mechanics. In the evaluation of cracks and material imperfections common to experimental mechanics, micro and even nanoscale precision is accomplished from this technique [1]. DIC techniques have even allowed strain measurements within open-cell structures such as bones in our bodies. Verhulp et al. describes the application of DIC in measuring the trabecular bone in the nanoscale [2]. Another group from the University of Texas at Austin has develop a method to measure deformation of rotating blades, such as those on helicopters, using DIC [3].

Inspiration to investigate acquisition of audio came from the news attention given to a group who developed the visual microphone from The Massachusetts Institute of Technology which uses video in order to extract complex spatial sub-bands which are then mapped into motion data [4]. The proposed method seeks to use a simpler, faster, and more well-established method in the form of DIC. Using high speed cameras, it is possible to record displacement data at a very high frame rate. With sound, a medium is stimulated and caused to vibrate at frequencies related to pitch. Such mediums may include pieces of paper or plastic bags. These vibrations, while sometimes invisible to the human eye, can easily be seen by the high speed cameras.

Traditional methods of sensing vibrations of objects are typically divided into contact and non-contact methods which fall into the field of acoustics. Contact microphones measure vibration from structures such as that of electrically-stimulated vibrating metal discs common in piezo devices. A very popular use of a contact method in measuring vibrations is seen in non-audible murmur microphones such as the one demonstrated by the works of Nakajima et al. [5] which features a device attached to the skin of a patient and is used in a similar fashion as a medical stethoscope. Non-contact microphones do not requires the adherent of measurement devices on an object but can rather depends on lasers. In interferometry, Laser Doppler

J. Quisberth (✉) • H. Nguyen
Department of Mechanical Engineering, The Catholic University of America, 620 Michigan Ave. N.E., Washington, DC 20064, USA

Department of Electrical Engineering and Computer Science, The Catholic University of America,
620 Michigan Ave. N.E., Washington, DC 20064, USA
e-mail: 61quisberth@cardinalmail.cua.edu

Z. Wang
Department of Mechanical Engineering, The Catholic University of America, 620 Michigan Ave. N.E., Washington, DC 20064, USA

S. Bossuyt et al. (eds.), *Residual Stress, Thermomechanics & Infrared Imaging, Hybrid Techniques and Inverse Problems, Volume 9*, Conference Proceedings of the Society for Experimental Mechanics Series, DOI 10.1007/978-3-319-21765-9_14

vibrometers require delicate setup of sophisticated lasers, beam splitters, and photo detectors in making vibration measurements. Measurement of vibration comes from amplitude changes related to Doppler shifts in frequency. Applications of Laser Doppler vibrometers in experimental mechanics include bridge structural health monitoring [6].

Since vibrations are simply displacements which can be periodic, capturing of images at high frame rates would allow for vibration measurement. DIC measurement focused on accuracy typically require artificial patterns to be imprinted on the test subject so frames of reference may more easily become established. The proposed method will only make use of natural patterns as seen on printed papers (such as this one if printed out). Key advantages of the proposed technique include a singular sensor in the high speed camera, no need for artificial patterns on the object, and rapid results due to a reduced region of interest (ROI).

14.2 Acquisition Process

The acquisition process can be divided into a series of four simple steps. This section will explain each in the order enumerated below.

i. Capture images of test subject using a high speed camera
ii. Specify region of interest, subset size, and reference parameters
iii. Employ DIC to obtain displacement data and calculate means
iv. Using mean displacements per frame, convert displacement into audio wave amplitude

Using a high speed camera, images are recorded over a set period of time at a high frame rate. This high frame rate is typically around 1000 frames per second. The test subject is to be a thin and flexible object that allows for displacement while stimulated by audio. A case study involving subjects of various material characteristics has already been conducted and used in determining preferable objects for audio acquisition experiments [4].

The specification of a region of interest (ROI) greatly reduces computational work required. In the proposed method, the ROI is divided into subsets of pixel groups. Displacement is the correct mapping of the movement of these subsets in particular the center pixel. Analyzing the entirely of the image of the subject will only be redundant as long as an appropriate region of interest is declared. In experimental mechanics, if a test subject is put under stress, then the ROI would typically be located around the areas of high stress gradients [7]. In experiments, the center of the images are designated as the ROI. The ROI is also divided into a point grid which features pixels as points and reduces processing time by measuring displacement using these points within the grid rather than pixels. Image 1 demonstrates the ROI division.

In reference to Fig. 14.1a demonstrates the static reference image, (b) is the target image which changes per iteration, (c) is the grid and subset division of the ROI, (d) represents displacement in the horizontal direction, (e) represents displacement in the vertical direction, and (f) is a combined displacement amplitude. Figure 14.1d–f use color maps in order to show disparity amongst displacement.

Employing DIC to the images outputted from the high speed camera will allow for displacement data to be obtained. Vendroux et al. describes that sub-nanoscale precision can be obtained with 640 × 480 camera resolution [9]. Traditionally it was thought that DIC is limited to pixel precision, but using interpolation methods such as the bi-cubic or b-spline interpolation, sub-pixel precision is easily attainable. Data in the proposed method's DIC algorithm outputted as two dimensional planar displacement. The first image is used as the reference from which displacement will be measured from. The overall cost function which is used for correlation criteria as introduced by Pan et al. [10] is written as:

$$C = \sum_{i=-1}^{N} \left[af(x_i,\ y_i) + b - g\left(x_i^{'},\ y_i^{'}\right) \right]^2, \tag{14.1}$$

where $\boldsymbol{N}$ is the total pixel count of a subset, $\boldsymbol{a}$ is a scaling factor, $\boldsymbol{b}$ is an intensity offset, and $\boldsymbol{f}(\boldsymbol{x_i}, \boldsymbol{y_i})$ represents the $\boldsymbol{i}^{\text{th}}$ pixel intensity value of the reference subset and $\boldsymbol{g}(x_i^{'}, y_i^{'})$ represents the $\boldsymbol{i}^{\text{th}}$ intensity value of the matching pixel within the target subset.

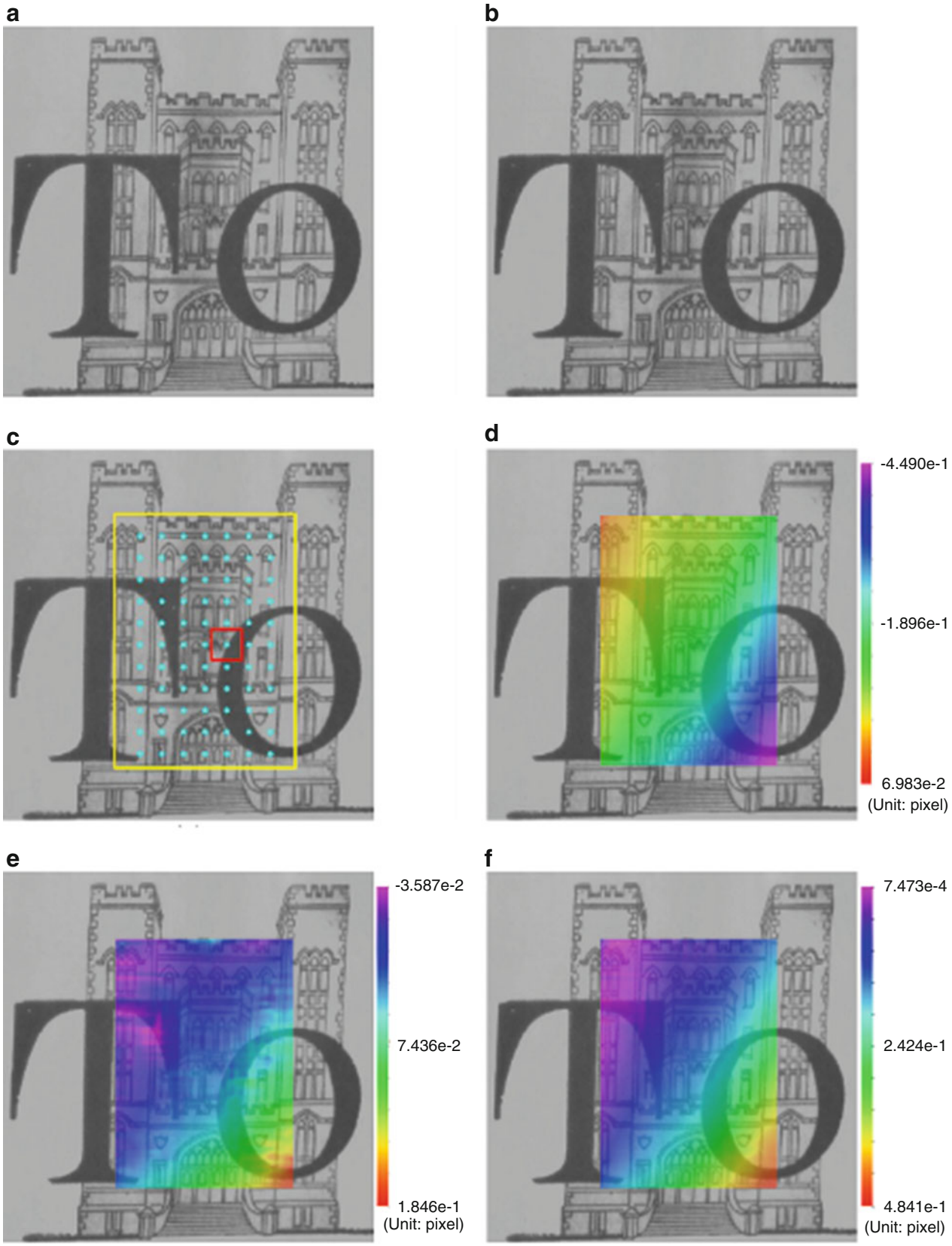

Fig. 14.1 ROI division into equally spaced subsets with point grid [8]

$$\begin{cases} x_i^{'} = x_i + \ \xi + \xi_x \Delta_i + \xi_y \Delta_i \\ y_i^{'} = y_i + \ \eta + \eta_x \Delta_i + \eta_y \Delta_i \end{cases} \tag{14.2}$$

Equation (14.1) can be re-written into a more compact form to further illustration its use as an iterating function.

$$C(p) = \sum_{i=-1}^{N} [\xi_i(p)]^2 \tag{14.3}$$

In (14.3), a transposed vector presented by $\boldsymbol{p} = \left[\xi, \eta, \xi_x, \xi_y, \eta_x, \eta_y\right]^T$ summarizes there parameters involved in (14.1) and (14.2). Within (14.3), the function of parameter $\boldsymbol{p}$ is written as:

$$\xi_i = af(x_i, \ y_i) + b - \ g\left(x_i^{'}, \ y_i^{'}\right), \tag{14.4}$$

where the right side of this equation is the information inside the brackets of (14.1). The compressed form of (14.3) allows for the application of a commonly used iterative approach known as the Gauss-Newton algorithm [11]. The Gauss-Newton algorithm is an iterative algorithm which is used to solve non-linear least squares problems. It is useful when attempting to solve for the minimum value of a function. The goal of this method is to minimize (14.3) as much as possible. When dealing with the minimization of a multivariable function, the Jacobian must be calculated in order to determine the next iteration's input. The next iteration's input $\boldsymbol{p_{n+1}}$ may be written as:

$$p_{n+1} = \ p_n - \left[\sum_{i=1}^{N} \boldsymbol{J}_i J_i^T\right]^{-1} \cdot \left[\sum_{i=1}^{N} \xi_i(p) \boldsymbol{J_i}\right], \tag{14.5}$$

where the Jacobian is expressed as:

$$J_i = {}^{\partial \xi_i(p)}/_{\partial p} = -\left[g_{x_i^{'}}, g_{y_i^{'}}, g_{x_i^{'}} \Delta x_i, g_{x_i^{'}} \Delta y_i, g_{y_i^{'}} \Delta x_i, g_{y_i^{'}} \Delta y_i, \ - f_i, \ -1\right]^T, \tag{14.6}$$

Audio wave amplitude is obtained using the equation below, where S denotes a grid pixel count, $\boldsymbol{\xi}$ represents horizontal displacement, and $\boldsymbol{\eta}$ represents vertical displacement of the center of subsets. Displacement in the x and y direction are averaged in the equation that obtains audio wave amplitude. Averaging of displacement data allowed for reduction of audible noise obtained during the image capturing process.

$$A \ = \frac{1}{S} \sum_{j=1}^{S} \sqrt{\xi_j^2 + \eta_j^2} \tag{14.7}$$

These wave amplitudes should then be normalized in order to attain the range $[-1, 1]$ such that volume may be adjusted to be made audible.

14.3 Experimental Procedure

Once a test subject is selected for audio acquisition, it is placed within the experimental setup. The experimental setup includes a high speed camera and a speaker. The high speed camera used for this manuscript is the Phantom V310 high speed camera. The speaker used is a generic shelf computer speaker whose specifics are not necessary. The resolution at which the high speed camera obtains images is 256 × 256 and they are taken at a frame rate of 1000 frames per second. Audio samples used in experimentation were the following: Symphony 40 by Mozart, Fur Elise by Beethoven, and a commercial by GEICO.

The audio samples are played by the speaker and their sound is transmitted to the test object. The high speed camera takes images for durations ranging from 4 to 6 s. The outputted images are then taken as inputs into the DIC scheme. A ROI is set

at starting from the center and is divided into 21 × 21 subsets which are equally spaced by a distance of 15 pixels. Figure 14.1 demonstrates how images are analyzed using an ROI and subsets.

Iterating for each subset within the ROI, pixels are matched according to the correlation criteria in (14.2). The first image is used as a reference image where displacement is measured. Matching of the reference's current subset's center to the current frame's subset's center is how displacement in two dimensions is acquired. The Newton–Raphson algorithm is employed in order to iteratively determine planar displacement. The convergence tolerance is set to 0.001 which typically is reached under ten cycles. The algorithm is given an iteration limit which is 30. This iteration limit prevents divergence and caps the processing time per frame. For those iterations that surpass the iteration limit, they are discarded from the final result. Some pseudo-code is shown below to further explain the pixel matching process.

Algorithm 1. DIC Pixel Matching Algorithm.

```
1:. procedure PIXELMATCH(a, b)
2:.   for sub : ROI do
3:.     p = [0, 0, 0, 0, 0, 0, 1, 0]
4:.     numIter = 0
5:.     while numIter < 30 do
6:.       min(Eq. (14.3))
7:.       if tol < 1.0e^-4 then
8:.         return
```

Figure 14.2 displays output waveform normalized amplitudes over time. The image does not tell much about the audio other than the acquired audio now includes audible noise which can be heard. The power spectral density plot in Fig. 14.3 consists of the power spectral densities of both audio files. This plot is a study of the variance of amplitudes with respect to frequency. The data is superimposed on one another in order to view overlaps over time. It is clear to see sections where the circles and X's overlap indicating matches in output audio. Areas where little correlation is observed is partially in due to the simplification of the assumed proportional relationship between planar motion and audio waveform amplitude. Within the frequency range of 250 and 1000 Hz there is a not as much overlap due to this region consisting of great audible noise. Figures 14.3 and 14.4's purposes are to give the reader a clearer view as to the correlation between original and acquired audio. In the case of those figures, we observe the frequency domain.

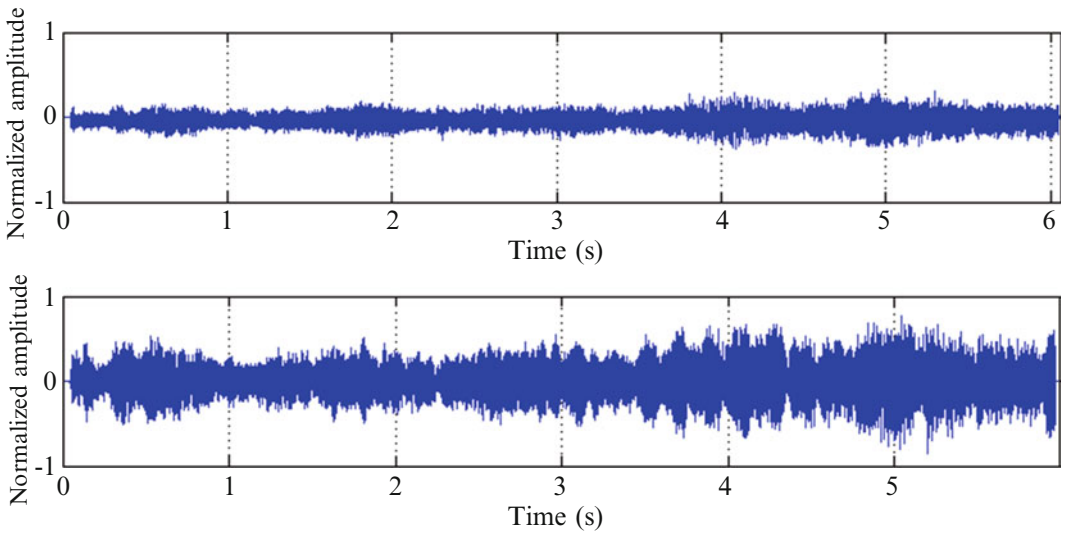

Fig. 14.2 Audio waveform output: the top plot is original audio and bottom plot is acquired audio

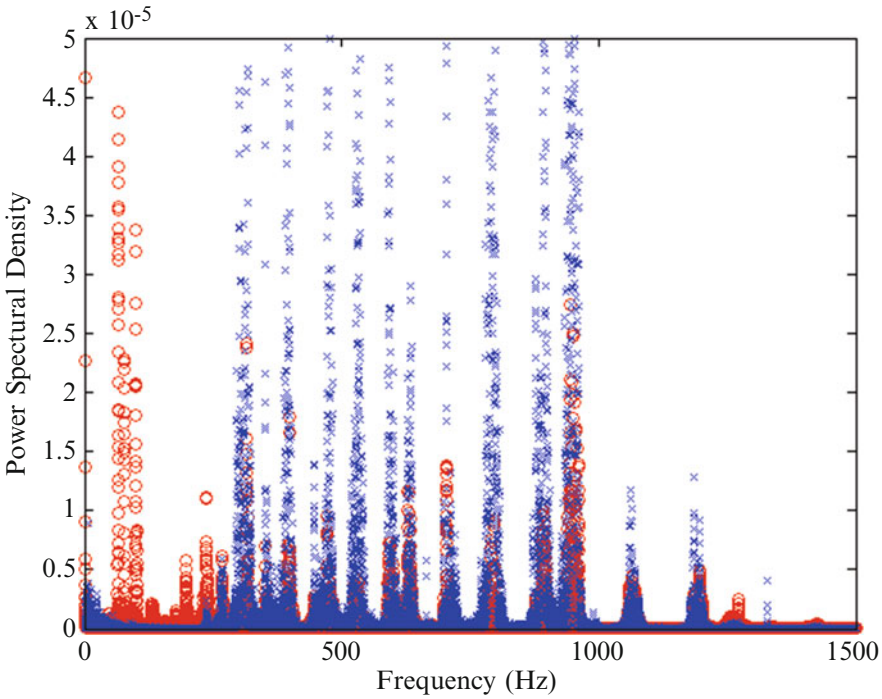

Fig. 14.3 Power density spectrum: circles indicate original audio and X's indicate acquired audio

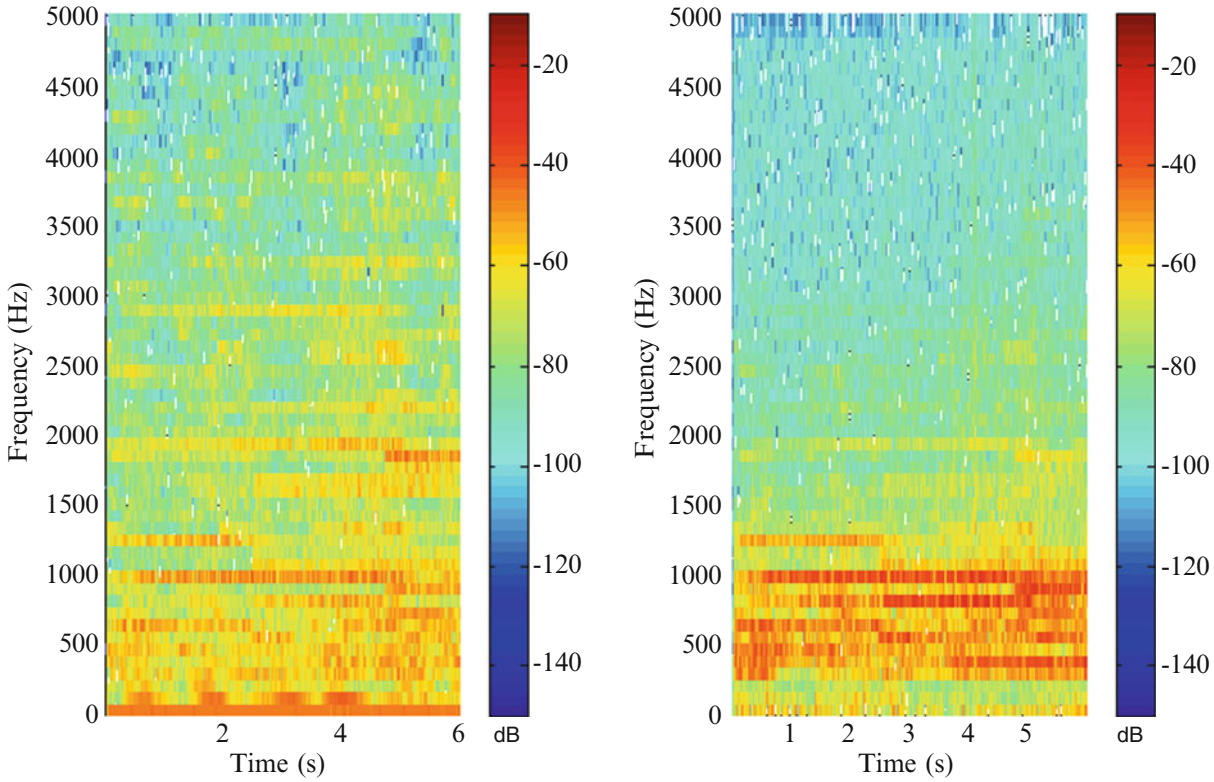

Fig. 14.4 Spectrogram plot of original and acquired audio

14.4 Conclusion

The proposed method proved a great success. The acquired audio from silent video was clearly audible even when played to subjects who have not heard the original audio sample. In the case of the GEICO commercial, each word can be clearly distinguished. These results were produced in about 2 min of processing time. Results may be obtained in under a minute given a larger ROI and coarser grid but accuracy may suffer. If the goal is to acquire audio signals of higher quality, then the frequency of image capturing should be increased. This increase, however, will result in greater processing times. Spectrograms provide more quantifiable information as to correlation between original and acquired audio. Spectrograms are graphical representations of frequency with respect to time or another variable. It is common to graph frequency vs time as to determine the frequency composition over time. Spectrograms prove useful when studying audio signatures and acoustic fingerprints which allow for identification of music. Acquisition of audio signatures is describes in the works of Radhakrishnan et al. which observes projections of various spectrograms [12]. A popular music identification software is called Shazam which allows for users to submit a snapshot of audio which is then sent to the software and returns a title of a song and artist [13]. It is shown that DIC is not just limited to the field of experimental mechanics. Wang et al. [14] describes its practicality and various compliments with the field of computer vision.

It would be even more beneficial to obtain a singular value for correlation measurement ranging from the range [0, 1], where 0 is no match and 1 is a perfect match. From there, one may observe various material properties of potential test subjects and attempt to construct an equation that related audio acquisition correlation to material properties such as density, hardness, and stiffness. Future work should also include case studies amongst various image resolutions as to determine ideal resolutions. An iterative approach may be employed that tests various resolutions and maximizes audio acquisition correlation. The proposed method should be automated starting from video recording up to calculation of audio acquisition correlation. Future improvements on the method include ways of optimizing performance to meet real-time processing requirements. If the system would reach real-time performance, applications in this method would increase exponentially as more work in done involving DIC and audio acquisition.

References

1. T. Berfield, J. Patel, R. Shimmin, P. Braun, J. Lambros, N. Sottos, Micro- and nanoscale deformation measurement of surface and internal planes via digital image correlation. Exp. Mech. **47**, 51–62 (2007)
2. E. Verhulp, B. Rietbergen, R. Huiskes, A three-dimensional digital image correlation technique for strain measurements in microstructures. J. Biomech. **37**, 1313–1320 (2004)
3. J. Sicard, J. Sirohi, Measurement of the deformation of an extremely flexible rotor blade using digital image correlation. Meas. Sci. Technol. **14**, 065203 (2013)
4. A. Davis, M. Rubinstein, N. Wadhwa, G. Mysore, F. Durand, W.T. Freeman, The visual microphone: passive recovery of sound from video. ACM Trans. Graphics (Proc. SIGGRAPH) **33**, 1–10 (2014)
5. Y. Nakajima, H. Kashioka, K. Shikano, N. Campbell, Non-audible murmur recognition input interface using stethoscopic microphone attached to the skin. in Acoustics, Speech, and Signal Processing, 2003. Proceedings (ICASSP'03). 2003 IEEE International Conference on, IEEE, vol. 5, pp. V-708
6. H.H. Nassif, M. Gindy, J. Davis, Comparison of laser Doppler vibrometer with contact sensors for monitoring bridge deflection and vibration. NDT & E Int. **38**, 213–218 (2005)
7. W. Peters, W. Ranson, Digital imaging techniques in experimental stress analysis. Opt. Eng. **21**, 213427 (1982)
8. Z. Wang, H. Nguyen, J. Quisberth, Audio extraction from silent high-speed video using an optical technique. Opt. Eng. **53**, 110502 (2014)
9. G. Vendroux, W. Knauss, Submicron deformation field measurements: part 2. improved digital image correlation. Exp. Mech. **38**, 86–92 (1998)
10. B. Pan, H. Xie, Z. Wang, Equivalence of digital image correlation criteria for pattern matching. Appl. Opt. **49**, 5501–5509 (2010)
11. J. Nocedal, S.J. Wright, *Numerical Optimization*, 2nd edn. (Springer, New York, 2006)
12. R. Radhakrishnan, C. Bauer, C. Cheng, K. Terry, Audio signature extraction based on projections of spectrograms. in Multimedia and Expo, 2007 IEEE International Conference, 2110–2113, (2007)
13. A. Wang, The shazam music recognition service. Commun. ACM **49**, 44–48 (2006)
14. Z. Wang, H. Kieu, H. Nguyen, M. Le, Digital image correlation in experimental mechanics and image registration in computer vision: similarities, differences and complements. Opt. Lasers Eng. **65**, 18–27 (2015). doi:10.1016/j.optlaseng.2014.04.002

Chapter 15
Overview of the Effects of Process Parameters on the Accuracy in Residual Stress Measurements by Using HD and ESPI

C. Barile, C. Casavola, G. Pappalettera, and C. Pappalettere

Abstract Several researches have been recently carried out about the feasibility of adopting optical methods, such as Electronic Speckle Pattern Interferometry (ESPI), in combination with hole-drilling. Using this kind of approach instead of adopting strain gage rosette, as usual, can be advantageous in view of the fact that costs and time of the measurement can be reduced. However it should be taken into account that several parameters involved in the whole measurement process can significantly determine the final accuracy of the measurement. In this paper an overview of the effects of some of those parameters is presented: errors on the knowledge of some of geometrical paramters, direction of the sensitivity vector of the system with respect to the principal stress direction, drilling rotation speed.

Keywords Electronic speckle pattern interferometry (ESPI) • Hole drilling method (HDM) • Process parameters • Residual stress • Titanium grade 5

15.1 Introduction

Residual stresses are present in almost all materials [1]. They may be created during the manufacture or during the life of the material. If not recognized and accounted for in the design process, residual stresses can be a major factor in the failure of a material, particularly if subjected to alternating service loads or corrosive environments. Residual stress may also be beneficial, for example, the compressive stresses produced by shot peening.

The hole-drilling strain-gage technique is a practical method for determining residual stresses [2]. It involves attaching a strain gage rosette to the surface [3], drilling a hole at the geometric center of the rosette, and measuring the resulting relieved strains. The residual stresses within the removed material are then determined from the measured strains using a series of equations. It is a consolidated approach for stress determination and it is ruled by the ASTM test standard [1]. Although their wide application, strain gauges have some disadvantages: the surface of the material has to be accurately prepared, the specimen surface has to be flat and smooth so that the rosettes can be attached, the hole has to be drilled exactly in the center of the rosette in order to avoid eccentricity errors, and costs and time associated with installing rosettes are remarkable. Furthermore the amount of available data is limited: for each measurement, only three discrete readings are available (six in the case of some special rosettes), just sufficient to fully characterize the in-plane residual stresses.

The application of optical techniques could promisingly overcome the difficulties connected with the use of strain gauges [4]. In the last years different methods were explored for implementing hole drilling with optical devices. Several techniques can be used to generate fringe patterns, from which the local displacements, in the neighborhood of the hole, can be calculated. The use of moiré interferometry to determine residual stresses was investigated in many scientific papers since McDonach et al. [5] and Martínez et al. [6]. Even if bonding a grating could also be time consuming. The feasibility of using holographic interferometry was shown by Antonov [7]. Hung et al. [8] have used shearography combined with a small ball indentation instead of a hole and also a phase shift shearography [9] was adopted. Also the possibility to release residual stresses by using local heat treatment, as in [10], was used by Pechersky et al. [11] combined with digital speckle pattern interferometry (DSPI). Instead Zhang [12] has investigated the practicability of the combination between DSPI and hole drilling. Electronic Speckle Pattern Interferometry (ESPI) which is an optical method based upon the speckle effect [13] has been increasingly used in the last decades. ESPI was successfully used to measure displacement fields in anisotropic specimen made by selective laser melting [14–16], or orthotropic materials [17] as laminated wood [18] but also in combination with hole drilling method to evaluate the residual stress relieving [19] avoiding rigid-body motions [20].

C. Barile • C. Casavola (✉) • G. Pappalettera • C. Pappalettere
Dipartimento di Meccanica, Politecnico di Bari, Matematica e Management, Viale Japigia 182, Bari 70126, Italy
e-mail: katia.casavola@poliba.it

S. Bossuyt et al. (eds.), *Residual Stress, Thermomechanics & Infrared Imaging, Hybrid Techniques and Inverse Problems, Volume 9*, Conference Proceedings of the Society for Experimental Mechanics Series, DOI 10.1007/978-3-319-21765-9_15

In this paper the advantages of using ESPI technique in contrast to the classical method are underlined. Moreover all the parameters connected with the use of the ESPI technique that could become source of errors are investigated. In defining the set-up it is necessary to have a good control of all the geometrical parameters involved, such as the angles that define the illumination and detection directions. If their values are not properly evaluated this introduces an error in the determination of the displacement field which introduces an error in the calculation of the stress field [21]. Another factor that must be taken into account is the sensitivity vector of the ESPI, that represents the vector along which displacement are measured. In this paper the influence of the relative angle between the sensitivity direction and the principal stress is evaluated. Fundamental is also the choice of the drilling rotation speed [22]. It can affect the heat input to the material during the drilling process modifying the plasticization zone and introducing problems connected with the choice of the internal radius of analysis area [23]. Also the combination of these effects [24, 25] must be taken adequately into account if high accuracy measurements are required.

15.2 Sources of Errors in ESPI-HDM

In this section the set-up will be described as well as the list of potential sources of errors connected with the system, the analysis technique and the hole drilling process. Also the magnitude of the potential errors introduced will be estimated.

The ESPI hole-drilling measurement system used in this work is schematically reported in Fig. 15.1.

A beam from a DPSS laser source is splitted into two beams and focused into two monomode optical fibers. One beam is collimated and illuminates the sample, while the second beam passes through a phase shifting piezoelectric system and then it goes to the CCD camera where it interferes with the light diffused by the optically rough surface of the specimen. Initial phase and final phase are evaluated by the four-step phase shifting technique, which allows to calculate the amount of displacement of each point into the analysis area at each step of the hole-drilling process. The holes are drilled by means of a high speed turbine, electronically regulated; turbine is mounted on a precision travel stage in order to allow accurate positioning of the drilling device. Experimental measurements were performed on a Ti6Al4V specimens.

15.2.1 Geometrical Parameters

The geometry and mutual position of laser, CCD and specimen should be accurately defined to correctly measure the displacement map. The xyz reference system of the specimen and the $x'y'z'$ reference system of the CCD camera

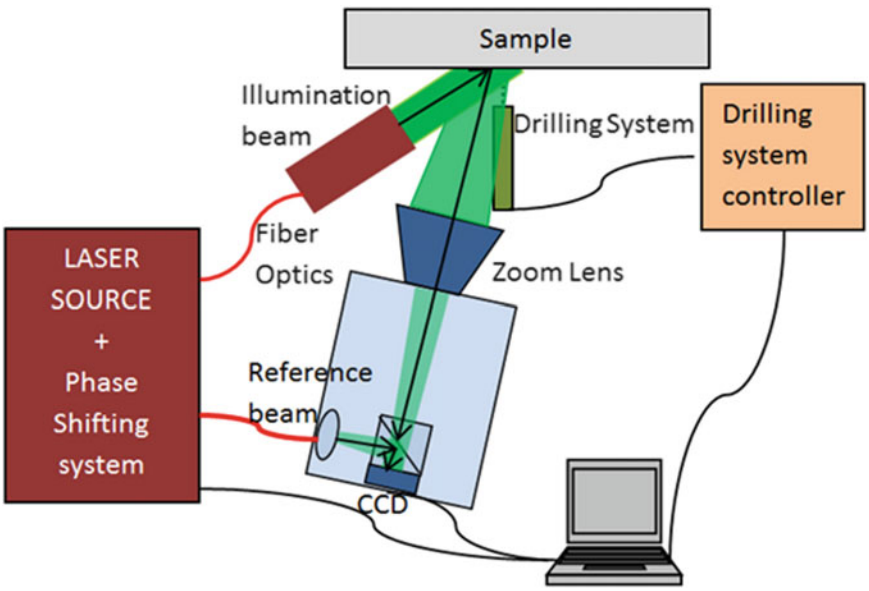

Fig. 15.1 ESPI + HDM set-up

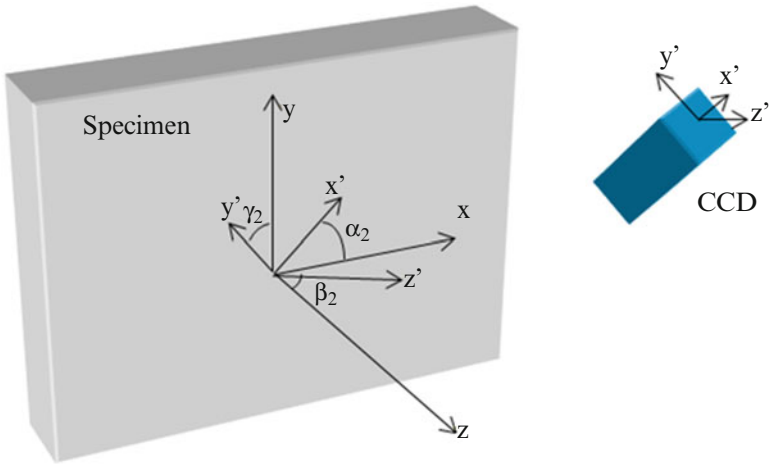

Fig. 15.2 Schematic of the geometrical set-up with the CCD camera and the specimen

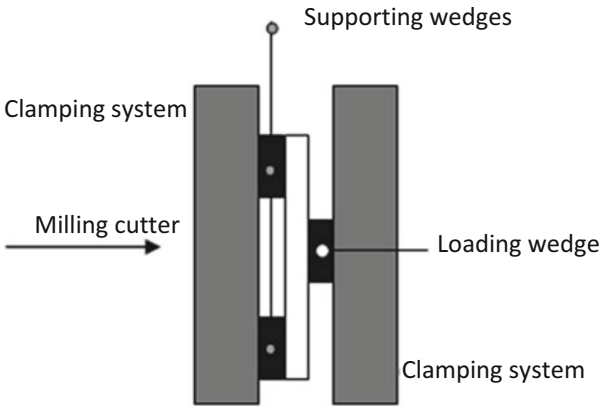

Fig. 15.3 Top view of the three-point bending load frame

are considered as shown in Fig. 15.2. To exactly calculate stresses from measured displacements, it is necessary to evaluate the pixel size along x and y directions, this means that the angles of CCD camera with respect to the specimen reference system xyz are needed. The α_2 angle defines the x axis and the x' axis; the β_2 angle defines the z axis and the z' axis; the γ_2 angle defines the y axis and the y' axis.

Moreover, to calculate stresses from measured displacements, it is necessary to know the phase changing of the pattern, detected during tests, and the sensitivity of the optical set-up that depends on the geometry of the illumination system. Due to the cylindrical symmetry of the illumination beam around the propagation direction of the laser, only two angles are necessary in this case to relate the specimen reference system and the illumination reference system. Being $x''y''z''$ the illumination beam reference system, the α_1 angle defines the x axis and the x'' axis, while the β_1 angle defines the z axis and the z'' axis. These geometric angles can be initially measured by a goniometer. The uncertainty in this measurement is estimated to be $\Delta = \pm 2^\circ$ because of the difficulties to correctly positioning the goniometer inside the measurement system. In order to assess the influence that an error in measuring geometrical parameters can have on the results in terms of measured stress, simple experimental tests were run. Rectangular cross section titanium specimen was subjected to three point bending load and induced stresses were measured as shown in Fig. 15.3.

The profile of the induced stresses was measured. The angle values were $\alpha_1 = 42.5^\circ$; $\beta_1 = 0^\circ$; $\alpha_2 = 24^\circ$; $\beta_2 = 0^\circ$; $\gamma_2 = 0^\circ$. Then stress profile was recalculated by hypothesizing an error $\pm 2^\circ$ on each of the considered angles and compared in order to detect the error on stress values $\Delta\sigma_{xx}$.

It was found that a $\pm 2^\circ$ of the in-plane detection angle α_2 can introduce the higher error on the measured stress profile with respect to the other angles. Figure 15.4 shows the effect of an error $\Delta\alpha_2 = \pm 2^\circ$ while in Table 15.1 are reported the numerical results and the effects in terms of percentage error on the calculated stress profile.

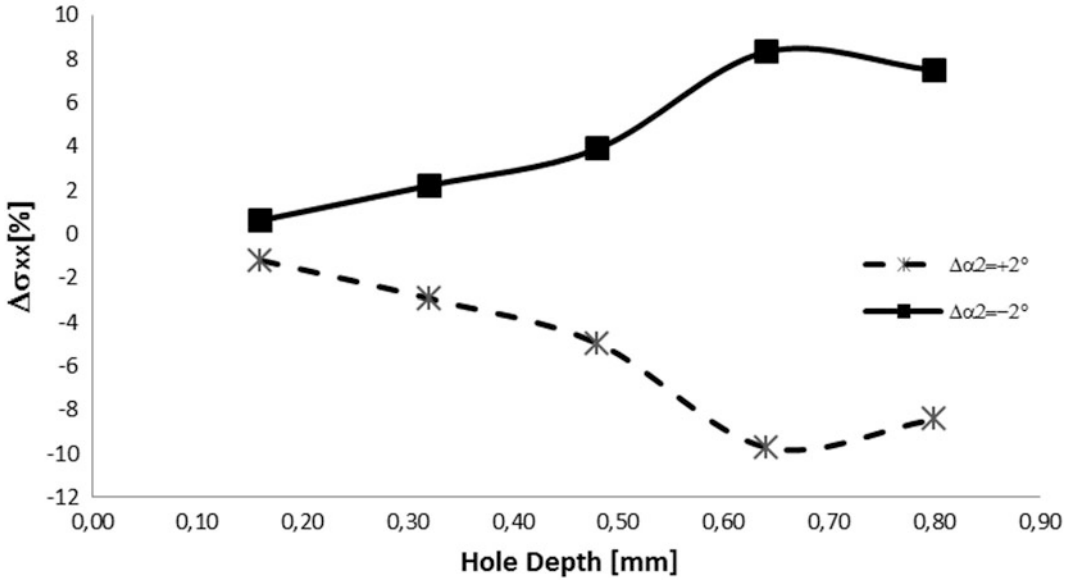

Fig. 15.4 Percentage differences in calculated σ_{xx} in correspondence of an error of $\Delta\alpha_2 = +2°$ and $\Delta\alpha_2 = -2°$ with respect to the measured angle

Table 15.1 Calculated stress σ_{xx} for measured $\alpha_2 = 24°$ and percentage errors for $\Delta\alpha_2 = \pm 2°$

Depth [mm]	σ_{xx} [MPa] ($\alpha_2 = 24°$)	σ_{xx} [MPa] ($\alpha_2 = 22°$)	σ_{xx} [MPa] ($\alpha_2 = 26°$)	$\Delta\sigma_{xx}$ % ($\Delta\alpha_2 = -2°$)	$\Delta\sigma_{xx}$ % ($\Delta\alpha_2 = +2°$)
0.16	−393	−396	−389	0.6	1.2
0.32	−314	−321	−305	2.2	2.9
0.48	−268	−279	−255	3.9	5.0
0.80	−213	−229	−195	7.5	8.4

15.2.2 Sensitivity Vector

In the measurement system displayed in Fig. 15.1 the in-plane displacements consequent to the stress relaxation are measured only along the *x* direction. This is an important consideration to take into account, since it describes the sensitivity vector of the set-up. For this reason the system appears to be different respect to the strain gage rosette where each extensimeter grid measures strain along different directions. The measured amount of displacement depends on the angle between the relieved stress and the sensitivity vector. If a perfect uniaxial load is applied, as tensile or simple bending test, the stress field can be identified by the maximum principal stress σ_1 while the minimum principal stress, σ_2, can be set equal to 0. If measurements are executed with σ_1 direction overlapped to the sensitivity vector one, the relieved strain is proportional to σ_1 according to the Hooke's law. On the other hand if the sample is put in the measurement system with σ_1 direction perpendicular to the sensitivity vector, the relieved strain results proportional to $\nu\sigma_1$, according to the transversal contraction of the material. Starting from these observations it seems to be relevant the investigation of the effects of the principal stresses' orientation with respect to the ESPI sensitivity direction, on the accuracy of the measurement. To this scope specimen were bent in a four-points bending frame to obtain an uniaxial stress state with an applied stress $\sigma_1 = 133$ MPa and $\sigma_2 = 0$ MPa.

Results can be summarized as follows:

- in all cases the θ angle between the maximum principal stress and the *x* axis was correctly identified and with a small percentage error. It was found a value of $\theta = -0.45°$ for measurement in which the specimen is oriented with the maximum principal stress parallel to the *x* axis and $\theta = -89.76°$ when the specimen is oriented perpendicularly to the *x* axis;
- the measurement of the maximum principal stress is not significantly affected by the orientation of the specimen; the entity of the error is about 10 % and this is a value consistent with errors reported in other studies [26, 27];
- concerning with the measurement of the minimum principal stress and in particular to its value along the thickness it was found that better results are obtained when the longitudinal axis of the specimen is oriented at 90° with respect to the *x* direction, that is to say when the minimum stress is oriented along the sensitivity direction of the ESPI system (Table 15.2).

Table 15.2 Results of the measurement of the minimum principal stress, σ_2, at 0.4 mm

Specimen angle [°]	σ_2 ESPI [MPa]	σ_2 expected [MPa]	$\Delta\sigma 2$ [MPa]
0	13.2	2.3	10.9
90	5.7	2.3	3.4

Table 15.3 Values of measured stress at the different rotations speed of the cutter

σ_x at 5000 rpm [MPa]	σ_x at 35,000 rpm [MPa]	σ_x at 50,000 rpm [MPa]	
118.0	153.8	152.6	
152.8	165.2	145.2	
170.2	171.2	150.2	
147.0	163.4	149.3	Mean value
26.6	8.8	3.8	Std Dev

Results seem to be in contrast with the general theory that encourages the overlapping of σ_1 with the sensitivity vector, but this attitude could be justified considering that the amplitude of load applied in all cases is large enough to be detected at all orientations. The limit condition could be reached decreasing the four-point bending load up to reduce at minimum the number of fringes in correspondence of different angles with respect to the sensitivity vector [28, 29]. This attitude is underlined when minimum principal stress is measured with sensitivity vector oriented at 90° respect to its own direction.

15.2.3 Drilling Speed

The effects of the drilling speed have been analyzed too. An electronic controlled drilling machine is used to drill the holes. Holes are drilled at three different velocities: 5000, 35,000, and 50,000 rpm. The first and the last values represent, respectively, the minimum and the maximum rotation speed attainable by the drilling system. ESPI was used to detect the displacement map in correspondence of each drilling step. Also in this case specimen were loaded in a four-point bending frame in order to introduce a well-known stress field, whose expected average value is 143.6 MPa. As it can be inferred from Table 15.3 the average value of the measured stress state is coherent with the expected theoretical value but data corresponding to lower speed appear more scattered than data recorded at the maximum speed. In fact the standard deviation for the measurement at 5000 rpm is about 20 % of the expected value. This value decreases at 35,000 rpm being about 6 % of the nominal expected value and it reaches the minimum at 50,000 rpm where it is less than 3 % of the expected theoretical value. In other words the accuracy and the repeatability of the measurement diminishes by decreasing the rotation speed, because the quality of the hole at low drilling speed is worse than at higher rotation speeds.

15.3 Conclusions

Hole-drilling method is one of the most useful and reliable approach for measuring residual stress and it can take advantages by its application in combination with ESPI because this can result in cheaper and faster measurements. However getting accurate results with this technique requires a good control over the many factors that can affect the final results. In this paper a review of some major sources of errors were presented and their effects were evaluated for the case of measurements on grade 5 Titanium samples. A good evaluation of the geometrical parameters it is relevant. In particular, for the adopted configuration, it is important to correctly determine the illumination angle α_2. It was found that an error of $\pm 2°$ on this parameter can introduce an error varying between 0.6-8 % on the final calculated stress. Finally it should be reminded that the final quality of the drilled hole is a key factor in determining a good measurement. This issue is strictly connected with the particular material under study, its machinability and the use of proper drilling material. However, final quality is also related with the proper choice of the drilling rotation speed, that must be optimized as a function of the material under study. It was found that, for Ti6Al4V, much better quality is obtained by using higher velocity (50,000 rpm), which is suggested

therefore for measurements on this specific material. Care must be taken, however, to avoid that fine chips resulting from drilling operations, at this speed, stick to the material degrading the quality of the speckle fringe pattern and, as a consequence, the accuracy of the measurement itself.

References

1. Standard test method for determining residual stresses by the hole-drilling strain-gage method standard E837-13a (American Society for Testing and Materials, West Conshohocken, PA, 2013)
2. N.J. Rendler, I. Vigness, Hole-drilling strain-gage method of measuring residual stresses. Exp. Mech. **6**, 577–586 (1966)
3. G.S. Schajer, Advances in hole-drilling residual stress measurements. Exp. Mech. **50**, 159–168 (2009)
4. F.M. Furgiuele, L. Pagnotta, A. Poggialini, Measuring residual stresses by hole drilling and coherent optics techniques: a numerical calibration. J. Eng. Mater. Technol. **113**, 41–50 (1991)
5. A. McDonach, J. McKelvie, P.M. MacKenzie, C.A. Walker, Improved moiré interferometry and applications in fracture mechanics, residual stresses and damage composites. Exp. Tech. **7**, 20–24 (1983)
6. A. Martínez, R. Rodríguez-Vera, J.A. Rayas, H.J. Puga, Fracture detection by grating moiré and in-plane ESPI techniques. Opt. Lasers Eng. **39**(5–6), 525–536 (2003)
7. A.A. Antonov, Inspecting the level of residual stresses in welded joints by laser interferometry. Welding Prod. **30**, 29–31 (1983)
8. Y.Y. Hung, J.D. Hovanesian, Fast detection of residual stress in an industrial environment by thermoplastic-based shearography. SEM Spring Conference on Experimental Mechanics, (Albuquerque, USA, 1990), pp. 769–775
9. M.Y.Y. Hung, K.W. Long, J.Q. Wang, Measurement of residual stress by phase shift shearography. Opt. Lasers Eng. **27**(1), 61–73 (1997)
10. C. Barile, C. Casavola, G. Pappalettera, C. Pappalettere, Feasibility of local stress relaxation by laser annealing and X-ray measurement. Strain **49**(5), 393–398 (2013)
11. M.J. Pechersky, R.F. Miller, C.S. Vikram, Residual stress measurements with laser speckle correlation interferometry and local heat treating. Opt. Eng. **34**, 2964–2971 (1995)
12. J. Zhang, Two-dimensional in-plane electronic speckle pattern interferometer and its application to residual stress determination. Opt. Eng. **37**, 2402–2409 (1998)
13. G.L. Cloud, *Optical Methods of Engineering Analysis* (Cambridge University Press, New York, 1995)
14. C. Barile, C. Casavola, G. Pappalettera, C. Pappalettere, Mechanical characterization of SLM specimens with speckle interferometry and numerical optimization. Conference Proceedings of the Society for Experimental Mechanics Series, vol. 6 (Springer, New York, 2011), pp. 837–843
15. C. Barile, C. Casavola, G. Pappalettera, C. Pappalettere, Experimental and numerical characterization of sinterized materials with speckle interferometry and optimization methods. 10th IMEKO TC15 Youth Symposium on Experimental Solid Mechanics (Chemnitz, Germany, 2011), pp. 35–36
16. C. Barile, C. Casavola, G. Pappalettera, C. Pappalettere, Mechanical characterization of SLM specimens with speckle interferometry and numerical optimization. Society for Experimental Mechanics—SEM Annual Conference and Exposition on Exp. and Applied Mech., vol. 3 (2010), pp. 2523–2529
17. A. Baldi, Full field methods and residual stress analysis in orthotropic material. Part I. Linear approach. Int. J. Solids Struct. **44**(25–26), 8229–8243 (2007)
18. C. Barile, C. Casavola, G. Pappalettera, C. Pappalettere, Hybrid characterization of laminated wood with ESPI and optimization methods. Conference Proceedings of the Society for Experimental Mechanics Series, vol. 3 (2013), pp. 75–83
19. O. Sedivý, C. Krempaszky, S. Holý, Residual stress measurement by electronic speckle pattern interferometry. 5th Australasian Congress on Applied Mechanics, ACAM 2007, 10–12 December (Brisbane, Australia, 2007)
20. G.S. Schajer, M. Steinzig, Full-field calculation of hole drilling residual stresses from electronic speckle pattern interferometry data. Exp. Mech. **45**(6), 526–532 (2005)
21. C. Barile, C. Casavola, G. Pappalettera, C. Pappalettere, Residual stress measurement by electronic speckle pattern interferometry: a study of the influence of geometrical parameters. Struct. Integrity Life **11**(3), 177–182 (2011)
22. C. Barile, C. Casavola, G. Pappalettera, C. Pappalettere, Drilling speed effects on accuracy of HD residual stress measurements. Conference Proceedings of the Society for Experimental Mechanics Series, vol. 8 (2014), pp. 119–125
23. C. Barile, C. Casavola, G. Pappalettera, C. Pappalettere, Remarks on residual stress measurement by hole-drilling and electronic speckle pattern interferometry. Scientific World J. **2014**, 7 (2014)
24. M. Steinzig, E. Ponslet, Residual stress measurement using the hole drilling method and laser speckle interferometry: part III. Exp. Tech. **27**(5), 45–48 (2003)
25. C. Barile, C. Casavola, G. Pappalettera, C. Pappalettere, Analysis of the effects of process parameters in residual stress measurements on Titanium plates by HDM/ESPI. Meas: J. Int. Meas. Confederation **48**(1), 220–227 (2014)
26. M. Steinzig, T. Takahashi, Residual stress measurement using the hole drilling method and laser speckle interferometry part IV: measurement accuracy. Exp. Tech. **27**(6), 59–63 (2003)
27. M.R. Viotti, A.G. Albertazzi Jr., W. Kapp, Experimental comparison between a portable DSPI device with diffractive optical element and a hole drilling strain gage combined system. Opt. Lasers Eng. **46**(11), 835–841 (2008)
28. C. Barile, C. Casavola, G. Pappalettera, C. Pappalettere, Considerations on the choice of experimental parameters in residual stress measurements by hole-drilling and ESPI. Frattura ed Integrità Strutturale **30**, 211–219 (2014)
29. C. Casavola, C. Pappalettere, F. Tursi, Calibration of barkhausen noise for residual stress measurement. Conference Proceedings of the Society for Experimental Mechanics Series, vol. 4 (2013), pp. 255–266

Chapter 16
Near Weld Stress Analysis with Optical and Acoustic Methods

Sanichiro Yoshida, Tomohiro Sasaki, Masaru Usui, Shuuichi Sakamoto, Ik-keun Park, Hyunchul Jung, and Kyeongsuk Kim

Abstract Residual stress induced by brazing and bead welding have been analyzed based on acousto-elasticity and optical interferometry. Acousto-elasticity is to probe compressive or tensile residual stresses from acoustic velocity measurements and optical interferometry is to measure strain induced by an external tensile load. It has been theorized that a compressive residual stress increases the elastic modulus and that an external tensile stress reduces the increase in the elastic modulus. From the tensile stress that brings back the elastic modulus to the nominal value, the residual stress can be estimated. Compressive residual stresses have been estimated in this fashion for a butt-brazed and a butt-bead-welded steel specimens to be of the order of 5 MPa and 50 MPa respectively.

Keywords Residual stress • Electronic speckle-pattern interferometry • Acousto-elasticity • Welding • Brazing • Strain analysis

16.1 Introduction

Welding processes always cause stresses on the work. The material near the weld is thermally expanded by the welding torch as it passes by and compressed by ambient air as the torch leaves. Since these heating and cooling off processes occur not uniformly, they create stresses known as residual stresses. When dissimilar materials of substantially different thermal expansion and thermal conductivity are butt-welded, the effect is significant. A number of methods have been developed for analysis of residual stresses [1–3], and many studies have been reported for residual stress due to welding [4–7]. The fundamental difficulty is that residual stresses are locked in the material. Unless the locking mechanism is removed, the stress does not change and therefore the residual stress is invisible. From this standpoint, residual stress analysis is essentially invasive, or at least needs some action to change the stress status.

Nondestructive techniques are also available for residual stress analysis. X-ray diffraction and acousto-elastic methods [8, 9] are most popular techniques to estimate residual stresses. The former measures averaged inter-atomic distance of the region where the residual stress is to be analyzed. The latter estimates the residual strain from the change of elastic modulus from the non-stressed state via acoustic velocity measurement. Both methods measure residual strain and estimate the corresponding stress with the use of an elastic modulus. They do not directly measure the residual stress.

The idea that this study attempts to demonstrate is a combination of the acousto-elastic technique and the electronic speckle-pattern interferometry. An acoustic transducer is used to measure acoustic velocity at various location of the specimen to identify spots of residual stresses. Tensile/compressive residual stress is identified as a decrease/increase in the acoustic velocity from the nominal (non-stressed) value. Subsequently, low-level tensile/compressive loads are applied to the specimen and resultant strain is measured with ESPI (Electronic Speckle-Pattern Interferometry.) The loads are applied stepwise with a small increment, and the strain measurement is made at each step by evaluating the deformation occurring

S. Yoshida (✉)
Department of Chemistry and Physics, Southeastern Louisiana University, SLU 10878, Hammond, LA 70402, USA
e-mail: syoshida@selu.edu

T. Sasaki • M. Usui • S. Sakamoto
Department of Mechanical Engineering, Niigata University, IkarashinNinocho 8050, Nishi-ku, Niigata-shi, Niigata 950-2181, Japan

I.-k. Park
Department of Mechanical and Automotive Engineering, Seoul National University of Science and Technology, 232 Gongneung-ro, Nowon-gu, Seoul 139-743, South Korea

H. Jung • K. Kim
Department of Mechanical Design Engineering, Chosun University, 309 Pilmun-daero, Dong-gu, Gwangju 501-759, South Korea

S. Bossuyt et al. (eds.), *Residual Stress, Thermomechanics & Infrared Imaging, Hybrid Techniques and Inverse Problems, Volume 9*, Conference Proceedings of the Society for Experimental Mechanics Series, DOI 10.1007/978-3-319-21765-9_16

between the steps. When a tensile/compressive load is applied, the region of compressive/tensile residual stress show smaller strain as the applied load neutralizes the residual stress. We have conducted a series of experiments based on this idea. The aim of this paper is to report on some preliminary results.

16.2 Theoretical

Details of the acousto-elastic techniques can be found elsewhere. The gist of it is provided here. The potential energy of elastic media generally has a quadratic dependence on the inter-atomic distance near the equilibrium, and steeper/less steeper dependence on the shorter/longer side of the equilibrium as illustrated schematically by Fig. 16.1. Considering the force-displacement relation for a unit volume, we can Taylor expand the potential energy function around the equilibrium as follows.

$$U(\varepsilon) = U_0 + C^{(1)}\varepsilon + C^{(2)}\varepsilon^2 + C^{(3)}\varepsilon^3 \tag{16.1}$$

Here, $U(\varepsilon)$ is the potential energy of the unit volume as a function of strain ε, U_0 is the reference potential energy, $C^{(i)}$ is the coefficient of the i^{th}-order term of ε, and 4^{th}-order and higher terms are ignored. By differentiating (16.1) with respect to ε, we obtain the stress σ as a function of ε.

$$\sigma = \frac{dU(\varepsilon)}{d\varepsilon} = C^{(1)} + 2C^{(2)}\varepsilon + 3C^{(3)}\varepsilon^2 \tag{16.2}$$

By differentiating (16.2) once again with respect to ε, we obtain the constitutive relation of the medium.

$$\frac{d\sigma}{d\varepsilon} = 2C^{(2)} + 6C^{(3)}\varepsilon \tag{16.3}$$

In (16.3), the first term on the right hand side is a constant known as the Young's modulus $E = 2C^{(2)}$. The second term represents the non-linear behavior of the elasticity. Since compressive strain ($\varepsilon < 0$) makes the slope of the potential curve Fig. 16.1 steeper, the coefficient of the second term $6C^{(3)} \equiv -A < 0$. When the displacement from the equilibrium is small and hence $\varepsilon \ll 1$, the second term is negligible. This is the case where the deformation dynamics can be treated with the law of linear elasticity.

In the context of residual stress, even if the strain due to the external load satisfies the condition of $\varepsilon \ll 1$, the second term of (16.3) cannot be neglected if the residual strain is substantial. Putting the residual strain as ε_{res}, the strain due to external force as ε where $\varepsilon \ll \varepsilon_{res}$, we can express the constitutive relation as follows.

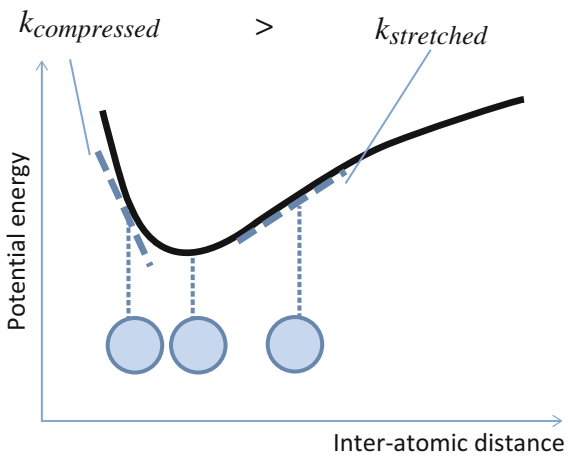

Fig. 16.1 Elastic energy potential as a function of inter-atomic distance

$$\frac{d\sigma}{d\varepsilon} = E - A(\varepsilon_{res} + \varepsilon) \tag{16.4}$$

Consider the equation of motion for a unit volume experiencing residual stress. Setting up a coordinate axis x parallel to ε, we can express the differential force acting on the unit volume as follows.

$$\frac{d\sigma}{dx} = \frac{d\sigma}{d\varepsilon}\frac{d\varepsilon}{dx} = (E - A\varepsilon_{res})\frac{d\varepsilon}{dx} \tag{16.5}$$

Here ε is dropped on the rightmost hand side as $\varepsilon \ll \varepsilon_{res}$. Using displacement ξ and $\varepsilon = d\xi/dx$, we can put the equation of motion in the following form.

$$\rho\frac{d^2\xi}{dt^2} = \frac{d\sigma}{dx} = (E - A\varepsilon_{res})\frac{d^2\xi}{dx^2} \tag{16.6}$$

Here ρ is the density of the elastic medium. Equation (16.6) yields a longitudinal wave solution that travels with phase velocity v_{ph} in the following form.

$$v_{ph} = \sqrt{\frac{E - A\varepsilon_{res}}{\rho}} \tag{16.7}$$

With the assumption that the residual stress does not alter the density, (16.7) indicates that a tensile residual stress $\varepsilon_{res} > 0$ decreases the phase velocity of an acoustic wave and a compressive residual stress $\varepsilon_{res} < 0$ increases it from the nominal value of v_{ph0}

$$v_{ph0} = \sqrt{\frac{E}{\rho}} \tag{16.8}$$

This is the operation principle of the acousto-elastic techniques for residual stress analysis. In principle, from the deviation of the acoustic phase velocity from the nominal value the residual stress can be evaluated. However, in reality, the residual stress evaluated in this method is substantially greater than a possible value. Among various causes for the discrepancy, possible causes include the accuracy of the coefficient A. Even if the value is accurate for a given elastic medium under the condition where the medium is under a purely elastic deformation, it is likely that the region of residual stress where the acoustic wave is applied for the velocity measurement can be represented by a pure nonlinear elasticity. It is likely that some portion of the region is plastically deformed or within the region the residual stress varies greatly so that it cannot be represented by a single value of ε_{res}. To overcome this problem, the present idea is to apply an external load just to cancel the residual stress so that the elastic modulus returns to the nominal value. Apparently, the applied load must be small enough not to cause plastic deformation.

16.3 Experimental

The specimen was a steel (skh51) plate of 18.5 mm wide, 50 mm long and 3.37 mm thick and a cemented carbide (cc) plate of the same dimension butt-brazed on their 18.5 mm sides and finished with grinding work. Thus, after the brazing, the specimen was 18.5 mm wide, 100 mm long and 3.37 mm thick (Fig. 16.2). The acoustic phase velocity measurements were made with the use of an ultrasonic transducer (Olympus M110 RM for the longitudinal wave and M156-RM for the shear waves) driven by square wave pulser/receiver (Model 5077PR) and a scanning acoustic microscope (Olympus UH3). The acoustic transducer had two types of sensor head, one operates in the longitudinal mode and the other in the shear mode. The sensor head was applied on the in-plane surface of the specimen for the measurement of the longitudinal wave velocity in the z-direction and of the shear wave velocity. Here, in accordance with (16.7), the longitudinal and shear wave velocities probed the elastic moduli along the thickness and parallel to the xy-plane, respectively. For the elastic modulus along the x- and y-axis, the sensor head was rotated by 90° about a line perpendicular to the specimen surface. Figure 16.2 shows

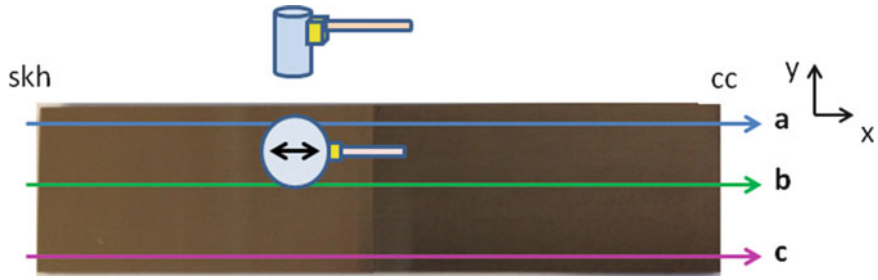

Fig. 16.2 Specimen and transducer head

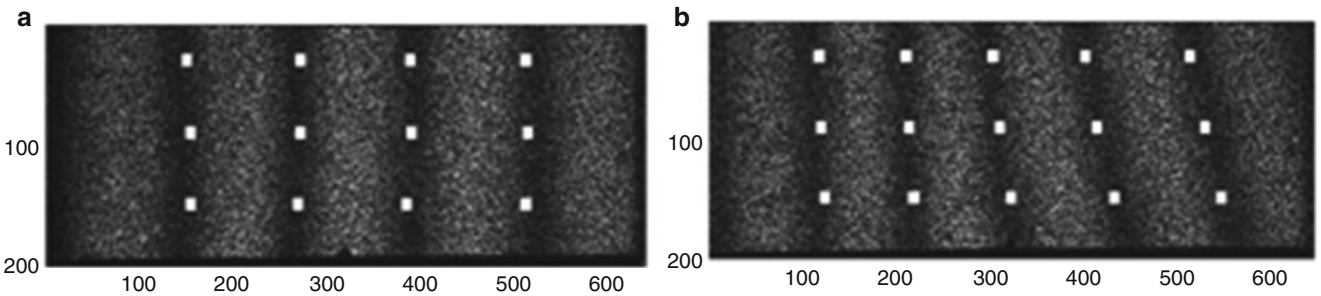

Fig. 16.3 Carrier fringes (**a**) and carrier fringe plus deformation fringes (**b**)

an arrangement for the measurement of shear wave oscillating along the *x*-axis or the elastic modulus in the *x*-direction. The scanning acoustic microscope (SAM) used an acoustic lens with focal plane 250 μm or less from the *xy*-surface of the specimen; thus, it probed the elastic modus of the subsurface region.

The external tensile load was applied along the *x*-axis to the specimen, and the resultant strain was measured with an in-plane displacement sensitive dual beam Electronic Speckle-Pattern Interferometric (ESPI) setup. The displacement was read out based on the analysis of dark fringes; a fringe order was assigned to each dark fringe and the displacement between the dark fringes was estimated via interpolation. A system of carrier fringes was introduced prior to the application of the tensile load (Fig. 16.3a). This was important for two reasons. First, when a tensile load was applied to a butt-joint specimen perpendicular to the joint, the specimen tended to stretch more on one end of the joint than the other end due to the non-uniformity in the joint strength. This made the displacement contours practically parallel to the tensile axis (in other words, the deformation involved bodily rotation) and therefore the number of fringes along the tensile axis small making the interpolation difficult. Second, since the elastic modulus of the cemented carbide (cc) was higher by a factor of three, the displacement on the cc side is much smaller than the skh side. With the introduction of the carrier fringes, the displacement due to tensile load could be read as the change of the dark fringe location, as Fig. 16.3b indicates. The tensile load was applied with an increment of 0.2 kN, or an average stress of 3.2 MPa.

16.4 Results and Discussions

Figure 16.4 plots the acoustic wave velocity measured for the *z*-direction (a), the *x*-direction (b) and *y*-direction (c), along with the nominal values [(16.8)] of the skh and cc specimens. The wave velocity in the *z*-direction was measured with the SAM and the acoustic transducer in the longitudinal wave mode. The wave velocities in the *x*- and *y*-directions were measured with the acoustic transducer in the shear wave mode. The measurements were made along the three reference lines a, b and c shown in Fig. 16.2.

Analyze the acoustic velocity data presented in Fig. 16.4. Consider the cc side first. Along all three reference-lines in common, the normalized acoustic velocity appears lower than the nominal value in the *z*-direction, and higher the *x*- and *y*-directions. These trends are rather uniform over the entire length of the cc side. As indicated by Fig. 16.1, the elastic modulus of a medium becomes higher/lower when it is compressed/stretched. According to (16.7), the higher/lower elastic modulus increases/decreases the acoustic velocity. The observed changes in the acoustic velocity from the nominal values on the cc side indicate that this side of the specimen is stretched along the thickness and compressed along the *xy*-plane

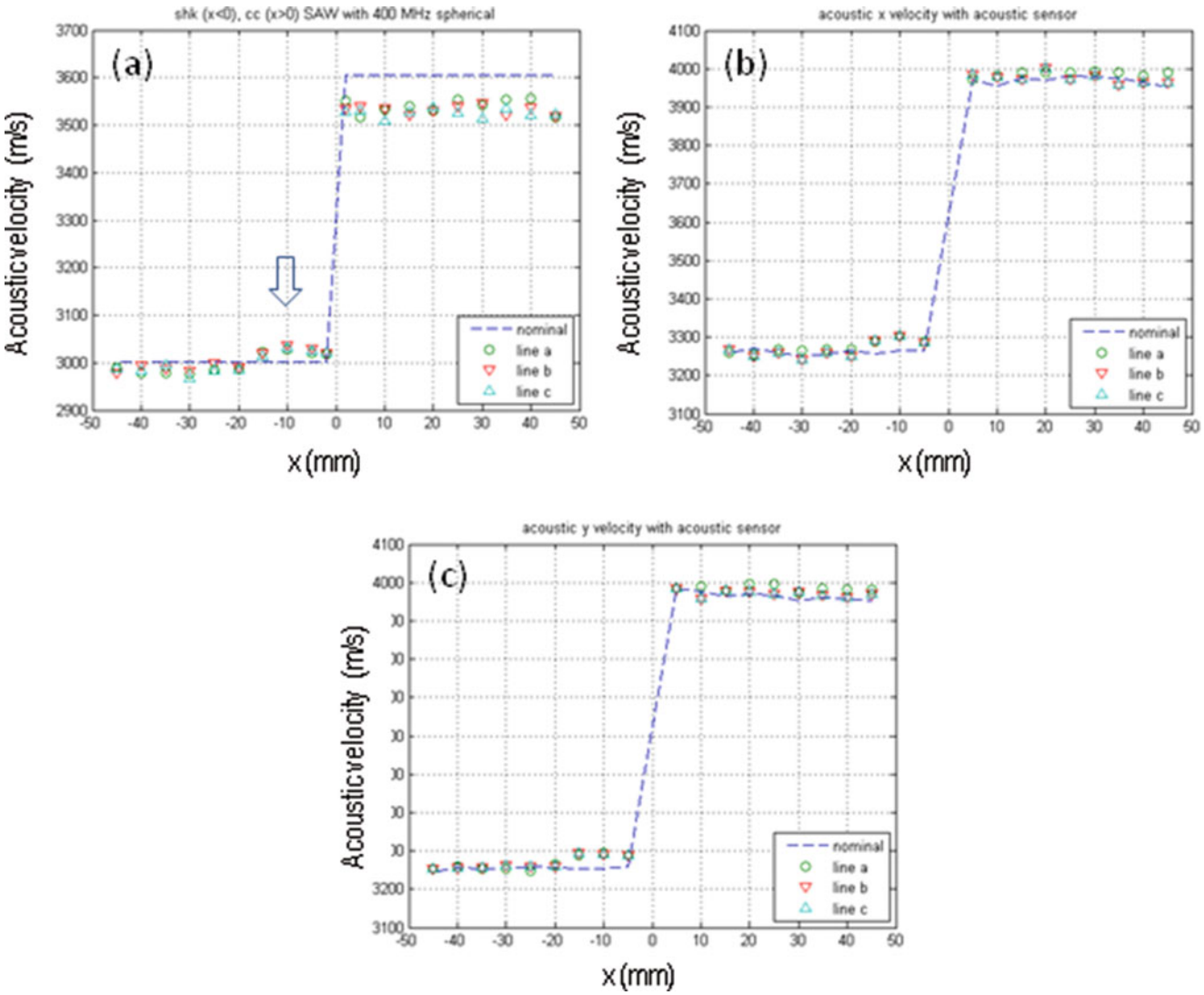

Fig. 16.4 Acoustic velocity in z (**a**), x (**b**) and y (**c**) directions

uniformly. On the skh side, on the other hand, the situation is different. Unlike the cc side, the acoustic velocity changes from the nominal values are not uniform for all the three directions. In the near joint regions highlighted by an arrow in Fig. 16.4a ($-20 < x < 0$ mm), the normalized acoustic velocity appears to be greater than the nominal values in all three directions, indicating that the skh plate is compressed three-dimensionally in this region. In the rest of the skh side, the acoustic velocity is somewhat lower than the nominal value in the *z*-direction, and similar to the nominal values in the *x*- and *y*-directions.

These observations all together are illustrated in Fig. 16.5 and can be explained as follows. During the brazing operation, two plates to be joined were held at the far ends from the joint. Consequently, the plates had less constraint to be thermally expanded along the thickness than along the *x*- or *y*-axes. The more uniform nature of the thermal deformation observed on the cc side can be ascribed to the higher thermal conductivity in cc than skh. The compressive deformation along the *x*- or *y*-axes represents the Poisson's effect where the medium selects the z-axis to be the preferred axis of thermal expansion due to the less constraint. The observations on the skh side can be explained accordingly. The lower thermal conductivity of skh makes this side to be heated more slowly and less uniformly than the cc side. Skh has a lower elastic constant and a higher thermal expansion coefficient than cc. Consequently, the skh side responds to the heat input by the brazing operation in the following way. As the joint region is heated, the cc side expands faster than the skh side. When the cc side is thermally expanded as discussed above, it tends to expand towards the skh side because it is softener along the *xy*-plane than the cc side because of the lower elastic modulus and higher thermal expansion coefficient. While this thermal deformation is taking place on the skh side near the joint, the region closer to the end at $x = -50$ mm is colder than the near joint due to the low

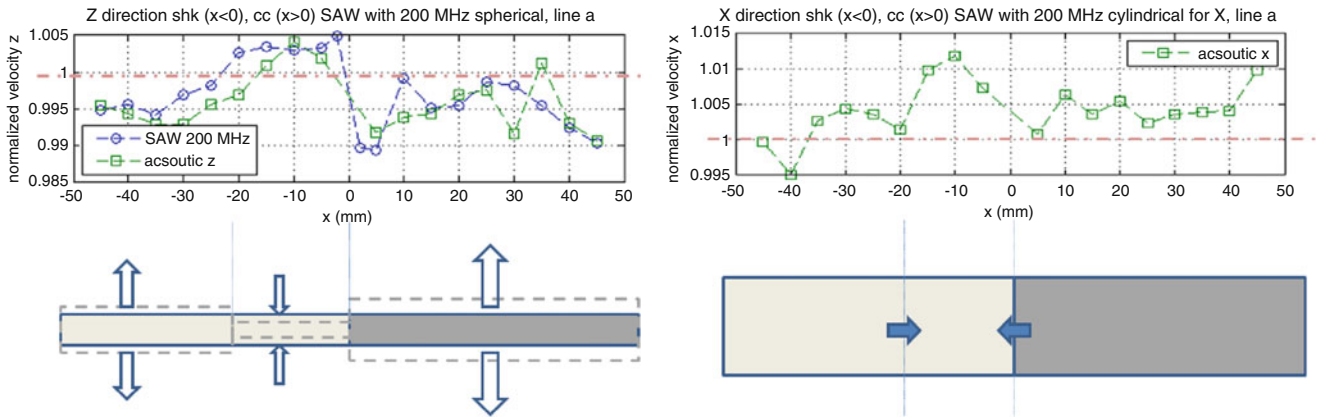

Fig. 16.5 Acoustic velocity profile (*top*) and resulting thermal expansion and compression (*bottom*). The *left* is for the *z*-direction and *right* is for the *x*-direction. The acoustic velocity profile for the *z*-direction show both those measured with the acoustic transducer in the longitudinal wave mode and with the scanning acoustic microscope

Table 16.1 Material constants

	Elastic modulus (GPa)	Thermal expansion (10^{-6} K^{-1})	Thermal conductivity (Wm^{-1} K^{-1})
High speed steel (skh 51)	219	11.9	23.0
Cemented carbide (V30)	580	5.3	67.0

thermal conductivity. These all situations make the near joint region of the skh side be compressed by being sandwiched by the thermally expanding cc side and relatively cold and rigid skh near end region. The constraints at the x $=-50$ mm end enhances this sandwiching effect. Table 16.1 summarizes the material constants of cc and skh pertinent to the discussion.

Figure 16.6 plots the normalized acoustic velocities along the *z*- and *x*-axes as a function of *x* measured for all the three-reference lines. For the velocity along the *z*-axis, the data obtained with the acoustic transducer and SAM are compared. As mentioned above, in the present study the SAM probed the elastic modulus of the subsurface region (<0.25 mm from the surface for the thickness of 3.37 mm). The agreement between them indicates that the observed trend is uniform along the thickness. The normalized acoustic velocity along *y*-axis shows a very similar behavior to the *x*-axis, indicating that the thermal effect and resultant deformation is similar to each other.

The *x*-component of the displacement resulting from the tensile load is plotted in Fig 16.7 as a function of *x* for reference line a (Fig. 16.2). Also plotted is the acoustic velocity along the *x*-axis measured with the acoustic transducer. Near $x = -10$ mm where the acoustic velocity has a peak and therefore the skh presumably experiences compressive residual-stress along the *x*-axis, the displacement from 0 to 0.2 kN shows a small hump. The displacement from 0.2 to 0.4 kN does not have such a hump, making the space between these two displacement curves greater than other range of *x*. The greater space between the two displacement curves indicates that the skh is deformed less when the load was increased from 0 to 0.2 kN than from 0.2 to 0.4 kN. Notice that in the displacement from 0.2 to 0.4 kN, the displacement curve in the near $x = -10$ mm range indicate more or less uniform deformation. These observations can be interpreted as that the compressive residual stress near $x=-10$ mm region is neutralized by the external tensile stress when the external load of 2.2 kN was applied. Assuming that the residual compressive stress is neutralized by the applied stress when the load is 0.4 kN, the residual stress can be estimated as 0.4 kN/(18.5 $\times$ 3.37 mm^2) $=$ 6.4 MPa.

Figure 16.8 plots the results of a similar tensile experiment with an in-plane displacement sensitive ESPI setup where a dog-bone shaped, welded steel (ASTM AH 36) specimen was pulled in a similar fashion. The central portion of the specimen was 70 mm long, 12.5 mm wide, 6 mm thick, and the middle of the 70 mm portion (i.e., 35 mm from one end of the shoulder) was butt-welded with CO_2 shielded bead welding. The current of the welding arc was varied in a range of 120–150 A. The vertical axis labeled "elastic modulus" was evaluated by dividing the averaged stress by the strain of the fusion zone on the tensile axis. Here the averaged stress was obtained by dividing the applied load by the cores sectional area of the fusion zone, and the strain was by dividing the stretch of the fusion zone along the tensile axis at the center of the weld by the weld length along the tensile axis. The lowest plot labeled "base" is the same plot for the non-welded specimen of the same material and dimension. The fact that the elastic modulus is constant for the base data indicates that the applied load did not cause plastic deformation. This constant value is 200 GPa, which is reasonable for AH 36 steel.

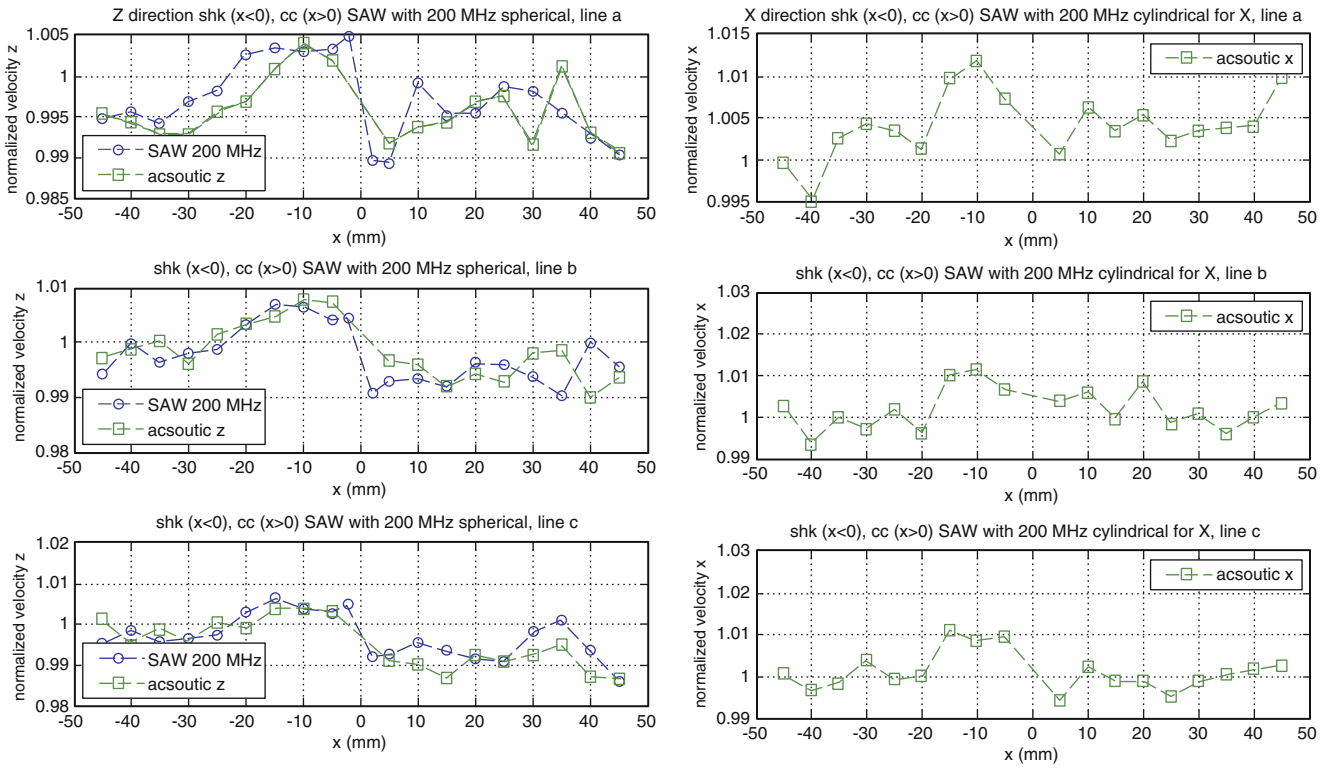

Fig. 16.6 Acoustic velocity normalized to nominal value along the axis (*left*) and axis (*right*)

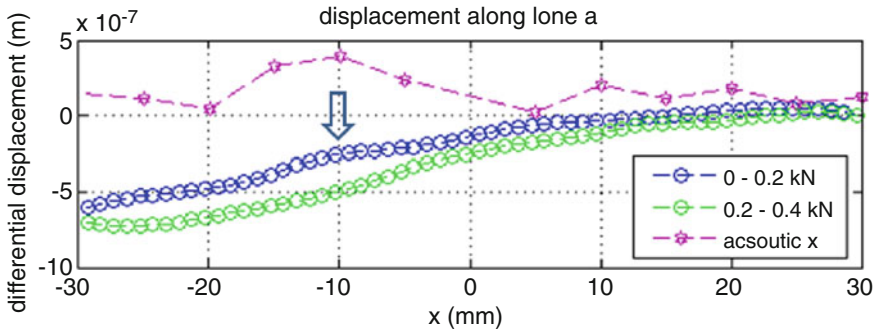

Fig. 16.7 Change in the elastic modulus with applied tensile load for a CO_2 bead-welded steel (ASTM AH36) specimen of 70 × 12.5 × 6 mm gauge dimension

In most welded cases in Fig. 16.8, the elastic modulus decreases as the applied load is increased, showing a minimum in the range of the applied load. The minimum elastic modulus increases with the welding current, indicating that the specimen became more rigid with the increase of the welding heat. As compared with the base case, the increases in the elastic modulus is more than 5 GPa, or 5/200 = 2.5 %. Using a typical value of 500–800 GPa for the third order elastic coefficient [9] [$6C^{(3)}$ in (16.3)], the corresponding residual strain is 0.6–1 %, or the residual stress is 200 × 0.006 to 200 × 0.01 or 1.2–2 GPa. This value is an order of magnitude higher than the ultimate tensile strength of steels, and it is impossible that the residual stress causes this. The reason of this behavior is unclear at this time.

The decrease in the elastic modulus toward the minimum can be interpreted as the compressive residual stress is being reduced as the increase of the applied load. It is interesting to note that the minimum appears at a lower external load in the 120 A case than the 150 A case. When the current is 120 A/150 A, the minimum appears when the load is 9 kN/12 kN. From the measured cross-sectional areas of $7.88 \times 10^{-5}(\mathrm{m}^2)$ and $1.06 \times 10^{-4}(\mathrm{m}^2)$ for the 120 and 150 A cases, the corresponding increases in the stress from the 6 kN load to the respective loads for the minimum can be estimated as $[(9-6) \times 10^3]$ (N)/$7.88 \times 10^{-5}(\mathrm{m}^2)$ = 38 (MPa) and $[(12-6) \times 10^3]$ (N)/$1.06 \times 10^{-4}(\mathrm{m}^2)$ = 56 (MPa), respectively. This value is an order of magnitude higher than the above-argued case of the brazed steel specimen.

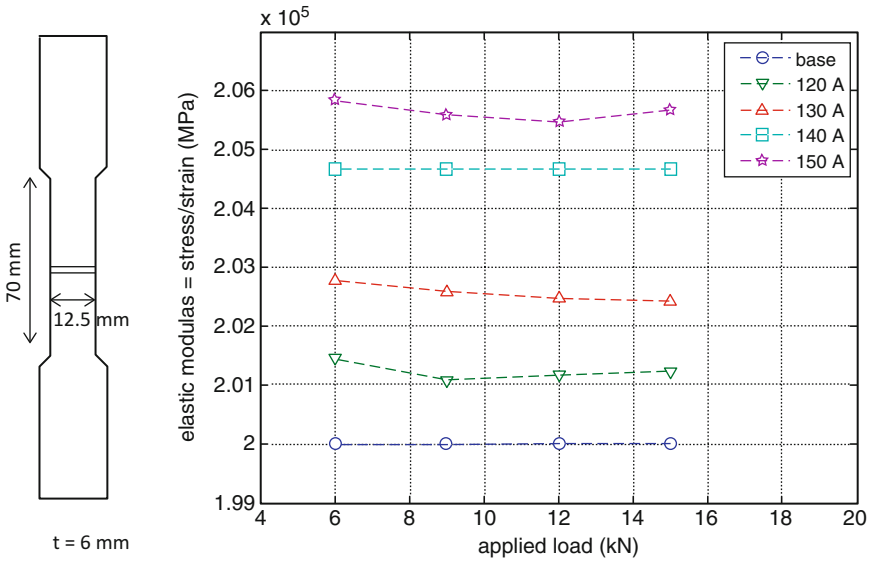

Fig. 16.8 Differential deformation along line a (from 0 to 0.2 and 0.2 to 0.4 kN)

In these two cases, the curve tends to increase with the load after the minimum. This observation can be interpreted as follows. After the compressive residual stress is neutralized by the applied tensile stress, the fusion zone starts to be stretched with the nominal elastic modulus. While this happens some other part, presumably the mostly heat-affected zone, starts to be deformed plastically. This makes the deformation of the fusion zone relatively smaller, and that makes the curve rises with the increase of the load.

16.5 Conclusions

Compressive residual stresses induced by brazing and welding joint processes were analyzed based on acousto-elasticity and optical interferometry. The brazed specimen was a butt joint of dissimilar materials, and the welded specimen was a butt joint of similar materials. Increase and decrease in the acoustic velocity from the nominal value were observed at different locations on the specimen, indicating distribution of compressive and tensile residual stresses. The observed distribution of the residual stresses was explained qualitatively through consideration of thermal expansion and the difference in the thermal conductivity and elastic modulus between the dissimilar materials. The optical interferometer was used to measure the strain induced by an external tensile load. Both specimens showed a behavior that can be interpreted as the external tensile stress neutralized the residual stress. Based on this interpretation, the compressive residual stresses were estimated to be of the order of 5 and 56 MPa for the respective specimens.

Acknowledgement The present study was supported by the National Research Foundation of Korea (NRF) grants funded by the Korean government MEST, NRF-2013R1A2A2A05005713, NRF-2013M2A2A9043274.

References

1. M.P.I.M. Eijpe, P.C. Powell, Determination of residual shear stress in composites by a modified layer-removal method. J. Mater. Sci. **33**, 2019–2026 (1998)
2. S.J. Roberts, L.N. McCartney, W.R. Broughton, A novel method of determining stress distribution in plates using the incremental slitting technique. J. Strain Anal. Eng. Design **46**, 280–297 (2011)
3. C.S. Vikram, M.J. Pchersky, C. Feng, D. Engelhaupt, Residual-stress analysis by local laser heating and speckle-correlation interferometry. Exp. Tech. **20**, 27–30 (1996)
4. G.S. Schajer, L. Yang, Residual-stress measurement in orthotropic materials using the hole-drilling method. Exp. Mech. **12**, 324–333 (1994)
5. S. K. Bate, D. Green, D. Buttle, A review of residual stress distribution s in welded joints for the defect assessment of offshore structures. Health and Safety Exclusive—Offshore Technology Report, ISBN 0-7176-2411-0, Her Majesty's Stationery Office (1997)

6. P. Colegrove, C. Ikeagu, A. Thistlethwaite, S. Williams, T. Nagy, W. Suder, A. Steuwer, T. Pirling, The welding process impact on residual stress and distortion. Sci. Technol. Weld. Joining **14**(8), 717–725 (2009)
7. L. Karlsson, Residual stresses due to welding of a nozzle to a pressure vessel, Master's dissertation. Division of Solid Mechanics, Lund University, Sweden (2005)
8. A.G. Every, W. Sachse, Determination of the elastic constants of anisotropic solids from acoustic-wave group-velocity measurements. Phys. Rev. B (Condensed Matter) **42**, 8196–8205 (1990)
9. D. D. Muir, One-sided ultrasonic determination of third order elastic constants using angle-beam acoustoelasticity measurements. Master's thesis, School of Electrical and Computer Engineering, Georgia Institute of Technology (2009)

Chapter 17
Nondestructive Characterization of Thin Film System with Dual-Beam Interferometer

Hae-Sung Park, David Didie, Daniel Didie, Sanichiro Yoshida, Ik-Keun Park, Seung Bum Cho, and Tomohiro Sasaki

Abstract A dual-beam Michelson interferometer has been built with two thin-film specimens configured as end mirrors. The two specimens have been prepared by coating a 10 nm thick titanium film on a silicon substrate and coating a 100 nm thick platinum over the titanium film. For one of the specimens, the silicon surface has been treated prior to the coating (the treated specimen). Each specimen is oscillated from the rear surface of the substrate with an acoustic transducer at a driving frequency ranging from 6 to 14 kHz, and the resultant film surface displacement is measured with the interferometer. The dual-beam configuration is important to compare the treated and untreated specimens under the same experimental conditions. The oscillation amplitude of the transducer's surface has been calibrated so that the specimens can be oscillated with the same acoustic amplitude for the entire frequency range. The study has confirmed our previous observation that the film-substrate interface of the treated specimen shows a resonance-like behavior near 8 kHz, exhibiting higher oscillatory displacement than the untreated specimen.

Keywords Thin-film • Opto-acoustic technique • Adhesion strength • Metal-silicon interface • Michelson interferometer

17.1 Introduction

Thin film systems are used in a variety of applications ranging from microelectronic products to artificial joints. In all these applications, without an exception, the adhesion strength of the film onto the substrate is an extremely important factor that determines the life of the product. As an example, slight degradation of the interface region between thin-layers of dissimilar materials used in a microelectronic assembly can cause a fatal malfunction of the devise. The quality control of these interfacial layers is more important than ever. On the other hand, the evaluation of the adhesion strength of dissimilar materials is not a simple task. In particular, nondestructive evaluation of the adhesion strength, which is obviously much more preferable than destructive methods, is complex. Most nondestructive methods in this field use ultrasonic techniques. The ultrasonic waves are used to either detect abnormality in the interfacial region or probe the elastic behavior of the interfacial layers. While the ultrasonic technologies used in these applications are matured and reliable, these techniques have limitations. The detection of abnormality is possible only after a problem occurs; the method cannot predict generation of abnormality. Often abnormality such as a micro-crack is generated during the routine use of the device, causing immediate failure of the functionality. In the technique to probe the interfacial elastic behavior, the operation frequency has an intrinsic issue. Normally, these techniques excite ultrasonic wave inside the film and substrate materials, and probe the interfacial strength from analysis of the wave's propagation characteristics. The recent trend of thin-film systems is to reduce the film thickness for better performance as the whole system. Accordingly, the ultrasonic frequency tends to be increased. The acoustic velocity in the film or substrate materials is typically in the range of km/s. If the film thickness is 100 nm, for example, the wavelength must be of the order of 10 nm, leading to the operation frequency of 100 GHz. The elastic modulus of the interface is normally orders of magnitude lower than the film or substrate. As a simple physical

H.-S. Park (✉) • I.-K. Park • S.B. Cho
Department of Mechanical Engineering, Seoul National University of Science and Technology, Seoul, Republic of Korea
e-mail: acas_hs@naver.com

D. Didie • D. Didie • S. Yoshida
Department of Chemistry and Physics, Southeastern Louisiana University, Hammond, LA 70402, USA

T. Sasaki
Department of Mechanical Engineering, Niigata University, IkarashinNinocho 8050,
Nishi-ku, Niigata-shi, Niigata 950-2181, Japan

S. Bossuyt et al. (eds.), *Residual Stress, Thermomechanics & Infrared Imaging, Hybrid Techniques and Inverse Problems, Volume 9*, Conference Proceedings of the Society for Experimental Mechanics Series, DOI 10.1007/978-3-319-21765-9_17

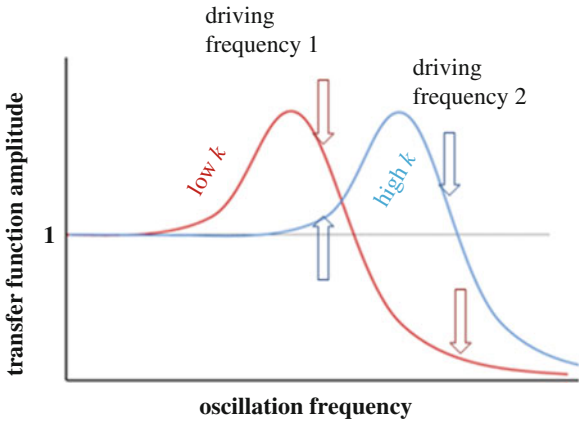

Fig. 17.1 Resonance curve

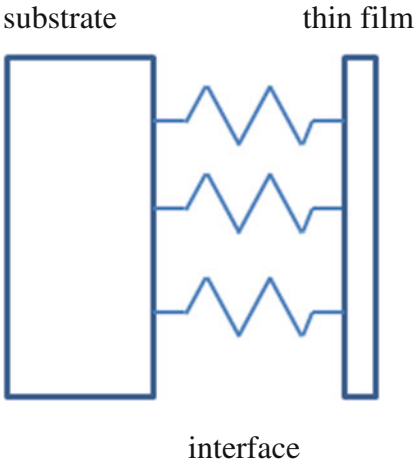

Fig. 17.2 Physical model of interface

consideration would indicate, this means that the response of the interfacial region is expected to be very low. Figure 17.1 illustrates the power spectra of two harmonic oscillators, one with high stiffness and the other with low stiffness. Consider the system consisting of these two harmonic oscillators is driven at the two frequencies indicated in the figure. If the driving frequency is high (frequency 2), the oscillator with the low stiffness (low k) would exhibit lower oscillation amplitude than the other. If the driving frequency is low (frequency 1), the oscillator with the lower stiffness would exhibit higher oscillation amplitude. In the context of a thin film system, if the specimen is driven at an ultrasonic frequency, the output signal is dominated by the response of the substrate and film materials rather than the interface. To probe the elastic behavior of the interface, it is important to lower the driving frequency so that the interfacial region would respond more sensitively. Figure 17.2 schematically illustrates the situation where the substrate and film as rigid bodies are connected with the spring-like interface. More description regarding this spring model will be provided in a later section.

Considering this situation, we started a project in which we use acoustic energy to oscillate thin film specimens and read out the response of the interface with an optical interferometer. The idea is that with the use of an acoustic frequency low enough to oscillate both the substrate and film as rigid bodies and high enough to excite spring-like vibratory motion in the interfacial region with reasonably high amplitude. We configured a Michelson interferometer with one of the end mirror replaced with a thin film specimen having the film-side surface inward, oscillated the specimen from the rear side of the substrate and read out resultant film surface oscillation as relative optical path length difference with the other interferometric path reflected from a still optical reflector [1]. Using this setup, we previously analyzed the interfacial elastic behavior for several types of thin film specimens. With the driving frequency ranging from 5 to 30 kHz, we tested several pairs of thin film systems of identical substrate and film materials and dimensions, one coated on a pre-coating surface treated substrate (called the treated specimen) and the other on the same substrate without surface treatment (called the untreated specimen). Consequently, we observed resonance-like behavior in both types of specimens [2]. The treated specimen was considered to generate stronger adhesion, and past ultrasonic analysis [3] verified it at a certain frequency. More recently, in a specimen of

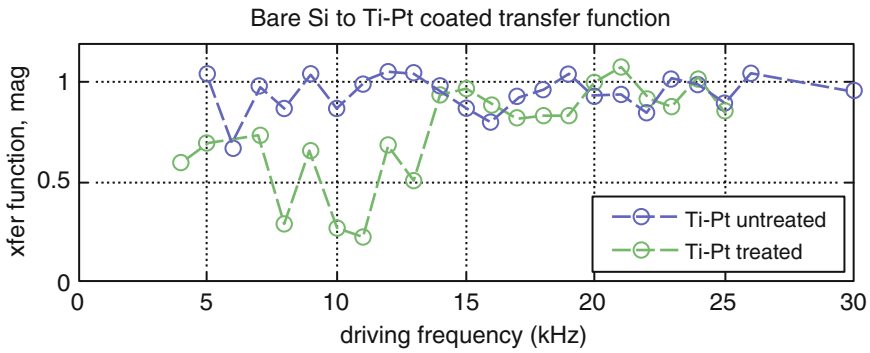

Fig. 17.3 Interferometric fringe contrast for untreated and treated specimens normalized to bare Si

platinum-titanium coated on a silicon substrate, we found the treated specimen showed substantially higher interface displacement amplitude in a certain driving frequency range than the untreated specimen. In these experiments, we tested uncoated silicon specimens for comparison, and observed that the surface oscillation was much lower than the film surface, confirming that the coated specimens revealed the interfacial behaviors. Figure 17.3 [4] shows the decrease in the optical fringe contrast due to the film surface oscillation. The specimen is a 10 nm thick titanium (Ti) film coated on a silicon (Si) substrate with a 100 nm thick platinum (Pt) film coated over the Ti film. In Fig. 17.3, the lower the value, and the greater the oscillation amplitude is, and the data points are normalized to the value for the bare silicon case.[1] Thus, the plot effectively represents the transfer function from the Si surface displacement to the film surface displacement. Our previous results indicated the possibility that those valleys as the one observed in Fig. 17.3 near 10 kHz for the treated specimen represent resonance of the interface oscillation [1, 2].

Although we had anticipated that the film surface of the treated specimen could oscillate greater than that of the untreated specimen in a certain frequency range, it was a bit surprising to us that the treated specimen showed greater oscillation amplitude than the untreated specimen at the level shown in Fig. 17.3. There were two uncertainties regarding the experiment that produced Fig. 17.3. The first was the transducer's frequency characteristics. In the past experiment, we used constant voltage amplitude to operate the transducer and constantly observed that the interferometric fringe contrast decreased drastically when the driving frequency was lower than 10 kHz. It was not clear if it was because the optical setup has resonance in or near this frequency range or the transducer oscillates with too largely so that it motion itself lowers the fringe contrast. Since in Fig. 17.3 the data for the treated and untreated were normalized to the bare silicon case, the absolute amplitude of the transducer oscillation was theoretically cancelled. However, it was possible that in the low frequency range the transducer's amplitude was so large that the interferometric arm was misaligned to cause an extra factor to decrease the fringe visibility. If this was the case, the treated specimen, which showed the resonance-like valley in the lower frequency range, could have the extra factor to decrease the fringe contrast. Apparently, it was much better to calibrate the transducer's motion so that its oscillation amplitude was constant over the frequency sweep. However, we were unable to measure the transducer's oscillation absolutely. The other uncertainty was the temporal fluctuation of the fringe contrast. In these past experiments, we evaluated one specimen at a time. We were aware that the fringe contrast fluctuated over time even if the transducer was turned off. This caused the comparison of the treated and untreated specimens inaccurate.

To solve the above problem, we recently made two modifications. First, we measured the transducer's displacement as a function of the driving frequency so that we can oscillate the specimen with the same input amplitude in the actual thin-film analysis. Second, to compare the untreated and treated specimens under as close as possible conditions, we introduced an additional pair of interferometric paths in the optical interferometer and captured the fringe images of both specimens exactly at the same time. Consequently, we confirmed that the Ti-Pt film on the treated Si substrate oscillated with greater amplitude than on the untreated substrate in the near 9 kHz frequency range. The aim of this paper is to report on these recent results.

[1] More explanation will be provided later in this paper about this plot and the way we evaluate the displacement from the interferometric optical data.

17.2 Theoretical

17.2.1 Physical Model

When metal atoms are deposited on the surface of a silicon substrate, various chemical bonds are formed [5]. The potential well of all these chemical bonds is approximately quadratic near the equilibrium position, and therefore the force associated with small displacement from the equilibrium position can be considered as elastic force. Depending on the quantum mechanical configuration, each bond has its own stiffness. The interface can be modeled as parallel and serial connections of these springs, and hence, as a single spring of the combined spring constant (Fig. 17.2). It is a good assumption that the spring constant of the interface is lower than the film or substrate. Otherwise, when a peeling-off force is applied to the film surface, the film or the substrate would stretch more than the interface. It is unlikely. Based on this assumption, it is possible to argue that if the entire thin-film system is subject to vibratory motion at a frequency low enough to oscillate the substrate and film as rigid bodies and high enough to induce vibration in the interface region the interfacial displacement is substantially greater than the substrate. In other words, the interface spring is stretched/compressed more than the substrate or film, making the displacement of the film surface is substantially greater than the substrate surface. If such vibratory motion is induced by an acoustic transducer attached to the rear surface of the substrate, the film surface oscillation indicates the interfacial vibration. The method we use is based on this idea, where the film surface oscillation is read out optically as relative optical path change in a Michelson interferometer. The optical configuration and the principle of operation will be described in the following section.

17.2.2 Michelson Interferometer and Principle of Operation

Figure 17.4 illustrates the Michelson interferometer schematically. Two pairs of interferometric paths, labeled 1 and 2, respectively, share the same laser source and the beam splitter. Each pair consists of light beams reflected off a mirror and a specimen. The beam reflected off the specimen is slightly tilted with respect to the beam from the mirror, as the close-up illustration on the right indicates for path 1, so that an interferometric fringe pattern consisting of parallel dark fringes is formed on the screen. Here ϕ is the optical phase, l_{10} is the path length for the beam off the mirror and l_1 is that from the specimen, d is the amplitude of the film-surface oscillation, Ω is the driving frequency of the acoustic transducer, and k is the wave number of the laser light. On the screen, the relative optical phase is a linear function of x where the x-axis is

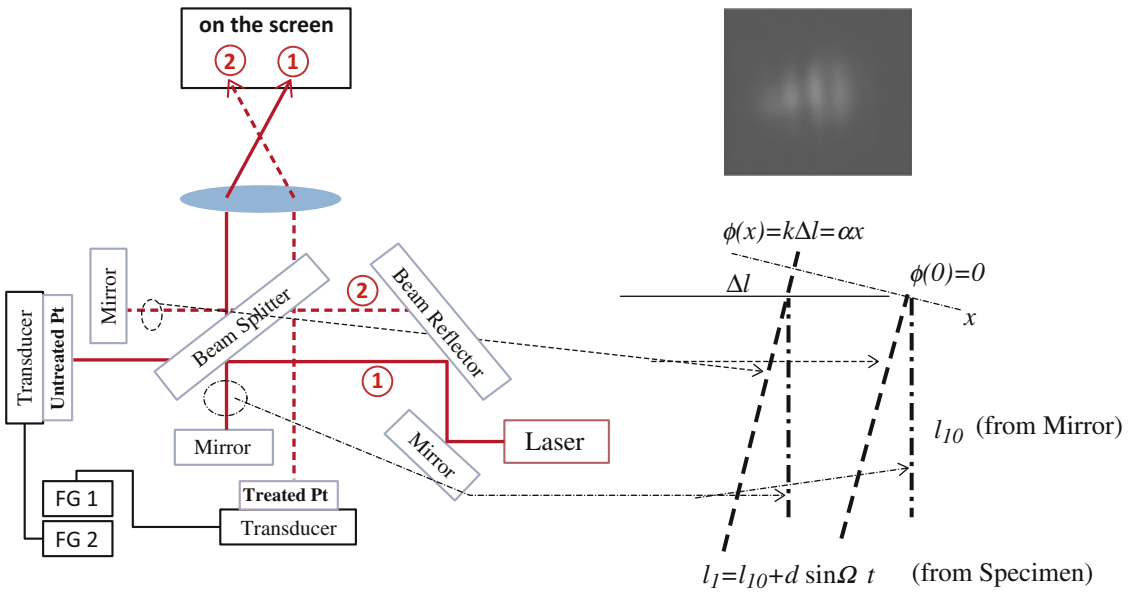

Fig. 17.4 Interferometer entire setup (*left*) and close-up view of the two beams of path 1 (*right*). In the close-up view, the *dashed lines* indicate the beam reflected off the specimen and the *dash-dotted lines* indicate the other beam from the mirror

perpendicular to the dark fringes. As the film surface oscillate with amplitude d, the optical path varies as a function of time as $l_1(t) = l_{10} + d \sin \Omega t$. Consequently, the dark fringes oscillate at the same frequency. Since the digital camera that captures the fringe pattern has a frame rate much lower than Ω, this fringe motion decreases the contrast of the fringe pattern.

The decrease in the fringe contrast is evaluated in the frequency domain. Spatial intensity variation along a line perpendicular to the dark fringes (i.e., along the x-axis in Fig. 17.4) is Fourier transformed. The top left plot of Fig. 17.5 shows power spectrum densities of three sample cases where the profile with the highest peak is the case when the transducer is turned off, the profiles with the medium and low peaks are respectively the cases when the film surface displacement is medium and large. The peak frequency corresponds to the fringe interval (see the insert in Fig. 17.4) or the spatial frequency of the dark fringes. As the film oscillation amplitude d increases, the dark fringe shifts largely on the screen, making the fringe pattern more blurry at the camera's frame rate an order of lower than the frequency of the film surface oscillation. Consequently, the spectrum peak decreases. The three fringe patterns shown in Fig. 17.5 indicate the highest, medium, and lowest fringe contrasts, corresponding to the three peaks in the power spectrum plot. The decrease in the fringe contrast can be quantified as a function of the film oscillation amplitude and the wave number.

$$S \propto J_0(\delta) = J_0(kd) \tag{17.1}$$

Here $\delta = kd$ is the optical path length change due to the film surface displacement of d, $J_0(\delta)$ is the Bessel function of the first kind with order 0. The top right plot of Fig. 17.5 show the change in the spectrum peak for the three cases as a function of the amplitude of the voltage applied to the transducer; as the voltage increases, the amplitude of the transducer surface increases in proportion, decreasing the fringe contrast.

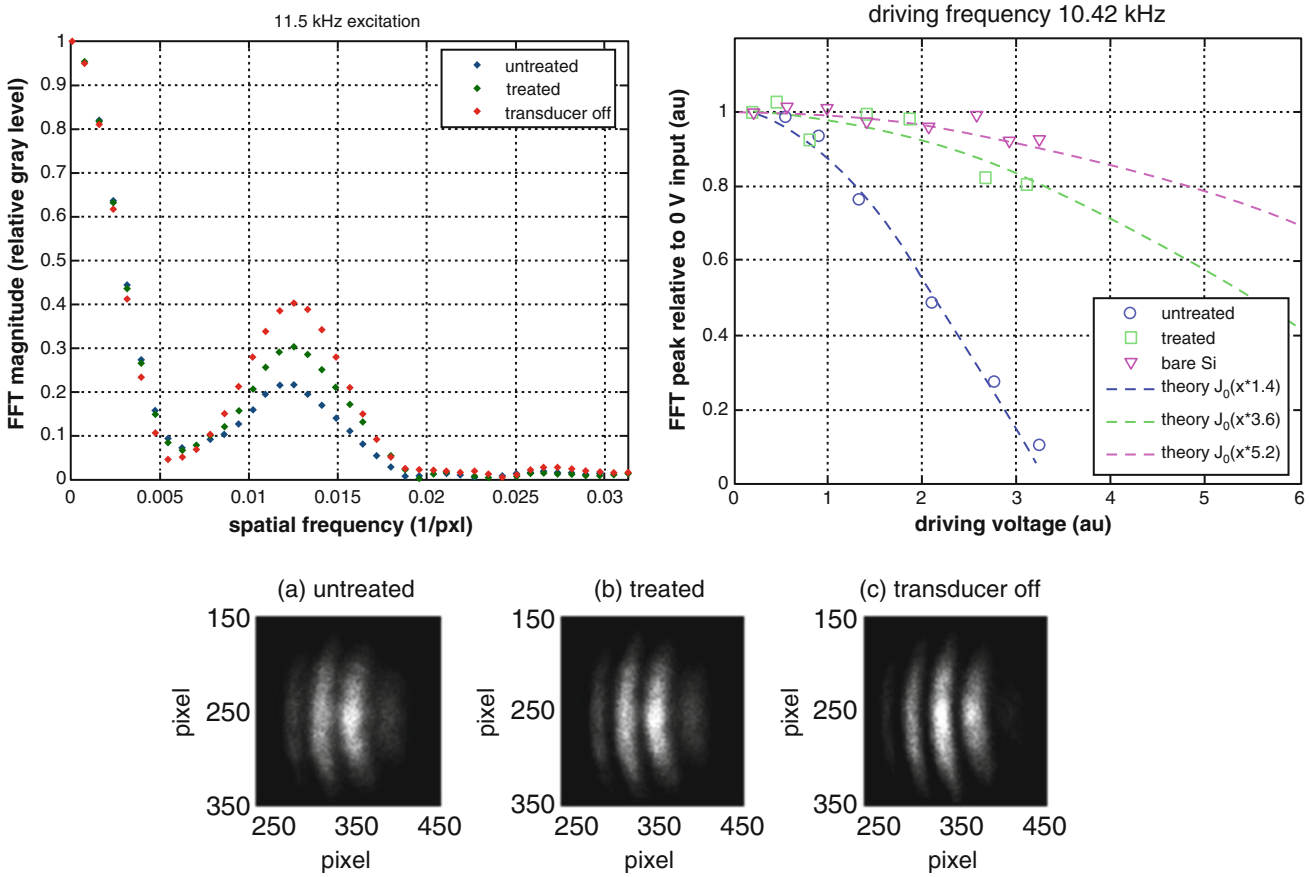

Fig. 17.5 High and low contrast fringe patterns and Bessel function

17.3 Experimental

17.3.1 Information of Pt Specimens

The thin-film specimens we used in this study were prepared with the sputtering method. On top of a silicon (Si) substrate cut along the [100] plane, first a 10 nm layer of titanium (Ti) was coated followed by 100 nm of platinum (Pt) over the Ti layer. For comparison, bare silicon specimens were tested as well. One specific question we are interested in answering through this project is the effect of pre-coating surface treatment. Oxygen-plasma bombardment is a common technique used to strengthen the adhesion between a metal film and a silicon substrate. There are two prevailing theories regarding the strengthening mechanism; the first is that the oxygen atoms knock off hydrocarbon on the Si surface making the surface hydrophobic and therefore more favorable for the metal atoms to be attached with the higher polarity. The other explanation is that the plasma bombardment makes the silicon surface rough, effectively increasing the surface area. Detailed mechanism has not been understood.

17.3.2 Operation Acoustic Frequency and Transducer Calibration

Figure 17.6 plots the amplitude of the transducer surface ξ_0 measured with a capacitive position sensor (MicroSense, Model 4810) as a function of the reciprocal of the square of the driving frequency, $\xi_0 \propto f^{-2}$, along with a linear trend line. The amplitude of the driving voltage was kept constant at 5 V peak-to-peak. The observed linearity of the oscillation amplitude to the driving frequency can be explained as follows. The acoustic transducer used in this study is magnetic or a speaker. The inductive reactance of the solenoid increases in proportion to the frequency, making the electric power at a given voltage decreases in proportion to the frequency; $P_e \propto f^{-1}V_0$. The mechanical power necessary to oscillate the transducer surface is proportional to the product of the kinetic energy of the film and the oscillation frequency. Here the film velocity is the time derivative of the displacement or in the form of the product of the displacement amplitude and the angular frequency, or proportional to $f\xi_0$. Thus, the kinetic energy is proportional to the square of the velocity, and the overall mechanical power has cubic dependence on the oscillation frequency; $P_m \propto f(f\xi_0)^2 = f^3{\xi_0}^2$. Since the mechanical and electric power are proportional to each other, ${\xi_0}^2 \propto P_m f^{-3} \propto P_e f^{-3} \propto \left(f^{-1}V_0\right)f^{-3} = V_0 f^{-4}$. So, under the condition of constant V_0, $\xi_0 \propto f^{-2}$.

To test the fluctuation of the spectrum peak signal, we kept running the interferometer with the acoustic transducer off for 1 h. Figure 17.7 shows the result. The spectrum peak appears to fluctuate approximately by 20 % over a period of 10 min.

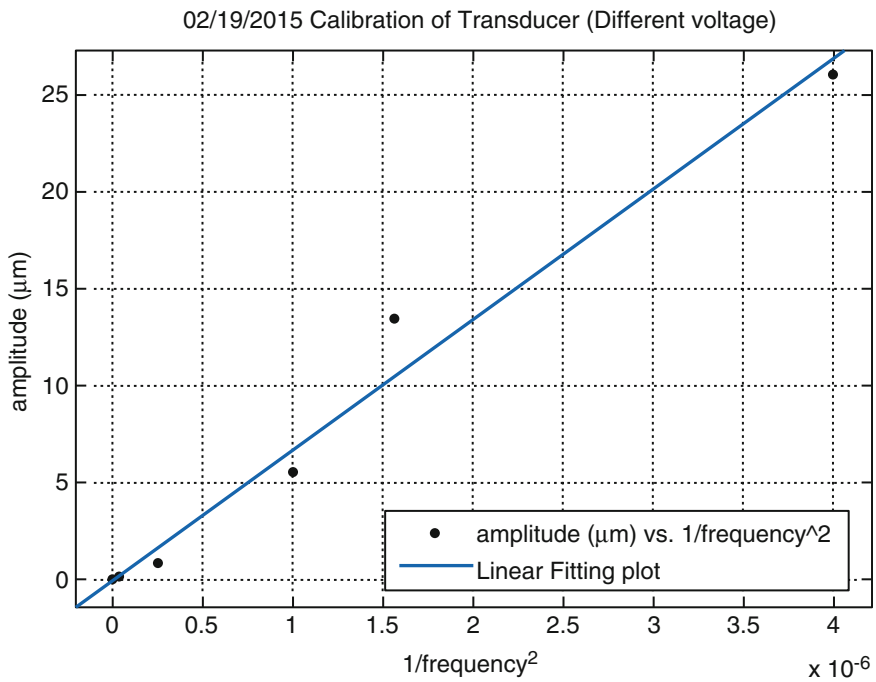

Fig. 17.6 Transducer calibration

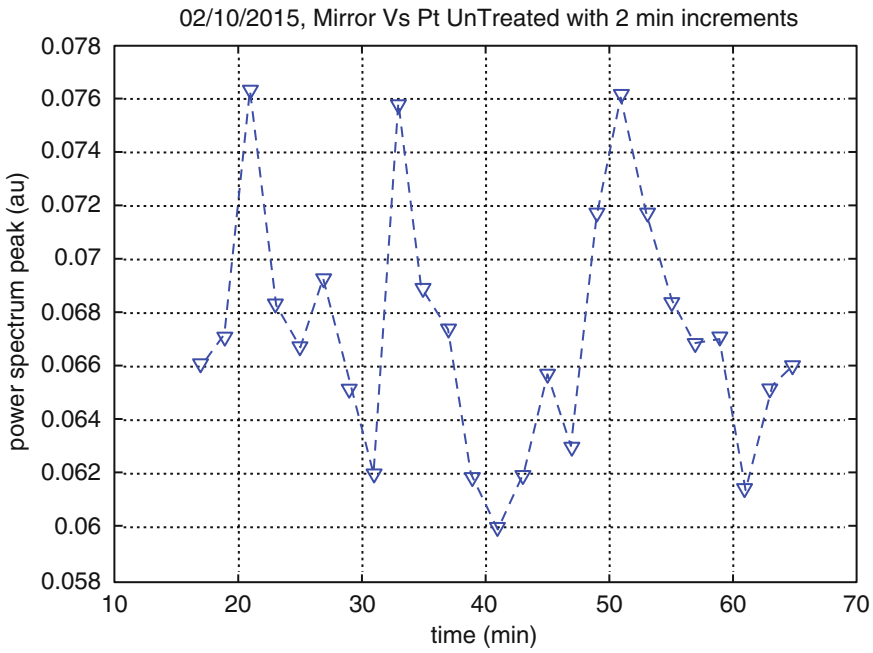

Fig. 17.7 Long term trend of spectrum peak

Any fluctuation in the relative path length difference between the two interferometric paths can cause the change in the spectrum peak. Based on (17.1), the observed spectrum peak change of 20 % corresponds to $d\delta = 0.9$ as $J_0(0.9) = 0.80$.[2] From $\lambda_0 = 632.8$ (nm) for the He-Ne laser, $d\delta = kdl = 0.9$ leads to $dl = 90$ nm. This defines the precision of the interferometer under the given noise presented by Fig. 17.7. It is interesting that the maxima appearing with this period in Fig. 17.7 are at the same level. This indicates that the maxima correspond to the situation where the interferometer condition maximizes the fringe contrast, and that the condition is reproducible. Below we discuss the cause of the relative optical path responsible for the fluctuation shown in Fig. 17.7 semi-quantitatively.

The optical path over a physical distance l can be given by (17.2).

$$OPL = 2\pi \frac{l}{\lambda} = 2\pi \frac{l}{\lambda_0} n = \left(\frac{2\pi}{\lambda_0}\right) ln \tag{17.2}$$

Here n is the refractive index of air, λ_0 is the reference wavelength corresponding to $n = 1$. The change in the optical path length, whatever the cause may be, is due to a change either in the physical length or in the refractive index, and can be written as follows.

$$dOPL = \left(\frac{2\pi}{\lambda_0}\right)(dln + ldn) = k(dln + ldn) \tag{17.3}$$

As for the change in the physical length of the interferometric arm, dl, seismic noise is the most likely cause. However, in Southeast Louisiana where the experiment was carried out, the seismic noise has a peak around 50 mHz, or 20 s in the period. This period is a factor of 30 smaller than the period of 10 min observed in Fig. 17.7. The seismic noise cannot be a significant cause for the observed fluctuation in the spectrum peak.

As far as the change in the refractive index of air, dn, is concerned, the ambient temperature fluctuation is the most-likely cause.

$$d\delta = kldn = kl\frac{dn}{dT}dT \tag{17.4}$$

[2] The maximum spectrum peak value corresponds to $J_0(0) = 1$ or $\delta = 0$. As δ increases from 0, the spectrum peak decreases as the top right plot of Fig. 17.5 indicates.

Assuming that ambient temperature change is responsible for the optical path length change $d\delta = 0.9$, using the round-trip arm length of the interferometer 13.0 cm and the temperature coefficient of refractive index for air $dn/dT = 1 \times 10^{-6}$ (1/°C) for room temperature, we can calculate $dT = 0.7$ °C as the relative air temperature change in the two interferometric arms. Our actual air temperature measurement near the interferometer arm indicates the absolute fluctuation of approximately 2 °C over a period of 10 min. With the absolute temperature change of this level, the relative temperature change of $dT = 0.7$ °C is realistic. It is possible that the 20 % fluctuation of the spectrum peak value observed in Fig. 17.7 is due to ambient air temperature fluctuation.

17.3.3 Experiment with Treated/Untreated Ti-Pt Thin-Film Specimens

We conducted experiment to compare the treated and untreated Ti-Pt thin-film specimens by mounting each specimen for the two interferometric paths 1 and 2 shown in Fig. 17.4. To investigate the resonance-like behavior observed in the treated specimen in Fig. 17.3, we focused on a driving frequency range of 7–14 kHz. To use the same transducer surface displacement for all frequencies, we varied the applied voltage based on the inverse quadratic dependence on the frequency observed in Fig. 17.6 and discussed above. The test procedure was as follows. We set the amplitude of the voltage applied to the transducer at 6 V peak-to-peak at the highest frequency of 14 KHz, and reduced the voltage amplitude as $6 \times (f/14)^2$V.[3] Here f is a driving frequency in kHz and 14 denotes the reference frequency of 14 kHz. We repeated this procedure for multiple frequency windows, always using 6 V peak-to-peak for the maximum frequency of the window. The use of multiple windows was necessary because if the frequency window was too large, the voltage at the lowest frequency became too low. This procedure resulted in applying different voltages for the same driving frequency; for instant, 6 V (peak-to-peak) was used for 10 kHz when the frequency window was 5–10 kHz, but 1.5 V was used if the window was 10–20 kHz. We calibrated the spectrum peak values resulting from these different frequency windows using the Bessel function dependence on the applied voltage shown in Fig. 17.5.

From Fig. 17.6, it is found that the voltage amplitude of 6 V at 14 kHz, and normalized for other frequencies accordingly, drives the transducer surface with amplitude of 58.3 nm. Note that this is lower than the optical path fluctuation of 90 nm caused by ambient noise discussed in Fig. 17.7. From this standpoint, the oscillation of the transducer surface can be assumed null in the assessment of the film-surface displacement.

Figure 17.8 shows the spectrum peak values obtained with the above procedure. The results of Bare Si case are shown in this figure for comparison. The two plots labeled “Bare Si” are from the two optical paths 1 and 2. The treated specimen shows the highest spectrum peak value at the lowest frequency of 7 kHz, sharply decreasing toward the minimum at 8 kHz, and gradually increases with the driving frequency. The untreated specimen, on the other hand, shows a minimum around 12–13 kHz. It is interesting to note that the maximum spectrum peak value for the treated and untreated specimens respectively approaching to the two Bare Si cases. It is possible that this is just a coincidence, but it may indicate that the film surface of the treated and untreated specimen did not show displacement relative to the substrate surface when they were driven at frequency far from the resonance.

The right plots in Fig. 17.8 are normalized to the maximum value for each data series. Note that the untreated frequency dependence appears sharper than the treated, indicating that the resonance behavior of the untreated case is a higher in the quality factor (less damping) than the treated case. This observation agrees with our previous experiment in which we used a Doppler Vibrometer to evaluate the resonance behavior of untreated and treated specimens with a single frequency measurement [6].

Figure 17.8 Spectrum peak observed with treated and untreated Ti-Pt specimen along with Bare Si. The left plots present raw data and the right plots are normalized to the maximum of each data series.

[3] At 7 kHz, for instance, the applied voltage was $6 \times (7/14)^2$=1.5 V, peak-to-peak.

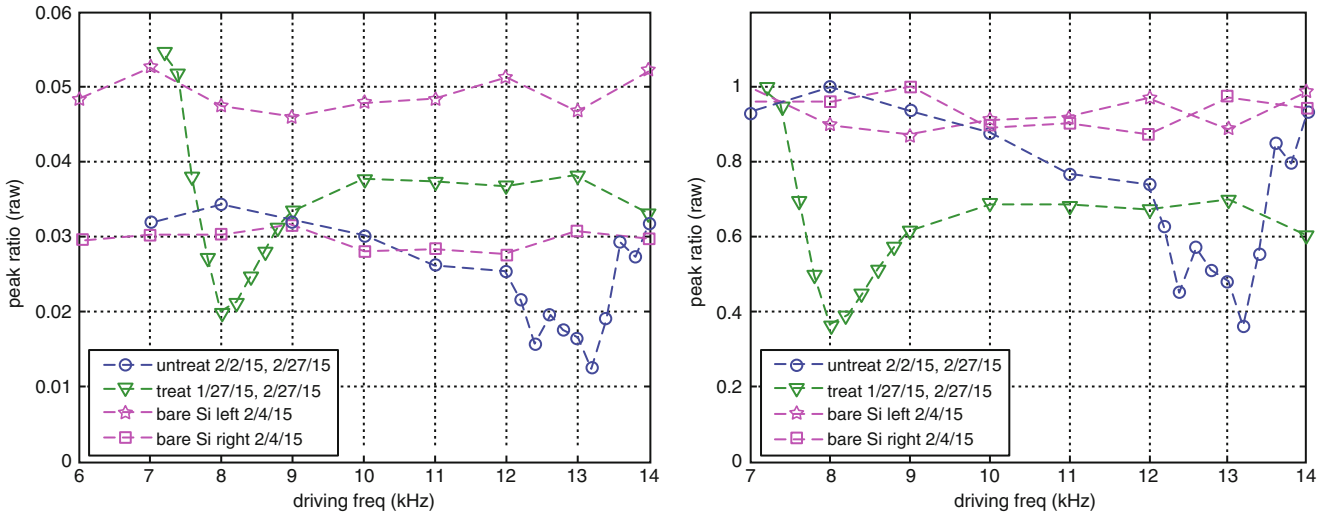

Fig. 17.8 Spectrum peak observed with treated and untreated Ti-Pt specimen along with Bare Si. The *left* plots present raw data and the *right* plots are normalized to the maximum of each data series

17.4 Summary

The present study confirmed our previous preposition that the treated specimen had a resonance-like peak in the frequency dependence of the film surface oscillation, and thereby could exhibit greater oscillation amplitude than the untreated specimen when driven at or near the resonant frequency. The dual-beam Michelson interferometer setup along with the transducer calibration provided us with the opportunity to conduct the interferometric experiment under better-controlled conditions. The untreated specimen also exhibited a resonance-like behavior at a higher frequency. The treated specimen's resonance curve seems to be broader than the untreated case, agreeing with our previous observation made with the use of Doppler Vibrometry at a single driving frequency.

Acknowledgement The present study was supported by the National Research Foundation of Korea (NRF) grants funded by the Korean government MEST, NRF-2013R1A2A2A05005713, NRF-2013M2A2A9043274.

References

1. S. Yoshida, S. Adhikari, K. Gomi, R. Shrestha, D. Huggett, C. Miyasaka, I. Park, Opto-acoustic technique to evaluate adhesion strength of thin-film systems. AIP Adv. **2**(2), 022126-1–022126-7 (2012)
2. D. Didie, D. Didie, B. Ghimire, K. Kabza, S. Adhikari, S. Yoshida, C. Miyaska, I.-K. Park, Optical interferometry for evaluation of adhesion strength of thin-film systems. Advancement of Optical Methods in Experimental Mechanics, vol. 3, Conference Proceedings of the Society for Experimental Mechanics Series, pp. 259–266 (2014)
3. J.N. Kim, R. Tutwiler, D.R. Kwak, I.-K. Park, C. Miyasaka, Multilayer transfer matrix characterization of complex materials with scanning acoustic microscopy. Proc. SPIE 8694, Nondestructive Characterization for Composite Materials, Aerospace Engineering, Civil Infrastructure, and Homeland Security 2013, 86941O (2013)
4. S. Yoshida, D. Didie, D. Didie, S. Adhikari, I.-K. Park, Opto-acoustic technique to investigate interface of thin-film systems. SEM 2014 Annual Conference, June 2–5, 2014 Greenville, SC (2014)
5. Q. Liao, J. Fu, X. Jin, Single-chain polystyrene particles adsorbed on the silicon surface: a molecular dynamics simulation. Langmuir **15**, 7795–7801 (1999)
6. M. Basnet, S. Yoshida, B.R. Tittmann, A.K. Kalkan, C. Miyasaka, Quantitative nondestructive evaluation for adhesive strength at an interface of a thin film system with opto-acoustic techniques. 47th Annual Technical Meeting of Society of Engineering Science, Oct 4–6, Iowa State University, Ames, IA (2010)

Chapter 18
Effect of Horn Tip Geometry on Ultrasonic Cavitation Peening

Tomohiro Sasaki, Kento Yoshida, Masayuki Nakagawa, and Sanichiro Yoshida

Abstract The ultrasonic horns with cylindrical concave surfaces (concaved horn) have been designed and the effect of the concave on cavitation bubbles generation in water has been investigated. High speed camera observation was made on the vibrating horn tip in water and the generation behavior and the impact force of the cavitation bubbles were investigated. In the measurement of impact force, load vibration occurred as the cavitation bubbles collapsed, and peak frequencies were observed at the vibratory frequency of the horn and its harmonic frequency. The impact force was evaluated based on the above peak frequency. The result showed that the concaved horn provide the higher impact force compared to the horn without the concave. Frequency analysis of the load vibration showed that the concaved horn enhanced the generation of cavitation bubbles in the number. The distribution of cavitation bubbles on the horn-tip was evaluated using high-speed image. It was confirmed that the cavitation bubbles flow was effectively converged to the center of concave.

Keywords Cavitation • Peening • Ultrasound • Surface treatment • Fatigue

18.1 Introduction

In recent years, applications of cavitation have received considerable attention in various fields such as metalworking, industrial cleaning and biochemistry. "Ultrasonic cavitation peening" has been developed as a means of surface treatment for fatigue life improvement [1, 2]. In this technique, cavitation bubbles are generated by an ultrasonic horn submerged in water and impact force induced by the cavitation bubbles upon collapsing on the work is utilized to cause compressive deformation of the surface layer. Compressive residual stress induced by the surface deformation improves the fatigue life of metals by counteracting on the crack initiation. In particular, the cavitation generation using ultrasonic vibration has the advantages of compactness of the equipment and ease of the control by electrical power. However, compared to the other cavitation techniques that utilize cavitation jet flow [3–6], the impact force of ultrasonic cavitation bubbles is small due to small momentary pressure variation. The present study focuses on the surface geometry of horn tip at which the pressure variation occurs to generate the cavitation bubbles. Horns with cylindrical concave surfaces were designed in order to enhance the cavitation generation. The effect of the tip geometry on the generation behavior and the impact force was investigated with high-speed camera observation.

18.2 Experimental Procedure

Figure 18.1 shows a schematic illustration of the equipment of ultrasonic cavitation. An ultrasonic transducer with the power of 2.5 kW and the resonance frequency of 17.5 kHz was used for the vibration source. The vibration of transducer was amplified by a stepped ultrasonic horn. The cavitation bubbles are generated by rapid momentary pressure variation at the horn-tip. The amplitude of horn vibration can be controlled by adjusting the supplying voltage to the transducer. The horn-tip

T. Sasaki (✉) • K. Yoshida
Department of Engineering, Niigata University, Ikarashininocho 8050, Nishi-ku, Niigata-shi, Niigata 950-2181, Japan
e-mail: tomodx@eng.niigata-u.ac.jp

M. Nakagawa
Industrial Research Institute of Niigata Prefecture (Japan), 1-11-1 Abuminishi, Chuou-ku, Niigata-shi, Niigata 950-2181, Japan

S. Yoshida
Department of Chemistry and Physics, Southeastern Louisiana University, SLU 10878, Hammond, LA 70402, USA
e-mail: syoshida@selu.edu

S. Bossuyt et al. (eds.), *Residual Stress, Thermomechanics & Infrared Imaging, Hybrid Techniques and Inverse Problems, Volume 9*, Conference Proceedings of the Society for Experimental Mechanics Series, DOI 10.1007/978-3-319-21765-9_18

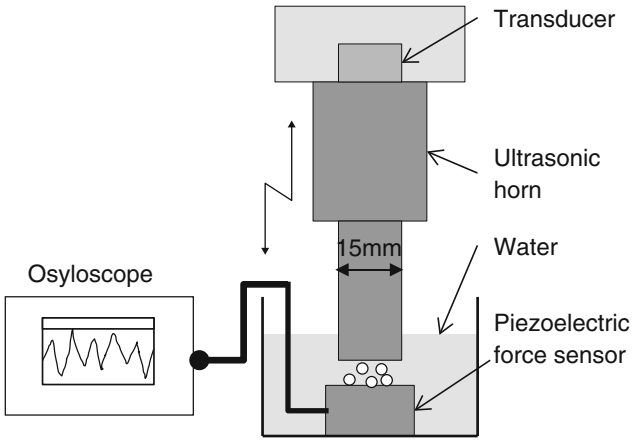

Fig. 18.1 Ultrasonic cavitation equipment

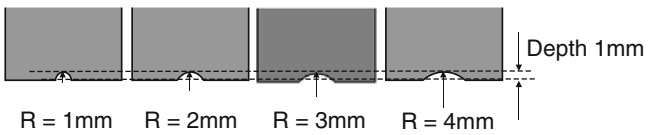

Fig. 18.2 Horn-tips with concaves used in this study

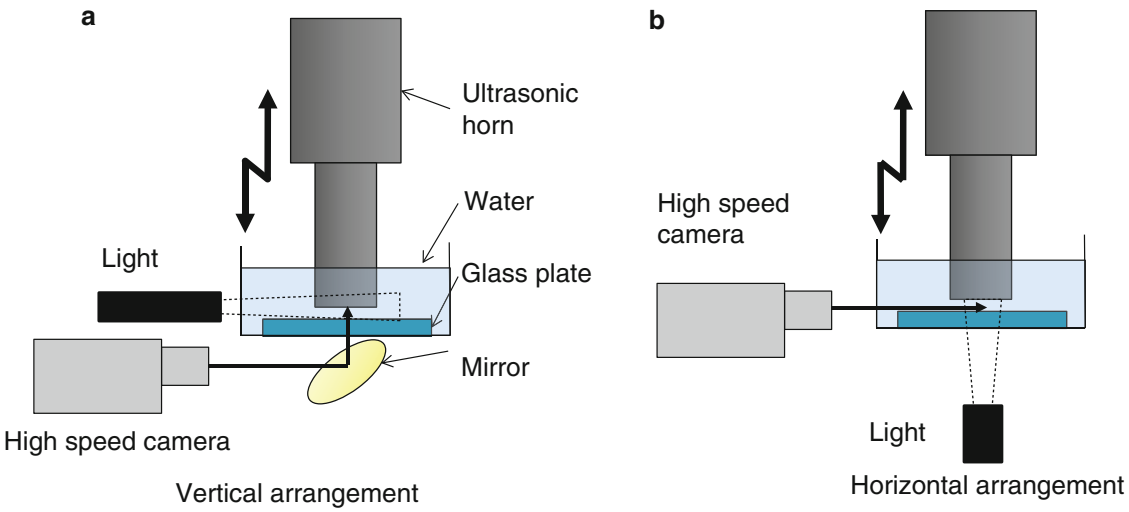

Fig. 18.3 Schematic illustration of high speed camera observation

diameter was 15 mm. In this study, the horn-tips were machined into faces having cylindrical concaves with the radii of 1 mm to 4 mm as shown in Fig. 18.2. The depth of concave from the horn-tip was constant at 1 mm. To evaluate the impact force due to the cavitation bubble collapse, a piezoelectric force sensor with the resonance frequency of 200 kHz was placed under the ultrasonic horn, and the voltage change output by the load sensor during the cavitation occurrence was measured for 0.5 s with an oscilloscope. The diameter of the sensitive face was 20 mm. The measurement was conducted five times per vibratory condition, changing the distance between the sensitive face and the horn-tip.

The behavior of cavitation bubbles on the applied surface was observed by a high-speed camera, as shown in Fig. 18.3. The observations were conducted in a vertical direction and a horizontal direction to the horn surface. In Fig. 18.3a, a transparent acrylic resin sheet was placed instead of the work piece or the force sensor, and the surface of horn was observed from the bottom of the equipment via a mirror. Light irradiated from a halogen light was introduced in the direction horizontal to the cylindrical axis. In addition, the horn-tip face was observed in the direction horizontal to the horn surface with the light irradiation from the bottom (Fig. 18.3b). The frame rate and the capture time were 100,000 fps and 1.0 s, respectively.

18.3 Result and Discussion

18.3.1 Impact Force Caused by Cavitation Bubbles

Figure 18.4 shows an example of the voltage change output by the force sensor during the cavitation occurrence in the horn-tip with a flat surface (no concave). Positive voltage change indicates compressive force to the sensitive surface. Waveform turbulence occurred periodically during the vibration, as shown in Fig. 18.4a. The pair of dashed lines in Fig. 18.4a indicates the duration of ten cycles of the ultrasonic vibration applied to the horn. In the enlarged view of the turbulence shown in Fig. 18.4b, load peaks were observed within one cycle of the ultrasonic vibration. These peaks are presumably due to the impulse of cavitation bubbles collapse. Amplitude spectrum obtained by analyzing the frequency of the waveform of Fig. 18.4 through FFT is shown in Fig. 18.5. A peak frequency at 17.5 kHz, which corresponds to the vibratory frequency of ultrasonic horn, and peaks of its higher harmonic frequencies (35.0 and 52.5 kHz) were confirmed in the FFT spectrum. Thus, the following arguments can be made regarding these three frequencies. The amplitudes at load vibration of 17.5, 35.0, and 52.5 kHz obtained from the FFT spectrum are plotted against the output voltage of the

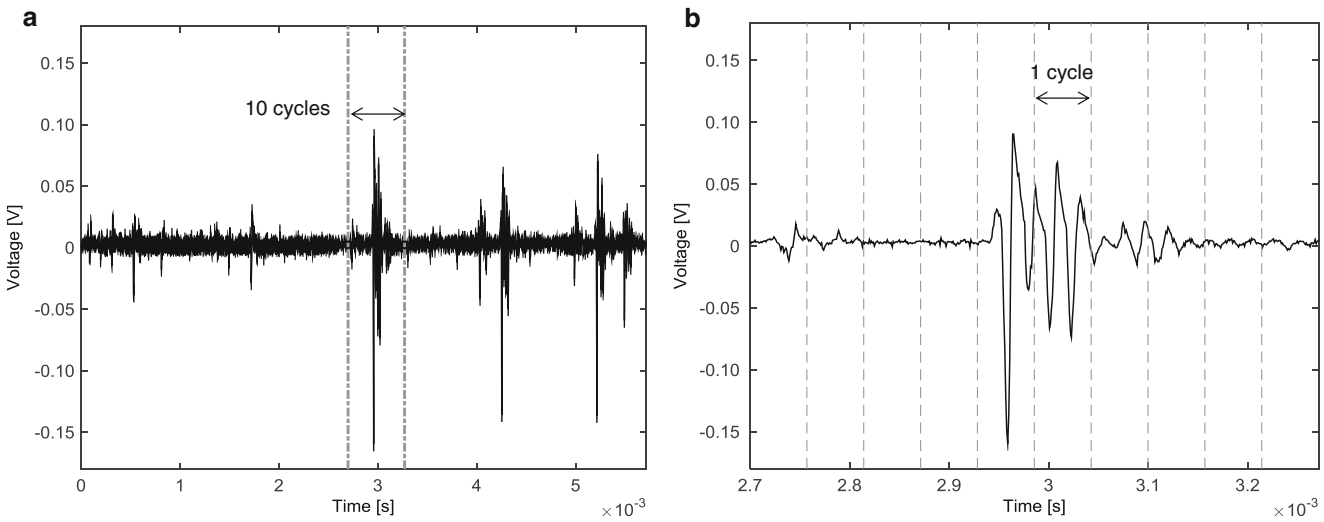

Fig. 18.4 (**a**) Voltage change of load sensor during cavitation in the flat surface horn. (**b**) is an enlarged view of the waveform shown in (**a**) by *dashed lines*

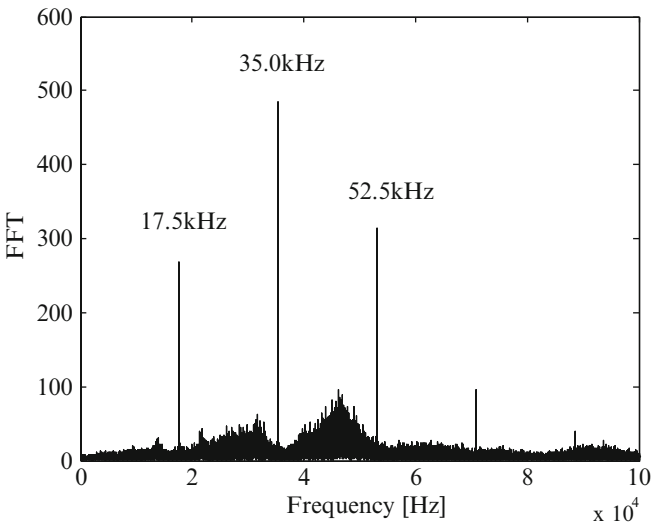

Fig. 18.5 FFT spectrum obtained from the waveform of Fig. 18.4

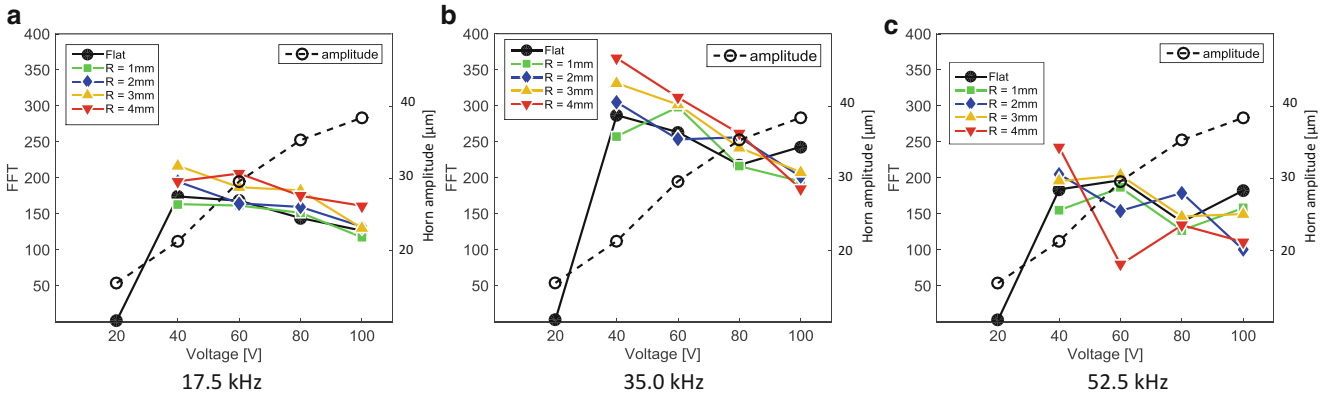

Fig. 18.6 Variations of load amplitude measured by load sensor and horn amplitude with supplying voltage

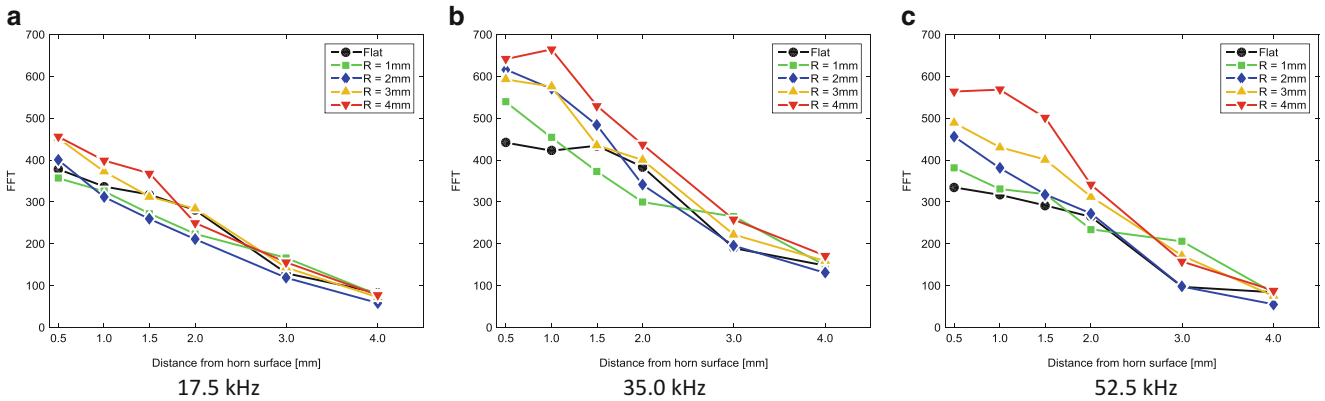

Fig. 18.7 Changes in load amplitudes with distance between horn-tip and sensitive face, d_h, at (**a**) 17.5 kHz, (**b**) 35.0 kHz, and (**c**) 52.5 kHz

transducer in Fig. 18.6. In addition, the vibration amplitude of the horn-tip in the air measured by a capacitance type displacement sensor is shown along with the load vibration. The vibration amplitude of the horn-tip almost linearly increased with the output voltage. In contrast, the load vibration on the load sensor was not observed up to the voltage of 40 V. The amplitude of load vibration rapidly increased up to 40 V and then flattened out. The occurrence of cavitation bubbles corresponded to the change in load amplitude; the cavitation bubbles were not observed at the load amplitude lower than 20 μm (supplied voltage 40 V). This trend was observed in the all peak frequencies as shown in Fig. 18.6a–c. Therefore, the peak frequencies observed in the FFT spectrum can be regarded as the result due to the impulse of cavitation collapses. It was found that the impact force due to the cavitation bubbles was independent on the horn amplitude.

18.3.2 Effect of Concave Radius on Impact Force

The load amplitude at 17.5 kHz, and the harmonic frequencies were observed in the horn-tips having concaves as well as the flat-surface horn. Figure 18.7 shows changes in the load amplitudes with the distance between the horn-tip and the sensitive surface, d_h. In the frequency of 17.5 kHz shown in Fig. 18.7a, the load amplitude linearly decreased with increasing d_h for the all horn-tips. In addition, at 17.5 kHz, there was little difference in the horn geometry. On the other hand, in the harmonic frequencies of 35.0 and 52.5 kHz shown in Fig. 18.7b, c, the load amplitude of the concaved horn-tips showed larger values especially in the smaller d_h below 1.5 mm. These results indicates that the impact force of cavitation bubbles increased by using the concaved horn-tips. The concaved horn-tip with the radius of 4 mm showed the

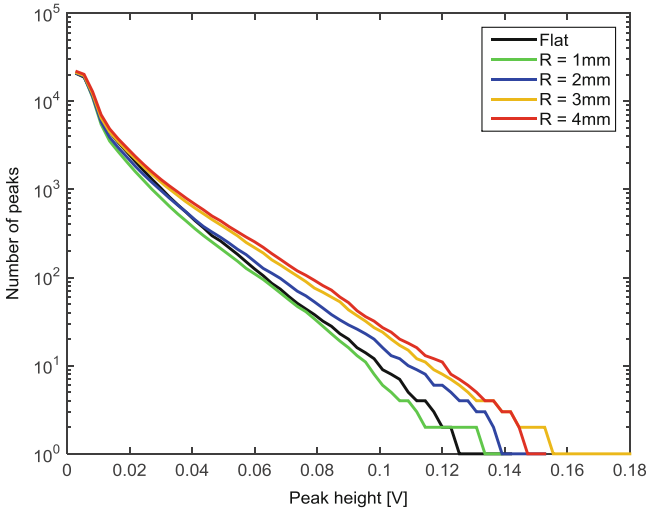

Fig. 18.8 Frequency distribution of load peak at the horn-tip/ sensitive face, $d_h = 1.0$ mm

largest amplitude in this study. There are two possible causes of the higher impact force in the concaved horn-tip: an increase in the number of cavitation bubbles generation on the sensitive surface, and an increase of the impact force due to each bubble collapse. Thus, frequency of cavitation bubble occurrence was estimated from the number of load peak. Figure 18.8 shows the frequency distribution of the load peak measured in the waveform in $d_h = 1.0$ mm where the large difference was observed. The number of positive voltage peaks representing compressive force was counted. The result showed that the number of peaks was higher in the concaved horn-tips for the all peak heights. The sensitive face of load sensor had a diameter of 20 mm which was much larger size than that of the cavitation bubble. Although it cannot be clearly confirmed whether each load peak is attributed to the impact force by a single cavitation bubble or not, it can be stated that the concaved horn-tip increased the frequency of cavitation generation on the sensitive face, and the sum total of the impacts due to the cavitation bubbles increased.

18.3.3 Behavior of Cavitation Bubbles Near Horn-Tip

Figure 18.9 shows an example of the high-speed camera images in which the surface of horn-tip was observed from the bottom. Time interval between frames was 10 μs, and the time for about six frames corresponds to the vibratory cycle (57.1 μs) of the horn. Cavitation bubbles were observed in white color and the intensity of pixels changed in accompanying with the horn vibration. Light irradiated in the direction vertical to the vibration direction is reflected on the surfaces of cavitation bubbles and enters the camera. Thus, the change in light intensity implies the cavitation generation. The captured images in Fig. 18.7 indicate that the cavitation bubbles repeated generating and collapsing on the horn surface. In addition, the momentary distribution of cavitation bubbles was inhomogeneous on the surface. Figure 18.10 shows the high-speed camera images observed sidewise in the horn vibration. In the flat horn shown in Fig. 18.10a, the cavitation bubbles were observed between the horn-tip and the glass plate. The larger bubbles which may be indicative of bubbles collapse were confirmed near the surface of glass. It is considered that the cavitation bubbles were generated near the horn-tip and collapse on the surface flowing down to the surface of glass surface. On the other hand, in the concaved horn-tip (Fig. 18.10b–d), the generation of cavitation bubbles were concentrated near and under the concaves.

In order to evaluate the frequency of cavitation bubbles distribution, the distribution of pixel intensities in the captured image was computed by a following process. First, to neglect background intensity of the image, nominal intensity was obtained by calculating the time and spatial average of pixel intensity of the movie. The nominal intensity is expressed as follow.

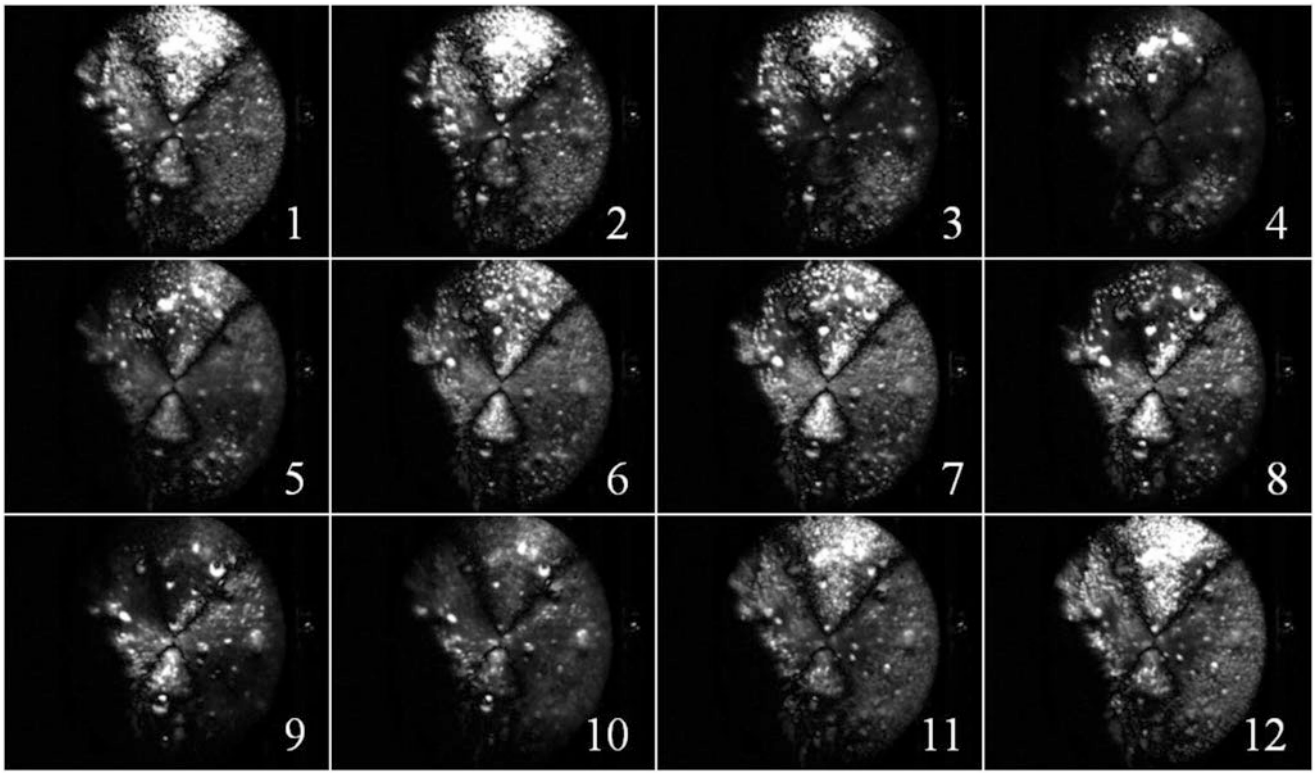

Fig. 18.9 High speed camera images captured in the vertical direction to horn surface in case of flat surface horn

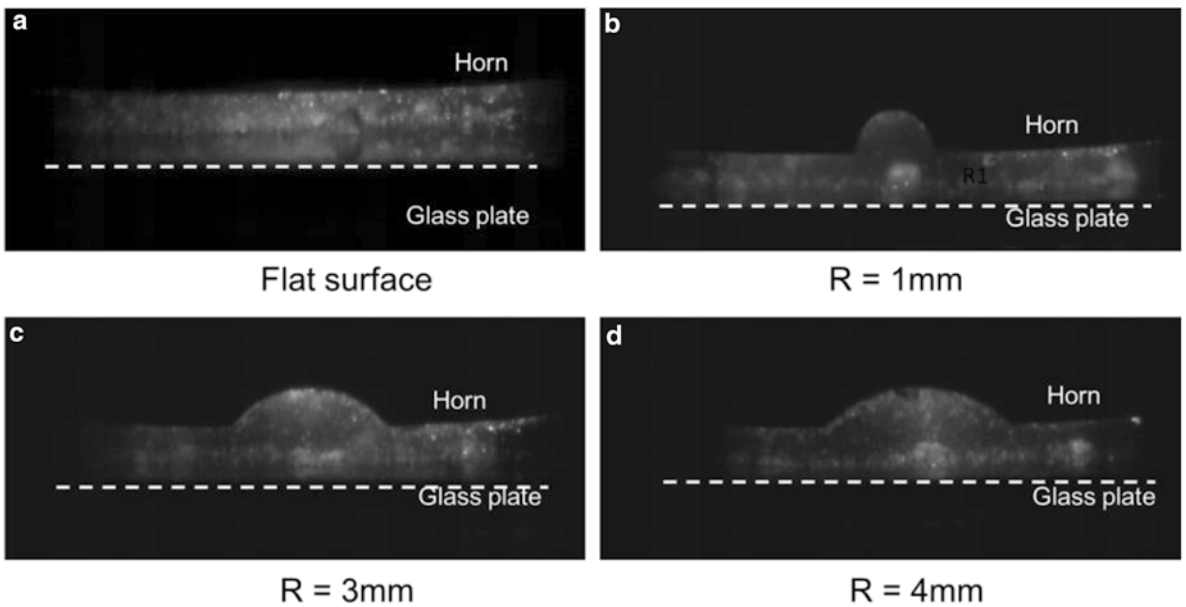

Fig. 18.10 High speed camera images captured in the horizontal direction to horn surface

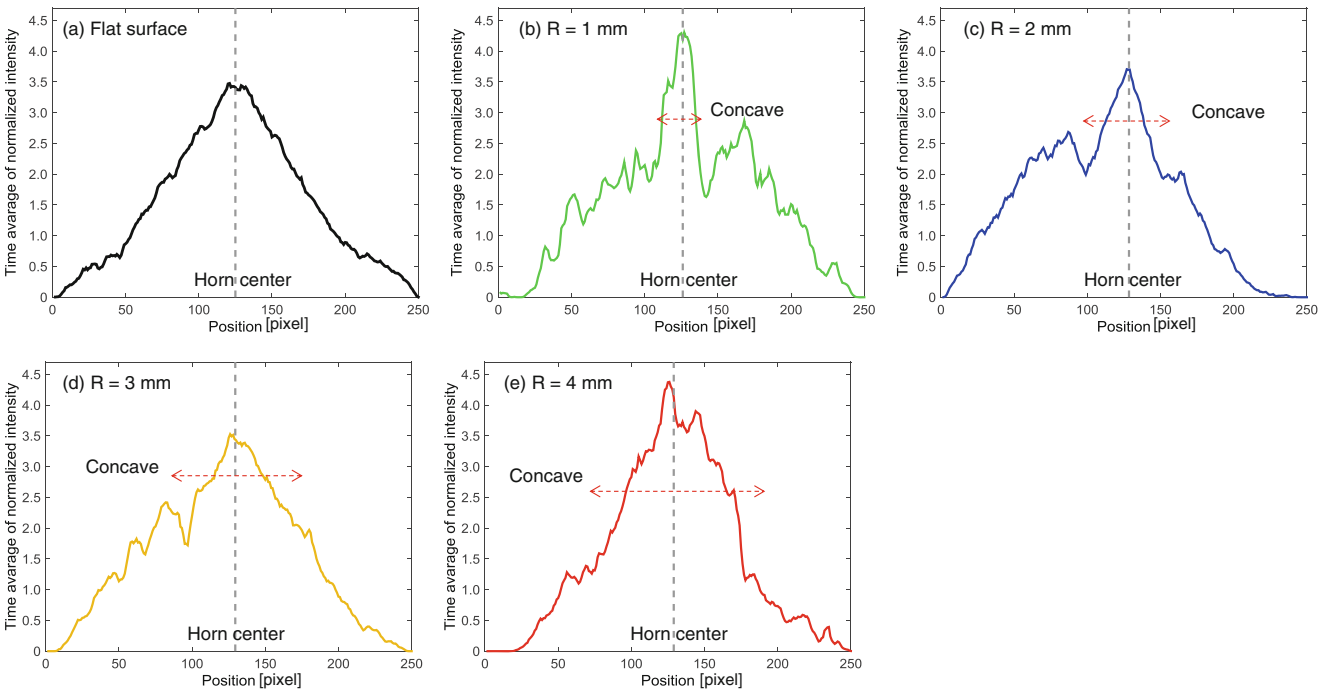

Fig. 18.11 Intensity profile on the image of cavitation bubble

$$I_{nominal} = \frac{\sum_{i=1}^{m}\sum_{j=1}^{n}\sum_{t=1}^{T} I_{i,j,t}}{mnT} \tag{18.1}$$

where m, n, and T are height and width of image in the number of pixel, and capture time, respectively. Normalized pixel intensity in the images was obtained by dividing each pixel intensity, $I/I_{nominal}$.

Figure 18.11 shows the normalized intensity profile in the direction vertical to the concave obtained by the images in which the surface of horn-tip was observed from the bottom. The profile in the concaved horn-tips had a peak at the center of concave. This result indicates that the frequency of cavitation generation was higher and the flow of bubbles converged to the center of concave. It is noted that the wavelength of acoustic wave in the water estimated from the vibration frequency (17.5 kHz) is much larger than the distance between the horn-tip and the surface of specimen. Thus, focusing of acoustic wave by the concaved lens is probably not the major cause of the increase of impact force. In the flat surface, the cavitation flow may be dispersed on the surface of specimen, while in the concaved surface, the cavitation flow is trapped in the concaved. Therefore, the larger impact force measured by the load sensor can be explained in term of the convergence effect of the cavitation flow.

18.4 Summary

Horn-tip of ultrasonic horn was machined into the concaved face and the effect of concave on the ultrasonic cavitation was investigated. Cavitation bubbles were generated by phase transformation caused by the water pressure variation. In this study, generation of cavitation bubbles was observed in the horn amplitude greater than approximately 20 μm. The impact force due to the cavitation collapse was independent on the horn amplitude. In contrast, the concaved horn-tip showed the higher impact force than that in the flat surface horn. This means that changing the horn-tip geometry is more effective in increasing the impact force. It was found that the increase of impact force were mainly the results of the increase of occurrence frequency on the applied surface. In addition, as observed by the high speed camera, cavitation bubbles flow was converged to the concave. The reason for the increase in occurrence frequency is not well understood, the above observation implies that the control of cavitation flow and the enhancement of bubbles nucleation are effective for the improvement of the ultrasonic cavitation.

References

1. M. Nakagawa, T. Watanabe, Introducing compressive residual stress on metal surfaces by irradiating ultrasonic wave with a horn in water: surface modification by irradiating ultrasonic wave in liquid (Report 1). Quart. J. Jpn. Welding Soc. **22**, 587 (2004) (in Japanese)
2. M. Nakagaw, T. Watanab, Introducing compressive residual stress on hard materials surface by irradiating ultrasonic wave with a horn in water: surface modification by irradiating ultrasonic wave in liquid (Report 2). Quart. J. Jpn. Welding Soc. **25**, 501 (2007) (in Japanese)
3. Y. Yamauchi, H. Soyama, Y. Adachi, K. Sato, T. Shindo, R. Oba, R. Oshima, M. Yamabe, Suitable region of high-speed submerged water jets for cutting and peening. JSME Int. **B38**, 31 (1995)
4. H. Soyama, T. Kusaka, M. Saka, Peening by the use of cavitation impacts for the improvement of fatigue strength. J. Mater. Sci. Lett. **20**, 1263 (2001)
5. H. Lee, S. Mall, H. Soyama, Tribology letters fretting fatigue behavior of cavitation shotless peened Ti-6Al-4 V. Tribology Lett. **36**, 89 (2009)
6. M. Ramulu, S. Kunaporn, M. Jenkins, M. Hashish, J. Hopkins, Improvement of fatigue strength of aluminum alloy by cavitation shotless peening. J. Press. Vessel Technol. Trans. ASME. **124**, 118 (2002)

Chapter 19
Fatigue Damage Analysis of Aluminum Alloy by ESPI

Tomohiro Sasaki, Shun Hasegawa, and Sanichiro Yoshida

Abstract In this study, Electronic Speckle Pattern Interferometry (ESPI) and acoustic microscopy were applied to analysis of the fatigue of aluminum alloy. Effect of fatigue damage on the macroscopic deformation behavior during a tensile test has been analyzed with the interferometric fringes. Resultant fringe pattern showed that the elastic compliance in the damaged area increased as the fatigue cycle before the tensile test (Pre-fatigue cycle) increased, resulting in the occurrence of strain localization. In order to know the relation of between the deformation behavior and the microstructural change of the specimen, the acoustic property on the surface has been investigated by a scanning acoustic microscope. It was found that the surface acoustic velocity in the load direction in the pre-fatigue test increased with increasing the pre-fatigue cycle. The results have been discussed based on the fatigue stages of the change in residual stress, local plastic deformation, and the crack initiation.

Keywords Speckle interferometry • Aluminum alloy • Deformation measurement • Fatigue • Acoustic property

19.1 Introduction

Fatigue of metals has been intensively studied because of the importance in industry. It is well known that the micro-cracks which occur in materials subjected to cycling loading cause a macroscopic fracture of metal components. A number of fatigue diagnosis techniques using X-ray, ultrasonic wave, and acoustic emission have been proposed [1–4]. These methods inspect the fatigue damage by detecting the micro-cracks and monitoring their lengths. However, evaluating individual cracks is a time-consuming process. In addition, the micro-crack is generated through microstructural changes such as crystal slippages and increase dislocation density deformation. Most of fatigue life of metals is generally spent by the process before the crack initiation. Thus, it is difficult to inspect the fatigue damage and diagnose the fatigue life at the earlier stage.

Electronic speckle pattern interferometry (ESPI) is a technique capable of measuring displacement fields on the surface of materials, and has been developed as a non-destructive and full field method of deformation materials. Our previous studies demonstrated that strain localization due to the occurrence of micro-cracks or the local plastic deformation affects to the macroscopic deformation behavior of metals [5–7]. These results suggest that the fatigue diagnosis might be possible by analyzing the correlation between the deformation behavior and the microscopic change. In the present study, the effect of fatigue damage on the deformation behavior of aluminum alloy has been analyzed with ESPI. Two-dimensional displacement fields on the surface were measured as images consisting of fringe contours. Microscopic changes were investigated by measurements of the acoustic property with a scanning acoustic microscope. The changes in the mechanical properties have been discussed on the basis of the fatigue stages of the local plastic deformation and the crack initiation.

T. Sasaki (✉) • S. Hasegawa
Department of Engineering, Niigata University, Ikarashininocho 8050, Nishi-ku, Niigata-shi, Niigata 950-2181, Japan
e-mail: tomodx@eng.niigata-u.ac.jp

S. Yoshida
Department of Chemistry and Physics, Southeastern Louisiana University, SLU 10878, Hammond, LA 70402, USA
e-mail: syoshida@selu.edu

S. Bossuyt et al. (eds.), *Residual Stress, Thermomechanics & Infrared Imaging, Hybrid Techniques and Inverse Problems, Volume 9*, Conference Proceedings of the Society for Experimental Mechanics Series, DOI 10.1007/978-3-319-21765-9_19

19.2 Experimental Procedure

19.2.1 Specimen

The material used in this study was industrial aluminum alloy sheet, AA7075 with 3.0 mm in thickness. Specimens for fatigue test were cut from the sheet into a neck shape as shown in Fig. 19.1 using electronic discharge machining. The yield strength of specimen measured by a static tensile test was 13.5 kN. The specimens were subjected to cyclic loadings within the fatigue life (Pre-fatigue test). The pre-fatigue test was conducted under load control condition at tensile load ratios from 0.1 to 0.5, with a sinusoidal waveform of 40 Hz. The fatigue life (cycles) of specimen measured under this fatigue condition was approximately 24,000 cycles. Thus, the number of cycles applied in the pre-fatigue test (pre-fatigue cycle), N_P, were determined to 10, 100, 1000, 10,000, and 20,000.

19.2.2 Observation of Deformation Behavior of Pre-fatigued Specimen

The pre-fatigued specimens were deformed by a tensile test and the deformation process was observed with ESPI. The dual beam ESPI setup used in this study is shown in Fig. 19.2. Two optical interferometers were arranged to the vertical direction (*y-axis*) and the horizontal (*x-axis*) direction to the tensile machine. Optical paths in the two interferometers are shown by solid line and dashed line in Fig. 19.1. Each interferometer was sensitive to in-plane displacement component along only its parallel direction. The laser beam (semiconductor lasers with the wavelength of 660 nm) was expanded by an optical lens and split into two paths by a cube beam splitter. The surface of specimen was irradiated by the two beams via two reflective mirrors. The angle of incidence used in this study was 30°. Superposed speckle pattern on the irradiated surface resulting from the two optical arms was captured by a CCD camera. Since the optical intensity received by each pixel of the CCD changes depending on the in-plane displacement on the surface, the displacement field on the measured surface can be obtained as fringe contours by computing the intensity difference. The speckle pattern during the tensile test was captured by the CCD camera at a constant frame rate of 16.7 fps. The fringe contours for a certain time interval was calculated by subtracting each frame of image from a frame captured at a later frame. The individual fringe contour along the x or y direction was captured by switching the light source of interferometer being synchronized with the CCD camera at its frame capture. In addition, a system of carrier fringes [8] was introduced to the interferometer in the horizontal direction because the displacement vertical to the tensile direction (x-axis) is relatively small. A glass window with 5.2 mm thick and the refraction index of 1.53 was placed after the mirror for the one interferometric arm. Since the laser beam in the interferometer was expanded by the optical lens, the optical distance of the laser beam which passes through the glass window varies

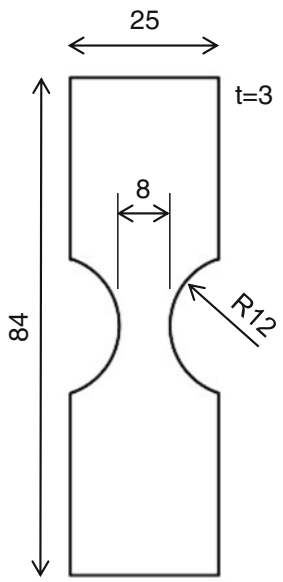

Fig. 19.1 Specimen used in this study

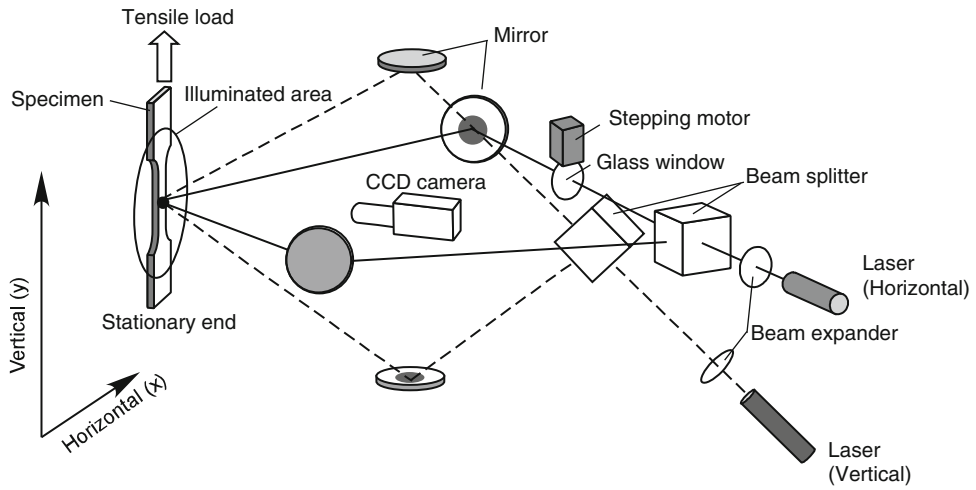

Fig. 19.2 Experimental arrangement of 2D-ESPI

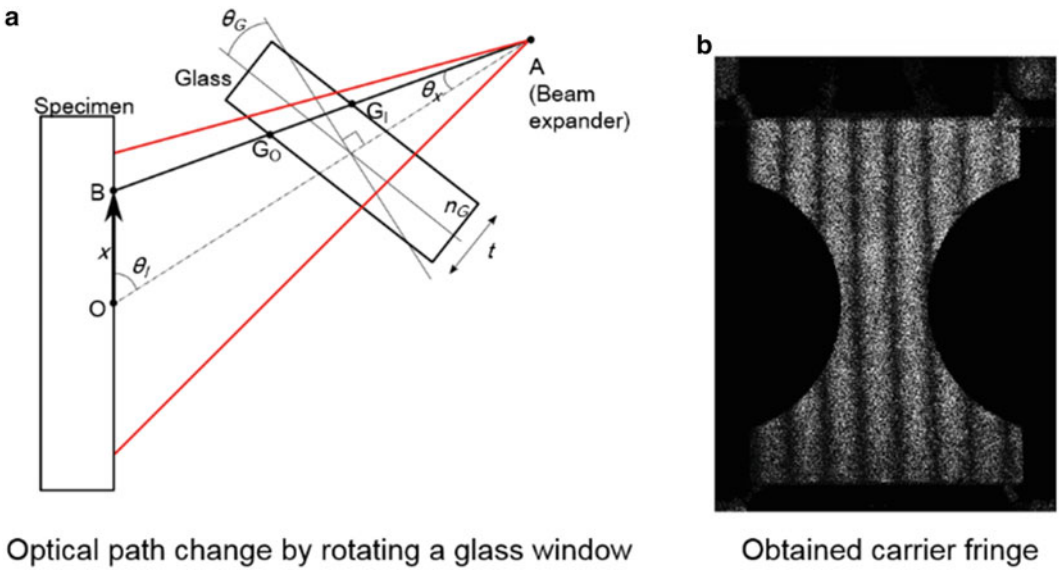

Fig. 19.3 Carrier fringes method

depending on its incident angle as shown in Fig. 19.3a. This leads to a gradient of optical distance in the x-direction on the irradiated surface. Consequently, as shown in Fig. 19.3b, the carrier fringes parallel to the tensile direction appear by rotating the window due to the difference in optical distance. When the horizontal displacement occur, the fringe contours represents the superimposing displacement resulting from the carrier and the horizontal displacement. The window was rotated at every 20 frames of the CCD capture, and eight carrier fringes were introduced.

19.2.3 Measurement of Surface Acoustic Wave Velocity

Surface acoustic wave (SAW) velocity on the surface of fatigued specimen was measured by a scanning acoustic microscope (Olympus UH3). The SAW velocity can be obtained by analyzing the relation of an electrical signal detected by the transducer and the distance between the specimen surface and an acoustic lens [9, 10]. As shown in Fig. 19.4, ultrasonic wave generated by an acoustic lens propagates into the specimen via a coupling medium (pure water).

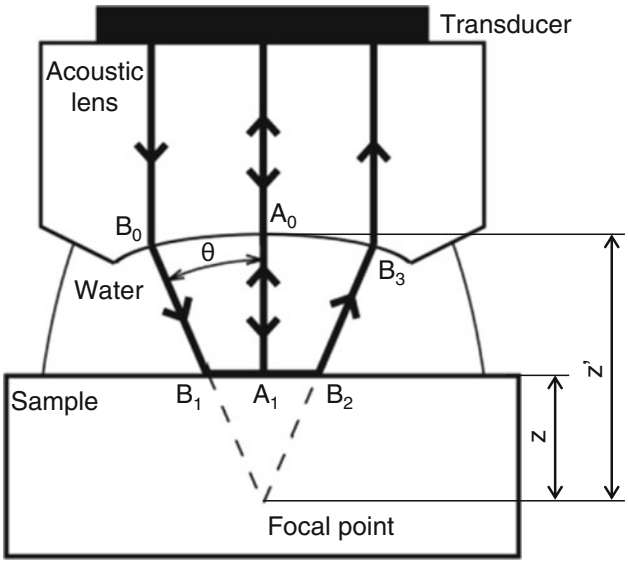

Fig. 19.4 Schematic illustration of scanning acoustic microscope and propagation paths of longitudinal wave and surface acoustic wave

The incident ultrasonic wave obliquely on the specimen surface causes SAW, and this propagates on the surface of specimen (B_0-B_1-B_2-B_3 in Fig. 19.4). This SAW interferes with the reflected longitudinal wave propagating the medium (A_0-A_1 in Fig. 19.4), electrical signal resulting from the interference was detected at the transducer. The voltage change at the transducer, V, was measured changing the distance between the specimen surface and the focal point of the acoustic lens, Z. The SAW velocity, v_R, was calculated from the V (Z) curve by (19.1) [6].

$$v_R = \frac{v_w}{\left\{1 - \left(1 - \frac{v_w}{2f\Delta z}\right)^2\right\}^{0.5}} \tag{19.1}$$

Where, v_W and f are the sound velocity in the coupling medium, and the vibratory frequency of the transducer. A cylindrical surface lens with the vibration frequency of 200 MHz was used in this study. The obtained data using the cylindrical lens indicates the SAW velocity propagating along the direction vertical to the cylindrical axis. The SAW velocities on the specimen surface were measured in the horizontal and vertical directions (x−y).

19.3 Result and Discussion

19.3.1 Influence of Fatigue Damage on Macroscopic Deformation

Figure 19.5 shows a load displacement curve and the fringe patterns observed in the tensile test of the specimen before the pre-fatigue test. The fringe patterns of Fig. 19.5 (y1)–(y5) were obtained at various load levels indicated in the load displacement curve by 1–5. The patterns represent displacement along the tensile axis resulting from a constant time interval of 3.3 s (50 frames in CCD capture). The fringes of the y-displacement (y-fringe) concentrate to the neck of specimen with increasing the tensile load, resulting in a formation of white band due to the strain concentration at the yielding. The strain concentration at the neck can be confirmed in the fringes to the x-displacement (Fig. 19.5 (x5)) as a discontinuous region.

Figure 19.6a, b show the changes in the fringe pattern for the pre-fatigued specimens of $N_P = 10{,}000$ and 20,000. In the y-fringe, all the pre-fatigued specimens except for the pre-fatigue cycle $N_P = 20{,}000$ showed the similar change to the non-fatigued specimen. The specimen of $N_P = 20{,}000$ showed asymmetric fringe patterns before the yielding as observed in Fig. 19.6a,F = 12.0–13.0 kN, and the formation of white band occurred at the smaller tensile load. This indicates that the strain concentration occurs at one side of the neck. Figure 19.7 shows an optical micrograph of the specimen of $N_P = 20{,}000$ after the tensile test. A crack with approximately 250 μm length was observed on the neck part. Therefore, it was confirmed that the deformation behavior of $N_P = 20{,}000$ was due to the presence of the major crack. In the x-fringes including the

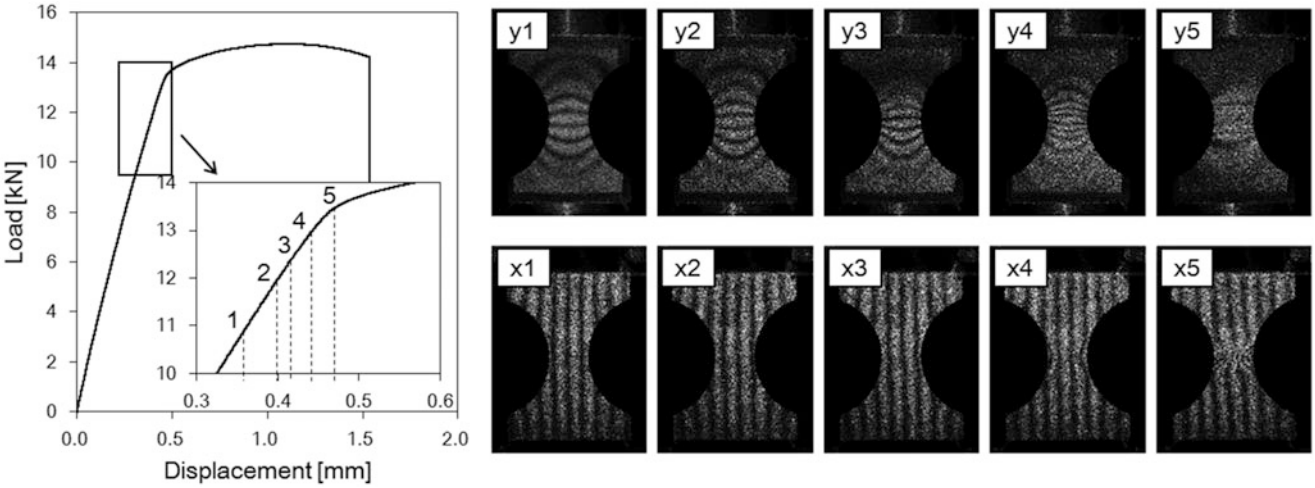

Fig. 19.5 Load–displacement curve and fringe pattern observed in tensile test of a non-fatigued specimen. The tensile load is indicated in the load–displacement curve by "1–5"

carrier fringes showed a wavy shape with the occurrence of strain concentration to the crack (Fig. 19.6b,$N_P = 20{,}000$). On the other hand, as observed in Fig. 19.6b,$N_P = 10{,}000$, the x-fringe in the specimens of $N_P < 10{,}000$ showed slightly curved shapes, and their curvature increased as the pre-fatigued cycle increased. These curved fringes in the x-fringe imply the occurrence of shear deformation in the neck part, and are probably due to the fatigue damage. Thus, the strain analysis was conducted on the neck part of specimen.

The mean value of shear strain in the 4.0 mm × 8.0 mm area near the neck part was computed from the fringe patterns observed in the tensile test. The result is shown in Fig. 19.8. The data was plotted against the tensile load. The shear strain rate $d\varepsilon_{xy}/dt$ represents the strain for the time interval which corresponds to the frame interval of the subtraction. $d\varepsilon_{xy}/dt$, monotonically increases with the increase of tensile load, reaching the maximum at the yielding. There was no difference in the yield strengths of the pre-fatigued specimen, while $d\varepsilon_{xy}/dt$ began to increase at smaller tensile load in greater N_P. The shear strain may be caused by the local plastic deformation before the macroscopic yielding. The result means that the pre-fatigue load enhanced the local plastic deformation.

19.3.2 Surface Acoustic Velocity on the Surface of Pre-fatigued Specimen

SAW velocities of the non-fatigued and the pre-fatigued specimens are shown in Fig. 19.9. The result of Fig. 19.9a, b respectively indicate the sound velocity propagating in the tensile direction, y, and the direction vertical to the tensile direction, x. The sound velocity in the direction y decreased as the pre-fatigue cycles increased up to 10,000, then, it showed a slight increase at $N_P = 20{,}000$. In contrast, the sound velocity in the direction x showed an increase. In theory, the sound velocity which propagates in solid materials depend on the density and the elastic modulus, $(E/\rho)^{1/2}$. In addition, the elastic modulus in atomic scale depends on stress because of the non-linear relationship between the elastic modulus and the interatomic distance. Thus, the sound velocity in the material is essentially affected by the microscopic factors such as dislocation density in metals, crystal orientation and residual stress. In particular, it has been reported that the tensile stress leads to a decrease in the sound velocity propagating in the tensile direction [11]. In this study, the tensile load during the pre-fatigued test may causes the crystal slips in a local area resulting in the increase of tensile residual stress. Since almost no change was confirmed in the microstructure after the pre-fatigue test except for $N_P = 20{,}000$, the decrease in the SAW velocity in the direction y is considered to be due to the increase of tensile residual stress. Moreover, the increase in the horizontal SAW velocity may be caused by the decrease in the interatomic distance by the Poisson's effect. The slight increase of the SAW velocity in the y-direction at $N_P = 20{,}000$ is surmised to be due to the stress relaxation by the occurrence of micro-crack as observed in Fig. 19.7 and the increase of the dislocation density around the crack tip. From the above results, the pre-fatigue of $N_P < 10{,}000$ can be interpreted as an increasing process of the tensile residual stress. When the pre-fatigued specimen is subjected to a tensile load, the residual stress due to the pre-fatigue is applied to the specimen in addition to the tensile stress. Thus, the localization of plastic deformation observed in the macroscopic deformation behavior may be a consequence of the tensile residual stress in the fatigued region.

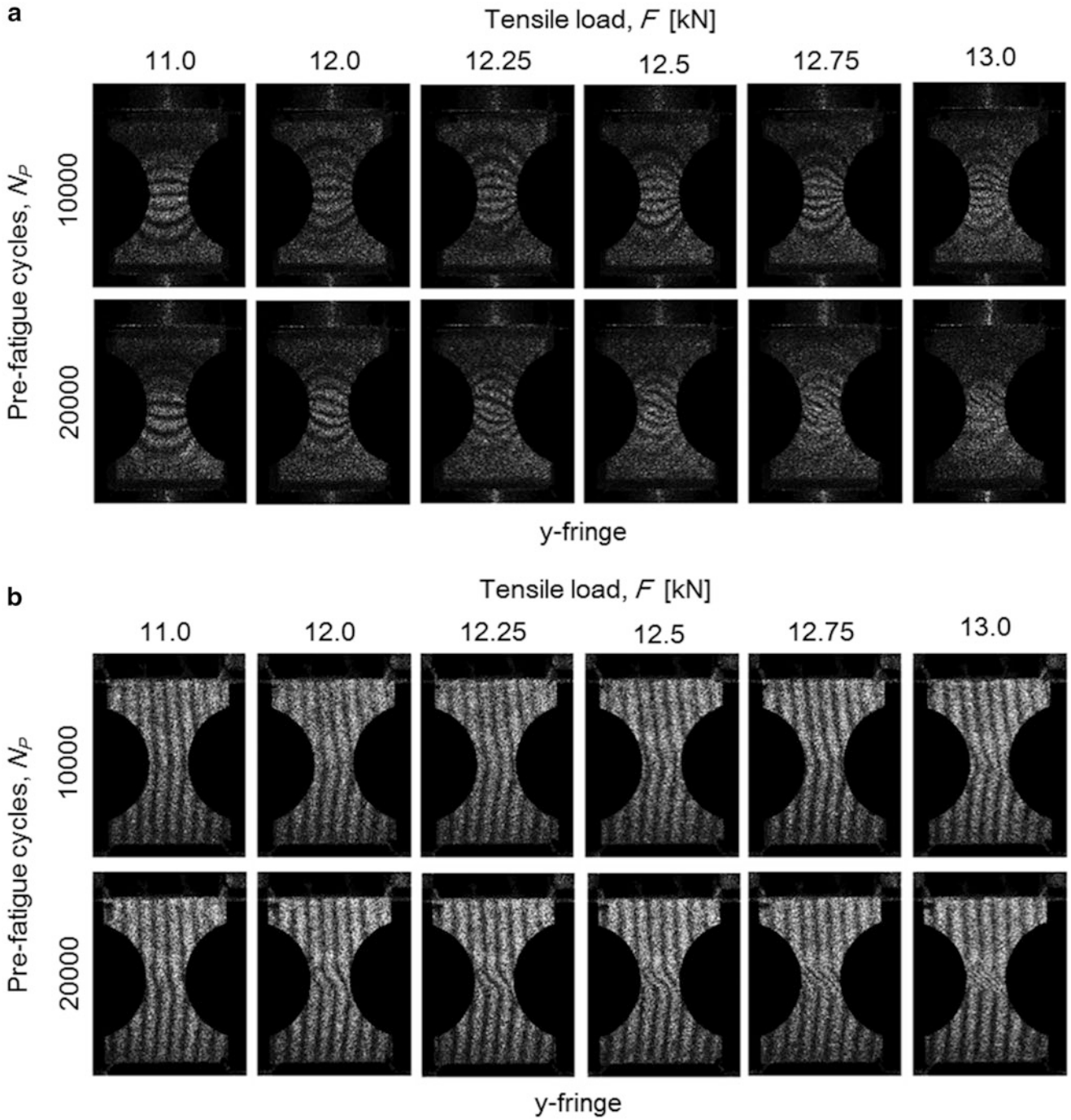

Fig. 19.6 Fringe patterns in tensile test of pre-fatigued specimen. (**a**) and (**b**) are fringe patterns showing displacement field in the tensile direction, y, and in the horizontal direction, x. In the pattern of horizontal direction, eight fringes are introduced to as the carrier fringe

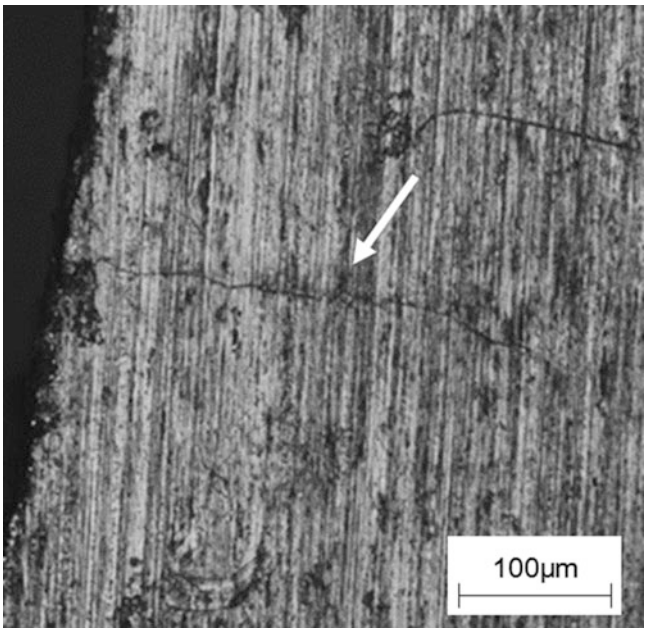

Fig. 19.7 Crack observed in a pre-fatigued specimen of $N_P = 20{,}000$

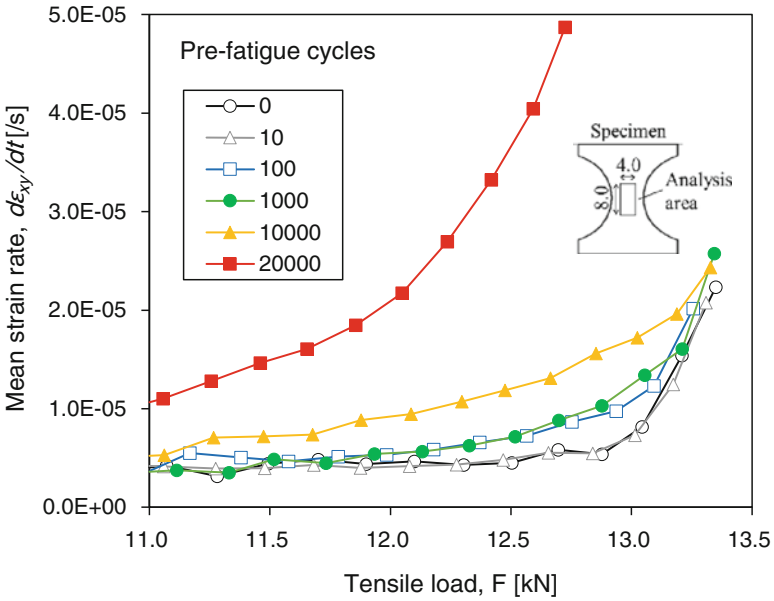

Fig. 19.8 Mean strain rate $d\varepsilon_{xy}/dt$ plotted against the applied tensile load

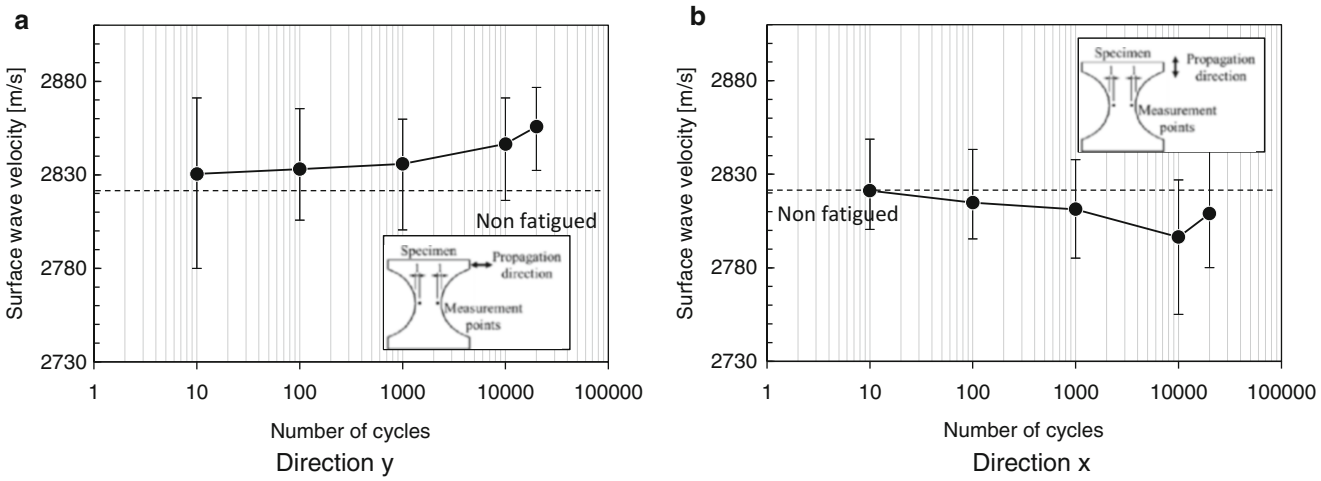

Fig. 19.9 SAW velocity on the surface of pre-fatigued specimen in (**a**) tensile direction, y, and (**b**) vertical direction to the tensile direction, x

19.4 Summary

The deformation behavior of pre-fatigued aluminum alloys was visualized using ESPI. The strain concentration behavior during the tensile test was dependent on the pre-fatigue cycle, N_P. In the pre-fatigued specimen, the strain localization occurred before the macroscopic yielding, and the resultant optical fringe showed a curved shape. The strain analysis by the fringe contours showed that the strain localization began at the lower tensile load as the pre-fatigue cycle increased. This trend appeared in the lower N_P than 10,000 cycles at the earlier fatigue stage in which no crack was observed. The SAW velocity measurement suggested that the residual stress in the tensile direction induced by the pre-fatigue, and this enhanced the strain localization in the tensile test. The result indicated that the microscopic change due to the residual stress can be detected by the evaluation of the macroscopic deformation behavior using ESPI.

References

1. K. Ogura, Y. Miyoshi, M. Kayama, A study of X-ray analysis of fatigue fracture surface. Eng. Fract. Mech. **22**, 123 (1985)
2. A. Steuwer, L. Edwards, S. Pratihar, S. Ganguly, M. Peel, M.E. Fitzpatrick, In situ analysis of cracks in structural materials using synchrotron X-ray tomography and diffraction. Nucl. Instrum. Methods Phys. Res. B **246**, 246 (2006)
3. A. Steuwer, M. Rahman, A. Shterenlikht, M.E. Fitzpatrick, L. Edwards, P.J. Withers, The evolution of crack-tip stresses during a fatigue overload event. Acta. Mater. **58**, 4039 (2010)
4. V. Moorth, T. Jayakumar, B. Raj, Influence of microstructure on acoustic emission behavior during stage 2 fatigue crack growth in solution annealed, thermally aged and weld specimens of AISI type 316 stainless steel. Mater. Sci. Eng. **A212**, 280 (1996)
5. T. Sasaki, S. Yoshida, Revealing load hysteresis based on electronic speckle pattern interferometry and physical mesomechanics. Phys. Mesomech. **15**, 47 (2012)
6. T. Sasaki, H. Suzuki, T. Watanabe, S. Yoshida, Effect of loading history of aluminum on fringe pattern in electronic speckle pattern interferometry. Conf. Proc. Soc. Exp. Mech. **3**, 141 (2013)
7. S. Hasegawa, T. Sasaki, S. Yoahida, S.L. Hebert, Analysis of fatigue of metals by electronic speckle pattern interferometry. Conf. Proc. Soc. Exp. Mech. **3**, 127 (2014)
8. S. Yoshida, T. Sasaki, S. Craft, M. Usui, J. Haase, T. Becker, I.-K. Park, Stress analysis on welded specimen with multiple methods. Conf. Proc. Soc. Exp. Mech. **3**, 143 (2015)
9. R.D. Weglein, A model for predicting acoustic material signature. Appl. Phys. Lett. **34**, 179 (1979)
10. W. Parmon, H.L. Bertoni, Ray interpretation of the material signature in the acoustic microscope. Electron. Lett. **15**, 684 (1979)
11. A. Todoroki, H. Kobayashi, H. Nakamura, W. Park, Y. Arai, H. Iida, Approach for measuring elastic modulus of thin film by scanning acoustic microscope. Trans. ASME J. **59**, 2977 (1993) (In Japanese)

Chapter 20
Dynamic Failure Mechanisms in Woven Ceramic Fabric Reinforced Metal Matrix Composites During Ballistic Impact

Brandon A. McWilliams, Jian H. Yu, and Mark Pankow

Abstract The complex interaction of dynamic stress waves during ballistic impact provides the opportunity to simultaneously observe the high strain rate loading response under various triaxialities including tension, compression, and shear. In this work the dynamic failure mechanisms of woven ceramic fabric reinforced aluminum metal matrix composites (MMC) during ballistic impact are experimentally investigated. In addition to experimental characterization, an orthotropic elastic-plastic constitutive model with hydrostatic pressure dependent yield is implemented in an explicit finite element code to quantify the stress states present during the progressive damage and failure of the MMC during the penetration and perforation process.

Keywords Metal matrix composites • Penetration mechanics • Dynamic failure mechanisms • Failure modeling • High strain rate behavior

20.1 Introduction

Ceramic fiber reinforced metal matrix composites (MMC) combine the high stiffness and high strength of ceramics with the plastic dissipation energy capacity of metallic alloys which offers promise as lightweight alternatives to traditional high strength monolithic metallic alloys. These materials have the added benefit of tunable properties in which mechanical properties, such as Young's modulus, tensile strength, and elongation, can be altered to meet design requirements by varying the volume fraction of reinforcement phase [1–3]. Unidirectional continuous fiber reinforced MMC offer the greatest increase in stiffness and strength in the longitudinal direction [4, 5]. However the resulting transverse properties are typically poor [6, 7], which is remedied by designing laminated cross ply or woven fabric structures. In this chapter, the effect of weave architecture on the impact response of two different woven fabric MMCs is investigated. Numerical modeling is used to offer insight into the damage mechanisms occurring during ballistic impact of woven fabric reinforced MMC.

20.2 Experimental

An inert gas pressure infiltration casting process by CPS Technologies (Norton, MA, USA) was used to produce fabric reinforced aluminum metal matrix composite plates of 0.25″ (6.35 mm) nominal thickness. The matrix alloy used was aluminum with 2 % copper (0.01 wt% Si, 0.01 wt% Fe and 2.17 wt% Cu). The fabrics were woven using rovings consisting of continuous Nextel 610TM (3M, St. Paul, MN, USA) alumina (Al_2O_3) fibers. The ceramic fiber is greater than 99 % α-Al_2O_3 with a diameter of 10–12 μm, density of 3.9 g/cm^3, tensile modulus of 380 GPa, and tensile strength of 3100 MPa [8]. Two fabrics with different weave architectures were investigated in the present study, which are shown schematically in Fig. 20.1. In the first fabric, 2D fabric plies consisting of 3000 denier rovings woven in an 8-harness satin weave configuration plies were laid up such that all rovings were in a 0/90 configuration prior to infiltration (will be further referred to as 0/90 3K). 2D fabric plies consisting of 20,000 denier rovings woven in a 2D plain weave configuration which were laid up such that all rovings were in a 0/90 configuration (will be further referred to as 0/90 20K).

B.A. McWilliams (✉) • J.H. Yu
US Army Research Laboratory, Aberdeen Proving Ground, Aberdeen, MD 21005, USA
e-mail: brandon.a.mcwilliams.civ@mail.mil

M. Pankow
Department of Mechanical and Aerospace Engineering, North Carolina State University, Raleigh, NC 27695, USA

S. Bossuyt et al. (eds.), *Residual Stress, Thermomechanics & Infrared Imaging, Hybrid Techniques and Inverse Problems, Volume 9*, Conference Proceedings of the Society for Experimental Mechanics Series, DOI 10.1007/978-3-319-21765-9_20

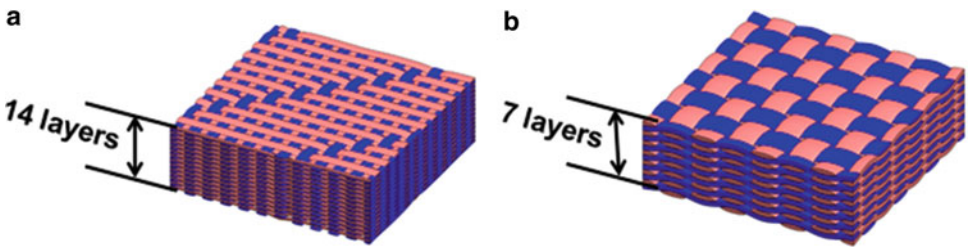

Fig. 20.1 Schematic of the ceramic weave architectures used as reinforcement in the MMCs investigated in this chapter: 8-harness satin weave with 3K denier tows laid up in 0/90 configuration (**a**), and plain weave with 20K denier tows (**b**)

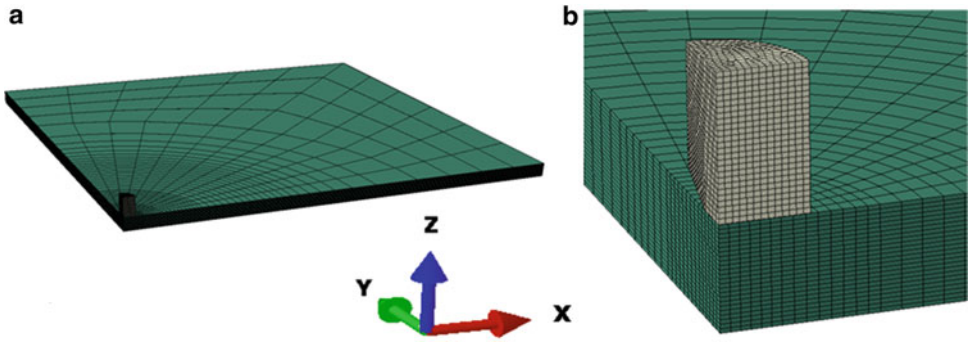

Fig. 20.2 Finite element model for FSP impact on MMC panel; full view (**a**); close up of FSP and impact region mesh (**b**)

Ballistic impact testing was conducted on all MMC materials to determine the effect of weave architecture on the ballistic limit of the targets. The MMC targets were 8 × 8 × 0.25 in. plates mounted on a square frame and clamped rigidly 1 cm on all sides. The MMC targets were impacted by 0.30 caliber fragment simulating projectiles (FSP) launched from a smooth bore gas gun with a plastic sabot. The target stand is located 0.5 m from the gun muzzle. The velocities of the projectiles were determined by a high speed video camera shooting at 100,000 frames per second perpendicular to the flight path of the projectile at the point of impact. The projectile impacted on the target surface with less than 5° of obliquity. The shot locations on each target were carefully spaced to ensure that the ballistic performance of the target from one impact was not affected by the damage caused by the other neighboring impacts. The validity of the shot spacing was verified non-destructively via post-test c-scan (ultrasound) testing [9]. The ballistic limit velocity (V_{50}^{BL}) for each target was calculated by averaging the striking velocities of the three lowest complete penetrations and three highest partial penetrations per target according to the guideline from MIL-STD-662 F [10]. The targets were sectioned post mortem for analysis of the penetration cavities generated by the impact and penetration of the FSP to observe dynamic damage mechanisms occurring in fabric reinforced MMC.

20.3 Numerical Modeling

A 3D finite element model (FEM) was used to conduct ballistic impact simulations of the 0/90 3K fabric reinforced MMC plate in order to validate a newly developed constitutive model and to gain physical insight into the progression of failure observed during the experiments. Simulations were conducted on a plate considered as a homogeneous continuum through the thickness (individual plies were not explicitly modeled) using a quarter symmetry model in the commercial software package ABAQUS/Explicit (Fig. 20.2). The projectile and MMC plate were both modeled as Lagrangian parts. Rigid displacement boundary conditions were applied to the outer 1 cm of the perimeter to emulate the clamping used during testing. Eroding contact between the projectile and the target was modeled as frictionless.

An elastic-plastic orthotropic material model with progressive damage and failure was developed to model the continuum response of the 0/90 3K fabric MMC. A hydrostatic pressure dependent yield surface was implemented via a user subroutine

Table 20.1 Summary of material properties used in ballistic impact simulations

ρ (g/cm^3)	3.2
E_{11} (GPa)	139
E_{22} (GPa)	139
E_{33} (GPa)	120
σ_y^T (MPa)	52.5
σ_u^T (MPa)	326
σ_u^C (MPa)	377
ε_f^T	0.0041
ε_f^S	0.036

to capture the asymmetric plastic behavior that this material exhibits in tension versus compression and is commonly observed in other MMC materials [11, 12]. The properties used in the simulations are summarized in Table 20.1. ρ is the density; $E_{11} = E_{22}$ are the in-plane elastic moduli; σ_y is the initial yield strength; $\sigma_u{}^t$ is the ultimate tensile strength; ε_f^t is the tensile failure strain [7]; E_{33} is the through thickness (normal to plane of fabric weave) modulus; and $\sigma_u{}^c$ is the compressive strength from quasi-static compression testing using ASTM standards [13]. An equivalent plastic strain failure criterion with triaxiality dependence was used to define damage initiation of the MMC in tension, compression, and shear modes. The in-plane (matrix) shear failure strain ($\varepsilon_f{}^{12}$) was obtained from ASTM standard tensile testing of 0/90 samples tested at a 45° orientation to the weave of the fabric [13]. The FSP was modeled with elastic-plastic material response using Johnson-Cook rate dependent plasticity with constants obtained from literature for 4340 steel [14].

20.4 Results and Discussion

The experimentally determined ballistic limit for the two Al_2O_3 woven fabric composite materials investigated were statistically the same with an average of 65.7 (m/s) per pound per square foot (areal density). The results were determined in a per weight basis to account for small variations in thickness due to processing. This result suggests that the particular 2D weave pattern does not significantly affect the overall response to dynamic impact at or near the ballistic limit as the 3K fabric had an 8-harness satin weave while the 20K fabric had a plane weave pattern. This result also suggests that the denier of the reinforcement yarn (3 vs. 20K) does not play a significant role in the dynamic impact behavior of these materials. Both MMCs exhibited generally brittle behavior with damage dominated by their inherently low in-plane tensile elongation [7]. All impacts that completely penetrated the panels created smooth entrance holes roughly the same diameter as the FSP, and varying degrees of spall on the exit holes indicating that the dominant failure modes were a combination of shear plugging and tensile failure through spalling.

The targets were cross sectioned in order to conduct post-mortem analysis of the fracture surfaces generated by the ballistic impact and penetration of the projectile and investigate the damage mechanisms occurring in the material. Both MMCs qualitatively exhibited the same deformation and damage characteristics as a result of the ballistic impact. SEM micrographs of different regions of the impact fracture surface are presented in Fig. 20.3. In both cases, high compressive loading directly under the projectile, and confinement by the surrounded material, results in shear plugging and the fracture surface observed in Fig. 20.3a. The grooves that can be observed are indicative of the hard 4340 steel FSP cutting through the comparatively soft Al-2 %Cu matrix. This failure mode occurred through approximately the first 50 % through thickness behind the target's strike face. At the mid-plane of the target the failure mode transitions sharply from shear plugging to tensile failure. It is believed, and will be demonstrated with the simulation results, that this is where damage initiates when the tensile wave reflected off the rear surface of the target interacts with the incident compression wave. As a result, spall failure initiates when the in-plane tensile strength of the MMC is exceeded and tensile fracture of warp and weft rovings is observed as the dominant damage mode. The tensile fracture is very similar to that observed in uniaxial tension tests [7] with the exception that the fractured yarns and regions of unreinforced matrix are typically deformed out of plane by the ballistic impact as seen in Fig. 20.3b. The out of plane deformation is caused by travel of the projectile as it passes through the thickness of the target. The out of plane plastically deformed matrix material can be seen covering fractured MMC yarns (Fig. 20.3b) that clearly failed in an in-plane tensile mode. This result indicates that the spall failure of the rear surface occurs early in the impact event. The spalling creates void space behind the intact material which is under compression directly in front of the projectile which allows material to be deformed into the space created by spalling and covers the previously fractured fibers. Additional MMC damage mechanisms are active in the material and contribute to the overall energy

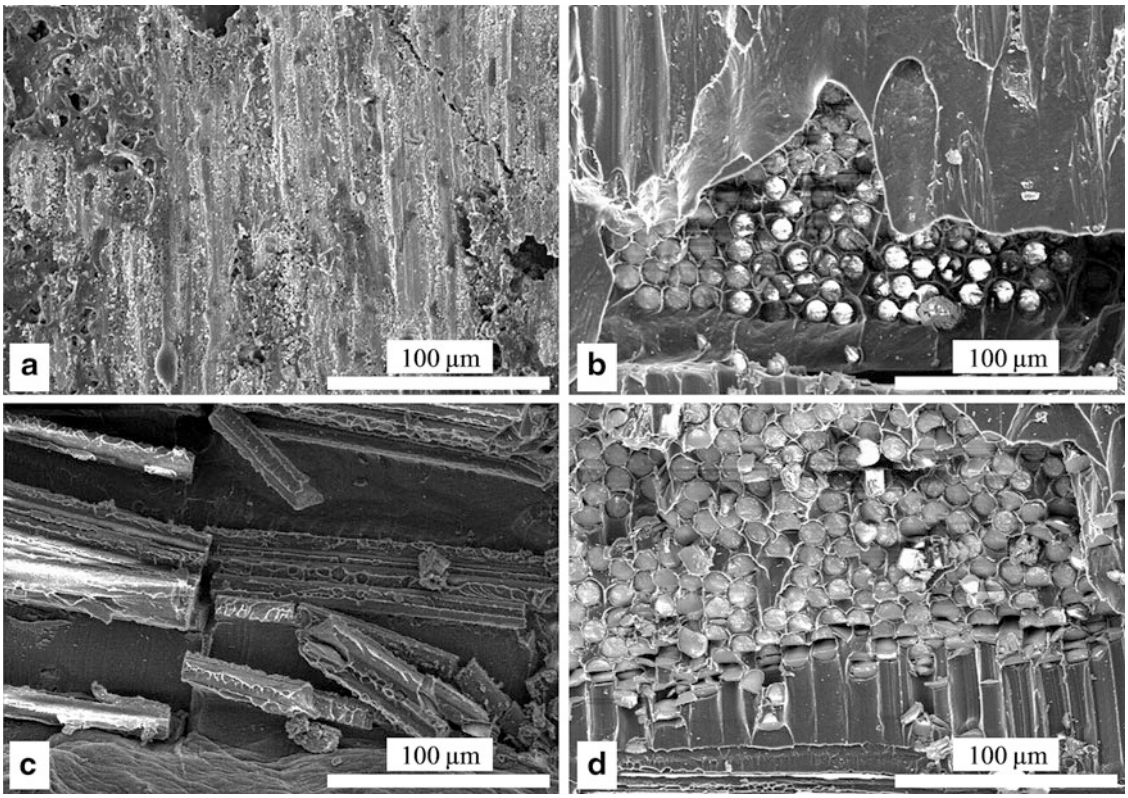

Fig. 20.3 SEM micrographs of post ballistic impact fracture surface of 0/90 3K MMC showing various damage mechanisms: shear plugging (**a**), in-plane tensile failure of roving and fibers and out of plane plastic deformation of matrix (**b**), fracture of transverse rovings and ductile damage (dimpling) of matrix where fibers have pulled out (**c**), and axial splitting of Al_2O_3 fibers (**d**). Direction of projectile travel is from top to bottom in all micrographs

absorbing capacity of the targets. In nearly all micrographs evidence of interfacial decohesion between the fibers and the matrix and the rovings (fiber bundles) and the matrix can be observed. This is consistent with prior work [7] which demonstrated that interfacial decohesion is a major contribution to the overall damage progression in longitudinal and transverse loading of MMC rovings. In some areas there is evidence of ductile matrix deformation (dimpling) where fibers have pulled out of the weft rovings (Fig. 20.3c) indicating good adhesion was formed between the fibers and matrix. Axial splitting of the alumina fibers was observed in both MMC targets investigated and is shown in Fig. 20.3d. This damage mechanism has not been observed at low strain rates but is expected based on prior work on high strain rate testing of unidirectional Al_2O_3 reinforced composites [15] and contributes to the overall energy absorbed by the target during ballistic impact.

The simulation results offer valuable insight into the progression of damage mechanisms that were experimentally observed after impact testing. Figure 20.4 presents hydrostatic pressure contours in order to visualize the regions of compression and tension. In this case tensile stress states are black while color contours represent regions of compressive hydrostatic stress. It can be seen in Fig. 20.4a that tensile failure near the mid plane of the target initiates very early in the impact event. Damage initiates at this location which is where the reflected tensile wave interacts with the incident compression wave. The material directly under the projectile is under high a level of compression which leads to the smooth failure surface representative of shear plugging observed in the experimental fracture surfaces. As the impact event progresses (Fig. 20.4b) it can be seen that the tensile damage rapidly progresses in the material near the exit surface. As more material is spalled from the rear, there is less intact material directly in the path of the projectile. Eventually, the volume of intact material becomes thin enough that it can be deformed plastically down into the void created by the tensile spall failure which creates the regions of deformed fractured MMC yarns visible perpendicular to the original plane of the weave seen in the fracture surfaces in Fig. 20.3.

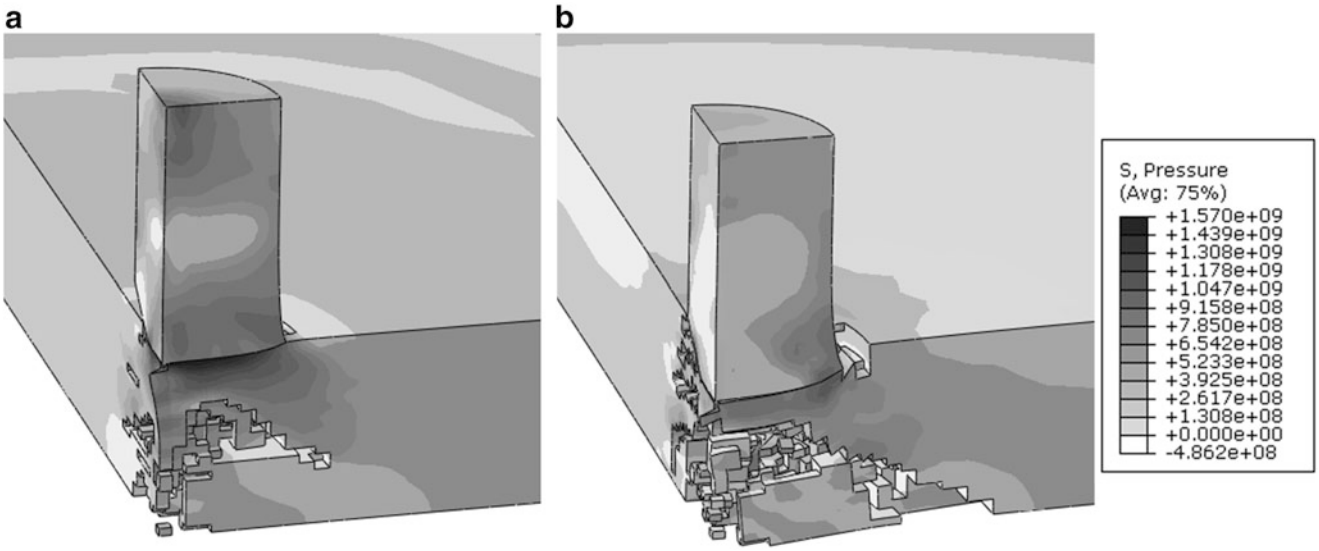

Fig. 20.4 Simulation predictions of hydrostatic pressure (Pa) during ballistic impact indicating regions of compressive (+, *grayscale*) and tensile (−, *white*) stress states at 2.5 μs (**a**) and 10 μs (**b**) which show the progression of tensile failure through spalling in the rear face, and high compression with shear plugging in the strike face of the 0/90 3K fabric MMC target

20.5 Conclusions

The effect of weave architecture on the ballistic impact response of two ceramic fabric reinforced aluminum composites was characterized. The underlying damage mechanisms occurring during ballistic impact with an FSP were characterized and found to be dominated by shear plugging with a sharp transition, about the mid-way through the specimen thickness, to an in-plane dominated tensile failure (spall) near the rear surface. A finite element model incorporating orthotropic plasticity and failure was developed to offer insight into the progression of damage mechanisms through the course of the impact event.

References

1. S. Suresh, A. Mortensen, A. Needleman, *Fundamentals of metal matrix composites* (Stoneham, Butterworth–Heinemann, 1993)
2. E.S.C. Chin, Mat. Sci. Eng. A **259**, 155–161 (1999)
3. A. Mortensen, J. Llorca, Annu. Rev. Mater. Res. **40**, 243–270 (2010)
4. U. Ramamurty, F.W. Zok, F.A. Leckie, H.E. Deve, Strength variability in alumina fiber-reinforced aluminum matrix composites. Acta Mater. **45**, 4603–4613 (1997)
5. B. Moser, A. Rossoll, L. Weber, O. Beffort, A. Mortensen, Damage evolution of Nextel 610 alumina fibre reinforced aluminum. Acta Mater. **52**, 573–581 (2004)
6. M. Guden, I.W. Hall, High strain rate deformation behavior of a continuous fiber reinforced aluminum metal matrix composite. Comput. Struct. **76**, 139–144 (2000)
7. B. McWilliams, J. Dibelka, C.-F. Yen, Multi scale modeling and characterization of inelastic deformation mechanisms in continuous fiber and 2D woven fabric reinforced metal matrix composites. Mat. Sci. Eng. A **61**, 142–152 (2014)
8. 3M Nextel™ Ceramic Textiles Technical Notebook, Ref. No. 98-0400-5870-7, 2004
9. B. McWilliams, C.-F. Yen, J. Yu, in *Experimental and Numerical Characterization of Fiber Reinforced Metal Matrix Composite Impact Behavior*. Proceedings of the American Society for Composites 27th Annual Conference (Arlington, 2012)
10. Dept. of Defense Test Method Standard: MIL-STD-662F, V_{50} Ballistic Test for Armor, 18 December 18 1997
11. B. McWilliams, J. Yu, E. Klier, C.-F. Yen, Mechanical response of discontinuous ceramic fiber reinforced metal matrix composites under quasi-static and dynamic loadings. Mat. Sci. Eng. A **590**, 21–29 (2014)
12. H. Zhang, K.T. Ramesh, E.S.C. Chin, A multi-axial constitutive model for metal matrix composites. J. Mech. Phys. Solids **56**, 2972–2983 (2008)
13. J. A. Dibelka, S. W. Case, in *Extracted Fiber Properties and their Effects on Composite Strength Through Damage Evolution Modeling*. Proceedings of the American Society for Composites 27th Annual Conference (Arlington, 2012)
14. G.R. Johnson, W.H. Cook, Fracture characteristics of 3 metals subjected to various strains, strain rates, temperatures and pressures. Eng. Fract. Mech. **20**, 31–48 (1985)
15. I.W. Hall, A. Tasdemirci, J. Derrick, Quasi-static and high strain rate properties of a cross-ply metal matrix composite. Mater. Sci. Eng. A **507**, 93–101 (2009)

Chapter 21
Digital Image Correlation Analysis and Numerical Simulation of the Aluminum Alloys under Quasi-static Tension after Necking Using the Bridgman's Method

Jian H. Yu, Brandon A. McWilliams, and Robert P. Kaste

Abstract The Bridgman method of true stress correction in tensile loading is revisited. With the current advances in 3D DIC technique, the implementation of the Bridgman method becomes very simple. The equivalent true stress-strain relation from the correction is readily and directly implementable into FEM simulation. The Bridgman method can yield a high degree of accuracy in predicting flow stress in post-necking for some aluminum alloys, especially where the radius of curvature around the neck is small before failure. However, if the actual triaxiality deviates too much from the uniaxial assumption that it is constant across the neck radius, the Bridgman's correction would still over estimate the equivalent stress. Subsequent FEM simulation can determine whether the Bridgman's correction is adequate to predict the true stress-strain relation beyond necking.

Keywords Bridgman's correction • Digital image correlation • Necking • FEM • Tensile • Stress-strain

21.1 Introduction

Finite Element Method (FEM) has become an indispensable and a prevalent engineering tool in solving mechanical problem, material design, and product development. In solving non-linear plastic problems, FEM requires the input of the von Mises equivalent stress, σeq, as function of equivalent plastic strain, εeq. The standard quasi-static tensile test is the simplest experiment to obtain this relation:

$$\sigma_{eq} = \frac{\mathrm{F}}{\mathrm{A}_o} e^{\varepsilon_{eq}} \tag{21.1}$$

where F is the loading force and Ao is the initial cross-sectional area. However, at the onset of necking, the stress state on the test specimen is no longer uniform nor uniaxial. Equation (21.1) is no longer valid.

There are a few ways to obtain the correct true stress-strain relation. Zhang and Li used a reiterative optimization model in FEM to match the simulated load vs. strain relation to the referent experimental data [1]. Although an accurate true stress-strain modeling curve can be obtained using this method, the implementation of optimizing a nonlinear model is rather complex. Joun et al. simplified the reiterative method to predict the necking process by extrapolating a reference true stress-strain curve using the Hollomon's constitutive relation [2].

For isotropic cylindrical specimen under tensile load, Bridgman had formulated a geometric approximation to obtain the equivalent stress-strain relation on the onset of necking and after necking, under the assumption that the von Mises strain is independent of the radial position across the neck [3]:

J.H. Yu (✉) • B.A. McWilliams • R.P. Kaste
Army Research Laboratory, Aberdeen Proving Ground, Aberdeen, MD 21005, USA
e-mail: jian.h.yu.civ@mail.mil

S. Bossuyt et al. (eds.), *Residual Stress, Thermomechanics & Infrared Imaging, Hybrid Techniques and Inverse Problems, Volume 9*, Conference Proceedings of the Society for Experimental Mechanics Series, DOI 10.1007/978-3-319-21765-9_21

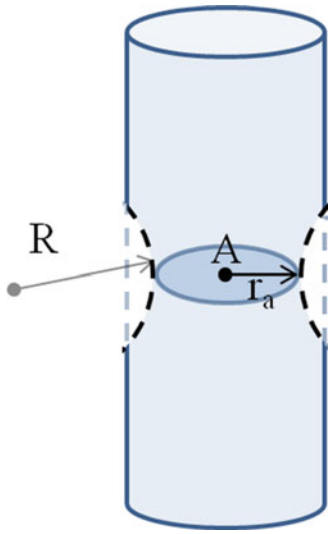

Fig. 21.1 An idealized illustration of necking

$$\sigma_{eq} = \frac{F}{A}\left[\left(1+\frac{2R}{r_a}\right)\ln\left(1+\frac{r_a}{2R}\right)\right]^{-1} \tag{21.2}$$

and

$$\varepsilon_{eq} = \ln\left(\frac{A_o}{A}\right) \tag{21.3}$$

where R is the radius of curvature of neck, r_a is the radius of the neck, and A is the cross-sectional area of the neck (Fig. 21.1).

The reliability of the Bridgman method is weighted heavily on accuracy in measuring the R value. In this report, 3D Digital Image Correction (3D-DIC) technique was used to obtain all the necessary geometric properties of a cylindrical tensile specimen, which are required in determining the Bridgman's correction to the true stress-strain relation. The obtained equivalent stress-strain relation was then input into a finite element method (FEM) model to simulate the tensile experiment. Subsequently, these results were used to validate the applicability of the Bridgman method.

21.2 Material and Methods

Cylindrical specimens were machined from three different aluminum alloy plates: AA-5456, AA-7017, and AA-2040. These three alloys were chosen to illustrate the different degrees of strain hardening and subsequent necking. Figure 21.2a shows the nominal dimension of the machined specimens. A thin layer, 0.01–0.02 mm, of speckled paint pattern was sprayed onto the surface of the specimen for 3D DIC (Fig. 21.2b).

A two-CCD camera stereovision system was used to perform the 3D DIC on the tensile experiment. The angle between the two cameras was 17°. Nikon lenses (Nikkor AF) were attached to the two CCD cameras. The f-stop and the focal length were set to f/8 and 105 mm, respectively. Figure 21.1b is an actual image that was taken from the camera viewing from the left. A pair of stereo images (640 × 480 pixels) was taken every second with an exposure time of 1/100 s during the experiment. The specimen was tested in a tensile loading frame (Instron Model 1331) at a cross-head speed of 0.02 mm per second. The recording of the force loading, F, was synchronized with the cameras' acquisition at 1-s intervals.

The stereo images were analyzed using the commercially available photogrammetric software program Vic-3D (Correlated Solutions, Inc.). Seventeen pairs of calibration images were used to calibrate the cameras. The overall average error for the stereo system is 0.038 pixels. For the 3D DIC analysis, the subset size and the step size were set to 11 pixels and 7 pixels, respectively. All other DIC parameters were set to the built-in default settings. The standard deviations of the 3D positional calculation were 0.006, 0.006, and 0.030 mm for x, y, and z displacements, respectively. The Cartesian coordinate system was transformed to a cylindrical coordinate system in which the Cartesian y-axis became the central axis

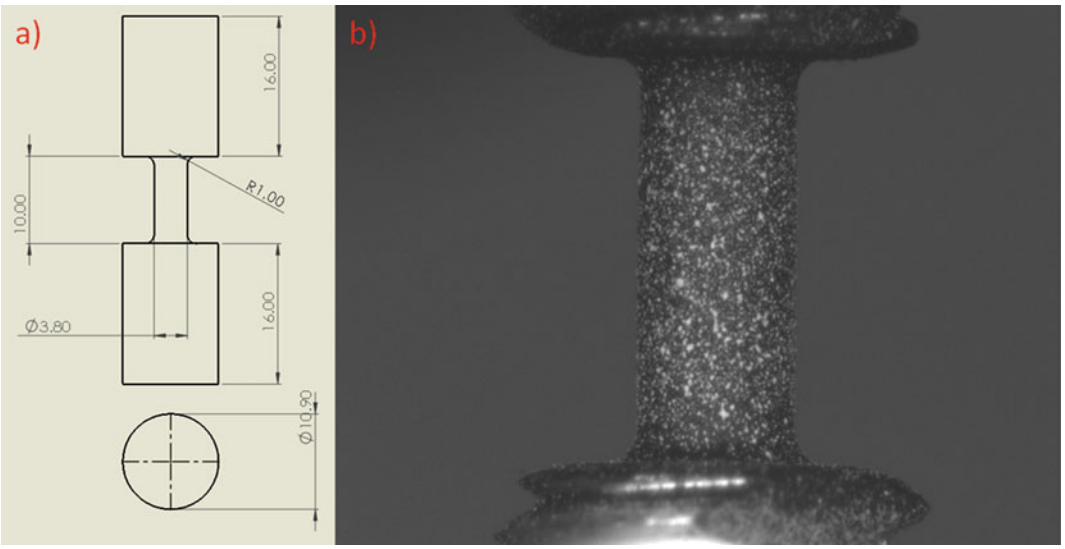

Fig. 21.2 (**a**) The dimensions of the cylindrical specimen are in millimeters; (**b**) the speckled pattern on the specimen surface

of the cylinder. The standard deviation of the calculated radial position was 0.031 mm. The local curvature of the cylinder surface during necking was calculated using the built-in post-processor tool.

21.3 Analysis

For brevity, this paper presents only the DIC analysis for AA-7017 alloy as an example. The onset of necking occurs when the strain hardening of the material exceeds the load-bearing capacity of the material due to reduction of the cross section area due to Poisson effect. The strain at which this plastic instability occurs and strain starts to localized thus is given by Considere's criterion:

$$\frac{d\sigma_t}{d\varepsilon_t} = \sigma_t \tag{21.4}$$

where σ_t and ε_t are the true stress and strain, respectively. In our analysis, we fit a smooth spline to the loading force as a function of the elongation. Where the first derivative of spline function equals zero, it demarcates the beginning of strain localization—the onset of diffuse necking. In terms of constitutive modeling importance, the uniaxial stress-strain curve can be considered valid as an equivalent stress–equivalent strain curve prior to this point and must be corrected to account for triaxial stress state after this point.

Figure 21.3 shows the 3D DIC full-field contour plots for the radius and the local curvature of the AA-7017 alloy specimen. The contour plots of the change of radius illustrate that the deformation of the cylindrical specimen is uniform until the onset of necking. After necking initiates, a very distinct band of curvatures develops on the middle of the specimen. The values of 2R and r_a are taken at the r, θ-plane of the cylinder, where r_a has the smallest value. Until the diffused neck is fully developed, the values of the curvature are quite scattered, particularly just after the onset of necking. This is due to the limitation of the spatial resolution of the cameras. The curvature is too small to detect at the onset of necking. However, these scattered data do not significantly affect the calculation of the correction factor. The limit is rapidly converging to unity as 2R approaches large values. The correction value is sensitive to small values of 2R. After the corresponding values of R and r_a were obtained, the Bridgman correction was applied to the true stress. AA-5456 has a minimal degree of necking before failure; on the other hand, AA-2040 necks severely before failure. The final necking area reduction percentages are −21, −33 and −46 % for AA-5456, AA-7017, and AA-2040, respectively. It can be observed on stress-strain relation that AA-2040 is the most strain-hardening material among the three alloys. It also has the greatest neck reduction and the

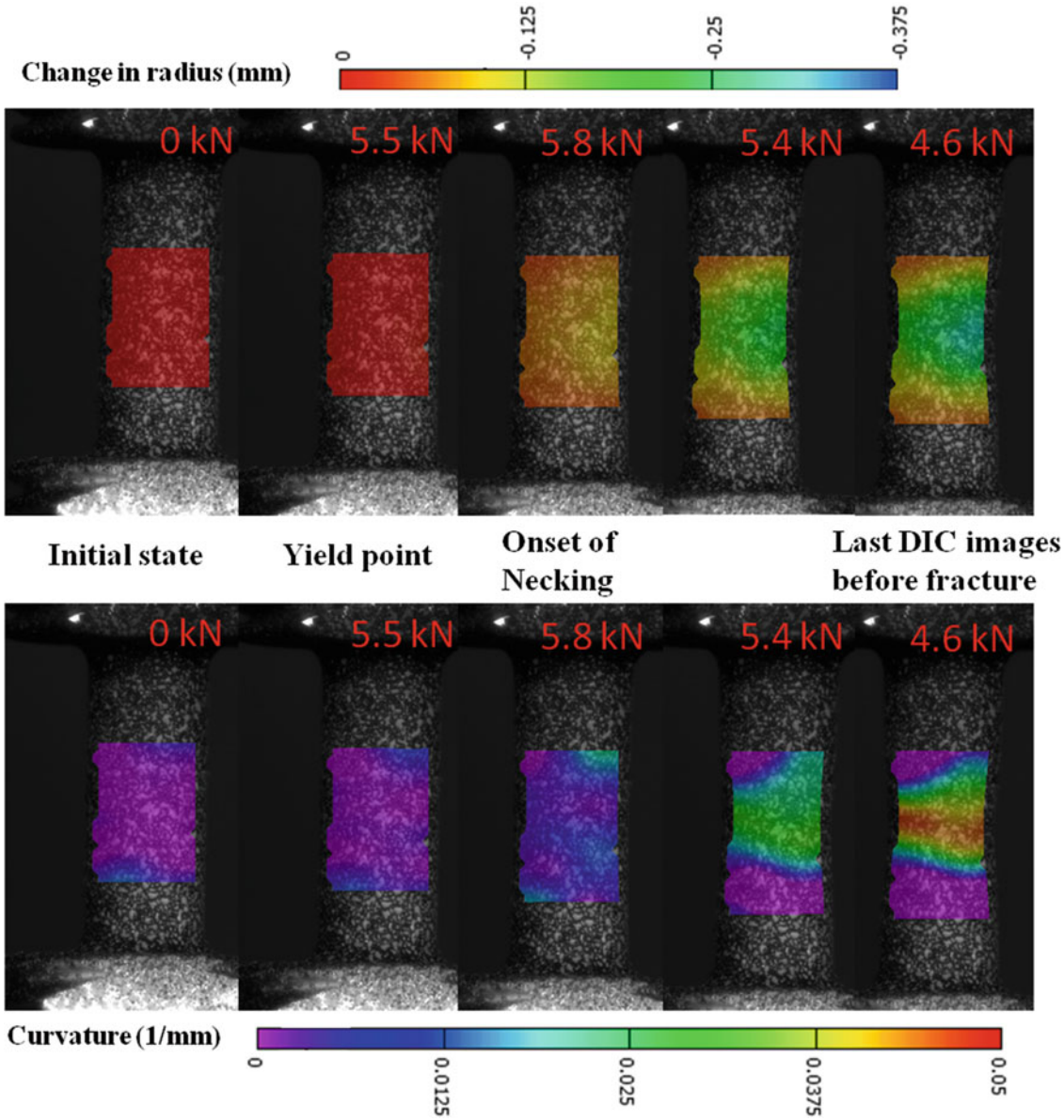

Fig. 21.3 3D full-field strain DIC results used to determine local change in radius (*top*) and the maximum principal curvature (*bottom*) for AA-7017 alloy

smallest curvature diameter before failure. On the other hand, AA-5456 has a curvature diameter greater than 20 before failure, which means the correction factor, C, is close to unity; the correction is almost not needed.

3D finite element simulations were used to model the quasi-static tension experiments up to and including failure of three aluminum alloys using Abaqus/Explicit. Predicted engineering stress–engineering strain curves were then compared to the experimental results in order to validate the constitutive material models obtained using the correction for post-necking behavior. In addition, simulations using the raw (uncorrected) stress-strain data from the experiment (true stress obtained from instantaneous area measured by DIC) were conducted to quantify the increase in accuracy obtained when using the correction.

21.4 Results and Discussion

Figure 21.4 presents the comparison between the simulated and experimental results for the three aluminum alloys. It shows how well the simulation model is able to predict the engineering stress-strain behavior.

The AA-5456 specimen failed just after necking. The Bridgman's correction was very small for AA-5456, which means the correction was almost not necessary. There was a significant improvement in simulating the AA-7017 specimen in terms of predicting the engineering failure strain and reducing the mean square error after applying the Bridgman's correction. For the most severely necked specimen, AA-2040, the Bridgman's correction had reduced the mean square error; however, it still over-predicted the engineering stress and failure strain. The further the specimen deviates from pure uniaxial tension, the lesser the effectiveness the Bridgman's correction is to the stress-strain relation. The equivalent strains as a function of the radial position are becoming less and less constant across the necking area. The Bridgman's correction method assumes the strain is constant across the neck. It is not so surprising that the Bridgman's correction method cannot be applied successfully for localized necking that has a highly non-uniform strain distribution.

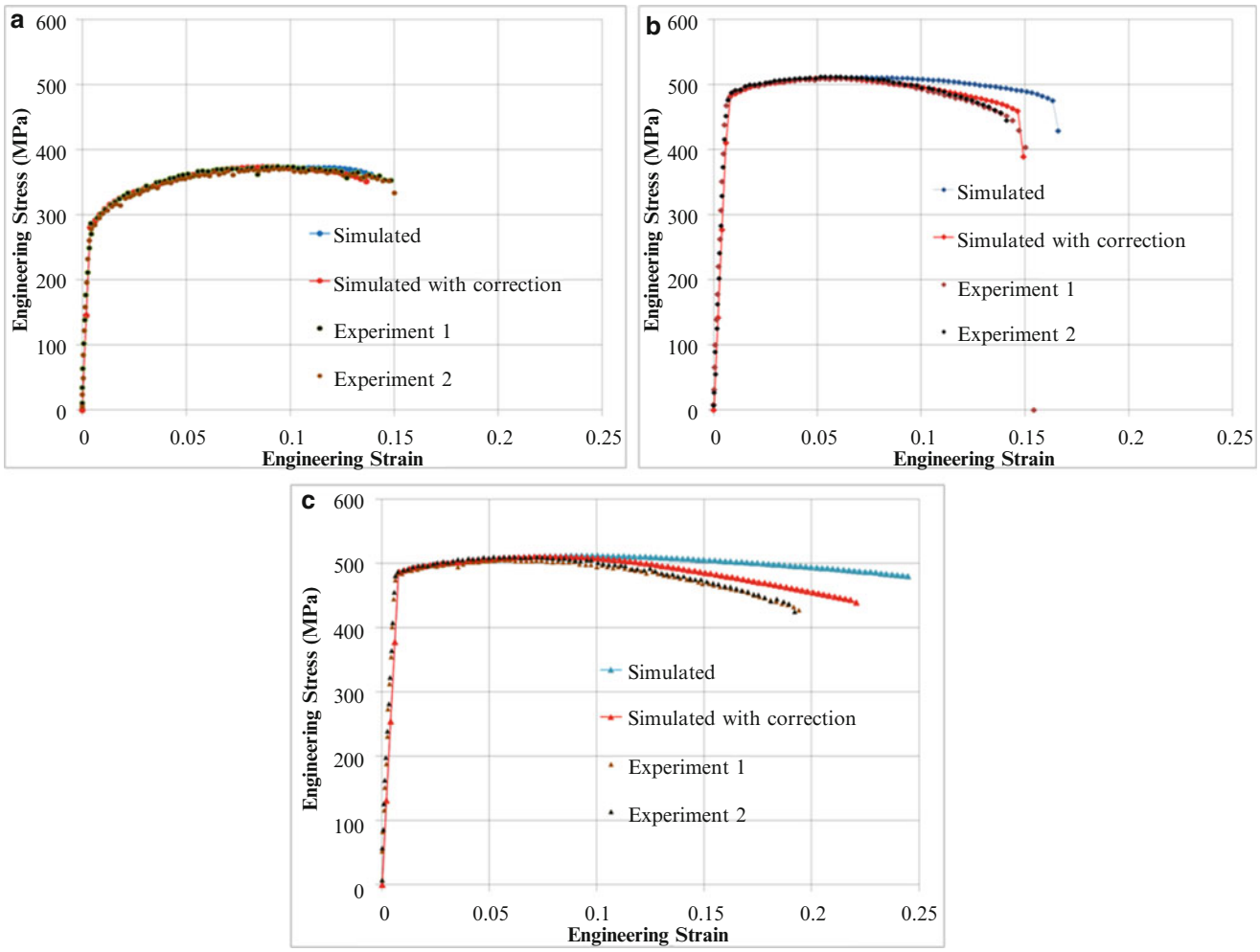

Fig. 21.4 Comparison among simulated and experimental data: (**a**) AA-5456; (**b**) AA-7017; (**c**) AA-2040

21.5 Conclusions

Bridgman's correction method of true stress correction in tensile loading is revisited, and its suitability for use in determining the post-necking constitutive behavior of three aluminum alloys exhibiting various degrees of strain hardening is quantified. With the current advances in 3D DIC techniques, the implementation of the Bridgman method becomes a convenient method to directly determine the constitutive behavior of aluminum alloys after the onset of diffuse necking. It was shown that the equivalent true stress-strain relation in the post-necking regime from the correction is readily obtained and suitable for direct use in FEM simulation for aluminum alloys that exhibit moderate necking behavior. As long as R and r_a are accurately measured, the Bridgman method yields a high degree of accuracy in predicting flow stress in the post-necking regime for some aluminum alloys, especially where the radius of curvature around the neck is small before failure. However, if the strain-hardening behavior of the alloy leads to significant strain localization and reduction in cross-sectional area, the Bridgman's correction would still overestimate the equivalent stress. It is noteworthy that the full-field 3D strain data obtained in this work can be used to apply additional techniques, such as inverse methods, to obtain more accurate constitutive parameters than could be obtained by using 1D or 2D strain data sets.

References

1. K.S. Zhang, Z.H. Li, Numerical analysis of the stress-strain curve and fracture initiation for ductile material. Eng. Fract. Mech. **49**(2), 235–241 (1994)
2. M. Joun, J.G. Eom, M.C. Lee, A new method for acquiring true stress–strain curves over a large range of strains using a tensile test and finite element method. Mech. Mater. **40**, 586–593 (2008)
3. P.W. Bridgman, *Studies in large plastic flow and fracture with special emphasis on the effects of hydrostatic pressure* (New York, McGraw, 1952). p. 23

Chapter 22
Robust Intermediate Strain Rate Experimentation Using the Serpentine Transmitted Bar

W.R. Whittington, A.L. Oppedal, D.K. Francis, and M.F. Horstemeyer

Abstract The stress-strain behavior of a material at intermediate strain rates (between 5/s and 500/s) is important for characterizing dynamic deformation events. A material's mechanical behavior can be strain rate dependent; calibrating constitutive models at actual strain rates of interest are essential for high fidelity simulations. Strain rates below 5/s are easily accomplished with conventional electro-mechanical or servo-hydraulic load frames. Strain rates above 500/s are typically performed with the split Kolsky/Hopkinson pressure bar (SHPB) and other devices depending upon the strain rate. The intermediate strain rate regime is a difficult test regime in which researchers have tried to extend the use of specially instrumented servo-hydraulic load frames or very long Hopkinson bars. We describe a novel design of a serpentine Hopkinson transmitted bar that allows for accurate and robust load acquisition in the intermediate strain rate regime. This design produces repeatable stress-strain results without the stress oscillations typical of a specially instrumented servo-hydraulic load frame and produces data for a longer test time than a conventional Kolsky/Hopkinson bar of the same length.

Keywords Intermediate strain rate • High strain rate • Kolsky bar • Split Hopkinson pressure bar

22.1 Introduction

Deformation of many materials is known to depend on strain rate [1]. In high strain rate testing (500–5000/s), the Hopkinson techniques are widely used to extract the stress-strain behavior [1–6] of these materials. In Split Hopkinson Pressure Bar (SHPB) experiments, a shock wave is imparted to the specimen and by using stress wave theory, stress-strain relations can be extracted from strain gages mounted on the bars. One drawback of SHPB setup is the total time duration of the test is limited based on the length of the bars. If strain rates in the intermediate strain rate regime (5–500/s) are of interests, then the testing apparatus would become too large to fit in conventional laboratories. Some select laboratories do have the ability to implement intermediate strain rate bar systems on the order of 30 m in length and researchers have been successful in producing this limited data [7, 8]. Other researchers have modified conventional SHPBs to provide a long loading duration with hydraulic or other means with load acquisition using multiple strain gages on each bar to monitor the stress strain relationship. In these systems, a multi-gage solution to the stress wave propagation extends the total time duration even if the relatively long stress waves traverse the bars multiple times [9, 10]. This method, however, presents a new problem as the strain rate jumps at every instance that the wave traverses the bars and comes into contact again with the specimen. Also, the many oscillations during the tests may show unfavorable stress strain rendering at intermediate strain rates.

Still other researchers approach testing materials in the intermediate strain rate regime by modifying existing hydraulic load frames [11, 12]. In these systems, deformation of the specimen is induced by high speed servo-hydraulics while the sample grips and fixtures are modified to improve the load acquisition [11, 12]. The modified grips and fixtures are intended to improve the load train with a natural frequency as high as reasonably possible which allows the machine to reaches equilibrium early in the tests. The load then can be measured by a strain gage mounted on the fixture or grip section of the specimen, or by use of a small piezoelectric load washer [13]. These test setups have achieved acceptable data up to approximately 100/s [11, 12]. Shown in Fig. 22.1 is a comparison of a purchased high rate testing apparatus from a manufacturer (Fig. 22.1a) and the best case modified improvement to the system (Fig. 22.1c). Although modified servo-

W.R. Whittington • A.L. Oppedal (✉) • D.K. Francis
Center for Advanced Vehicular Systems, Mississippi State University, Mississippi State, MS 39762, USA
e-mail: aoppedal@cavs.msstate.edu

M.F. Horstemeyer
Center for Advanced Vehicular Systems, Mississippi State University, Mississippi State, MS 39762, USA

Department of Mechanical Engineering, Mississippi State University, Mississippi State, MS 39762, USA

S. Bossuyt et al. (eds.), *Residual Stress, Thermomechanics & Infrared Imaging, Hybrid Techniques and Inverse Problems, Volume 9*, Conference Proceedings of the Society for Experimental Mechanics Series, DOI 10.1007/978-3-319-21765-9_22

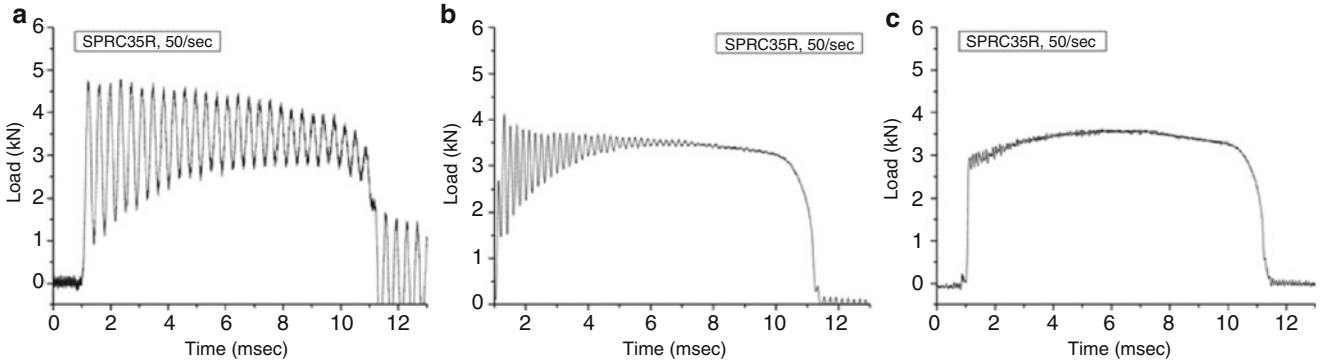

Fig. 22.1 Tensile load ringing in three different modified servo-hydraulic specimen fixtures at three different natural frequencies: (**a**) 2500 Hz, (**b**) 4800 Hz, (**c**) 13,000 Hz [Reproduced with permission from Huh et al. [14]]

hydraulics are typically rated for high loading rates (>10 m/s), at strain rates above 100/s these systems become unreasonably difficult to acquire load data. To extend the achievable strain rates some researchers perform data filtering and curve fitting techniques to remove undesirable oscillations [12].

Due to the aforementioned bar systems having a minimum strain rate limitation in the intermediate regime and modified servo-hydraulic systems having a maximum strain rate limitation also in this regime, improvements to one or both systems is paramount to provide significant strain rate overlap between the testing practices. The main objective of this paper is to provide a solution that acquires accurate load data in the intermediate strain rate regime without complex implementation, in an effort to provide laboratories with an avenue of load acquisition in this environment. A more substantial paper on this intermediate strain rate testing method will be published shortly [15].

22.2 Design Strategy

22.2.1 Bar System Methodology

As previously discussed, a major issue with intermediate rates by use of bar techniques is due to the size limitation. This issue is mainly due to the stress wave propagating along the length of the bar, reflecting off of the free end, and returning to the specimen [9]. Once the stress wave reaches the specimen, the energy applied to the specimen changes, and can then change the applied strain rate. Hopkinson bar experiments are typically performed at such a high rate that the specimen has deformed to the desired amount before the stress wave traverses the bar. Conventional Hopkinson Bar techniques then have a lower strain rate limit determined by the time duration of a single traversing stress wave. The minimum strain rate that can be achieved with a single continuous applied load to conventional bar system can be estimated by:

$$\dot{\varepsilon}_{\min} = \frac{\varepsilon_{\max} c}{2L} \tag{22.1}$$

where L is the length of the transmitted bar, c is the longitudinal wave speed of the bar material, and $\varepsilon_{\max}$ is the maximum strain incurred by the specimen. To reduce the minimum strain rate of these experiments, the longitudinal wave speed of the bar could be reduced by changing the bar material. However, materials with lower wave speeds, such as polymeric materials, also have a significant reduction in strength; this reduction in strength nullifies its use for testing metals which are much stronger than the bars themselves. Another parameter in (22.1) that is possible to change is the bar length. Changing the bar length can be performed only to the extent that a laboratory can accommodate such a testing apparatus. As previously mentioned, some researchers [7, 8] have adopted this practice by increasing their length (~30 m). However, the majority of labs would have to undergo infrastructure changes to acquire these systems.

Repackaging the bar system in a way that allows conventional laboratories to perform intermediate strain rate tests would be beneficial and that is the purpose of our design. Many labs that perform SHPB experiments can house a system of 6 m but need the capabilities of a longer system (>18 m) for smooth load acquisition durations in the intermediate strain rate range. The time duration of a bar with length of 18 m would be enough for testing nominal strain rates of about 70/s for a specimens

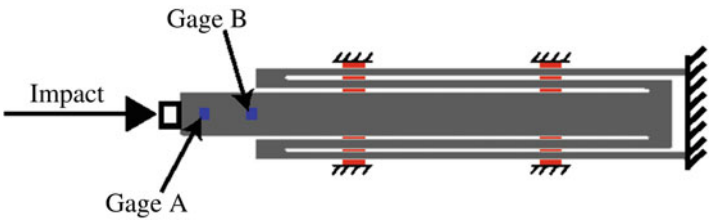

Fig. 22.2 Setup of our proposed serpentine transmitted bar loaded in compression, with two strain gage stations (*blue*), the specimen location (*white*), and bushings (*grey*)

tested to 0.5 strain if a metallic bar ($c = 5000$ m/s) was used. Because modified servo-hydraulics are capable of strain rates up to 100/s, this technique could provide enough overlap for complete testing throughout the intermediate strain rate regime if a laboratory had acquired both systems.

22.2.2 The Serpentine Bar Approach

Figure 22.2 shows the setup of a serpentine, or folded, bar that can provide increased time duration to achieve large strains. A serpentine bar has the advantage over a conventional long bar in the since the stress wave, propagating from the sample, can be transferred into a series of tubes. These tubes are impedance matched to the original solid bar to eliminate the reflection due to the added tubes, and the joint is made small and stiff to reduce the reflections at the joint. Tubes have been successfully used previously to trap the stress wave energy in recovery Hopkinson bar setups [16]. The recovery Hopkinson bar uses a tube that is located near a flange on the free end of the bar to allow a certain amount of bar movement before the stress wave enters the tube and is trapped from returning to the specimen. Furthermore, this setup has been shown to transmit the stress wave very well when careful consideration is taken in designing the transfer flange. Here, we adapt this concept for increasing the stress wave possible in a given bar length, rather than trapping a shorter stress wave inside a detachable tube. The main difference in our setup is that in the serpentine bar, a series of tubes are rigidly connected at alternating ends of the bar. The setup shown in Fig. 22.2 shows a serpentine bar with two attached tubes that multiply the effective length of the bar by a factor of three. If manufacturing techniques permit, any number of tubes can be attached to increase the effective length of the bar. With attachment of this bar to a direct Hopkinson bar loading system as the transmitted bar, or to the fixed end of a servo-hydraulic load frame, elimination of high frequency ringing with long time duration can be achieved efficiently in a bar of substantial reduced length.

22.3 Prototype Fabrication

A serpentine transmitted bar with a single attached tube, designed for compression testing, was selected to provide a conceptual demonstration. This setup was also compared directly to a longer bar of equal effective length, detailed in the Experiments section. The serpentine bar was built using a 15 mm diameter rod of 1.5 m length with a 1 m long tube (giving an equivalent length of 2.5 m), both being the same grade 350 maraging steel. The diametrical gap between the tube and the rod was 1.5 mm and the tube was machined to match the effective cross sectional area of the solid rod. Joining the bars was performed using a gas-tungsten arc welding (GTAW) process without filler. Threaded connections between the bars were also attempted but the load did not transmit smoothly through the joint. Bronze rings were placed in the gaps in between the bar and tube at 300 mm intervals to ensure rigidity of the bar inside the tube. Two gage stations were placed near the specimen approximately 300 mm apart from each other with the closest strain gage 100 mm from the sample to provide load sampling and monitoring of any reflections that may occur. The entire bar was then mounted on a SHPB frame in a similar fashion to conventional Hopkinson bar mounting. Images of the fabricated serpentine bar are shown in Fig. 22.3.

The physical limitations of making a serpentine bar became clear during the fabrication of the prototype. If each tube would have the same characteristic impedance, i.e. cross sectional area, then the tube's thickness becomes very small as the number of tubes increases. A practical limitation of two tubes for a 12–15 mm diameter bar was observed during the project. However, and initial larger diameter rod would allow more attached tubes. A 25 mm diameter rod may be able to achieve four tubes.

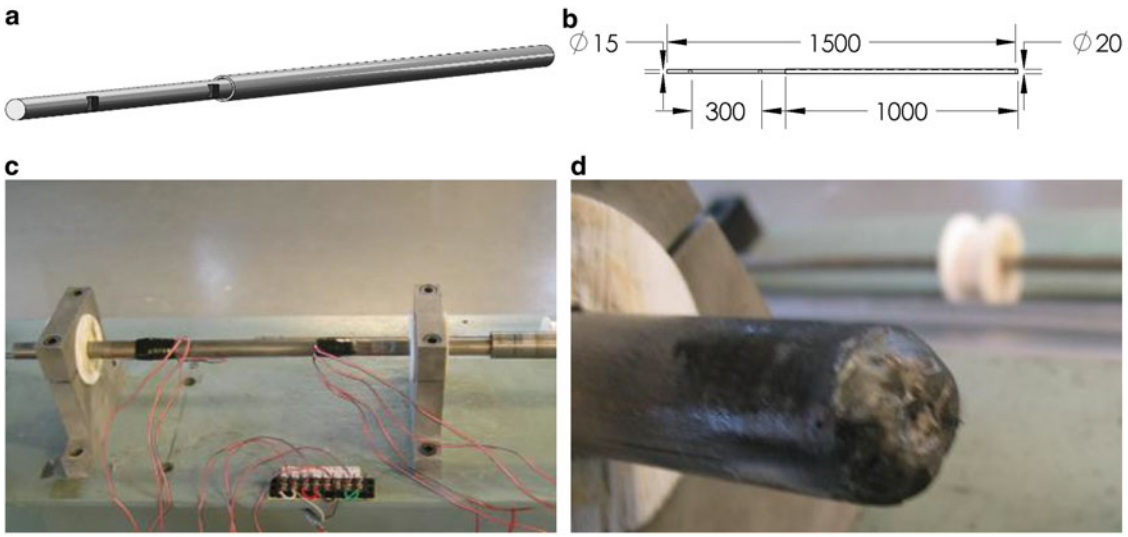

Fig. 22.3 Schematic of the serpentine bar (**a**, **b**). Front half of the two pass bar (**c**) and close-up of the welded joint at the far left of the serpentine bar (**d**)

22.4 Experiments

22.4.1 Dynamic Joint Behavior

When constructing the serpentine bar, the authors' hypothesized that the welded joint may cause unwanted reflections of the stress wave to propagate towards the specimen and subsequently produce unwanted ringing in the specimen. The Lagrange diagram, shown in Fig. 22.4a, shows the theoretical position versus time of the transmitted stress wave front, as well as an illustration of the gage positions in the bar. The tube is shown unfolded for viewing purposes of the stress wave frontal. Using an experimentally determined bar wave speed of 4783 m/s, a hypothetical first order reflected wave from the welded joint was anticipated to be captured by Gage A after 0.00057 s of record time. To investigate this notion, an experiment was constructed on the serpentine bar prototype in which a striker bar of 0.6 m long was fired at the serpentine bar. The striker bar length was chosen to allow the initial wave to transmit through the joint and enter the attached tube while any reflection from the joint could be monitored without interference. The striker, originally moving at 10 m/s, was fired at the serpentine bar, which had a small 3 mm thick aluminum pulse shaper inserted between the two bars, to eliminate dispersion effects [9].

Notice in Fig. 22.4b that the stress wave generated is smooth in nature and ends at a time of approximately 0.00047 s. After this time, the signal should remain null if no reflections from the joint occur. However, at 0.0005385 s, a small wave was detected which is negative (tension) and then positive (compression) in nature. A single wave of this size is not likely to affect the specimen strain rate behavior; however, this wave could pose a problem for data analysis. If the final design also has a reflection wave of this size, Gage B, depicted in Fig. 22.4a, can be placed at an appropriate distance from Gage A can be used to provide more accurate accounting of the stress versus time. The data reduction method by a two point strain methodology proposed by Zhao and Gary [9] is suitable. The form of the equations used to solve for the actual elastic strain in the serpentine bar near the specimen is the following:

$$\varepsilon(t) = \left\{ \begin{array}{lll} \varepsilon_A(t - L_A/c) & \text{for} & t < 2(L - L_A)/c \\ \varepsilon_B(t - L_B/c) & \text{for} & 2(L - L_A)/c \le t < (2L + L_B)/c \\ \varepsilon_A(t - L_A/c) & \text{for} & (2L + L_B)/c \le t \end{array} \right\} \tag{22.2}$$

where L, L_A, and L_B are the distances from the sample to joint, Gage A, and Gage B, respectively. By providing an appropriate distance between Gage A and Gage B, the stress wave, free of the reflection of the joint, can be produced using

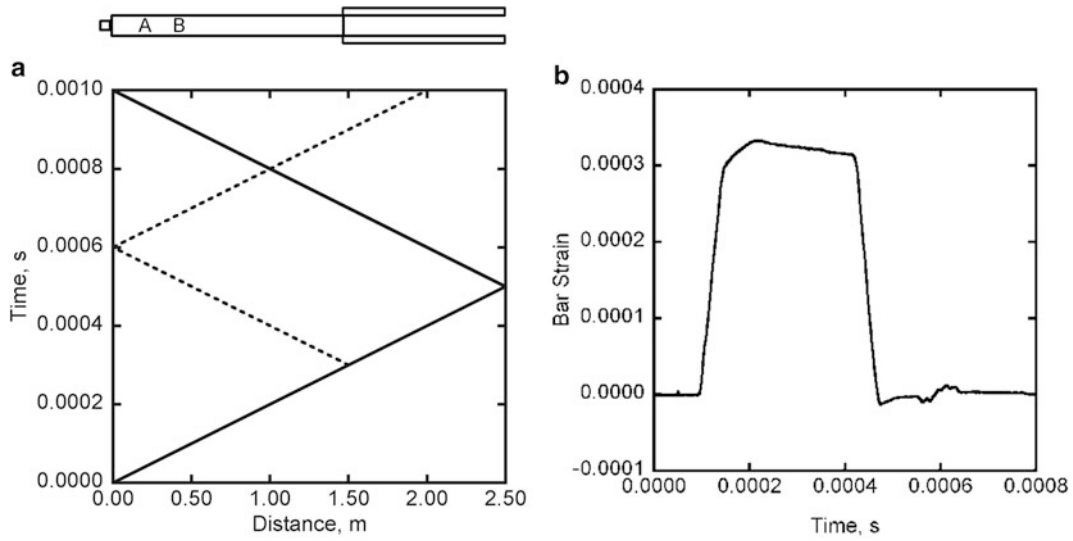

Fig. 22.4 Stress wave position diagram in the serpentine bar prototype (**a**) and the experimental data gathered from Gage A (**b**) from an impact of a striker bar with pulse shaper. The serpentine bar illustration is shown with the attached tube in reverse direction for comparison to diagram

the appropriate strain gage signal at the appropriate time. This will not remove the inflection due to the reflected wave bouncing off of the specimen, as this is a real stress existing on the specimen bar interface.

If the reflection for the final design does not show a significant reflection, Gage B is not needed and a single strain gage can be used to monitor the stress history similar to long bar systems [8].

22.4.2 Intermediate Strain Rate Experiment

To investigate the robustness of the new serpentine bar in operation, an intermediate strain rate compression test was performed on a 6061-T6 aluminum sample material. For this experiment, a long striker of 2.5 m was used. A compression specimen was placed at the end of the transmitted bar and impacted by the long striker at the free end of the specimen at 2 m/s in a direct Hopkinson bar fashion. The striker bar velocity was chosen to give a nominal strain rate in the intermediate strain rate regime. The aluminum specimen was machined to a right cylinder of 12.7 mm diameter and a high elongation EP style strain gage was attached to the specimen to monitor strain. For monitoring of load, the previously used transducer class strain gages, Gage A and Gage B, were mounted to the bar at selected locations, shown in Fig. 22.4a. Figure 22.5 shows the raw data from the test.

Figure 22.5 exhibits the bar strain vs. time as recorded from the two strain gages mounted on the bar. In Fig. 22.5, the Specimen Gage record becomes static at approximately 0.001 s. At this time at which the stress wave has traversed the entire bar length, including the tube, and has finally unloaded the specimen. This is the time that both Gage A and B now significantly drop, except for some ringing due to the stress wave now free to ring in the bar. The Gage B record is slightly shorter in time duration than Gage A due to the wave not reaching Gage B until after Gage A (because it is further away from the specimen) and then Gage B dropping off before Gage A (because it is closer to the free end of the bar). Notice at the time between 0.0005 and 0.001 s that there are two inflections in the Gage A and Gage B results during the specimen loading. Also, the inflections in Gage B are separated by a larger distance than in Gage A. This is due to Gage B being placed further from the specimen end of the bar. These inflections in the data appear to be a direct result of the joint. The signals show promise as compared to long bar and servo-hydraulic systems [7, 8, 10–12].

22.4.3 Long Bar Verification Experiment

To compare signals of the serpentine bar to that of a traditional long bar system, an experiment was conducted using a long transmitted bar of equal effective length to the serpentine bar. A 2.5 m solid bar was instrumented with a single strain gage in

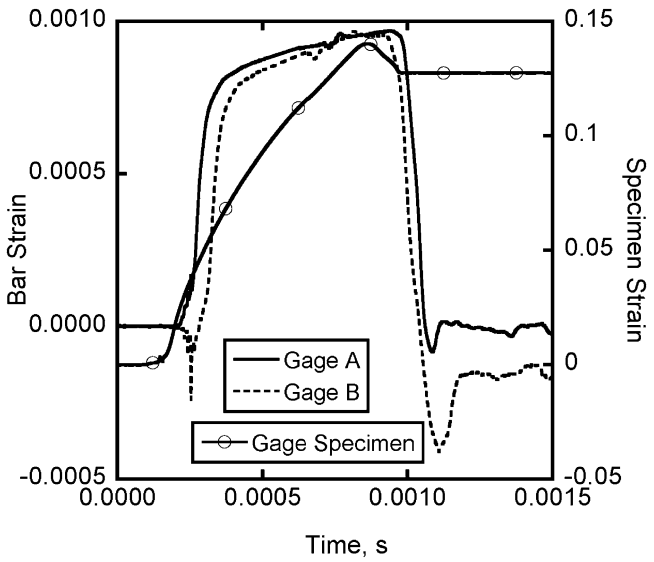

Fig. 22.5 Raw strain gage data from a direct compression test of 6061-T6 aluminum with a striker impact at 2 m/s using the serpentine bar

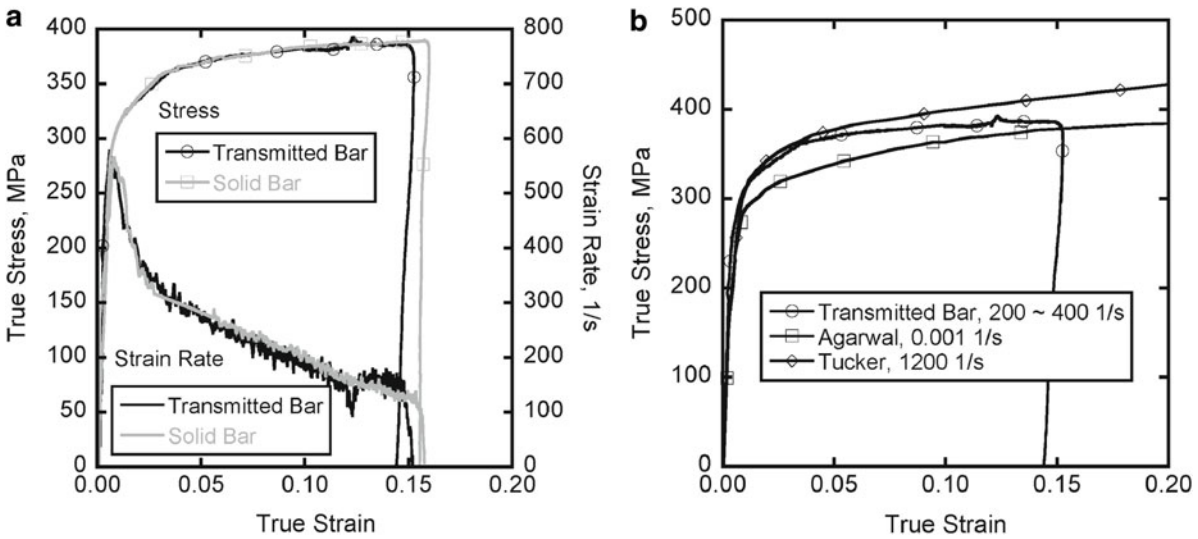

Fig. 22.6 (**a**) Comparison of a compression stress-strain curves and strain rate-strain curves of the solid 2.5 m long bar (*solid bar*) and the new serpentine bar (*transmitted bar*), and (**b**) comparison of the serpentine bar data with published compression data at a higher and lower strain rate for the same sample material with results from Tucker et al. [18] and Agarwal et al. [17] for a 6061-T6 aluminum alloy

the same approximate distance from the sample as Gage A in the serpentine bar arrangement. Stress in the specimen was calculated by gathering the transmitted bar strain gage data as a force measurement. This force in the specimen-bar interface is related to the raw transmitted bar strain gage record by the relationship:

$$F(t) = \varepsilon\left(t - L_g/c\right)EA \tag{22.3}$$

where $\varepsilon(t-L_g/c)$ is the transmitted bar strain gage record at some time $t-L_g/c$. L_g is the distance from the transmitted bar strain gage to the specimen-bar interface, c, E and A are the wave speed, elastic modulus and cross sectional area of bar, respectively.

True stress and true strain cures were then calculated for both the long bar and the serpentine bar tests and are shown in Fig. 22.6. Figure 22.6 shows that the stress-strain curves and strain rate-strain curves compare very well to each other for the two different systems. The two point strain data reduction method employed for the serpentine bar experiments improved the stress strain curve by removal of the first inflection in the data. A key aspect of the serpentine bar experiment is that robust stress strain data in the intermediate strain rate regime is achieved without filtering or curve fitting. Figure 22.6b also shows

that the serpentine experimental data for a 6061 aluminum alloy compares well with other high and low strain rate data with the exception of the hardening rate [17, 18]. The hardening rate drop is likely due to the drastic drop in strain rate during the direct Hopkinson bar experiment. However, many of the researchers have worked diligently at providing constant strain rate experiments using hydraulic or other means [9, 13].

22.5 Conclusion

The design of a serpentine, or folded, Kolsky/Hopkinson bar, is described that can produce useful stress-strain measurements in the intermediate strain rate regime. The device produces results free of stress oscillations that are typical of a modified servo-hydraulic load frame and is able to reach lower strain rates and longer test times than Kolsky/Hopkinson bar devices of the same length. Experimental stress-strain results of 6061-T6 aluminum at a strain rate of ~300/s on the device reproduce nearly exactly published conventional Kolsky/Hopkinson bar results [18]. This serpentine Hopkinson transmitted bar design can be useful in providing longer recording times than conventional bars of the same effective length. This method may be employed for intermediate strain rate experiments in laboratories that cannot house a long bar system. Furthermore, this system may be employed when load ringing exists in experiments performed using modified servo-hydraulics systems.

Acknowledgments The authors would like to acknowledge the Center for Advanced Vehicular Systems (CAVS) at Mississippi State University for supporting this work.

References

1. U.S. Lindholm, High Strain Rate Testing, Part 1: Measurement of Mechanical Properties, in *Techniques of Metals Research*, ed. by R.F. Bunshah, vol. 5 (Wiley Interscience, New York, 1971), pp. 199–271
2. P. Follansbee, "The split Hopkinson bar," *Mechanical Testing,* 8, 9th ed., vol 198 (ASM International, Brook Park, 1985). p. 203
3. H. Kolsky, An investigation of the mechanical properties of materials at very high rates of loading. Proc. Phys. Soc. B **62**(11), 676–700 (1949)
4. H. Zhao, G. Gary, On the use of SHPB techniques to determine the dynamic behavior of materials in the range of small strains. Int. J. Solids Struct. **33**(23), 3363–3375 (1996)
5. G.T.I. Gray, in *Methods in Materials Research*, ed. by E. Kaufmann. High-Strain-Rate Testing of Materials: The Split-Hopkinson Pressure Bar, (John Wiley & Sons, New York, 1999)
6. T. Nicholas, Tensile testing of materials at high rates of strain. Exp. Mech. **21**(5), 177–185 (1981)
7. B. Song, C.J. Syn, C.L. Grupido, W. Chen, W.-Y. Lu, A long split hopkinson pressure bar (LSHPB) for intermediate-rate characterization of soft materials. Exp. Mech. **48**(6), 809–815 (2007)
8. A. Gilat, T.A. Matrka, A new compression intermediate strain rate testing apparatus. EPJ Web Conf. **6**, 39002 (2010)
9. H. Zhao, G. Gary, A new method for the separation of waves. Application to the SHPB technique for an unlimited duration of measurement. J. Mech. Phys. Solids **45**(7), 1185–1202 (Jul. 1997)
10. J. Shim, D. Mohr, Using split Hopkinson pressure bars to perform large strain compression tests on polyurea at low, intermediate and high strain rates. Int. J. Impact Eng. **36**(9), 1116–1127 (Sep. 2009)
11. M. Borsutzki, D. Cornette, Y. Kuriyama, A. Uenishi, B. Yan, and E. Opbroek, "Recommendations for dynamic tensile testing of sheet steels. Intern. Iron Steel Inst. (2005).
12. D. Zhu, B. Mobasher, S.D. Rajan, P. Peralta, Characterization of dynamic tensile testing using aluminum alloy 6061-T6 at intermediate strain rates. J. Eng. Mech. **137**(10), 669–679 (Mar. 2011)
13. R. Bardenheier, G. Rogers, Dynamic impact testing with servohydraulic testing machines. J. Phys. IV (Proceedings) **134**, 693–699 (2006)
14. H. Huh, J.H. Lim, S.H. Park, High speed tensile test of steel sheets for the stress-strain curve at the intermediate strain rate. Int. J. Automot. Technol. **10**(2), 195–204 (2009)
15. W.R. Whittington, A.L. Oppedal, D.K. Francis, M.F. Horstemeyer, A novel intermediate strain rate testing device: the serpentine transmitted bar. Int. J. Impact Eng. (2015) doi:10.1016/j.ijimpeng.2015.02.009
16. S. Nemat-Nasser, J.B. Isaacs, J.E. Starrett, Hopkinson techniques for dynamic recovery experiments. Proc. R. Soc. Lond. A Math. Phys. Sci. **435**(1894), 371–391 (1991)
17. H. Agarwal, A.M. Gokhale, S. Graham, M.F. Horstemeyer, Anisotropy of intermetallic particle cracking damage evolution in an Al-Mg-Si base wrought aluminum alloy under uniaxial compression. Metallurgical Mater. Trans. A **33**(11), 3443–3448 (2002)
18. M.T. Tucker, M.F. Horstemeyer, W.R. Whittington, K.N. Solanki, P.M. Gullett, The effect of varying strain rates and stress states on the plasticity, damage, and fracture of aluminum alloys. Mech. Mater. **42**(10), 895–907 (2010)

Chapter 23
Testing Program for Crashworthiness Assessment of Cutaway Buses

Michal Gleba, Jeff Siervogel, Jerry W. Wekezer, and Sungmoon Jung

Abstract The State of Florida acquires over 300 cutaway buses every year. The increasing popularity of such buses raised concerns about passenger safety and overall crashworthiness of this transportation mode. An extensive research program was initiated at Crashworthiness and Impact Analysis Laboratory (CIAL) to facilitate experimental testing and computational mechanics as two integral parts for crashworthiness evaluation of the cutaway buses. The major objective of the evaluation program is to ensure that bus structures perform well during actual accidents, especially rollovers. Multi-level testing program includes testing of: small samples for material characterization, larger passenger compartment connections, impact testing of wall panels, as well as full scale roll-over and side impact tests of the inspected vehicles. Due to dynamic nature of rollover accidents, the program was originally based on dynamic testing. However, further research led to introduction of several simpler yet equivalent, quasi-static tests. Testing data is also used to support verification and validation of detailed finite element models of the buses, which are developed for LS-DYNA—an explicit, non-linear finite element solver. The program was well received by cutaway bus industry and it resulted in strong commitment and collaboration with bus manufacturers.

Keywords Testing techniques • Dynamic behavior of materials • Experimental user facilities • Vehicle crashworthiness • Cutaway bus rollover

23.1 Introduction

Cutaway bus transportation in North America in increasing in popularity as each state acquires more of these vehicles each year. However, this increasing trend has raised concerns about passenger safety and overall crashworthiness of this transportation mode.

The main safety concern is that cutaway buses are designed and built in a specific way which distinguishes them from other types of commonly used buses in transportation. The most significant difference is their assembly process. Unlike large coaches, the cutaway buses are built in two separate stages [1]. In the first stage, the vehicles chassis with the driver's cab is built by a major car manufacturer. Next, a smaller company adds a passenger compartment structure per client request. The main issue of such a process is that the smaller companies in contrast to major automotive manufacturers cannot afford conducting the same level of R&D and testing. Another feature that makes these vehicles unique is the lack of applicable crashworthiness standards in the United States. Cutaway buses often exceed the 10,000 lbs. Gross Vehicle Weight Rating (GVWR) which in combination with the two stage manufacturing process exempts them from most federal safety standards. In order to improve the safety and crashworthiness of this transportation node an extensive research program was initiated in 1999 by the Crashworthiness and Impact Analysis Laboratory (CIAL) located at the FAMU-FSU College of Engineering in Tallahassee FL. Experimental testing procedures and computational mechanics studies were initiated in order to accurately assess the overall crashworthiness of the cutaway buses [2]. The multi-level testing program includes testing of: small samples for material characterization, larger passenger compartment connections, impact testing of wall panels, as well as full scale roll-over and side impact tests of the inspected vehicles [3].

M. Gleba (✉) • J. Siervogel • J.W. Wekezer • S. Jung
Department of Civil and Environmental Engineering, FAMU-FSU College of Engineering,
2525 Pottsdamer Street, Tallahassee, FL 32310-6046, USA
e-mail: mgleba2@fsu.edu

S. Bossuyt et al. (eds.), *Residual Stress, Thermomechanics & Infrared Imaging, Hybrid Techniques and Inverse Problems, Volume 9*, Conference Proceedings of the Society for Experimental Mechanics Series, DOI 10.1007/978-3-319-21765-9_23

23.2 Initial Testing and Material Characterization

The evaluation of the cutaway buses begins with the characterization of the structural members from which the passenger compartment is composed. Parameters for the steel and composite members are obtained using a simple tension test with dog-bone shaped samples (Fig. 23.1). Results are utilized in further investigations using Finite Element methods.

Other testing methods for material characterization include: testing of bus skin glued to steel member components, static three point testing and impact testing of structural members. The testing setup for static bending and impact testing is shown in Fig. 23.2 An impactor for dynamic testing was designed and fabricated by the Crashworthiness and Impact Analysis Laboratory (CIAL). The height and mass of the impacting hammer are adjustable and can be modified according to testing needs.

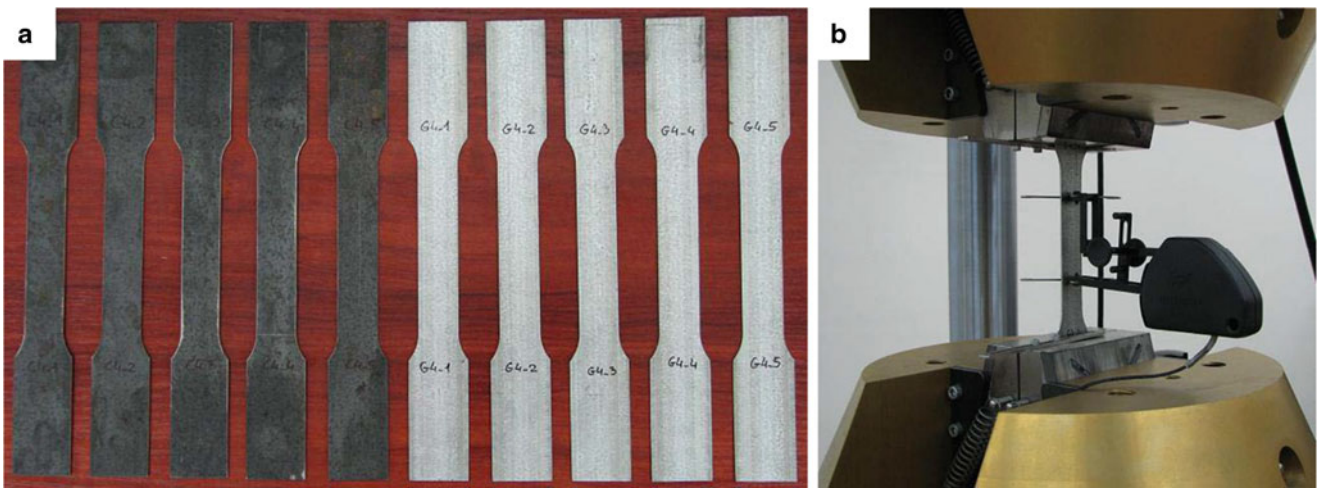

Fig. 23.1 (**a**) Steel specimens prepared for tensile testing (**b**) specimen with extensometers in testing grips of the INSTRON machine

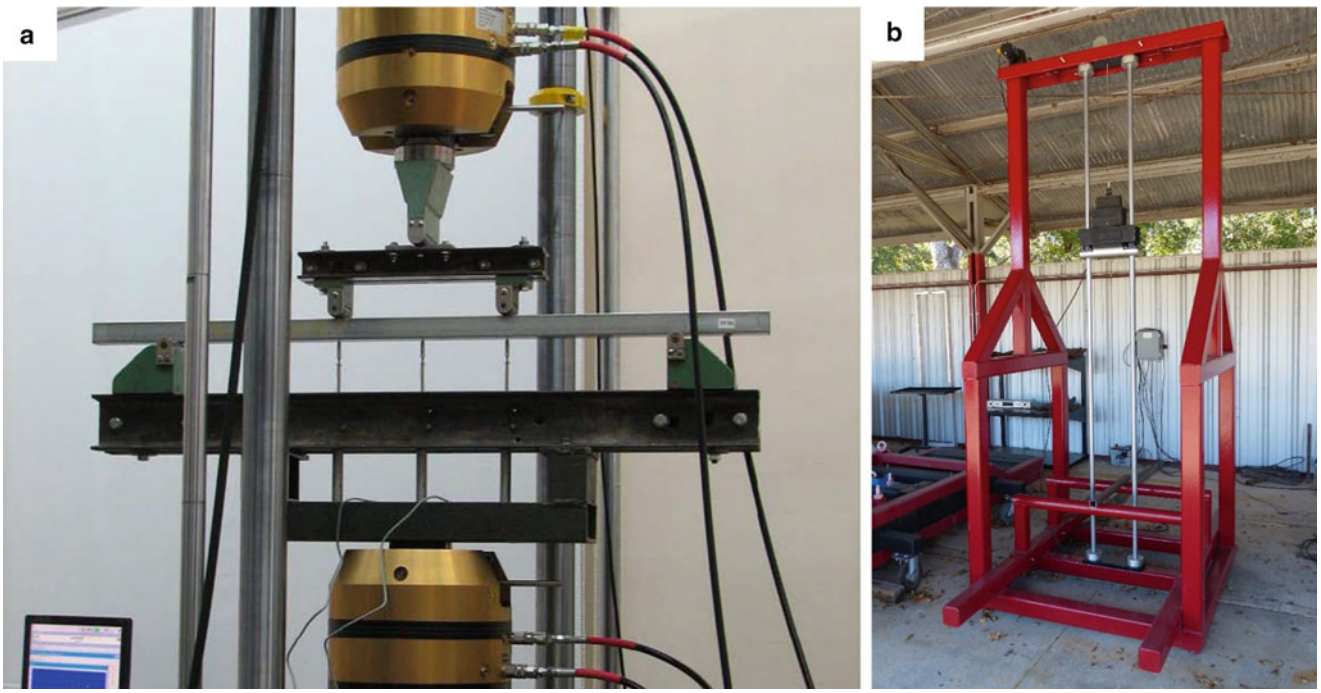

Fig. 23.2 (**a**) Static bending test setup (**b**) impact testing machine with the impacting hammer

23.3 Component Testing

After several years of the cutaway bus testing program it became apparent that crashworthiness of structural connections is critical especially during roll-over accidents [4]. It was also found out that cutaway buses with low floors may be prone to side impact accidents. Figure 23.3 shows a typical cutaway bus with indicated components which are being tested as a part of the component testing program. The aim of the test is to measure the energy needed to deform the element until its failure (failure is defined as a critical angle for which the element deformation penetrates the so called 'survival space').

The testing methods and devices were designed and fabricated by the Crashworthiness and Impact Analysis Laboratory. Figure 23.4 shows a schematic representation of a wall to floor connection test with a set of prepared connection samples. The width of the floor panel is equal to the typical longitudinal distance between two adjacent columns (vertical tubes). The vertical part of the tested specimen consists of only one column (tube or open channel). The column is cut at the level just under the window or the waistrail of the tested vehicle. During the tests the floor panel is fixed to the ground and the loading is applied to the column along the direction going through a fixed point, as it is shown in Fig. 23.4.

The wall to floor test requires the panel to dissipate a minimum of 290 J per meter of panel length over 16.7° of rotation [5]. Similar testing is carried out for the roof to wall connection. However, in the later case the panel is required to dissipate at least 140 J per meter. The test setup and the failure mode of some of the samples is shown in Figs. 23.5 and 23.6 respectively.

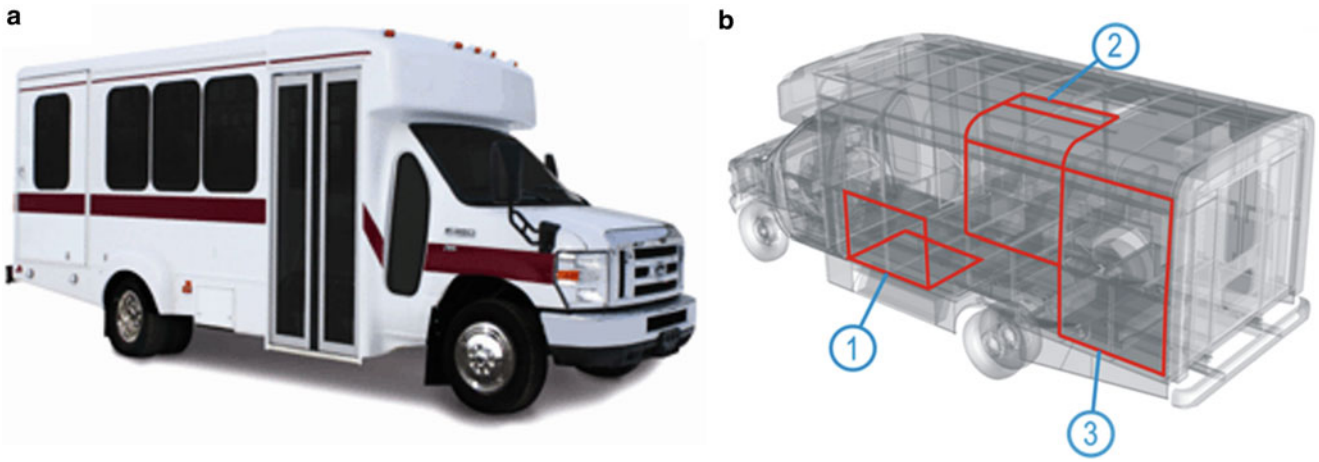

Fig. 23.3 (**a**) View of a typical cutaway bus (**b**) key structure components examined in the component testing program (1—wall to floor connection, 2—roof to wall connection, 3—sidewall)

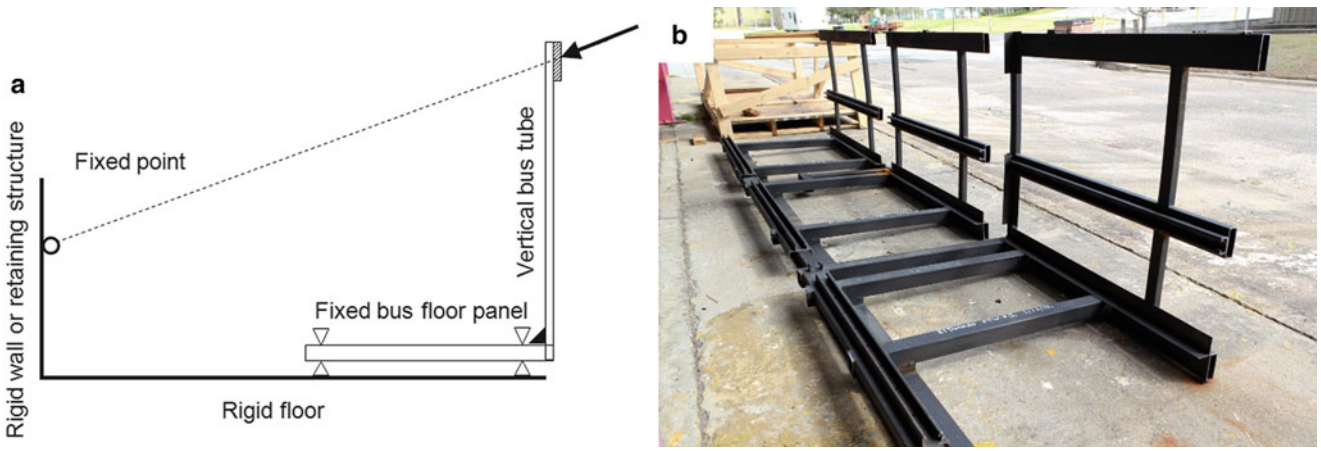

Fig. 23.4 (**a**) Schematic representation of the wall to floor connection, (**b**) connection samples prepared for testing

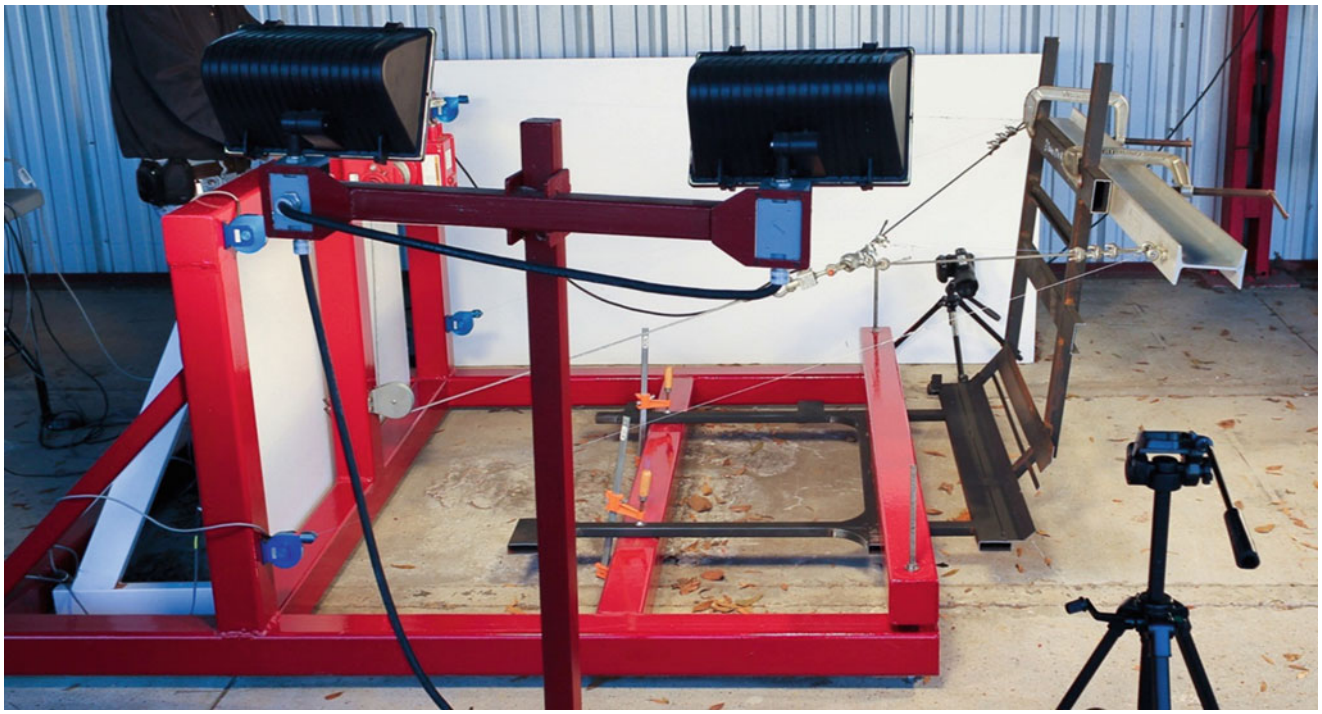

Fig. 23.5 Roof to wall connection test setup

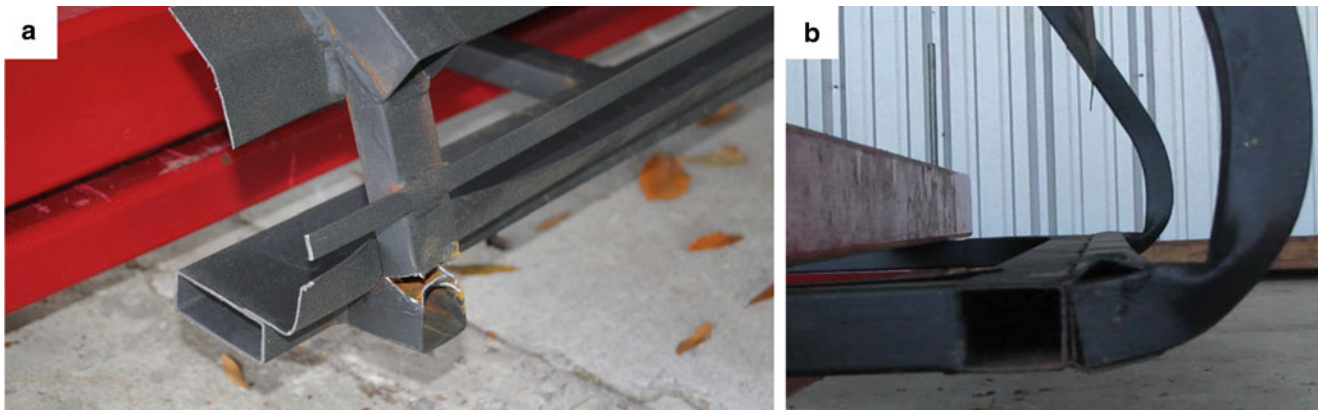

Fig. 23.6 Selected failure modes (**a**) wall to floor connection (**b**) roof to wall connection

The panel component test is the last test in the component testing section. The major objectives of the impact tests on panels are to check dynamic characteristics of plastic zones at the waistrail connection and to evaluate the amount of energy which can be absorbed by the bus outer skin. This data is also used to support validation and verification efforts for finite element models of the buses developed for computational mechanics studies. Experience shows that the waistrail connection, especially with a discontinuous pillar (divided by a continuous rail), can be very vulnerable during the rollover test. The dynamic performance of such flawed connection can be worse than static due to the notch effect generated at the welds. The sidewall panels are required to dissipate 600 J of energy per meter of panel length with less than 150 mm of residual deflection [5]. An actual testing apparatus with a placed specimen is shown in Fig. 23.7.

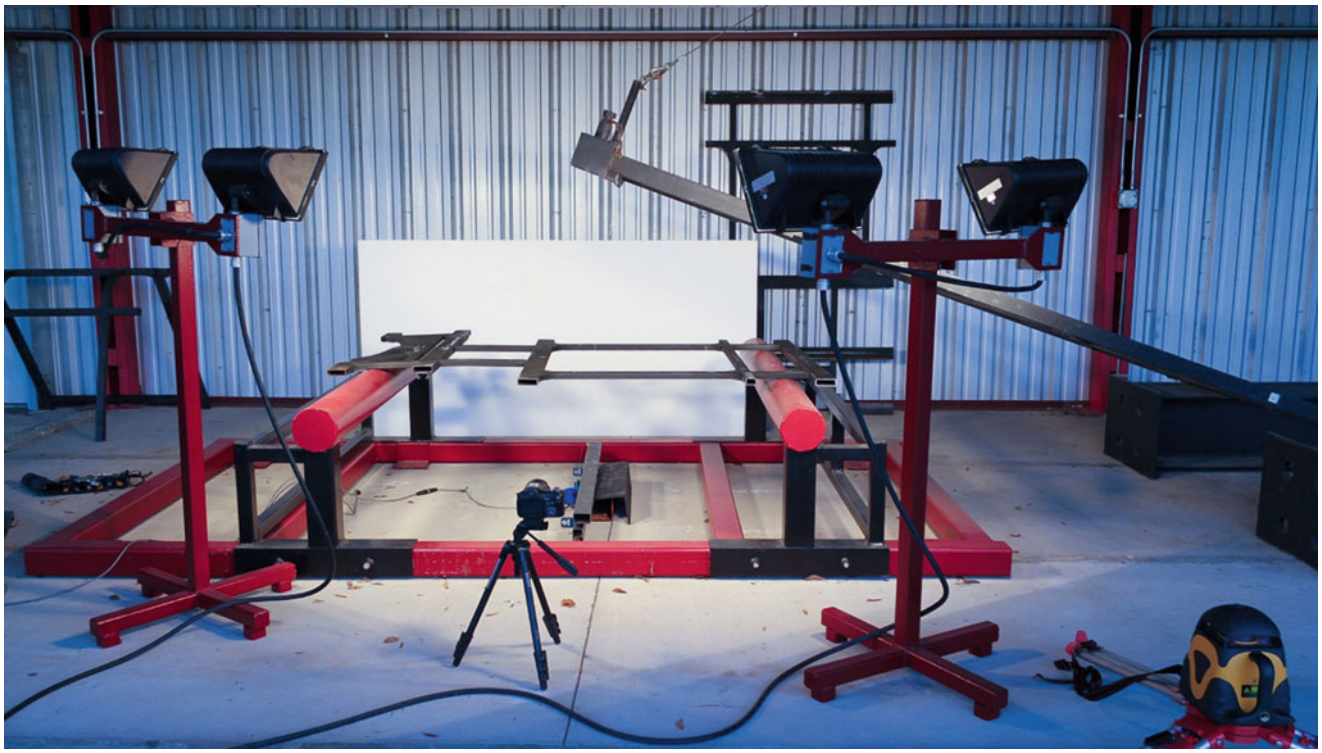

Fig. 23.7 Sidewall panel testing apparatus

23.4 Full Scale Testing

There are two major full scale tests performed by the Crashworthiness and Impact Analysis Laboratory. The first one is a rollover test where a cutaway bus is positioned on a specially designed tilt table and tilted until it falls freely onto a concrete slab 800 mm (31.5 in) below. The tested vehicle is equipped with a data acquisition system and additional load ballast dummies (75 kg each) to simulate the weight of passengers. Water ballasts are belted to the bus seats with seat belts. Additional ballasts are used to represent two disabled passengers seating in wheelchairs. During the test deformation of the sidewalls is measured using previously attached string transducers to examine the level of the passenger compartment deformation and to check for possible penetrations into the 'survival space' (a predefined space for which no intrusion is allowed [6]). The test setup is shown in Fig. 23.8, whereas Fig. 23.9 depicts bus deformation after the rollover.

The second full scale test is designed to evaluate the crashworthiness of the cutaway bus during a side impact scenario. The test setup is comprised of a stationary cutaway test bus struck on the driver's side with an impactor. The impactor consists of a crash bogie cart fitted with an IIHS deformable barrier in front. The impactor is suspended from two towers and is raised and swung into the bus in a pendulum motion. The impactor with its deformable barrier weighs a minimum of 4400 lbs. and has an impact velocity of 30 mph. The impactor strikes the bus orthogonally on the driver's side, which represents a tee bone accident of a bus impacted by a full size pickup. High speed cameras are placed around the bus to capture the test in detail. Figure 23.10 shows a screen capture from the experiment just after the moment of impact.

23.5 Computational Testing

All experimental tests are supported with detailed computational analyses using LS-DYNA, a non-linear Finite Element code. Finite Element models for each test are developed. Validation and verification of the models exhibit high level of their compliance with the actual experiments. An example of a Finite Element model from the wall panel component testing is shown in Fig. 23.11.

Fig. 23.8 Test setup for the full scale rollover test

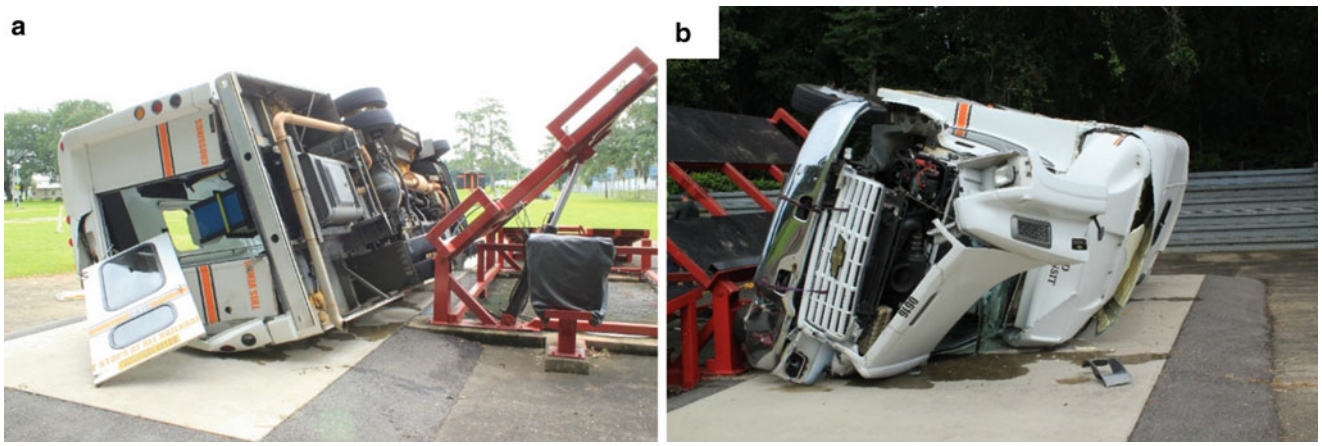

Fig. 23.9 (**a**) Rear view of the bus after the rollover test (**b**) front view of the bus after the rollover test

Complete Finite Element models of the cutaway buses were also developed. Detailed models are composed from more than one million elements. All models were validated and verified using experimental results from actual tests. Figure 23.12 shows one of the Finite Element models and its deformation after a computational rollover test.

Fig. 23.10 Frame capture from the side impact experiment

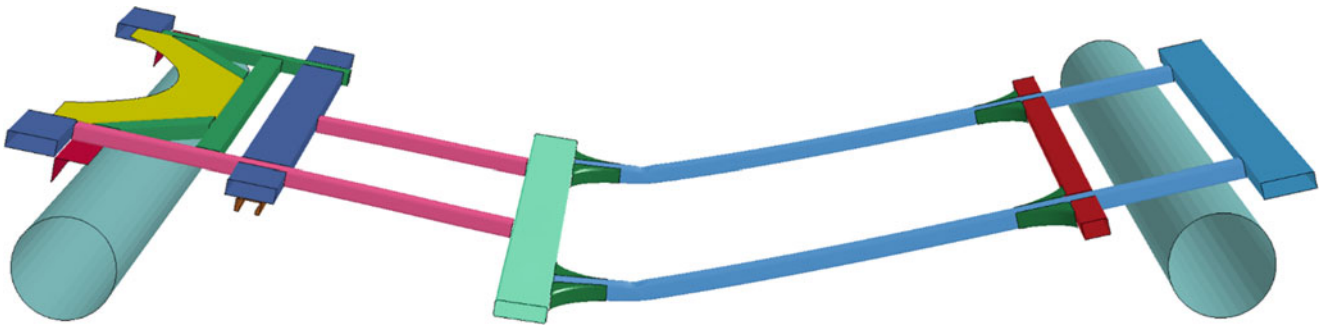

Fig. 23.11 Finite Element model of a wall panel after testing it in the wall panel component testing apparatus

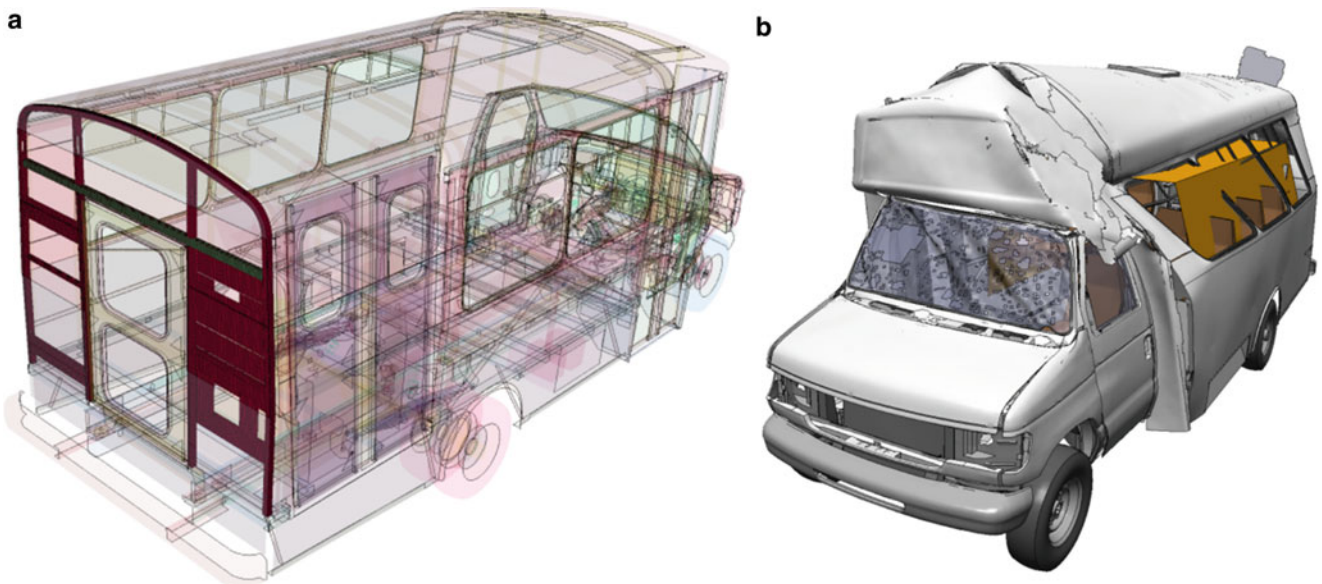

Fig. 23.12 (**a**) Finite Element model of the cutaway bus (**b**) deformation of the bus after a computational rollover test

23.6 Summary

The crashworthiness assessment program presented in this paper was well received by paratransit bus operators and cutaway bus industry. It resulted in strong commitment and collaboration with bus manufacturers. Several full scale rollovers were performed and multiple component tests are being carried out every year. The Crashworthiness and Impact Analysis Laboratory provides detailed reports and feedback to bus manufacturers and the Florida Department of Transportation which results in increasing safety of passengers travelling with this transportation mode.

References

1. C. Bojanowski, B. Gepner, L. Kwasniewski, C. Rawl, J. Wekezer, in *Roof Crush Resistance and Rollover Strength of a Paratransit Bus*, 8th European LS-DYNA Users Conference, (Strasbourg, 2011)
2. L. Kwasniewski, C. Bojanowski, J. Siervogel, J.W. Wekezer, K. Cichocki, Crash and safety assessment program for paratransit buses. Int. J. Impact Eng. **36**(2), 235–242 (2009)
3. C. Bojanowski, J.W. Wekezer, L. Kwasniewski, J. Kownacki, in *Florida Standard for Crashworthiness and Safety Evaluation of Paratransit Buses*, 21st International Technical Conference on the Enhanced Safety of Vehicles, US DOT NHTSA, Paper (No. 09-0299, pp. 15–18), (2009)
4. C. Bojanowski, Verification, validation and optimization of finite element model of bus structure for rollover test. Ph.D. dissertation, Florida State University, 2009
5. L. Kwasniewski, J.W. Wekezer, B. Gepner, J. Siervogel, *Development of Simplified Safety Assessment Procedure for Paratransit Buses* (CMM-2011—Computer Methods in Mechanics, Warsaw, Poland, 2011)
6. United Nations; Strength of the superstructure of large passenger vehicles. Regulation 66. Revision 1 (2006), http://www.unece.org/trans/main/wp29/wp29regs/r066r1e.pdf.

Chapter 24
In-Situ DIC and Strain Gauges to Isolate the Deficiencies in a Model for Indentation Including Anisotropic Plasticity

Jacob S. Merson, Michael B. Prime, Manuel L. Lovato, and Cheng Liu

Abstract A 60-mm diameter disk of 2024 aluminum was indented by opposing steel indenters over a central 10 mm region. Residual stress measurements made using neutron diffraction and the contour method matched each other, but not a finite element (FE) model with a calibrated model for plastic anisotropy of the aluminum. Since residual stresses are only the endpoint of the process, *in situ* data was needed to determine which portion of the load/unload process was causing model deficiencies. The indentation process was repeated on a new specimen with three-dimensional Digital Image Correlation (3D-DIC) to map full-field strain information and with resistance strain gauges to obtain high fidelity strain information at discrete locations. The DIC data was too noisy to extract strains, so displacements were analyzed after rigid body motion was removed. The deformation field revealed geometric imperfections of the indenters that were within tolerance, but had significant effect on the stress state. An updated FE model including geometric imperfections in the indenters gave better agreement with the DIC data. It did not however allow the material model to become the dominant effect and thus model calibration was unsuccessful.

Keywords Residual stress • Digital image correlation • Plastic anisotropy • Finite element model • Strain gauges

24.1 Introduction

Residual stresses play a significant role in many material failure processes like fatigue, fracture, fretting fatigue, and stress corrosion cracking [1–3]. Residual stresses are the stresses present in a part free from external load, and they are generated by virtually any manufacturing process. Because of their important contribution to failure and their almost universal presence, knowledge of residual stress is crucial for prediction of the life of any engineering structure. However, the prediction of residual stresses is a very complex problem. In fact, the development of residual stress generally involves nonlinear material behavior, phase transformation, coupled mechanical and thermal problems and also heterogeneous mechanical properties [4–15].

This paper discusses *in situ* data collection to improve a process model used to predict residual stresses. It shows how the use of different measurement techniques and multiple channels of data can help improve problem understanding.

24.2 Backstory

To provide specimens for development and validation of techniques for residual stress measurement, solid disks were indented plastically by opposing, hardened-steel indenters, see Fig. 24.1, a process occasionally used to introduce residual stresses for testing purposes [16]. A first set of specimens had 316 L stainless steel as the disk material and the residual stresses were measured using neutron diffraction and the contour method [17, 18]. An early finite element (FE) model, which used a calibrated stress-strain curve but assumed isotropic hardening, did not match the measurements very well [19]. Further testing of the 316 L steel revealed a modest Bauschinger effect in cyclic stress-strain data. After calibrating a combined hardening model to the cyclic data, the FE model was able to match the measured stresses quite well [17].

Additional specimens were later made with the same indentation process but using 60-mm diameter, 10-mm thick disks of 2024-T351 Aluminum [20]. Based on the experience with 316 L steel, a combined hardening model was calibrated on

J.S. Merson • M.B. Prime (✉) • M.L. Lovato • C. Liu
Los Alamos National Laboratory, P.O. Box 1663, Los Alamos, NM 87545, USA
e-mail: prime@lanl.gov

S. Bossuyt et al. (eds.), *Residual Stress, Thermomechanics & Infrared Imaging, Hybrid Techniques and Inverse Problems, Volume 9*, Conference Proceedings of the Society for Experimental Mechanics Series, DOI 10.1007/978-3-319-21765-9_24

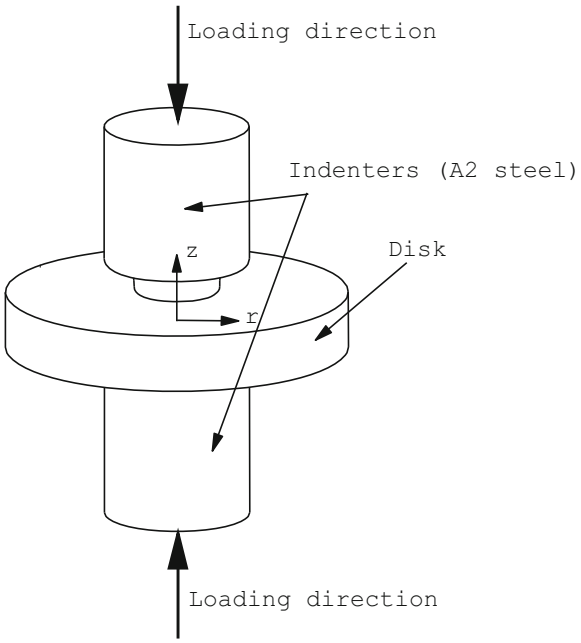

Fig. 24.1 Indented disk residual stress specimens were made using 2024-T351 Aluminum disks

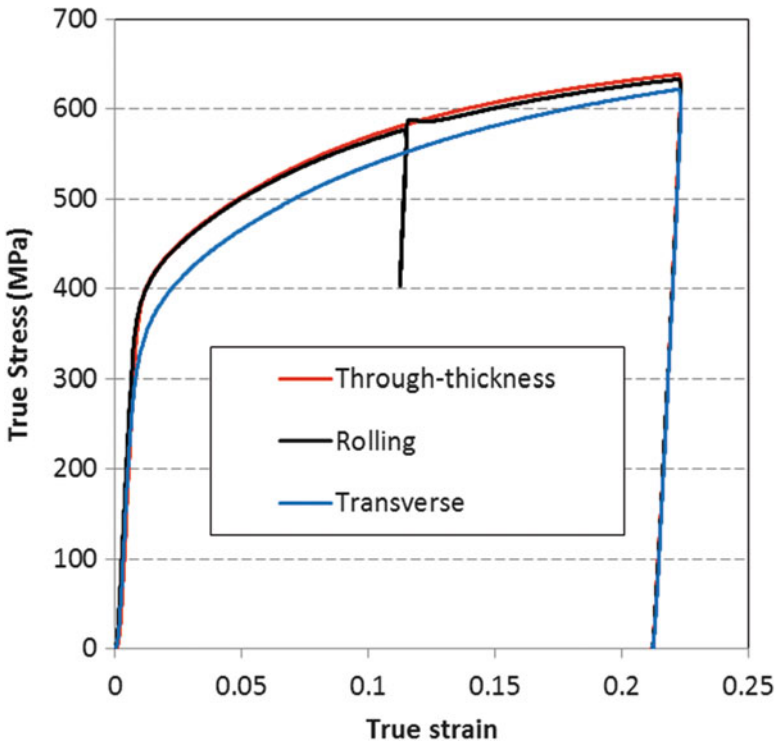

Fig. 24.2 Mild plastic anisotropy in stress-strain curves for 2024 Aluminum

cyclic data, but the resulting FE model did not agree very well with measured residual stresses and strains. Further testing revealed that the 2024 Aluminum was mildly plastically anisotropic, see Fig. 24.2, with lower strength in the in-plane direction transverse to the rolling direction of the original plate material, and higher but equal strength in the other two directions. An anisotropic plasticity model was calibrated to the data in Fig. 24.2 and used to model the indentation. Figure 24.3 shows that neutron diffraction measurements were made along orthogonal paths along the rolling and transverse directions in the disk. Figure 24.4 shows residual hoop stresses along those two measurement scans (note that unplotted contour method [21] and slitting method [22] measurements validate the neutron results [20, 19]). Switching to the anisotropic plasticity model significantly improved the model prediction, which now matches the difference in the residual stresses along the two measurement directions, but the predictions are still off of the data by about 50 MPa.

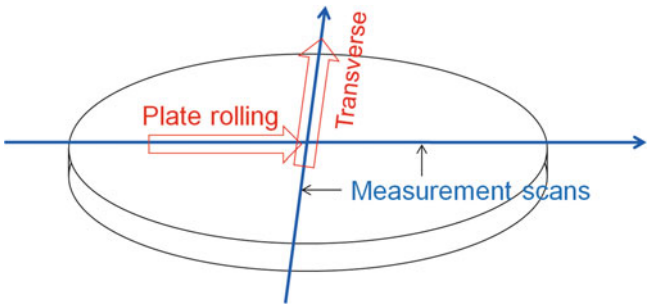

Fig. 24.3 Neutron diffraction scans were made along two orthogonal directions

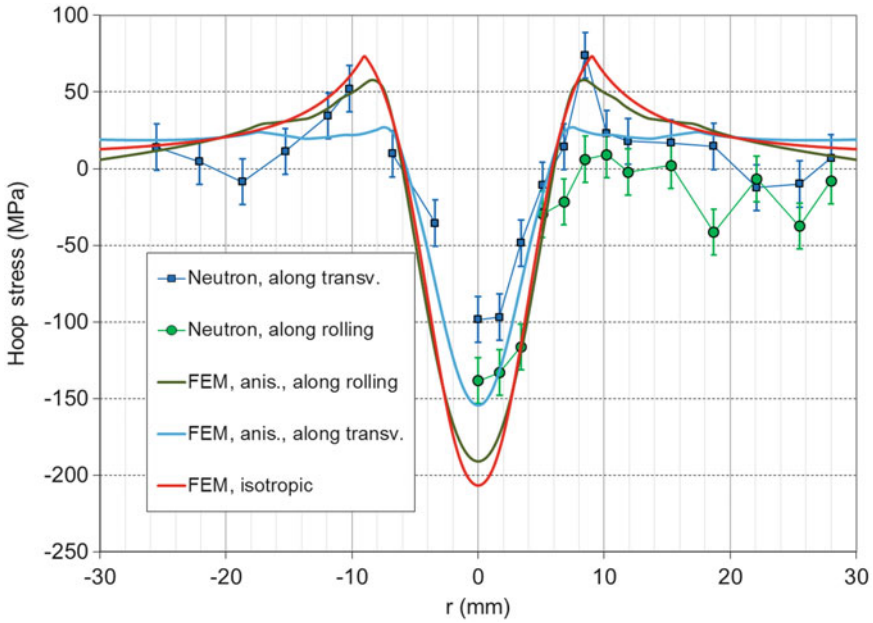

Fig. 24.4 Even the anisotropic plasticity model does not agree well with the neutron measurements

24.3 Purpose

The work in this paper aims to improve the FE model prediction shown in Fig. 24.4. Several possible issues with the model have been discounted based on previous work:

- The anisotropic constitutive model already matches uniaxial compression data in all three material directions.
- Calculational studies have demonstrated that the Bauschinger effect in 2024 Aluminum, measured in uniaxial cyclic testing, does not seem to have any effect on the prediction.
- Since there is significant hydrostatic compression under the indenter, a model for pressure-dependent plasticity in 2024 Aluminum [23] was implemented, and also shown to not significantly improve the model prediction [24].

The current data on these disks, mostly residual stresses and strains, only give information about the end state of the indentation process. End state data is insufficient to identify when during the process the model is deficient. The approach in this work, therefore, is to identify the deficiencies in the model by taking *in situ* data throughout the loading and unloading process of indentation in order to hopefully identify where the model has gone wrong and then fix it.

Fortunate, because modeling combined hardening simultaneously with anisotropic plasticity is quite limited using only the built-in functionality in the Abaqus commercial finite element code.

24.4 Methods

24.4.1 Experimental

The opposed indentation test sketched in Fig. 24.1 was conducted with a 2024-T351 aluminum disk in an MTS 1125 load frame. The overall setup is shown in Fig. 24.5. The indenters were coated in Molicote lubricant to reduce friction. Two PMMA rings were used to center the indenters on the disk. To accommodate DIC measurements, the top centering ring was removed before loading the sample. The crosshead was moved at 0.14 mm/min to reach a maximum load of 99.5 kN in about 10 min. Once maximum loading was achieved, the crosshead was reversed until the disk was completely unloaded.

Strain gauges were used on one face of the disk, and the locations of strain gauges were optimized to be most sensitive to material modeling. A finite element model was run with several variations on the anisotropic material model for Al 2024. The predicted strain output at many locations was compared for the various material models to see where the differences were most significant. Based on the simulations, strain gauges were placed at five discrete locations shown in Fig. 24.6. Three locations used stacked gauges to measure both hope and radial strain and the two other locations measured radial strain, for 8 total channels of strain. Most of the gauges were along either the plate rolling or transverse directions, with some 10 mm from the center and others at 15 mm, and one gauge was at 45° to these axes in accordance with [24]. Strain was recorded at a sampling frequency of 1 Hz. The 8 strain gauges were calibrated, and the data was collected with two Vishay model P3 Strain Indicator and Recorders.

In order to get a full field deformation map an optical technique called three-dimensional digital image correlation (3D-DIC) was used. DIC uses a computer vision approach to get a deformation field by comparing a set of before and after pictures. To capture the *in situ* strain field a series of images are taken and compared to the initial image. In order to capture out of plane motion a stereoscopic two camera system is used. A more detailed description of the DIC technique can be found in literature e.g. [26]. To measure the strain field the internal camera parameters must be calibrated. These parameters include the focal length, image center, distortions, skew, etc. Also, the relative positions and orientations of the cameras must be known for triangulation. Calibration allows calculation allows calculation of parameters such as accuracy, uncertainty, and sensitivity.

To use 3D-DIC a speckle pattern must be added onto the surface of the disk. Black spray paint was used to create the speckles directly on the aluminum surface, see Fig. 24.7. The thickness of these speckles is on the order of 1 μm. Since the black highly contrasted with the aluminum color, no background painting was necessary. In this experiment, the central 15 mm and far half of the aluminum disk are hidden from view by the indenter and load frame during the indentation.

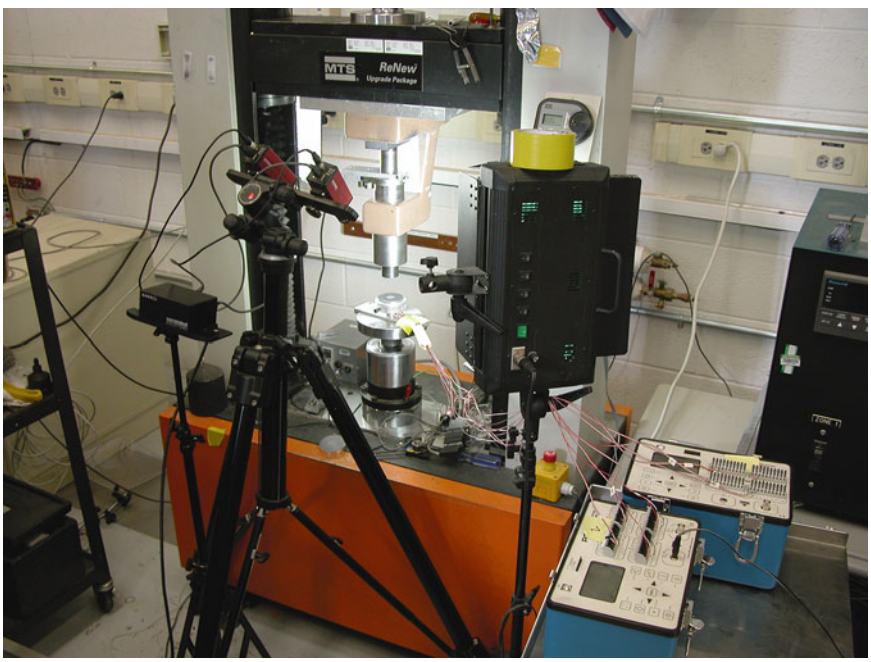

Fig. 24.5 Experimental setup prior to inserting the top indenter

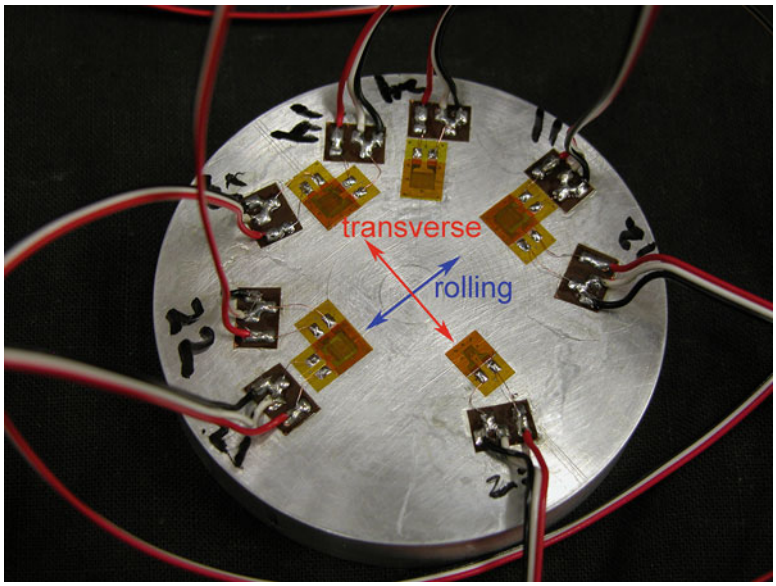

Fig. 24.6 A total of 8 resistance strain gauges were used to measure hoop and radial strain in multiple directions

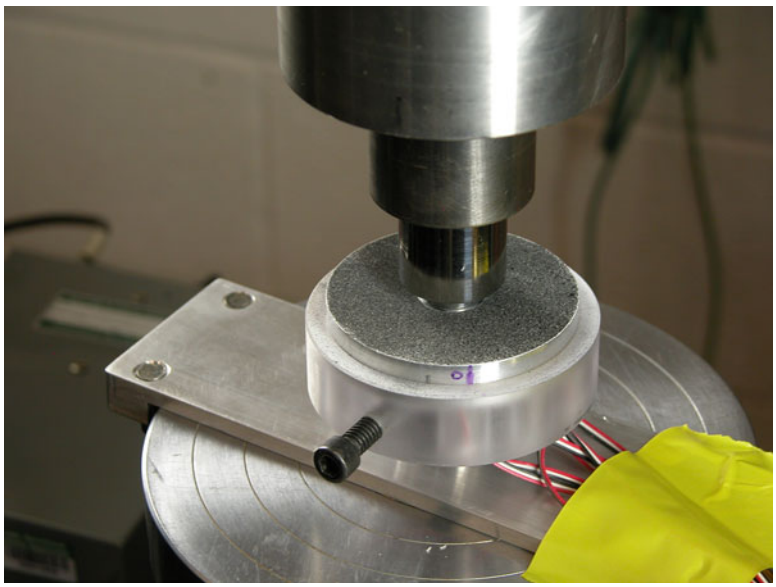

Fig. 24.7 The disk specimen shown during the indentation test. The DIC speckle pattern is visible on the top face of the disk

However, pictures taken before and after the test allowed the final deformation to be determined over the full 360° disk surface minus the central 15 mm where the indenter had contacted the disk. During the indentation process DIC images were recorded at a frequency of 0.5 Hz.

Quantitative investigations regarding the confidence margins and errors in experimental measurements using DIC, both 2D and 3D, have been carried out in recent years [27–29]. One detailed investigation found a resolution in determining the in-plane motion within 0.006 pixels and the resulting variability for in-plane strain in the range of 20–90 με [28]. However, there are many factors that will affect the resolution and accuracy of DIC measurement, and the more significant uncertainty comes from the calibration of the 3D-DIC system. In our particular system, the calibration process indicates the uncertainty is less than 0.05 pixels. With spatial resolution of 45.5 μm/pixel, we expect the uncertainty in the in-plane displacement measurement to be about 2.3 μm and out-of-plane displacement measurement to be about 4.5 μm, which is twice of that in-plane uncertainty [27]. Scaling up from the reported results for 0.006 pixel resolution [28] to our value of 0.05 pixels, we estimate strain variability in the range 170–750 με.

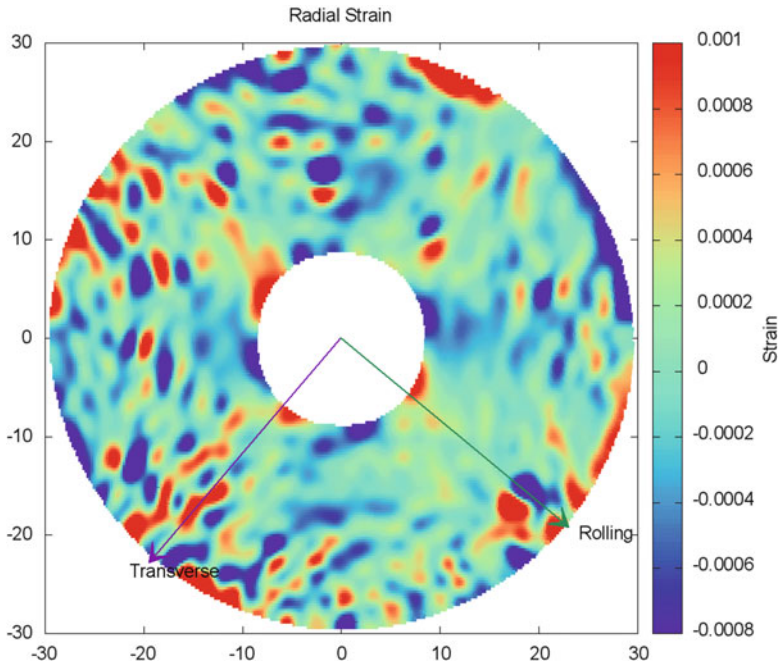

Fig. 24.8 A plot of radial strain from the DIC shows that the strain is low and, therefore, too noisy to be helpful

LED lights are used to provide sufficient light on the testing specimen for DIC measurements. The load cell and the DIC cameras use a synchronized clock and the clock on the strain gauge data is matched using a manual timing synchronization (e.g. strain gauges started at $t=0$s, loading starts at $t=30$s) and this is confirmed by matching the time of peak loading.

Due to the relatively low deformations because of the highly constrained nature of the loading conditions, the strains measured with DIC were very noisy and were not very informative, see Fig. 24.8. Therefore, displacements were used for comparing with the finite element model. To compare displacements, rigid body motion in the DIC of the part was calculated using a least squares fit of Q and b in (24.1).

$$Y = QX + b \tag{24.1}$$

Where Y is the position vector (e.g. $Y=(x+u,\ \ y+v,\ \ z+w)$), Q is a third order orthogonal (rotation) tensor, X is the original position of each point, and b is the translation vector. From the DIC outputs, Y and X are known. Therefore, the displacement with no rigid body motion U can be written as (24.2).

$$U = Y(Qx + b) \tag{24.2}$$

These rigid body motions were subtracted from the deformation field, and a transformation into a cylindrical coordinate system was done for visual inspection of the deformation field. This inspection gave a good comparison of the deformation field to the finite element model.

Considering that the loading was nominally axisymmetric but that the aluminum was anisotropic as shown in Fig. 24.2, the deformation field was expected to be different in the rolling and transverse directions but symmetric about those two axes. Instead the deformation was asymmetric, as is shown later in Fig. 24.12, with the transverse-direction deformations notably greater on one side of the indenter than the other. This asymmetry indicated that the loading was not as axisymmetric as intended.

In order to investigate and quantify this asymmetry the indenters and disk indentations were inspected using a coordinate measuring machine (CMM). Figure 24.9 shows the results for the bottom surface of the disk. Using least squares fit of a plane on the bottom of the indent, a tilt of 0.064° was estimated, which translates to about 15 μm of tilt over a 15 mm diameter, or about 60 % of the average indent depth. This is within the specified machining tolerances of the indenters, but is significant relative to the assumption of axisymmetric loading. The indent on the top surface of the disk, the surface measured by DIC in Fig. 24.7, was tilted by about 0.019° relative to the surface of the disk, corresponding to about 5 μm of tilt or 20 % of the indent depth. On both the top and bottom surfaces, the low point of the indentation

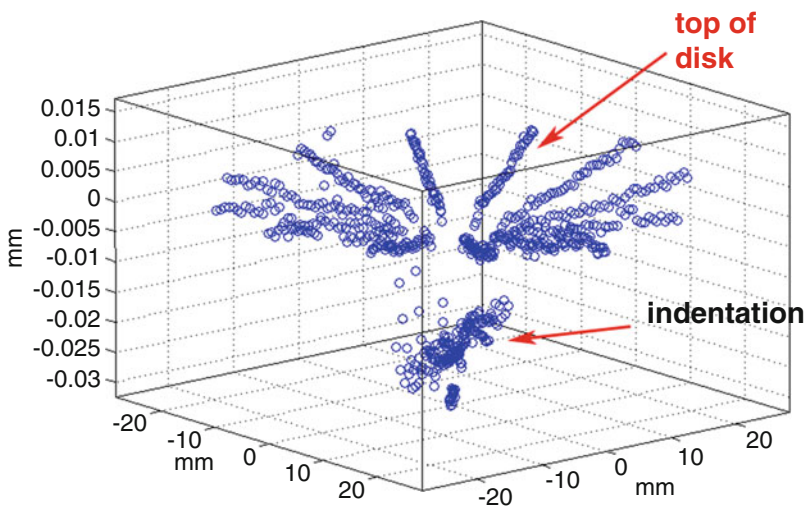

Fig. 24.9 CMM inspection data on the bottom of the indented disk. The data is plotted such that the top of the surface is approximately flat at a height of 0. The bottom of the indent is tilted

Table 24.1 Number of elements in rough and fine meshes used in finite element calculations

Part	Elements in rough mesh	Elements in fine mesh
Top indenter	384	4032
Bottom indenter	384	3976
Disk	7794	70,686
Total	8562	78,694

aligned with neither the rolling or transverse axis but was rather between the two. Inspection of the two indenters revealed that the indentation surfaces were tilted 0.033 and 0.008° relative to the opposite surface if the indenter, but the precision of the alignment of the platens on the load frame is not known, so it is not clear what angle the indenter actually makes with the disk surface. Indenter tilt turns out to be an important factor which must be accounted for in the finite element models.

24.4.2 Finite Element Modeling

The disk indentation process was modeled as a quasi-static process in Abaqus/Standard finite element code. All models were assumed to have nonlinear geometries. In previous work, the model progressed from a 2D axisymmetric model [19], which could only look at isotropic material behavior, to a 1/8th symmetry 3D finite element model in order to model material anisotropy. Based on DIC and inspection results (e.g., Fig. 24.9), a 1/8th symmetry model was no longer adequate so a full 3D model which accounted for indenter tilt and in-plane angle (where the low point of the indenter was aligned) was created. Table 24.1 shows the number of 20 noded reduced integration elements (C3D30R) used in the rough and fine meshes. The rough mesh, shown in Fig. 24.10, was used for most of the calculations in this paper as the difference in the strain and contour outputs was negligible. The mesh in the contact zone was selected to be fine enough to help reduce local perturbations at the edge of the contact region.

Determining the boundary conditions for problem was challenging. A displacement condition was used to apply the load on the indenters, and the displacement value was adjusted so the total load matched the experiment (99.5 kN). The indenter had rotation about its own axis constrained as we assume the friction between the platen and indenter is strong enough to oppose rotation. The disk was constrained so it couldn't rotate out of plane because unconstrained models predicted such a rotation (Fig. 24.11) and failed to match observed indentation patterns. We believe that the PMMA fixture used to align the indenter and disks provided sufficient constraint to prevent such rotation.

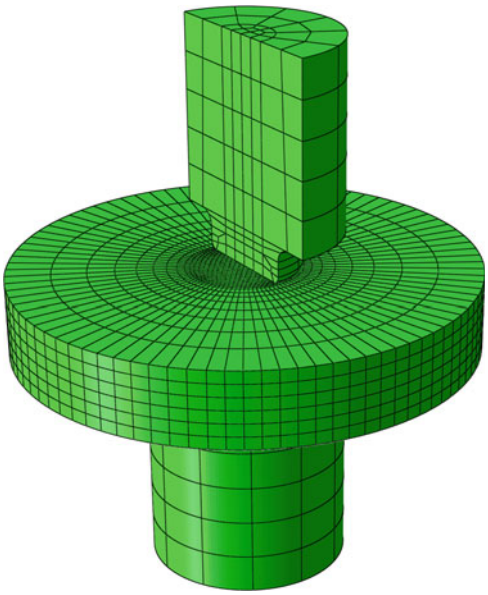

Fig. 24.10 The mesh for the indentation process model is most refined in the indentation region where the largest gradients occur. In this graphic, half of the upper indenter is removed to expose the underlying mesh

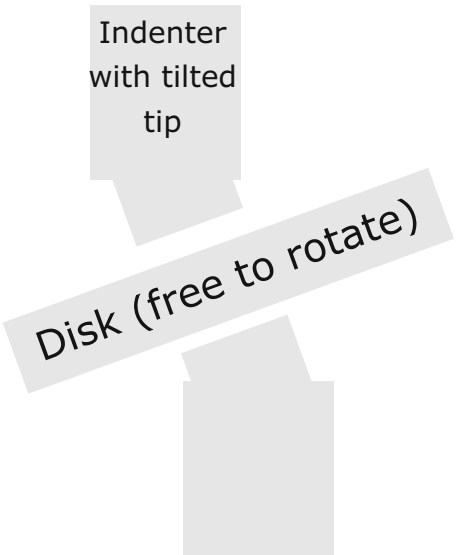

Fig. 24.11 Unconstrained models allowed a disk rotation that was not observed experimentally. Hence, constraints were added to the model

Correctly modeling the contact also presented a challenge. Abaqus surface to surface contact was used with a stabilization factor of one, and end of step stabilization factor of 0.1. These stabilization values were chosen to maximize solution speed while keeping the associated dissipative energies below 1 % of the total system energy.

24.4.3 Material Models

The material modeling was similar to previous efforts to model this indentation process [24]. The indenter material used was A2 tool steel characterized by a high hardness (58 HRC) and a high yield stress (about 1300 MPa), so the indenter was modeled as elastic with Young's modulus of 204 GPa and Poisson's ratio of 0.3. For the Al 2024, the Young's modulus was 73.2 GPa and Poisson's ratio was 0.33. As discussed previously, an anisotropic plasticity model using isotropic

hardening (no Bauschinger effect) was used. Plastic anisotropy was modeled using Hill's potential function [24] in ABAQUS. Because the conversion of uniaxial stress-strain curves to effective-stress—effective-strain curves depends on the *R* ratios, the ratios between the strengths in different directions, an iterative process was used to fit the *R* ratios to the data [24]. This fit was applied in ABAQUS using the *POTENTIAL function to define the anisotropy and a tabular description of the stress-strain curve.

24.5 Results and Discussion

The finite element model was able to reasonably reproduce the tilt in the bottom of the indentation (e.g., Fig. 24.9) measured by the CMM. The model predicted a tilt of 0.055˚ on the bottom indent compared to the measured value of 0.064˚, and the predicted tilt on the top surface was 0.022˚ compared to the measured value of 0.019˚, so both within 16 % of experiment. Because the alignment of the platens in the load frame is uncertain, it would be reasonable to iterate on the initial indenter tilt until even better agreement was achieved. However, the current level of agreement is sufficient to evaluate the effects on indenter tilt on predictions of deformation and strain.

Figure 24.12 shows the radial deformation field at the end of the indentation and unloading process measured by 3D-DIC, after removal of rigid body motions. Visually inspecting the deformation field shows that the areas of maximum radial deformation are asymmetric, being greater on one side (upper right quadrant of Fig. 24.12) than the opposite side. This key observation led to the inescapable conclusion that the load was asymmetric, which led to geometry quantification using CMM measurements, and then model refinement. Figure 24.13 shows that the finite element model including indenter tilt predicts a similar asymmetry in the deformation field.

It was challenging to get useable DIC data since the strains resulting from indentation were very small. Practical use of DIC data required analysis of the deformations and thus removal of the rigid body motion. The process used to remove rigid body motion from the before and after picture with full disk visibility did not work on the *in situ* measurements when only half of the disk was visible. For the *in situ* deformation field, further work must be done to remove the rigid body motions so that the results can be compared with FEM.

We now present comparisons of the FE model to representative strain gauge data. The title of each plot identifies which strain gauge from Fig. 24.6 is shown using three identifiers in order at the end of the plot title:

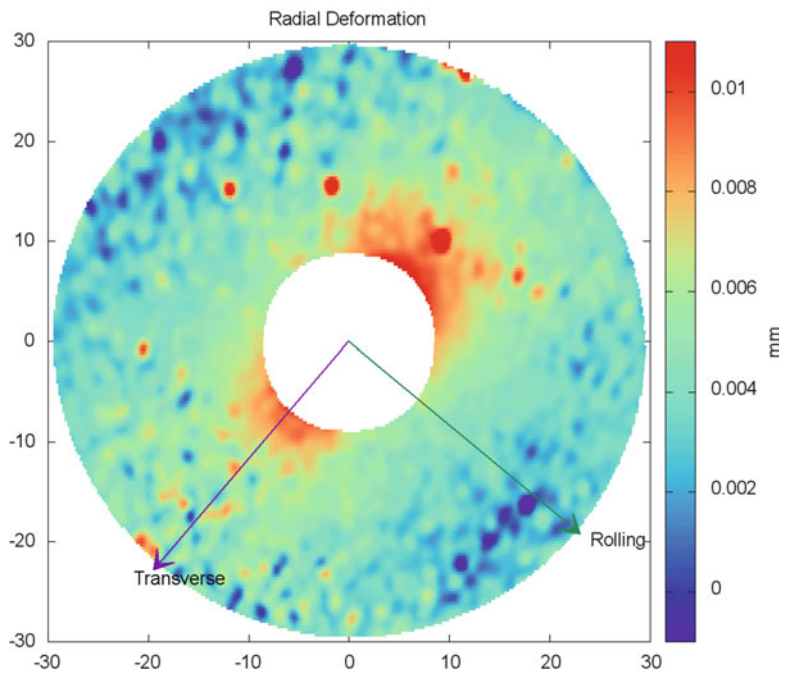

Fig. 24.12 Radial deformation field from DIC results. Note that the asymmetry around the indent helped to diagnose the tilt in the indenter

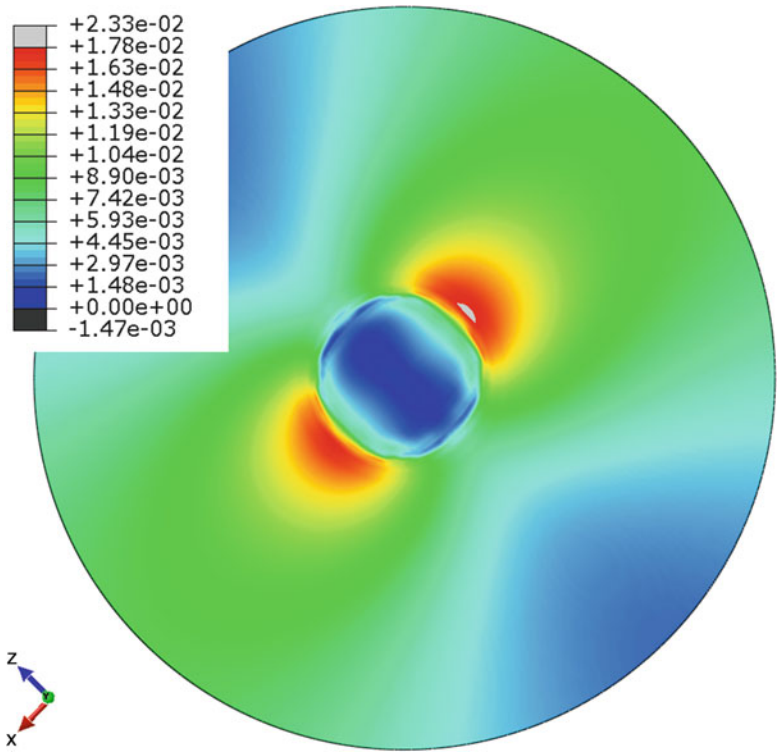

Fig. 24.13 Contour Plot of radial deformation (in mm) from finite element model. Here the transverse axis is pointing down. Note asymmetry in the deformation field around the indentation

- The radial distance from the center of the disk to the strain gauge center, either 10 or 15 mm
- The *location* of the gauge, either rolling axis (along the blue line in Fig. 24.6), transverse (red line in Fig. 24.6) or 45°.
- The component of strain being measured, either hoop or radial.

The comparisons will also show two variations on the anisotropic plasticity model. "Anisotropic plasticity 1" was an earlier rough version of the model, with slightly greater strength and anisotropy than version 2, which better matched the calibration data. For the case of anisotropic model 2, predictions are presented with and without indenter tilt. For an isotropic plasticity model, and anisotropic model 1, results are only presented for a flat (untilted) indenter.

To aid interpretation of the strain plots, one should first understand the basic deformation modes [17]. During indentation, the material under the indenter is compressed thinner and therefore wants to expand radially. The material radially outside the indenter (where the strain gauges are) then deforms like a ring under internal pressure: compression in the radial direction and tension in the hoop direction.

Figures 24.14 and 24.15 show the only load-strain curves where adding the indenter tilt made a notable improvement to the prediction, and even there the improvement is debatable. These are the two radial strain measurements closer to the indenter ($r = 10$ mm), and they show an unusual shape. Unlike all the other curves, these two have a change in the sign of the slope during loading, and unlike we just described in the previous paragraph, these radial strain start out positive. Near but outside the indenter region, the surface material of the disk is pulled axially towards the disk mid thickness, which stretches that material into tension. Later, the aforementioned radial expansion of the material under the indenter begins to dominate and turn the trains towards compression. Adding the indenter tilt has improved the model prediction near the peak load, although in the case of Fig. 24.14, all of the models do a poor job of predicting the data.

Both of those figures, along with Fig. 24.16 and others show that adding the indenter tilt predicts a significant nonlinear transient at early loads. The data generally shows linear elastic behavior, especially all the data taken at $r = 15$ mm. At this time, the reason for the discrepancy is not fully understood, but it is striking. It appears to be a geometric nonlinearity before there is any yielding, and may have something to do with the contact numerics.

The tilted-indenter model also did not significantly change the residual stress prediction of Fig. 24.4, which was the main purpose of this effort. Therefore, the effort to model the indenter tilt and related geometric issues may have been an unproductive effort—a red herring. Adding indenter tilt did improve comparison with two sets of data: the DIC deformations and the CMM-measured shapes of the indentations. Adding the tilt generally made the strain predictions worse. Adding the tilt did not change the most important comparison with data: the residual stresses. Overall, the tilted indenter model gave a very mixed result with better agreement on only two out of four measures.

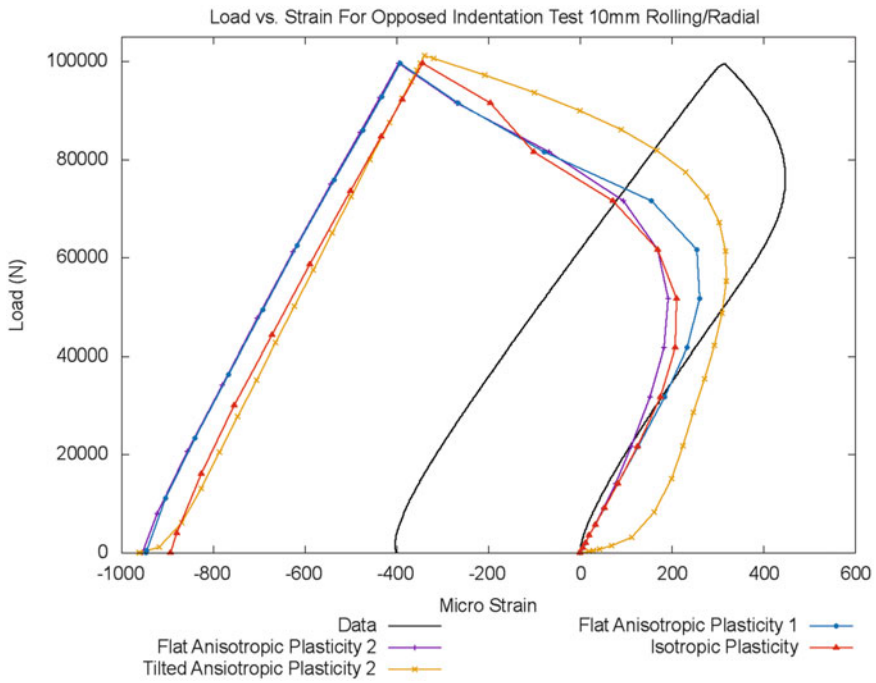

Fig. 24.14 Load vs. strain curve at 10 mm on the rolling axis in the radial direction

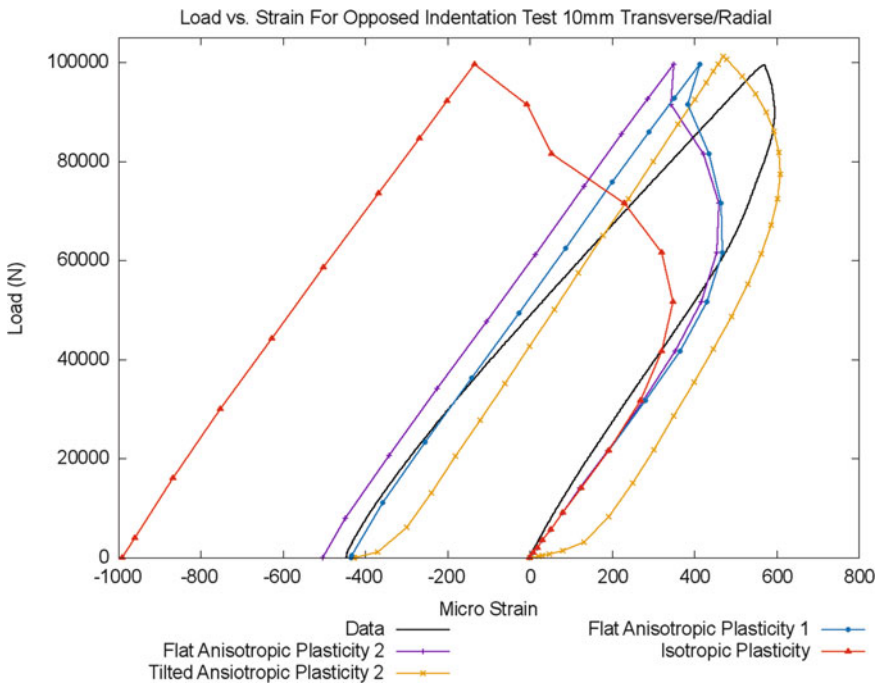

Fig. 24.15 Load vs. strain curve at 10 mm on the transverse axis in the radial direction

Figures 24.15 and 24.16 show that changing from an isotropic plasticity model to either of the anisotropic models has significantly improved the prediction, which is encouraging. In a few cases, like Fig. 24.14, there is no noticeable improvement from an anisotropic model although it is also no worse.

Some of the strain data is also quite sensitive to the variations in the material model. To see this compare the untilted (flat) predictions of the two anisotropic models. In some cases, like Fig. 24.17 and Fig. 24.18, anisotropic model 1, gives a noticeably superior prediction. In other cases, like Fig. 24.16, model 2 is superior and in others, like Fig. 24.19, none of the models predict the data well.

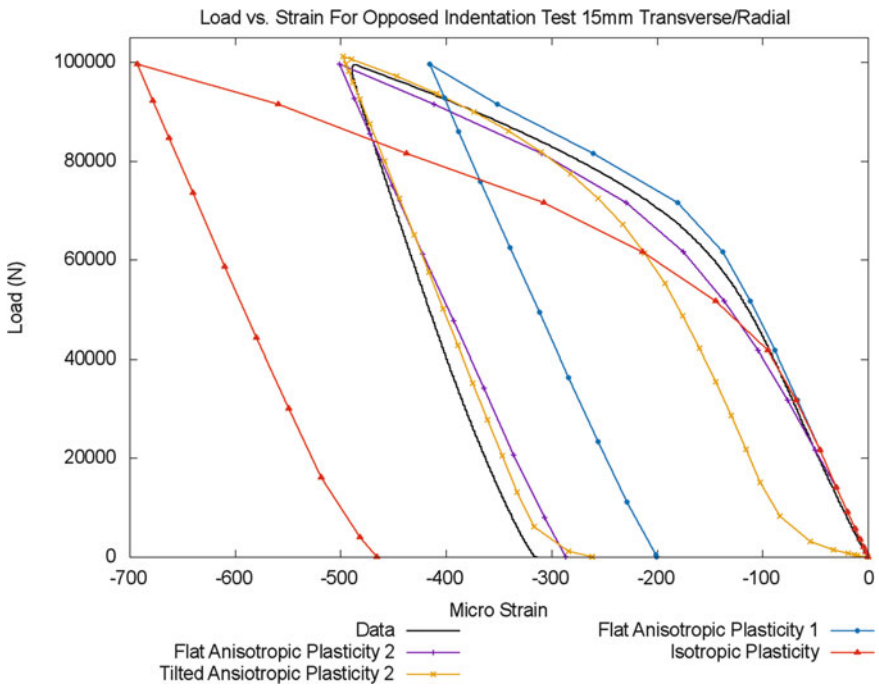

Fig. 24.16 Load vs. strain curve at 15 mm on the transverse axis in the radial direction

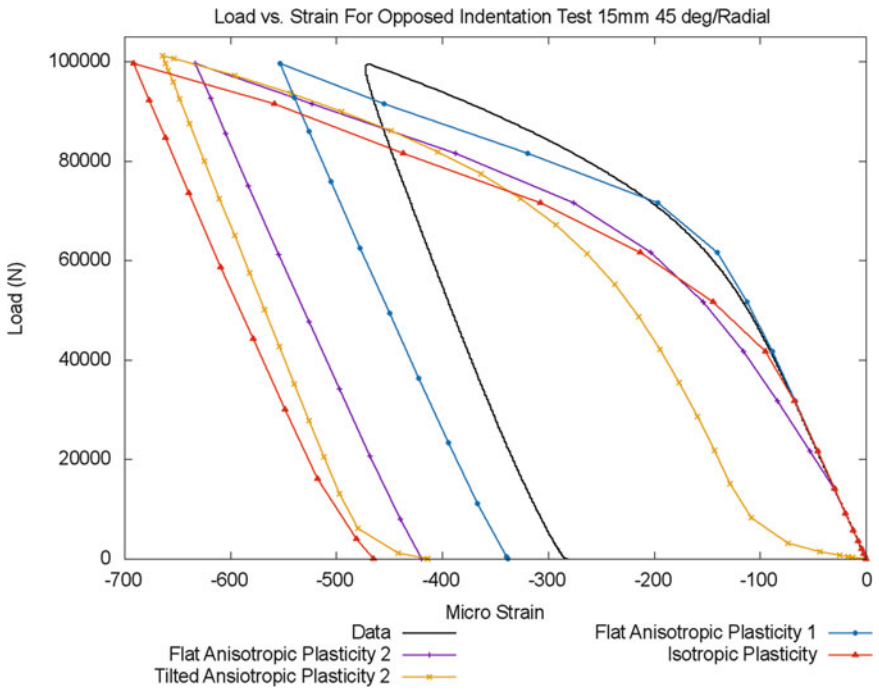

Fig. 24.17 Load vs. strain curve at 15 mm on the 45° axis in the radial direction

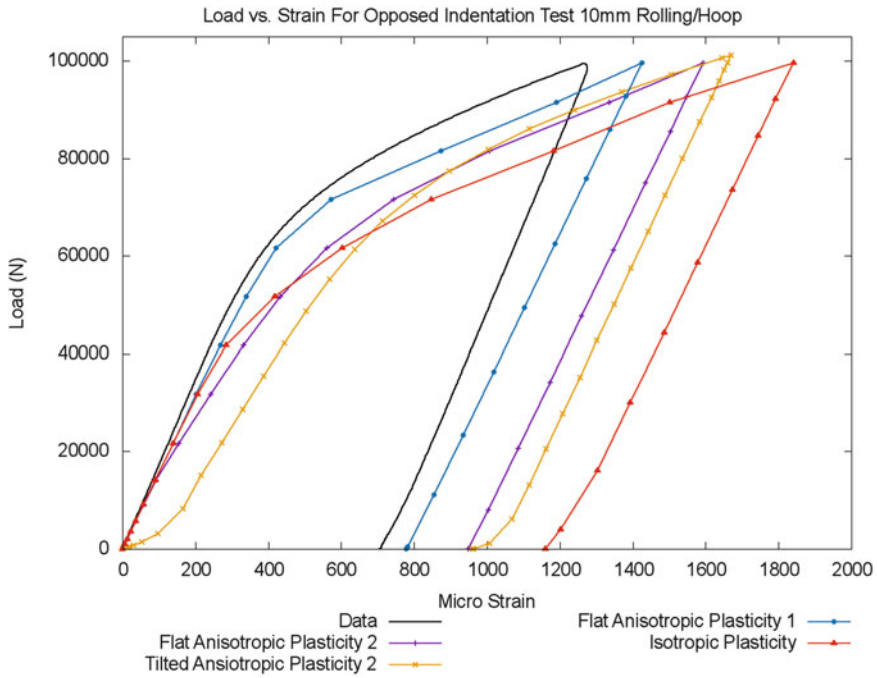

Fig. 24.18 Load vs. strain curve at 10 mm on the rolling axis in the hoop direction

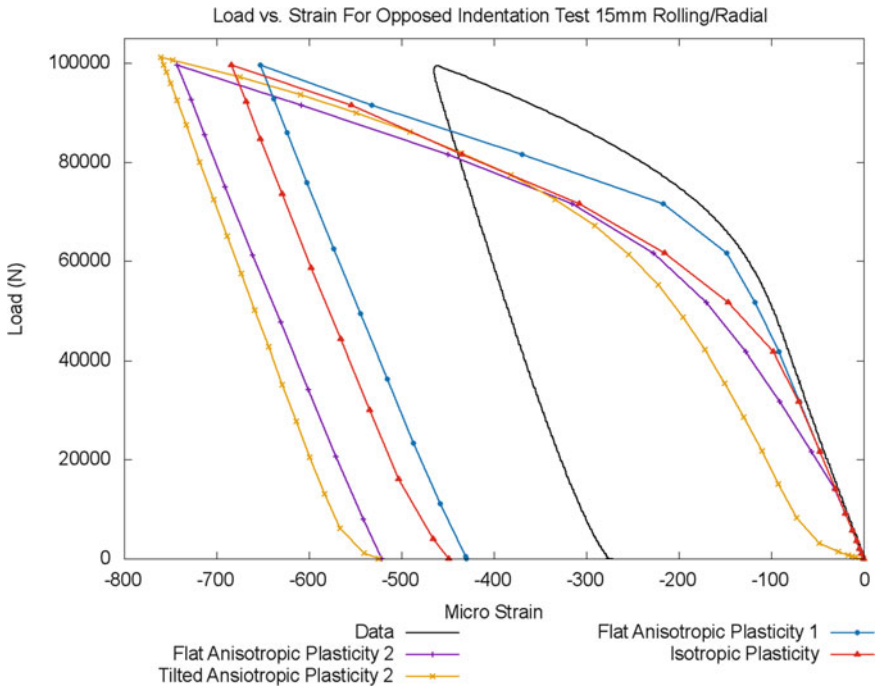

Fig. 24.19 Load vs. strain curve at 15 mm on the rolling axis in the radial direction

The inability of the titled indenter model to match more of the data was disappointing and led to further investigation. The previous CMM data had been collected independently on each face of the disk. More CMM data was collected but on both faces simultaneously. It was determined that the disk faces were tilted 0.024° in relation to each other, which is significant relative to the indentation tilts measured relative to each face (0.064 and 0.019°). These face tilts could have a significant impact on the measured strain field because it will affect the loading alignment with the tilted indenters. However, we do not expect that changing only that issue in the models would results in a wholesale improvement of the prediction.

In this indentation process the hydrostatic loading conditions (stiff indenter on a stiff disk with deformation constrained in all three directions under the indenter) lead to high sensitivity to small geometric changes. The strain gauges are able to capture these changes with high sensitivity. The full-field DIC data is able to capture global physics; however in comparison to the strain gauges it has limited sensitivity.

One important aspect of this work is the use of multiple types and locations of data to create a unique inverse problem. This is important because it allows confidence that when agreement is found all of the underlying physical phenomenon have been captured. In this case, we have not achieved satisfactory agreement.

24.6 Conclusions

In this paper the use of multimodal data allowed a much deeper understanding of the problem physics at hand:

- Only the *full field data* from 3D-DIC was able to identify the key geometric issues (tilting) in the indenters. This would not have been discovered through the strain gauge data alone.
- Only the strain gauges had sufficiently high precision to be sensitive to small changes in geometry and material model.
- Unfortunately, the unexpected sensitivity to small geometric perturbations made it too difficult to isolate material modeling effects and study those.

As seen above, the strain gauge data improved in some locations and got worse in others while the DIC deformation field was insensitive to these changes. This shows that if we had collected data at only one or two points, then we might have matched our experimental data without getting the correct solution. Using many sources of data to interpret model agreement allows us to be certain that we have created a unique inverse problem (reduced the likelihood of falsely matching data).

In the end, we were unable to isolate all errors in the model and improve the prediction of residual stresses.

If we could capture all the geometric details perfectly, we might be able to isolate the effects of the material model. One approach would be to repeat the test with better controls. We could use the inspection data from the indenters to make the orientation and magnitude of the indenter tilt a known quantity. Also, to make the boundary conditions on the disk more obvious, both the top and bottom centering rings could be removed during the experiment and additional displacement measurements could be taken to check boundary conditions. On the other hand, a specimen re-design could be even more helpful. In order to remove geometric issues with the indenter tilt an indenter with a curved surface could be used. However, with this highly stiff and constrained loading configuration, other alignment issues might still be significant.

Acknowledgements This work was performed at Los Alamos National Laboratory, operated by the Los Alamos National Security, LLC for the National Nuclear Security Administration of the U.S. Department of Energy under contract DE-AC52-06NA25396. By acceptance of this article, the publisher recognizes that the U.S. Government retains a nonexclusive, royalty-free license to publish or reproduce the published form of this contribution, or to allow others to do so, for U.S. Government purposes.

References

1. P.J. Withers, Residual stress and its role in failure. Rep. Prog. Phys. **70**(12), 2211–2264 (2007)
2. M.N. James, Residual stress influences on structural reliability. Eng. Fail. Anal. **18**(8), 1909–1920 (2011)
3. K.K. Liu, M.R. Hill, The effects of laser peening and shot peening on fretting fatigue in Ti-6Al-4V coupons. Tribol. Int. **42**(9), 1250–1262 (2009)
4. L. Edwards, M.C. Smith, M. Turski, M.E. Fitzpatrick, P.J. Bouchard, Advances in residual stress modeling and measurement for the structural integrity assessment of welded thermal power plant. Adv. Mater. Res. **41–42**, 391–400 (2008)
5. C.C. Aydiner, E. Ustundag, M.B. Prime, A. Peker, Modeling and measurement of residual stresses in a bulk metallic glass plate. J. Non Cryst. Solids **316**(1), 82–95 (2003)
6. D.A. Tanner, J.S. Robinson, Modelling stress reduction techniques of cold compression and stretching in wrought aluminium alloy products. Finite Elem. Anal. Des. **39**(5/6), 369–386 (2003)
7. A.H. Yaghi, G. Hilson, S. Simandjuntak, P.E.J. Flewitt, M.J. Pavier, D.J. Smith, T.H. Hyde, A.A. Becker, W. Sun, A comparison between measured and modeled residual stresses in a circumferentially butt-welded P91 steel pipe. J. Press. Vessel Technol. **132**(1), 011206 (2010). doi:10.1115/1.4000347
8. J. Rolph, M. Preuss, N. Iqbal, M. Hofmann, S. Nikov, M.C. Hardy, M.G. Glavicic, R. Ramanathan, A. Evans, Residual Stress Evolution during Manufacture of Aerospace Forgings, in *Superalloys*, ed. by E.S. Huron, R.C. Reed, M.C. Hardy et al. (Wiley, Hoboken, 2012), pp. 881–891. doi:10.1002/9781118516430.ch97

9. H. Dai, J.A. Francis, P.J. Withers, Prediction of residual stress distributions for single weld beads deposited on to SA508 steel including phase transformation effects. Mater. Sci. Technol. **26**, 940–949 (2010). doi:10.1179/026708309x12459430509454
10. A.T. DeWald, M.R. Hill, Eigenstrain based model for prediction of laser peening residual stresses in arbitrary 3D bodies. Part 1: model description. J. Strain Anal. Eng. Des. **44**(1), 1–11 (2009)
11. M.B. Prime, V.C. Prantil, P. Rangaswamy, F.P. Garcia, Residual stress measurement and prediction in a hardened steel ring. Mater. Sci. Forum **347–349**, 223–228 (2000)
12. O. Muránsky, C.J. Hamelin, M.C. Smith, P.J. Bendeich, L. Edwards, The role of plasticity theory on the predicted residual stress field of weld structures. Mater. Sci. Forum **772**, 65–71 (2014)
13. P. Carlone, G.S. Palazzo, R. Pasquino, Finite element analysis of the steel quenching process: temperature field and solid–solid phase change. Comput. Math. Appl. **1**, 585–594 (2010). 10.1016/j.camwa.2009.06.006
14. D.A. Tanner, J.S. Robinson, Residual stress prediction and determination in 7010 aluminum alloy forgings. Exp. Mech. **40**(1), 75–82 (2000). doi:10.1007/bf02327551
15. S. Ismonov, S.R. Daniewicz, J.J.C. Newman, M.R. Hill, M.R. Urban, Three dimensional finite element analysis of a split-sleeve cold expansion process. J. Eng. Mater. Technol. **131**(3), 031007 (2009). doi:10.1115/1.3120392
16. A.H. Mahmoudi, D. Stefanescu, S. Hossain, C.E. Truman, D.J. Smith, P.J. Withers, Measurement and prediction of the residual stress field generated by side-punching. J. Eng. Mater. Technol. **128**, 451–459 (2006)
17. P. Pagliaro, M.B. Prime, B. Clausen, M.L. Lovato, B. Zuccarello, Known residual stress specimens using opposed indentation. J. Eng. Mater. Technol. **131**, 031002 (2009)
18. P. Pagliaro, M.B. Prime, H. Swenson, B. Zuccarello, Measuring multiple residual-stress components using the contour method and multiple cuts. Exp. Mech. **50**(2), 187–194 (2010). doi:10.1007/s11340-009-9280-3
19. P. Pagliaro, Mapping multiple residual stress components using the contour method and superposition. Ph.D. Dissertation, Universitá degli Studi di Palermo, Palermo, 2008
20. P. Pagliaro, M.B. Prime, J.S. Robinson, B. Clausen, H. Swenson, M. Steinzig, B. Zuccarello, Measuring inaccessible residual stresses using multiple methods and superposition. Exp. Mech. **51**(7), 1123–1134 (2011). doi:10.1007/s11340-010-9424-5
21. M.B. Prime, A.T. DeWald, in *The Contour Method*. ed. by G.S. Schajer. Practical Residual Stress Measurement Methods, (Wiley, Chichester, 2013). doi:10.1002/9781118402832.ch5
22. M.R. Hill, The Slitting Method, in *Practical Residual Stress Measurement Methods*, ed. by G.S. Schajer (Wiley, Chichester, 2013), pp. 89–108. doi:10.1002/9781118402832.ch4
23. Y. Bai, T. Wierzbicki, A new model of metal plasticity and fracture with pressure and Lode dependence. Int. J. Plast. **24**(6), 1071–1096 (2008)
24. MB. Prime, in *Anisotropic and Pressure-Dependent Plasticity Modeling for Residual Stress Prediction*. ed. by C.E. Ventura, W.C. Crone, C. Furlong. Experimental and Applied Mechanics, Conference Proceedings of the Society for Experimental Mechanics Series. Conference Proceedings of the Society for Experimental Mechanics Series, vol. 4 (Springer, New York, 2013), pp. 415–427. doi:10.1007/978-1-4614-4226-4_49
25. R. Hill, A theory of the yielding and plastic flow of anisotropic metals. Proc. R. Soc. Lond. A Math. Phys. Sci. **193**(1033), 281–297 (1948). doi:10.1098/rspa.1948.0045
26. M.A. Sutton, S.R. McNeill, J.D. Helm, Y.J. Chao, Advances in Two-Dimensional and Three-Dimensional Computer Vision, in *Photomechanics*, ed. by P. Rastogi. Topics in Applied Physics, vol. 77 (Springer, Berlin, 2000), pp. 323–372. doi:10.1007/3-540-48800-6_10
27. Y.Q. Wang, M.A. Sutton, X.D. Ke, H.W. Schreier, P.L. Reu, T.J. Miller, On error assessment in stereo-based deformation measurements. Exp. Mech. **51**(4), 405–422 (2011). doi:10.1007/s11340-010-9449-9
28. X.D. Ke, H.W. Schreier, M.A. Sutton, Y.Q. Wang, Error assessment in stereo-based deformation measurements. Exp. Mech. **51**(4), 423–441 (2011). doi:10.1007/s11340-010-9450-3
29. P.L. Reu, Experimental and numerical methods for exact subpixel shifting. Exp. Mech. **51**(4), 443–452 (2011). doi:10.1007/s11340-010-9417-4

Chapter 25
Analysis of Laser Weld Induced Stress in a Hermetic Seal

Ryan D. Jamison, Pierrette H. Gorman, Jeffrey Rodelas, Danny O. MacCallum, Matthew Neidigk, and J. Franklin Dempsey

Abstract Laser welding of glass-to-metal electrical connectors is a common manufacturing method for creating a hermetically sealed device. The materials in these connectors, in particular the organic glass, are sensitive to thermal induced residual stress and localized heating. An analytical laser weld model is developed that provides simulation and analysis of both thermal and mechanical effects of the welding process. Experimental studies were conducted to measure the temperature at various locations on the connector. The laser weld is modeled using both surface and volumetric heating directed along the weld path to capture the thermal and mechanical response. The weld region is modeled using an elastic-plastic weld material model, which allows for compliance before welding and stiffening after the weld cools. Results from a finite element model of the glass-to-metal seal are presented and compared with experimental results. The residual compressive stress in the glass is reduced due to the welding process but hermeticity is maintained.

Keywords Laser weld • Residual stress • Hermetic seal • FEA • Thermomechanical

25.1 Introduction

Glass-to-metal hermetic seals are found in many engineering applications, such as semiconductor electronics, thermostats, optical devices, switches, and electrical connectors. The hermetic seal is traditionally created using one of two methods [1]. First, "matched seals" are seals in which the glass and metal packaging have similar coefficients of thermal expansion (CTE) and rely on chemical bonds between the glass and metal oxide to provide a seal. Second, compression seals, or "mismatched seals," are designed such that the metal surround will shrink more rapidly than the glass, putting the glass in compression and creating a seal. Hermetic seals used as electrical connectors typically involve a metallic shell, contact(s) and sealing glass. A common approach for designing hermetic connectors is to use a contact material whose CTE matches that of the sealing glass and a shell material that creates compression seal around the glass and contact. Figure 25.1 shows an example of a hermetic connector. In the figure, the hermetic connector consists of a metallic shell, sealing glass, and single contact. Because the hermetic seal is created by taking the connector through a glass sealing cycle at temperatures typically greater than 500 °C, residual stresses are commonly present in the sealing glass and need to be carefully characterized to determine design margin.

Hermetic connectors must be attached to surrounding material using a method that will maintain an airtight seal. Methods used to mount hermetic seals include laser, TIG, or MIG welding. One of the most common methods is to laser weld the hermetic seal to the surrounding bulkhead. Laser welding has been studied extensively and many methods have been developed to allow for finite element simulations of the laser welding process [2–6] as well as residual stress in weld members [7–9]. The strategies and implementation of laser welding and residual stress calculations vary in complexity, such as only considering conduction during welding to capturing the fluid-solid interaction during keyhole formation. When welding the hermetic connector, large amounts of energy are deposited locally in the connector, which can result in large temperature gradients and high-localized temperatures. This change in temperature magnitude and distribution can result in transient thermal stresses in the connector. Because of the nature of the "matched" and compression seals found in hermetic connectors, the residual stress in the glass is sensitive to large changes in temperature. Therefore, it is import to understand the residual stress state in the sealing glass after the sealing cycle and welding process.

In this paper, experimental work to characterize the temperature distribution through a hermetic connector and finite element simulations to determine the residual stress in the sealing glass is presented. The experimental setup and results are discussed in Sect. 25.2. Finite element simulations of the glass sealing cycle are discussed in Sect. 25.3. Also in Sect. 25.3,

R.D. Jamison (✉) • P.H. Gorman • J. Rodelas • D.O. MacCallum • M. Neidigk • J.F. Dempsey
Sandia National Laboratories, Albuquerque, PO Box 5800, NM 87185-0346, USA
e-mail: rdjamis@sandia.gov

S. Bossuyt et al. (eds.), *Residual Stress, Thermomechanics & Infrared Imaging, Hybrid Techniques and Inverse Problems, Volume 9*, Conference Proceedings of the Society for Experimental Mechanics Series, DOI 10.1007/978-3-319-21765-9_25

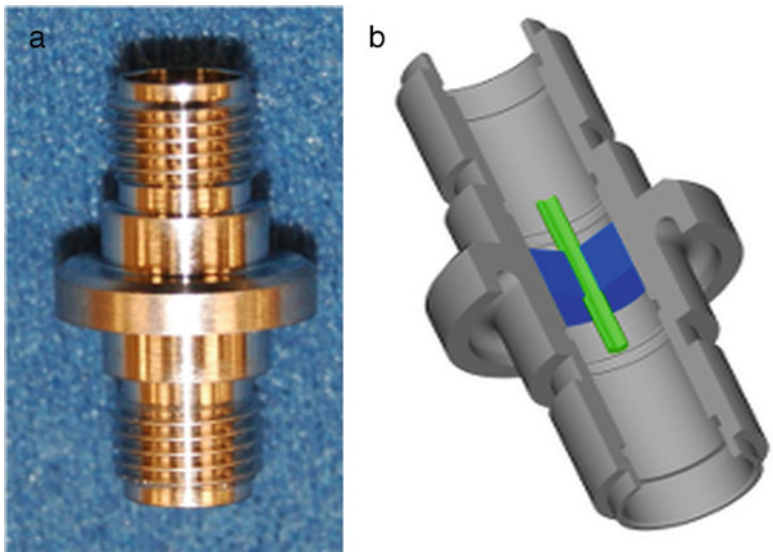

Fig. 25.1 (**a**) Photo and (**b**) cross-section of the single contact glass-to-metal seal analyzed in this paper

the finite element simulation of the laser weld with resultant temperature distribution and residual stress is. Finally, concluding comments are in Sect. 25.4.

25.2 Experimental

25.2.1 Experimental Procedure

Laser welding is a high-energy density process that produces high heating and cooling rates during welding. The purpose of this study is to capture the peak welding temperatures and cooling rates in the hermetic connector during the welding process. The laser system used is an IPG YLS-2000, Ytterbium-Doped Fiber Laser System (1070 nm) with motion control and work station integrated by Mundt & Associates, Inc. Laser power measurements were performed using an Ophir power meter 5000W-ROHS. Tack welding of specimens was performed on the LaserStar Model 1900 spot welder. Temperature data was captured using the iOtech Personal DAQ3000 with a sample rate of 520 Hz. The Type K (Chromel/Alumel) 0.010″ diameter thermocouples were attached to the hermetic connector and test plate using a Unitek Model 350 resistance welder. Measurements of thermocouple placement were performed on the Vision Engineering Hawk Elite Mono Dynascope.

Prior to welding the hermetic connector, a series of weld bead on sheet experiments were conducted. These experiments were used to provide insight into the power settings of the laser in association with the materials of used in the hermetic connector. The sheets used were type 304L stainless steel. Weld passes at power levels of 300, 350, 400, 450, and 500 W were done. Metallography was performed on the 300, 400, 450, and 500 W samples to visualize the cross-section of the resulting weld bead. For example, Fig. 25.2 shows the cross-section of the weld beads for 300 and 400 W. The weld depth is 135 and 640 μm for the 300 and 400 W samples, respectively. Since metallography was not performed on the specimen welded at 350 W, the 300 and 400 W samples provide a bound of what the weld bead may look like at power levels associated with welding the hermetic connector (350 W).

The hermetic seal was welded to a 0.5″ thick 304L stainless steel test plate. A hole was machined in the center of the test plate, with geometric features representing a weld flange. Four thermocouples (channels 0–3) were placed at 90° increments on the underside of the connector (opposite the side that is welded). One thermocouple (channel 4) was placed near the weld joint on the underside of the test plate and another (channel 5) was placed on the topside of the test plate near the weld joint, directly opposite of channel 4. The placement of the thermocouples is shown in Fig. 25.3. In the figure, the white circle in image b highlights the location of the weld joint.

The hermetic connector was cleaned with isopropyl alcohol and thermocouples were resistance welded to the 304L sheet. Inert gas shielding (argon) was delivered to the hermetic connector coaxially with the laser beam at a flow rate of 100 cfh.

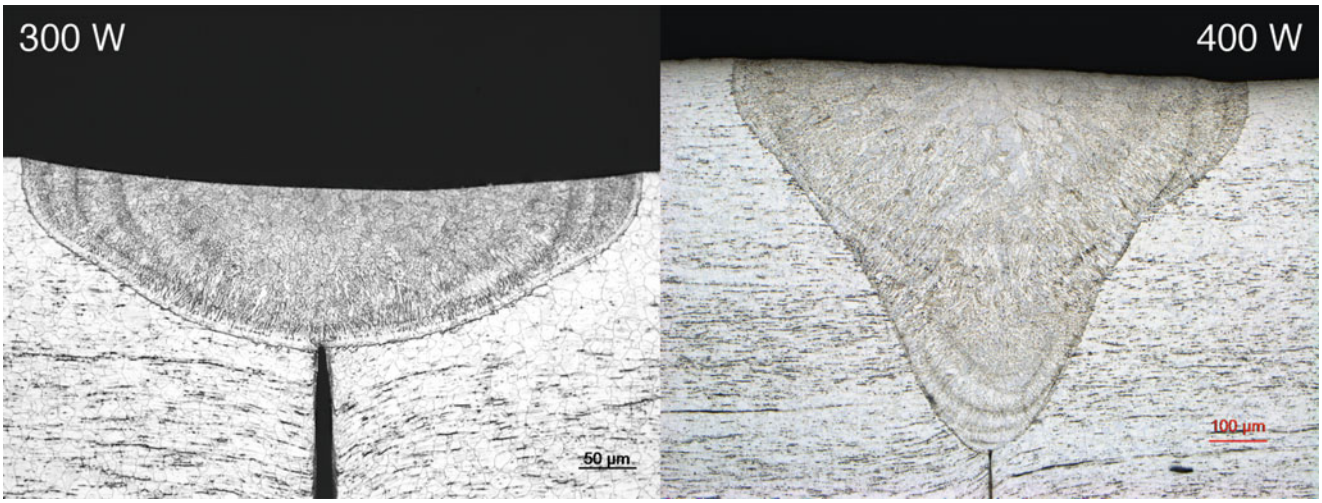

Fig. 25.2 Metallography of weld bead on 304L stainless steel sheets for power levels of 300 and 400 W

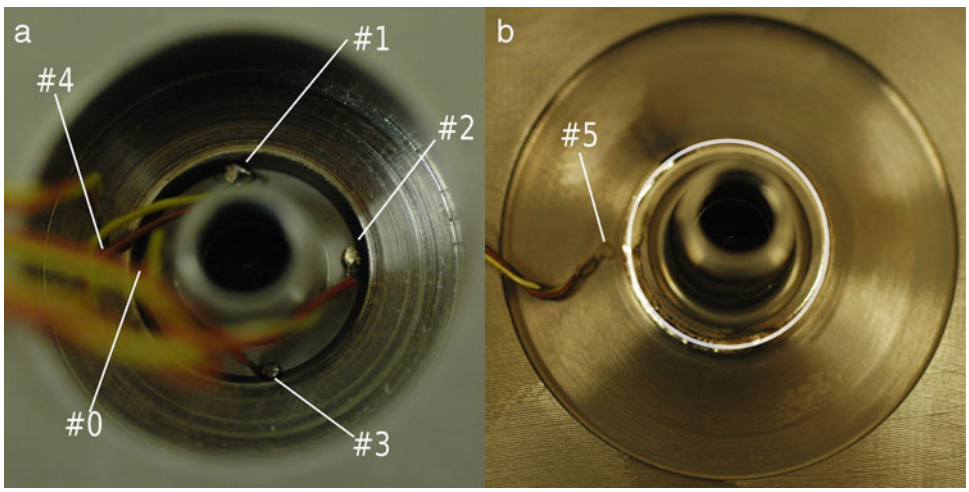

Fig. 25.3 (**a**) The underside of the connector showing thermocouples #0 through #4 and (**b**) the topside of the connector showing thermocouple #5 located on the test plate near the weld joint

Prior to welding, the connector was tack welded to the test plate at 90° increments around the perimeter of the connector. The sample was welded at 33.8 mm/s (80 in/min) travel speed at a nominal power of 350 W (338 W measured at the weld). The weld was performed using continuous wave output without modulation. After traveling the full circumference of the connector, the weld was overlapped by 40° at full power and then the power was ramped down to zero over an additional 40°. The weld penetration was nominally 508 µm and the weld spot size was approximately 280 µm. Traditionally, when welding a hermetic seal, only one weld pass is required. Since the connector used in this study is for experimental purposes only and in an effort to gather more data, two weld passes were made directly on top of each other; the second after the first had cooled to room temperature.

25.2.2 Experimental Results

The temperature at six thermocouple locations was measured during the welding process. The temperature at each thermocouple for both weld passes is shown in Fig. 25.4. During the first weld pass (image a), the weld transitioned

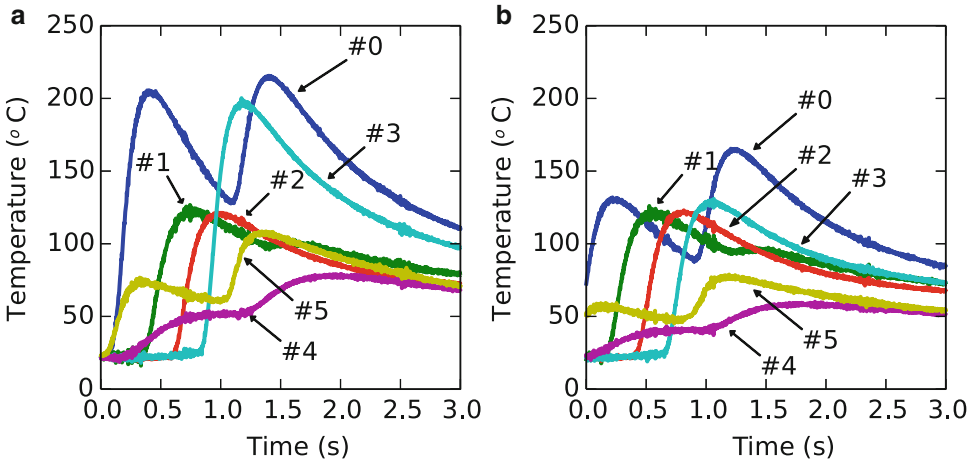

Fig. 25.4 Experimentally measured temperature at thermocouple locations for (**a**) first weld pass and (**b**) second weld pass

between conduction and keyhole mode welding [10]. At 338 W, the laser power density was too low for the unwelded joint, causing the jump between welding modes. As a result, energy transfer efficiency varied along the weld length. The high temperatures in the shell of the hermetic connector are because the virgin weld joint minimizes heat transfer from the connector to the test plate. During the second pass, the peak temperatures are lower due to an increase in allowable heat transfer through the shell and test plate.

25.3 Finite Element Model

Though the experimental technique described above is capable of evaluating the temperature in the shell of the hermetic connector during the welding process, it remains difficult to evaluate the temperature of the sealing glass or contact. Also, because of the small size of this particular hermetic connector, it is also difficult to gather any meaningful strain measurements during the welding process. Therefore, finite element modeling is used to analyze the temperature and residual stress in the hermetic connector. The finite element model is composed of two parts—thermal and mechanical. Both codes are built on the SIERRA framework, a massively parallel, finite element code. The thermal modeling of the laser weld is performed in Sierra Thermal/Fluid [11], which specializes in incompressible flow and heat transfer modeling. The residual thermal stresses are calculated using Sierra Solid Mechanics [12], a three-dimensional solid mechanics code capable of modeling nonlinear materials, large deformation, and contact. SIERRA allows the laser weld induced stress analysis to be performed fully coupled or uncoupled.

25.3.1 Material Models

The materials used in the hermetic connector presented here are those commonly found in many applications. The shell is type 304L Stainless Steel, the contact is Paliney 7, and the sealing glass is Schott S8061. The room temperature thermal and mechanical properties used in the finite simulations are shown in Table 25.1. Due to a lack of thermal material data at elevated temperatures, and because the temperature in the glass and contact remain low, room temperature data is used for both Paliney 7 and Schott S8061 for the thermal simulation. Temperature dependent specific heat and thermal conductivity is assumed for the type 304L Stainless Steel.

Three separate solid mechanics material models are used in calculation of the thermal residual stress. All materials models used are rate independent. The 304L Stainless Steel is modeled as a thermoelastic-plastic material with temperature dependent Young's modulus, yield stress, and hardening modulus. Paliney 7 is modeled as an elastic-plastic material. Schott S8061 is modeled as a thermoelastic material with temperature dependent Young's modulus. Glass is actually a viscoelastic material, but the glass transition region is significantly higher than the peak temperature of the sealing cycle (460 °C) and the viscous behavior is negligible. A temperature dependent elastic assumption for the Schott S8061 is therefore appropriate.

Table 25.1 Room temperature thermal and mechanical material properties for the hermetic connector

Material Property	304L SS	Paliney 7	Schott S8061
Density, ρ (kg/m^3)	8,000	11,790	260
Young's modulus, E (GPa)	193[a]	117	68[a]
Poisson's ratio, ν	0.26[a]	0.30	0.21
CTE (ppm/°C)	18.5	15.1	9.5
Yield stress, σ_y (MPa)	241[a]	620	-
Specific Heat, c_p (J/kg-K)	502[a]	240	837
Thermal Conductivity, k (W/m-K)	9.4[a]	71.8	1.05
Melt Temperature, T_m (K)	1,873	-	-

[a]Temperature dependent

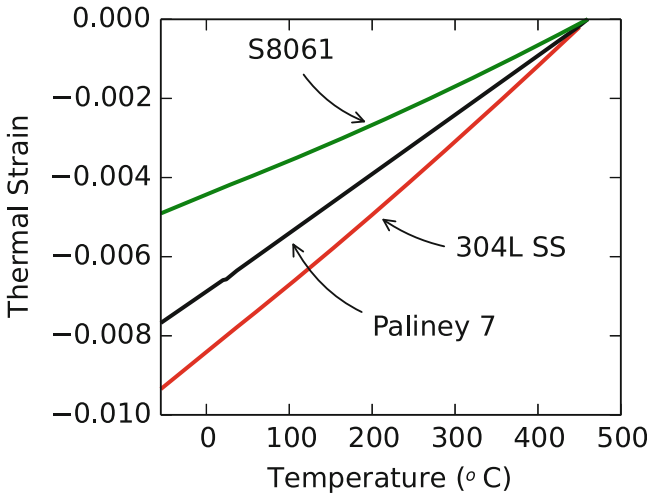

Fig. 25.5 Linear thermal strain as a function of temperature over sealing cycle temperature range

The thermal strain profile over the sealing cycle temperature range (−55 °C to 460 °C) for each material is shown in Fig. 25.5. Lastly, the model assumes the materials are perfectly bonded at all material interfaces and glass menisci are neglected.

25.3.2 Boundary Conditions

Modeling thermal induced residual stresses in a hermetic connector requires both thermal and mechanical simulations. The laser weld modeling capability was developed to evaluate the performance of hermetic connectors and other glass-to-metal seals subject to laser weld heating. In both simulations, the welded joint is modeled as a thin layer of elements that connect the hermetic shell to the surrounding bulkhead. The solid mechanics material model is assumed elastic-plastic. This assumption allows for simplicity in creating the finite element model while not decreasing the effectiveness of the overall simulation.

In the thermal simulation, the heat transfer in the hermetic connector is modeled assuming Fourier's law heat conduction, surface convection, and black body radiation. The laser weld itself is modeled using both surface and volumetric flux boundary conditions. The surface flux is assumed circular in shape and applies a flux normal to the surface of the weld joint. The radius of the surface flux is assumed to be the spot size of the laser. The volumetric flux is assumed cylindrical in shape and applies a flux to any nodes found within the cylinder. The depth of the volumetric flux is modeled as the nominal penetration depth of the weld and the radius is the same as the spot size (if experimentally measured weld profiles are available, actual depth and radius at base of the keyhole is used). Both surface and volumetric fluxes move in unison in a prescribed path to simulate the welding process. The magnitude of the flux is equal to the measured laser power. To account for losses through the system, both the surface and volumetric flux magnitudes can be scaled independently. The combination of both a surface and volumetric flux is capable of creating a melting zone that approximates the keyhole shape that is

characteristic of a laser weld. The material at the weld joint is assumed to be the same as the bulk material, i.e. the keyhole shape of the laser weld is not explicitly meshed and provided with melt zone specific properties.

The residual stress calculation in the hermetic connector is composed of two simulation steps. The first step consists of isothermal cooling of the entire hermetic connector from 460 °C to room temperature. The model is assumed to be stress free at 460 °C. As the connector cools, residual stress is generated in the shell, sealing glass, and contact. This modeling step generates accounts for compression in the sealing glass. The second step consists of applying the resulting temperature field from the thermal simulation. The temperature field from the thermal laser weld simulation is passed to the solid mechanics code as a temperature boundary condition to calculate the thermal residual stress. Prior to heating the weld joint has nearly zero stiffness. Upon heating to melt temperature and subsequent cooling, the material stiffens, producing weld distortion at the weld joint. Combining simulations that include the weld distortion, thermal expansion of the surrounding material, and the sealing cycle residual stress more accurately predicts the final stress state of the hermetic connector.

25.3.3 Sealing Cycle

Isothermally cooling the hermetic connector from 460 °C to room temperature produces residual stress in the shell, contact, and sealing glass. The residual stress is caused by the mismatched CTE in the sealing glass, contact, and shell. Traditionally for a hermetic connector, it is desired to minimize the maximum principal stress (SMAX) in the sealing glass and prevent (or minimize) plastic strain in the contact and shell. Figure 25.6 shows the deformed state of the hermetic connector (magnified ×50) and the maximum residual stress in the sealing glass post sealing cycle. The shell and contact have a greater CTE than the sealing glass, compressing the seal in both the radial and axial directions. In Fig. 25.6b, the image is colored such that only tensile stress is emphasized. The gray represents compressive stress in the connector.

The stress in the glass post sealing cycle is dominantly compressive. Both "matched" and compression seals require that the sealing glass remain in a compressive state. Tensile stress in the sealing glass can lead to glass fracture and loss of hermeticity. For this particular connector, the peak maximum principal stress is less than 1 MPa, which is sufficiently low to be of no concern. The ring of tensile principal stress that forms (Fig. 25.6b) is dominated by an axial stress component; therefore, there is little concern of loss of hermeticity in the connector. During the sealing cycle, the contact remains elastic and there is a small amount of plasticity developed at the shell-glass interface.

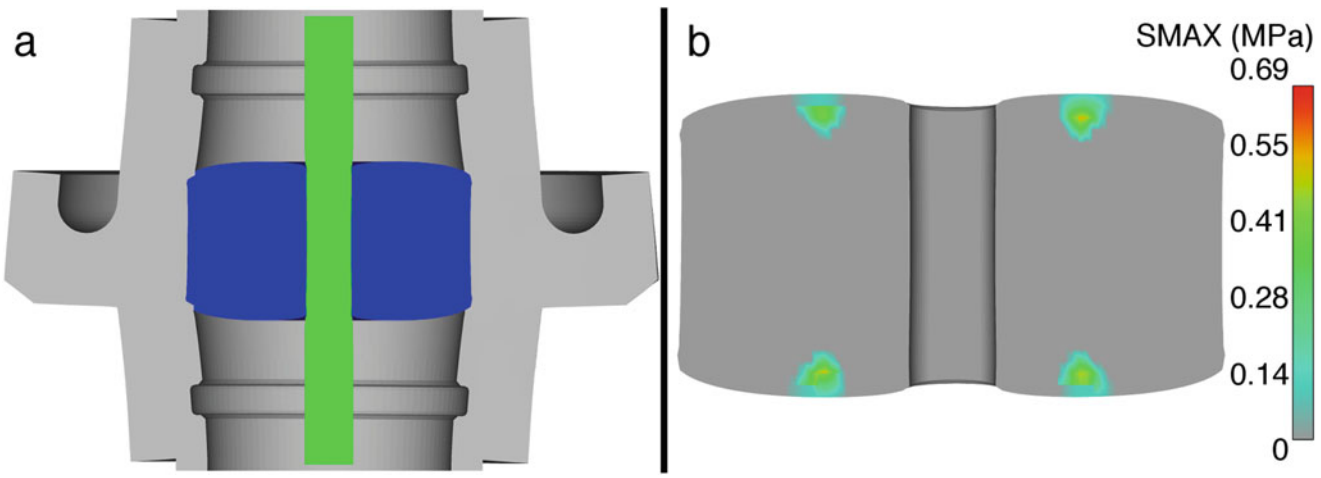

Fig. 25.6 Hermetic connector post sealing cycle (**a**) deformation magnified ×50 and (**b**) maximum principal stress in sealing glass in a deformed state (×50 magnification) where grey represents compressive stress

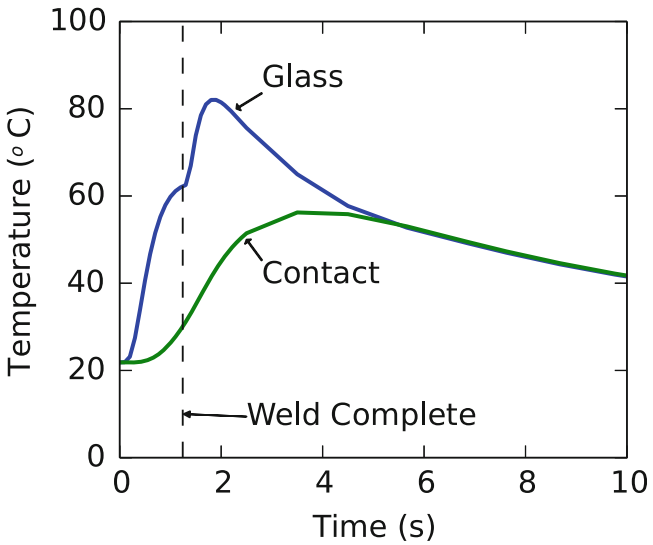

Fig. 25.7 The maximum temperature anywhere in the sealing glass and contact during the laser weld and post-weld cool down

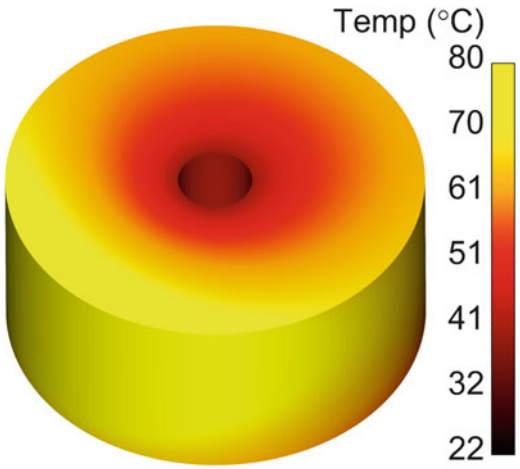

Fig. 25.8 Temperature distribution in the sealing glass caused by the laser weld at the time corresponding to the peak temperature in the glass

25.3.4 Laser Weld

The experiment outlined in Sect. 25.2 was able to capture the temperature on the surface of the shell at various locations. The temperature data was used to calibrate the finite element thermal model inputs. The finite element model provides insight into the temperature and stress throughout the sealing glass and contact. The maximum temperature anywhere in the sealing glass and contact is shown in Fig. 25.7. The peak temperature in the sealing glass is approximately 80 °C and peak temperature in the contact is 55 °C. The peak temperature in the contact occurs at the axial center of the contact near the contact-glass interface. Furthermore, the peak temperature in both the sealing glass and contact occur after the welding process has completed.

The temperature distribution throughout the glass is shown in Fig. 25.8. The temperature is shown at the time corresponding to the peak temperature anywhere in the glass (see Fig. 25.7). The temperature in the glass is not uniformly distributed and there is a large portion of the glass at or near the peak temperature. The peak temperature occurs near the location of the Ch. 0 thermocouple, which corresponds to the overlap portion of the weld. The resulting temperature gradient in the sealing glass is as high as 40 °C. The peak temperature in the glass is sufficiently below the glass transition temperature to avoid any viscoelastic effects.

The increase in temperature and asymmetric distribution can lead to an increase in residual stress in the sealing glass. Furthermore, the welding process can affect the radial compression of the sealing glass. Figure 25.9 shows the post-weld residual maximum principal stress in the sealing glass as well as the radial compression at the shell-glass and contact-glass

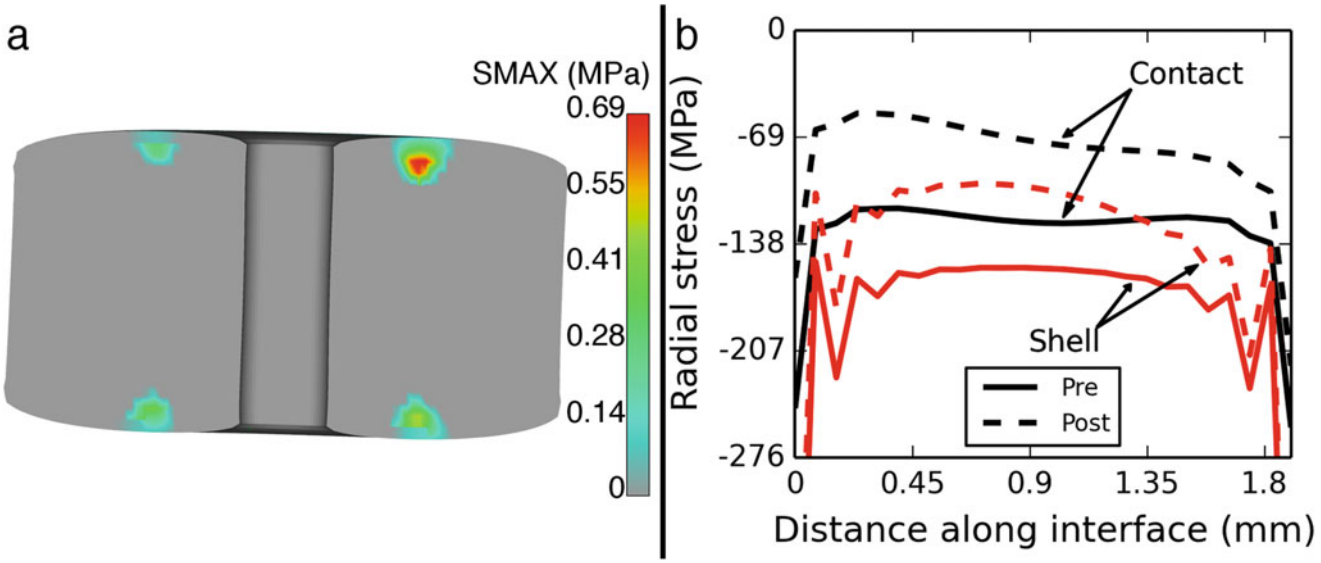

Fig. 25.9 The post-weld room temperature (**a**) maximum principal stress (SMAX) in the sealing glass and (**b**) pre and post-weld compression along the shell-glass and contact-glass interface

interface. The maximum principal stress is shown at the time corresponding to the peak stress during the welding process. The solid lines show the radial compression prior to welding at room temperature and the dashed lines show the radial compression post welding at room temperature. The abscissa of Fig. 25.9b represents the axial distance along the shell-glass and contact-glass interface starting at the bottom increasing to the top of the glass (ref. Fig. 25.9a). The difference in stress in the sealing glass during the welding process is less than 5 %. Though the change in maximum principal stress is small, the radial compression decreases by nearly 70 MPa at both the contact and shell interfaces (Fig. 25.9b). The laser weld appears to cause the shell to contract at the weld location, effectively decreasing the compression imposed on the sealing glass and contact.

25.4 Conclusion

An experimental and numerical analysis of the temperature and residual stress in a hermetic glass-to-metal connector due to laser welding has been conducted. The hermetic connector was welded to a test plate at nominally 350 W and the temperature in the hermetic shell and test plate was measured. It was found that at 350 W, the weld transitioned between keyhole and conduction mode welding. The connector was welded a second time, resulting in a consistent keyhole mode weld. The temperature at the exterior of the shell measured as high as 200 °C. A laser weld modeling technique has been described that allows for modeling the laser welding process and evaluating the temperature and stress in a hermetic connector. The temperature of the glass reached as high as 80 °C during welding. It was shown that there was little change in the residual stress of the sealing glass before and after the laser welding process. The radial compression in the sealing glass was decreased by as much as 70 MPa due to laser welding.

Acknowledgements Sandia National Laboratories is a multi-program laboratory managed and operated by Sandia Corporation, a wholly owned subsidiary of Lockheed Martin Corporation, for the U.S. Department of Energy's National Nuclear Security Administration under contract DE-AC04-94AL85000. The authors would like to acknowledge Derek Luu for his support of this project. Also, the authors would also like to thank Kurtis Ford and Russell Teeter for their advice and guidance.

References

1. Glenair Inc: Introduction to Glenair Hermetic Connector Products, www.glenair.com. 2013
2. M.R. Frewin, D.A. Scott, Finite element model of pulsed laser welding. Weld. Res. Suppl. **78**, 15–22 (1999)
3. A. De, S.K. Maiti, C.A. Walsh, H.K.D.H. Bhadeshia, Finite element simulation of laser spot welding. Sci. Technol. Weld. Joining **8**(5), 377–384 (2003)

4. A.P. Mackwood, R.C. Crafer, Thermal modelling of laser welding and related processes: a literature review. Opt. Laser Technol. **37**, 99–115 (2005)
5. B.S. Yilbas, A.F.M. Arif, B.J. Abdul Aleem, Laser welding of low carbon steel and thermal stress analysis. Opt. Laser Technol. **42**, 760–768 (2010)
6. J. Rońda, A. Siwek, Modelling of laser welding process in the phase of keyhole formation. Arch. Civ. Mech. Eng. **3**, 739–752 (2011)
7. P. Martinson, S. Daneshpour, M. Koçak, S. Riekehr, P. Staron, Residual stress analysis of laser spot welding of steel sheets. Mater. Des. **30**, 3351–3359 (2009)
8. F. Kong, K. Radovan, 3D finite element modeling of the thermally induced residual stress in the hybrid laser/arc welding of lap joint. J. Mater. Process. Technol. **210**, 941–950 (2010)
9. M. Zain-ul-abdein, D. Nélias, J.F. Jullien, D. Deloison, Experimental investigation and finite element simulation of laser beam welding induced residual stresses and distortions in thin sheets of AA 6056-T4. Mater. Sci. Eng. A **527**, 3025–3039 (2010)
10. Z. Feng, *Processes and Mechanisms of Welding Residual Stress and Distortion* (Woodhead Publishing, Oxford, 2005)
11. P.K. Notz, S.R. Subia, M.M. Hopkins, H.K. Moffat, D.R. Noble, ARIA Manual Aria 1.5: User's Manual, (Sandia National Laboratories, SAND 2007-2734, 2007)
12. SIERRA Solid Mechanics Team, Sierra/Solid Mechanics 4.22 User Guide, (Sandia National Laboratories, SAND 2011-7597, 2011)

Chapter 26
A Summary of Failures Caused by Residual Stresses

E.J. Fairfax and M. Steinzig

Abstract Residual stress (RS) is often implicated in the failure of parts or assemblies, but there has not been any quantification or statistics collected on RS induced failures. Using the ASM Failure Analysis Database™, 147 individual case histories of failure analysis involving residual stress were identified and categorized based on various criteria. Information about the type of failure, material, processing, severity, date and other pertinent facts were extracted from the failure write-ups and the statistics on date of publication, material type, and failure type are compiled here. This information is used in conjunction with other compiled information on residual stress induced failures to estimate the impact of various residual stress induced problems in manufacturing and industry.

Keywords Residual stress • Failure • Statistics • Database • Industry

26.1 Introduction

Mechanical failures involving residual stress are of interest to many sectors of industry as they can occur in a wide variety of metals and alloys [1]. Using the ASM Failure Analysis Database™ [2], 147 unique accounts of mechanical failure due at least in part to residual stress were identified and the articles documenting each failure compiled for statistical analysis. The failures discussed here are examined in the context of severity, type of failure, material affected, and occurrence date. The statistical analysis of these failures was conducted to provide insight into patterns in the causes and conditions surrounding the failures that may help guide efforts to reduce the overall impact of the failures.

26.2 Methods

The ASM Failure Analysis Database™ was searched for the key words "residual stress." After that initial search all of the articles returned were read and it was determined whether residual stress was implicated as a cause of the failure, or discussed in some other context in the article. Of those where residual stress was implicated as a cause of the failure, the articles were then read again to determine if there were multiple articles documenting a single instance of failure. At the end of the sorting, it was determined that there were 147 unique articles in the ASM Failure Analysis Database™ that implicate residual stress as a cause of failure.

The 147 articles were then used to generate a spreadsheet tabulating the article name, year of publication, type of failure, and material affected Fig. 26.1.

First the articles were analyzed temporally by year of publication. The year of publication of the articles was then binned into three decades: 1970s, 1980s, and 1990s. The ASM Failure Analysis Database™ did not contain articles published past 2004 at the time of the analysis, so any articles published between 2000 and 2004 were discarded from the temporal analysis due to the fact that the 2000s decade had an incomplete record.

Second, the articles were analyzed according to type of failure. The articles were categorized based on the type(s) of failures that occurred as described in the text of the articles. The failure types identified in the articles were stress corrosion cracking, joining-related failures, brittle fracture, fatigue fracture, intergranular fracture, hydrogen damage and embrittlement, intergranular corrosion, transgranular fracture, corrosion fatigue, surface treatment related, pitting corrosion, mixed-mode fracture, creep fracture, stress rupture, casting-related failures, liquid metal induced brittlement, high temperature corrosion, metalworking

E.J. Fairfax (✉) • M. Steinzig
Los Alamos National Laboratory, Los Alamos, NM 87544, USA
e-mail: fairfaxe@lanl.gov

S. Bossuyt et al. (eds.), *Residual Stress, Thermomechanics & Infrared Imaging, Hybrid Techniques and Inverse Problems, Volume 9*, Conference Proceedings of the Society for Experimental Mechanics Series, DOI 10.1007/978-3-319-21765-9_26

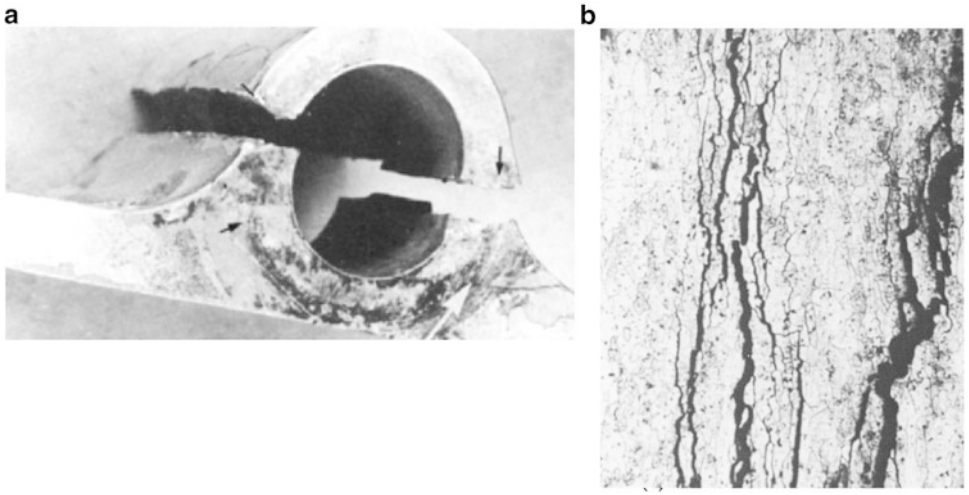

Fig. 26.1 Examples of residual stress induced mechanical failures (**a**) Fractured aircraft component examined in a case history in the ASM Failure Analysis Database™. (**b**) Example of mechanical failure due to stress corrosion cracking caused by residual stresses in aircraft components. Note the intergranular mode of branching typical of stress corrosion attacks at the grain boundaries. Images courtesy of J.B. Shah [3]

related failure, and thermal fatigue fracture. Many of the articles had more than one failure type, and were counted once for each failure type they implicated. For example, if an article listed stress corrosion cracking and corrosion fatigue as failure types, it would be included in both the total number of incidences of stress corrosion cracking as well as in the total number of incidence of corrosion fatigue failures. The most common failure type (stress corrosion cracking) was examined in more detail to determine if there are any commonalities between the articles citing that failure type.

Finally, the articles were analyzed by material type. To determine the material type, the specific materials affected by the residual stress were extracted from each of the 147 articles. The specific materials were then binned into 6 general categories: steel, aluminum, non-metal, brass, cast iron, and other. Several of the articles listed more than one material affected. In those cases where more than one material was affected, the article was counted once for each material type listed. In the event that an article listed two specific materials that fall under the same material type, i.e. two varieties of stainless steel, then the article was counted only once under the general material category, "steel."

26.3 Results and Discussion

The results of each analysis method (temporal, failure type, and material type) are shown in the subsections below. Any patterns illuminated by the analysis are discussed. Special attention is paid to the possible implications of the results for persons in manufacturing or industry with an emphasis on information that could reduce the magnitude or frequency of high impact failures.

26.3.1 Temporal Analysis

The articles accounting for unique individual residual stress failures were binned into decade of publication and the results of that are shown in Fig. 26.2.

It was clear looking at the data that the number of documented case histories of residual stress induced mechanical failures has increased steadily over the past three decades. However, it cannot be assumed that this is because there are more residual stress induced mechanical failures occurring. It is possible that the sheer number of failures has remained constant or even decreased, but they have been better documented as time goes on.

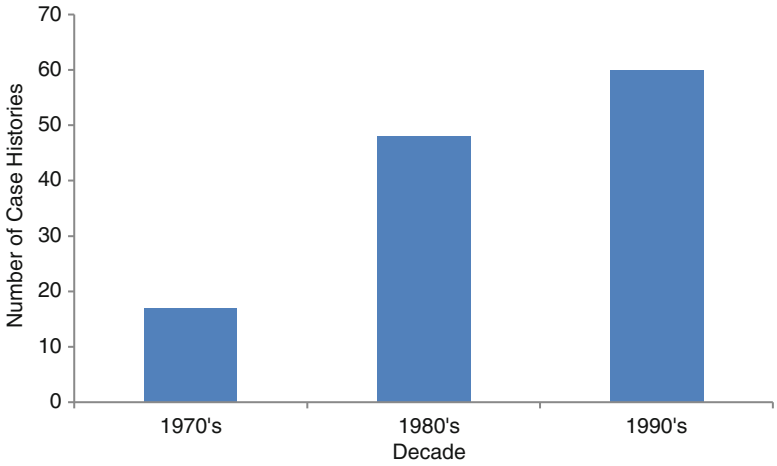

Fig. 26.2 Number of case histories describing a residual stress related mechanical failure (dependent variable) broken down by decade of occurrence (independent variable)

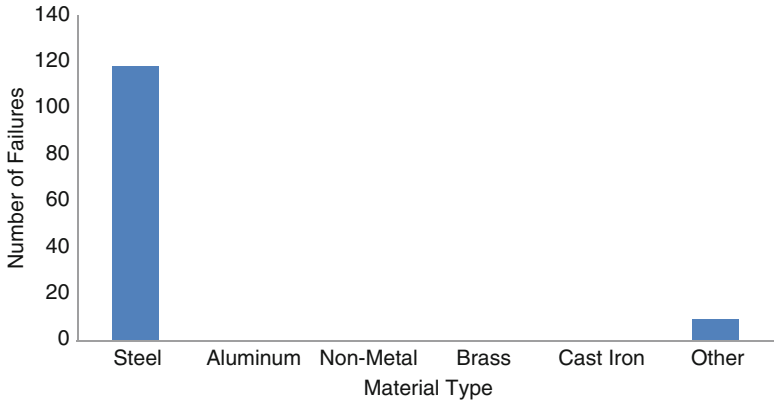

Fig. 26.3 Number of case histories describing a residual stress related mechanical failure (dependent variable) broken down material type (independent variable)

Regardless of whether the actual number of residual stress induced failures is increasing, decreasing, or remaining constant, the fact that more of them are being documented implies that more information is becoming available to people in industry and manufacturing. With more information publicly available from the increased number of articles documenting the details of the failures, it should become easier to predict and avoid conditions that lead to these failures. By keeping up with the latest articles published, persons in industry and manufacturing should be able to use the historical mechanical failure instances to better inform their current processes and procedures.

Another take away point from the temporal analysis is that the types of failures and materials affected did not vary significantly by decade. The distribution of those two characteristics was roughly even over all three decades, which implies that no one material is performing better with advancing material production technologies, and that no types of failure have been successfully mitigated with advancing material processing and treatment technologies. Details on why there is such an even distribution of failure type and material affected amongst the examined case histories over time is beyond the scope of this analysis, and is a possible avenue for further research.

26.3.2 Material Analysis

The articles accounting for unique individual residual stress failures were binned by material type and the results of that are shown in Fig. 26.3.

It is clear that materials that fall under the steel category account for the largest portion of residual stress induced failures. In total, 118 out of the 147 total failures examined listed some type of steel as an affected material.

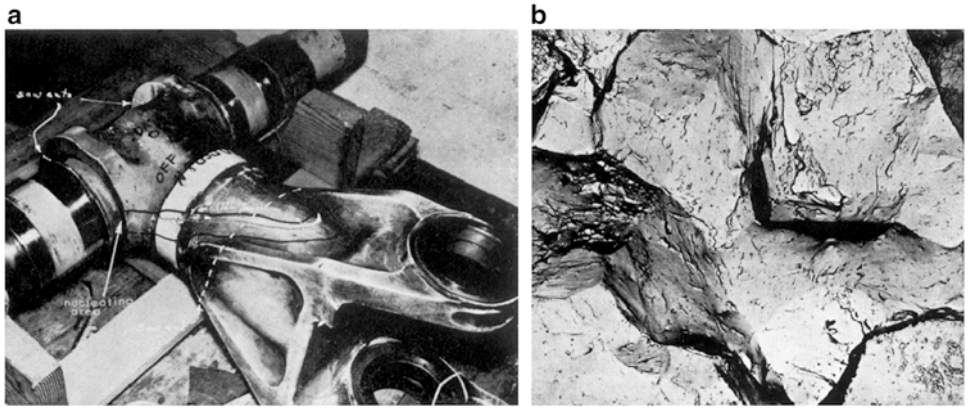

Fig. 26.4 (**a**) A failed ultra high strength steel aircraft landing gear. (**b**) An electron micrograph showing the brittle intercrystalline fracture in the ultra high strength steel aircraft landing gear in (**a**). Images courtesy of W.L. Holshouser [8]

Interestingly, a variety of types of steel were implicated. Case histories ranged from common type 304 stainless steel failures in everyday applications like ice cream mix drinkers [4] to the high impact failures of ultra-high strength steel leading to aircraft landing gear failure [5] and bridge collapse [6]. Steel is often chosen as a material in many industrial and manufacturing projects due to its low cost, high strength, and ease of machinability [7].

However, the material analysis of the ASM Failure Analysis Database™ clearly shows that steel is most often the metal affected by residual stress related failures. Whether this is because steel is more prone to failure than other materials or because steel is simply used more often cannot be determined from the data. Regardless, persons who choose steel to be their main structural material should be made aware of the fact that residual stress needs to be monitored closely cradle to grave throughout its useful life Fig. 26.4.

The variety of steels that failed due to residual stresses included stainless steels, carbon steels, welded steels, low carbon steels, chromium plated steels, structural steels, high strength steels and heat treated steels. The fact that there was such variety shows that it is not just standard stainless steel that is prone to these types of failures, but is instead indicative that residual stresses are a serious consideration for persons using any variety of steel.

26.3.3 Failure Mechanism Analysis

The articles accounting for unique individual residual stress failures were binned by failure mechanism and the results of that are shown in Fig. 26.5.

Of the 147 case studies examined, 111 of the failures involved stress corrosion cracking, followed by 55 joining-related failures, 48 brittle fractures, 46 fatigue fractures, and 40 intergranular fractures. Stress corrosion cracking occurs in more than twice the number of case histories as the next common failure mechanism, so a more in depth look at the stress corrosion cracking failures is warranted.

It is non-trivial that the material most commonly affected was steel and the mechanism of failure was most often stress corrosion cracking. Stress corrosion cracking generally speaking is a failure mechanism where a crack formation grows in corrosive environments. It is known for causing sudden, often unexpected failures of ductile metals (such as stainless steel) when they are subjected to tensile stress [9]. The correlation between the high number of steel failures and the high number of stress corrosion cracking failures is predictable, although the question still remains as whether the high number of steel failures is caused by the high rate of steel usage or if steel is an inherently more failure prone material.

The source of the tensile stress in stress corrosion cracking failures is often residual stresses, so its high prevalence in residual stress case histories is also predictable. The residual stresses can be relieved by annealing and other surface treatments, however it is not easy to completely relieve all residual stresses from a machined part such as those used in manufacturing and industry [10].

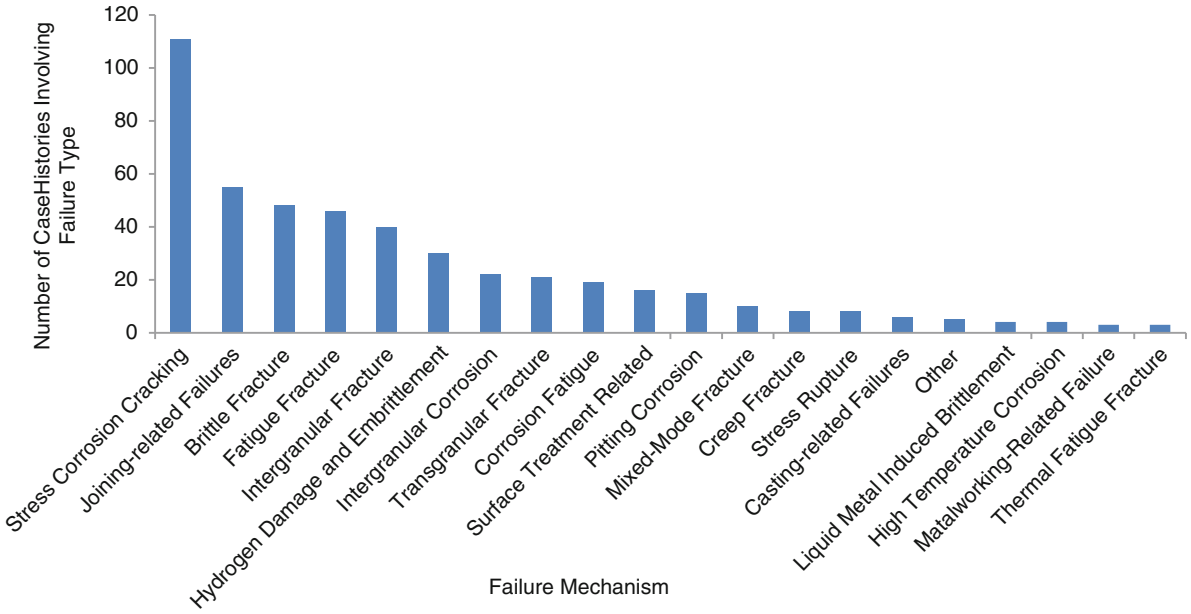

Fig. 26.5 Number of case histories describing a residual stress related mechanical failure (dependent variable) broken down failure type (independent variable)

26.4 Impact of Failures on Industry

In summary, steel is the material most often cited as failing due to residual stress. This is likely correlated, if not caused by the fact that steel is very commonly used in a wide variety of applications in manufacturing and industry. These failures are most often cause by stress corrosion cracking, a mechanism of failure that requires three things: a susceptible ductile material (such as steel), the presence a specific corrosive agent (such as chlorides, even in low concentration), and tensile stresses. The tensile stresses are often simply residual stresses from the formation processes that have not been fully relieved by annealing or other surface treatments.

The upfront cost of relieving residual stresses in every single component or part made from steel is no doubt steep. However, many of the case histories in the ASM Failure Analysis Database™ citing both steel and stress corrosion cracking are those that describe high impact failures.

The impact of a failure can be thought of in two ways: in terms of danger to human life and in terms of financial cost of the failure. Several case histories would be considered high impact in both regards—such as the failure of the high strength steel frame in a U.S. military fighter aircraft [8]. In fact, six of the examined case histories describe aircraft part failures that cite both stress corrosion cracking and stainless steel [3, 5, 8, 11–13].

Another case history describes the failure of a bridge [6]. Clearly these examples demonstrate that something as seemingly small as residual stresses can cause very high impact failures.

A number of the case histories describe failures of pipes or storage tanks for a variety of liquids and also cite steel and stress corrosion cracking. While these failures tend to be lower impact in terms of danger to human life (with the exception of three case histories describing failures in tanks at nuclear power plants [14–16]), they can be very expensive in terms of financial costs. When a pipe or storage tank fails, the response often includes repairing or replacing the failed part, clean-up of any leaked fluids, and sometimes the shutdown of operations until the failed part is dealt with. When the failed part is underground, the cost of excavation and reburying is added [17].

As persons in manufacturing and industry make decisions regarding the preventative measures taken to avoid failures involving residual stresses, there are many variables to consider. Particularly for those who work with steel that may be exposed to corrosive environments, the risk of residual stress involved failures has been shown in this paper to be a serious consideration. Even so, the best course of action in response to these findings is still quite complicated. To take every precaution possible would not be effective because it would be simply too financially expensive and time consuming. To take no precautions would be irresponsible considering the historical record of high impact—both financially and in terms of danger to human life—residual stresses related failures.

When establishing processes and procedures for a given operation, it would be prudent to perform a quick search of the ASM Failure Analysis Database™ and identify all residual stress case histories similar in nature. Using the information contained in the articles regarding specific conditions of failure, preventative measures taken, effectiveness of the measures, etc., a balance between upfront preventative costs and potential for high impact failures can be achieved.

Acknowledgements This paper was written with the support of Los Alamos National Laboratory, a U.S. Department of Energy Laboratory. Los Alamos National Laboratory strongly supports academic freedom and a researcher's right to publish; as an institution, however, the Laboratory does not endorse the viewpoint of a publication or guarantee its technical correctness. It has been approved for release with number LA-UR-15-21819.

References

1. W.F. Hosford, "Residual Stresses." In *Mechanical Behavior of Materials*, (Cambridge University Press, New York, 2005), pp. 308–321
2. The ASM Failure Analysis Database™, ASM International, 2013
3. J.B. Shah, Failure analyses of aircraft accidents—part III. Met. Eng. Q. **15**(1), 33–39 (1975)
4. J.J. Scutti, W.J. McBrine, *Ice Cream Drink Mixer Blade Failures, Introduction to Failure Analysis and Prevention, Failure Analysis and Prevention,* Vol 11, ASM Handbook, ASM International, pp. 3–23, 2002
5. W.L. Holshouser, Failure in aircraft parts made of ultra-high-strength steel, *Met. Eng. Q.* **4**(3) (1964) as published in Source Book in Failure Analysis, American Society of Metals, (1974) pp. 108–114
6. H. Czyzewski, Brittle failure: the story of a bridge. Metal Progress **107**(3), W6–W12 (1975)
7. H. Adeli, in *Advantages And Disadvantages Of Steel As A Structural Design Material*. Department of Civil & Environmental Engineering and Geodetic Science at Ohio State University, http://hcgl.eng.ohio-state.edu/~ceg532/chap1/chap1_2.htm. Accessed 9 Feb. 2015
8. T.N. White, S Kantimathi, in *Stress-Corrosion Cracking of a High-Strength Steel Frame in a Fighter Aircraft*, ed. by K.A. Esakul. Handbook of Case Histories in Failure Analysis, vol 1 (ASM International, 1992)
9. ASM International, Metals Handbook (Desk Edition) Chapter 32 (Failure Analysis), American Society for Metals, (1997) pp. 32–24 to 32–26
10. J. Toribio, Residual stress effects in stress-corrosion cracking. J. Mater. Eng. Perform. **7**(2), 173–182 (1998)
11. C.E. Witherell, in *Aircraft Landing Gear Fracture*, ed. by K.A. Esakul. Handbook of Case Histories in Failure Analysis, vol 1. (ASM International, 1992)
12. J.B. Shah, Corrosion cracking of aircraft components. Met. Eng. Q. **15**(1), 33–39 (1975)
13. C.H. Craft, Failure of aircraft engine crankshaft, *Met. Progress* **98** (5) (1970) as published in Source Book in Failure Analysis, American Society for Metals, (1974), p. 170
14. D.R. Diercks, Analysis of failed nuclear plant components. J. Mater. Eng. Perform. **2**(6), 799–806 (1993)
15. C.J. Czajkowski, in *SCC of a Nuclear Steam-Generator Vessel at Low Concentrations of Chloride Ion*, Failures of Pressure Vessels, Failure Analysis and Prevention, vol 11 (ASM Handbook, ASM International, 1986), pp. 643–669
16. P. Muraleedharan, J.B. Gnanamoorthy, in *Metallurgy Division, Indira Gandhi Centre for Atomic Research, Stress-Corrosion Cracking in a Stainless Steel Emergency Injection Pipe in a Nuclear Reactor*, ed. by K.A. Esakul. Handbook of Case Histories in Failure Analysis, vol 2 (ASM International, 1992)
17. P. Gaewski, *Analysis of Total Cost of Large Diameter Pipe Failrues* (Awwa Research Foundation, 2007)

Chapter 27
Comparative Analysis of Shot-Peened Residual Stresses Using Micro-Hole Drilling, Micro-Slot Cutting, X-ray Diffraction Methods and Finite-Element Modelling

B. Winiarski, M. Benedetti, V. Fontanari, M. Allahkarami, J.C. Hanan, G.S. Schajer, and P.J. Withers

Abstract Micro-Hole Drilling (μHD) and Micro-Slot Cutting (μSC) methods for the measurement of residual stress at the micron scale have recently been proposed but have yet to be evaluated and validated against other methods such as X-ray Diffraction (XRD). In this paper near surface and sub-surface residual stresses were measured in ceramic-shot peened and fatigued Al-7075-T651 double notched samples using μHD and μSC methods, and compared to XRD micro-diffractometer results and Finite-Element (FE) predictions. The micron-seized sampling volumes enabled the stress to be evaluated in individual impact craters (dimples) showing significant point-to-point variation (~±150 MPa) (with certain dimples even recording tensile stresses). At a depth of around 30 μm the heavily deformed region had largely been removed and the stress became much more homogeneous. At this depth the μHD and μSC results were in good accord with those from XRD and FE modelling showing a stress of around 150 MPa far from the notch with stress increasing at the notch being to about 200 MPa for the blunt (2 mm) notch and 500 MPa for the sharp (0.15 mm).

Keywords XRD • FEA • focused ion beam (FIB) micro-slot cutting • FIB micro-hole drilling • Shot-peening

27.1 Introductions

Residual stresses (RS) are induced by almost all manufacturing and surface finishing processes, e.g. plastic forming, casting, welding, friction-stir welding, grinding, polishing, etc. [1]. In many cases they can be neglected but in others they can extend or shorten component lifetimes. For large components they can vary over meter dimensions but they can also be present at the micron scale. Such stresses can significantly affect the performance of thin-films [2, 3], the durability micro-welds of electronic devices [4], mechanical properties of micro/nano-electro-mechanical systems (MEMS/NEMS) [5], etc.

For many years residual stresses have been evaluated by a variety of destructive (hole-drilling (HD) [6], slitting technique (SC) [7], contour methods (CM) [8], etc.) and non-destructive (X-ray diffraction (XRD) $\sin^2\psi$ method [9], synchrotron and neutron diffractions [10], Raman, ultrasonic, magnetic, etc., see [11]) residual stress measurement methods. The most common, well-established and reliable techniques for RS evaluation are the hole-drilling, slitting technique, and X-ray diffraction which usually show good agreement [12]. Discrepancies can arise because of spurious peak shifts associated with changes in strain free lattice spacing, geometrical effects on entering/exiting the surface or elastic/plastic anisotropy effects on the diffraction side [13] or plasticity effects associated with material removal [12, 14]. Experiments show that when the residual stresses exceed 60–70 % of the materials yield's strength, the plasticity incurred using HD can cause stresses to be

B. Winiarski (✉)
School of Materials, University of Manchester, Manchester M13 9PL, UK

FEI Company, Achtseweg Noord 5, Bldg 5651 GG, Eindhoven, The Netherlands
e-mail: b.winiarski@manchester.ac.uk

M. Benedetti
Department of Industrial Engineering, University of Trento, Trento, Italy

V. Fontanari • M. Allahkarami • J.C. Hanan
Department of Mechanical and Aerospace Engineering, Oklahoma State University, Tulsa, OK, USA

G.S. Schajer
Department of Mechanical Engineering, University of British Columbia, Vancouver, BC, Canada

P.J. Withers
School of Materials, University of Manchester, Manchester M13 9PL, UK

S. Bossuyt et al. (eds.), *Residual Stress, Thermomechanics & Infrared Imaging, Hybrid Techniques and Inverse Problems, Volume 9*, Conference Proceedings of the Society for Experimental Mechanics Series, DOI 10.1007/978-3-319-21765-9_27

overestimated 8–15 % [12, 14]. The SC method is less sensitive to yielding, particularly if the cuts are shallow with respect to the sample thickness [15].

There is currently a strong interest in quantifying the local residual stresses (RS) in variety of amorphous and crystalline components and micro-devices by Micro-Hole Drilling (μHD) [16–18], Micro-Slot Cutting (μSC) [19–22] and other [23–26] mechanical relaxation methods scaled down to the micron scale using Scanning Electron Microscope-Focused Ion Beam (SEM-FIB) dual beam systems. Applying μHD and μSC methods at the same measuring point for amorphous materials leads to fairly consistent results [18, 19]. An attempt has been made to compare the performance of SEM-FIB ring-core method for crystalline thin film chromium nitride against X-ray diffraction (XRD) $\sin^2\psi$ method [26]. Here the analyses shows somewhat comparable results (qualitative) of the both methods when taking into account residual stresses >4 GPa, RS gradients in the film, and highly anisotropic crystal elastic properties [27], which are not normally considered using the ring-core method. Our recent work on mapping intragranular residual stresses by the micro-slotting method shows that cubic crystals with low elastic anisotropy (Zener ratio <1.5) can be accurately measured assuming isotropic elastic properties in the stress calculation procedures [22].

The present experimental study is intended to investigate the reliability of the μHD and μSC methods for measuring ceramic-shot peened and fatigued residual stresses compared to micro-diffractometer XRD and finite-element simulations as reported in [27–30]. The residual stress field in the vicinity of the notch of ceramic-shot peened fatigue specimens was measured. For the purpose of this study we choose fairly isotropic Al-7075-T651 (Zener ratio <1.5 [22]) with the maximum residual stresses much lower than the yield strength of material (515 MPa) [30]. This allowed us to minimise sources of errors related to the plasticity effect and the anisotropy of elastic properties. The effects of the notch shape, ceramic-shot peening on the residual stress field are presented and discussed in details in our accompanying paper [29], whereas the fatigue aspects are presented in [27].

27.2 Materials and Methods

An 4 mm thick rolled plate of aeronautical grade aluminium alloy Al-7075-T651 [27, 29] was used in these investigations. Plain and double notch shape specimens were electro-discharge machined (EDM) from the plate (Fig. 27.1) according to the ISO 3928 standard, with the notch fillet radius R of 2 mm (blunt notch), 0.5 and 0.15 mm (sharp notch).

Both sides and the notch regions of the central parts of specimens were shot-peened at 90° impingement angle using small ceramic (ZrO_2 and SiO_2) beads of 60–120 μm diameter and Almen intensity of 4.5 N; details of the experimental setup are presented in [30, 31]. This treatment leads to a gentle and near surface RS profile, giving higher fatigue performance as compared with that peened using larger shots [32, 33].

Three sets of XRD measurements were carried out on plain samples to investigate the in-depth residual stress profile, as reported in [27]. For this purpose, an AST X-Stress 3000 X-ray diffractometer operated with Cr Kα radiation was used. The region of interest was limited by a collimator to 1 mm^2 in area. Depth profiling was conducted step-by-step by removing a very thin layer of material in a 2 mm × 2 mm region by electropolishing. The classical $sin^2\psi$ method was applied using of 9 ψ angles between −45° and +45° for each measurement. The<311>diffracting planes were chosen (i) in order to obtain

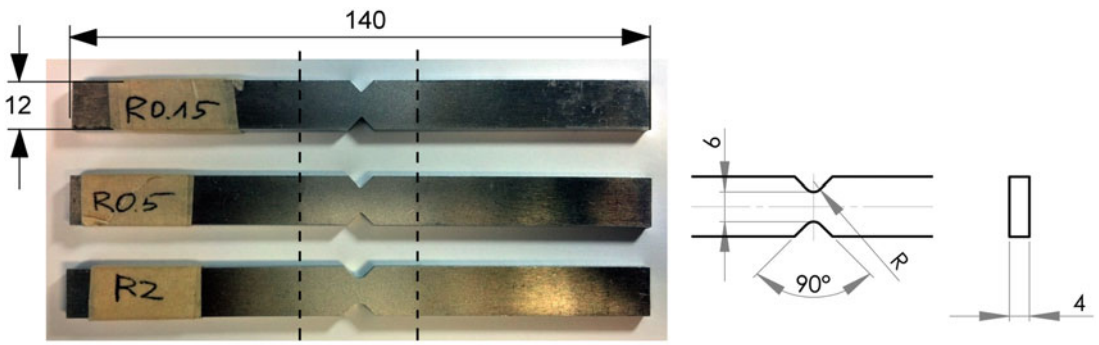

Fig. 27.1 Geometry of specimens and locations of shot-peened areas (between *dashed lines*)

high angle measurements (2θ angle 139.0°) with higher strain sensitivity, and (ii) because they do not accumulate significant intergranular stresses and hence exhibit similar behavior to that of the bulk.

Subsequently, load-controlled cyclic ($R = 0.05$) 4-point bending tests were carried out under ambient conditions; as reported in [27]. Tests were undertaken at the stress level of $\sigma_{max} = 240$ MPa and 10^8 cycles with a nominal frequency of 110 Hz using a resonant testing machine (Rumul Mikrotron 20 kN) equipped with a 1 kN load cell.

The residual stress field was reconstructed in the companion paper [29] on the basis of experimental measures. For this purpose, a FE model of the notched samples has been set up with the ANSYS 15 commercial code using 8 nodes isoparametric brick elements. In order to take advantage of the symmetry, only one eighth of the specimen has been modelled. The mesh in the surface region was particularly refined with the purpose of better reproducing stress and strain gradients in the hardened layer due to the peening treatment. The minimum thickness of the elements in the surface region was 10 μm.

Next, μXRD measurements were carried out on notched specimens to map the residual stress field in the X-direction in the vicinity of the notch root along the line between the two notch roots (as shown in Fig. 27.2b). This was done using a Bruker's D8 Discover XRD2 micro-diffractometer (Fig. 27.2a) equipped with General Area Diffraction Detection System (GADDS) and Hi-Star 2D area detector. Tube parameters of 40 kV/40 mA using Cu-Kα radiation at a detector distance of 30 cm were used. This setting covers approximately the area of 20° in 2θ and 20° in γ with 0.02° resolution was used. A motorized five axis (X, Y, Z (translation), ψ (tilt), φ (rotation)) stage was used giving 12.5 μm position accuracy and 5 μm repeatability. The gauge area was limited using an 800 μm pinhole collimator. Exposure time per frame was 120 s. For the given angular resolution of 0.01°, a residual stress with magnitude of ±1.04 MPa was measured. The surface residual stress profile between the two notches was mapped through 11 measurements spaced 50 μm apart starting from the notch tip (Fig. 27.2b). The penetration depth of Cu K_α is about 40 μm, thus each XRD measurement gives an average values of the RS over this depth, as reported in [27, 31].

After XRD measurement the longitudinal stress was mapped at the same locations using SEM-FIB Micro-Hole Drilling and Micro-Slot Cutting methods directly on the as-peened surface and about 30 μm below the peened surface after polishing away the top surface. These measurements were performed using a FEI Nova NanoLab 600i Dualbeam SEM-FIB microscope with digital image correlation of Pt features. Since the residual stress profile changes with the depth from the surface (reported in [27, 33]), the second set of measurements are designed to sample at the same depth as that probed by XRD. This is important because the slotting and hole drilling measurements sample much smaller gauge volumes than XRD (μHD:5 × 5 × 0.5 μm^3 and μST 30 × 30 × 5 μm^3 [19] compared with 800 × 800 × 40 μm for XRD).

To reduce the rate of re-deposition of the excavated material, improve the topographic contrast and prevent overexposure to Ga+ [18, 19, 34] when FIB milling we used a Gatan PECS 682 etching-coating system equipped with a Gatan 681.20000 thickness metre to sputter a ~10 nm-thick carbon film on the specimen surface prior to FEGSEM imaging and FIB milling. The carbon target was exposed to a broad argon-ion beam of the current of 550 μA accelerated with the electric potential of 10 kV in a vacuum environment of ~2 × 10–5 Torr.

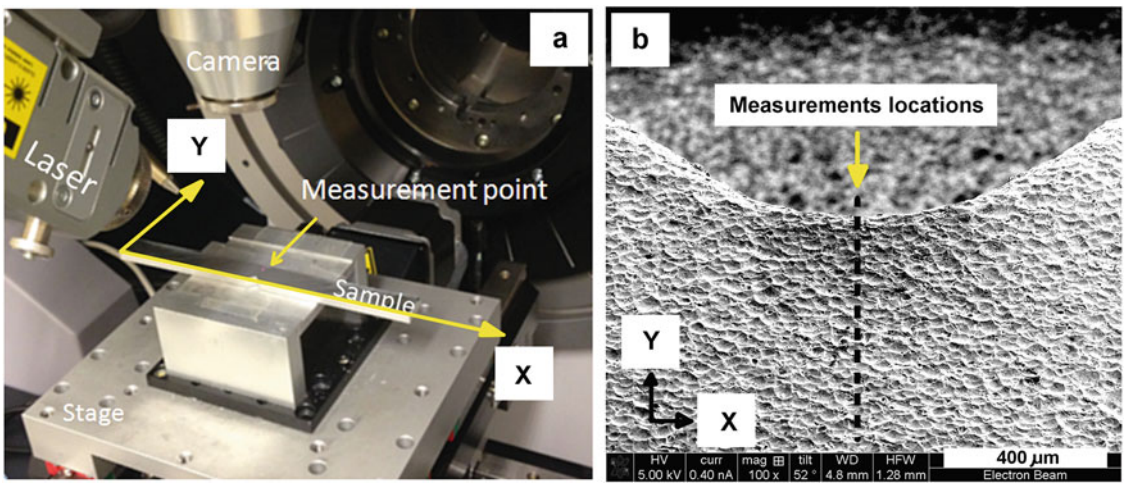

Fig. 27.2 (**a**) XRD2 micro-diffractometer used to map the residual stress line profile in the notch specimen along the notch bisector [27]; (**b**) SEM image showing the measurement locations

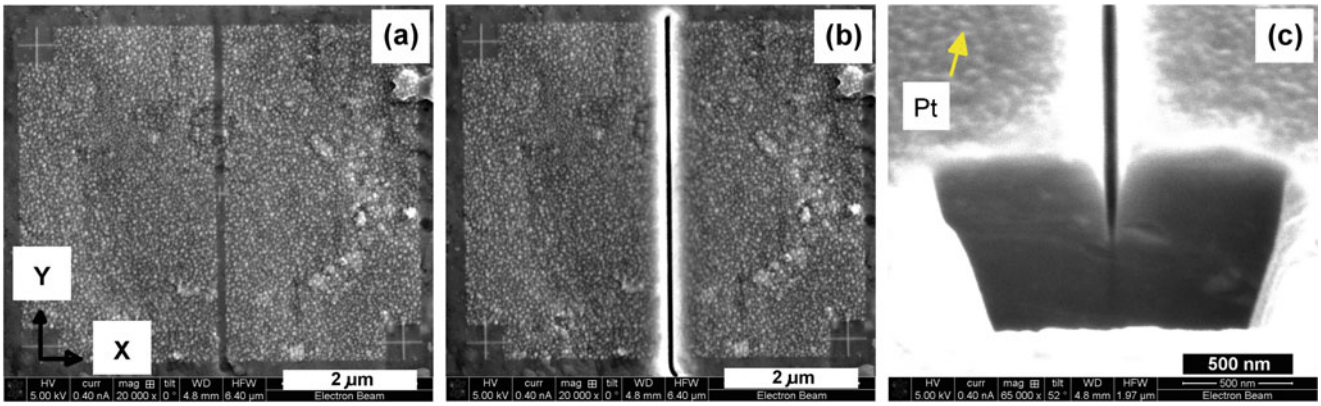

Fig. 27.3 FEGSEM images show patterned area before (**a**) and after (**b**) micro-slotting. The slot size is 6 × 0.6 × 0.1 µm^3. The actual slot depth is measured from an end trench FIBed after slotting (**c**)

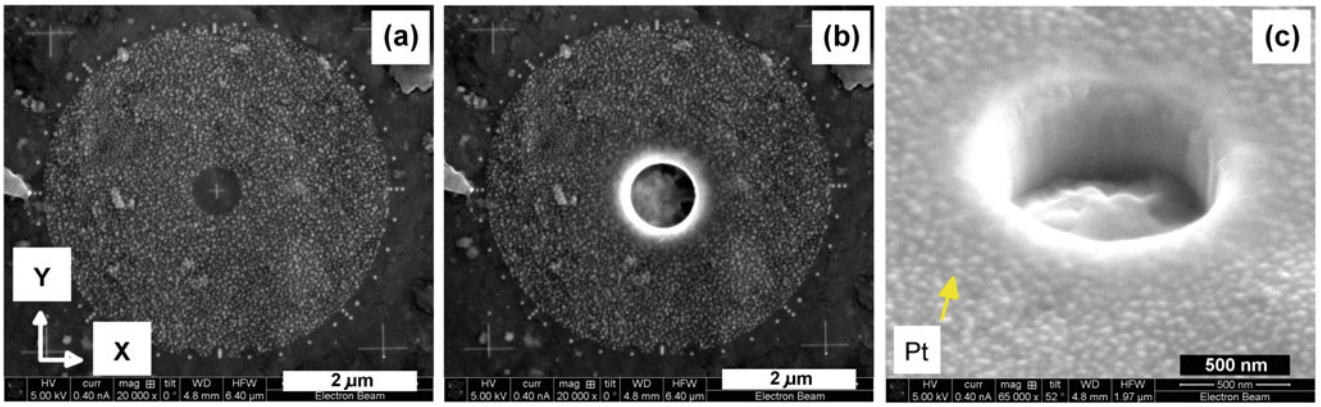

Fig. 27.4 FEGSEM images show patterned area before (**a**) and after (**b**) micro-hole milling. The hole is 1 µm diameter and 0.5 µm deep as measured from SEM image taken at oblique angle (**c**)

Next, platinum (Pt) nano-dots (diameter ~20 nm) were laid down as illustrated in Figs. 27.3 and 27.4. The Pt nano-dots enhance the topological contrast of FEGSEM imaging and improve the accuracy of DIC displacement/strain measurement [34].

A series of 6 × 0.5 × 0.1 µm^3 micro-slots (depicted in Fig. 27.3b) and then 1 µm diameter by 0.5 µm deep micro-holes of (depicted in Fig. 27.4b), spaced about 4–5 times the slot length, were milled (48 pA at 30 kV) along the notch bisector near the notch root (as shown in Fig. 27.2b). A sequence of FEGSEM images (D_t = 3 µs, 8 frames averaged, ETD detector) of the patterned areas were then acquired at 0° stage tilt before (Figs. 27.3a and 27.4a) and after milling (Figs. 27.3b and 27.4b). The dimensions of the holes and slots were selected so, that the gauge volumes are similar.

After milling each slot, an end trench is milled at 52° stage tilt in order to monitor the depth and shape of each FIB-processed slot (Fig. 27.3c), whereas the actual hole depths were measured from FEGSEM directly after hole milling (Fig. 27.4c). Monitoring the depth is important because it is not possible to excavate deep micro-slots having perfectly rectangular walls, and the predefined slot depth may vary substantially from the actual depth since the FIB milling rate depends both on the material milled and its crystallographic orientation [35]. Later FEGSEM images and the actual shapes of slot and holes were used in the automated stress calculation algorithms for the µSC [19, 22] and µHD [17] methods using LaVision Davis 8.1 DIC to calculate full-field 2D displacements in the stress estimations. Based on arguments in [22] isotropic elastic properties (E = 73 GPa, ν = 0.33) were used in these calculations.

After the measurements on the top surface, the samples were polished using sand papers (800, 1200, 2500), aqueous silica suspensions (9, 6, 3, 1, 0.25 µm) and finally 0.05 µm colloidal silica. Then the samples were cleaned in ethanol. After drying the samples were carbon coated and the µHD and µSC measurements were repeated at the same locations.

27.3 Results and Discussion

The longitudinal residual stress (σ_{xx}) variation with the depth from the bead-pinned surface measured by AST X-Stress 3000 X-ray diffractometer has a typical peened shape with the peak of compressive stresses at a depth about 15 μm (in Fig. 27.5).

When taking in to consideration that the D8 Discover XRD2 averages the residual stresses over about 40 μm depth is it clear from Fig. 27.5 that this average residual stress is close both to the RS measured at the surface and RS measured at depth of about 30 μm. This implies that RS determined by micro milling, where the depth is a micron or so, should be similar to that from XRD if measured at a depth of about 30 μm.

Figure 27.6 shows comparison between residual stress profiles along the notch bisector inferred by FE simulations, XRD measurements and the micro-milling methods for two samples notch radii of 0.15 and 2 mm. The results for 0.5 mm notch are presented in our companion paper [29], and herein are omitted for space saving reason. For the sharp notch there is fairly good agreement between FE and XRD measurements up to 300 μm from the notch root. The detailed analyses of the role of the residual stress field ahead of the notch root is beyond of the scope of this paper and can be found elsewhere [27, 31]. The micro-milling methods display large variations of residual stress results. Taking into account the complex deformation state introduced by the impact of individual 60–120 μm shot [36] it is not surprising that the residual stresses are heterogeneous very close to the surface.

While bead-peened surfaces are typically much smoother than shot peened ones [30, 31], these surfaces have considerable surface roughness with pattern of overlapping dimples, see Fig. 27.7. The surface roughness determines the locations where micron-size slots/holes can be introduced. In this case, micro-slots and micro-holes were introduced at the bottom of dimples on a concave surface, as shown in Fig. 27.7, spaced apart at least 4–5 times the slot length. In several locations the dimples were too small to accommodate two measurement points, thus these were milled in the adjacent dimples (see Fig. 27.7b).

Inspections of the surface also reveal a network of surface cracks (marked with chequered arrows in Fig. 27.7). Subsurface investigation by FIB cross-sectioning in the vicinity of one of the cracks clearly shows that cracks propagate and branch below the surface to a depth of at least 6 μm where distinctive material deformation patterns could be observed; as illustrated in Fig. 27.8c. Multiple voids of size of hundreds of nm and light grey Al_2CuMg eutectic phase precipitates are observed as well; depicted in Figs. 27.3c and 27.8c. Bearing in mind the heterogeneous and damaged topography (Fig. 27.8) and the means by which it was introduced the scatter in the surface micro-milling measurements is not surprising. Indeed the micron sized footprints of the slots and holes have enabled a measure the heterogeneity in residual stress (~±150 MPa) at the surface to be quantified for the first time.

Given the microstructure of the dimples one would expect by St Venant's principle the microstresses to decay quickly with distance from the surface to give the long range stress field typically sampled by XRD. We found that by electropolishing to a depth of ~30 μm it was possible to remove the highly deformed and defective layer to obtain a

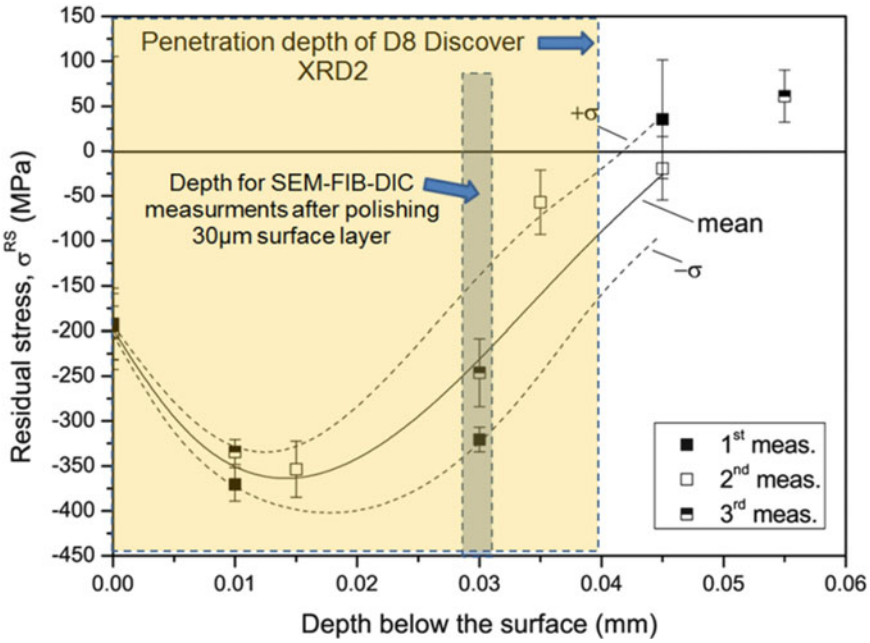

Fig. 27.5 Depth profile of residual stress in bead-pinned Al-7075-T651 measured by AST X-Stress 3000 X-ray diffractometer [29]

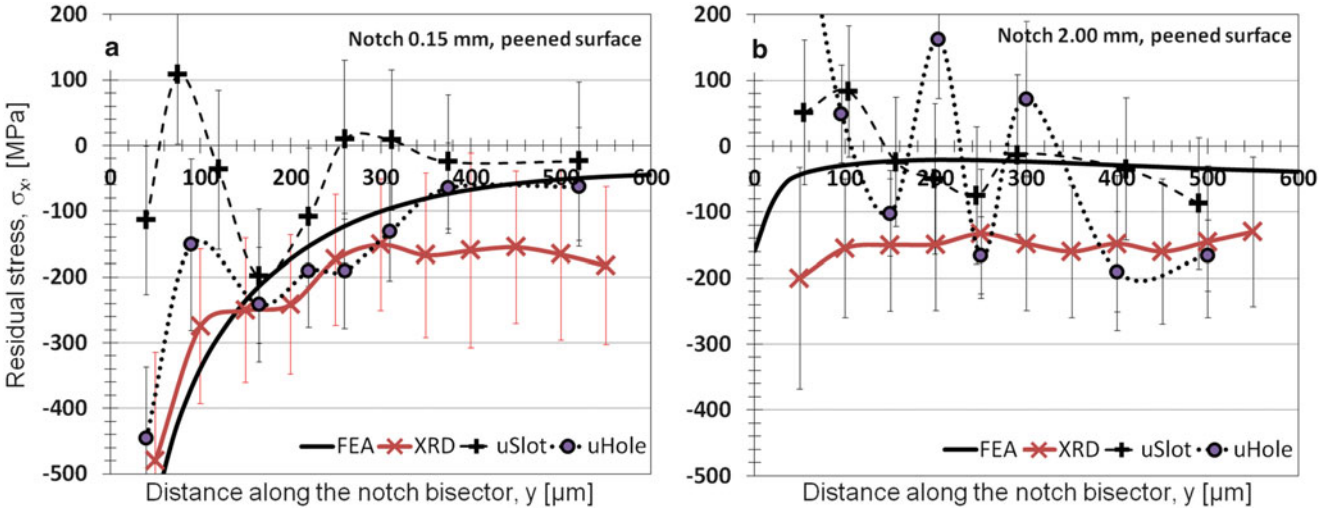

Fig. 27.6 Comparison between stresses (σ_{xx}) measured at the peened surface (1 μm depth) by μHD and μSC as well as those sampled over the penetration depth (~40 μm) by XRD alongside numerical (FE) predictions for peened samples with (**a**) a 0.15 mm and (**b**) a 2 mm notch radius

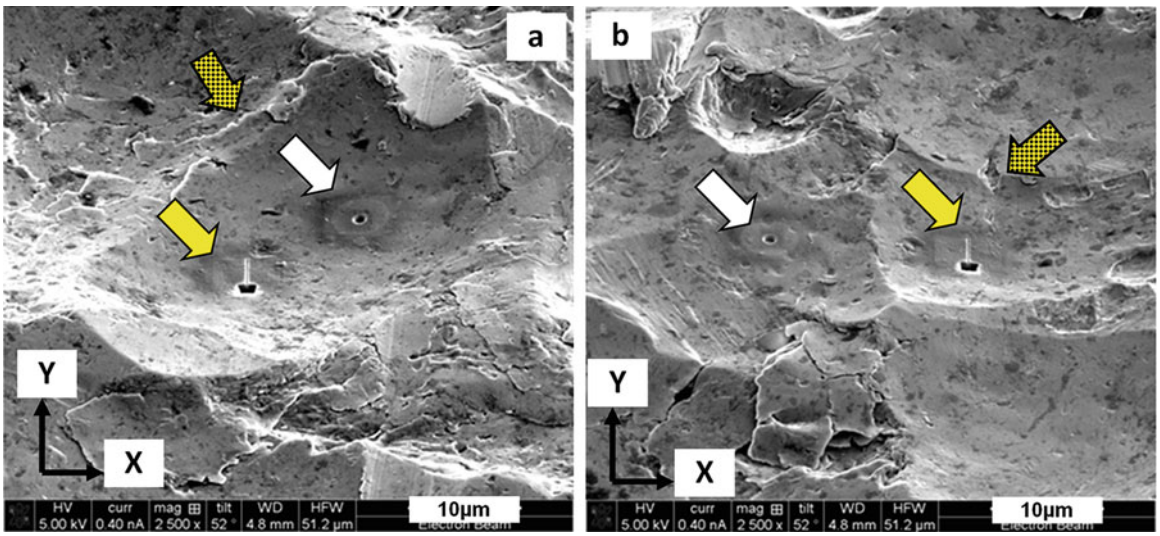

Fig. 27.7 FEGSEM images show micro-slot of size 6 × 0.6 × 0.1 μm^3 (*yellow arrows*) and micro-hole of 1 μm diameter and 1 μm deep (*white arrows*) introduced at the bottom of bead-peened dimple: (**a**) in the same dimple, (**b**) in adjacent dimples. Note end trenches milled for each slot. *Chess-patterned arrows* indicate surface cracks

smooth surface. Figure 27.9c shows FEGSEM images FIB-ed cross-section near a micro-slot on the polished surface. The cross-section reveals little evidence of damage of severe plasticity with uniformly distributed Al_2CuMg precipitates and large aluminium grains. The residual stress profiles measured at 30 μm below the peened layer are presented in Fig. 27.10.

As one might expect the micro-milled stress profiles are now much smoother and are in good agreement with the XRD measurements which are representative of a similar depth. The scatter measured for the μSC and μHD is associated with three factors: (a) the relatively small gauge volume of both methods, which is similar to, or smaller than, the grain size. RSs varies from grain to grain (as recently measured by the μSC in [22]); (b) each grain is elastically anisotropic and this has not been accounted for here (c) the Al_2CuMg eutectic phase precipitates are twice as stiff as the Al-rich matrix [37], and these are not taken into account in RS estimates. Since the Al-rich grains are fairly isotropic (the Zener ratio is 1.2 [22]) thus (a) and (b) may have small impact on the RSs scatter (discussed in details in [22]). The large Al_2CuMg precipitates are of the comparable size particularly to the micro-hole, thus the effective elastic modulus in the gauge volume is different than the matrix material and measurement taken from the immediate vicinity of large participate can be considerable altered [22].

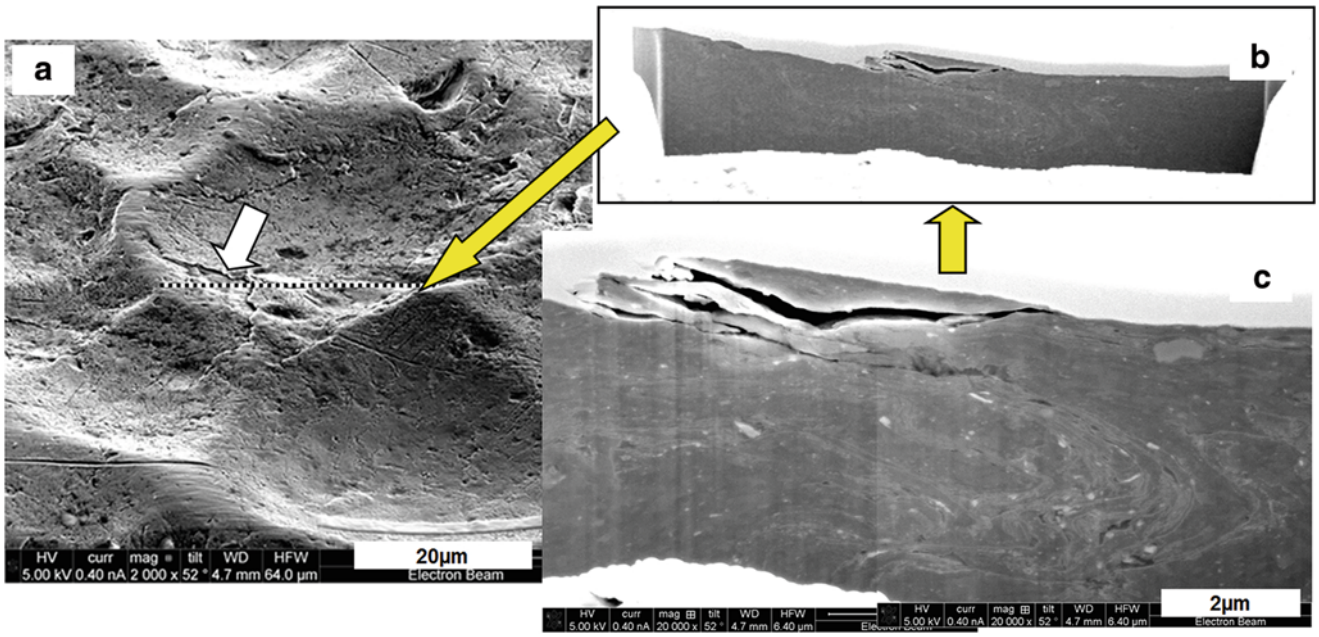

Fig. 27.8 FEGSEM images show surface cracks (**a**) and FIBed cross-section that reveals the scale of sub-surface damage, (**b**, **c**), caused by the peening treatment. Note *light grey areas* are Al_2CuMg precipitates

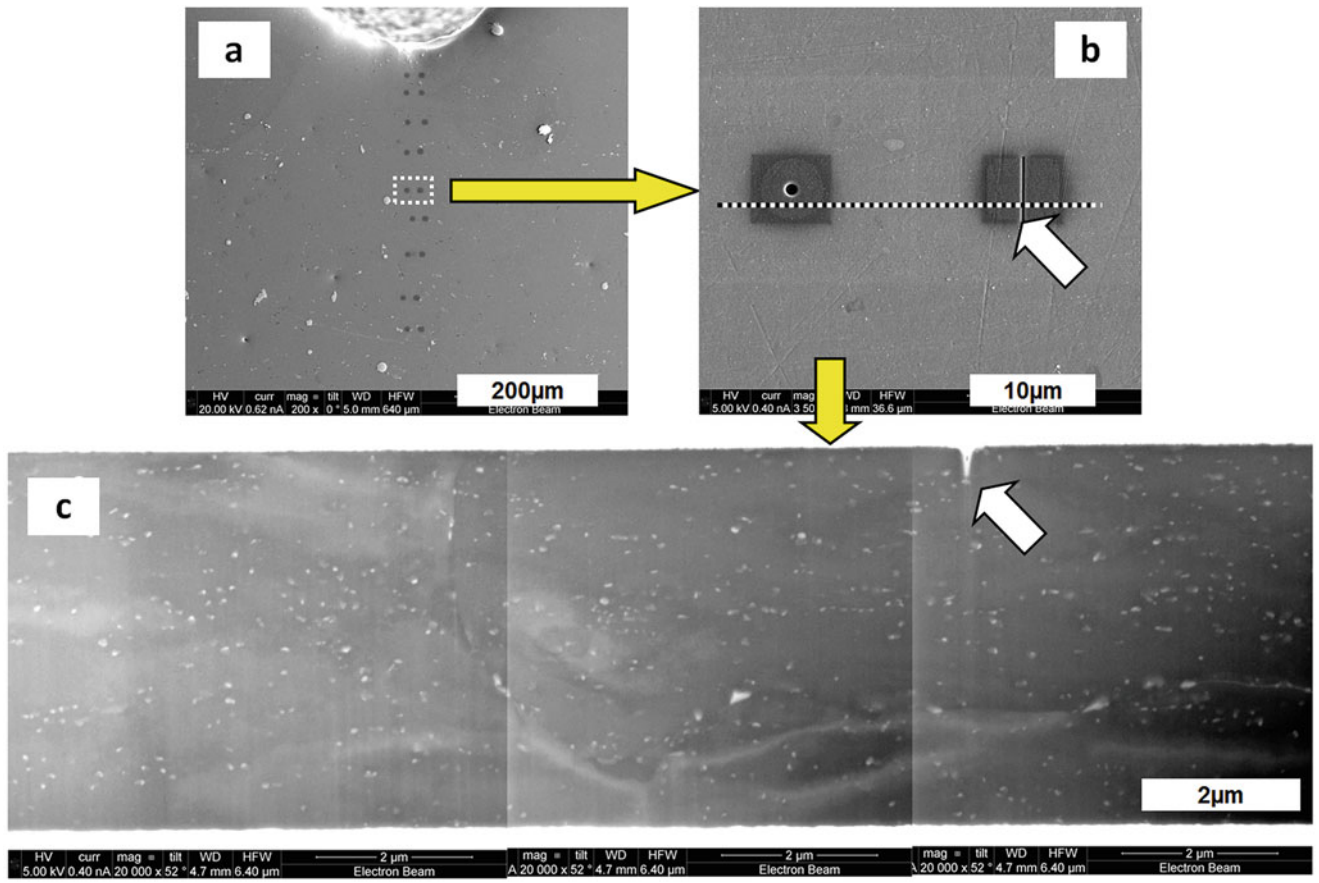

Fig. 27.9 FEGSEM images show polished surface of R0.15 specimen with SEM-FIB-DIC measurement locations (**a**, **b**), and FIBed cross-section that reveals sub-surface severe-damage-free microstructure near a micro-slot (**c**). Note *light grey areas* are Al_2CuMg precipitates

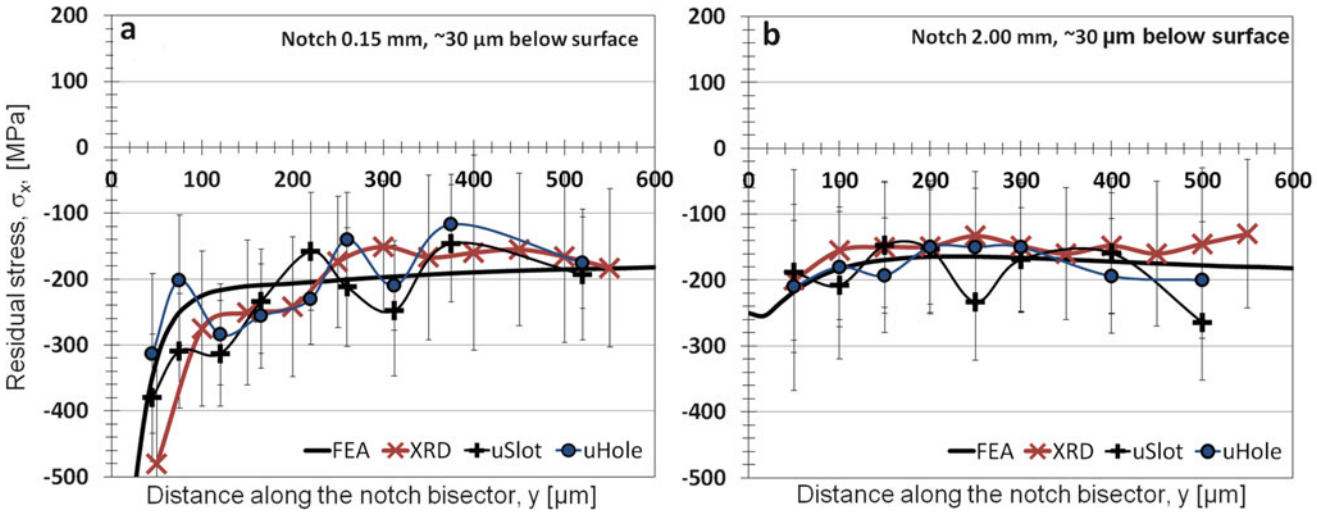

Fig. 27.10 Comparison between experimentally measured ~30 µm below the surface (for µSC and µHD) and numerically predicted residual stress distribution along the notch bisector: (**a**) the notch radius 0.15 mm and (**b**) 2 mm

27.4 Conclusions

In this paper, a comparison between XRD, FE, and SEM-FIB-DIC micro-hole drilling and micro-slotting residual stress measurement methods has been performed. The µHD and µSC methods have much smaller measurement volumes that the X-ray diffraction. Consequently it was possible for the first time to record the heterogeneity of residual stresses (±150 MPa) in the overlapping dimples caused by the shot impacts material. The stress is much more homogeneous at a depth of 30 µm giving much smoother µHD and µSC profiles. While these are still affected by scatter they compare well XRD measurements.

The analysis of the measurement clearly showed that the most critical factors to be considered when planning and performing the experimental measurements using the SEM-FIB-DIC based methods are:

(a) *the size of representative gauge volume and its microstructural features*. In cases where, the gauge volumes are of the same size inclusions, precipitates, etc. the residual stress estimates can be significantly altered if their different elastic properties are not accounted for in the analyses. For micron-size gauge volumes elastic anisotropic behaviour of a specimen is dominant, therefore the proper choice of the elastic modulus to be used for stress evaluations in the SEM-FIB-DIC methods represents an additional source of error. Further the gauge volumes could be corrupted by existence of micro-cracks, voids, thus generating misleading stress estimates.

(b) *the depth of penetration with respect to the stress gradients*. µSC and µHD methods average residual stress over the excavated depth (the penetration depth). Therefore the results obtained by these methods can be directly compared for the same penetration depth. Alternatively, for different penetration depths the incremental variants of micro-hole drilling and micro-slotting methods, i.e. IµSC [21] and IµHD [18], can be used.

References

1. P.J. Withers, H. Bhadeshia, Overview—residual stress part 2—nature and origins. Mater. Sci. Technol. **17**(4), 366–375 (2001)
2. R. Daniel, J. Keckes, I. Matko, M. Burghammer, C. Mitterer, Origins of microstructure and stress gradients in nanocrystalline thin films: the role of growth parameters and self-organization. Acta Mater. **61**(16), 6255–6266 (2013)
3. M. Sebastiani, E. Bemporad, F. Carassiti, On the influence of residual stress on nano-mechanical characterization of thin coatings. J. Nanosci. Nanotechnol. **11**(10), 8864–8872 (2011)
4. A.B. Horsfall, J.M.M. dos Santos, S.M. Soare, N.G. Wright, A.G. O'Neill, S.J. Bull, A.J. Walton, A.M. Gundlach, J.T.M. Stevenson, Direct measurement of residual stress in sub-micron interconnects. Semicond. Sci. Technol. **18**(11), 992–996 (2003)
5. N. Sabate, D. Vogel, A. Gollhardt, J. Keller, C. Cane, I. Gracia, J.R. Morante, B. Michel, Measurement of residual stress by slot milling with focused ion-beam equipment. J. Micromech. Microeng. **16**(2), 254–259 (2006)
6. G.S. Schajer, Advances in hole-drilling residual stress measurements. Exp. Mech. **50**(2), 159–168 (2009)

7. G.S. Schajer, M.B. Prime, Residual stress solution extrapolation for the slitting method using equilibrium constraints. J. Eng. Mater. Technol. Trans. ASME **129**(2), 227–232 (2007)
8. M.B. Prime, *The contour method: simple 2-D mapping of residual stresses American Society of Mechanical Engineers,* vol 415 (Pressure Vessels and Piping Division (Publication) PVP, 2000), p. 121–127
9. I.C. Noyan, J.B. Cohen, *Residual Stress—Measurement by Diffraction and Interpretation* (Springer, New York, 1987)
10. P.J. Withers, Depth capabilities of neutron and synchrotron diffraction strain measurement instruments. II. Practical implications. J. Appl. Crystallogr. **37**, 607–612 (2004)
11. G.S. Schajer, *Practical Residual Stress Measurement Methods.* (Wiley, Chichester, 2013)
12. J.P. Nobre, M. Kornmeier, A.M. Dias, B. Scholtes, Comparative analysis of shot-peening residual stress using hole drilling and x-ray diffraction methods. Mater. Sci. Forum **347–349**, 138–143 (2000)
13. M.T. Hutchings, P.J. Withers, T.M. Holden, T. Lorentzen, *Introduction to the Characterisation of Residual Stresses by Neutron Diffraction* (CRC Press, London, 2005)
14. M. Beghini, L. Bertini, P. Raffaelli, Numerical analysis of plasticity effects in the hole-drilling residual-stress measurement. J. Test. Eval **22**(6), 522–529 (1994)
15. M.B. Prime, Plasticity effects in incremental slitting measurement of residual stresses. Eng. Fract. Mech. **77**(10), 1552–1566 (2010)
16. B. Winiarski, P.J. Withers, Mapping residual stress profiles at the micron scale using FIB micro-hole drilling. Appl. Mech. Mater. **24–25**, 267–272 (2010)
17. G.S. Schajer, B. Winiarski, P.J. Withers, Hole-drilling residual stress measurement with artifact correction using full-field DIC. Exp. Mech. **53**(2), 255–265 (2013)
18. B. Winiarski, P.J. Withers, Micron-scale residual stress measurement by micro-hole drilling and digital image correlation. Exp. Mech. **52**(4), 417–428 (2012)
19. B. Winiarski, R.M. Langford, J. Tian, Y. Yokoyama, P.K. Liaw, P.J. Withers, Mapping residual-stress distributions at the micron scale in amorphous materials. Metall. Mater. Trans. A **41**, 1743–1751 (2009)
20. B. Winiarski, G. Wang, X. Xie, Y. Cao, Y. Shin, P.K. Liaw, P.J. in *Proceedings of MRS Fall Meeting,* Withers, Mapping Residual-Stress Distributions in a Laser-Peened Vit-105 Bulk-Metallic Glass Using the Focused-Ion-Beam Micro-Slotting Method, Boston, 29 November–3 December 2010, (2011)
21. B. Winiarski, A. Gholinia, J. Tian, Y. Yokoyama, P.K. Liaw, P.J. Withers, Submicron-scale depth profiling of residual stress in amorphous materials by incremental focused ion beam slotting. Acta Mater. **60**(5), 2337–2349 (2012)
22. B. Winiarski, P.J. Withers, in *Proceedings of the SEM 2014 Annual Meeting & Exposition on Experimental and Applied Mechanics,* Mapping stresses within Grains by the Micro-slot Cutting Method, Hyatt Regency Greenville, Greenville, 2–5 June 2014
23. S. Massl, J. Keckes, R. Pippan, A new cantilever technique reveals spatial distributions of residual stresses in near-surface structures. Scr. Mater. **59**(5), 503–506 (2008)
24. S. Massl, H. Kostenbauer, J. Keckes, R. Pippan, Stress measurement in thin films with the ion beam layer removal method: influence of experimental errors and parameters. Thin Solid Films **516**(23), 8655–8662 (2008)
25. M. Sebastiani, C. Eberl, E. Bemporad, G.M. Pharr, Depth-resolved residual stress analysis of thin coatings by a new FIB-DIC method. Mater. Sci. Eng. A **528**(27), 7901–7908 (2011)
26. E. Bemporad, M. Brisotto, L.E. Depero, M. Gelfi, A.M. Korsunsky, A.J.G. Lunt, M. Sebastiani, A critical comparison between XRD and FIB residual stressmeasurement techniques in thin films. Thin Solid Films **572**, 224–231 (2014)
27. Y. Liang, X. Yuan, W. Zhang, The effect of magnetostructural coupling on mechanical behaviors in CrN. Solid State Commun. **150**(41–42), 2045–2048 (2010)
28. M. Benedetti, V. Fontanari, M. Allahkarami, J.C. Hanan, in *SEM Annual Conference and Exposition*, Notch Fatigue Behaviour of Shot Peened High-strength Aluminium Alloys: Role of the Residual Stress Field Ahead of the Notch Root, SEM, SEM: Greenville, 2014
29. M. Benedetti, V. Fontanari, M. Allahkarami, J.C. Hanan, B. Winiarski, P.J. Withers, P.J. in *Proceedings of the SEM 2015 Annual Conference & Exposition on Experimental and Applied Mechanics,* Modelling the Residual Stress Field Ahead of the Notch Root in Shot Peened V-Notched Samples, Costa Mesa, 8–11 June 2015
30. M. Benedetti, V. Fontanari, P. Scardi, C.L.A. Ricardo, M. Bandini, Reverse bending fatigue of shot peened 7075-T651 aluminium alloy: the role of residual stress relaxation. Int. J. Fatigue **31**(8–9), 1225–1236 (2009)
31. M. Benedetti, V. Fontanari, C. Santus, M. Bandini, Notch fatigue behaviour of shot peened high-strength aluminium alloys: experiments and predictions using a critical distance method. Int. J. Fatigue **32**(10), 1600–1611 (2010)
32. K. Oguri, Fatigue life enhancement of aluminum alloy for aircraft by Fine Particle Shot Peening (FPSP). J. Mater. Process. Technol. **211**(8), 1395–1399 (2011)
33. M. Benedetti, V. Fontanari, M. Bandini, E. Savio, High- and very high-cycle plain fatigue resistance of shot peened high-strength aluminum alloys: the role of surface morphology. Int. J. Fatigue **70**, 451–462 (2015)
34. B. Winiarski, G.S. Schajer, P.J. Withers, Surface decoration for improving the accuracy of displacement measurements by digital image correlation in SEM. Exp. Mech. **52**(7), 793–804 (2012)
35. M. Nastasi, J.W. Mayer, *Ion Implantation and Synthesis of Materials* (Springer, Berlin, 2006)
36. G.H. Majzoobi, R. Azizi, A. Alavi Nia, A three-dimensional simulation of shot peening process using multiple shot impacts. J. Mater. Process. Technol. **164–165**, 1226–1234 (2005)
37. J. Zhang, Y.N. Huang, C. Mao, P. Peng, Structural, elastic and electronic properties of θ (Al2Cu) and S (Al2CuMg) strengthening precipitates in Al–Cu–Mg series alloys: first-principles calculations. Solid State Commun. **152**(23), 2100–2104 (2012)

Chapter 28
Thermal Deformation Analysis of an Aluminum Alloy Utilizing 3D DIC

Jarrod L. Smith, Jeremy D. Seidt, and Amos Gilat

Abstract The thermally induced behavior of a 6000 series Aluminum Alloy is investigated in this study. The objective of this experiment is to replicate the deformation and the heating cycles a sheet of the Aluminum Alloy is subjected to during production. Various surface strains are achieved by introducing the sample geometries to different loading conditions. Axial strains are induced in thin flat dogbone specimens via static tension tests with varying displacement. In addition, bending strains are generated in thin flat rectangular specimens via a three point bend test with varying punch radii. The specimens are then placed in a furnace with a heat cycle that ranges from 130 to 190 °C. Three dimensional digital image correlation is used to measure the surface strain during the initial deformation and heating cycle for all experiments. The resulting surface strain and temperature data is used to investigate the effect of temperature and initial strain on the permanent thermally-induced strain from the heating cycle.

Keywords 3D-DIC • Thermal deformation • Residual strain • Thermal buckling • Aluminum

28.1 Introduction

Competition throughout the automotive industry has been a driving force for research and modification of manufacturing processes. Recently the focus of the industry has been centered on reducing the weight of each vehicle to increase the fuel efficiency, improve driving performance, and meet the meet the strict requirements of energy saving and environmental protection outlined by governing bodies [1]. To accomplish these goals considerable efforts were taken to replace the steel body panels of cars with aluminum. An estimated 50 % total energy savings from production to end of service life was obtained for every 20 t of steel replaced by 1 t of aluminum [2]. Initially, several car manufacturers selected 2000 series aluminum-copper alloys for the outer body of the car while Magnesium-based 5000 series aluminum alloys is used for the inner body elements of each vehicle [3]. However, the 2000 series alloys were incompatible with the 5000 series alloys in recycling processes due to their differences in composition. Also, the 2000 series alloys strain hardened during paint-bake heating cycle of 180 °C for 30 min while the 5000 series alloys experienced softening effects. A new Magnesium-Silicon based Aluminum 6000 series alloy with was developed to assist in recycling compatibility while retaining paint-bake strengthening properties [1]. As the need for weight reduction has increased, the thickness of the 6000 series alloys sheets has decreased dramatically creating a need for better understanding the response of the sheet to prestrained conditions, differences in paint-bake cycle, and the boundary conditions emplaced on the sheet during assembly. The behavior of several 6000 series aluminum alloy sheets during the paint-bake cycle has been simulated by several researchers to better understand the mechanical property changes of the material. Balderach et al. [4] cold rolled three different Al-Mg-Zn alloys to a sheet thickness 4.1 mm and subjected the tension and disk samples to four different types of aging treatments combining natural and artificial aging. After heat treatment the samples were subjected to Vicker's hardness, tension, and differential scanning calorimetry tests. Samples subjected to the paint-bake cycle of 175 °C for 30 min were found to have an increase in ultimate tensile strength and hardness when compared with the solution-treated condition. Natural aging of the samples for 1 year after the simulated paint-bake cycle increased the hardness and ultimate tensile strength by 41–78 %. Zhen and Kang [5] studied the effects of pre-aging on two Al-Mg-Si alloys under a paint-bake condition. After cold rolling the specimens were solution treated and then quenched at room temperature. Each set of specimens was then subject to either a natural aging for three months, a pre-aged condition at 150 °C for 5 min or a combination of the two and then half were subjected to the 180 °C simulated paint-bake cycle for 30 min. The yield strength of each alloy was increased by the paint-bake cycle but the greatest increase came from samples that were pre-aged due to the increase in density of precipitates. Birol [6] prepared uniaxial

J.L. Smith (✉) • J.D. Seidt • A. Gilat
Department of Mechanical Engineering, The Ohio State University, Scott Laboratory, 201 W 19th Ave, Columbus, OH 43210, USA
e-mail: smith.6575@osu.edu

S. Bossuyt et al. (eds.), *Residual Stress, Thermomechanics & Infrared Imaging, Hybrid Techniques and Inverse Problems, Volume 9*, Conference Proceedings of the Society for Experimental Mechanics Series, DOI 10.1007/978-3-319-21765-9_28

samples and subjected them to a uniaxial strain between 0 and 5 %. A paint-bake treatment of 180 °C for 30 min was then applied to each specimen and the microhardness of each sample was recorded. It was discovered that as the amount of prestrain increased, the hardness of the sample increased as well. Lastly, Ratchev et al. [7] recrystallized tension and disk specimens of Al-Cu-Mg alloy by means of a 550 °C salt bath treatment to study the effects of 4 different cooling rates from 2 to 500 °C/s on the strength and precipitation behavior of the material. Several of the tension samples were baked at 180 °C for 30 mins to compare to the recrystalized samples. Baking each sample increased the strength of the material, however the yield stress after baking was nearly constant and did not depend on the cooling rate. Interrupted tensile tests were also performed on uniaxial specimens to give a uniaxial prestrain between 0 and 10 %. In general, the strength of the material increased with increasing prestrain due to work hardening of the material while specimens subjected to a paint-bake cycle displayed greater strength due to the nucleation of precipitates along dislocations. The goal of the current study is to relate the amount of permanent thermally-induced strain to the test variables to improve modeling efforts and to avoid excessive deformation during production.

28.2 Experimental Procedures and Techniques

28.2.1 Tension Experiments

Tension tests are performed on an aluminum 6000 series alloy to study the material response to various prestrains, loadings, thermal cycles, and boundary conditions. The experimental test plan for the tension tests is shown in Table 28.1 Experimental test plan for uniaxial specimens.

Thermal testing consists of two soak periods at a specified temperature followed by a return to 30 °C during two cooling periods. A summary of the thermal profiles is displayed in Table 28.2.

A 20 % uniaxial prestrain is induced in a uniaxial tension specimen subjected to an A-type heat cycle. Thermal buckling tests are completed by prestraining a specimen from 0 to 20 % and constraining the sample using a specially designed plate before exposure to a C-type thermal heat cycle. The uniaxial samples for the uniaxial expansion, failure behavior, thermal buckling, and combined strain tests are predeformed to strains of 0–20 % using the set-up in Fig. 28.1.

Tests are conducted using a 20 kip servo-hydraulic load frame at a strain rate of 1×10^{-3} s^{-1}. The specimen is placed in two slotted adapters and pinned in place. The slotted adapters are connected to two Inconel 718 push rods which are mounted to the LVDT and 20 kip load cell. Two Point Gray Research 20S4M-C cameras equipped with a Schneider 30 mm lens are positioned 1.5 ft away from the sample to capture images at 2 frames per second while fiber optic lamps provide illumination on the specimen surface. Approximately 430 images are taken of each deformation event and are processed by Correlated Solutions VIC-3D 7 software to calculate the displacements on the specimen. The specimen is loaded by placing the controller in stroke control and displacing the actuator at a rate of 1.2×10^{-3} ft/s a pre-determined distance of 0.170″ or 0.317″ depending on the desired prestrain of 10 % or 20 % respectively. Failure testing and DIC is conducted on prestrained and unstrained uniaxial samples at room temperature and 190 °C using a furnace attached to the load frame. Rust-oleum High Heat paint is used to provide a base coat and speckle pattern on each specimen. Digital image correlation is used to

Table 28.1 Experimental test plan for uniaxial specimens

Test no.	Test type	Axial prestrain (%)	Heat cycle
1	Uniaxial	20	A
2	Combined	10	C
3	Thermal Buckling	0	A
4		20	

Table 28.2 Overview of thermal profiles

Thermal cycle	First Dwell temperature (°C)	Second Dwell temperature (°C)	Cooling temperature (°C)	Dwell hold time (min)
A	190	160	30	20
C	160	160	30	20

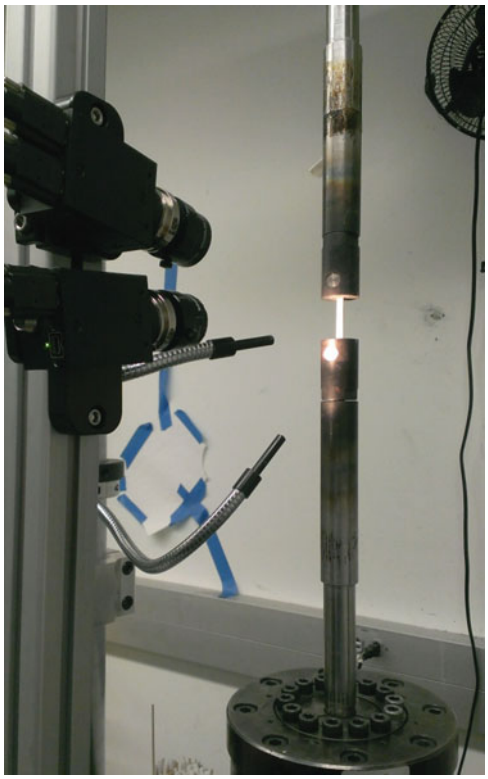

Fig. 28.1 Uniaxial prestrain experimental setup

Table 28.3 Experimental test plan for bending experiments

Test no.	Test type	Bending prestrain	Heat cycle
1	Bending	10 %	A
2			C
3		20 %	A
4			C
5	Combined		C

measure and record displacements and strains. The engineering and true stress and strain to failure are calculated for each specimen using the collected data from the load cell and DIC analysis.

28.2.2 Bend Testing

Bend tests are completed on uniaxial and bend specimens to observe the behavior of combined and bending strain states in an aluminum 6000 series alloy under thermal cycle loading. A summary of the bending experiment plan is shown in Table 28.3. Samples undergo bending strains of 0, 10, and 20 % before being exposed to A and C type thermal cycles. Samples are also bent in the transverse direction to study the effect of material anisotropy on thermal expansion. Lastly, samples that were previously prestrained with a uniaxial strain of 10 % are subject to a bending strain of 20 % to observe the effects of combined loading.

The procedure for prestraining the bend samples is displayed in Fig. 28.2. The apparatus is based upon the ASTM 190 and 290 standards for guided bend tests [6, 7] and was designed in collaboration with HRA to allow DIC measurements on the surface of the bend specimen during mechanical testing. The base plate provides a platform for a mirror fixture that sits 45° from the shoulder plates and allows DIC measurements on the outer surface of each specimen during deformation. Two different plungers were designed with radii of 0.177″ and 0.079″ to create bending strains of 10 and 20 % in the aluminum strips. Bend testing is carried out by attaching the entire bend apparatus to an Inconel 718 push rod and the load cell of the servo-hydraulic load frame. Next, the plunger with the appropriate bending radius for the desired strain is attached

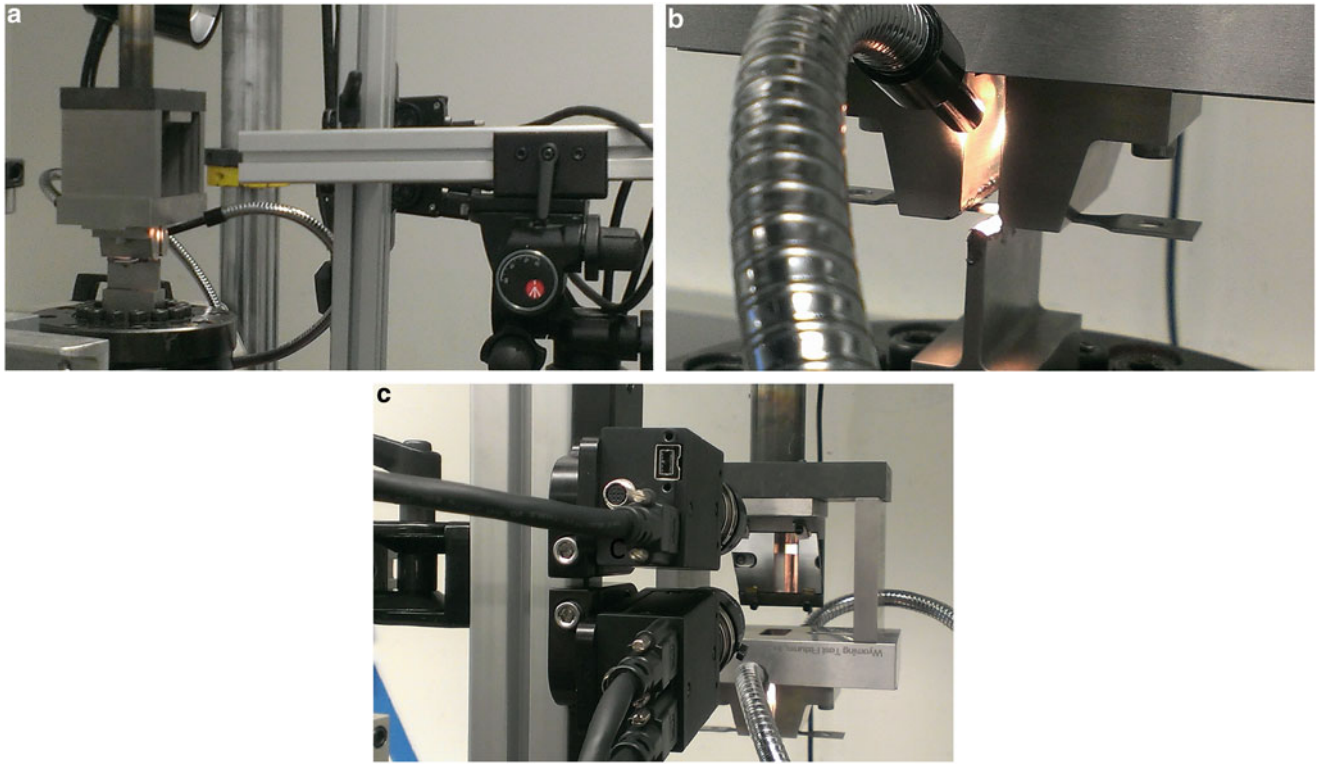

Fig. 28.2 (**a**) Overview of bend test experimental setup (**b**) specimen placement (**c**) DIC setup

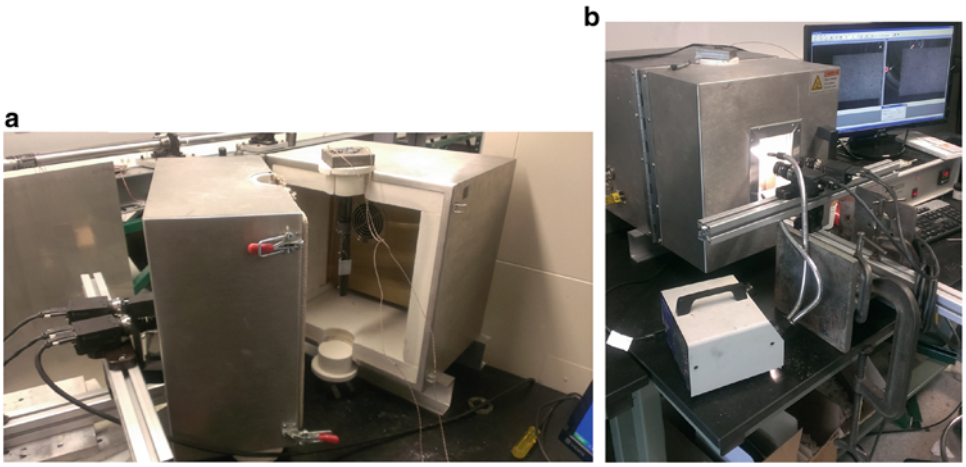

Fig. 28.3 (**a**) Furnace setup for thermal cycle testing (**b**) inside of furnace

to the actuator with a 1″ steel rod. The surfaces of the plunger and the shoulders are greased using a high pressure resistant G-N Metal Assembly Paste to ensure the sample can bend without seizing.

28.2.3 Thermal Testing

Each specimen is subjected to a specific temperature profile meant to replicate the paint-bake cycle experienced during manufacturing. Thermal cycle profiles remain within ±5 °C of the prescribed temperature as measured by a K-type thermocouple while soak times are to be +1/−0 min from the specified times. The thermal cycles are applied to the specimens by a modified split-box furnace as shown in Fig. 28.3.

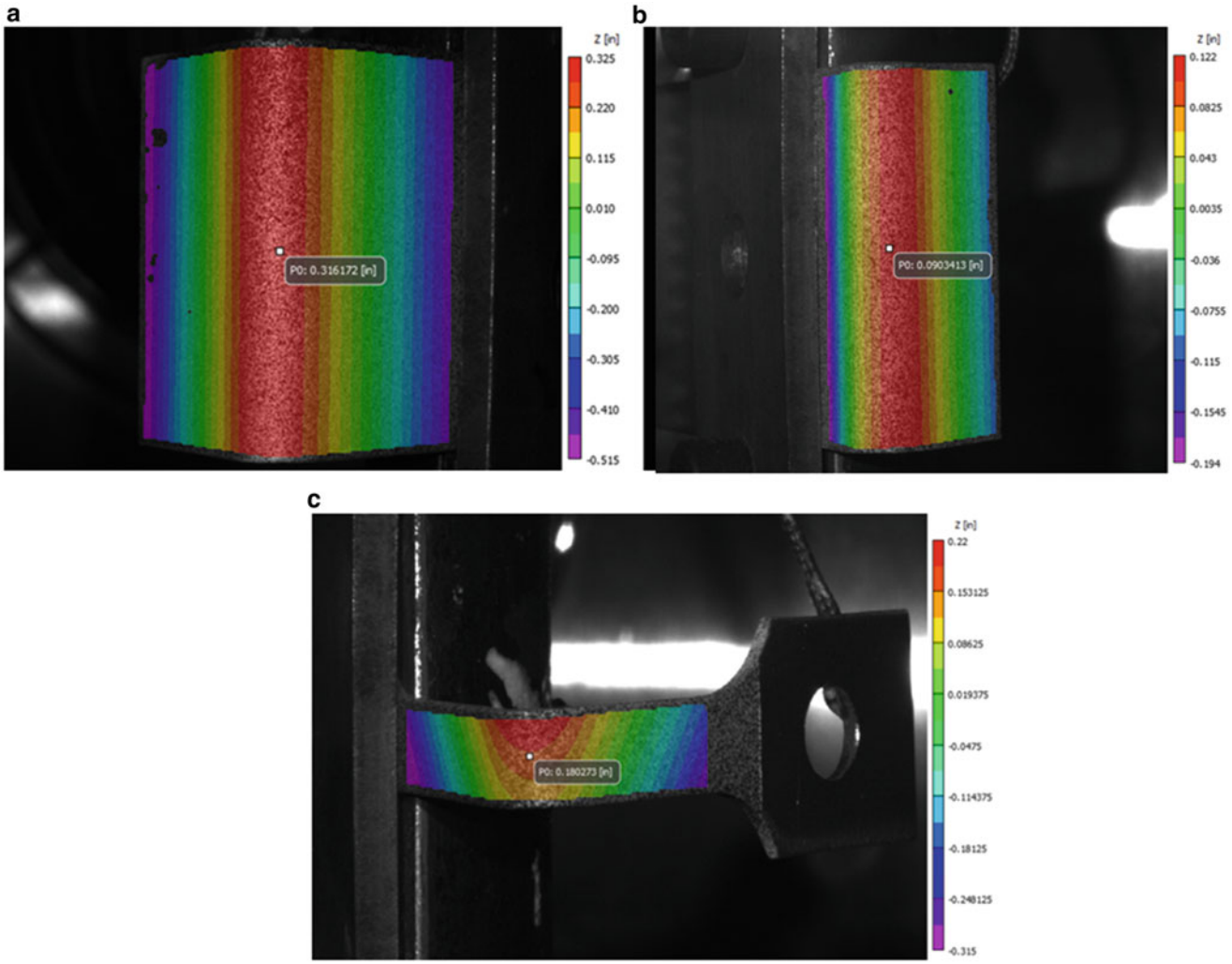

Fig. 28.4 (**a**) 3D DIC images for a Bending sample. (**b**) Transverse specimen. (**c**) Combined specimen

The oven has a 4 × 5″ optical quartz window in the door to allow DIC measurements to be taken from cameras outside the furnace. Temperature measurements are taken at 0.1 Hz by attaching a K-type thermocouple to each specimen using Omega CC high temperature cement.

The displacements and strains for each specimen during deformation and the thermal cycles are recorded using a combination of 1″ extensometers and data points. For each uniaxial tension test an extensometer was placed over the gage section and a data point was located at the point of maximum strain for prestraining operations or the failure point for mechanical tests to failure. During bending prestrain experiments a data point was used to capture the strain along the bend axis and the vertical displacement of the specimen during deformation. Throughout thermal cycle testing a single data point was placed in the center of the bend for samples prestrained to 10 and 20 % bending strain as shown in Fig. 28.4

28.3 Experimental Results

Experimental results from a data point center of a uniaxially prestrained dogbone and an undeformed bend sample are presented in Fig. 28.5. The strains are measured in both the deformed (X-direction) and transverse (Y-direction) and compared to the estimated strain due to thermal expansion. After cooling to room temperature the specimens show no noticeable signs of residual thermal strain.

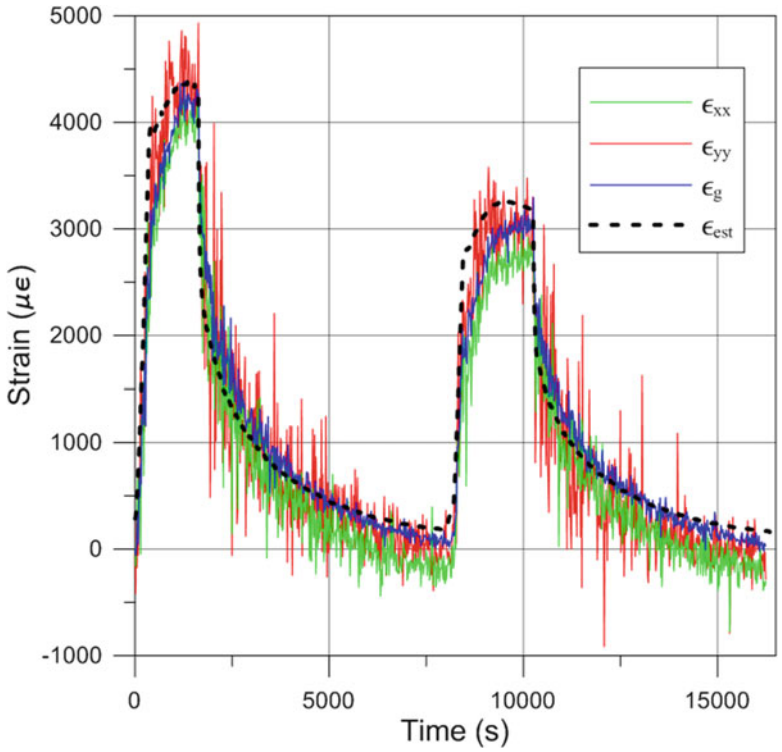

Fig. 28.5 Strains measured at the center of a 20 % uniaxially prestrained dogbone sample subjected to a A-type thermal cycle

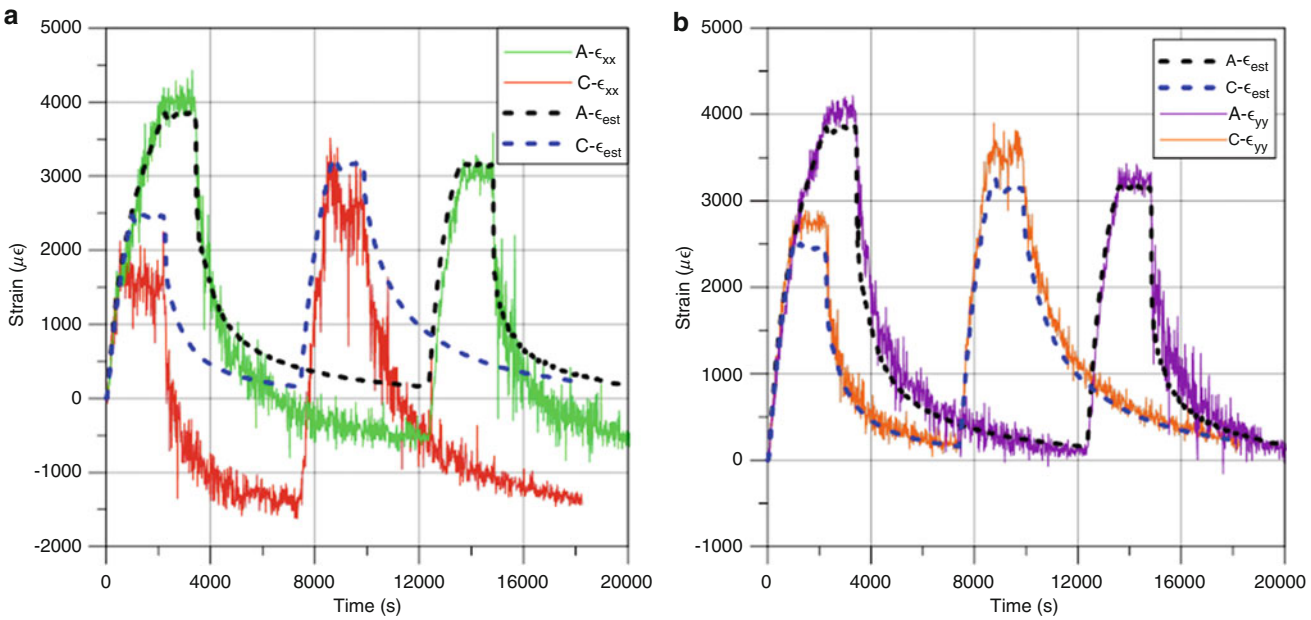

Fig. 28.6 Experimental data from a 10 % prestrained bending specimen during A and C thermal cycles: (**a**) Strains measured around the bend axis compared to the estimated thermal strain. (**b**) Strains measured parallel the bend axis compared to the estimated thermal strain

The representative curves for bending specimens prestrained to 10 and 20 % bending strain, are shown in Figs. 28.6 and 28.7. The strains around the bend axis of the sample are shown in (a) and the strains parallel to the bend axis are shown in (b). The estimated thermal expansion curve is once again used for comparison against the measured strains. The different heating cycles are also represented in each graph and are evident in the difference in strains during the first temperature dwell. A negative residual strain exists around the bend axis for all specimens when they are returned to room temperature after heating.

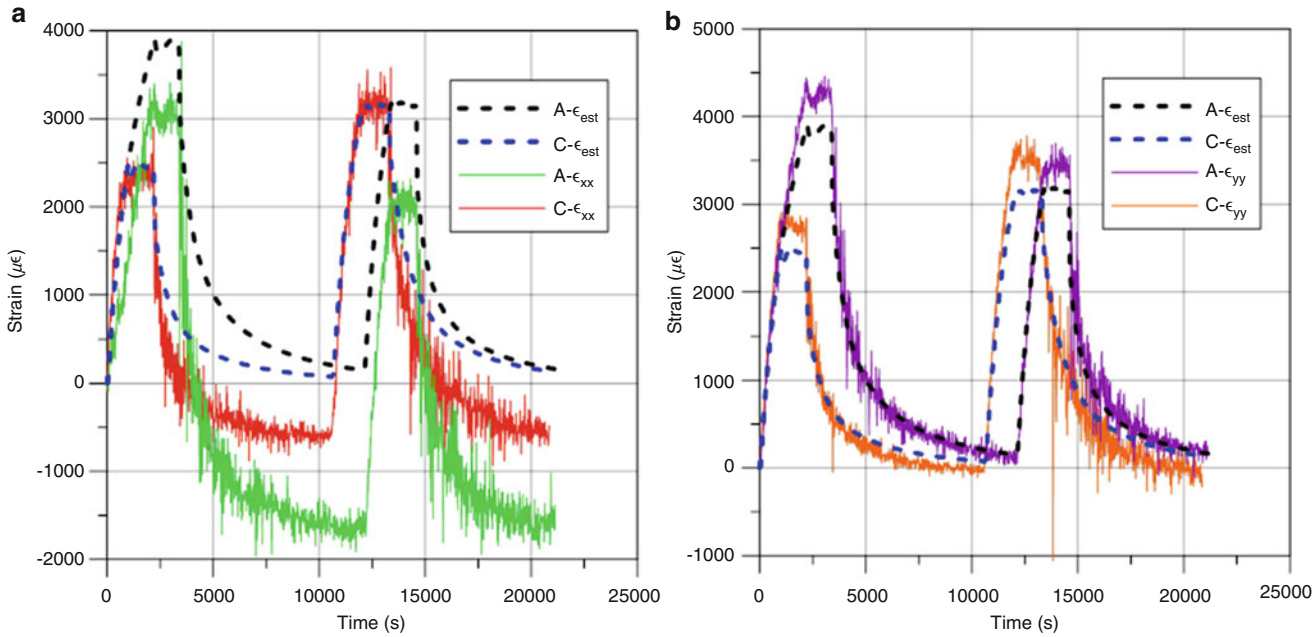

Fig. 28.7 Experimental data from a 20 % prestrained bending specimen during A and C thermal cycles: (**a**) Strains measured around the bend axis compared to the estimated thermal strain. (**b**) Strains measured parallel the bend axis compared to the estimated thermal strain

The measured strains for the combined and transverse specimens are presented in Fig. 28.8. The directions for the strains on the surface of each sample is shown in Fig. 28.8a. Each specimen was subjected to a C-type thermal cycle. The dwell strains for both the combined and transverse bending specimens decrease during the first heat cycle stage. Residual strains for the combined and tranverse specimens range from 1500 μ. The measured negative residual strain in all samples is due to the unwrapping of the bend due to stress relaxation.

A comparison of the strain offset between the estimated thermal strain due to thermal expansion and the measured strains for each specimen subjected to varying heat cycles is shown in Fig. 28.9. The average strain offset for all of the experiments is −617.90 μ/°C and the 95 % confidence interval lies between −312.71 and −923.10 μ/°C. The plot displays that for unstrained specimens or unstrained specimen directions residual strains are held to a minimum. Once the strain offset occurs after the initial cooling sequence the subsequent reheating of the sample to 160 °C has a minimal effect on the residual strains in each specimen. This plot also suggests that the residual strain is not sensitive to level of non-zero strain, prestrain type, nor the heating profile.

The radius of curvature was calculated around the bend for each sample throughout the thermal testing process as shown in Fig. 28.10. As the temperature of each specimen increased the radius of the sample increased as well. After the initial increase in radius due to the first dwell of the heating cycle, a residual increase in radius remained in the sample after cooling and was not affected by the second dwell of the heating cycle. Overall, the increase in radius for each specimen was small but the specimens with the largest increase also had the largest residual strains. The increase in strain supports the assumption that the bend is unwrapping during thermal cycling. A summary of the increase in radius for each specimen is displayed in Table 28.4.

The vertical displacement at the center of the gage section for a dogbone specimen subjected to uniaxial prestrains of 0 and 20 % then bolted to a steel plate and subjected to an A type thermal cycle is displayed in Fig. 28.11. The displacements after the two separate cooling periods show little deviation. The amount of prestrain also has little effect on the residual displacements as each experiment lands between 0.1 and 0.2 mm. Initial modeling of the metal under these conditions adequately predicts the out of plane deformation as well as the residual strain in the specimen.

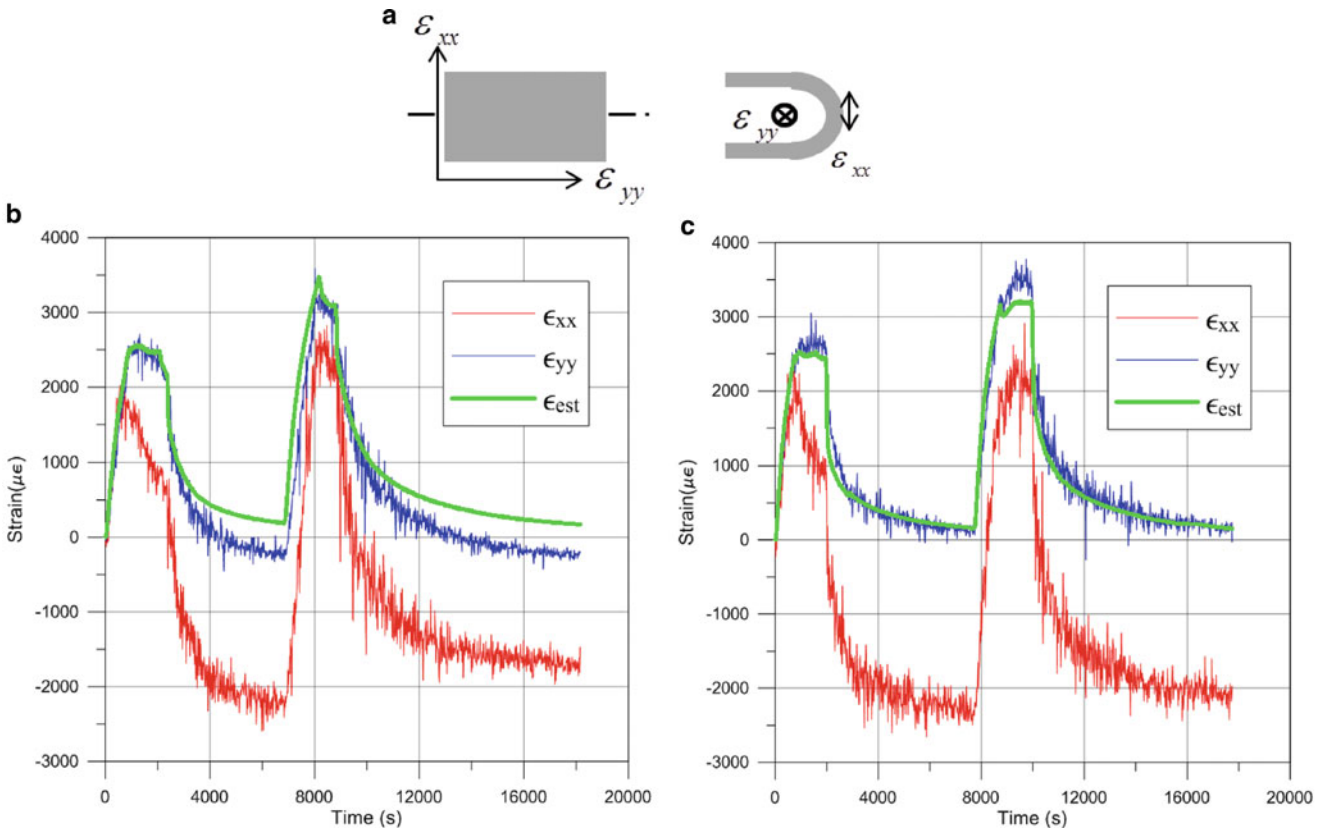

Fig. 28.8 (**a**) Representation of the measured strain directions on the surface of each bend. (**b**) Measured strains for a combined specimen compared to the estimated thermal strain. (**c**) Measured strains for a transverse specimen compared to the estimated thermal strain

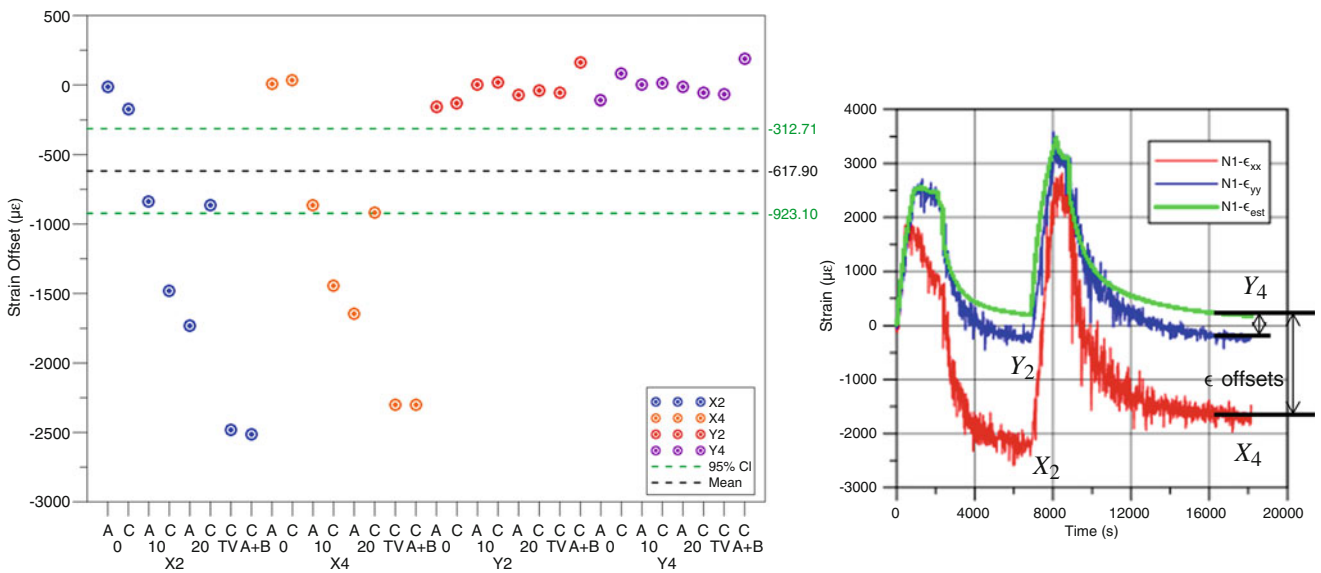

Fig. 28.9 (**a**) Strain offsets in the X and Y directions during the first and second cooling sequences of A and C type heating cycles for all bending and combined tests. (**b**) Representation of strain offsets

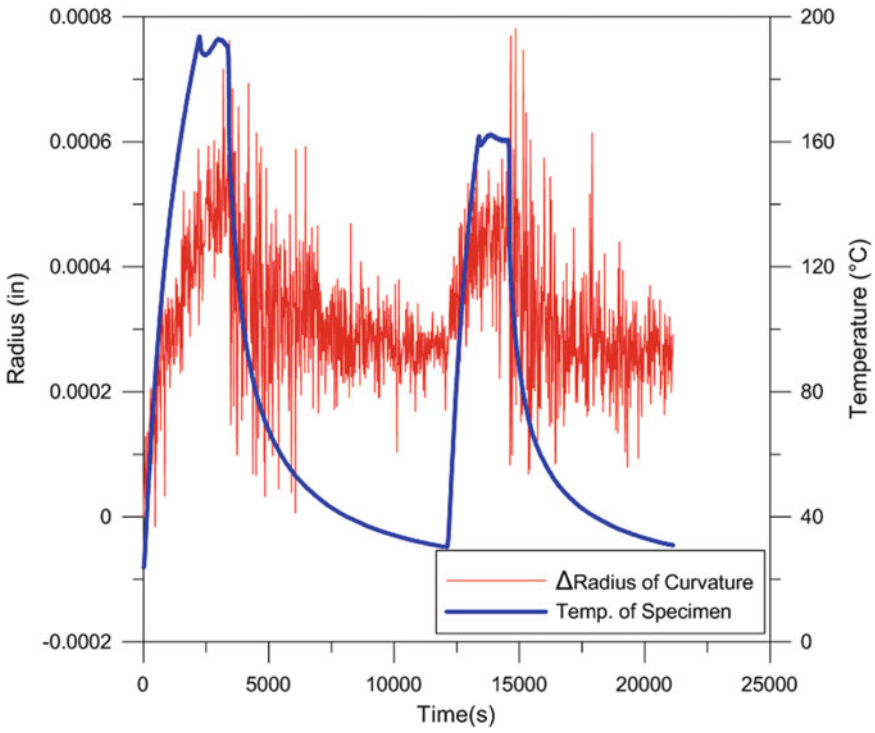

Fig. 28.10 Measured increase in bend radius for a 20 % prestrained bend specimen

Table 28.4 Overview of bend radius values for varying bend specimens subject to A and C type thermal cycles

	10 %-A	10 %-C	20 %-A	20 %-C	Transverse-C	Combined-C
Radius change at first cooling period (in.)	2.10E-04	3.00E-04	2.45E-04	3.88E-04	5.13E-04	6,69E-04
Radius change at second cooling period (in.)	2.08E04	4.11E-04	2.65E-04	4.19E-04	6.12E-04	6.89E-04

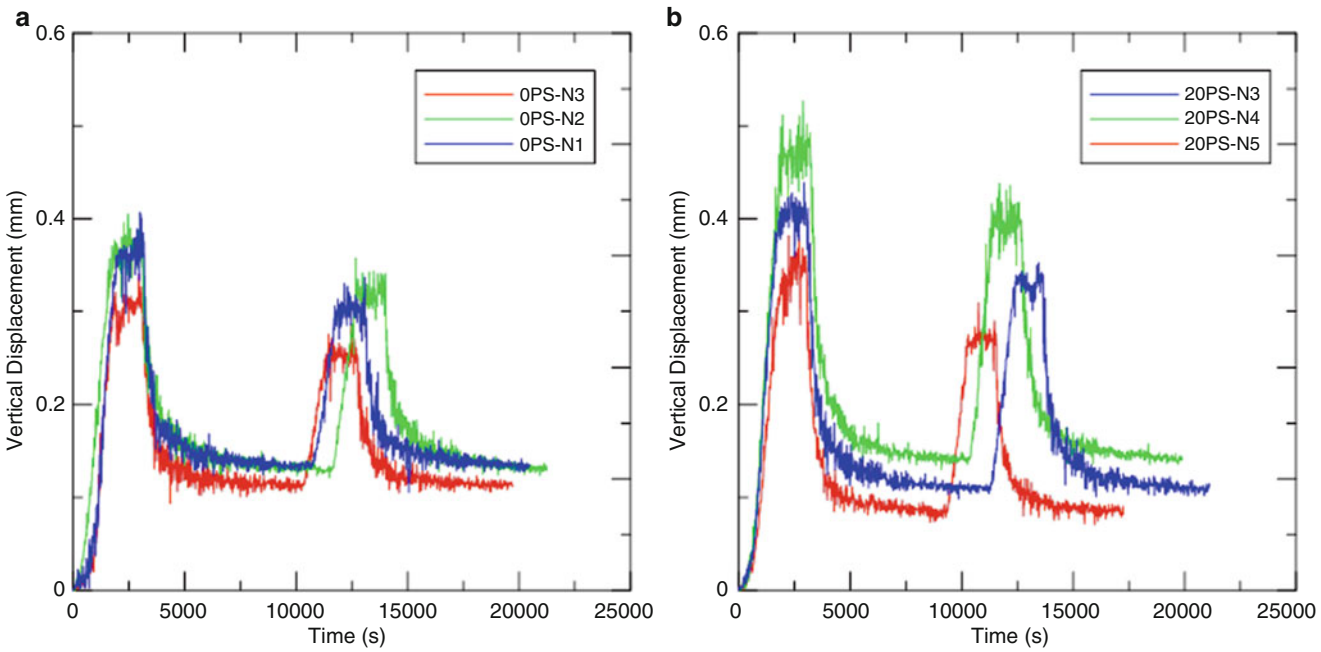

Fig. 28.11 Vertical displacement of the centerpoint of the gage section for dogbone specimens in the (**a**) undeformed and (**b**) 20 % prestrained conditions during an A-type thermal cycle

28.4 Summary and Conclusions

The thermal strain behavior of a 6000 series aluminum alloy is studied under a variety of different prestrains, specimen orientations and temperatures. Uniaxial dogbone specimens were tested to failure in tension under different prestrains and different temperatures. Bend specimens were subjected to bending strains of 0–20 % while uniaxial specimens were subject to 20 % axial strains and a combination of 10 % axial strain and 20 % bending strain then placed in a furnace and exposed to a thermal cycles that replicate the conditions of a paint-bake cycle during manufacturing. Uniaxial samples were bolted to a steel plate to observe the effects of thermal buckling. After each thermal cycle a residual strain and vertical displacement was seen in the gage section of the sample. The amount of displacement and strain was not sensitive to the prestrain in each sample. The recorded displacements and strains will be used in conjunction with the material property study to create an LS-DYNA model for the effects of thermal cycles on 6000 series aluminum alloys.

Acknowledgements This work was supported by Honda Research America. Thanks are due to Ryan Hahnlen of Honda Research America.

References

1. E. Romhanji, M.M. Popović, D.M. Glišić, M. Stefanović, M. Milovanović, On the Al-Mg alloy sheets for automotive application: problems and solutions. Metalurgija **10**(3), 205–216 (2004)
2. S. Das, The life-cycle impacts of aluminum body-in-white automotive material. JOM **52**(8), 41–44 (2000)
3. D.C. Balderach, H. Jennifer, E. Leung, J. Qiao, M.C. Tejeda, E. Taleff, The paint–bake response of three Al–Mg–Zn alloys. Mater. Sci. Eng. A **339**(1–2), 194–204 (2003)
4. Y. Birol, Pre-straining to improve the bake hardening response of a twin-roll cast Al–Mg–Si alloy. Scr. Mater. **52**(3), 169–173 (2005)
5. T.L. Jin, N.S. Ha, N.S. Goo, A study of the thermal buckling behavior of a circular aluminum plate using the digital image correlation technique and finite element analysis. Thin-Walled Struct. **77**, 187 (2013)
6. K.D. Murphy, D. Ferreira, Thermal buckling of rectangular plates. Int. J. Solids Struct. **38**(22–23), 3979–3994 (2001)
7. R.H. Plaut, L.N. Virgin, Use of frequency data to predict buckling. J. Eng. Mech. **116**(10), 2330 (1990)

Chapter 29
Hybrid Full-Field Stress Analysis of Loaded Perforated Asymmetrical Plate

S. Kurunthottikkal Philip and R.E. Rowlands

Abstract This chapter demonstrates the ability to determine experimentally the complete state of stress throughout a compressively-loaded rectangular aluminum plate containing an irregularly-shaped asymmetrically orientated hole. This is achieved by processing the recorded associated stress-induced temperature information with a stress function and discretely imposing the boundary conditions. The challenges include handling the total lack of symmetry and satisfying the traction-free conditions on the edge of the irregularly-shaped inclined hole.

Keywords Thermoelasticity • TSA • Stresses • Holes • Asymmetry

29.1 Introduction

Thermoelasticity (TSA) is a contemporary method of determining the stresses in loaded structures and machine components [1, 2]. Advantages of the stress analysis technique include that one neither needs to know the values of the elastic constitutive properties nor differentiate the measured information. However, and not unlike most experimental methods, traditional TSA does not provide accurate edge results, rendering it difficult to determine reliable stress concentrations. This edge issue is circumventer here by ignoring temperature data on and near the edges of the analyzed member, processing the recorded temperature information away from the edges using an applicable Airy stress function and satisfying the traction-free boundary conditions discretely on the edge of the hole. The particular situation here is the compressively loaded plate of Fig. 29.1.

29.2 Prior Relevant Analyses

References [3–6] are previously relevant experimental stress analyses whereupon measured information was combined with a stress function. Reference [3] used TSA to determine the stresses in the neighborhood of a round hole beneath an edge load. While enjoying symmetry about the vertical axis, the analysis used a complicated stress function which was developed by superposition to account for the contributions of the applied top concentrated load and the traction-free circular hole. Reference [4] provides the stresses at and near holes utilizing simpler stress function. References [5, 6] used recorded temperature or displacement data to evaluate the stresses in loaded plates containing elliptical holes. Although the cases of References [3–5] had symmetry about the vertical axis, that of Reference [6] does not. However, the perforated shapes in References [4–6] were all simple, *i.e.*, circular or elliptical, thereby simplifying the task of satisfying the traction-free conditions on the edge of the cutout. Reference [7] combined TSA and a stress function to evaluate the stresses in rectangular plate containing an irregularly-shaped, but symmetrically orientated hole. Having symmetry about the vertical axis again simplified the analysis.

Processing measured information using a stress function for unsymmetrical situations like the present, Fig. 29.1, is aggregated by the need for a more extensive stress function, more Airy coefficients and the implication of needing more measured input data. However, this demonstrates the ability to thermoelastically analyze a very general and practical class of engineering problems.

S.K. Philip • R.E. Rowlands (✉)
Department of Mechanical Engineering, University of Wisconsin-Madison, Madison, WI 53706, USA
e-mail: rowlands@engr.wisc.edu

S. Bossuyt et al. (eds.), *Residual Stress, Thermomechanics & Infrared Imaging, Hybrid Techniques and Inverse Problems, Volume 9*, Conference Proceedings of the Society for Experimental Mechanics Series, DOI 10.1007/978-3-319-21765-9_29

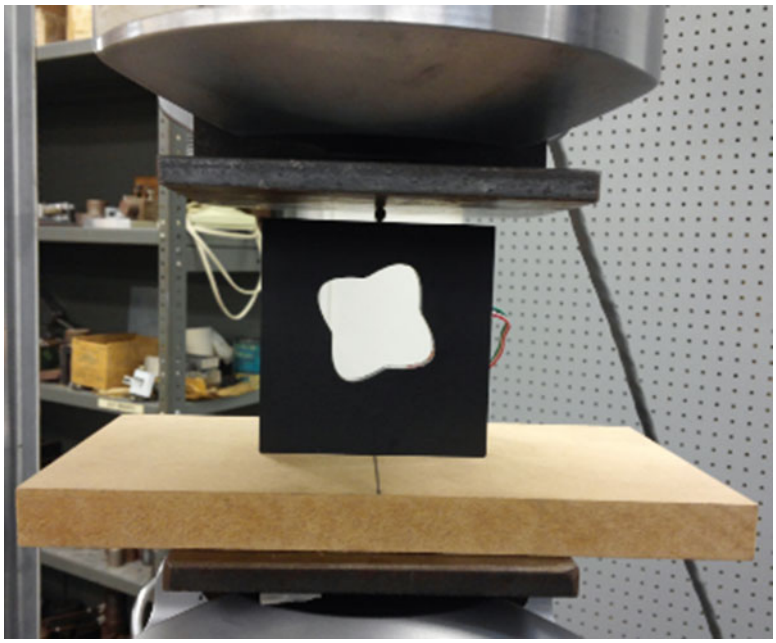

Fig. 29.1 Irregularly and unsymmetrically perforated supported plate subjected to top concentrated load

The state of stress at and in the neighborhood of a discontinuity in an unsymmetrical structure is achieved by coupling the measured stress data with an Airy's stress function and applying traction-free boundary conditions analytically on the edge of the hole. Combining these two features to form a hybrid provides the individual components of stresses.

The Airy stress function ϕ of (29.1), which is a solution of the bi-harmonic equation $\nabla^4\phi = 0$ so as to satisfy equilibrium and compatibility, is applicable for the unsymmetrical loaded plate of Fig. 29.1.

$$\phi_{unsym} = \begin{bmatrix} a_0 + b_0 \cdot ln\, r + c_0 \cdot r^2 + A_0 \cdot \theta \\ + \left(a_1 \cdot r + \frac{c_1}{r} + d_1 \cdot r^3\right) sin\ \theta + \left(a_1' \cdot r + \frac{c_1'}{r} + d_1' \cdot r^3\right) cos\ \theta \\ + \sum_{n=2,3,4\ldots}^{N} \left[a_n \cdot r^n + b_n \cdot r^{(n+2)} + c_n \cdot r^{-n} + d_n \cdot r^{-(n-2)}\right] (sin\ n\theta) \\ + \sum_{n=2,3,4\ldots}^{N} \left[a_n' \cdot r^n + b_n' \cdot r^{(n+2)} + c_n' \cdot r^{-n} + d_n' \cdot r^{-(n-2)}\right] (cos\ n\theta) \end{bmatrix} \tag{29.1}$$

From (29.2, 29.3, 29.4), the individual polar components of stress can be written as in (29.5, 29.6, 29.7), Fig. 29.2 [7]. Combining (29.5, 29.6, 29.7, 29.8) gives the components of stress at points on the boundary of the hole in the directions normal, ξ, and tangential, η, to the edge of the hole, *i.e.*, (29.9) and (29.10). The angle ψ in the transformation matrix of (29.8) is the angle between the normal, ξ, and the polar radial, r, directions, Fig. 29.3 [7].

$$(\sigma_{rr})_{unsym} = \frac{1}{r} \cdot \frac{\partial \phi_{unsym}}{\partial r} + \frac{1}{r^2} \frac{\partial^2 \phi_{unsym}}{\partial \theta^2} \tag{29.2}$$

$$(\sigma_{\theta\theta})_{unsym} = \frac{\partial^2 \phi_{unsym}}{\partial r^2} \tag{29.3}$$

$$(\sigma_{r\theta})_{unsym} = -\frac{\partial}{\partial r} \cdot \left(\frac{1}{r} \cdot \frac{\partial \phi_{unsym}}{\partial \theta}\right) \tag{29.4}$$

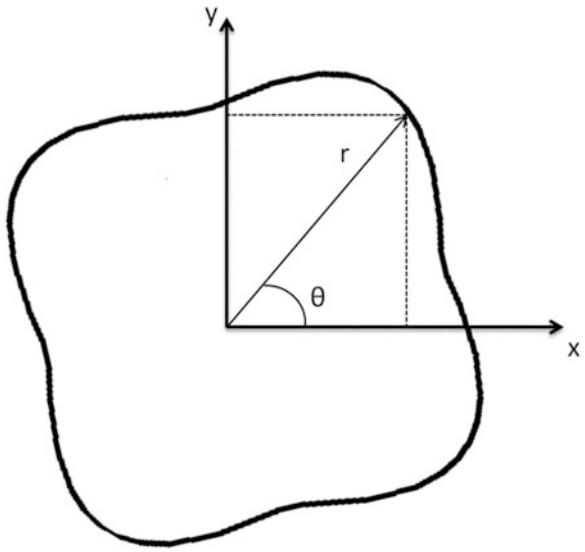

Fig. 29.2 Polar and Cartesian coordinate systems

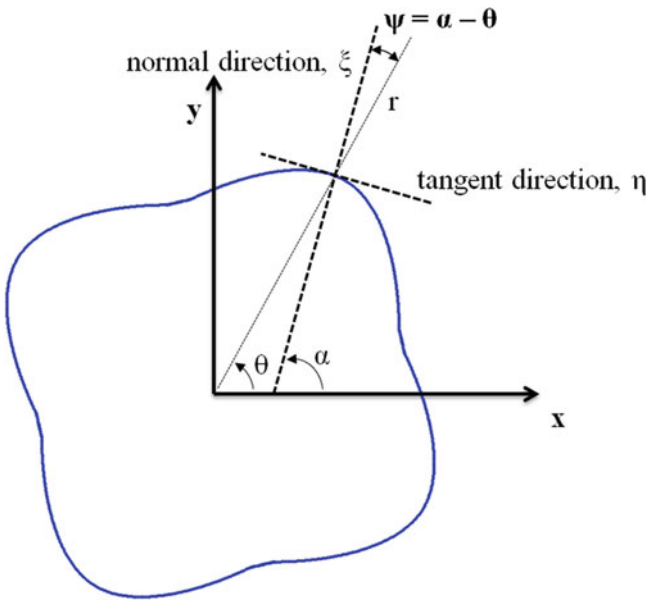

Fig. 29.3 Coordinate system representation

$$(\sigma_{rr})_{unsym} = \begin{pmatrix} \dfrac{b_0}{r^2} + 2c_0 + \left(-\dfrac{2c_1}{r^3} + 2d_1 r\right)\sin\theta + \left(-\dfrac{2c_1'}{r^3} + 2d_1' r\right)\cos\theta \\ -\sum\limits_{n=2,3,4..}^{N} \begin{pmatrix} a_n n(n-1)r^{n-2} + b_n(n+1)(n-2)r^n \\ +c_n n(n+1)r^{-(n+2)} + d_n(n-1)(n+2)r^{-n} \end{pmatrix} \sin(n\theta) \\ -\sum\limits_{n=2,3,4..}^{N} \begin{pmatrix} a_n' n(n-1)r^{n-2} + b_n'(n+1)(n-2)r^n \\ +c_n' n(n+1)r^{-(n+2)} + d_n'(n-1)(n+2)r^{-n} \end{pmatrix} \cos(n\theta) \end{pmatrix} \tag{29.5}$$

$$(\sigma_{\theta\theta})_{unsym} = \begin{pmatrix} -\dfrac{b_0}{r^2} + 2c_0 + \left(\dfrac{2c_1}{r^3} + 6d_1 r\right)\sin\theta + \left(\dfrac{2c_1^{'}}{r^3} + 6d_1^{'} r\right)\cos\theta \\ + \displaystyle\sum_{n=2,3,4..}^{N} \begin{pmatrix} a_n n(n-1)r^{n-2} + b_n(n+1)(n+2)r^n + c_n n(n+1)r^{-(n+2)} \\ +d_n(n-1)(n-2)r^{-n} \end{pmatrix} \sin(n\theta) \\ + \displaystyle\sum_{n=2,3,4..}^{N} \begin{pmatrix} a_n^{'} n(n-1)r^{n-2} + b_n^{'}(n+1)(n+2)r^n + c_n^{'} n(n+1)r^{-(n+2)} \\ +d_n^{'}(n-1)(n-2)r^{-n} \end{pmatrix} \cos(n\theta) \end{pmatrix} \tag{29.6}$$

$$(\sigma_{r\theta})_{unsym} = \begin{pmatrix} \dfrac{A_0}{r^2} + \left(\dfrac{2c_1}{r^3} - 2d_1 r\right)\cos\theta - \left(\dfrac{2c_1^{'}}{r^3} - 2d_1^{'} r\right)\sin\theta \\ - \displaystyle\sum_{n=2,3,4..}^{N} \begin{pmatrix} a_n n(n-1)r^{n-2} + b_n n(n+1)r^n - c_n n(n+1)r^{-(n+2)} \\ -d_n n(n-1)r^{-n} \end{pmatrix} \cos(n\theta) \\ + \displaystyle\sum_{n=2,3,4..}^{N} \begin{pmatrix} a_n^{'} n(n-1)r^{n-2} + b_n^{'} n(n+1)r^n - c_n^{'} n(n+1)r^{-(n+2)} \\ -d_n^{'} n(n-1)r^{-n} \end{pmatrix} \sin(n\theta) \end{pmatrix} \tag{29.7}$$

$\sigma_\xi = \sigma_{\xi\eta} = 0$ at boundary of the irregularly $-$ shaped hole

$$\begin{Bmatrix} \sigma_\xi \\ \sigma_\eta \\ \sigma_{\xi\eta} \end{Bmatrix} = \begin{bmatrix} \cos^2\psi & \sin^2\psi & 2\cos\psi\sin\psi \\ \sin^2\psi & \cos^2\psi & -2\sin\psi\cos\psi \\ -\sin\psi\cos\psi & \sin\psi\cos\psi & (\cos^2\psi - \sin^2\psi) \end{bmatrix} \begin{Bmatrix} \sigma_r \\ \sigma_\theta \\ \sigma_{r\theta} \end{Bmatrix} \tag{29.8}$$

$$(\sigma_\xi)_{unsym} = \begin{pmatrix} \left(\dfrac{\cos 2\psi}{r^2}\right)b_0 + 2c_0 + \left(\dfrac{2\sin\psi\cos\psi}{r^2}\right)A_0 \\ +\left(-\dfrac{2}{r^3}\sin\theta\cos 2\psi + \dfrac{4}{r^3}\cos\theta\sin\psi\cos\psi\right)c_1 \\ +\left(2r\sin\theta\{\cos^2\psi + 3\sin^2\psi\} - 4r\cos\theta\sin\psi\cos\psi\right)d_1 \\ +\left(-\dfrac{2}{r^3}\cos\theta\cos 2\psi - \dfrac{4}{r^3}\sin\theta\sin\psi\cos\psi\right)c_1^{'} \\ +\left(2r\cos\theta\{\cos^2\psi + 3\sin^2\psi\} + 4r\sin\theta\sin\psi\cos\psi\right)d_1^{'} \\ + \displaystyle\sum_{n=2,3,4...}^{N} \begin{bmatrix} (-n(n-1)r^{n-2}\{\sin n\theta\cos 2\psi + 2\cos n\theta\sin\psi\cos\psi\})a_n \\ +(-(n+1)r^n\{\sin n\theta[n\cos 2\psi - 2] + 2n\cos n\theta\sin\psi\cos\psi\})b_n \\ +\left(n(n+1)r^{-(n+2)}\{-\sin n\theta\cos 2\psi + 2\cos n\theta\sin\psi\cos\psi\}\right)c_n \\ +((n-1)r^{-n}\{\sin n\theta[-n\cos 2\psi - 2] + 2n\cos n\theta\sin\psi\cos\psi\})d_n \end{bmatrix} \\ + \displaystyle\sum_{n=2,3,4...}^{N} \begin{bmatrix} (-n(n-1)r^{n-2}\{\cos n\theta\cos 2\psi - 2\sin n\theta\sin\psi\cos\psi\})a_n^{'} \\ +((n+1)r^n\{\cos n\theta[2 - n\cos 2\psi] + 2n\sin n\theta\sin\psi\cos\psi\})b_n^{'} \\ +\left(n(n+1)r^{-(n+2)}\{-\cos n\theta\cos 2\psi - 2\sin n\theta\sin\psi\cos\psi\}\right)c_n^{'} \\ +((n-1)r^{-n}\{\cos n\theta[-n\cos 2\psi - 2] - 2n\sin n\theta\sin\psi\cos\psi\})d_n^{'} \end{bmatrix} \end{pmatrix} \tag{29.9}$$

$$
\left(\sigma_{\xi\eta}\right)_{unsym} = \left(\begin{array}{l}
\left(-\dfrac{2\sin\psi\cos\psi}{r^2}\right)b_0 + \left(\dfrac{\cos 2\psi}{r^2}\right)A_0 \\
+\left(\dfrac{2}{r^3}\{2\sin\theta\sin\psi\cos\psi + \cos\theta\cos 2\psi\}\right)c_1 \\
+(2r\{2\sin\theta\sin\psi\cos\psi - \cos\theta\cos 2\psi\})d_1 \\
+\left(\dfrac{2}{r^3}\{2\cos\theta\sin\psi\cos\psi - \sin\theta\cos 2\psi\}\right)c_1' \\
+(2r\{2\cos\theta\sin\psi\cos\psi + \sin\theta\cos 2\psi\})d_1' \\
+\sum\limits_{n=2,3,4..}^{N} \left[\begin{array}{l}
(n(n-1)r^{n-2}\{2\sin n\theta\sin\psi\cos\psi - \cos n\theta\cos 2\psi\})a_n \\
+(n(n+1)r^{n}\{2\sin n\theta\sin\psi\cos\psi - \cos n\theta\cos 2\psi\})b_n \\
+\left(n(n+1)r^{-(n+2)}\{2\sin n\theta\sin\psi\cos\psi + \cos n\theta\cos 2\psi\}\right)c_n \\
+(n(n-1)r^{-n}\{2\sin n\theta\sin\psi\cos\psi + \cos n\theta\cos 2\psi\})d_n
\end{array} \right] \\
+\sum\limits_{n=2,3,4..}^{N} \left[\begin{array}{l}
(n(n-1)r^{n-2}\{2\cos n\theta\sin\psi\cos\psi + \sin n\theta\cos 2\psi\})a_n' \\
+(n(n+1)r^{n}\{2\cos n\theta\sin\psi\cos\psi + \sin n\theta\cos 2\psi\})b_n' \\
+\left(n(n+1)r^{-(n+2)}\{2\cos n\theta\sin\psi\cos\psi - \sin n\theta\cos 2\psi\}\right)c_n' \\
+(n(n-1)r^{-n}\{2\cos n\theta\sin\psi\cos\psi - \sin n\theta\cos 2\psi\})d_n'
\end{array} \right]
\end{array} \right) \tag{29.10}
$$

For proportional loading under plane stress, the recorded TSA system signal, S^*, is related to the change in the isopachic stress, $\sigma = \sigma_{rr} + \sigma_{\theta\theta}$ according to

$$S^* = K^* \Delta\sigma \tag{29.11}$$

where K is a thermal mechanical coefficient.

29.3 Experimental Details

Figure 29.4 shows some strain gages which were bonded on the transverse curved surface of the hole while Fig. 29.5 is a TSA thermogram of the plate of Fig. 29.1 recorded at 25 Hz. The 25 Airy coefficients employed were evaluated from (29.11), 45,156 recorded values of S^* from throughout the TSA image of Fig. 29.5 and satisfying the traction-free conditions

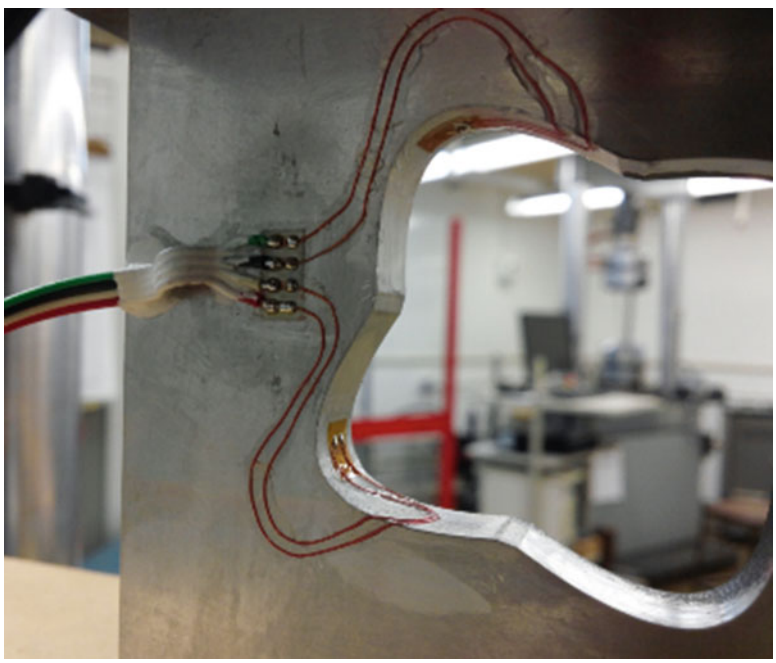

Fig. 29.4 Strain gages on edge of hole

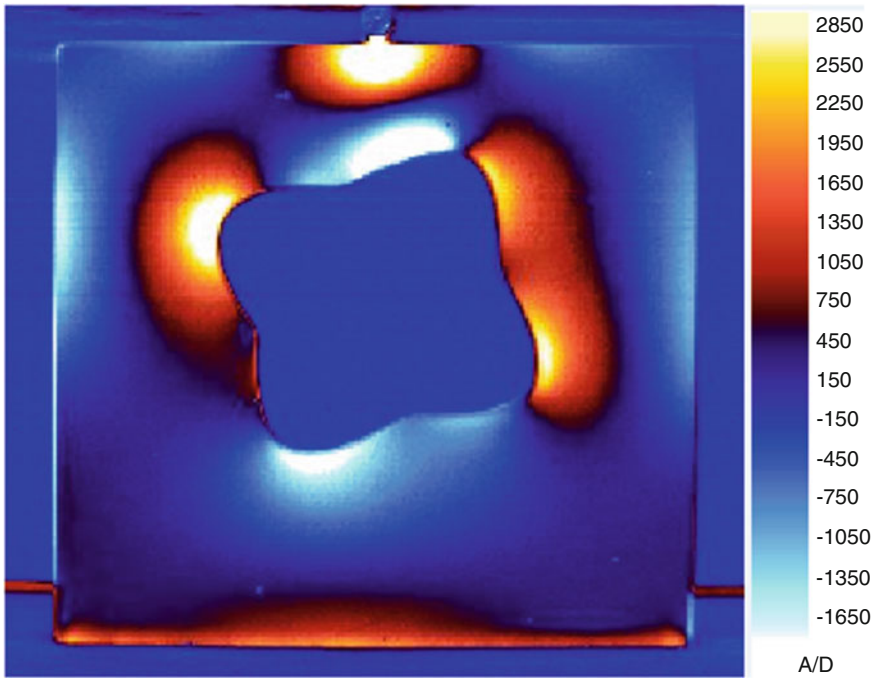

Fig. 29.5 TSA Thermogram recorded at 890 N (200 lbs)

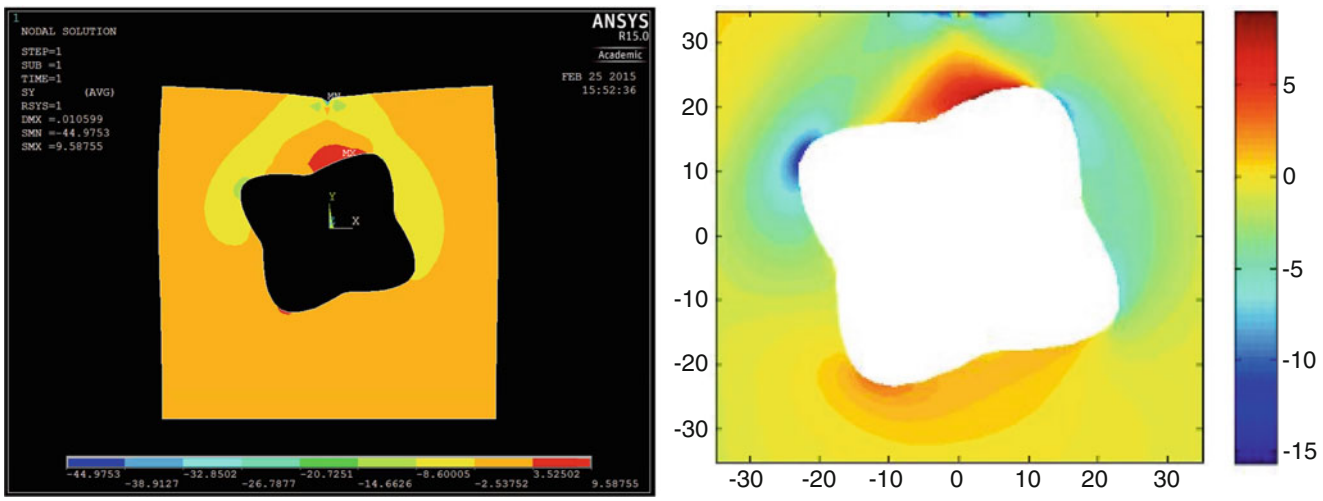

Fig. 29.6 Comparison of FEM and TSA determined contours of normalized hoop stress $\sigma_{\theta\theta}/\sigma_o$ throughout the plate

at 288 locations on the edge of the hole according to (29.9) and (29.10). Knowing the magnitudes of the Airy coefficients, the stresses available from (29.5, 29.6, 29.7) were determined. Figures 29.6 and 29.7 show TSA and ANSYS determined hoop stresses, whereas Table 29.1 compares the hoop stress on the edge of the hole at $\theta = 60^o$ and 330^o. Reliability of the TSA results is confirmed by those from FEM and strain gages.

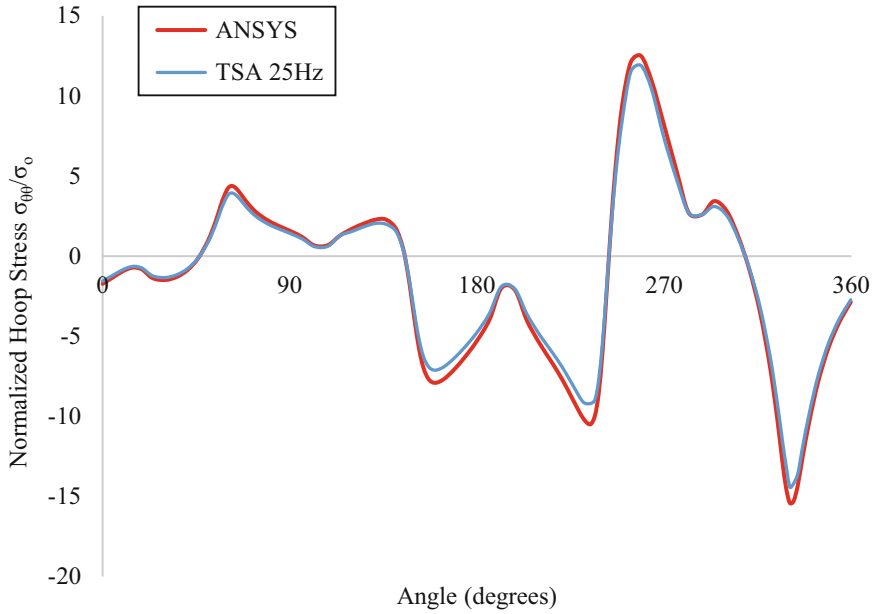

Fig. 29.7 Normalized Hoop Stress $\sigma_{\theta\theta}/\sigma_0$ at the edge of the hole by TSA and ANSYS

Table 29.1 Comparison of results from TSA, FEM and strain gages

Stress values (MPa) at a boundary of the hole at a static load of 889.64 N (200 lbs)			
Angle (degrees)	Strain gage	TSA	ANSYS
60	−8.28	−8.302	−8.3194
330	−5.679	−5.413	−5.4706

References

1. R.J. Greene, E.A. Patterson, R.E. Rowlands, Thermoelastic Stress Analysis, Ch. 26, in *Handbook of Experimental Solid Mechanics*, ed. by W. M. Sharpe (Springer, New York, 2008)
2. S.J. Lin, W.A. Samad, A.A. Khaja, R.E. Rowlands, Hybrid thermoelastic stress analysis. Exp. Mech. (Special Issue) (2013, in press)
3. S.J. Lin, S. Quinn, D.R. Matthys, A.M. New, I.M. Kincaid, B.R. Boyce, A.A. Khaja, R.E. Rowlands, Thermoelastic determination of the individual stresses in the vicinity of a near edge hole beneath a concentrated load. Exp. Mech. **51**, 797–814 (2011)
4. A.A. Khaja, R.E. Rowlands, Experimentally determined stresses at geometric discontinuities using simple stress functions. J. Eng. Mech. (2015, in press)
5. A.A. Khaja, R.E. Rowlands, Experimentally determined stresses associated with elliptical holes using polar coordinates. Strain **49**(2), 116–124 (2013)
6. W.A. Samad, R.E. Rowlands, *Full-Field Thermoelastic Stress Analysis of an Unsymmetrically-load Elliptically-Perforated Structure* (Photomechanics, Montpellier, 2013)
7. W.A. Samad, R.E. Rowlands, Full-field thermoelastic stress analysis of a finite structure containing an irregularly-shaped hole. Exp. Mech. **54** (3), 457–469 (2014)

Chapter 30
Automated Detection of CFRP Defects by Infrared Thermography and Image Analysis

Terry Yuan-Fang Chen and Guan-Yu Lin

Abstract Carbon fiber reinforced polymers (CFRP) have experienced widespread use in the aerospace industry. However, the very different internal structure and properties of woven composites presents a challenge to defect detection in such structures. An automated scheme for determination of the location and size of defects using image processing techniques is reported. The scheme includes local thresholding to binarize the image and reduce non-uniform thermal energy effect, morphology procedures to reduce larger noises and separate the defect from the specimen. Test of the scheme on various specimens having artificial defects embedded in different depth is shown. The contrast is lower as the defect is embedded deeper. Nevertheless, the defects can be detected accurately from the IRT images while comparing to the observed ones.

Keyword CFRP • Defect detection • Infrared thermography • Image analysis • Local thresholding

30.1 Introduction

Carbon fiber reinforced polymers (CFRP) have experienced widespread use in the aerospace industry. The advantages of composites over other materials include high strength/weight, high fatigue resistance, low thermal expansion, and good resistance to corrosive damages. However, the nature of the material is susceptible to internal defects, foreign bodies and glued adverse that affect the aviation safety. Therefore, it is necessary to detect the defect regions in advance and improving them before usage.

Infrared thermography (IRT) inspections have become a widely accepted method for inspecting these composite structures due to nondestructive and wider detecting area. However these methods must provide inspectors with the ability not only to detect defects, but also has automated scheme to quantify the defects to eliminate the human error, and thus improve the system's detection accuracy and effectiveness. A wide variety of image processing methods has been adapted for analyzing thermographic image to evaluate the defects quantitatively. A good review of preprocessing, processing and quantification levels for pulsed thermography methods can be found in Ref. [1, 2]. The detection is based on the calculation of the first time and second time derivative images. Further development of automated fuzzy expert system which can effectively eliminate the error of the human eye to improve detection capability, and improve the system of detection capability on specific defect size is also reported [3].

In this study, an automated scheme for determination of the location and size of defects using image processing techniques is reported. The scheme includes local thresholding to binarize the image and reduce non-uniform thermal energy effect, morphology procedures to reduce larger noises, extract connected set and separate the defect from the sample, the area and size of defects can be identified automatically. Test of the scheme on various samples having artificial defects embedded in different depth is shown and discussed.

T.Y.-F. Chen (✉) • G.-Y. Lin
Department of Mechanical Engineering, National Cheng Kung University, Tainan 70101, Taiwan, ROC
e-mail: ctyf@mail.ncku.edu.tw

S. Bossuyt et al. (eds.), *Residual Stress, Thermomechanics & Infrared Imaging, Hybrid Techniques and Inverse Problems, Volume 9*, Conference Proceedings of the Society for Experimental Mechanics Series, DOI 10.1007/978-3-319-21765-9_30

30.2 Materials and Methods

30.2.1 IRT

Objects will emit infrared above 0K, when the light passes through the lens of IR camera, the IR sensors receive infrared light and generate electrical signal that is proportional to the radiation energy received. After signal amplification, it will be converted into temperature data by the data conversion circuit. In general, different IR sensor has its own energy detection wavelength range and the detection range. The temperature range and emissivity for testing the object need to be set and calibrated before starting the measurement.

30.2.2 IRT Experimental System

A photograph of step heating experimental system is shown in Fig. 30.1. It consists of an IR camera, a computer system, and a hood with 4000 W of heat source lamp at the top inside. The IR camera (TAS-G100EXD, NEC, Japan) used in this study has wavelength of 8~14 μm and temperature range −40 to 1500 °C, with a resolution of 0.04 °C and a measurement accuracy of ±2 % or 2 °C of reading, 320 × 240 pixels and 30 frames/s. A shutter is set at the bottom of hood to extract after preheating. Since the conversion of grey-level image to temperature field in not linear, a self-designed calibration method was applied to transfer the gray-level value image into a temperature image accurately [4].

30.2.3 Specimens and Test

The most common defects in CFRP are delaminations, voids, inclusions, and regions having non uniform distribution of fibers [5]. The CFRP sample used is shown in Fig. 30.2. Artificial defect was made by inserting Teflon film of size 8 mm × 8 mm between layer 2 (0.05 cm), layer 4 (0.1 cm), and layer 6 (0.15 cm) at known locations. The size of specimens

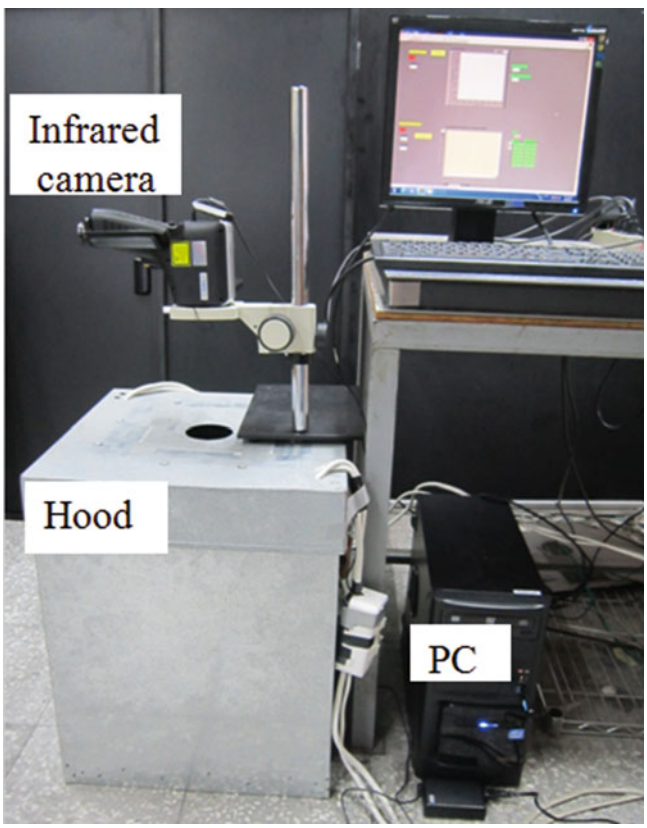

Fig. 30.1 Step heating experimental system

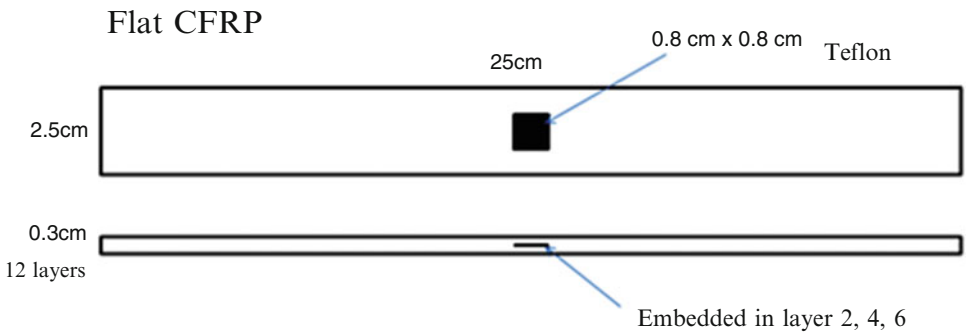

Fig. 30.2 Schematic of CFRP sample

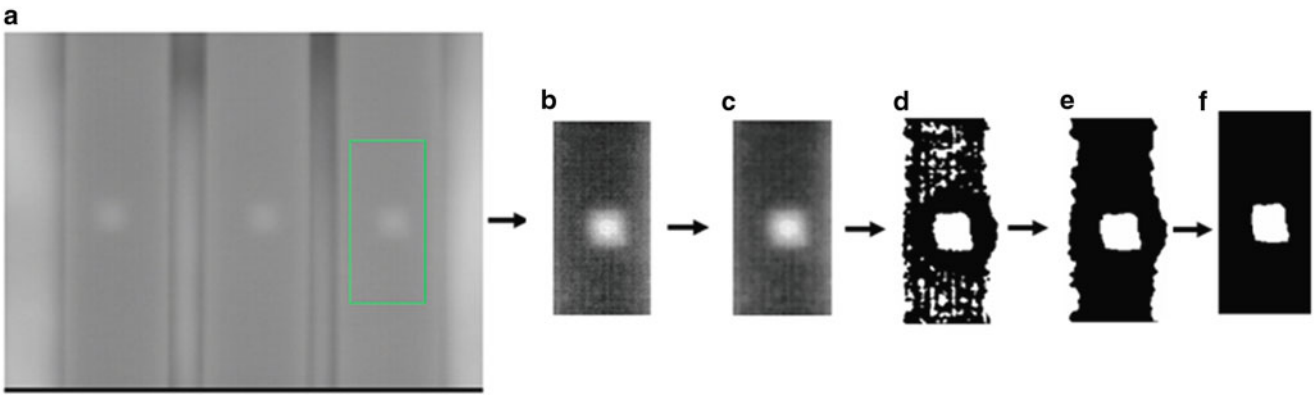

Fig. 30.3 (**a**) Original IRT image of a specimen after being (**b**) enhanced, (**c**) filtered, (**d**) binarized, holes filled, and (**f**) edge filled

is 250(L) × 25(W) × 3(T) mm. One face of the specimen was subjected to a constant and uniform heat flux, and the surface temperature response was recorded on the same face. The hood was preheated for 5 s and applied for 5 s with heat source, and then the specimen was allowed to cool down. The IR camera recorded the data from the start of the heat flux application and up to 5 s after the heat source was turned off. The recorded IR image was fed into computer directly for further examination and image processing.

30.2.4 Software Development

The IRT images (Fig. 30.3a) are typically analyzed for temperature difference which may indicate the suspected defects. Usually the contrast of defect in IRT image is low, image enhancement process can be applied to make the defect more visible (Fig. 30.3b). For automated detection, the image having the highest temperature difference among the 300 temperature-time history data is chosen for further detection of defects. Since noise of multiple nature and non-uniform distribution of thermal energy could make the interpretation of the defect difficult, the reduction of noises on the image selected by using median filtering and/or neighborhood averaging is required. Figure 30.3c shows the filtered IRT image.

Image binarization methods usually select one threshold to distinguish the desired target or background from image. However, if the image is affected by non-uniform distribution, it's hard to distinguish the desired targets correctly. Niblack thresholding method [6] can effectively eliminate uneven areas and distinguish the desired target and background from image was adopted to reduce the non-uniform thermal effect. Niblack method calculates a pixel-wise threshold by sliding a rectangular window over the gray level image. The threshold is determined based on the local mean m(x, y) and the standard deviation s(x, y) of all the pixels in the window as given by (30.1) below:

$$T(x, y) = m(x, y) + k \bullet s(x, y) \tag{30.1}$$

where k is the coefficient of variation which is an empirical constant, and can be adjusted according to demand. The window size can be selected as the smallest defect size approximately. Figure 30.3d shows the binarized IRT image with defect area clearly distinguished from the background. There are some noises mainly due to thermal diffusivity changes in the CFRP orthotropic material. Niblack method tents to generate noise. With larger value of k, the noise will be reduced but the sensitivity of the target will also be reduced.

Morphology operations change the structure of objects in an image. Its main principle is using a structuring element to remove or increase the area of the object. Using the conditional dilatation to fill the enclosed region X_k in the binary image, the definition given below can be applied

$$X_k = \left(X_{k-1} \bigoplus S\right) \cap B^c \tag{30.2}$$

Where $X_{k-1} \bigoplus S$ means X_{k-1} is dilated by S, B^c is the complement of B set. When X_k=X_{k-1}, the iterative computation is ended, and small holes in the image can be filled. Figure 30.3e shows the result after those noisy holes, being filled. The resulting image after edge filled is shown in Fig. 30.3f

Finally a 8-adjacent element connected set extraction procedure can be applied to obtain the connected set, and separated by 8-adjacent element eroding first and dilated by using 4-adjacent element for defect size measurement. Figure 30.4 shows the flowchart of automated defect detection algorithm. The software was coded by LabView [7].

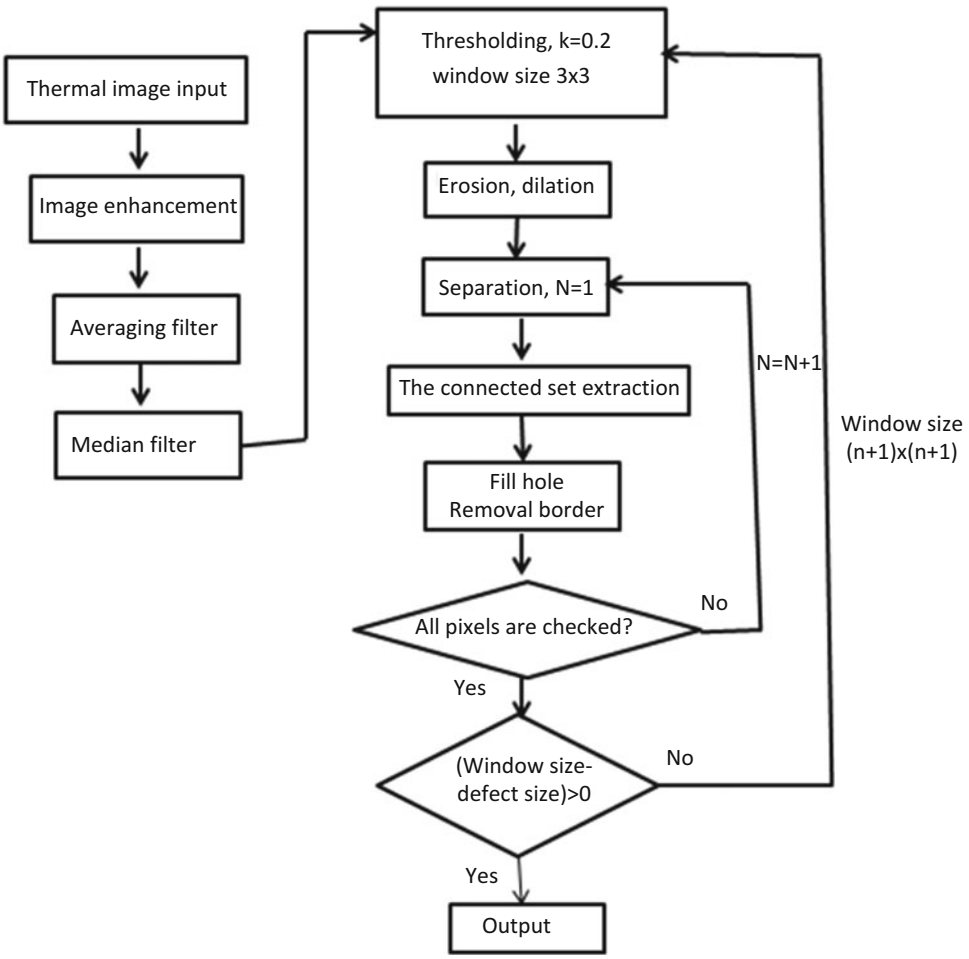

Fig. 30.4 Automated defect detection algorithm flowchart

30.3 Test Results and Discussion

Using the IRT temperature-time history data, the image having the largest temperature difference was found around 5–6 s for the three kinds of specimens. In general, the time is longer as the defect is embedded deeper. The enhanced and processed IRT images of the three specimens are shown in Fig. 30.5. The number listed below the processed image represents the window size used for Niblack binarization. The window size varies a little It can be seen that the contrast of defect become

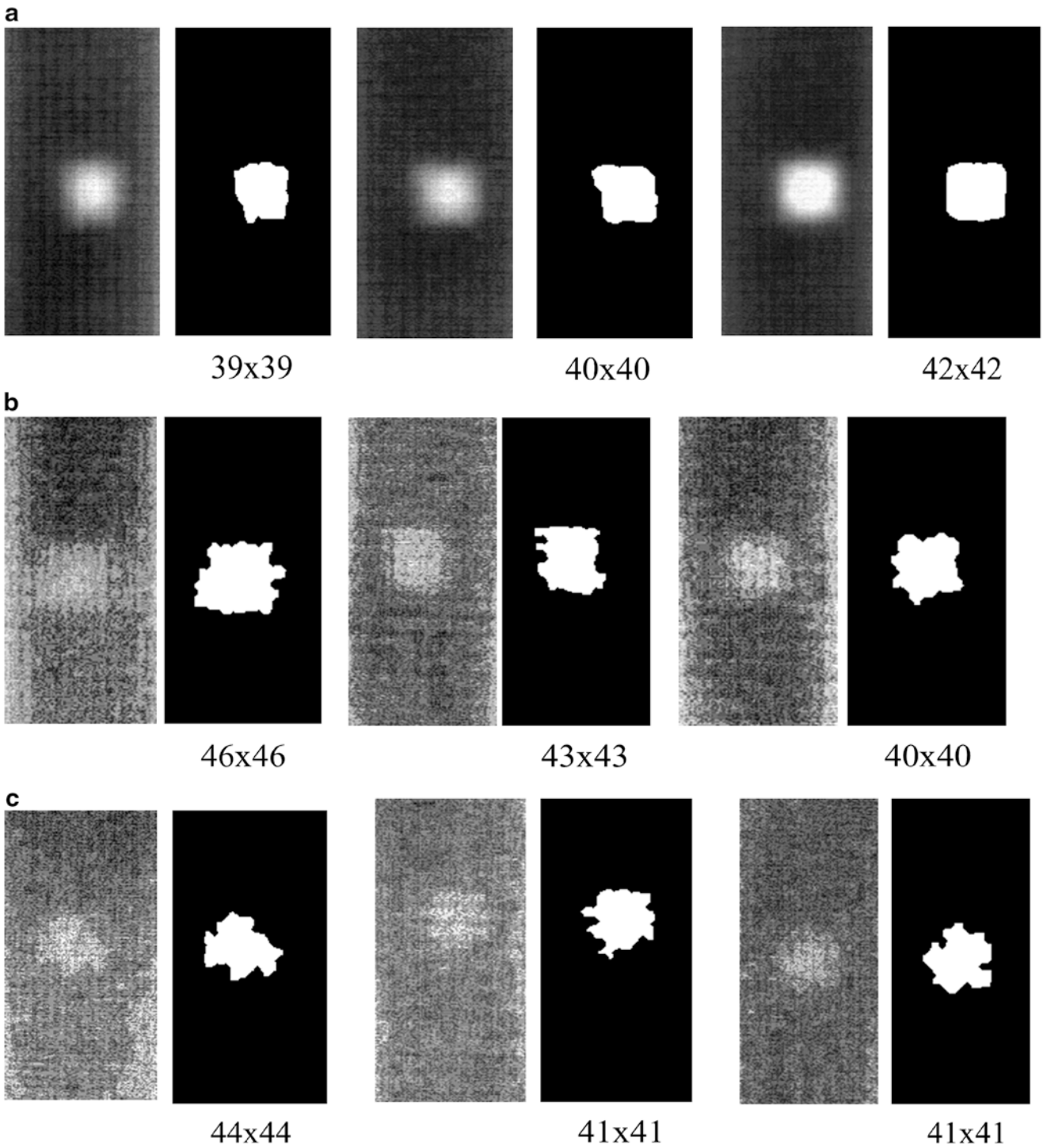

Fig. 30.5 Enhanced and processed IRT images of three specimens with defect embedded in (**a**) layer-2, (**b**) layer-4 and (**c**) layer-6

worse as the defect deposed deeper. The shape is also changed more from the original artificial shape. Nevertheless, the location and shape of the detect defects resemble to the ones observed in the enhanced original image. The size of defects of layer-2 specimen detected are 57.1 mm^2, 56.6 mm^2, 52.3 mm^2, and that for layer-4 and layer-6 are 57.7 mm^2, 63.6 mm^2, 66.2 mm^2, and 50.4 mm^2, 47.3 mm^2, 47.5 mm^2, respectively. The sizes of most detected defects are smaller than the Teflon film size of 64 mm^2.

30.4 Conclusion

An automated scheme for determination of the location and size of defects using image processing techniques is reported. The scheme includes local thresholding to binarize the image and reduce non-uniform thermal energy effect, morphology procedures to reduce larger noises, extract connected set and separate the defect from the specimen. Test of the scheme on various specimens having artificial defects embedded in different depth is shown. The contrast is lower as the defect is embedded deeper. Nevertheless, the defects can be detected accurately from the IRT images while comparing to the IRT image observed. Further study of the difference between the defect on IRT image and the embedded Teflon size maybe required.

Acknowledgement This work is supported by National Science Council, Republic of China under the contract no. MOST103-2221-E-006 -053

References

1. V. Vavilov, X. Maldague, B. Dufort, F. Robitaille, J. Picard, Thermal nondestructive testing of carbon epoxy composites: detailed analysis and data processing. NDT&E Int. Vol. **26**, 85–95 (1993)
2. X. Maldague, Applications of Infrared Thermography in Nondestructive Evaluation, in *Trends in Optical Nondestructive Testing*, ed. by P. Rastogi (Elsevier, Oxford, 2000), pp. 591–609
3. Y.P. Pan, T.P. Chu, Intelligent Non-Destructive Evaluation Expert System for Carbon Fiber Reinforced Plastics Panel Using Infrared Thermography. in *Thermomechanics and Infra-Red Imaging, vol. 7, Conference Proceedings of the Society for Experimental Mechanics Series 9999999*. doi:10.1007/978-1-4614-0207-7_12, 2011
4. T.Y. Chen, M.-H. Kuo, Converting the Infrared Thermal Image into Temperature Field for Detection the Defects Inside Materials, in *Proc. SPIE, 8759, Eighth International Symposium on Precision Engineering Measurement and Instrumentation*, p. 87594L. doi:10.1117/12.2015771, 2013
5. S. Marinetti, A. Musicio, P.G. Bison, E. Grinzato, Modeling of thermal non-destructive evaluation techniques for composite materials. Proc. SPIE Int. Soc. Opt. Eng. **4020**, 164–173 (2000)
6. W. Niblack, *An Introduction to Digital Image Processing* (Prentice Hall, Upper Saddle River, 1986), pp. 115–116
7. T. Klinger, *Image Processing with LabVIEW and IMAQ Vision* (Pretice Hall PTR, Upper Saddle River, 2003)

Chapter 31
Modelling the Residual Stress Field Ahead of the Notch Root in Shot Peened V-Notched Samples

M. Benedetti, V. Fontanari, M. Allahkarami, J.C. Hanan, B. Winiarski, and P.J. Withers

Abstract The knowledge of the residual stress field in the vicinity of the notch of shot peened fatigue specimens is of paramount importance to understand the fatigue resistance of components carrying stress raisers and subjected to surface treatments aimed at introducing compressive residual stresses. For this purpose, residual stresses were measured along the notch bisector using two experimental techniques, namely micro-XRD and FIB-DIC micro-slot cutting and micro-hole drilling. The measurements were used to reconstruct the residual stress field through FE analyses. The obtained results accord with both experimental techniques and indicate an increasing concentration of the longitudinal residual stress component with increasing sharpness of the notch. The proposed approach can be very useful to estimate the notch fatigue resistance of shot peened component on the basis of local stress and fracture mechanics approaches.

Keywords Shot peening • Notch fatigue • Al-7075-T651 • Residual stresses

31.1 Introduction

Residual stresses arise in most materials as a consequence of processing and/or in-service loading. Depending on their sign, magnitude, spatial distribution, and the scale over which they equilibrate, residual stresses can alter the mechanical and functional performances [1]. Consequently, their quantification is of great importance across many sectors. For instance, residual stresses are intentionally introduced into the surface layers of mechanical components to enhance their fatigue resistance. In fact, compressive residual stresses hinders crack nucleation owing to mean stress effect and retards the propagation of physically-small cracks [2]. Shot peening is a surface treatment that is commonly used to exploit the beneficial effects of residual stresses on the fatigue resistance of metallic materials. Shot peening proved to be particularly effective in enhancing the fatigue response in the presence of stress raisers, like notches in laboratory samples or holes, fillets and grooves associated with machined elements. In such cases, the concomitant increment in fatigue strength and the reduction in notch sensitivity are mostly attributed to compressive residual stresses [3]. However, the few papers published in the literature [4–6] do not seem to provide a convincing explanation of both the spatial distribution and the effect of residual stresses on the notch fatigue strength. Until now, attempts to estimate the fatigue resistance of peened notched components were done (1) by considering nominal residual stresses measured far from the notch [7], or (2) by adopting fatigue design codes based on empirical correction factors to account for surface treatment effects on notch fatigue [8], or (3) by reconstructing the notch residual stress field on the basis of Finite Element Analyses and XRD residual stress measurements on plain specimens [3], or taking (4) in-situ measurements of the residual stress field at the notch tip using experimental techniques suitable for far-field measurements [6]. To date the first three approaches lack experimental validation, while the last approach encounters considerable experimental challenges to stress measurement; namely, the shallow treatment depth (some hundreds of microns) and high lateral residual stress gradients (on the order of MPa/μm) meaning that most experimental techniques are not suitable. For instance, blind-hole-drilling, contour and slitting methods

M. Benedetti (✉) • V. Fontanari
Department of Industrial Engineering, University of Trento, via Sommarive 9, Trento 38123, Italy
e-mail: matteo.benedetti@ing.unitn.it

M. Allahkarami • J.C. Hanan
Department of Mechanical and Aerospace Engineering, Oklahoma State University,
700 N. Greenwood Ave., Tulsa, OK 74106, USA
e-mail: Jay.Hanan@okstate.edu

B. Winiarski • P.J. Withers
School of Materials, The University of Manchester, Grosvenor Street, Manchester M13 9PL, UK
e-mail: B.Winiarski@manchester.ac.uk

S. Bossuyt et al. (eds.), *Residual Stress, Thermomechanics & Infrared Imaging, Hybrid Techniques and Inverse Problems, Volume 9*, Conference Proceedings of the Society for Experimental Mechanics Series, DOI 10.1007/978-3-319-21765-9_31

can be applied only to macroscopic through-thickness residual stress fields in work-pieces of simple geometry; conventional X-ray and neutron diffraction probe regions of millimetre dimensions which are too large to resolve steep residual stress gradients [3]. In recent years, a few techniques have emerged for micron scale residual stress evaluation. Micro X-ray diffraction (μXRD) allows for the examination of very small sample areas using highly focussing optics [9] but the depth sampled is limited to tens of microns in most metals. The advent of dual beam focused ion beam—scanning electron microscope (FIB-SEM) imaging/milling systems in combination with digital image correlation (DIC) analysis has made it possible to carry out very fine excisions and to record the resulting displacements with nanometre precision. Recently, this has led to the development of a number of micro-scale analogues of conventional mechanical stress measurement methods, e.g. micro-slot cutting (μSC) [10, 11] and micro-hole (μHD) drilling [12] and ring-core methods [13]. Such micro-mechanical methods can determine residual stresses at micron scales laterally and as a function of depth.

In the present paper, we map the residual stresses in shot peened prismatic Al-7075-T651 specimens carrying two edge V-notches along the notch bisector using complementary microscopic techniques, namely μXRD, μHD and μSC with the aim of faithfully reconstructing the residual stress field by finite element modelling. A measure of the residual stress distribution in the presence of a notch is needed to evaluate the notch fatigue resistance on the basis of local stress and fracture mechanics approaches [3, 14]. A specific aim of this paper is to verify the method proposed in [3] where thermal eigenstrains were determined from in-depth residual stress measurements undertaken on plain specimens and then transferred to the notched geometry, neglecting the contribution of the peening treatment on the lateral surface at the notch root. Unfortunately, the resulting residual stress distribution was not validated through in-situ residual stress measurements, so the effect of the peening treatment on the lateral surface could not be estimated.

31.2 Material and Experimental Procedures

31.2.1 Sample Preparation

The experimentation was performed on the aluminium alloy Al-7075-T651, widely used for aeronautical applications, supplied in the form of 4 mm thick rolled plate. Microstructure and monotonic tensile properties are reported in [15]. The fatigue characterization of the material was carried out using prismatic specimens, whose geometry is shown in Fig. 31.1. The results of the fatigue tests are reported in [16]. The specimens were extracted from the plate with the stress axis parallel to the L-direction of the microstructure. Particular attention was paid in accurately electro-discharge machining the two edge V-notches (with aperture angle of 90°), which significantly affect the stress distribution. The notch root fillet radius was set to 2 mm (“blunt” notched samples), 0.5 mm (“sharp” notched samples) and 0.15 mm (“very sharp” notched samples), so that the theoretical stress concentration factor is 1.5, 2.4 and 3.7, respectively.

The fatigue specimens were subjected to a controlled shot peening treatment, whose process parameters are summarized in Table 31.1. Details about the air-blast machine used for shot peening can be found in Ref. [14]. The treatment employs small ceramic beads leading to a gentle and superficial effect, which allow for higher fatigue performance as compared with larger shots and better coverage of small geometrical details. All the specimen sides, including the notch root, were treated.

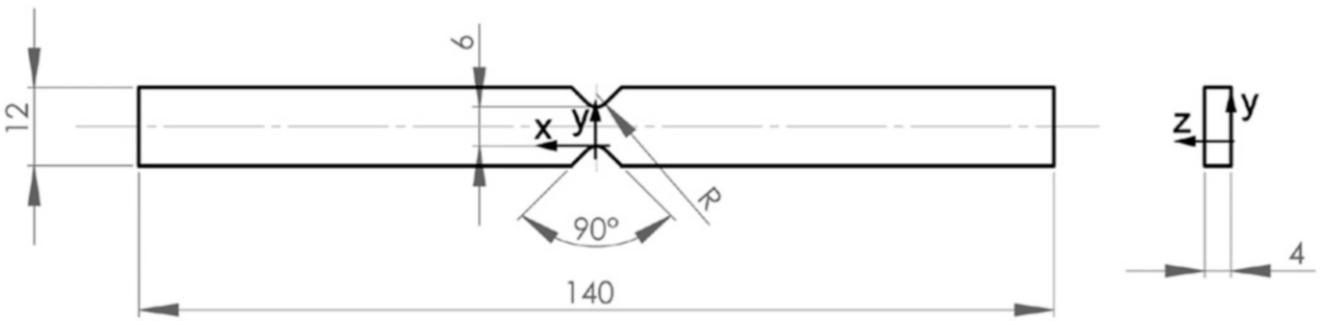

Fig. 31.1 Geometry of notched specimens used in this study. All dimensions are given in mm. Three types of notched samples were used; the notch root fillet radius R is 2, 0.5 and 0.15 mm in the blunt-notched, sharp-notched and very sharp-notched samples, respectively

Table 31.1 Shot peening parameters

Treatment	Material	Bead size (μm)	Bead hardness (HV_1)	Bead composition	Almen intensity	Angle of impingement	Coverage (%)
B120	Ceramic	60–120	700	ZrO_2 67 %	4.5N	90°	100
				SiO_2 31 %			

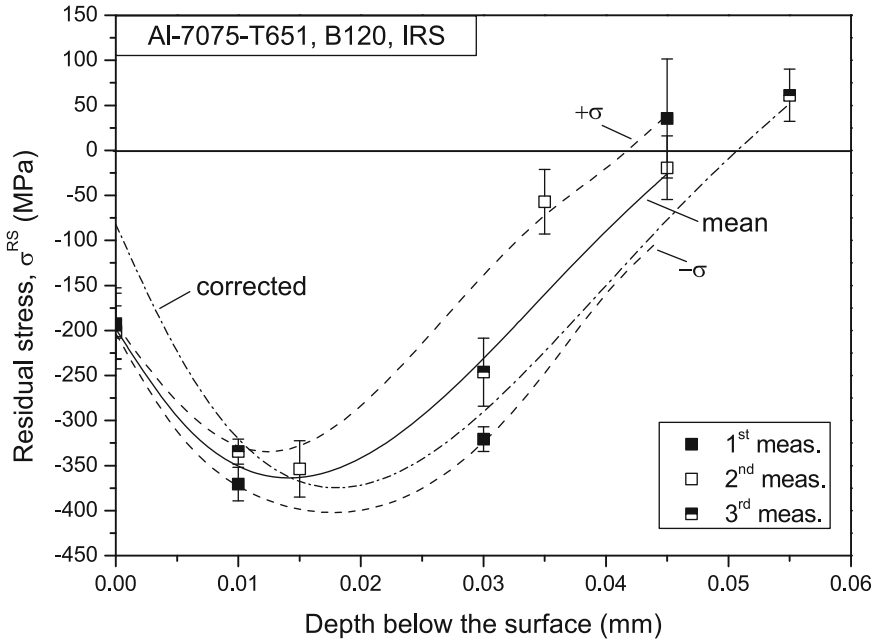

Fig. 31.2 Longitudinal residual stress in-depth profile measured by XRD technique in the centre of plain (unnotched) coupons. Three measurements were carried out in order to account for the variability in the residual stress field. Beside experimental data, the mean in-depth profile (*solid line*) and the [+σ,−σ] scatter band (*dashed lines*) are shown. The mean residual stress profile was corrected (*dash-dotted line*) to account for the penetration depth of the Cr radiation

In [14], the residual stress field produced by the peening treatment was characterized through in-depth XRD measurements carried out in the centre of plain (unnotched) coupons. Measurements were made with Cr Kα radiation (penetration depth ≈12 μm) in the longitudinal direction in the gage region. The analysis zone was limited by a collimator of 1 mm^2 in area. The classical $\sin^2 \psi$ method was applied for stress evaluation with the use of 9 diffraction angles (2θ) scanned at tilt angles ψ comprised between −45° and +45°. The ⟨311⟩ diffracting planes were chosen in order to obtain high angle measurements (2θ angle 139.0°) with higher strain sensitivity. The in-depth measurements were conducted step-by-step using an electro-polishing device by removing a very thin layer of material in a region (2 mm × 2 mm) localized at the gauge section of the specimen. Three measurements (dotted values) were performed in order to account for the variability in the residual stress field. The obtained residual stress profiles are shown in Fig. 31.2. The solid line represents the average in-depth profile, while the dashed lines identify the 1σ uncertainty band. The residual stress profile displays a sub-superficial compressive residual stress peak located nearly 15 μm below the surface and a depth of the surface layer interested by compressive residual stresses equal to about 50 μm. The average residual stress profile was corrected for the penetration depth of the radiation used for the XRD measurements and shown in figure as a dash-dotted line. It can be noted that the surface residual stress value decreases and the compressive residual stress peak is shifted to a deeper position, located about 20 μm below the surface.

31.2.2 Stress Field Around the Notch

In the present paper, we characterized the residual stress field in the notched peened samples by measuring residual stresses along the notch bisector through two complementary experimental techniques. (1) μXRD measurements were made using CuKα radiation with higher penetration depth (≈40 μm) to capture information about residual stresses throughout the entire surface layer modified by the peening treatment. (2) μHD and μSC measurements were made on specimens that had been previously polished to remove the outer 30 μm thick surface layer. In this way, information was obtained in a region of high

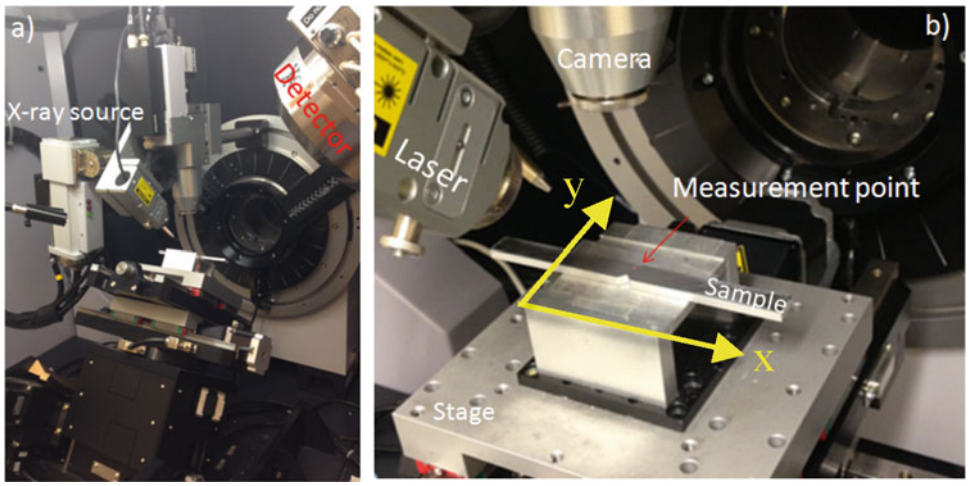

Fig. 31.3 Photograph of the XRD2 micro-diffractometer used to map the residual stress field in the notched specimens

compressive residual stresses, but the local point to point variations arising from the impact dimples and surface damage had been eliminated, as discussed in the companion paper [17].

μXRD measurements were carried out on notched specimens in the longitudinal direction employing a Bruker's D8 Discover XRD2 micro-diffractometer equipped with aGeneral Area Diffraction Detection System (GADDS) and Hi-Star 2D area detector. Tube parameters of 40 kV/40 mA using Cu-Kα radiation at a detector distance of 30 cm covering approximately an area of 20° in 2θ and 20° in γ with 0.02° resolution. For line scans, a motorized five axis (X, Y, Z (translation), ψ (tilt), φ (rotation)) stage was used for positioning which can move the measurement spot to the instrument centre within 12.5 μm position accuracy and 5 μm repeatability. A photograph of experimental set up is shown in Fig. 31.3. A focusing optic was used to achieve a beam diameter of 50 μm. Exposure time per frame was 120 s. The ⟨311⟩ diffracting planes were selected in order to include material isotropy and the possibility of obtaining high angle measurements with higher stress sensitivity. For the given angular resolution of 0.01°, a residual stress with magnitude of ±1.04 MPa can be measured. The surface residual stress profile along the notch bisector was mapped through 11 measurements spaced 50 μm apart starting from the notch tip with the height adjusted for each point. Two dimensional frame data were imported to Bruker's LEPTOS software for residual stress evaluation. Each frame was divided to sub regions and locally integrated along the y direction to obtain 1D diffraction pattern for each sub region. Corrections on polarization, background, $K\alpha_2$ were performed. The peak positions were determined by fitting Pearson VII type functions. Due to the large number of points available for a diffraction peak, the Pearson VII function is statistically reliable.

The μHD and μSC measurements were performed on notched peened samples. Their front surface was gently polished using emery papers (grit ranging from 600 to 2400), abrasive aqueous suspensions (particle size ranging from 9 to 0.25 μm) and 0.05 μm colloidal silica solution. In this way, a surface layer of about 30 μm thickness was removed. As shown in [14], the removal of a thin surface layer does not significantly affect the residual stress distribution in the underlying material. To measure the residual stresses, a series of micro-holes (1 μm in diameter and 1 μm deep) and micro-slots (6 μm long, 0.1 μm wide and 0.5 μm deep) were FIBed along the notch bisector using an FEI Nova Nanolab 600i, as shown in Fig. 31.4. Davis LaVision DIC software was used to record the surface relaxations as the holes and the slots are milled. Further detail can be found in the companion paper [17].

31.3 Experimental Results

Figure 31.5 shows the results of the μXRD measurements in terms of longitudinal residual stress distribution along the *y* coordinate (as defined in Fig. 31.7) aligned with the notch bisector and centred on the notch apex. Due to the high penetration of the Cu-radiation into the surface layers, each experimental data can be considered as an average value of the longitudinal residual stress acting, at the corresponding *y* location, on the outer 40 μm thick surface layers, as discussed in the following. Two measurements were done on opposite faces of the samples, showing a very good repeatability. It can be noted that the

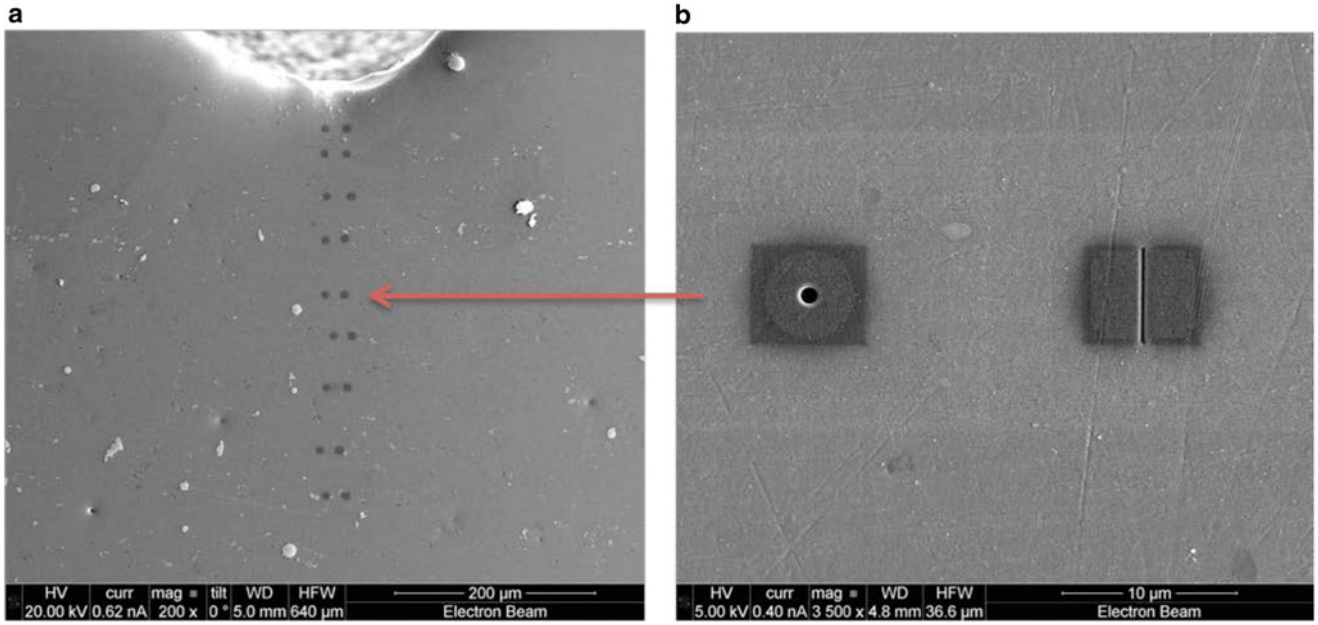

Fig. 31.4 (**a**) Overall view from SEM microscopy of polished notched sample, with a measurement location. (**b**) Detailed view of a micro-hole and a micro-slot

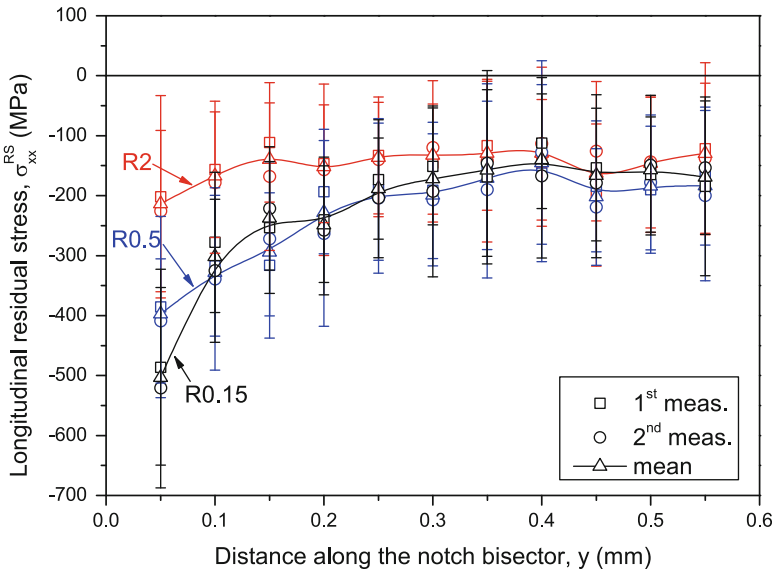

Fig. 31.5 Results of the µXRD measurements in terms of longitudinal residual stress distribution along the notch bisector. Error bars represent the 1σ uncertainty band. R2, R0.5 and R0.15 refer to the measurements undertaken on the blunt (R2), sharp (R0.5) and very sharp (R0.15) notched samples, respectively

longitudinal residual stress component is increases moving toward to notch and that the stress concentration effect scales with the severity of the notch. The region affected by the notch spans over about 0.25 mm from the notch root.

Figure 31.6a–c illustrate the results of the FIB/DIC measurements undertaken on the blunt (R2), sharp (R0.5) and very sharp (R0.15) notched samples, respectively. The longitudinal stress (σ_{xx}) was measured by the micro-hole and micro-slot techniques, showing good agreement and matching the trends in the µXRD measurements. In addition the micro-hole method allows simultaneous evaluation of both the shear (τ_{xy}) and the transverse (σ_{yy}) residual stress components.

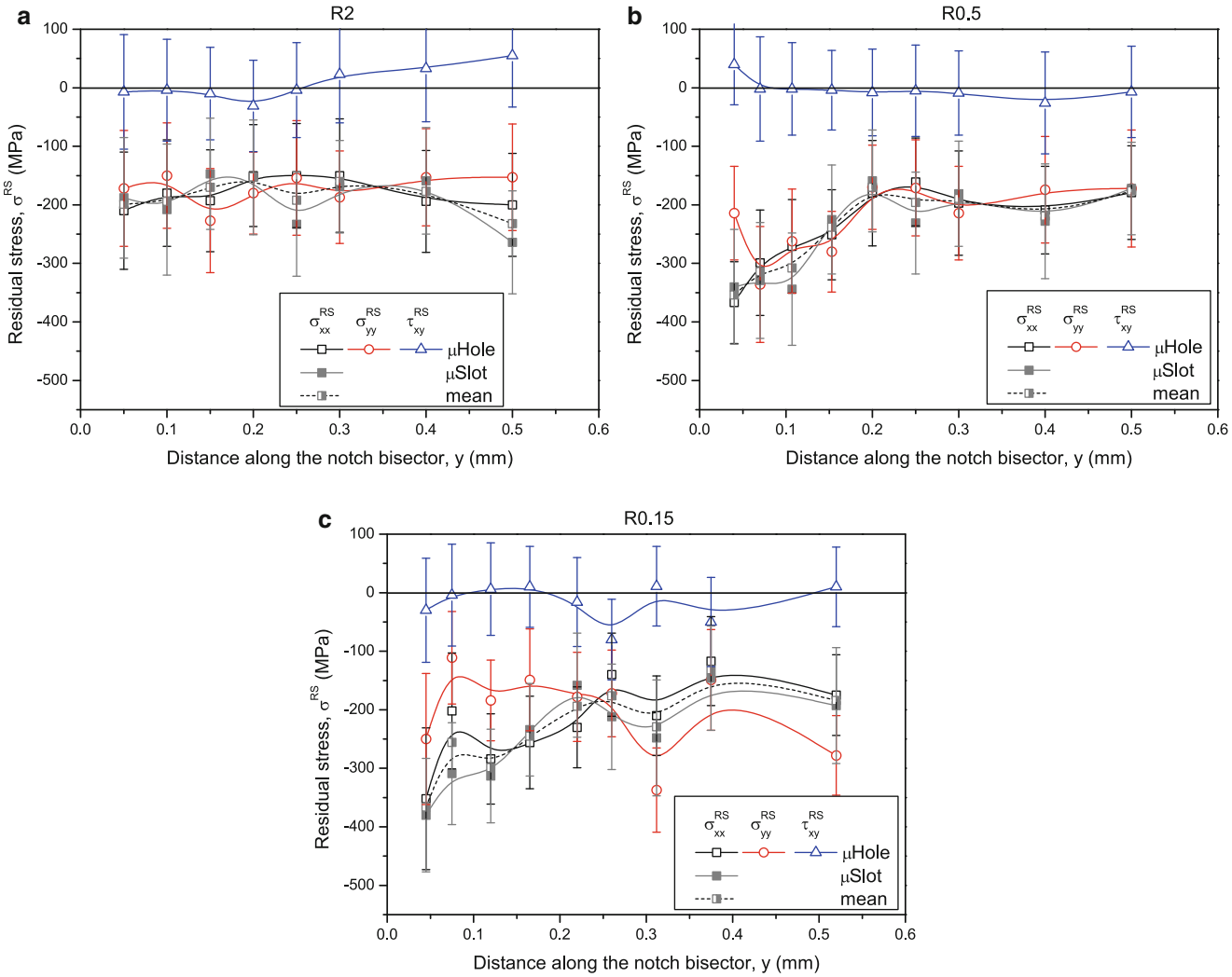

Fig. 31.6 Results of the FIB/DIC measurements of the residual stress distribution along the notch bisector. Error bars represent the 1σ uncertainty band. (**a**) Blunt (R2), (**b**) sharp (R0.5) and (**c**) very sharp (R0.15) notched samples

As expected, given that residual stresses were mapped along a symmetry plane, the shear stress is close to zero at all locations. The transversal residual stress component shows non-zero values also at close distances from the notch tip.

31.4 Numerical Reconstruction of the Residual Stress Field

In [3], the residual stress field in notched peened samples was numerically reconstructed. Accordingly, the same temperature distribution, which was estimated to reproduce the residual stresses in plain unnotched specimens on the basis of in-depth XRD measurements, was applied to nodal planes parallel to the frontal planar of the finite element model of the notched samples. In this paper, we propose to use the experimental results illustrated in Sect. 31.3 to reconstruct the whole residual stress field acting on the symmetry plane lying on the notch bisector. A specific aim of the paper is to investigate the influence that the peening treatment applied to the frontal and the lateral surfaces exerts on the residual stress field.

For this purpose, a FE model of the notched samples, depicted in Fig. 31.7, has been set up with the ANSYS 15 commercial code using 8 nodes isoparametric brick elements. In order to take advantage of the symmetry, only one eighth of the specimen was modelled. The mesh in the surface region is particularly refined with the purpose of better reproducing

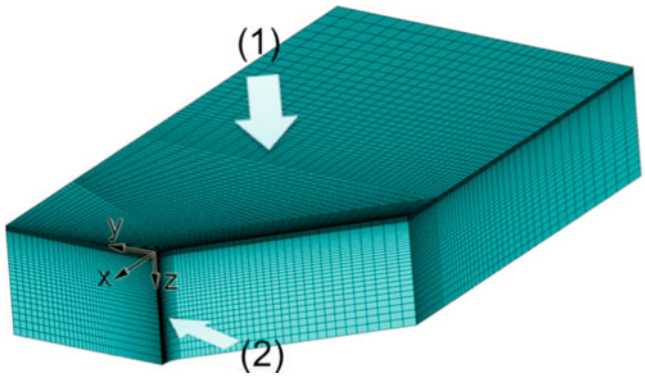

Fig. 31.7 Overview of the FE model of one eighth of the notched fatigue specimens illustrated in Fig. 31.1. (1) and (2) identify the frontal planar and fillet curved surfaces, respectively, to which a distribution of thermal eigenstrains has been applied to introduce residual stresses

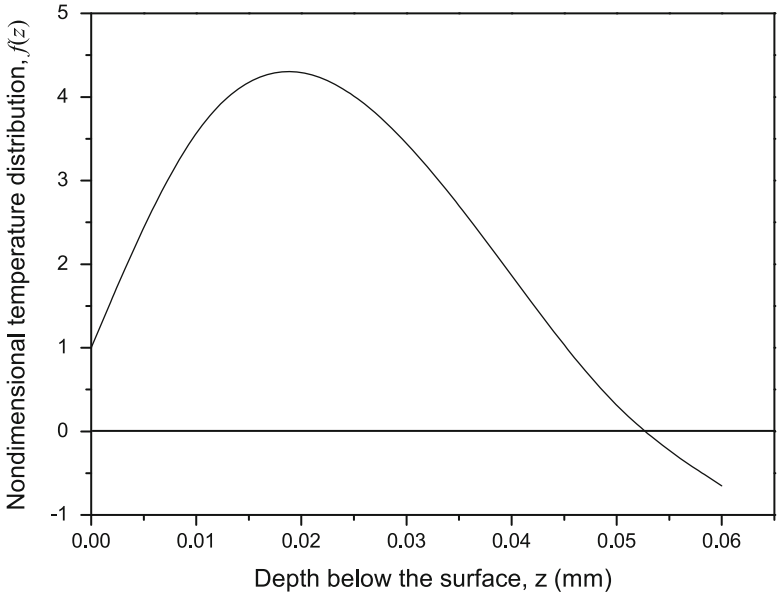

Fig. 31.8 In-depth variation of the function $f(z)$, which defines the shape of the temperature distribution applied to nodal planes parallel to the frontal surface

stress and strain gradients in the hardened layer due to the peening treatment. The minimum thickness of the elements in the surface region is 10 μm.

The analysis was conducted according to the technique presented in [3], whereby self-balancing residual stresses can be introduced into a body by applying a suitable distribution of thermal eigenstrains produced by a fictitious non-homogeneous temperature field.

First, the eigenstrain distribution needed to describe the residual stress variation with depth (Fig 31.2) introduced by peening in a flat surface was calculated. The temperature field T_1 applied to nodal planes parallel to the front surface was assumed to vary with the only depth z below the surface according to the following equation:

$$T_1(z) = A f(z) \tag{31.1}$$

where the function $f(z)$ defines the shape of the temperature distribution, shown in Fig. 31.8, and the intensity of the temperature field is controlled by the constant A.

Second, the temperature field T_2 applied to radial layers concentric to the notch root fillet was assumed to vary with the radial and angular coordinates r and θ of the polar reference frame shown in Fig. 31.9 according to the following equation:

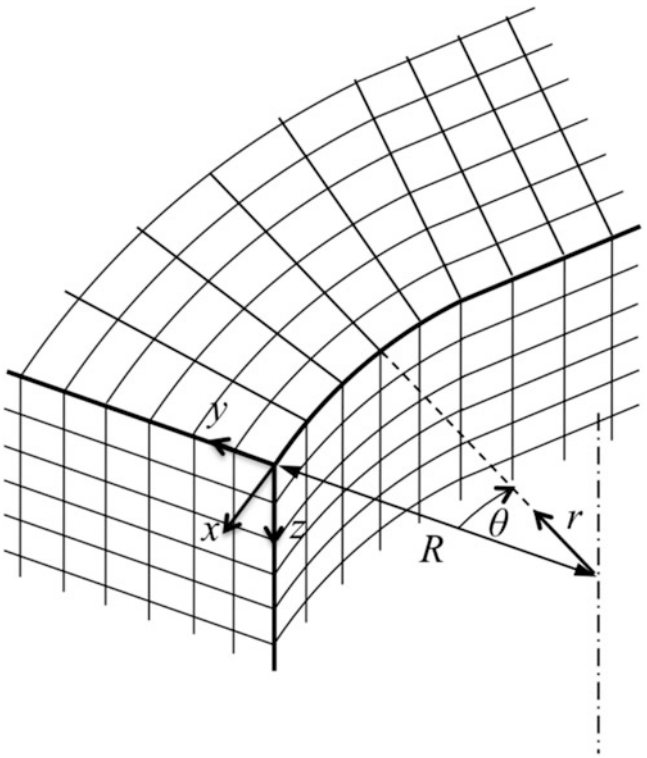

Fig. 31.9 Schematic view of the notch root region showing the reference frames considered in this work

$$T_2(r,\theta) = \sum_{i=1}^{n} B_i \cos\left[2(i-1)\theta\right] e^{-\frac{r-R}{\tau}} \tag{31.2}$$

where R is notch root fillet radius. This choice of the temperature field is based on the hypothesis that the deformation process produced by shot peening on the lateral curved surface varies not only with the depth below the surface but also with the angular position owing to the different angle under which the shots impact the surface. As before, B_i controls the intensity of the temperature field, τ its shape.

If the parameter τ is kept constant, the constants A and B_i, expressing the intensity of the temperature field, can be determined through linear fit of the experimental data. For this purpose, the influence coefficient matrices $[\alpha]$ and $[\beta_i]$ are calculated to express the residual stress at position j due to a unitary temperature applied to a nodal set located in position k. A reasonable compromise between the number of terms in (31.2) and the accuracy and stability in the solution of the fit was obtained by assuming n equal to 2. The unknown intensity of the temperature fields is calculated by solving the following equations system:

$$\left\{\sigma^{RS}\right\} = [\alpha]\{T_1\} + ([\beta_1] + [\beta_2])\{T_2\} = [M]\begin{Bmatrix} A \\ B_1 \\ B_2 \end{Bmatrix} \tag{31.3}$$

where the vectors$\{\mathrm{T_i}\}$ contain the nodal temperatures corresponding to the i-th thermal field. The vector $\{\sigma^{\mathrm{RS}}\}$ contains the experimental data shown in Sect. 31.3. Specifically, the average of the two μXRD measurements, the average of the longitudinal residual stress component measured with the μHD and μSC techniques, and the transversal residual stress component measured with the μHD method were considered. The FE stress results contained in the matrix $[M]$ to be fitted to the μXRD measurements were averaged over the penetration depth of the Cu-Kα radiation according to the following equation:

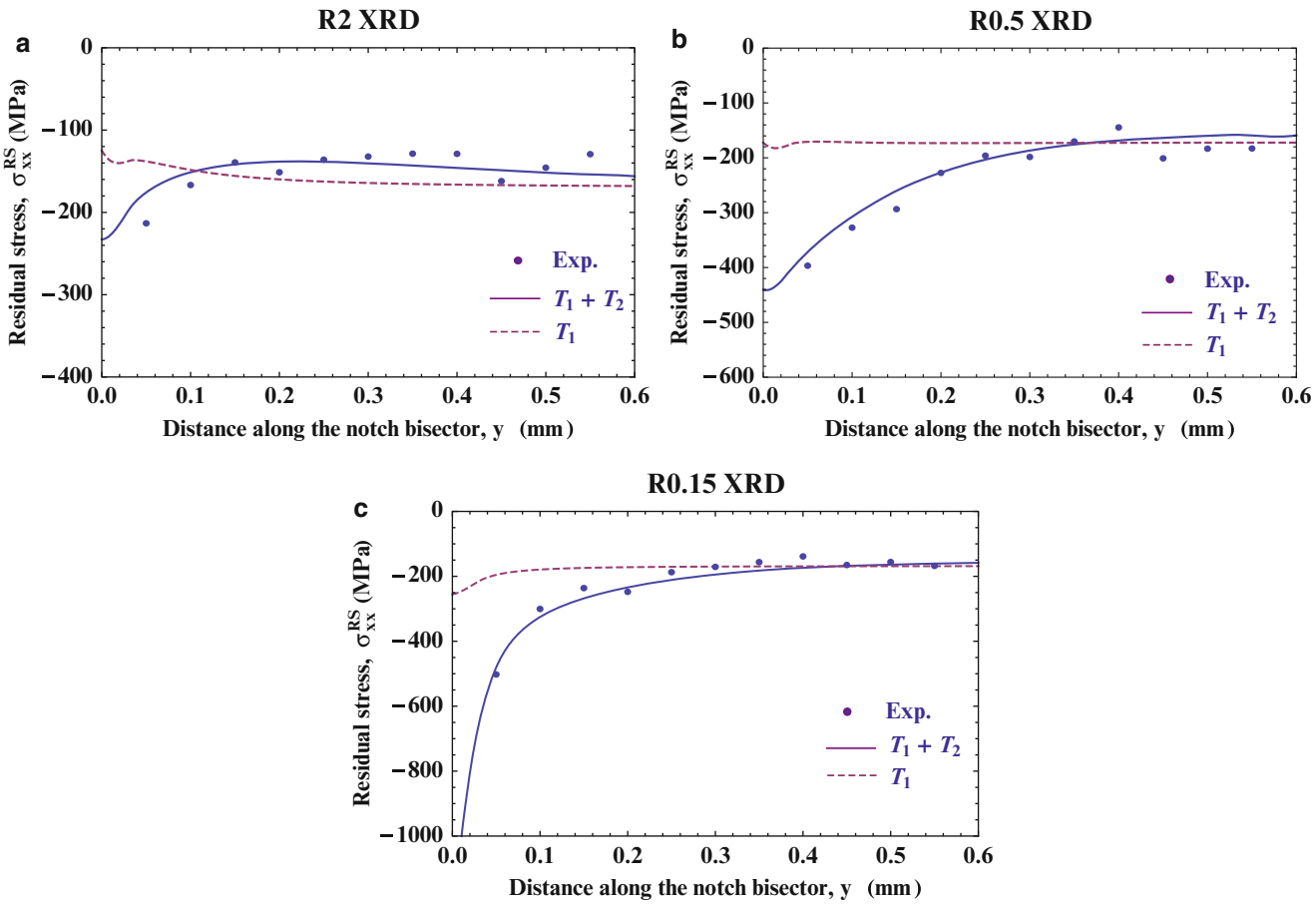

Fig. 31.10 Comparison between the residual stress values mapped with the μXRD technique (*dotted values*) and the corresponding predictions made by the numerical reconstruction. The *solid lines* refer to the contribution of both temperature fields, while the *dashed lines* indicate the contribution of the only temperature distribution T_1. (**a**) Blunt (R2), (**b**) sharp (R0.5), (**c**) very sharp (R0.15) notched samples

$$\overline{\sigma}_{xx}^{RS} = \frac{\int_0^{\infty} \sigma_{xx}^{RS}(z) e^{-\frac{z}{\xi}} dz}{\int_0^{\infty} e^{-\frac{z}{\xi}} dz}; \quad \xi = 0.0146 \text{ mm} \tag{31.4}$$

The matrix [M] is a non-linear function of the parameter τ. This problem was transformed into a linear fit and solved using the Normal Equation Method by keeping τ constant and selecting the value that minimizes the variance of the linear fit expressed by (31.3). It is very interesting to note that the fitting of the experimental data pertaining to the three notch geometries gave very similar measures of A. This means that the effect of shot peening on the curved lateral surface of the notch is effectively captured by the temperature field T_2, whose effect tends to extinguish about 0.3 mm from the notch tip. Beyond this distance, the residual stress field is mainly controlled by the temperature distribution T_1, which was found to be fairly independent of the notch geometry.

Figure 31.10 shows the comparison between the residual stress values mapped with the μXRD technique (dotted values) and the corresponding predictions made by the numerical reconstruction for the blunt (R2), sharp (R0.5) and very sharp (R0.15) notched samples, respectively. The solid lines refer to the contribution of both temperature fields, while the dashed lines indicate the contribution of the only temperature distribution T_1. It can be noted that the solid lines are in very good agreement with the experimental data, while considering the only effect of shot peening on the

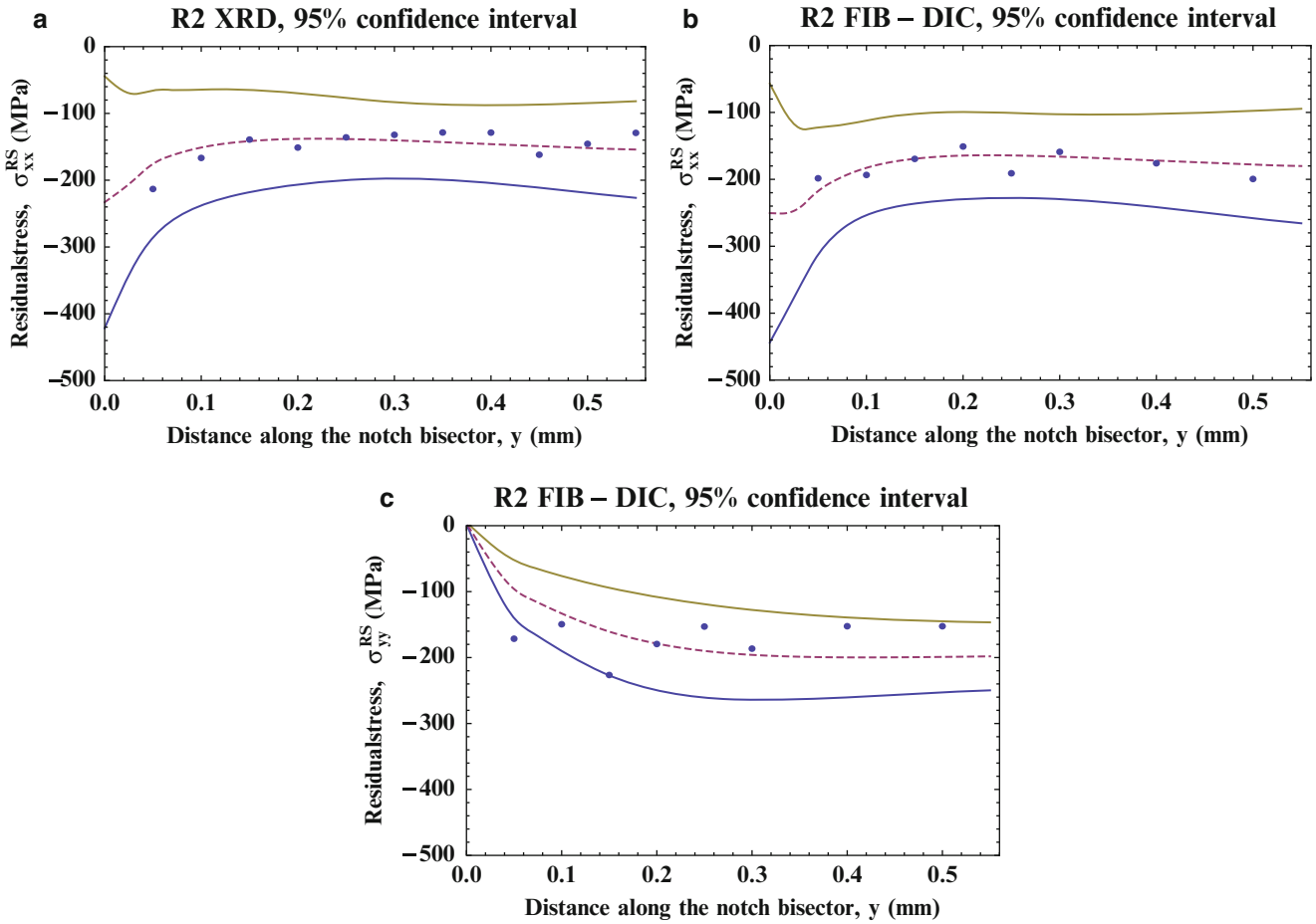

Fig. 31.11 Best fit (*dashed line*) and 95 % confidence interval (*solid lines*) of the residual stress field in the blunt (R2) notched sample. (**a**) Longitudinal residual stress measured through XRD, (**b**) longitudinal residual stress measured through FIB-DIC, (**c**) transversal residual stress measured through FIB-DIC. *Dotted values* indicate the experimental data

frontal surface will result in a significant underestimation of residual stresses close to the notch root, especially in the sharper notches.

The uncertainty on the residual stress field was estimated according to the Monte Carlo method. For this purpose, 10,000 trials were considered. In each trial, a population of residual stress data $\{\sigma^{RS}\}$ was randomly generated assuming a Gaussian probability density function with mean and standard deviation given by the experimental measures. For each trial, the unknowns A and B_i were calculated solving (31.3). The 95 % confidence interval was computed leaving 2.5 % of the trials on both sides.

The results of the residual stress field reconstruction performed through FE analyses and fit of the experimental data (dotted values) are shown in Figs. 31.11, 31.12 and 31.13 for the blunt (R2), sharp (R0.5) and very sharp (R0.15) notched samples, respectively. Figures a, b and c refer to the XRD and FIB-DIC longitudinal residual stress as well as the FIB-DIC transversal residual stress component, respectively. Dashed lines represent the best fit, while solid lines identify the 95 % confidence interval.

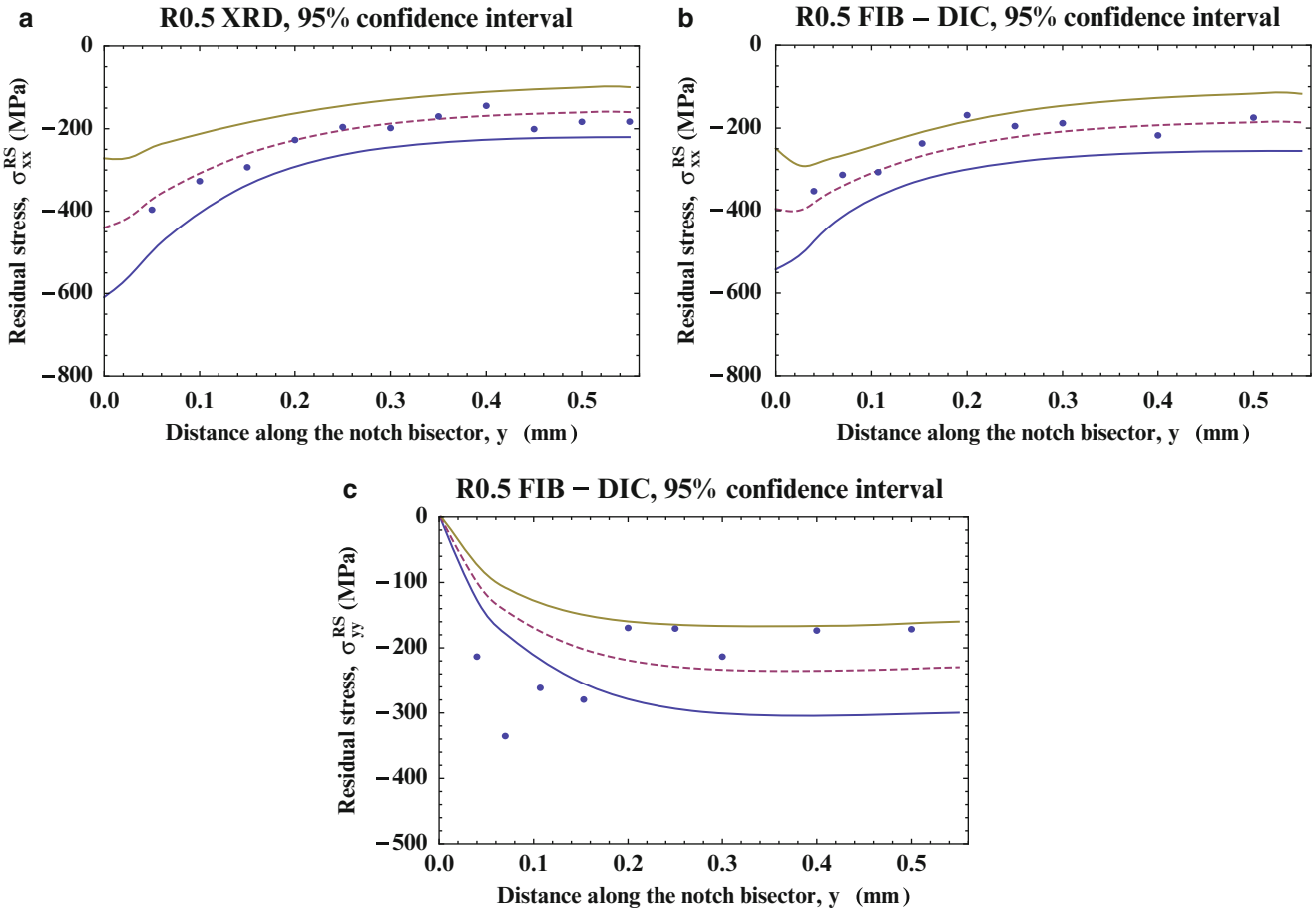

Fig. 31.12 Best fit (*dashed line*) and 95 % confidence interval (*solid lines*) of the residual stress field in the sharp (R0.5) notched sample. (**a**) Longitudinal residual stress measured through XRD, (**b**) longitudinal residual stress measured through FIB-DIC, (**c**) transversal residual stress measured through FIB-DIC. *Dotted values* indicate the experimental data

It can be noted that the reconstruction reasonably satisfies the constraints imposed by the measures of both experimental techniques. The uncertainty in the longitudinal residual stress component is higher at or close to the notch root while it declines with increasing distance from the notch. The uncertainty is particularly high on the value of the longitudinal residual stress value at the tip of the sharpest notch. In addition, the average 50 % probability value is far above the material's yield stress (515 MPa). This can be due to the fact that the analysis was purely linear-elastic, while no residual stress redistribution due to plastic flow was considered. This aspect will be further investigated in the next.

31.5 Conclusions

The residual stress field in the vicinity of the notch of shot peened fatigue specimens was measured experimentally. Specifically, two techniques, namely micro-XRD and FIB-DIC micro-slot cutting and micro-hole drilling, were used to map the residual stress field along the notch bisector. These measurements were used to reconstruct the residual stress field in the vicinity of the notch. In fact, the knowledge of the local residual stress field at the notch root is mandatory for estimating the notch fatigue resistance on the basis of local stress and fracture mechanics approaches. The residual stress field ahead of the notch was introduced into the finite element model of the notched samples using thermal eigenstrains applied to (1) nodal planes parallel to the front surface of the specimen to simulate the effect of peening on the frontal surface and (2) to nodal

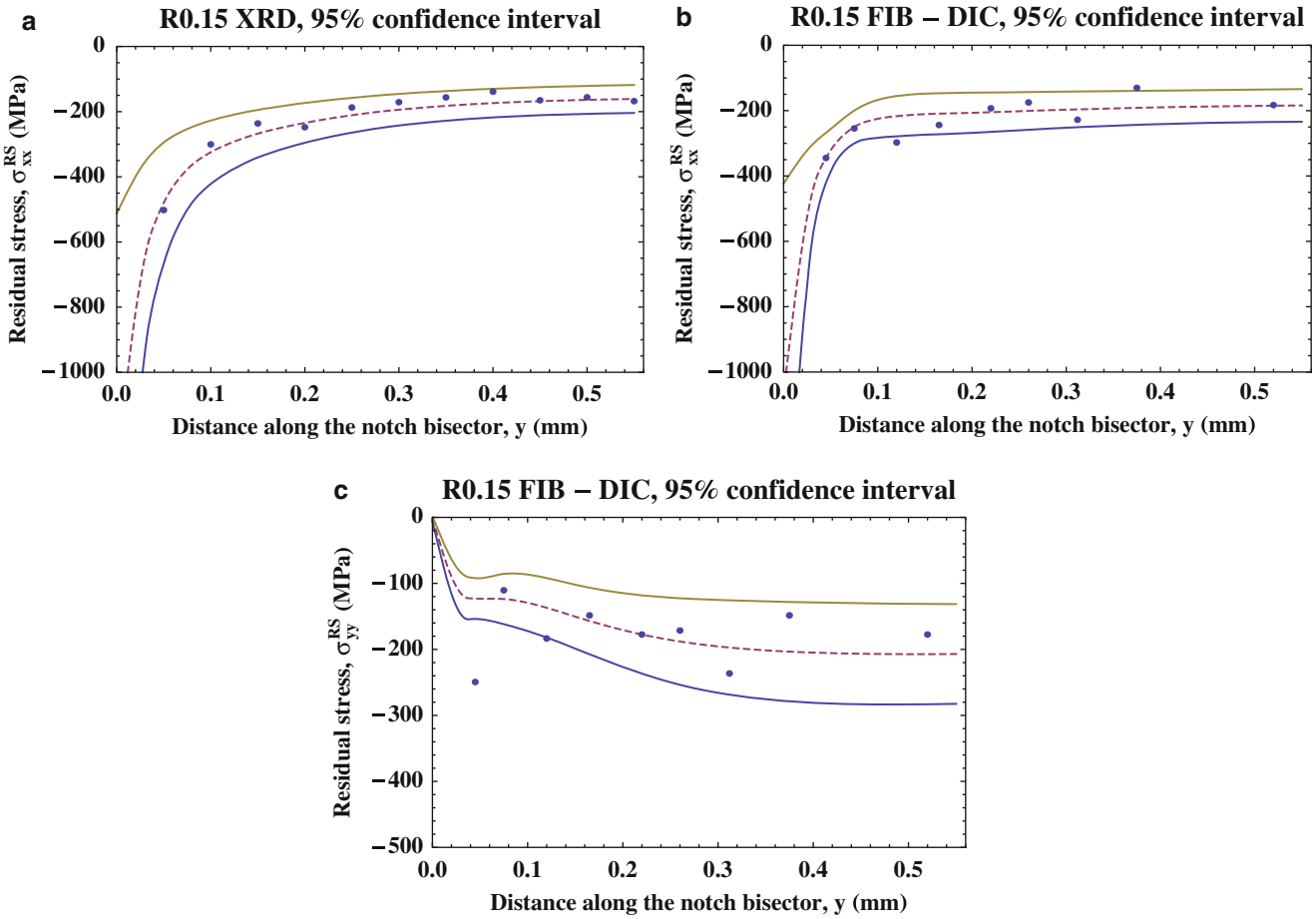

Fig. 31.13 Best fit (*dashed line*) and 95 % confidence interval (*solid lines*) of the residual stress field in the very sharp (R0.15) notched sample. (**a**) Longitudinal residual stress measured through XRD, (**b**) longitudinal residual stress measured through FIB-DIC, (**c**) transversal residual stress measured through FIB-DIC. *Dotted values* indicate the experimental data

radial layers concentric to the notch root fillet to account for the effect of the treatment on the lateral curved surface of the notch. It was found that the second contribution dominates the residual stress field at the root of the sharper notches. Therefore, simplified approaches published in the past and accounting only for the peening effect on the frontal surface lead to a significant underestimation of the residual stress field ahead of the notches.

References

1. P.J. Withers, Residual stress and its role in failure. Rep. Prog. Phys. **70**(12), 2211–2264 (2007)
2. E.R. de los Rios, A. Walley, M.T. Milan, G. Hammersley, Fatigue crack initiation and propagation on shot-peened surfaces in A316 stainless steel. Int. J. Fatigue **17**, 493–499 (1995)
3. M. Benedetti, V. Fontanari, C. Santus, M. Bandini, Notch fatigue behaviour of shot peened high-strength aluminium alloys: experiments and predictions using a critical distance method. Int. J. Fatigue **31**, 1600–1611 (2010)
4. J.A. Akber, S. Kyriacou, A.M. El-Zafrany, Effect of Shot Peening on the Fatigue Life of Axially Loaded Notched Components, in *Proceedings of the 5th International Conference on Shot Peening (ICSP5)*, Oxford, 1993, ed. by D. Kirk, pp. 349–358
5. K. Xu, J. He, Z. Huijiu, Effect of residual stress on fatigue behaviour of notches. Int. J. Fatigue **16**, 337–343 (1994)
6. J. Bergström, T. Ericsson, Relaxation of Shot Peening Induced Compressive Stress During Fatigue of Notched Steel Samples, in *Proceedings of the 2nd International Conference on Shot Peening (ICSP2)*, Chicago 1984, pp. 241–248
7. S. Bagherifard, C. Colombo, M. Guagliano, Application of different fatigue strength criteria to shot peened notched components. Part 1: fracture mechanics based approaches. Appl. Surf. Sci. **289**, 180–187 (2014)

8. G. Olmi, M. Comandini, A. Freddi, Fatigue on shot-peened gears: experimentation, simulation and sensitivity analyses. Strain **46**, 382–395 (2010)
9. M. Allahkarami, J.C. Hanan, Mapping the tetragonal to monoclinic phase transformation in zirconia core dental crowns. Dent. Mater. **27**, 1279–1284 (2011)
10. B. Winiarski, R.M. Langford, J. Tian, Y. Yokoyama, P.K. Liaw, P.J. Withers, Mapping residual stress distributions at the micron scale in amorphous materials. Metall. Mater. Trans. Phys. Metall. Mater. Sci. **41**, 1743–1751 (2010)
11. B. Winiarski, A. Gholinia, J. Tian, Y. Yokoyama, P.K. Liaw, P.J. Withers, Submicron-scale depth profiling of residual stress in amorphous materials by incremental focused ion beam slotting. Acta Mater. **60**(5), 2337–2349 (2012)
12. B. Winiarski, P.J. Withers, Micron-scale residual stress measurement by micro-hole drilling and digital image correlation. Exp. Mech. **52**(4), 417–428 (2012)
13. A.M. Korsunsky, M. Sebastiani, E. Bemporad, Residual stress evaluation at the micrometer scale: analysis of thin coatings by FIB milling and digital image correlation. Surf. Coat. Technol. **205**, 2393–2403 (2010)
14. M. Benedetti, V. Fontanari, M. Bandini, E. Savio, High- and very high-cycle plain fatigue resistance of shot peened high-strength aluminum alloys: the role of surface morphology. Int. J. Fatigue **70**, 451–462 (2015)
15. M. Benedetti, V. Fontanari, P. Scardi, C.L.A. Ricardo, M. Bandini, Reverse bending fatigue of shot peened 7075–T651 aluminium alloy: the role of residual stress relaxation. Int. J. Fatigue **31**, 1225–1236 (2009)
16. M. Benedetti, V. Fontanari, M. Allahkarami, J.C. Hanan, Notch Fatigue Behaviour of Shot Peened High-strength Aluminium Alloys: Role of the Residual Stress Field Ahead of the Notch Root, in *Proceedings of the SEM 2014 Annual Conference & Exposition on Experimental and Applied Mechanics*, Greenville, 2–5 June 2014
17. B. Winiarski, M. Benedetti, V. Fontanari, M. Allahkarami, J.C. Hanan, G.S. Schajer, P.J. Withers, Comparative Analysis of Shot-Peened Residual Stresses Using Micro-Hole Drilling, Micro-Slot Cutting, X-Ray Diffraction Methods and Finite-Element Modelling, in *Proceedings of the SEM 2015 Annual Conference & Exposition on Experimental and Applied Mechanics*, Costa Mesa, 8–11 June 2015

Chapter 32
Numerical Prediction of Temperature and Residual Stress Fields in LFSW

C. Casavola, A. Cazzato, V. Moramarco, and C. Pappalettere

Abstract In recent years important innovations have been introduced in FSW technology such as, for example, the Laser assisted friction stir welding (LFSW). In this technique the FSW process is assisted, during the weld, by the pre-heating of a de-focalized laser that allows an easier advancement of the tool. This technique should lead higher welding speeds, lower clamping forces and lower residual stress. Moreover, the prediction of residual stress is a relevant, complex and still open issue for welding process design. In this work an uncoupled thermo-mechanical finite element model has been developed to predict the temperature and residual stress fields in LFSW. Both the thermal and mechanical parts of the model have been validated on the base of experimental data. The temperature field has been recorded by an infrared camera, while residual stress field has been measured by X-ray diffraction analysis. The LFSW test was conducted on 6 mm thick 5754 H111 aluminium alloy plates.

Keywords Laser assisted friction stir welding • Residual stress • Temperature field • Finite element method • Infrared thermography

32.1 Introduction

Friction stir welding (FSW) is a joining process, invented in 1991 by The Welding Institute (TWI), with many application in bridge construction, railway, aerospace, shipbuilding and automotive industry [1]. The process consists in a rotating tool that is driven into the plates and, after a period of stationary rotation to heat and soften the material (dwell time), it is translated along the welding line to carry out the weld. In this process the material is not led to fusion but the joint is the combined result of the plasticization due to the heat generated by friction and stirring action of the pin due to the rotation and the displacement of the tool. First industrial applications of the FSW were on aluminium alloys and, in general, light alloy that are difficult to weld by traditional welding techniques [1]. Subsequently, this technology has been used with magnesium, copper, nickel, metal matrix composites (MMC) and polymeric materials [2–7]. In recent years, in order to use FSW on materials with higher melting point than aluminium light alloys (e.g. titanium, steel [8]), laser assisted friction stir welding (LFSW) has been invented and developed. In this technique, a defocused laser beam precedes the FSW tool during welding, increasing the temperatures reached in front of the tool and allowing an easier advancement of the same. This modification to FSW process should reduce the residual stress in materials where traditional FSW is already commonly used [9].

The temperature distributions and thermal histories have an important role in FSW and LFSW. Some studies [10, 11] have shown that the control of temperature during the welding process is essential to reduce the residual stresses and to obtain a good joint. Xu et al. [10], using thermocouples, found that the temperature increases with increasing the rotational speed or decreasing the transverse speed of the FSW tool. Maeda et al. [11], always using thermocouples, found that near FSW tool zone there is an asymmetric temperature distribution between the advancing side and the retreating side. Moreover, several papers have dealt with the residual stress distribution in FSW welds through experimental tests. Donne et al. [12] have measured FSW residual stress distribution on 2024Al-T3 and 6013Al-T6 welds. They have found that longitudinal and transverse residual stresses have a "M"-like distribution across the weld. Peel et al. [13] have measured the residual stress in FSW welded AA5083 specimens by synchrotron X-ray method showing that the longitudinal stresses increase with the traverse speed increase.

C. Casavola (✉) • A. Cazzato • V. Moramarco • C. Pappalettere
Dipartimento di Meccanica, Matematica e Management (DMMM), Politecnico di Bari, Viale Japigia 182, Bari 70126, Italy
e-mail: caterina.casavola@poliba.it

S. Bossuyt et al. (eds.), *Residual Stress, Thermomechanics & Infrared Imaging, Hybrid Techniques and Inverse Problems, Volume 9*, Conference Proceedings of the Society for Experimental Mechanics Series, DOI 10.1007/978-3-319-21765-9_32

Although experimental measures are fundamental to understand the thermal phenomenon and residual stress distribution in the FSW process, they present some limitations, (e.g. economic costs or internal temperature and residual stress distribution). For this reason, the implementation of numerical models that can predict the temperature distributions [14] and residual stress values have an important role. These could estimate the correct weld parameters and mechanical constraints [15] in order to improve mechanical properties of the welded joints and reducing the amount of trials and errors. Several papers, in the past years, have addressed FSW numerical models in different manner. Schmidt et al. [16] have developed an analytical model for heat generation in FSW based on different assumptions of the contact condition between the tool and the welded piece. Soundararajan et al. [17] have implemented a FSW thermo-mechanical numerical model validated by thermocouples and Song and Kovacevic [18] have carried out a 3D numerical model in a moving coordinate system validated by thermography. In the above cited model [17], the use of thermocouples shows some limitation because this technique allows to measure in single points losing the entire view of temperature distribution and, in special manner for LFSW, the temperature in the front zone of the tool. Many of these numerical simulations are only thermal model or thermo-mechanical models in which it is not considered the mechanical force that the tool exerts on the workpiece. These should be included into the thermo-mechanical model because FSW is mainly a mechanical process and the forces involved in this type of work are relevant. Finally, there are few experimental works on this new combined LFSW technique [9] and also less works that have addressed the numerical simulation of LFSW welding process.

In view of understanding, modelling and simulating the LFSW process an uncoupled 3D thermo-mechanical finite element analysis will be carried out. Also the mechanical effect of the tool will be implemented. The thermal FSW model, based on Schmidt et al. [16] equation, will be validated experimentally on temperature field recorded by an infrared camera during the LFSW process. The residual stress field behaviour, also, will be validated based on X-ray diffraction analysis measurement.

32.2 Material and Methods

The LFSW process has been carried out on 200 mm × 100 mm × 6 mm AA5754-H111 butt-welded plates, whose chemical composition appear in Table 32.1. Thermo-physical properties and mechanical characteristics at room temperature (20 °C) have been reported in Table 32.2. Table 32.3 sums up the parameters used in the LFSW process.

The tool, whose scheme has been reported in Fig. 32.1, has a flat shoulder of 10.75 mm radius ($R_{shoulder}$), a threaded cylindrical pin with a radius of 3 mm (R_{probe}) and 5.8 mm height (H_{probe}). The LFSW (Fig. 32.2) has been carried out along the welding line (Fig. 32.3) that was perpendicular to the rolling direction of the AA5754 sheets. In the same figure has been represented the configuration of the specimen constraints. Temperature measurement, residual stresses analysis and then numerical simulation have been carried out for the retreating side of the FSW welded plate, because the configuration of the FSW machine prevents access to both sides.

Table 32.1 Chemical composition Al5754

Al (%)	Si (%)	Fe (%)	Mn (%)	Mg (%)
96.1–95.5	0.4	0.4	0.5	2.6–3.2

Table 32.2 Physical and mechanical characteristics

Parameter	Value
Density (kg/m^3)	2650
Melting temperature (°C)	600
Thermal conductivity (W/m K)	138
Thermal expansion coefficient (K^{-1})	23.9×10^{-6}
σ_y (MPa)	103.4
σ_u (MPa)	215
Vickers hardness (HV)	55

Table 32.3 Process parameters of LFSW

Traverse speed (cm/min)	Dwell time (s)	Rotational speed (rpm)	Tilt angle (°)	Laser power (W)	Distance laser spot-FSW tool (mm)	Plunge force (N)
20	3	500	2	500	40	20,000

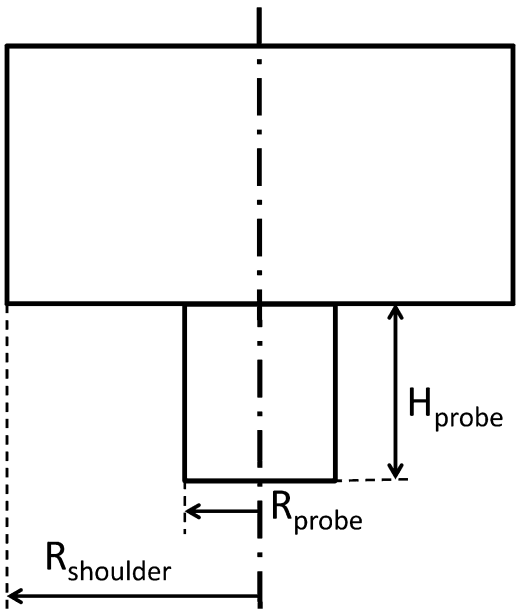

Fig. 32.1 Tool geometry scheme

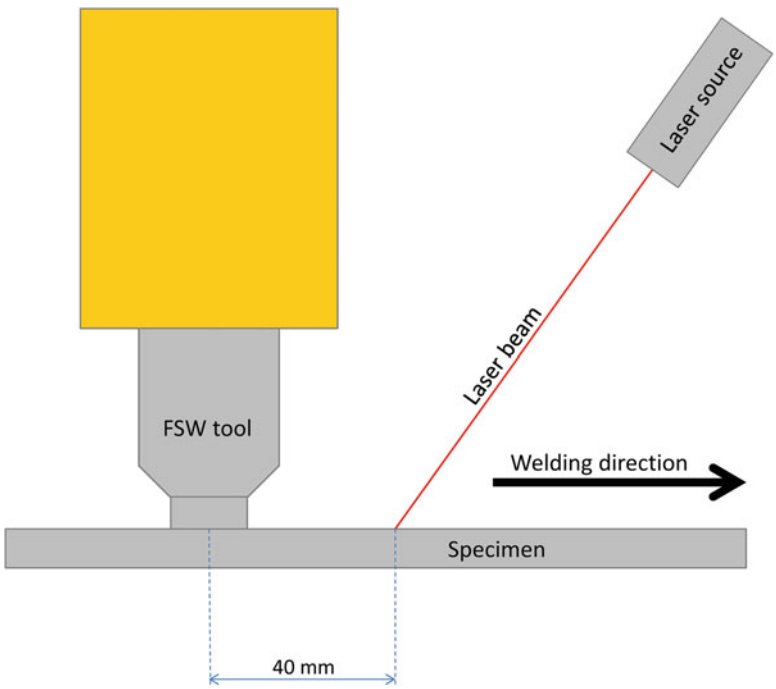

Fig. 32.2 LFSW scheme

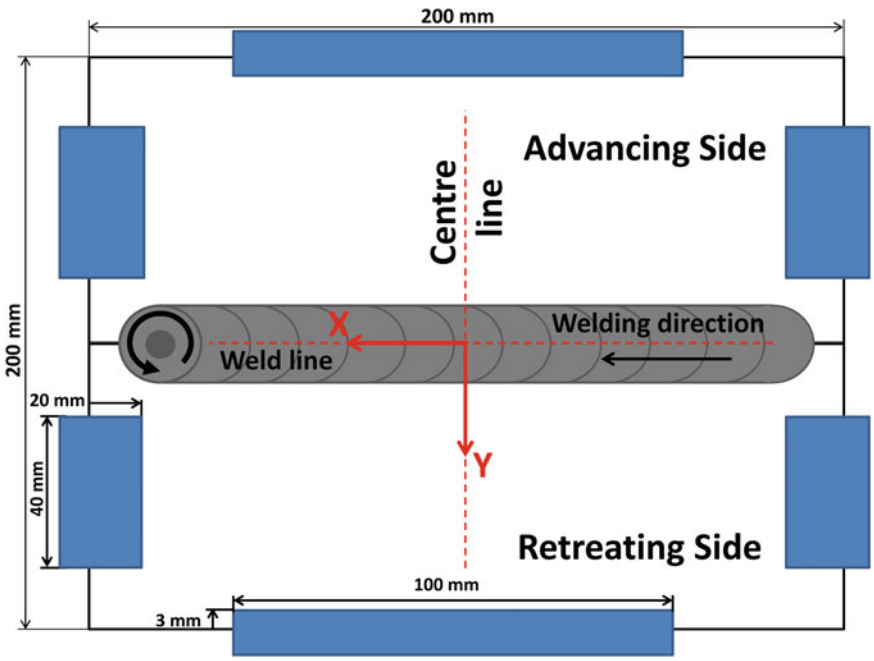

Fig. 32.3 Specimen and clamping system scheme

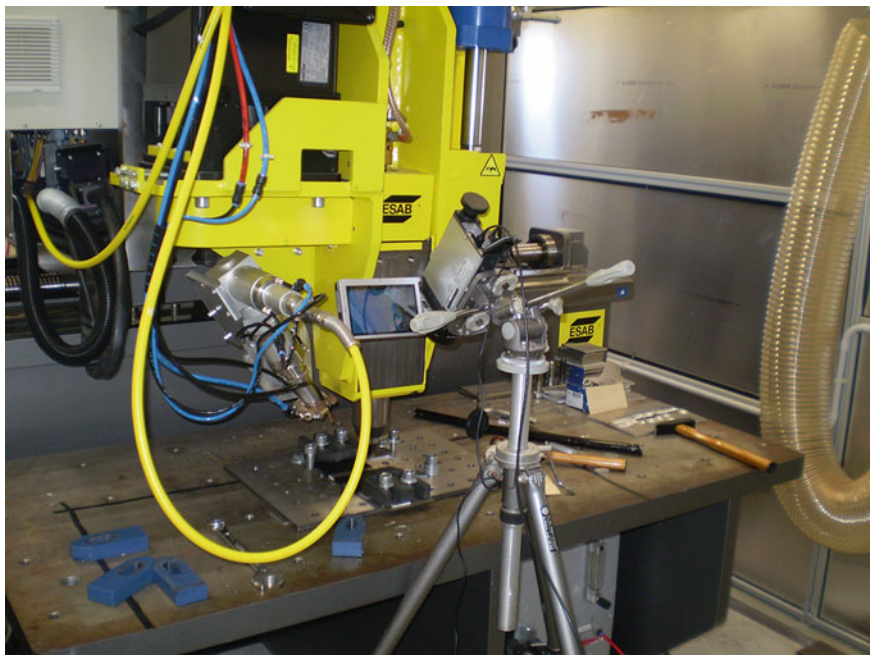

Fig. 32.4 Experimental setup

32.2.1 Temperature Measurement

A NEC H2640 infrared camera (Range 0–2000 °C; Resolution 0.06 °C; Accuracy ±2 °C or ±2 %; spectral range: 8–13 μm) has been used to acquire the temperature during the welding process. The experimental setup of the thermal camera has been reported in Fig. 32.4. The angle between the camera and FSW tool axis has been set to 30°. Due to reflection problems and low emissivity of aluminium, the specimen has been painted with matte black acrylic spray paint and an emissivity $\varepsilon = 0.95$ has been set on the camera. Moreover, in order to acquire the temperatures in front of the tool and to avoid the inclusion of paint into the bead, the LFSW temperatures have been acquired on 200 mm × 100 mm specimen in bead on plate configuration. Subsequently, an actual weld has been carried out to join two 200 mm × 100 mm plates.

32.2.2 Residual Stresses Measurement

Nowadays, several techniques have been developed to measure residual stress into the materials [19]. However, just some of these are quantitative and non-destructive. Probably, one of the most used technique is X-ray diffraction that can measure the residual stress on the surface of the structures without damaging. In this work, residual stresses measurements have been carried out using a Xstress 3000 G3R Stresstech X-ray diffractometer. A Cr tube ($\lambda = 0.2291$ nm) powered with a 30 kV, 8 mA current and a 3 mm collimator has been used. A 2θ diffraction angle of 156.7° has been selected for the measures. The residual stresses, both longitudinal (x axis direction) and transverse (y axis direction), have been measured along the centre line of the specimens as showed in Fig. 32.3. In order to increase the quality of the measure, the stress in each point has been measured at five different angles (0°, ±22.5°, ±45°) with a φ oscillation of ±3°. The detection distance has been set at 75 mm.

32.2.3 Numerical Model

A 3D uncoupled FE model analysis has been carried out to calculate the temperature and residual stress values. For this simulation the finite elements commercial code ANSYS 14.5 has been used. Initially, a thermal analysis on bead on plate configuration has been carried out to calculate the temperatures during the weld. These simulated temperature values have been compared to those experimental measured during the bead on plate welding process. Once the numerical model has been validated, it has been extended on the actual welding configuration to simulate the temperature during the joining of two 200 mm × 100 mm plates.

This calculated temperature field has been used as thermal input to the mechanical model to predict the residual stresses and strains. In order to carry out an accurate simulation of residual thermal stresses, temperature dependent thermo-physical and thermo-mechanical properties have been used. Due to a lack of literature data, the density of the material has been kept constant with the temperature. The temperature dependent parameters of the material have been summed up in Table 32.4 [20]. A multi-linear isotropic hardening has been adopted to describe the stress-strain behaviour of the material. Finally, in order to decrease the elements number and due to the geometrical symmetry of the problem, only half plate has been simulated.

The thermal model has been meshed using SOLID90 elements [21]. A gradual thicker mesh has been adopted near the welding line to describe more accurately the thermal and stress behaviour where the temperature gradient is higher (Fig. 32.5).

In the thermal model the natural convection between aluminium and air has been set to 20 W/m^2 °C on the top surface and on the lateral side of the specimen. The conduction between the specimen and the backing plate has been simulated (Fig. 32.5). A thermal contact conductance coefficient of 450 W/m^2 °C has been introduced between the bottom face of the specimen and the backing plate. This value has been chosen in the way to match the maximum temperature of the numerical model with experimental data. The backing plate is a 400 mm × 400 mm × 10 mm FE360 steel plate.

In Table 32.5 has been reported the thermo-mechanical properties of the FE360 steel backing plate. According to Chao et al. [22], the radiation heat loss has been neglected because temperature hardly exceeds 500 °C.

The welding process has been modelled as an uniform thermal source with a radius equal to $R_{shoulder}$ that moving along the welding line. The analytical expression used for simulate FSW tool heat generation is [16]:

$$Q = \frac{2}{3}\mu\omega\frac{F_n}{R_{shoulder}^2}\left(\left(R_{shoulder}^3 - R_{probe}^3\right)(1 + \tan\alpha) + R_{probe}^3 + 3R_{probe}^2 H_{probe}\right) \quad (32.1)$$

Table 32.4 Temperature dependent material properties for AA5754-H111 [20]

Temperature (°C)	Density (kg/m^3)	Specific heat (J/kg K)	Thermal conductivity (W/m K)	Thermal expansion (m/m °C)	Young's modulus (GPa)	Poisson's ratio
20	2650	891.6	138	23.90 E−6	103.4	0.34
100		950	147.2	24.40 E−6	–	0.34
200		988.4	152.7	25.13 E−6	97.88	0.35
300		1015.2	162.7	26.15 E−6	42.11	0.365
400		1045.6	152.7	27.15 E−6	23.07	0.365
500		1106.6	158.75	28.15 E−6	–	0.34

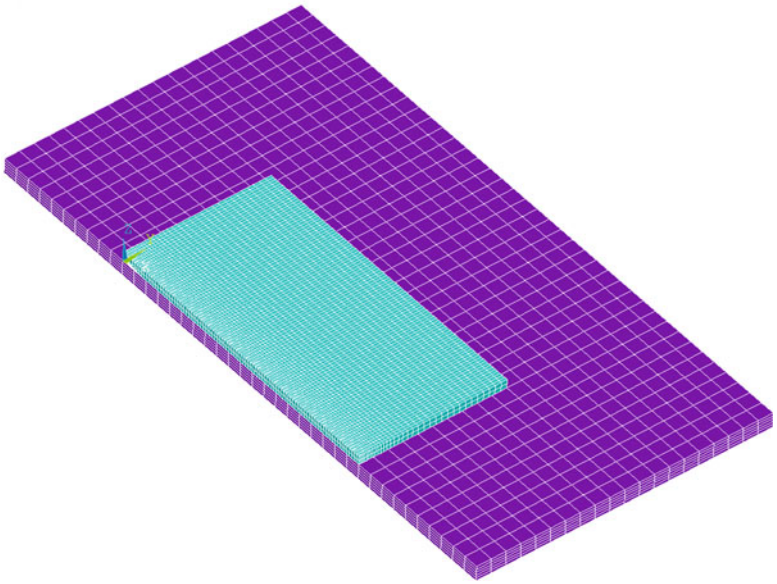

Fig. 32.5 LFSW scheme of model mesh

Table 32.5 Backing plate thermos-mechanical properties

Parameter	Value
Young's Modulus (GPa)	210
Density (kg/m^3)	7750
Thermal conductivity (W/m K)	48.9
Thermal expansion (m/m °C)	12.5×10^{-6}
Specific heat (J/kg K)	103.4
Poisson's ratio	0.29

Equation (32.1) provides the heat power based on the tool geometry. $R_{shoulder}$, R_{probe}, H_{probe} and α has been already indicated in Fig. 32.1. The remaining parameters are related to FSW process: μ and F_n are respectively the friction coefficient and the normal plunge force while ω is the rotational speed of the tool. The friction coefficient μ has been set equal to 0.237 according to the experimental tests F_n has been set to 20,000 N in the model. Finally, the laser source has been simulated as an uniform heat source of 2 mm radius that moves together to FSW tool.

Subsequently, the thermal histories simulated by the FE thermal model were used as an input in the mechanical model to evaluate the stress values. To this aim, the SOLID90 elements have been substituted with SOLID186 elements, keeping the same mesh and load step size. Moreover, also the mechanical effect due to the compression force applied by the tool has been taken into account introducing a uniform axial pressure distributed on tool area. The mechanical constrains have been set according to experimental set up (Fig. 32.3). For the left and right clamp an area of 20 × 40 mm has been constrained, instead, for the below clamp a centred 3 × 100 mm area has been constrained. These constraints block the movements in all direction. Moreover, the left side of Fig. 32.3 has been blocked in the x-axis direction. Finally, the bottom of the plate has been constrained in z-direction. Once that the welding simulation is concluded, the constraints are gradually released and the residual stresses due to LFSW process have been evaluated.

32.3 Results

The previously described model has been validated both for the thermal part and for the mechanical part on the basis of experimental data. The temperature of the thermal analysis on Bead on Plate configuration has been compared to the temperatures reached during the weld. Once the thermal model has been validated, it has been extended on the actual welding configuration to simulate the temperature during the joining of two 200 mm × 100 mm plates. The obtained temperature field has been used as thermal input to the mechanical model to predict the residual stresses and strains. Finally the numerical computed stress values have been compared to the X-ray residual stress experimental measured.

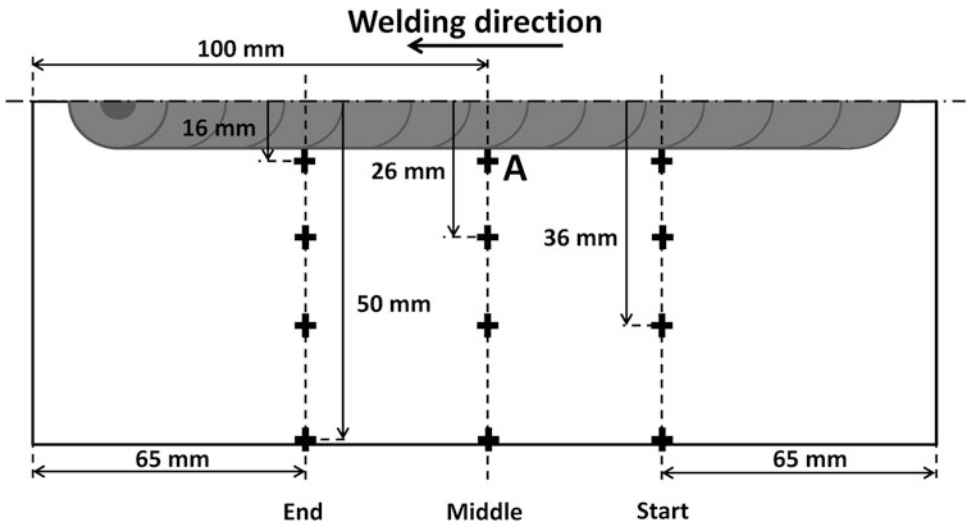

Fig. 32.6 Scheme of temperature measured points

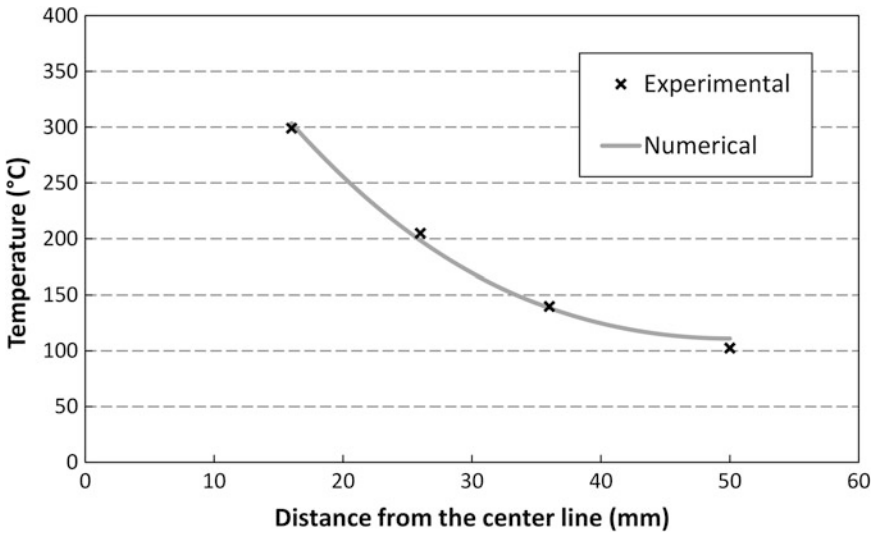

Fig. 32.7 Numerical vs. experimental data in the start phase

In Fig. 32.6 has been reported a scheme of the points that have been analysed to validate the thermal model. Three different steps have been studied and reported in the later graphs. In each step the tool has been aligned at the measured points and the temperature has been acquired in both numerical and experimental data. The start position and the end position correspond to the initial and final welding phases and they are about 65 mm from the right and left edges of the plate respectively. Instead, the middle step is in the half of the specimen. For each position the temperature has been measured at 16, 26, 36 and 50 mm from the welding line. It has not been possible to collect experimental data nearer the centre line for the presence of the FSW tool and the processing burrs that modifies the emissivity of the surface and thus the temperature.

The trends of the temperature versus distance from the weld line have been plotted for numerical and experimental data in the start (Fig. 32.7), middle (Fig. 32.8) and end (Fig. 32.9) phase. Generally, these graphs show that the temperature decreases moving away from the welding line and that the numerical model fits the experimental data with low errors. This is confirmed by R^2 value analysis defined as:

$$R^2 = 1 - \frac{SS_{res}}{SS_{tot}} \tag{32.2}$$

where SS_{res} is the sum of the squares of the distances between experimental data and the numerical curve, instead, SS_{tot} is the sum of the square of the distances of experimental values from a horizontal line through the mean of all Y values. The R^2 is 0.992 in the start step, 0.999 in the middle phase and, finally, 0.999 in the end step.

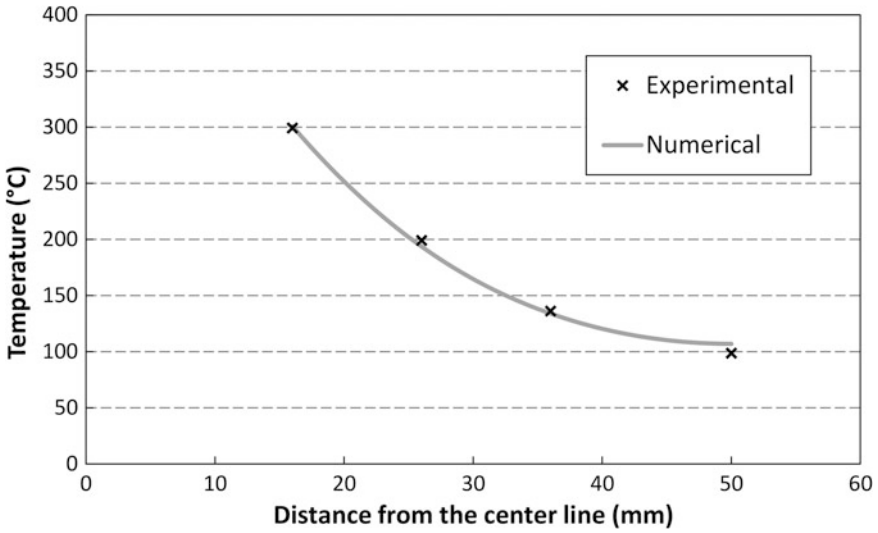

Fig. 32.8 Numerical vs. experimental data in the middle phase

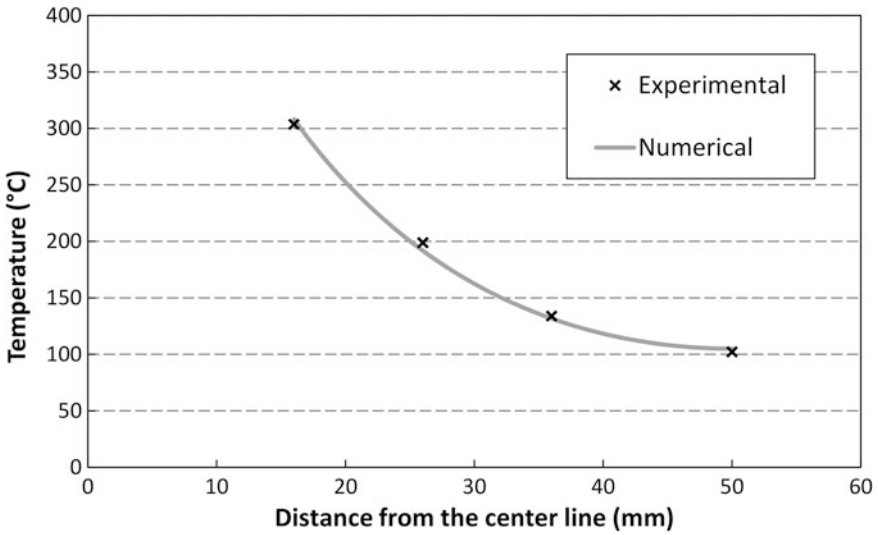

Fig. 32.9 Numerical vs. experimental data in the end phase

In order to accurately validate the FE model, in Fig. 32.10 has been reported the temperature versus time of the experimental data and the numerical model. This graph represents the temperatures of a central point distant 16 mm from the welding line (point A in Fig. 32.6). In general, there is a good agreement between the numerical model and the experimental data.

The value of the thermal contact conductance coefficient, between the backing plate and the aluminium sheets, has been chosen in the way to fit the numerical maximum temperature in the point A with the experimental data.

In Fig. 32.11 has been reported a qualitative comparison of thermal field measured experimentally and that obtained numerically. The white area in the figure describes the zone of the specimen where the temperature exceeds 250 °C. Moreover, the temperature of welded area behind the FSW tool is not correct because there is a variation of the emissivity due to the paint removal and change of roughness after the transit of FSW tool. Finally, in order to present the results in better way and because only a semi-plate has been modelled, the numerical results have been mirrored along the joint line.

In order to validate the mechanical part of the model, X-ray diffraction stress measures have been carried out. Both the superficial longitudinal stress (welding direction) and transverse stress (transverse to welding direction) has been measured and compared with the numerical model prediction. In Fig. 32.12, the numerical versus experimental longitudinal stress trend has been reported for the retreating side. The maximum stress value in the LFSW welds is located on the edge of the bead as has been showed in Fig. 32.12 by a vertical grey line at a distance of 10.75 mm from the joining line.

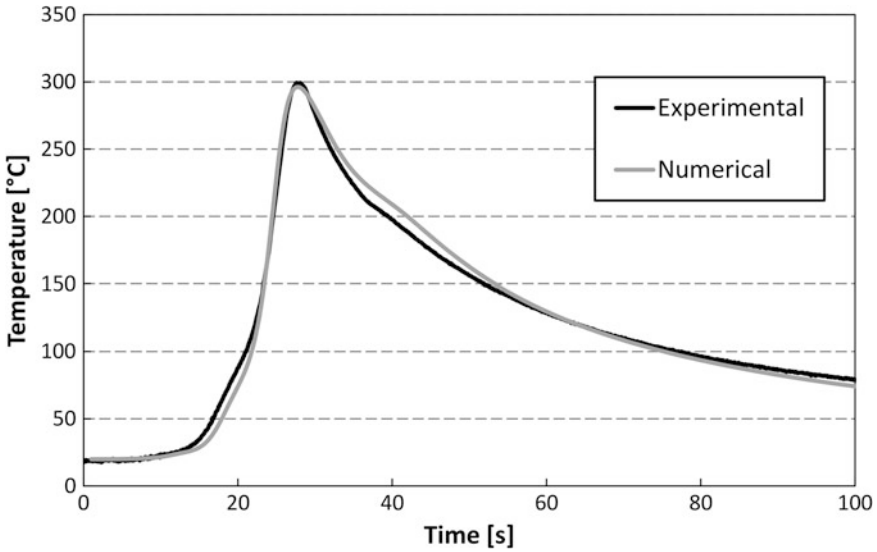

Fig. 32.10 Temperature vs. time trend of the middle point A

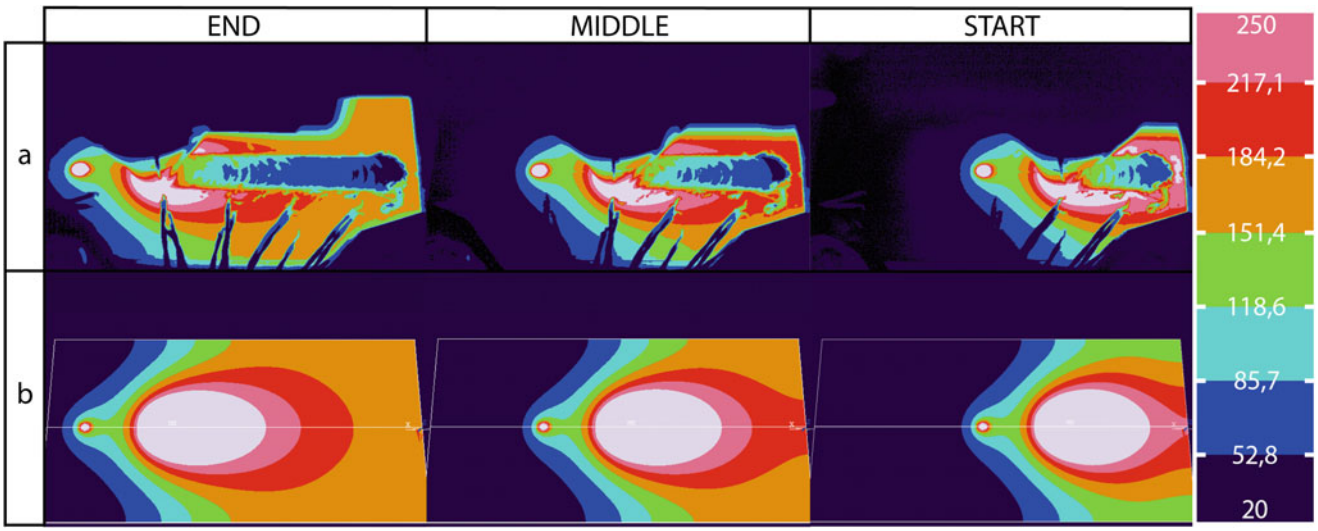

Fig. 32.11 Graphical comparison between the experimental data (**a**) and numerical results (**b**)

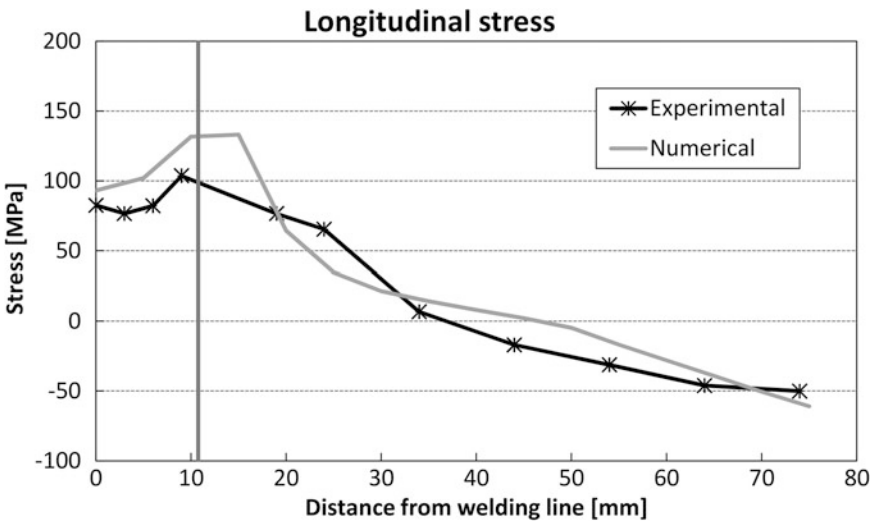

Fig. 32.12 Numerical vs. experimental comparison of longitudinal stress

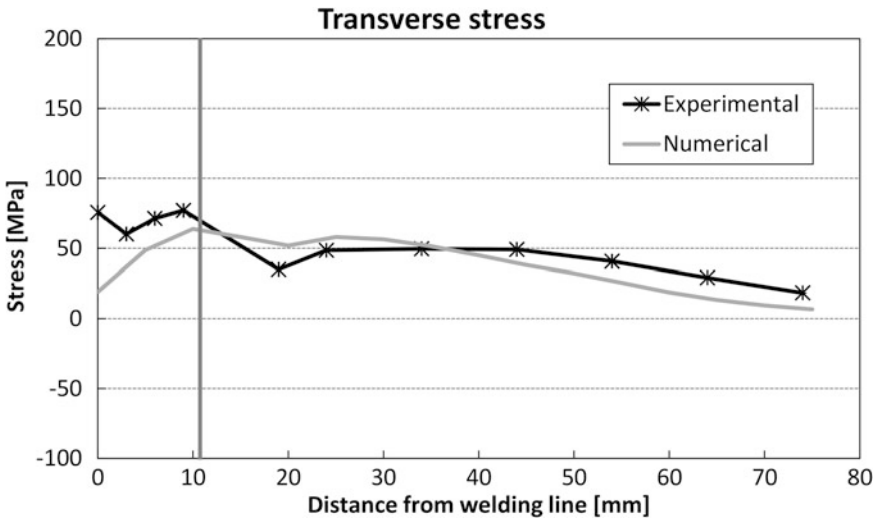

Fig. 32.13 Numerical vs. experimental comparison of transverse stress

In Fig. 32.13 the stress in the transverse direction, in the retreating side, has been reported. The trend of the stress is roughly constant along all the transverse direction of the plate. Only in the welded zone there is a small increment probably due to the laser presence. In general, the distribution of the residual stress, in both longitudinal and transverse direction, shows a good agreement with the experimental results.

32.4 Conclusion

One of the most important advantage of numerical models is the possibility of predict thermo-mechanical behaviour of the joints and to provide information where the experimental data cannot give results. In the present work a three-dimensional thermo-mechanical model of LFSW has been modelled. The aim of the FE simulation is to predict the temperature and residual stress developed during the weld. The model includes the mechanical action of the shoulder and the thermo-mechanical characteristic of AA5754 at different temperatures. A 200 mm $\times$ 100 mm $\times$ 6 mm 5754 H111 aluminium alloy plate has been welded in bead on plate configuration to validate the thermal part of the simulation. Once the thermal part has been validated, the model has been extended to weld two 200 mm $\times$ 100 mm plates in view to simulate the actual welding setup. The obtained temperature field has been used as thermal input to the mechanical part in order to predict the residual stresses. These values have been compared to the X-ray residual stress experimental measurements. The thermal FE model can describe the heat-transfer process in the LFSW with a good correspondence with experimental data.

The longitudinal residual stress measurements confirm, as pointed out by Campanelli et al. [9], that the maximum value in the LFSW welds is located on the edge of the bead. Moreover, the transverse stress has lower values than longitudinal stress confirming that this type of residual stress is a less critical issue also in this combined joining process. Finally, the mechanical part of the model is in a good agreement with experimental results. This highlights that the FE model is capable to predict the temperatures and the stresses in different configurations from those whereby has been validated.

References

1. W.M. Thomas, E.D. Nicholas, J.C. Needham, M.G. Murch, P. TempleSmith, C.J. Dawes, The Welding Institute, TWI, International Patent Application No. PCT/GB92/02203 and GB Patent Application No. 9125978.8, 1991
2. R.S. Mishraa, Z.Y. Ma, Friction stir welding and processing. Mater. Sci. Eng. R **50**, 1–78 (2005)
3. G. Padmanaban, V. Balasubramanian, Selection of FSW tool pin profile, shoulder diameter and material for joining AZ31B magnesium alloy—an experimental approach. Mater. Des. **30**, 2647–2656 (2009)
4. W.B. Lee, S.B. Jung, The joint properties of copper by friction stir welding. Mater. Lett. **58**, 1041–1046 (2004)
5. J.R. Fernández, A.J. Ramirez, Dissimilar friction stir welding of steel to Ni-based alloy 625—Butt and lap joints, in *Proceedings of the International Offshore and Polar Engineering Conference 2013*, 2013, pp. 207–210
6. F. Cioffi, R. Fernández, D. Gesto, P. Rey, D. Verdera, G. González-Doncel, Friction stir welding of thick plates of aluminum alloy matrix composite with a high volume fraction of ceramic reinforcement. Compos. A: Appl. Sci. Manuf. **54**, 117–123 (2013)

7. A. Bagheri, T. Azdast, A. Doniavi, An experimental study on mechanical properties of friction stir welded ABS sheets. Mater. Des. **43**, 402–409 (2013)
8. M. Merklein, A. Giera, Laser assisted friction stir welding of drawable steel-aluminium tailored hybrids. Int. J. Mater. Form. **1**, 1299–1302 (2008)
9. S.L. Campanelli, G. Casalino, C. Casavola, V. Moramarco, Analysis and comparison of friction stir welding and laser assisted friction stir welding of aluminum alloy. Materials **6**, 5923–5941 (2013)
10. W. Xu, J. Liu, G. Luan, C. Dong, Temperature evolution, microstructure and mechanical properties of friction stir welded thick 2219-O aluminum alloy joints. Mater. Des. **30**(6), 1886–1893 (2009)
11. M. Maeda, H. Liu, H. Fujii, T. Shibayanagi, Temperature field in the vicinity of FSW-tool during friction stir welding of aluminium alloys. Weld. World **49**(3–4), 69–75 (2005)
12. C. Dalle Donne, E. Lima, J. Wegener, A. Pyzalla, T. Buslaps, Investigations on residual stresses in friction stir welds, in *Proceedings of the Third International Symposium on Friction Stir Welding*, 2001
13. M. Peel, A. Steuwer, M. Preuss, P.J. Withers, Microstructure, mechanical properties and residual stresses as a function of welding speed in aluminium AA5083 friction stir welds. Acta Mater. **51**, 4791–4801 (2003)
14. C. Casavola, A. Cazzato, V. Moramarco, C. Pappalettere, Temperature field in FSW process: experimental measurement and numerical simulation, in *Conference Proceedings of the Society for Experimental Mechanics Series*, vol. 6, 2015, pp. 177–186
15. C. Casavola, A. Cazzato, V. Moramarco, C. Pappalettere, Influence of the clamps configuration on residual stresses field in friction stir welding process. J. Strain Anal. Eng. Des. **50**(4), 232–242 (2015)
16. H. Schmidt, J. Hattel, J. Wert, An analytical model for the heat generation in friction stir welding. Model. Simul. Mater. Sci. Eng. **12**(1), 143–157 (2004)
17. V. Soundararajan, S. Zekovic, R. Kovacevic, Thermo-mechanical model with adaptive boundary conditions for friction stir welding of Al 6061. Int. J. Mach. Tool Manuf. **45**(14), 1577–1587 (2005)
18. M. Song, R. Kovacevic, Thermal modeling of friction stir welding in a moving coordinate system and its validation. Int. J. Mach. Tool Manuf. **43**(6), 605–615 (2003)
19. N.S. Rossini, M. Dassisti, K.Y. Benyounis, A.G. Olabi, Methods of measuring residual stresses in components. Mater. Des. **35**, 572–588 (2012)
20. S.K. Khanna, X. Long, W.D. Porter, H. Wang, C.K. Liu, M. Radovic, E. Lara-Curzio, Residual stresses in spot welded new generation aluminium alloys, part A—thermophysical and thermomechanical properties of 6111 and 5754 aluminium alloys. Sci. Technol. Weld. Joining **10**(1), 82–87 (2013)
21. Swanson Analysis System Inc., The ANSYS 14.5 Users' Manual, 2012
22. Y.J. Chao, X. Qi, W. Tang, Heat transfer in friction stir welding-experimental and numerical studies. J. Manuf. Sci. Eng. **125**, 138–145 (2003)

Chapter 33
Residual Stress Measurement on Shot Peened Samples Using FIB-DIC

Enrico Salvati, Matteo Benedetti, Tan Sui, and Alexander M. Korsunsky

Abstract Shot peening is an established technique for improving the fatigue resistance of mechanical components by performing a deformation treatment that causes local near surface plastic deformation and introduces a layer of compressive residual stress. The knowledge of the residual stress distribution plays a crucial role in the correct prediction of fatigue life during service in the context of engineering design. Reliable prediction of safe fatigue life requires knowing how the residual stress state obtained after shot peening depends on the sample geometry, e.g. the presence of notches, and how it evolves during cyclic loading. The Focused Ion Beam milling coupled with Digital Image Correlation (DIC) analysis of SEM images (the FIB-DIC method) has been shown to be an efficient technique for stress evaluation at the (sub)micron-scale. The residual stresses in the vicinity of shot-peened rounded notch tips in Al-7075-T651 samples were studied as a function of notch radii ($\boldsymbol{\rho} = 2, 0.5, 0.15$ mm). The interpretation of the results is aided by comparison with a simple numerical model of eigenstrain cylinder.

Keywords Shot peening • FIB-DIC • Residual stress • SEM • Eigenstrain

33.1 Introduction

In most cases, mechanical failures initiate at component surfaces. In order to improve the mechanical part reliability, specific surface treatments are widely used. One of such treatments is known as shot peening (SP). This process consists of bombarding the surface to be treated with a large number of nearly spherical hard shots. The effect induced by this treatment is the generation of plastic deformation in a shallow surface region of the treated part leading to a compressive residual stress state being generated. The benefit given by the SP in terms of fatigue life extension is well reported and widely accepted [1–5].

Recently, some authors proposed various approaches for the prediction of the fatigue failure in shot peened mechanical components [1, 6]. Taking into account the effect of SP requires understanding of the induced residual stress field in the vicinity of the treated surface. Therefore, experimental measurements of the residual stress are required in order to incorporate this effect into numerical simulation of deformation and to estimate safe life on the basis of one of the possible failure criteria.

One approach to the measurement of residual stress at the micron scale is the micro-ring core FIB-DIC method. This technique has recently been developed into an efficient semi-destructive methodology for the evaluation of residual stresses and strains at the material surface [7, 8]. The material removal is executed by the use of Focused Ion Beam (FIB), and a ring-core marker is milled through the material surface. As consequence, a feature with a micro-pillar type geometry is generated. The displacements occurring during the material removal are evaluated by monitoring the top surface of the pillar by means of Digital Image Correlation (DIC) method using high resolution SEM images. As a result of DIC analysis, a strain relief curve is obtained as a function of the milling depth for two orthogonal directions. For the purposes of interpretation the relief curve is usually fit with a master function [9] that was originally derived on the basis of numerical modelling and allows the estimation of the complete strain relief at the end of the material removal process.

In the present paper, the FIB-DIC ring-core method was adopted for the evaluation of residual stress induced by SP in samples made from aluminium alloy Al-7075-T651 and having three different V-notch root radii. The measurements for each specimen were performed along the notch bisector and along a line perpendicular to it running at a certain distance from

E. Salvati (✉) • T. Sui • A.M. Korsunsky
Department of Engineering Science, University of Oxford, Parks Road, Oxford OX13PJ, UK
e-mail: enrico.salvati@eng.ox.ac.uk; tan.sui@eng.ox.ac.uk; alexander.korsunsky@eng.ox.ac.uk

M. Benedetti
Department of Industrial Engineering, University of Trento, via Mesiano 77, Trento 38123, Italy
e-mail: matteo.benedetti@ing.unitn.it

S. Bossuyt et al. (eds.), *Residual Stress, Thermomechanics & Infrared Imaging, Hybrid Techniques and Inverse Problems, Volume 9*, Conference Proceedings of the Society for Experimental Mechanics Series, DOI 10.1007/978-3-319-21765-9_33

the notch root. Taking full advantage of the DIC analysis it was possible to evaluate the residual strain in two orthogonal directions. A new fitting procedure is presented for the interpretation of the relief curve given by DIC. In fact, a modification of the master function seen in [9] is used in this work in order to improve the fit and thus reduce the standard deviation. The measurements are interpreted, and the results discussed in comparison with a small and efficient mathematical model based on the eigenstrain approach [10].

33.2 Experimental Procedure and Data Analysis

33.2.1 Sample Description and Measurement Locations

The samples used in the study were machined from a 4 mm-thick rolled aluminium alloy plate (Al7075-T651). They had different notches of varying severity machined in them in order to obtain three notched samples. All notches were V-shaped and differed from each other only in the fillet radius at the notch tip. The geometry and the main dimensions of the samples are depicted in Fig. 33.1. Table 33.1 shows the geometric characteristics related to Fig. 33.1a, and the corresponding values of the Stress Concentration Factor K_t.

The shot peening treatment was conducted using small ceramic beads of the size 60 ÷ 120 μm that provided complete coverage of the notch roots and the top surface (Fig. 33.1a). The top surface examined by FIB-SEM microscopy were first ground using abrasive cloths up to 1200 grit, followed by smooth cloth polishing with 1 μm diamond particle suspension in aqueous solution and then, as the final step, using colloidal silica solution. The grinding and polishing procedure has resulted in the removal of the material layer at the top surface that was affected by the shot peening treatment.

The milling micro-pillar markers (measurement sites) were placed as shown in Fig. 33.1b. In the very vicinity of the notch tip, a very high gradient of stress may be found. Consequently, the two closest milling points were spaced 12.5 μm apart from each other, with the first marker the same distance from the surface. The remaining measurement points were spaced 50 μm apart. Due to the requirement of final alignment between FIB and SEM beams prior to milling, the arrangement described

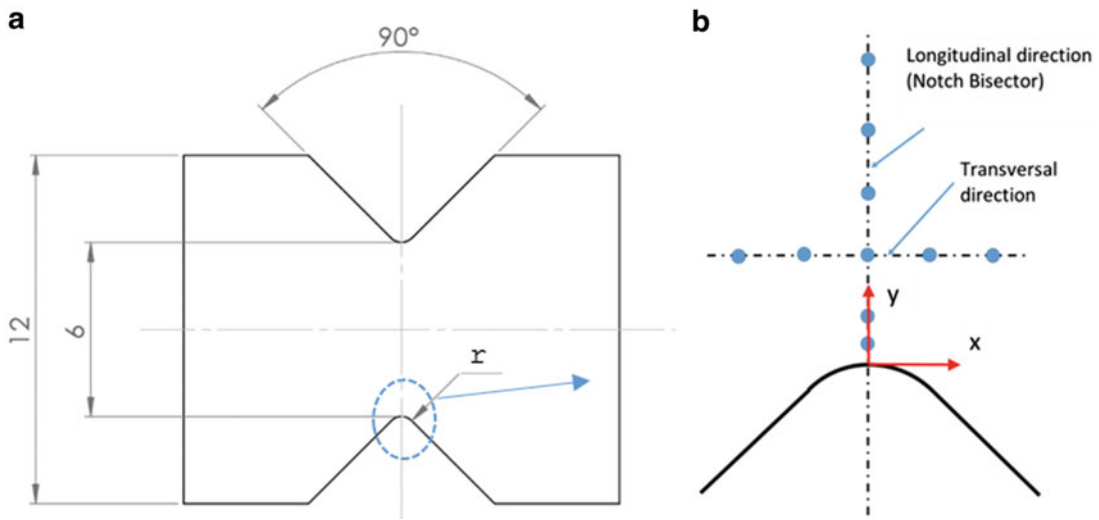

Fig. 33.1 Schematic representation of the milling locations. (**a**) Sample overview (circled the milling location). (**b**) Milling positions at the notch tip

Table 33.1 Samples' geometrical specifications

Sample n.	Fillet radius ρ (mm)	K_t
1	2	1.52
2	0.5	2.37
3	0.15	3.76

above may not always have been respected. However, the actual distances were used and the data points corrected accordingly. The transversal line of markers ran perpendicular to the notch bisector (Fig. 33.1b) at an actual distance of 75 μm from the notch root in all samples in the set.

33.2.2 FIB Milling Procedure

In order to perform DIC analysis, the surface must show good contrast derived from the features already present, e.g. roughness, precipitates etc., or be "decorated" to create such contrast to enable time-depending tracking of surface displacement. Since the surface of polished samples used in the present study did not present these characteristics, in-chamber electron beam deposition of a Pt pattern was used. The Gas Injection System (GIS) was used to deliver a local flow of a Pt-containing volatile organic compound, and electron beam was used to precipitate Pt onto the surface to create a so-called"sunflower"pattern of dots (Fig. 33.2b).

Micro-pillars of ring-core geometry of nominal diameters of $D_1 = 7.5$ μm and $D = 5$ μm (Fig. 33.2d) were milled at each measurement point (Fig. 33.2a). The milling procedure was subdivided into $n = 50$ steps, and SEM images of the micro-pillar top surface were acquired at each step. A micrograph of the monitored region of sample surface carrying the sunflower pattern is shown in Fig. 33.2c. Once the procedure was complete, the relative distances between the centres of the milling positions were measured by means of SEM at lower magnification.

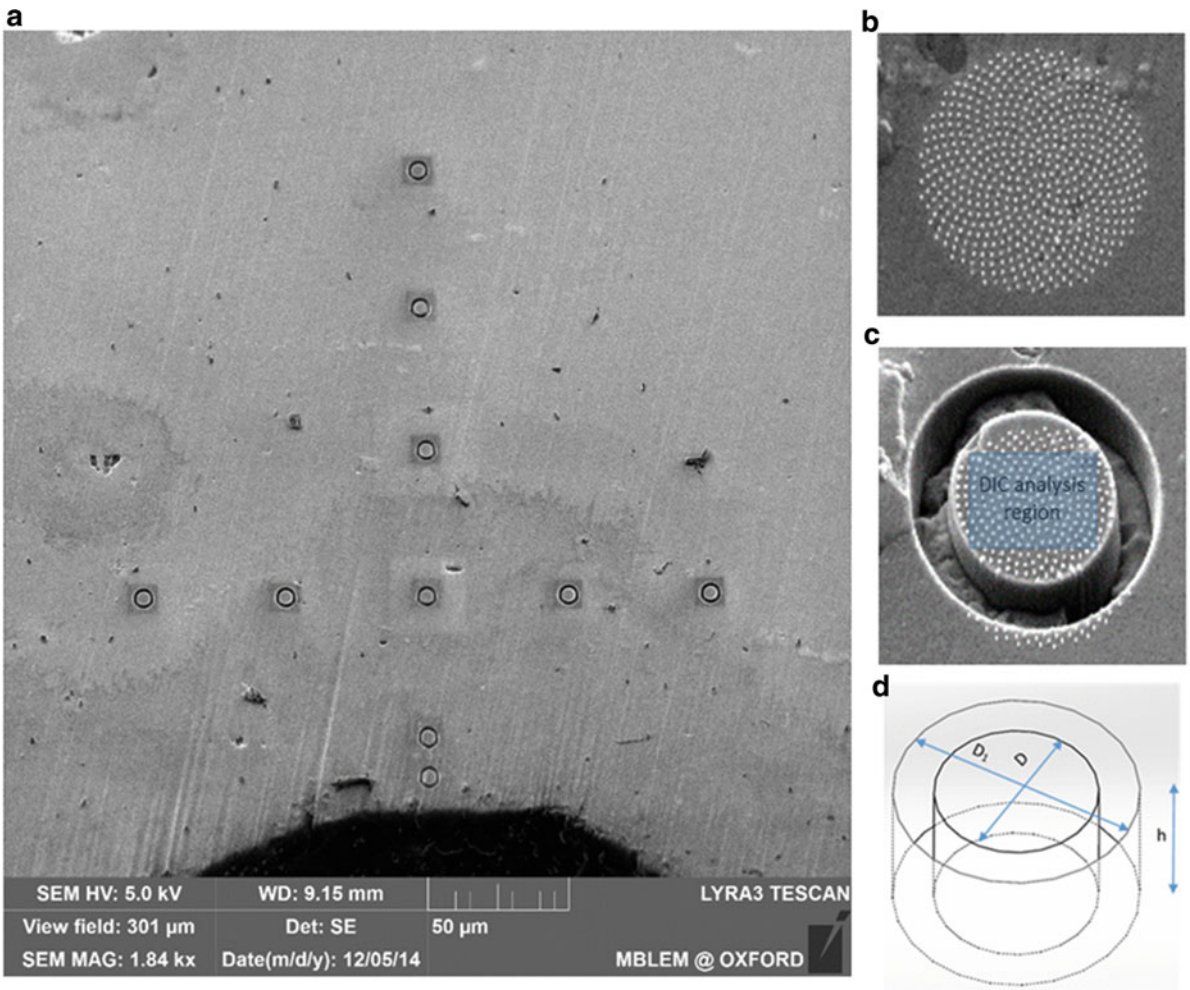

Fig. 33.2 Milling positions and ring core characteristics. (**a**) SEM image overview in correspondence of the notch ($\rho = 0.15$ mm) after FIB-DIC measurements. (**b**) Sunflower pattern created with Pt deposition. (**c**) Surface analysed with DIC during milling process. (**d**) Ring core geometry dimensions

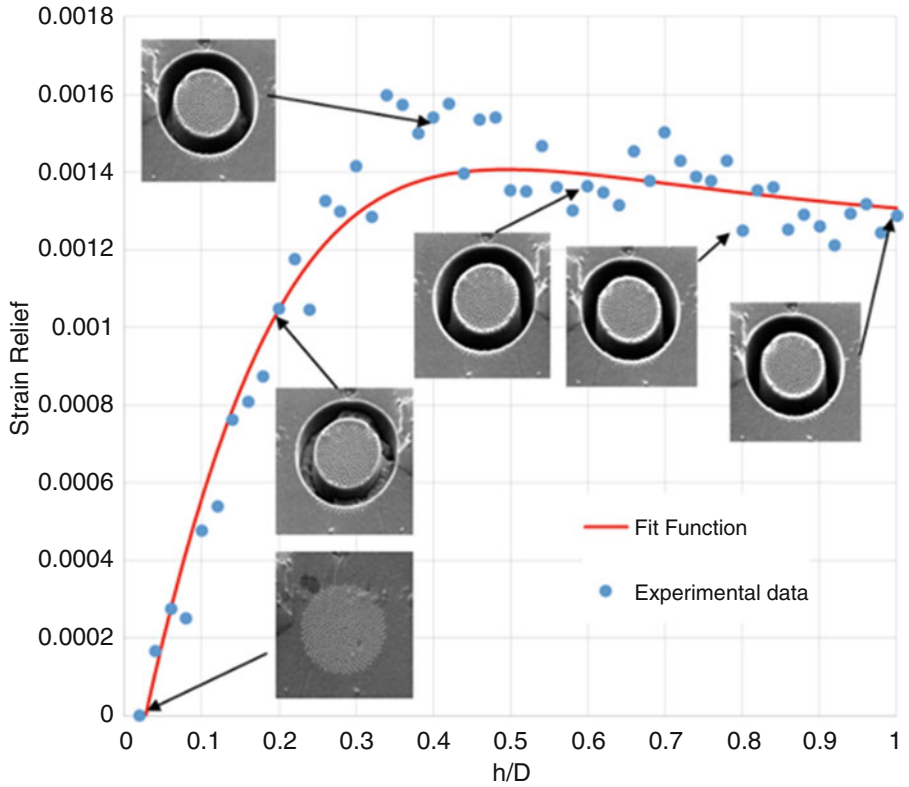

Fig. 33.3 Strain relief profile, fitting curve and cartoons of the images utilised for the DIC analysis. The figure shows the curve for strain component ε_{xx} at the position 0.0375 mm from the notch tip (sample $\boldsymbol{\rho} = 0.5$ mm)

33.2.3 DIC Analysis and Fitting Procedure

The images collected at each milling step were analysed by means of Digital Image Correlation (DIC). For the purpose of tracking the displacement occurring during the milling procedure, a reference grid was created on the sunflower pattern. Large scale rigid body displacements due to the SEM image drift were corrected for. The raw DIC tracking data were post-processed to remove outliers and to filter out the noise. This procedure produced the curve for the strain relief as a function of the milling step for two orthogonal directions x and y previously defined at the sample surface (Fig. 33.1b). Figure 33.3 shows the experimental result, in terms of the strain relief at each milling step, for a given direction (x or y) obtained as the average across the entire tracking grid. This strain evolution culminates in the achievement of complete relief to zero strain, with the overall increment providing the information necessary for the evaluation of the residual strain present in the material prior to milling.

The experimentally determined strain evolution can be described by a parametric function (33.1) developed on the basis of Finite Element Analysis (FEA) which contains two fitting parameters: the complete elastic strain relief $\Delta\varepsilon^{\infty}$, and the normalized milling depth z.

In the present study we propose a new definition of the normalized milling depth (33.2). Comparing this new definition with the previously established approach [9], we point out the difference in terms of additional free fitting parameters δ and κ being introduced in the evaluation of the normalised milling depth z:

$$\varepsilon^{*} = 1.12\Delta\varepsilon^{\infty}\left(\frac{z}{1+z}\right)\left[1+\frac{2}{(1+z^{2})}\right] \tag{33.1}$$

$$z = \frac{\left(\frac{h}{D} + \delta\right)}{k} \tag{33.2}$$

The physical meaning of parameter δ is the offset adjustment of the reference surface depth from which fitting begins. This helps accommodate the effect of surface roughness on the strain relief vs. depth curve. The parameter κ accounts for the possible imprecision in the calculation of milling depth that can be adjusted to obtain the best agreement with the theoretically predicted curve.

The fitting procedure was implemented in Matlab©. The algorithm adopted was based on the minimisation of the absolute residuals (LAR—Least Absolute Residuals). At the end, the standard deviation of the residual strain was evaluated at 95 % of confidence. An example result of fitting the new function (33.1) to the experimental data is shown in Fig. 33.3, together with small cartoons indicating the stage of the milling process.

33.3 Eigenstrain Modelling

For the purpose of this work we proposed a simple numerical model of the residual stress generation within the sample due to a distribution of eigenstrain induced by the plastic deformation during shot peening. Using the plane stress approximation, we modelled an annular domain in which the inner radius was set to be equal to that of the notch root of the samples examined. Accordingly, three different geometries were analysed. The imposed eigenstrain profile was chosen to be a function given by a product of an exponentially decaying function and a linear function of the form:

$$\varepsilon^*(y) = A(B - y)\, e^{-Cy} \tag{33.3}$$

where y denotes the distance from the surface. The profile given by this function is illustrated in Fig. 33.4 and is seen to correspond to the eigenstrain profile, as function of the depth normalized by the relative fillet radius, typically encountered after shot peening [3]. The normalised depth is the abscissa of the plot shown in Fig. 33.1.

For the purpose of the present brief discussion, only the hoop residual stress is compared with the experimental data. The magnitude and the shape of the eigenstrain profile was chosen to obtain broad general agreement with the set of measurements for three samples. Then statistical analysis was conducted to evaluate the confidence interval in the context of experimental observation. The results are presented in the following section.

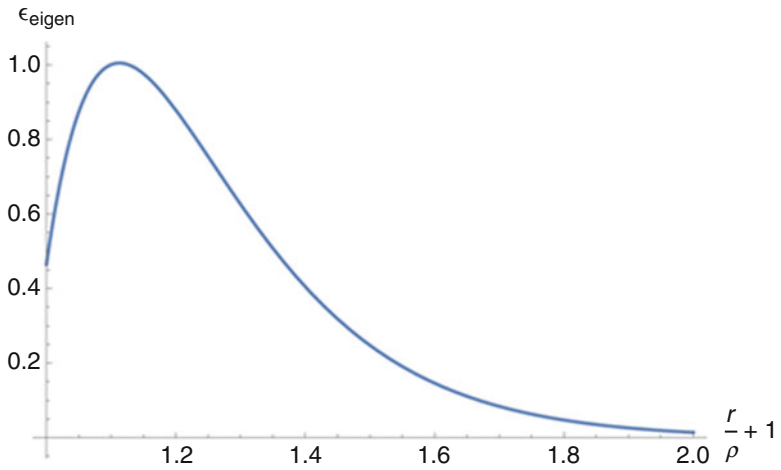

Fig. 33.4 Eigenstrain profile applied in the model

33.4 Results and Discussion

The fitting procedure returns the value $\Delta\varepsilon^{\infty}$, the experimentally evaluated residual strain. Since the interrogated volumes of material lie very close to the sample surface, the residual stress profiles were calculated under the assumption of plane stress. The version of Hooke's law that applies in this case has the form:

$$\sigma_{xx} = -\frac{E\varepsilon_{xx}}{(1-\nu)} \tag{33.4}$$

$$\sigma_{yy} = -\frac{E\varepsilon_{yy}}{(1-\nu)} \tag{33.5}$$

For the material analysed in this study Young's Modulus of $E = 73$ GPa and Poisson's Ratio of ν=0.33 were used.

The results obtained from the FIB-DIC analysis are shown in Fig. 33.5. The graphs reported include error bars that indicate the standard deviation derived from the fitting procedure. The error contribution from DIC analysis would result in error bars associated with each of the points in Fig. 33.3. However, these were not taken into account in this study, as their contribution was judged unlikely to cause a significant difference for the results.

The presence of the expected localised compressive residual stress σ_{xx} in the vicinity the notch tip is confirmed by the experimental results (Fig. 33.5a). The near-surface compressive layer was present in all of the samples examined in the present study. The residual stress trend typical for shot peened components that is well known for flat samples is confirmed: a high gradient of compressive stress from the surface extends over ~100 μm into the sample bulk. Typically in shot peened components the compressive residual stress reaches a maximum at a certain distance from the notch tip [1, 3, 6]. In the present study this peak was not observed directly due to the spatial resolution chosen.

Samples with the larger notch root radius show higher compressive residual stress magnitude. The difference between the $\boldsymbol{\rho} = 2$ mm sample and the $\boldsymbol{\rho} = 0.5$ mm sample was limited in terms of stress profiles. The $\boldsymbol{\rho} = 0.15$ mm one shows a somewhat lower compressive stress magnitude compared to the other samples, suggesting a reduced efficiency of shot peening treatment.

Figure 33.5b shows the results for the orthogonal component of stress σ_{yy}. In this case the near-surface region has low residual stress values, and the maximum compression is reached at depths of around $0.10 \div 0.15$ mm. The residual stress σ_{yy} is seen to have undergone relief at the vicinity of the free surface (notch root) as expected due to the traction-free boundary condition. A persistent largely uniform compressive stress σ_{yy} is found at distances larger than ~0.15 mm from the notch root. This background stress is likely to be associated with a compressive residual stress state present prior to shot peening due to some manufacturing process (e.g. rolling, or quenching prescribed by the T651 thermo-mechanical treatment of the alloy).

Regarding the stress variation along the path transversal to the notch bisector, the σ_{xx} component (Fig. 33.5c) shows more fluctuations in the samples with smaller fillet radius, although overall the variation is small, and no evident peaks can be identified. The same behaviour is observed for the other component of stress (σ_{yy}) along the same transversal path, except for a single outlier point (circled in Fig. 33.5d) that suggests an anomalously high value of stress. Conventional approach to the analysis of experimental data is to dismiss this point, associating the anomalous value with the errors in the experimental procedure and interpretation, e.g. reduced SEM image quality in y direction (slow scan) compared to the x direction (fast scan), and the possibility of presence of a microstructural feature such as a grain boundary.

The comparison of the eigenstrain modelling results with experimental observations shows adequate agreement for the general trend of the residual stress profile and magnitude (Fig. 33.6). The data are represented as function of the longitudinal direction normalised by the fillet radius of the relevant sample. The statistical analysis of the data dispersion based on the model used allowed the assessment of the confidence interval indicated by the shaded band. This confidence band for each sample defines the limits in which the experimental data are likely to lie with the probability of 95 %. The presence of compressive residual stress at the notch root is confirmed (σ_{xx}), as is its gradual decay with depth, followed by low level tensile stress in the bulk. Figure 33.6 reveals that the model agrees with the experimental data particularly well for sample 2, for which the confidence band is narrower than for other samples.

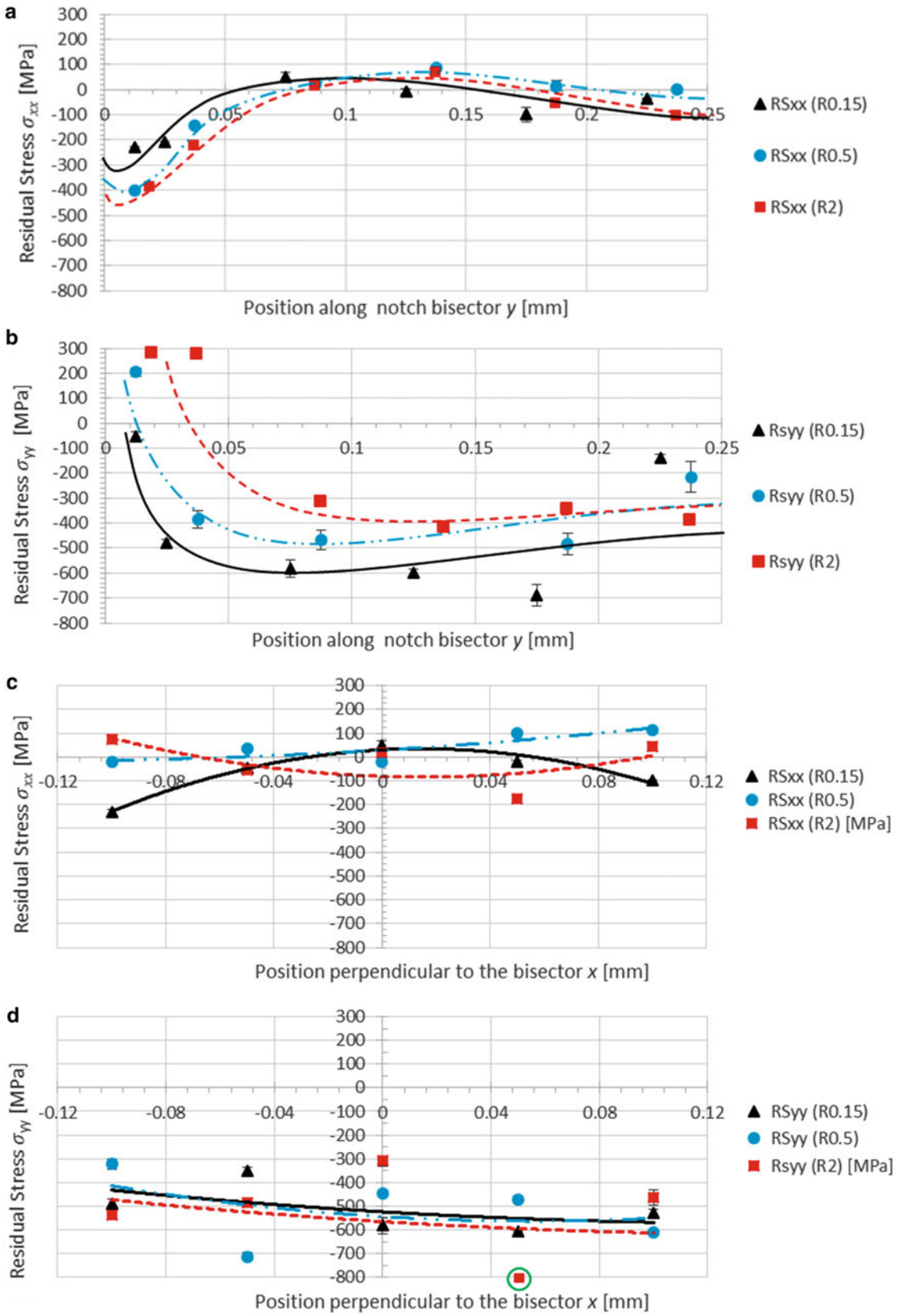

Fig. 33.5 Residual stress profiles. (**a**) σ_{xx} along the notch bisector. (**b**) σ_{yy} along the notch bisector. (**c**) σ_{xx} along the path transversal to the notch bisector at 0.75 mm from the notch tip. (**d**) σ_{yy} along the path transversal to the notch bisector at 0.75 mm from the notch tip

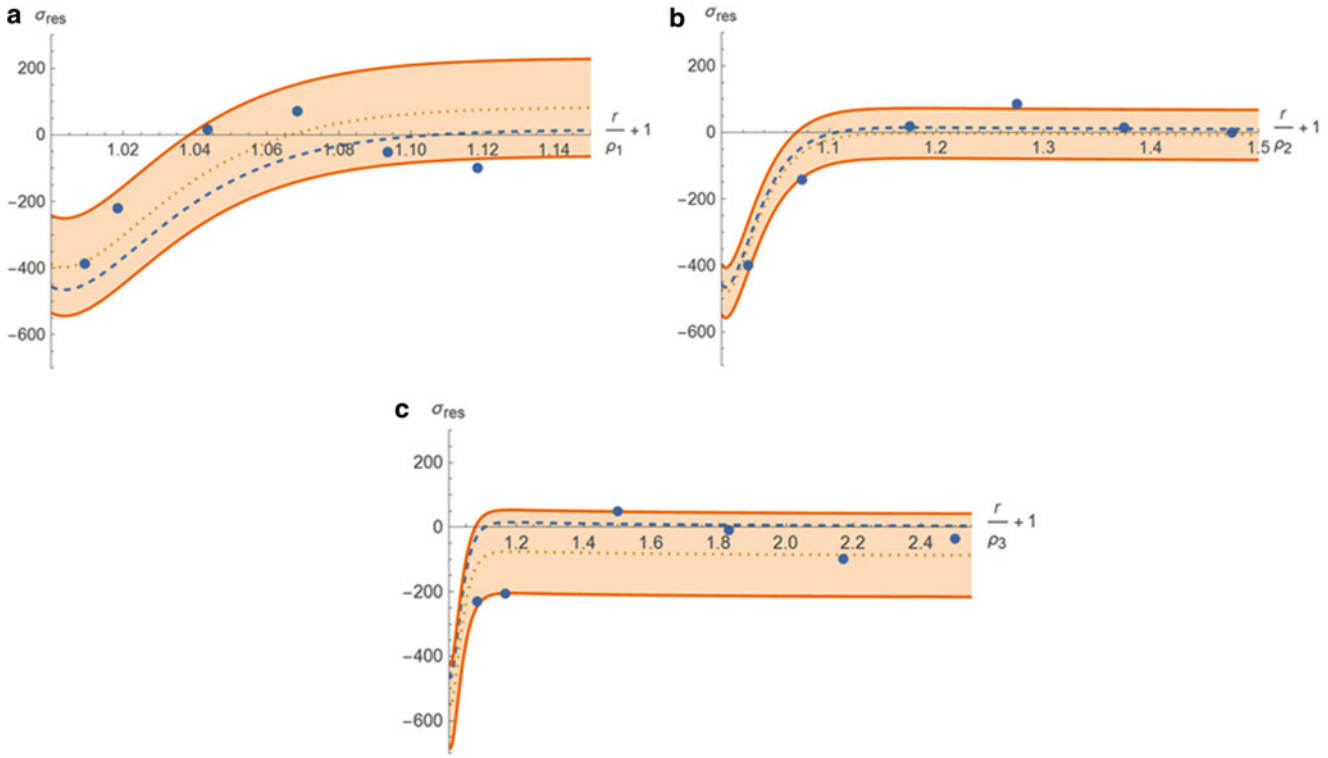

Fig. 33.6 Residual stress (σ_{xx}) result along the notch bisector and comparison with eigenstrain modelling result. The band in *orange colour* represent the confidence band at 97 % of probability based on the mathematical model. The *blue dotted line* represents the model's prediction. (**a**) Sample n.1 ($\boldsymbol{\rho_1} = 2$ mm). (**b**) Sample n.2 ($\boldsymbol{\rho_2} = 0.5$ mm). (**c**) Sample n.3 ($\boldsymbol{\rho_3} = 0.15$ mm)

33.5 Conclusion

The experimental evaluation of residual stresses carried out in the present study allowed the analysis of the residual stress profile along the bisector line for three shot-peened samples with different notch root radii. Stress evaluation was also conducted along an additional line extended perpendicularly to the bisector and running at 0.75 mm from the notch root. The polishing of the front surface, with consequent material removal, has eliminated the layer of material previously treated with shot peening. This conclusion emerges from the observation that no significant compressive residual stress σ_{xx} are present at distances greater than ~0.06 mm from the notch tip. The highest value of compressive residual stress σ_{xx} near the notch was found in the sample with the biggest notch radius ($\boldsymbol{\rho} = 2$ mm), whilst the lowest value was obtained for the smaller notch root radius sample. Regarding the other stress component σ_{yy}, the compressive state extends along the entire bisector extension. The effect of the shot peening is unlikely to extend up to such depths and we consider that it may be associated to a pre-existent compressive residual stress state prior the shot peening treatment due to some manufacturing process.

Given the fact that identical eigenstrain profiles were used in all cases, this effect is likely to be associated purely with the sample geometry, and the geometry-dependent mechanism of residual stress generation due to eigenstrain imposition.

The high spatial resolution given by the use of the FIB-DIC micro-ring core method allowed the residual stress evaluation in very narrowly defined regions of interest. The stress profiles evaluated by this method show good consistency between measurement points and lead to relatively narrow scatter band.

The comparison between the results presented in this work and the eigenstrain interpretation revealed general good agreement in terms of trend and magnitude. Particularly in the case of the sample having smallest notch root radius $\boldsymbol{\rho} = 0.15$ mm, the model agreed with the experimental observations with 95 % confidence.

Further more detailed analysis of residual stress generation can be carried out using either FEM or analytical modelling. This would provide a firm basis for reliable fatigue durability prediction of engineering components treated with this type of shot peening process. Further measurements, using different techniques, are required for the cross-validation of the results presented.

Acknowledgement This work was supported in part by EU FP7 project iSTRESS "Pre-standardisation of incremental FIB micro-milling for intrinsic stress evaluation at the sub-micron scale" EU FP7 iSTRESS 604646.

References

1. M. Benedetti, V. Fontanari, M. Bandini, D. Taylor, Multiaxial fatigue resistance of shot peened high-strength aluminum alloys. Int. J. Fatigue **61**, 271–282 (2014)
2. D. Liu, J. He, Effect of shot peening factors on fretting fatigue resistance of titanium alloys. Acta Metall. Sin. **37**, 156 (2001)
3. X. Song, W.C. Liu, J.P. Belnoue, J. Dong, G.H. Wu, W.J. Ding, S.A.J. Kimber, T. Buslaps, A.J.G. Lunt, A.M. Korsunsky, An eigenstrain-based finite element model and the evolution of shot peening residual stresses during fatigue of GW103 magnesium alloy. Int. J. Fatigue **42**, 284–295 (2012)
4. M. Benedetti, V. Fontanari, C. Santus, M. Bandini, Notch fatigue behaviour of shot peened high-strength aluminium alloys: experiments and predictions using a critical distance method. Int. J. Fatigue **32**, 1600–1611 (2010)
5. P.K. Sharp, J.Q. Clayton, G. Clark, The fatigue resistance of peened 7050-t7451 aluminium alloy-repair and re-treatment of a component surface. Fatigue Fract. Eng. Mater. Struct. **17**(3), 243–252 (1994)
6. M. Guagliano, L. Vergani, An approach for prediction of fatigue strength of shot peened components. Eng. Fract. Mech. **71**, 501 (2004)
7. A.M. Korsunsky, M. Sebastiani, E. Bemporad, Focused ion beam ring drilling for residual stress evaluation. Mater. Lett. **63**, 1961–1963 (2009)
8. E. Bemporad, M. Brisotto, L.E. Depero, M. Gelfi, A.M. Korsunsky, A.J.G. Lunt, M. Sebastiani, A critical comparison between XRD and FIB residual stress measurement techniques in thin films. Thin Solid Films **572**, 224–231 (2014)
9. X. Song, K.B. Yeap, J. Zhu, J. Belnoue, M. Sebastiani, E. Bemporad, K.Y. Zeng, A.M. Korsunsky, Residual stress measurement in thin films using the semidestructive ring-core drilling method using focused ion beam. Proc. Eng. **10**, 2190–2195 (2011)
10. A.M. Korsunsky, Eigenstrain analysis of residual strains and stresses. J. Strain Anal. **44**, 29–43 (2009)

Chapter 34
Residual Stress in Injection Stretch Blow Molded PET Bottles

Masoud Allahkarami, Sudheer Bandla, and Jay C. Hanan

Abstract Injection stretch blow molded poly(ethylene terephthalate) bottles show evidence of residual stresses. Some of these may develop as a result of cooling rate gradients through the material thickness. Others result from stretch crystallization as well as other forms of reduced entropy caused by rapidly stretching and quenching the amorphous PET matrix. A wide range of interdependent variables can change the magnitude and sign of residual stresses in bottles including the shape of the mold, resin properties, blowing pressure, preform temperature, thickness of the bottle wall, and cooling rate. Residual stresses can significantly influence bottle dimensional stability, top load, permeability, and consumer tactile feel. Here, the residual stresses were observed with photo-elasticity, which measures the changes in optical properties of the polymer in the presence of residual stresses. For observation of the time-dependence of stresses in the polymer film, a ring-cutting method was implemented. Depending on process and mainly on cooling rate, the rings have a tendency to open up or collapse under relaxation. X-ray diffraction crystallinity measurements with different incident angles were performed on both sides of the film to obtain information from different depths. XRD helped to explain the cause of collapsing instead of an expected opening in some ring tests. The change in distance between the two edges of the cut was measured with an image analyzing program. For the initial cut and 30 days after cutting, the residual stress was calculated. A chemical etching technique was used for validating the presence of tensile residual stress on one side of the polymer film. Applying chemicals to the surface of a polymer creates fracture on the more amorphous surface side of the film, depending on the magnitude of the tensile stress.

Keywords Residual stress • Ring-cutting test • Photo-elasticity • Etching PET • X-ray diffraction crystallinity measurement

34.1 Introduction

Polyethylene terephthalate (PET) is the most used raw material for packaging water and carbonated soft drink bottles [1, 2]. Demand for PET in beverage packaging is increasing, and PET bottles are very unlikely to be replaced by other materials in the near future. In order to significantly reduce the cost and carbon footprint, new bottles are designed with improved mechanical properties such as top load and with a lesser amount of PET per bottle [3, 4]. Comparing with metal cans, or glass bottles, bottles made from polymers present some level of time dependent dimension change. Due to the difference in cooling rate inside and outside of a bottle wall, mechanical stretching, or stretching from air blowing, a hoop residual stress is always present in the PET bottle wall due to gradient of cooling across the wall thickness. Depending on the manufacturing process, the inner and outer layer of wall experience different volume contraction or expansion. The level of residual stress is an important quality attribute of a blown PET bottle. There is lack of knowledge about the impact of residual stress on gas permeability through a polymeric bottle wall. Designing PET bottles with less PET material benefits from advancing accurate techniques for residual stress measurement. The bottle main body cylindrical wall is one of the locations that can more easily be used for residual stress measurement due to its less complex shape.

M. Allahkarami
Research and Development, Niagara Bottling LLC, Ontario, CA, USA

Mechanical and Aerospace Engineering, Oklahoma State University, Tulsa, OK, USA

S. Bandla • J.C. Hanan (✉)
Mechanical and Aerospace Engineering, Oklahoma State University, Tulsa, OK, USA
e-mail: jay.hanan@okstate.edu

S. Bossuyt et al. (eds.), *Residual Stress, Thermomechanics & Infrared Imaging, Hybrid Techniques and Inverse Problems, Volume 9*, Conference Proceedings of the Society for Experimental Mechanics Series, DOI 10.1007/978-3-319-21765-9_34

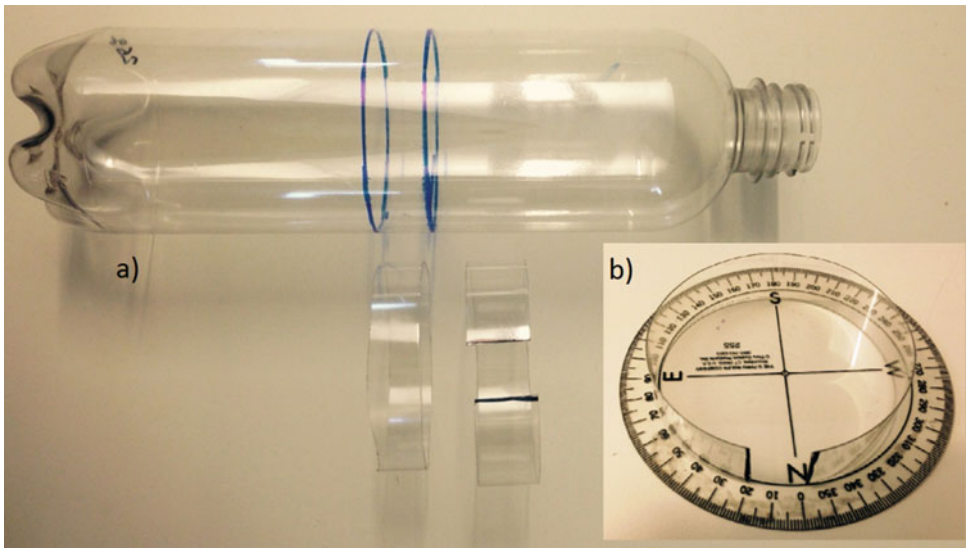

Fig. 34.1 (**a**) Ring-shaped specimens cut from the middle part of the bottle and (**b**) 20° of opening right after vertical slit

34.2 Material and Experimental Setup

Commercially available PET of M_w 36,000 g mol^{-1} (0.76 dL/g I.V.) was used for the current study. PET perform samples with a 26 g weight were injection molded using a cylindrical mold. Preforms were stretched to shape a bottle by stretch blow molding, as shown in Fig. 34.1a. Ring-shaped specimens of 55 mm inside diameter and around 400 μm thickness were cut by razor blade from the middle flat panel for testing. Figure 34.1b illustrates ring-shaped specimens and a similar ring being slit with a razor blade vertical cut. An opening of 20° was observed right after cutting due to stored residual stress.

34.3 Result and Discussion

The bottle wall could be considered a laminar structure. At the final stage of blowing, the outer layer of the bottle is in contact with the surface of the mold cooled with circulating chilling water. The outer layer cools down almost immediately while he interior layers of bottle are still quite fluid. Therefore no residual stress can be established at the rapidly solidified outer surface. As the rest of the layers solidify and contract, a residual stress freezes in as a result of shrinkage. This results in tensile stresses on the inside and compressive stress on the outside of the bottle. PET film was etched by suspending it in n-propylamine at room temperature. After a 60 min time interval, the sample was removed, rinsed in fresh propylamine, rinsed thoroughly in water, and dried. The etched sample was then examined by scanning electron microcopy.[1] This base film etched into random patterns, roughly similar to those of sun-dried clay, shown in Fig. 34.2. This was observed on an etched outer layer of the film with the amorphous structure created by instant freezing as indicated by XRD.

X-ray diffraction crystallinity measurements [5, 6] were performed on both sides of the film to obtain information from multiple depths. XRD revealed that the outside layer has a more amorphous content than the inner layer surface.

[1] Hitachi S-4800.

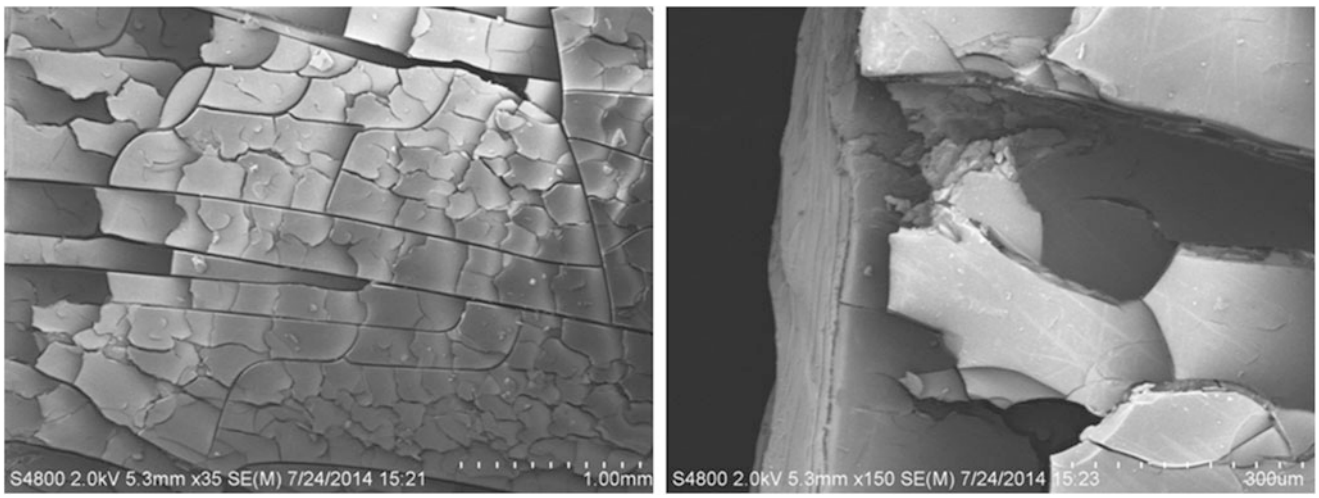

Fig. 34.2 SEM micrograph of etched PET film in n-propylamine showing cracks on the surface that cools down almost immediately

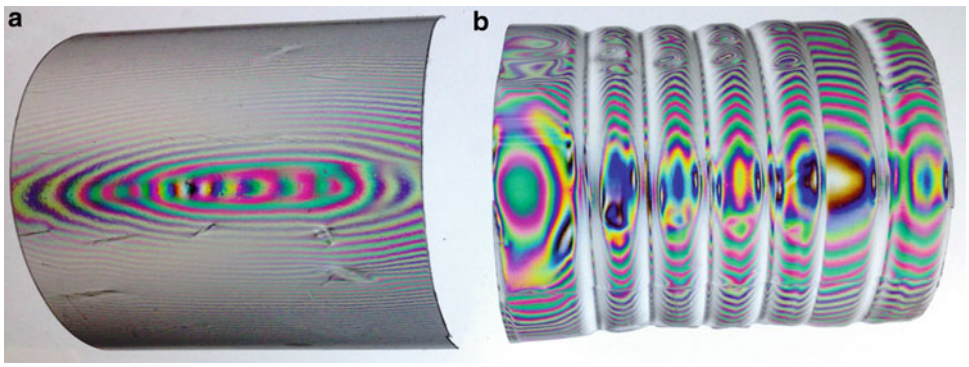

Fig. 34.3 (**a**) Typical fringes observed for semi-cylindrical cut of bottle and (**b**) typical fringe distortion by rib geometries

34.4 Photo-Elasticity Observation of Residual Hoop Stress

Residual stresses were observed with photo-elasticity, which measures the changes in optical properties of the polymer in the presence of residual stresses [7]. Fringes proportional to stress state were observed using cross-polarized light. The fringes are also dependent on geometry. These fringes might be trivial to predict analytically for the cylindrical shape shown in Fig. 34.3a, but can become more difficult to numerically resolve for complex shape in Fig. 34.3b.

34.5 Time-Dependence of Stresses in the Polymer Film

PET is viscoelastic, therefore the ring opening changes with time. For the initial cut and 30 days after cutting, the opening was recorded. The change in the opening with time is illustrated in Fig. 34.4. From the initial cut until 30 days after cutting the opening angle was measured and the data is presented in Fig. 34.5.

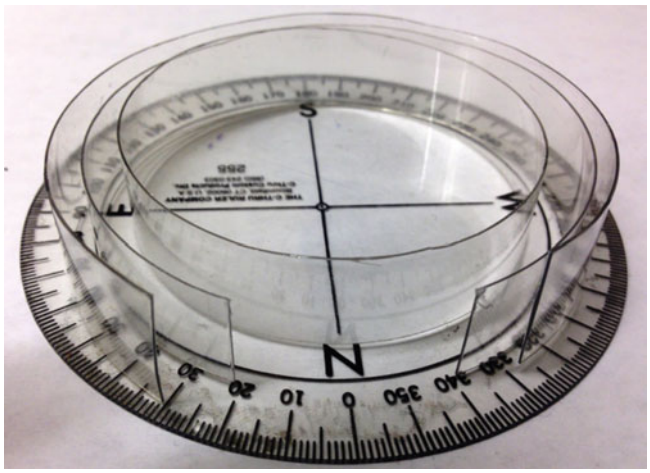

Fig. 34.4 Inner ring is a cylindrical cut of bottle. The middle ring is the slit ring after 20 days and the outer ring is after 30 days

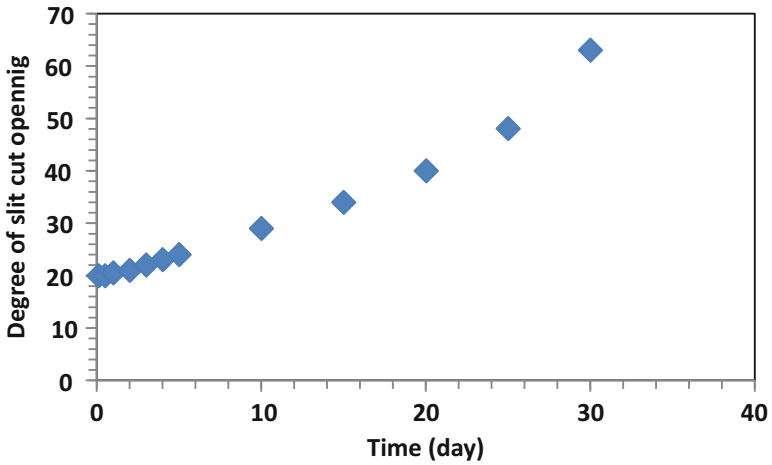

Fig. 34.5 Change in the opening angle of the slit-ring versus time

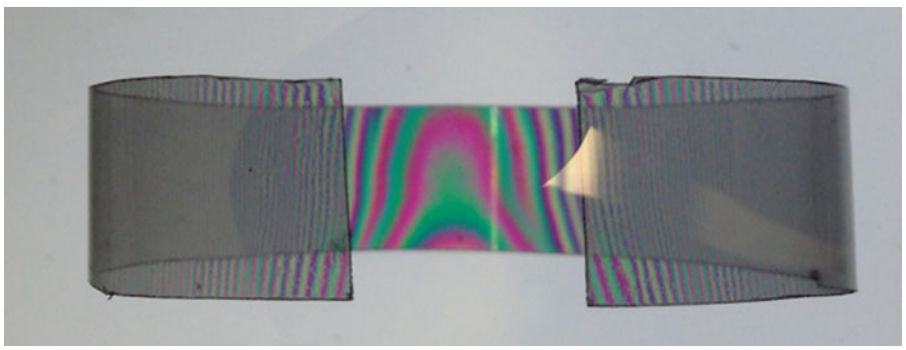

Fig. 34.6 Photoelastisity fringes for slit cut-ring cylindrical sample

34.6 Combined Photoelasticity and Residual Stress Measurement

Qualitative observation of residual stress in Fig. 34.6 was combined with a custom-built load cell setup shown in Fig. 34.7. In order to evaluate the amount of residual stress relaxed as function of time, slit-ring cut samples were mounted between a load cell and linearly movable fixture. Once the open ring was placed between the fixture and load cell, the load cell was balanced

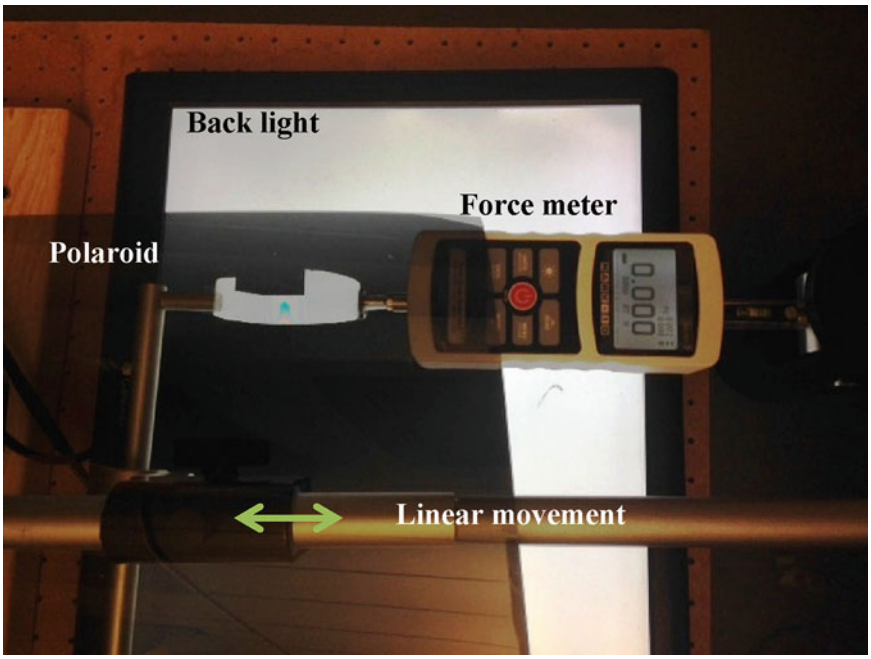

Fig. 34.7 Combined photo-elasticity tensile test set up

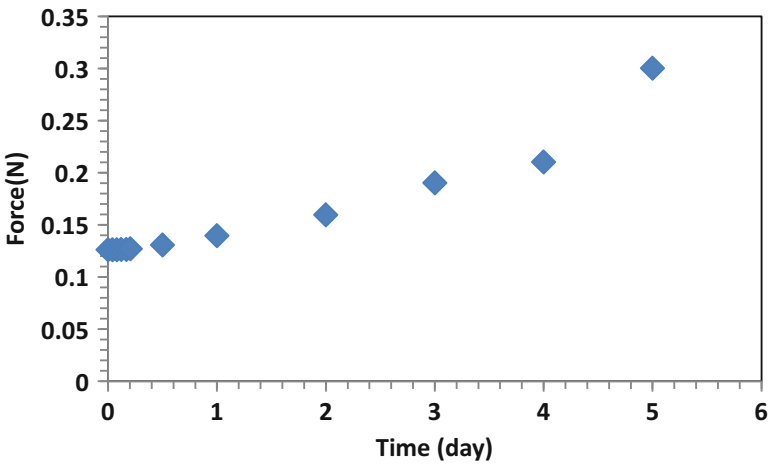

Fig. 34.8 Change in the force required to bring the opening angle to initial opening value

to zero. Then the fixture was moved to close the ring and when the opening was equal to the initial moment cut, the force from the load cell was recorded.

From initial cut until 5 days after cutting the required force to bring the opening angle to the initial opening state was measured and the data is presented in Fig. 34.8. As it can be seen from the force vs time graph, some residual stress relaxed as time progressed and more force was required for closing the ring.

34.7 Conclusion

There is a residual stress in blow molding PET bottles. The state of residual stress changes over time. Using photoelasticity residual stress in PET bottles can be observed qualitatively. Observing the amount of opening over a period of time revealed relaxation of stored residual stress in the bottles. The open ring cutting method combined with photoelasisity was used for creep study of the blow molded PET bottles. It is expected that this method of observing and measuring the residual stress will lead to greater efficiency in manufacturing stretch blow molded PET bottles.

References

1. J.C. Maddox, Strategic consulting and supply demand modeling for the PET raw material, resin and packaging industry, in *Packaging Conference*, LasVegas, 2011
2. F. Awaja, D. Pavel, Recycling of PET. Eur. Polym. J. **41**(7), 1453–1477 (2005)
3. J.C. Hanan, Plastic container having sidewall ribs with varying depth, United States Patent, US 2013/0140264 A1
4. J.C. Hanan, Preform extended finish for processing light weight ecologically beneficial bottles, United States Patent, US 2012/0263902 A1
5. S. Bandla, M. Allahkarami, J.C. Hanan, Thermal crystallinity and mechanical behavior of polyethylene terephthalate, in *Challenges in Mechanics of Time-Dependent Materials*, vol. 2, pp. 141–146
6. S. Bandla, M. Allahkarami, J.C. Hanan, Out-of-plane orientation and crystallinity of biaxially stretched polyethylene terephthalate. Powder Diffract. **29**(2), 123–126 (2014)
7. J.C. Hanan, Birefrengent residual stress and improved injection mold design. Mater. Sci. Forum **768–769**, 217–223 (2013)

Chapter 35
Applying Infrared Thermography and Heat Source Reconstruction for the Analysis of the Portevin-Le Chatelier Effect in an Aluminum Alloy

Didier Delpueyo, Xavier Balandraud, and Michel Grédiac

Abstract This study deals with the Portevin-Le Châtelier (PLC) effect in an aluminum alloy. Tensile tests are performed and the temperature variations are measured at the specimen surface during the loading by infrared thermography. In order to improve the spatio-temporal identification of the plastic instabilities, the heat sources are estimated by processing the temperature fields by using a two-dimensional version of the heat diffusion equation. Filtering is a key-point of the technique since the goal is calculate both temporal and spatial derivatives from noisy temperature fields. The idea is to convolve the temperature variation fields with a kernel chosen as a first and a second derivative of a Gaussian, in order to estimate the first-order temporal derivative and the second-order spatial derivative, respectively. The study focuses on the effect of the strain rate in terms of heat source band patterns associated with the PLC effect.

Keywords Portevin-Le Châtelier effect • Aluminum alloy • Infrared thermography • Heat source reconstruction • Thermomechanics of materials

35.1 Introduction

The Portevin-Le Châtelier (PLC) effect in certain dilute alloys has been studied extensively for some years [1]. It is characterized by plastic instabilities over time and in space during the stretching of the metal. These instabilities have been thoroughly studied in the literature as a function of the loading rate and the temperature considered for the specimen under test. Some theoretical and numerical investigations can be found in [2, 3] for instance. Among the experimental approaches, let us cite the use of optical techniques [4, 5] (including digital image correlation [6–9]), laser scanning [10, 11] and acoustic emission [12, 13]. Infrared (IR) thermography was also employed for studying plastic instabilities [14–16]. However, the temperature variation is not the most relevant parameter because of heat diffusion inside the specimen or heat exchange with the outside. Many authors suggest to deduce the heat sources (produced or absorbed by the material due to strain variation) from the measured temperature fields by using the heat diffusion equation [17, 18]. The mean difficulty of this approach is that input data are noisy. Different strategies of filtering have been tested in the past: local polynomial approximation [19], low-pass recursive filters [20], Fourier transform [14], modal filtering method [21] or proper orthogonal decomposition [22]. Filtering is indeed a key-point of the approach since the goal is calculate temporal and spatial derivatives from noisy temperature fields. In the present study, we used a derivative Gaussian filter [23]. The idea is to convolve the temperature change fields with a kernel chosen as a first or second derivative of a Gaussian in order to estimate the first-order temporal derivative and the second-order spatial derivative, respectively. In practice, a two-dimensional version of the heat diffusion equation is employed considering thin specimens (thus enabling us to assume a nearly homogeneous temperature distribution along the thickness). Uniaxial tensile tests were performed on an aluminum-magnesium alloy. The study focuses on the effect of the strain rate in terms of heat source band pattern associated with the PLC effect.

D. Delpueyo • M. Grédiac
Clermont Université, Université Blaise Pascal, Institut Pascal, BP 10448, Clermont-Ferrand 63000, France

CNRS, UMR 6602, Institut Pascal, Aubière 63171, France

X. Balandraud (✉)
CNRS, UMR 6602, Institut Pascal, Aubière 63171, France

Clermont Université, Institut Français de Mécanique Avancée, Institut Pascal, BP 10448, Clermont-Ferrand 63000, France
e-mail: xavier.balandraud@ifma.fr

S. Bossuyt et al. (eds.), *Residual Stress, Thermomechanics & Infrared Imaging, Hybrid Techniques and Inverse Problems, Volume 9*, Conference Proceedings of the Society for Experimental Mechanics Series, DOI 10.1007/978-3-319-21765-9_35

35.2 Experimental Conditions and Image Processing

The material under study was a 5052 aluminum alloy, hardened by rolling and stabilized by low-temperature heat treatment. Specimens were rectangular sheets with dimension 300 × 40 × 1 mm^3. Specimens were painted in black to maximize the thermal emissivity. Tests were performed an ambient temperature. A MTS ±15 kN testing machine was used to apply a uniaxial tensile loading up to specimen rupture. Two macroscopic strain rates were tested: 6.25 × 10^{-2} and 2 × 10^{-3} s^{-1}. The measurement of the temperature fields on the specimen surface was performed during the loading with a CEDIP Jade III-MWIR infrared camera featuring 320 × 240 pixels. The integration time used was 1500 µs and the noise equivalent temperature difference was about 20 mK.

Fields of temperatures $T(x, y, t)$, where x and y are the spatial coordinates in the specimen plane and t the time, are then post-processed using the heat diffusion equation. Indeed, the heat source s produced or absorbed by the material due to strain variation can be estimated by:

$$s = \rho C\left(\frac{\partial T}{\partial t} + \frac{T - T_{amb}}{\tau}\right) - \lambda \Delta T \tag{35.1}$$

where ρ is the density, C the specific heat and λ the thermal conductivity of the material assumed to be isotropic. Δ is the Laplacian operator. T_{amb} is the ambient temperature. Parameter τ is a time constant characterizing the heat exchange along z-direction with ambient air.

The idea here is to merge the filtering and derivation steps by convolving the temperature difference maps with a suitable kernel. This kernel is the derivative of a Gaussian function. On the one hand, the first-order time derivate in (35.1) is estimated by using the first-order derivative of the one-dimensional Gaussian function $G_{temporal}(t)$. On the other hand, the second-order spatial derivative is obtained with the Laplacian of the two-dimensional Gaussian function $G_{spatial}(x, y)$ as a kernel. These derivatives are defined respectively by:

$$\frac{\mathrm{d}G_{temporal}}{\mathrm{dt}} = \frac{t}{\sqrt{2\pi}\sigma_{temporal}^3}\exp\left(-\frac{t^2}{2\sigma_{temporal}^2}\right) \tag{35.2}$$

$$\Delta G_{spatial} = \frac{1}{2\pi\sigma_{spatial}^4}\left[1 - \frac{x^2 + y^2}{2\sigma_{spatial}^2}\right]\exp\left(-\frac{x^2 + y^2}{2\sigma_{spatial}^2}\right) \tag{35.3}$$

where $\sigma_{temporal}$ and $\sigma_{spatial}$ are the standard deviations of the Gaussian considered for the time derivative and the spatial derivative, respectively.

These functions defined in (35.2) and (35.3) are applied to the $T(x, y, t)$ field by convolution. Thanks to the basic properties of the convolution product, this procedure is equivalent to the calculation of the convolution of the derivate of the temperature field by the Gaussian. Since discrete temperature fields are available in practice, two parameters need to be considered: the width of the processing kernel and the number of standard deviations considered in this kernel. Reference [23] provides the details about the optimization of the kernel for the estimation of the second-order spatial derivative of the temperature fields.

35.3 Results

Figure 35.1 shows the macroscopic stress–strain curve for the test performed with a strain rate of 6.25 × 10^{-2} s^{-1}. The curve is smooth up to a strain value equal to about 3.8 %. Then some sudden drops of the stress are observed. They correspond to the existence of PLC bands. Figure 35.2 shows the temperature change field and the heat source field for a strain value equal to 4.8 %. A heterogeneous temperature change field is observed, the right-hand part of the specimen in the figure being hotter than the left-hand part. The unit of the heat sources in this figure is °C s^{-1}. This unit is simply obtained by dividing the heat source value by the ρC product. It can be noted that, as expected, the heat source distribution is more localized than the temperature change distribution. A specific heat source pattern is observed. It consists of inclined bands of high intensity forming crosses, while heat sources are nearly equal to zero in the other part of the specimen. This cross-shaped pattern was numerically predicted in [3] for aluminum alloys and in [24] for steel alloys.

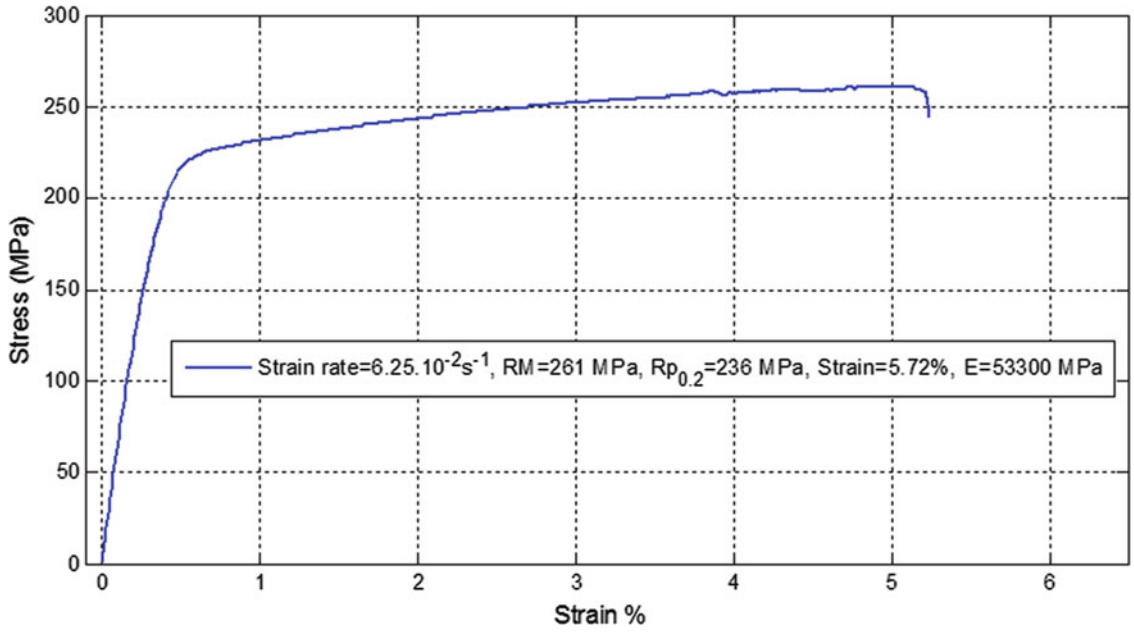

Fig. 35.1 Macroscopic stress–strain curve for a macroscopic strain rate equal to 6.25×10^{-2} s^{-1}

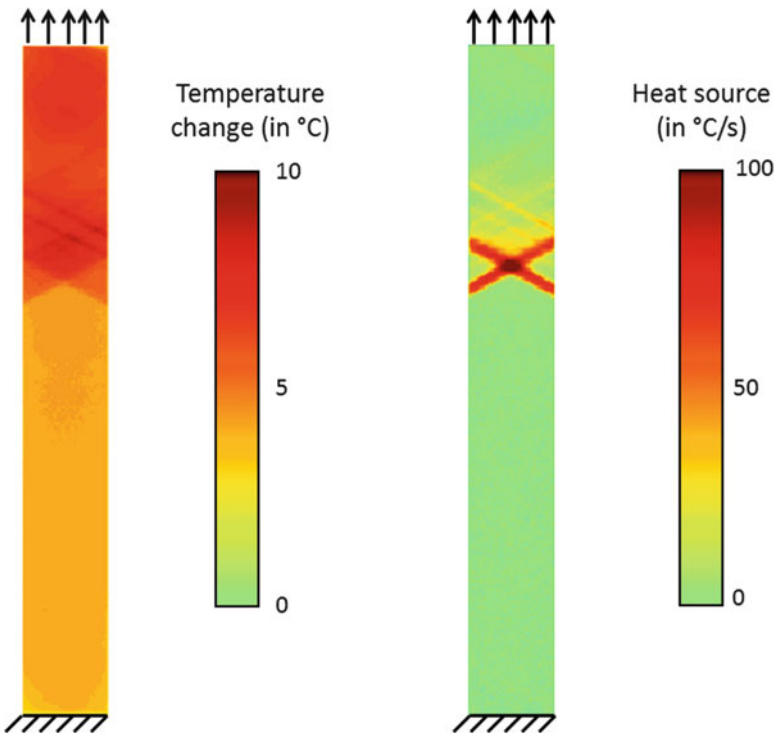

Fig. 35.2 Temperature change field and heat source field for a macroscopic strain equal to 4.8 %, during the test performed at a strain rate equal to 6.25×10^{-2} s^{-1}

Figure 35.3 shows the heat source field for a strain value equal to 4.8 %. It was obtained during the test performed at a strain rate of 2×10^{-3} s^{-1}. When comparing this map with that shown in Fig. 35.2, it appears that the shape of the heat source pattern is quite simple: it consists of individual inclined bands. The PLC effect appears to be very sensitive to the strain rate in terms of heat source patterns. This was confirmed by testing other strain rates. These results are not reported. They are given in [25]. As a general comment, the higher the strain rate, the more complex the heat source pattern associated to the PLC effect.

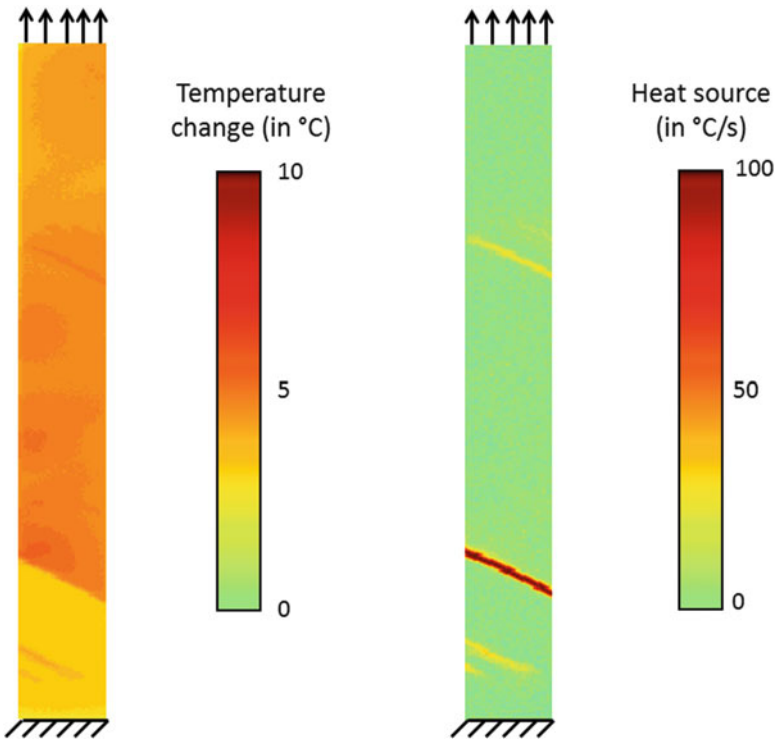

Fig. 35.3 Temperature change field and heat source field for a macroscopic strain equal to 4.8 %, during the test performed at a strain rate equal to 2×10^{-3} s^{-1}

35.4 Conclusion

The Portevin-Le Châtelier effect was studied on an aluminum alloy subjected to uniaxial tensile tests. These tests were performed while the temperature variations were measured at the specimen surface by infrared thermography. The heat sources were deduced from the temperature fields by using the heat diffusion equation. Gaussian derivative filters were used in order to calculate the temporal and spatial derivatives of the (noisy) temperature fields. By convolving the temperature variation fields with a kernel chosen as a first or second derivative of a Gaussian, it was possible to estimate the first-order temporal derivative and the second-order spatial derivative of the temperature variation fields, respectively. Specific patterns of heat source were obtained. They were composed of inclined bands along the specimen. It was observed that the higher the strain rate, the more complex the heat source pattern associated to the PLC effect.

References

1. Y. Ahmet, The Portevin-Le Châtelier effect: a review of experimental findings. Sci. Technol. Adv. Mater. **12**, 063001 (16pp) (2011)
2. E. Rizzia, P. Häner, On the Portevin-Le Châtelier effect: theoretical modeling and numerical results. Int. J. Plast. **20**, 121–165 (2004)
3. M. Mazière, J. Besson, S. Forest, B. Tanguy, H. Chalons, F. Vogel, Numerical aspects in the finite element simulation of the Portevin-Le Châtelier effect. Comput. Methods Appl. Mech. Eng. **199**, 734–754 (2010)
4. C.Y. Yu, P.W. Kao, C.P. Chang, Transition of tensile deformation behaviors in ultrafine-grained aluminum. Acta Mater. **53**, 4019–4028 (2005)
5. J. Kang, D.S. Wilkinson, M. Jain, J.D. Embury, A.J. Beaudoin, S. Kim, R. Mishira, A.K. Sachdev, On the sequence of inhomogeneous deformation processes occurring during tensile deformation of strip cast AA5754. Acta Mater. **54**, 209–218 (2006)
6. H. Halim, D.S. Wilkinson, M. Niewczas, The Portevin-Le Châtelier (PLC) effect and shear band formation in an AA5754 alloy. Acta Mater. **55**, 4151–4160 (2007)
7. A. Benallal, T. Berstad, T. Borvik, O.S. Hopperstad, I. Koutiri, R. Nogueira de Codes, An experimental and numerical investigation of the behaviour of AA5083 aluminium alloy in presence of the Portenin-Le Châtelier effect. Int. J. Plast. **24**, 1916–1945 (2008)
8. J. Coer, P.Y. Manach, H. Laurent, M.C. Oliveira, L.F. Menezes, Piobert-Lüders plateau and Portevin-Le Châtelier effect in an Al-Mg alloy in simple shear. Mech. Res. Commun. **48**, 1–7 (2013)
9. S. Nagarajan, N. Raghu, B. Venkatraman, Study on local zones constituting to band growth associated with inhomogeneous plastic deformation. Mater. Lett. **105**, 209–212 (2013)
10. H. Neuhäuser, F.B. Klose, F. Hagemann, J. Weidenmüller, H. Dierke, P. Hâhner, On the PLC effect in strain-rate and stress-rate controlled tests-studies by laser scanning extensometry. J. Alloys Compd. **378**, 13–18 (2004)

11. R. Shabadi, S. Kumar, H.J. Roven, E.S. Dwarakadasa, Characterisation of PLC band parameters using laser speckle technique. Mater. Sci. Eng. A **354**, 140–150 (2004)
12. I.V. Shashkov, M.A. Lebyodkin, T.A. Lebedkina, Multiscale study of acoustic emission during smooth and jerky flow in an Al-Mg alloy. Acta Mater. **60**, 6842–6850 (2012)
13. F. Chmelik, F.B. Klose, H. Dierke, J. Sachl, P. Lukac, Investigating the Portevin-Le Châtelier effect in strain rate and stress rate controlled tests by the acoustic emission and laser extensometry techniques. Mater. Sci. Eng. A **462**, 53–60 (2007)
14. H. Louche, A. Chrysochoos, Thermal and dissipative effects accompanying Lüders band propagation. Mater. Sci. Eng. A **307**, 15–22 (2001)
15. H. Louche, P. Vacher, R. Arrieux, Thermal observations associated with the Portevin-Le Châtelier effect in an Al-Mg alloy. Mater. Sci. Eng. A **404**, 188–196 (2005)
16. S. Nagarajan, R. Narayanaswamy, V. Balasubramaniam, Study on the kinetics of thermomechanical response accompanying plastic instability in mild steel. Mech. Mater. **80**, 27–36 (2015)
17. P. Schlosser, H. Louche, D. Favier, L. Orgeas, Image processing to estimate the heat sources related to phase transformations during tensile test of NiTi tubes. Strain **43**, 260–271 (2007)
18. D. Delpueyo, M. Grédiac, X. Balandraud, C. Badulescu, Investigation of martensitic microstructures in a monocrystalline Cu-Al-Be shape memory alloy with the grid method and infrared thermography. Mech. Mater. **45**, 34–51 (2012)
19. M.L. Pastor, X. Balandraud, M. Grediac, J.L. Robert, Applying infrared thermography to study the heating of 2024-T3 aluminium specimens under fatigue loading. Infrared Phys. Technol. **51**, 505–515 (2008)
20. X. Balandraud, A. Chrysochoos, S. Leclercq, R. Peyroux, Influence of the thermomechanical coupling on the propagation of a phase change front. C.R. Acad. Sci., Ser. II B: Mec. **329**, 621–626 (2001)
21. T. Pottier, H. Louche, S. Samper, H. Favreliere, F. Toussaint, P. Vacher, Proposition of a modal filtering method to enhance heat source computation within heterogeneous thermomechanical problems. Int. J. Eng. Sci. **81**, 163–176 (2014)
22. N. Ranc, A. Blanche, D. Ryckelynck, A. Chrysochoos A, POD preprocessing of IR thermal data to assess heat source distributions. Exp. Mech. **55**, 725–739 (2015)
23. D. Delpueyo, X. Balandraud, M. Grédiac, Heat source reconstruction from noisy temperature fields using an optimised derivative Gaussian filter. Infrared Phys. Technol. **60**, 312–322 (2013)
24. S. Dumoulin, H. Louche, O.S. Hopperstad, T. Brvik, Heat sources, energy storage and dissipation in high-strength steels: experiments and modelling. Eur. J. Mech. A Solids **29**, 461–474 (2010)
25. D. Delpueyo, X. Balandraud, M. Grédiac, Calorimetric signature of the Portevin-Le Châtelier effect in an aluminum alloy from infrared thermography and heat source reconstruction (2015, submitted for publication)

Chapter 36
Applying a Gad Filter to Calculate Heat Sources from Noisy Temperature Fields

Clément Beitone, Xavier Balandraud, Michel Grédiac, Didier Delpueyo, Christophe Tilmant, and Frédéric Chausse

Abstract This study deals with a post-processing technique to reconstruct heat source fields from temperature fields measured by infrared thermography. A Gradient Anisotropic Diffusion (GAD) image filter is used to process the data. The technique is first described. Synthetic temperature fields corrupted by added noise are then considered to assess the robustness of the procedure and the filter is optimized in order to reconstruct at best the heat source fields. Results are compared with those obtained with an averaging filter and a Gaussian derivative filter. The second part of the study presents an application to experimental temperature fields. Obtained results illustrate the relevancy of the GAD filter to reliably extract heat sources in thermomechanics of materials.

Keywords Heat source reconstruction • Filtering • Gradient Anisotropic Diffusion • Image processing • Thermomechanics of materials

36.1 Introduction

During the last decades, the use of infrared (IR) measurement techniques has spread in experimental mechanics to study the thermomechanical behavior of materials. With the constant improvement of IR cameras in terms of measurement resolution and number of pixels, it is now possible to measure accurately temperature variations which are representative of physical phenomena in materials such as thermoelastic coupling, plastic instabilities, phase transitions, fatigue or damage. The idea is to reveal the deformation mechanisms in a specimen from its thermal response under mechanical loading. However, the temperature variation is not the most relevant parameter because of both the heat diffusion inside the specimen and the heat exchange with the outside. A more relevant approach is thus to estimate the heat sources (which are produced/absorbed by the material due to deformation) from the measured temperature fields by using the heat diffusion equation [1–3]. Two main difficulties are encountered in this approach: measurements are available only at the specimen surface, and experimental input data are unavoidably noisy.

Two main types of approaches are available in the literature. The first one consists in minimizing the error between measured temperature fields and theoretical temperature fields provided by a numerical model (see [4, 5] for instance). The second one consists in using a suitable two-dimensional version of the heat diffusion equation and directly calculating the terms of the heat diffusion equation using the experimental temperatures. The method presented here belongs to this second type of approach. Various filtering strategies were tested in the past. Important results were obtained on the thermomechanical behavior of materials using different types of filtering methods: local polynomial approximation [6], low-pass recursive filters [7], Fourier transform [8], modal filtering method [9], proper orthogonal decomposition [10] or

C. Beitone • M. Grédiac • D. Delpueyo • C. Tilmant
Clermont Université, Université Blaise Pascal, Institut Pascal, BP 10448, Clermont-Ferrand 63000, France

CNRS, UMR 6602, Institut Pascal, Aubière 63171, France

X. Balandraud (✉)
CNRS, UMR 6602, Institut Pascal, Aubière 63171, France

Clermont Université, Institut Français de Mécanique Avancée, Institut Pascal, BP 10448, Clermont-Ferrand 63000, France
e-mail: xavier.balandraud@ifma.fr

F. Chausse
CNRS, UMR 6602, Institut Pascal, Aubière 63171, France

Clermont Université, Université d'Auvergne, Institut Pascal, BP 10448, Clermont-Ferrand 63000, France

S. Bossuyt et al. (eds.), *Residual Stress, Thermomechanics & Infrared Imaging, Hybrid Techniques and Inverse Problems, Volume 9*, Conference Proceedings of the Society for Experimental Mechanics Series, DOI 10.1007/978-3-319-21765-9_36

derivative Gaussian filter [11]. In the present study, we focus only on the thermal conduction term of the heat diffusion equation because it is the most difficult term to estimate in the procedure, the reason being that it involves spatial second derivatives (a Laplacian for isotropic materials) of noisy data. As the underlying process is linked to the heat equation, we expect a signal with a smooth curvature. We study the benefit of a filter which was specially designed to remove noise in the curvature of a signal: the so-called Gradient Anisotropic Diffusion (GAD) proposed first by Perona and Malik [12]. This filter was first designed for image smoothing purposes, but it can also be used to detect interest points in natural images. The objective here is to study the efficiency of the heat source determination employing such a GAD filter. Synthetic and experimental data are successively processed.

36.2 Heat Diffusion Equation and Processing by GAD Filter

Physical problem statement—Let us consider a rectangular plate in the (x, y) plane with small thickness in the z-direction. A two-dimensional version of the heat diffusion can be written as follows [1]:

$$s_t = \rho C\left(\frac{\partial \theta}{\partial t} + \frac{\theta}{\tau}\right) - \lambda \Delta \theta \tag{36.1}$$

where θ is the temperature variation, s_t the heat source produced or absorbed by the material due to deformation, ρ the density, C the specific heat and λ the thermal conductivity of the material assumed to be isotropic. τ is a time constant characterizing the heat exchanges by convection with air along the z-direction. By dividing this equation by ρC, we obtain:

$$s = \frac{\partial \theta}{\partial t} + \frac{\theta}{\tau} - D\Delta \theta \tag{36.2}$$

where D is the thermal diffusivity. In this expression, s is equal to the $(s_t/\rho C)$ ratio. It is referred to as the 'heat source' in the following. It is expressed in $^\circ\mathrm{C\ s}^{-1}$. From noisy temperature fields, the most difficult term to be calculated is the Laplacian term, especially for materials such as metals which feature a high thermal diffusivity compared to other types of materials. Hence the present study focuses on this term. Only the steady-state regime $\theta(x, y)$ of the temperature evolution $\theta(x, y, t)$ under constant heat source field $s(x, y)$ is considered in the following. Equation (36.2) becomes

$$s = \frac{\theta}{\tau} - D\Delta \theta \tag{36.3}$$

Equation (36.3) shows that the field of heat source $s\,(x, y)$ can be deduced from the field of temperature change $\theta(x, y)$ using the right-hand side of the equation.

Processing by anisotropic diffusion filtering—The GAD filtering method was specially designed to remove the noise in the curvature of a signal while respecting the causality principle, which claims that details at coarse scales remain present at finer scales [12]. It relies on a diffusion equation for which the raw noisy field $\theta(x, y)$ is used as initial condition:

$$\frac{\partial \theta^*}{\partial t^*} - div\left(c \nabla \theta^*\right) = 0 \tag{36.4}$$

$$\text{with } \theta^*(x, y, t^* = 0) = \theta(x, y) \tag{36.5}$$

where $c(x, y, t^*)$ is a scalar function. Exponent "*" in the symbols t^* and θ^* is here employed to distinguish the quantities from those used in (36.1) and (36.2). The variation in time of the field $\theta^*(x, y, t^*)$ provides smoother versions of the original field $\theta(x, y)$. In order to preserve the signal structure hidden by noise, function c must respect some properties. For instance, a common choice for this function is [12]:

$$c(x, y, t^*) = \exp\left[-\left(\frac{|\nabla\theta^*(x, y, t^*)|}{k}\right)^2\right] \tag{36.6}$$

where k is a scalar constant. As c is not constant in space, the filter is said to be heterogeneous and anisotropic [12]. Equation (36.4) is solved with an iterative method, namely the Euler method. The choice of the time step for this resolution is usually normalized [12], and the variation in time of θ^* can be expressed only as a function of the iteration number i. The objective here is to find the optimal iteration number i_{opt} providing the optimal filtered version $\theta_f(x, y)$ of $\theta(x, y)$ for the heat source reconstruction:

$$s = \frac{\theta_f}{\tau} - D\Delta\theta_f \tag{36.7}$$

Examples of data processing are given in next section.

36.3 Simulated Data

Figure 36.1 shows a theoretical field of temperature change resulting from a heat source in a rectangular plate. The heat source is non-null in the square zone with dimension a at the center of the plate, and null elsewhere. The objective is to reconstruct the heat source field $s(x, y)$ from the field of temperature change $\theta(x, y)$ in the presence of noise. A Gaussian noise with a standard deviation of 0.02 °C is added for the theoretical input data in order to simulate a noise which is typical of noise encountered in real IR cameras. The mean quadratic error between imposed and reconstructed heat source field can be calculated inside the central square zone (where the theoretical heat source is non-null), as well as in the remaining part of the rectangular plate. The global reconstruction error is defined here as the mean value of these two errors (see [11]).

Figure 36.2 shows the performance of the heat source reconstruction as a function of the number of iterations i used during the filtering procedure. It is observed that there is an optimum for the reconstruction which is equal here to 35 iterations. In our tests, parameter k was fixed empirically after some preliminary tests (not presented here): $k = 6$. A series of simulations was performed to identify the optimal number of iterations as a function of various parameters: the heat source intensity, the size a and the noise which corrupts the input data. It can be also noted from the curve in Fig. 36.2 that above the optimum number of iterations, the error increases quite slowly, highlighting that a non-optimal number of iterations still leads to a correct heat source reconstruction. This information is interesting in practice, while performing mechanical tests for instance. Indeed, defining the optimal filtering parameter is difficult during an experimental test as no reference solution is *a priori* available.

Figure 36.3 presents the comparison between three types of filtering applied on the same input data: the averaging filter, the Gaussian derivative filter and the GAD filter. The theoretical heat source profile is superimposed in red. Each filter was optimized to minimize its reconstruction error. The heat source field reconstructed using the averaging filter (Fig. 36.3a) clearly exhibits a higher level of noise compared to the others. The comparison between the derivative Gaussian and GAD

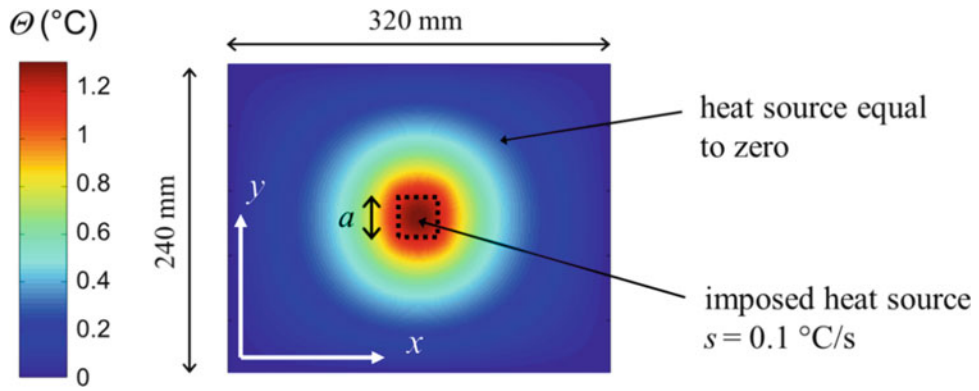

Fig. 36.1 Example of temperature field in an aluminum plate resulting from a heat source located at the center of the plate

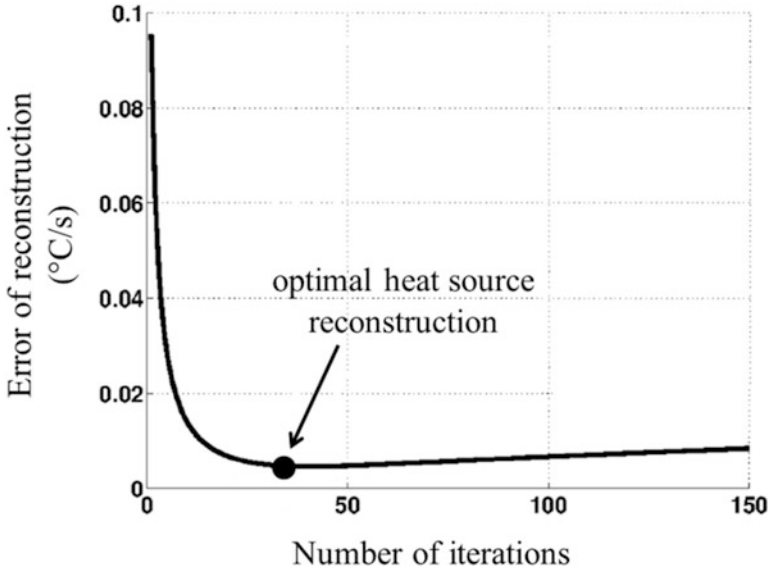

Fig. 36.2 Error in the heat source reconstruction as a function of the number of iterations

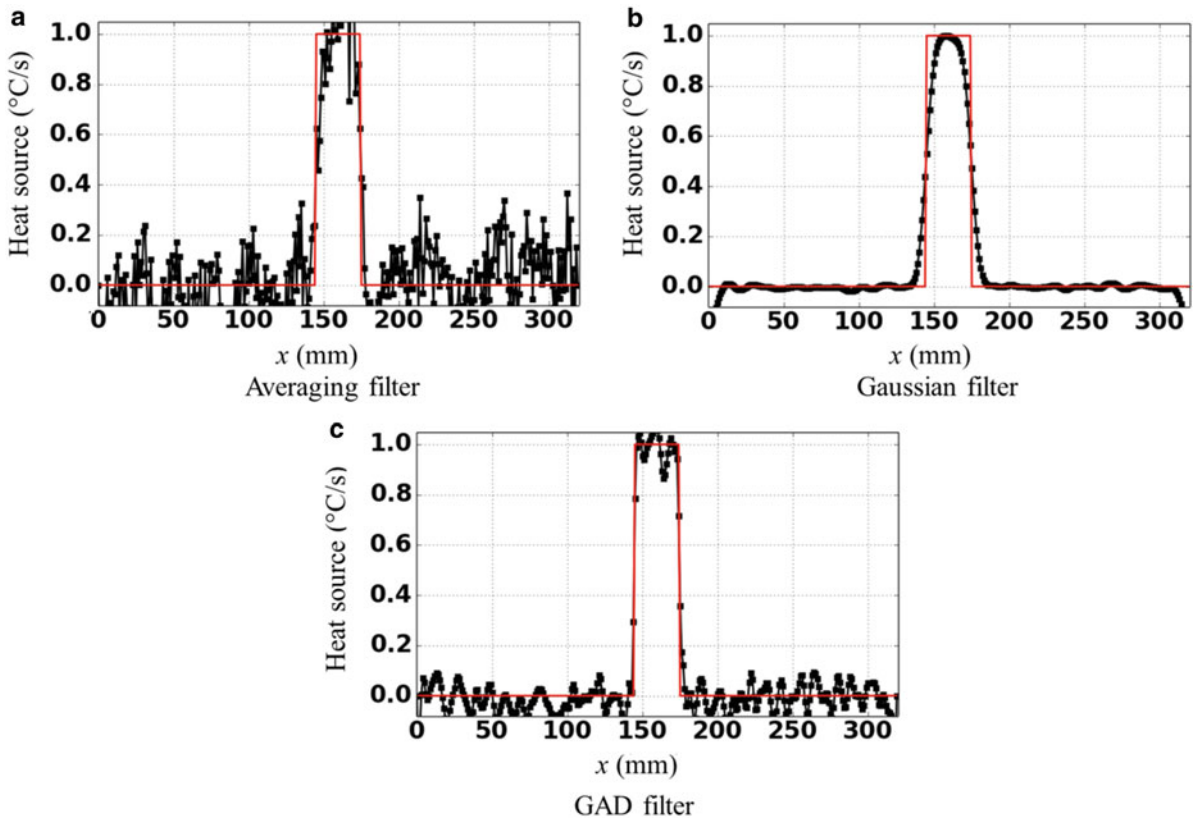

Fig. 36.3 Comparisons between three types of filtering procedures using the same input data: (**a**) averaging filter, (**b**) derivative Gaussian filter, and (**c**) GAD filter. Profiles are plotted as a function of coordinate x for $y = 120$ mm. The theoretical heat source profile is superimposed in *red*. Each filter was optimized to minimize the error of heat source reconstruction

filters (Fig. 36.3b and c) shows that the former leads to a lower level of noise. However, the mean error of heat source in the central zone is lower with the GAD filter. Indeed, the imposed value of 1 °C/s for the heat source in the central zone is reached only over a small zone with the derivative Gaussian filter, while the GAD filter better approximates (on average) the theoretical heat source in this zone.

36.4 Experimental Data

The approach is now applied to an experimental temperature field measured on an aluminum plate (dimensions $320 \times 240 \times 2$ mm^3). A heat source was imposed using an electric heating patch glued on the specimen surface: see Fig. 36.4a. The measurement of the temperature field was performed with a Cedip Jade III-MWIR infrared camera. The temperature map was encoded with 320×240 pixels. The value of the heat source produced by the patch can be deduced from its electrical resistance, the intensity and voltage of the electric current, and the volume of the material located under the patch. It is equal to 0.4 °C s^{-1} for the considered test. Figure 36.4b presents the results of the processing. It can be seen that the heat source is correctly identified at the center of the plate, both in terms of shape and intensity.

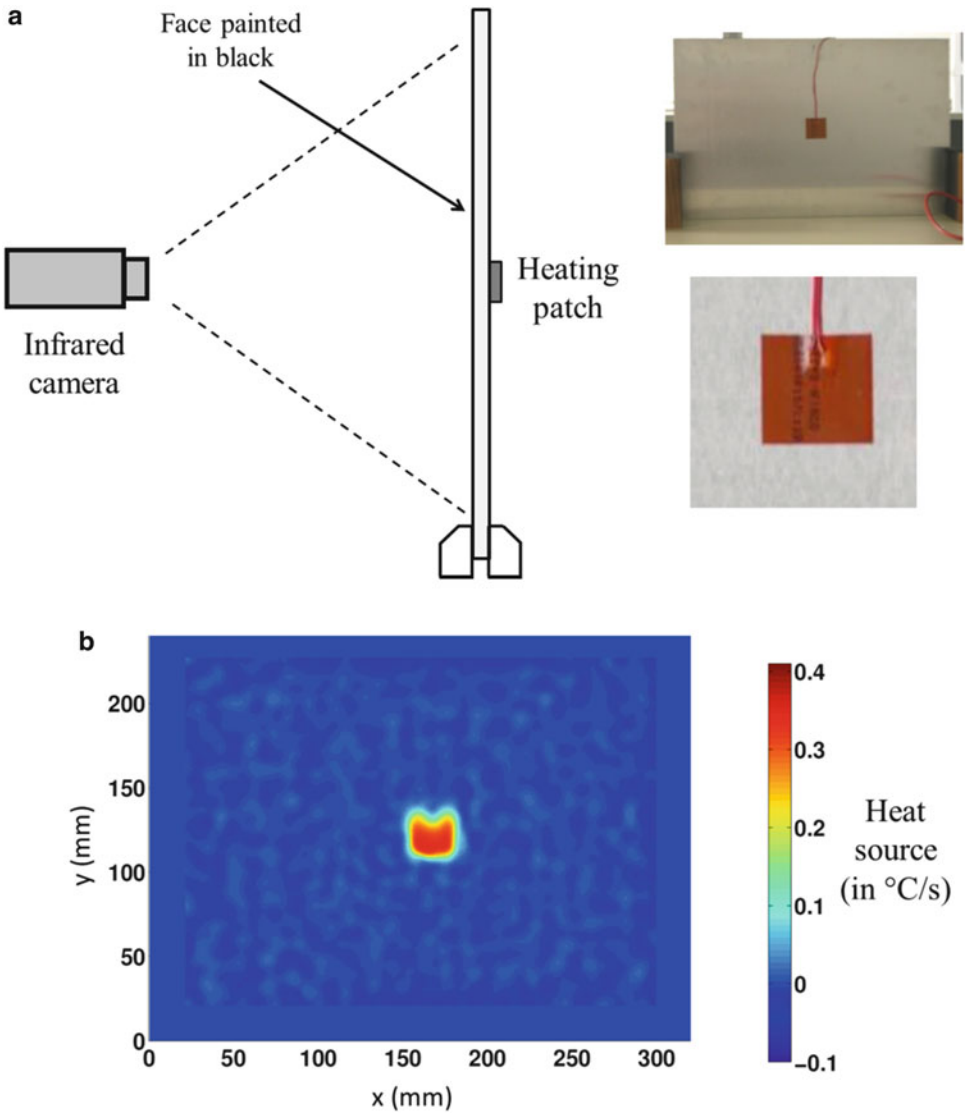

Fig. 36.4 Experimental validation of the procedure: (**a**) experimental set-up comprising an aluminum plate with a heating patch placed at the center to impose a constant heat source and (**b**) reconstructed heat source field from the measured steady-state temperature field

36.5 Conclusion

A post-processing technique using a Gradient Anisotropic Diffusion filter was used to reconstruct heat source fields from noisy temperature fields. The relevance of the GAD filter compared to two other types of filter (averaging filter and Gaussian derivative filter) was illustrated from synthetic data corrupted by Gaussian noise, and the heat source distribution was correctly identified from real experimental fields.

References

1. A. Chrysochoos, H. Louche, An infrared image processing to analyse the calorific effects accompanying strain localisation. Int. J. Eng. Sci. **38**, 1759–1788 (2000)
2. P. Schlosser, H. Louche, D. Favier, L. Orgeas, Image processing to estimate the heat sources related to phase transformations during tensile test of NiTi tubes. Strain **43**, 260–271 (2007)
3. D. Delpueyo, M. Grédiac, X. Balandraud, C. Badulescu, Investigation of martensitic microstructures in a monocrystalline Cu-Al-Be shape memory alloy with the grid method and infrared thermography. Mech. Mater. **45**, 34–51 (2012)
4. C. Le Niliot, P. Gallet, Infrared thermography applied to the resolution of inverse heat conduction problems: recovery of heat line sources and boundary conditions. Rev. Gen. Therm. **36**, 629–643 (2001)
5. N. Renault, S. André, D. Maillet, C. Cunat, A two-step regularized inverse solution for 2-D heat source reconstruction. Int. J. Therm. Sci. **47**, 834–847 (2008)
6. M.L. Pastor, X. Balandraud, M. Grediac, J.L. Robert, Applying infrared thermography to study the heating of 2024-T3 aluminium specimens under fatigue loading. Infrared Phys. Technol. **51**, 505–515 (2008)
7. X. Balandraud, A. Chrysochoos, S. Leclercq, R. Peyroux, Influence of the thermomechanical coupling on the propagation of a phase change front. C.R. Acad. Sci. Ser. II B: Mec. **329**, 621–626 (2001)
8. H. Louche, A. Chrysochoos, Thermal and dissipative effects accompanying Lüders band propagation. Mater. Sci. Eng. A **307**, 15–22 (2001)
9. T. Pottier, H. Louche, S. Samper, H. Favreliere, F. Toussaint, P. Vacher, Proposition of a modal filtering method to enhance heat source computation within heterogeneous thermomechanical problems. Int. J. Eng. Sci. **81**, 163–176 (2014)
10. N. Ranc, A. Blanche, D. Ryckelynck, A. Chrysochoos, POD preprocessing of IR thermal data to assess heat source distributions. Exp. Mech. **55**, 725–739 (2015)
11. D. Delpueyo, X. Balandraud, M. Grédiac, Heat source reconstruction from noisy temperature fields using an optimised derivative Gaussian filter. Infrared Phys. Technol. **60**, 312–322 (2013)
12. P. Perona, J. Malik, Scale-space and edge detection using anisotropic diffusion. IEEE Trans Pattern Anal Mach Intell **12**, 629–639 (1990)

Chapter 37
Contour Method Residual Stress Measurement Uncertainty in a Quenched Aluminum Bar and a Stainless Steel Welded Plate

Mitchell D. Olson, Adrian T. DeWald, Michael B. Prime, and Michael R. Hill

Abstract This paper describes a newly developed uncertainty estimate for contour method residual stress measurements and presents results from two experiments where the uncertainty estimate was applied. The uncertainty estimate includes contributions from random error sources including the error arising from noise in displacement measurements and the smoothing of the displacement surfaces. The output is a two-dimensional, spatially varying uncertainty estimate such that every point on the cross-section where residual stress is determined has a corresponding uncertainty value. The current paper describes the use of the newly developed uncertainty estimate in a quenched aluminum bar with a cross section of 51 × 76 mm and a stainless steel weld plate with a cross-section of 25.4 × 152.4 mm, with a 6.35 mm deep groove, filled with a multi-pass weld. The estimated uncertainty in the quenched aluminum bar is approximately 5 MPa over the majority of the cross-section, with localized areas of higher uncertainty, up to 10 MPa. The estimated uncertainty in the welded stainless steel plate is approximately 22 MPa over the majority of the cross-section, with localized areas of higher uncertainty, over 50 MPa.

Keywords Residual stress measurement • Contour method • Uncertainty quantification • Repeatability • Aluminum alloy 7050-T74 • Quenching

37.1 Introduction

The contour method is a residual stress measurement technique that is capable of generating a two-dimensional map of residual stress over a plane in a body. The theoretical underpinning of the method is given by Prime [1], and is based on the fact that when a residual stress bearing body is cut in half, stresses are released and redistributed within the body, which causes deformation. The out-of-plane displacements are directly related to the stresses released, and the technique comprises measurement of the out-of-plane displacements at the cut plane and use of the measured displacements to determine residual stress at the cut plane via elastic stress analysis (Fig. 37.1). The contour method has been used to measure residual stress for a variety of conditions [2–5].

Currently, only limited work has been performed for uncertainty estimation of the contour method. Some researchers have used an *overall* uncertainty estimate (e.g., a single uncertainty value for every measured point on the cross-section) based on the noise present in the surface topography data [6, 7] and measuring the surface topography with different instruments [8]. Another study found the uncertainty using differences in residual stress from different levels of smoothing [9], but required that the surface use a similar level of smoothing in both spatial directions. The newly developed uncertainty estimate [10] is the first to develop a single measurement uncertainty estimator for the contour method, where the estimated uncertainty is a function of in-plane position and is applicable for arbitrary surface smoothing, and to show the uncertainty

M.D. Olson (✉)
Hill Engineering, LLC, 3035 Prospect Park Drive Suite 180, Rancho Cordova, CA 95670, USA

Department of Mechanical and Aerospace Engineering, University of California, One Shields Avenue, Davis, CA 95616, USA
e-mail: molson@ucdavis.edu

A.T. DeWald
Hill Engineering, LLC, 3035 Prospect Park Drive Suite 180, Rancho Cordova, CA 95670, USA

M.B. Prime
Los Alamos National Laboratory, W-13, PO Box 1663, Los Alamos, NM 87545, USA

M.R. Hill
Department of Mechanical and Aerospace Engineering, University of California, One Shields Avenue, Davis, CA 95616, USA

S. Bossuyt et al. (eds.), *Residual Stress, Thermomechanics & Infrared Imaging, Hybrid Techniques and Inverse Problems, Volume 9*, Conference Proceedings of the Society for Experimental Mechanics Series, DOI 10.1007/978-3-319-21765-9_37

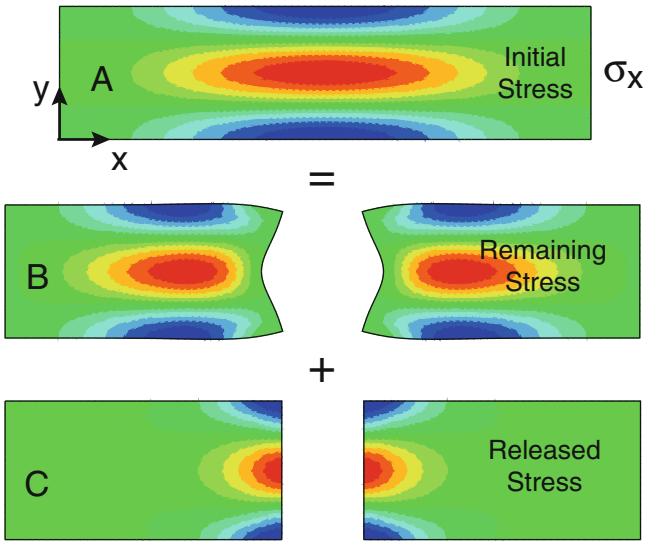

Fig. 37.1 Contour method steps: configuration A is a body containing residual stresses with the color scale corresponding to σ_{xx}; in configuration B, the body has been cut in half, creating a new stress-free surface; configuration C shows the stresses that were released in going from A to B, which can be found by reversing the cut surface deformation. Assuming elastic behavior, superposition provides A = B + C, and since σ_{xx} on the cut plane in B is zero (free surface), then σ_{xx} on the cut plane in A must be equal to σ_{xx} on the cut plane in C

estimator is a useful predictor of measurement uncertainty. The objectives of this work are to report the estimated uncertainty in two test cases using the newly developed uncertainty estimate.

37.2 Methods

The methodology for contour method uncertainty estimation is based on quantifying the uncertainty for random error sources [10]. Two random error sources identified for the contour method are the uncertainty due to noise in the displacement surfaces and the uncertainty arising from smoothing of the displacement surfaces. The uncertainty due to noise in the displacement surfaces is caused by the inherent surface roughness due to cutting, as well as the measurement error present in the displacement measurement signal. Both of these uncertainty sources show up as high frequency noise in the displacement surface, and cause what will be called the "displacement error." The other error source addressed is the uncertainty arising from the smoothing used in data processing that is required to extract the underlying form of the measured data. The amount of smoothing is selected based upon limited knowledge. Even if the optimal amount of smoothing were selected, there is no guarantee that the extracted form will exactly match the underlying trend in the displacement data. Thus, some amount of error is introduced from the data processing and this will be called the "model error." This approach for uncertainty estimation is similar to the methodology developed by Prime and Hill for uncertainty estimation in the slitting method for residual stress measurement [11].

37.2.1 Model Error

For contour method measurements, the analysis to extract the form of the experimental surface displacement (and simultaneously filter out the noise) is typically accomplished by fitting the measured surface displacements to a bivariate analytical surface. To illustrate the model error concept, consider a general bivariate, tensor product analytical surface

$$f(x,y) = \sum_{i=0}^{m} \sum_{j=0}^{n} C_{ij} P_i(x) P_j(y) \tag{37.1}$$

where x and y are spatial dimensions in the cut plane, C_{ij} are coefficients, $P_i(x)$ and $P_j(y)$ are known basis functions, and m and n are the highest order terms included in the series corresponding to the x and y spatial dimensions. The amount of smoothing is related to the choice of the fitting model (i.e., (37.1) and parameters m and n). The choice of the fitting model and parameters affects the contour method result. Earlier work on the slitting method for residual stress measurement [11] treated the smoothing model as a source of uncertainty, referred to as the "model error." Adapting that approach to the contour method, the model error is estimated by taking the standard deviation of the computed residual stresses over a range of smoothing parameters. The model error definition used is

$$U_{Model} = std(\sigma_{m,n}, \sigma_{m+1,n}, \sigma_{m,n+1}, \sigma_{m-1,n}, \sigma_{m,n-1}) \tag{37.2}$$

where U_{Model} is the model error, σ is residual stress determined by the contour method for a given smoothing model, and the subscripts refer to the amount of smoothing used in the contour data analysis. This definition of the model error includes a range of smoothing in both spatial directions and both higher and lower in spatial frequency, which provides a measure of the sensitivity of the computed residual stress to the selected fitting model. The model error is assumed to have a Gaussian distribution, which has been found to be appropriate for many experimental error sources [12], and implies that one standard deviation represents a confidence interval of 68 %.

37.2.2 Displacement Error

The contribution of the noise in the measured displacement field to the total uncertainty can be quantified using a Monte Carlo approach [13]. A statistical measure of the random noise in the experimental data is calculated from the residual of the displacement data, after the form of the surface has been extracted by fitting, where the residual is the difference between the measured surface profile and the smoothed surface profile. To estimate the influence of noise on measured residual stress, the contour method data analysis is repeated with normally distributed noise added to the measured displacements (i.e., the displacement data now contain the noise that was originally present plus random noise that was artificially introduced into the analysis). The added normally distributed noise has a standard deviation equal to the standard deviation of the residual of the displacement data. The residual stress is computed after introduction of the additional noise, and the process is repeated several times to develop a set of residual stress results, each computed with different random noise (but in every case the standard deviation of the noise is the same). The displacement error is estimated by computing the standard deviation of the set of residual stresses results with added noise, at each spatial location.

37.2.3 Total Uncertainty

The two uncertainty sources are combined together to estimate the total uncertainty. First, the root sum square of the two uncertainty sources is calculated according to

$$U_{RSS}(x,y) = \sqrt{U_{Disp}^2(x,y) + U_{Model}^2(x,y)}. \tag{37.3}$$

Next, the mean value of the root sum square uncertainty for all points on the cross-section is calculated

$$\overline{U}_{RSS} = \frac{\sum_{i=1}^{N} U_{RSS}(x_i, y_i)}{N}, \tag{37.4}$$

where (x_i, y_i) are a set of N points having roughly uniform spacing over the cross section. The pointwise measurement uncertainty is then defined as the greater of the root sum square uncertainty at each point, or the mean value

$$U_{TOT}(x, y) = \max\left(U_{RSS}(x, y), \overline{U}_{RSS}\right). \tag{37.5}$$

The inclusion of the mean value places a floor on the estimated uncertainty and ensures that it remains at a reasonable level over the entire cross section.

37.2.4 Experiments

Two contour method measurements were preformed and their associated uncertainties were estimated using the above approach. One experiment used a 7050-T74511 extruded aluminum bar that was used to confirm the usefulness of the uncertainty estimate [10] by determining the repeatability standard deviation (a measure of precision) in a set of repeat measurements (similar to a recent repeatability study for the contour method [14]). The bar cross section is 51.1 mm thick and 76.1 mm wide, with a length of 305 mm. The material properties for the bar are: E = 71 GPa, $\nu = 0.33$, with a yield strength of 490 MPa. The bar had residual stresses induced by heat treating to a T74 temper [15], which consisted of solution heat treatment at 477 °C for 3 h, immersion quenching in room temperature water with 16 % polyalkylene glycol (Aqua-Quench 260), and a dual artificial age at 121 °C for 8 h then 177 °C for 8 h. Based on earlier work, this treatment is expected to produce compressive residual stress on the bar exterior and tensile residual stress on the bar interior, both having magnitudes greater than 100 MPa [14, 16]. Contour method measurements were performed at the mid-length of the bar, as can be seen in Fig. 37.2.

The second contour method measurement was made in a long 316L stainless steel plate with an eight-pass groove weld of 308L stainless steel. The plate was the result of a concerted effort to design a sample to obtain data on the precision of residual stress measurements as described in [17]. The plate has a width of 152.4 mm (6 in.), height of 25.4 mm (1 in.), and a length of 1.22 m (48 in.) (Fig. 37.3a) with a groove along the plate length. The machined groove has a root width of 12.7 mm (0.5 in.), root depth of 6.35 mm (0.25 in.), and a wall angle of 70° (Fig. 37.3b). The material properties for the 316L stainless steel parent plate are: E = 206 GPa, $\nu = 0.3$, with a yield strength of 440 MPa, and the material properties for the 308L stainless steel weld filler metal are: E = 204 GPa, $\nu = 0.3$, with a yield strength of 350 MPa. The weld is made with machine controlled inert gas tungsten arc welding (GTAW). The details of the welding procedure can be found elsewhere [17]. A contour method measurement were performed at the mid-length of the plate at $z = 0$ (609.6 mm from each end), as can be seen in Fig. 37.3a.

A brief summary of the experimental steps of the contour method and its application for the two measurements will be given. Each sample was cut at the earlier described measurement plane using a wire electric discharge machine (EDM), while securely clamped. For each sample, the two resulting deformed cut surfaces were measured with a laser scanning profilometer along the cross-section with a measurement spacing of roughly 200 μm in both directions. The two surface profiles were then averaged on a common grid, and the average was fit to a smooth bivariate analytical surface. Residual stress on the contour plane was found by applying the negative of the smoothed surface profile as a displacement boundary

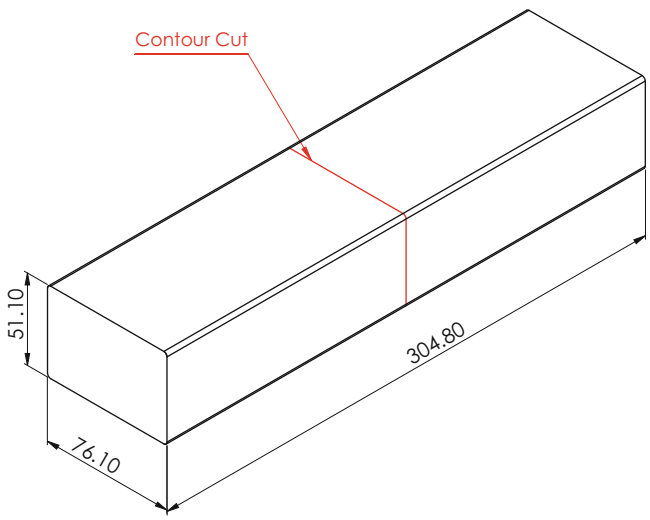

Fig. 37.2 Diagram of aluminum block and contour measurement location. Dimensions are in mm

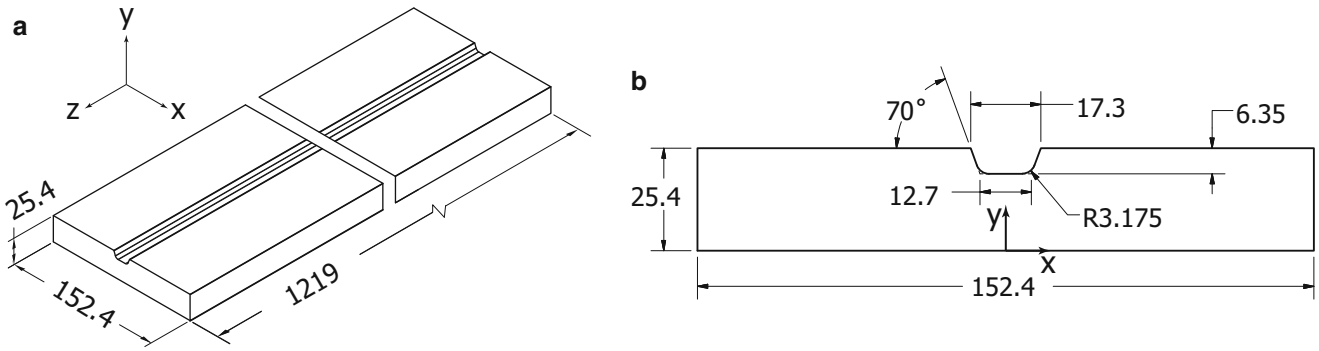

Fig. 37.3 Diagram of stainless steel weld plate (**a**) overall geometry and (**b**) cross-section with details of the machined groove. Dimensions are in mm

condition in a linearly elastic finite element (FE) model of the half plate. The FE analysis used commercial software [18], and a mesh of eight-node linear interpolation brick elements, with node spacing of roughly 1 mm on the cross-section in both directions, and biased node spacing in the out-of-plane direction.

37.3 Results

The results using the quenched aluminum bar can be seen in Fig. 37.4. The measured residual stress is shown in Fig. 37.4a. The contour method results are typical of a quenched aluminum component with compressive residual stress around the perimeter (−175 MPa) and tensile residual stress in the center (160 MPa). The calculated displacement error can be seen in Fig. 37.4b. The displacement error is very low at all points, but is slightly higher at the perimeter of the cross-section (around 2 MPa) than it is in the interior (around 1 MPa). The model error results can be seen in Fig. 37.4c. The results show that the model error is significantly higher at the perimeter of the cross-section (around 40 MPa) than in the interior (under 10 MPa at most locations). The total uncertainty estimate is shown in Fig. 37.4d.

Line plots of the of the measured residual stress with the total uncertainty estimate are shown as error bars in Fig. 37.5 for the quenched aluminum bar (labeled as Cut 1). These plots show the total uncertainty is relatively small compared to the range of the measured stress. Line plots of the displacement error, model error, and total uncertainty estimate are shown in Fig. 37.6 for the quenched aluminum bar. The results show that displacement error is very small compared to the model error, and in this case negligibly contributes to the total uncertainty estimate. The model error is under 10 MPa at most locations in the part interior, but is significantly higher at the perimeter of the cross section at a three localized areas toward the center of the bar.

The results for the stainless steel welded plate can be seen in Fig. 37.7. The measured residual stress is shown in Fig. 37.7a. The results show high tensile stress in the weld region, with a maximum near 450 MPa, giving way to nearby low magnitude compressive stresses (around −100 MPa), which is typical weld residual stress [19–21]. However, the results also show an area of larger compressive stress (about −250 MPa) toward the transverse edges, which was not expected, and may have been introduced during plate manufacture, prior to welding. The calculated displacement error can be seen in Fig. 37.7b. The displacement error is low at all points, but is slightly higher at the perimeter of the cross-section (some points as high as 10 MPa) than it is in the interior (around 2 MPa). The model error results can be seen in Fig. 37.7c. The results show that the model error is significantly higher at the perimeter of the cross-section (around 100 MPa) than in the interior (under 30 MPa at most locations). The total uncertainty estimate is shown in Fig. 37.7d, which has essentially the same distribution as the model error, but with the low uncertainty being replaced with a floor.

Line plots of the of the measured residual stress with the total uncertainty estimate are shown as error bars in Fig. 37.8 for the stainless steel welded plate (labeled as Cut 1). These plots show the total uncertainty is a significant percentage of the measured stress range. Line plots of the displacement error, model error, and total uncertainty estimate are shown in Fig. 37.9 for the stainless steel welded plate. The results show that displacement error is very small compared to the model error, and in this case negligibly contributes to the total uncertainty estimate. The model error is under 30 MPa at most locations in the part interior, but is significantly higher at the perimeter of the cross section which causes the mean of the uncertainty to be high (46 MPa), and thus dominates the total uncertainty distribution.

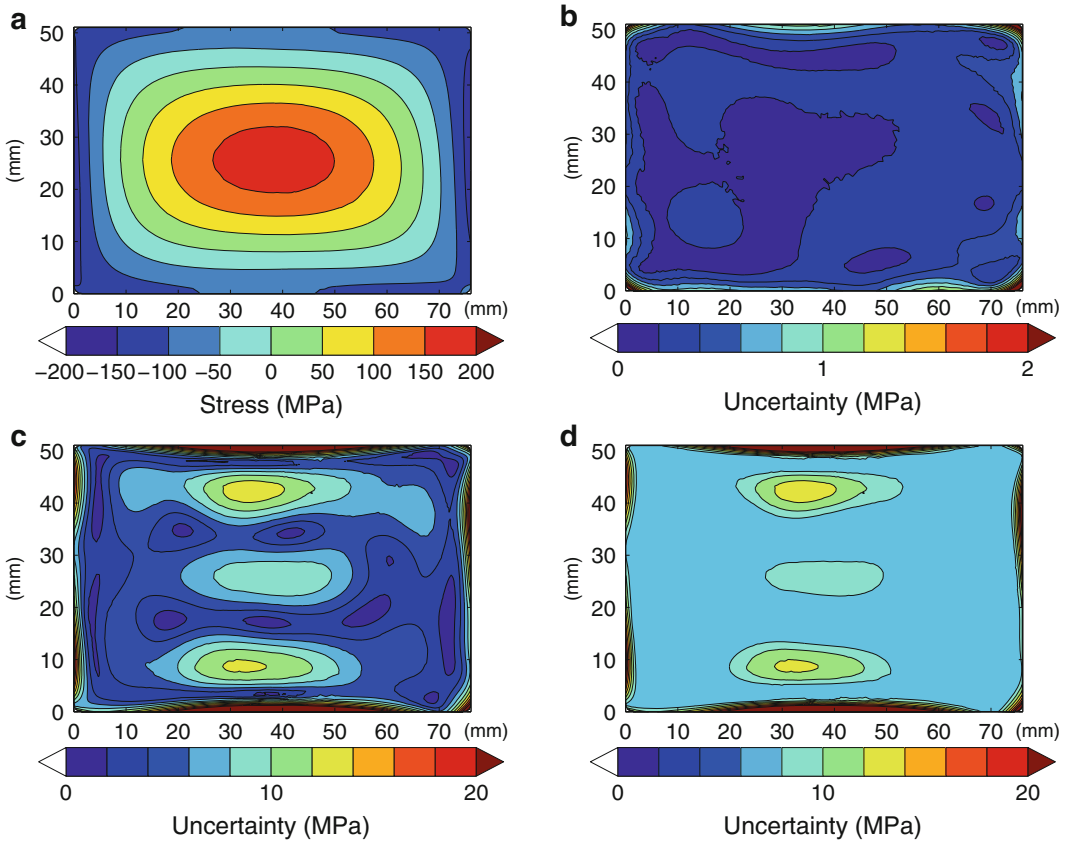

Fig. 37.4 Results from the contour method measurement in a quenched aluminum bar: (**a**) measured residual stress, (**b**) displacement error, (**c**) model error, and (**d**) total uncertainty

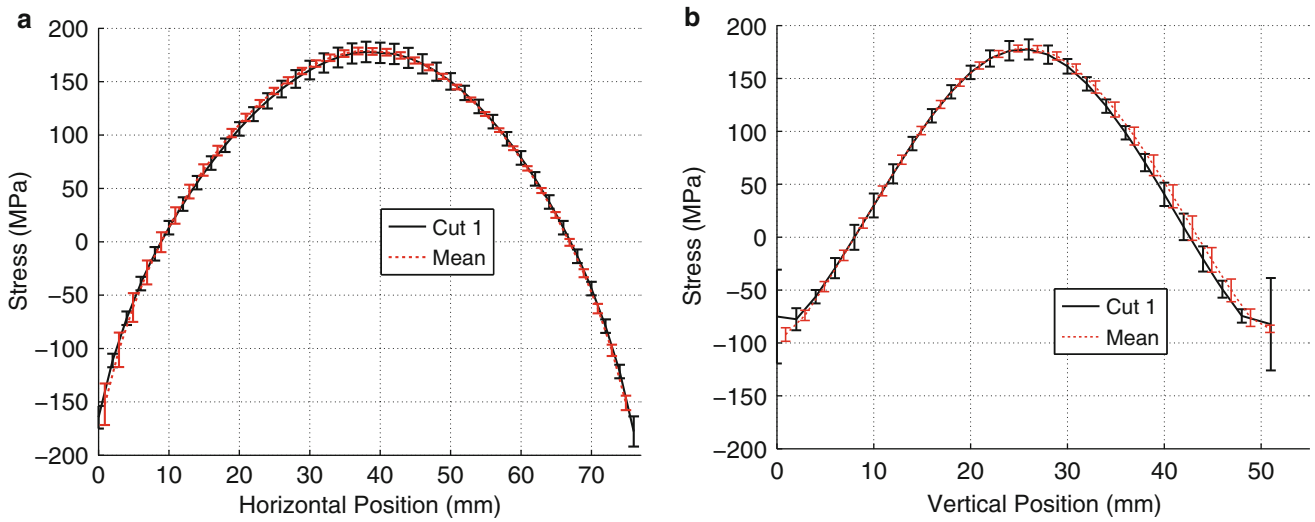

Fig. 37.5 Line plots of the measured residual stress in the quenched aluminum bar with the total uncertainty shown as error bars along the (**a**) horizontal direction at the mid-thickness (y = 25.4 mm) and (**b**) vertical direction at the mid-width (x = 38.1 mm)

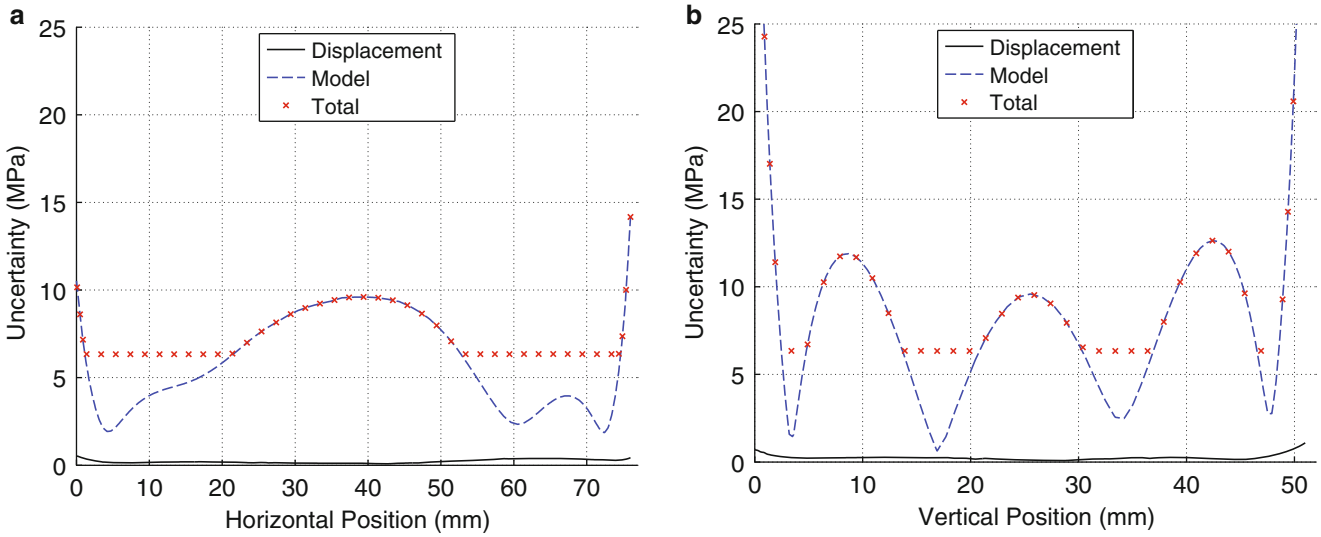

Fig. 37.6 Line plots of the displacement error, model error, and total uncertainty in the quenched aluminum bar along the (**a**) horizontal direction at the mid-thickness (y = 25.4 mm) and (**b**) vertical direction at the mid-width (x = 38.1 mm)

37.4 Discussion

The nominally small model error in both samples indicates that the smoothing tends to be robust in the part interior, whereas the smoothing is less stable at the part boundary, which is indicated by the larger uncertainties at the boundary.

The uncertainty is significantly larger in the stainless steel welded plate. There appears to be two reasons for that. One, as suggested in [10], the uncertainty does appear to scale with the elastic modulus. For a given amount of residual stress, a sample with a larger elastic modulus will exhibit a lower displacement, which is measured experimentally. The second reason for the larger uncertainty in the stainless steel welded plate is due to the more complicated stress field that is being measured, and as a result is more difficult to fit with a finite number of coefficients in the analytical surface.

Both of the measurements presented here were used in repeatability studies of the contour method. Repeatability studies are especially useful to compare with this study because they offer an alternative method to calculate uncertainty (assuming each measurement has the same underlying stress). The mean of the measurement population and the repeatability standard deviation can be seen in the line plots in Fig. 37.5 for the quenched aluminum bar. Comparing an individual measurement from that data set and its estimated uncertainty (Cut 1) to the mean of the measurement set and its repeatability standard deviation shows that the uncertainty estimate is reasonable. The two lines have error bars that overlap at all points, indicating that there is no statistical difference between the two lines with their associated uncertainties. Further details regarding the repeatability study in the quenched aluminum bars can be found in [10]. We find similar results when looking at the results for one measurement in the stainless steel welded plate compared with mean of a set of repeated measurements, as is shown in Fig. 37.8. As was found in the quenched aluminum bar results, the results for the stainless steel welded plate have error bars that overlap both lines at all points, indicating that there is no statistical difference between the two lines with their associated uncertainties. Further details regarding the repeatability study in the stainless steel welded plate can be found in [17].

Overall, the uncertainty estimates in both cases appear to be reasonable and give much needed uncertainty estimates for a single contour method measurement.

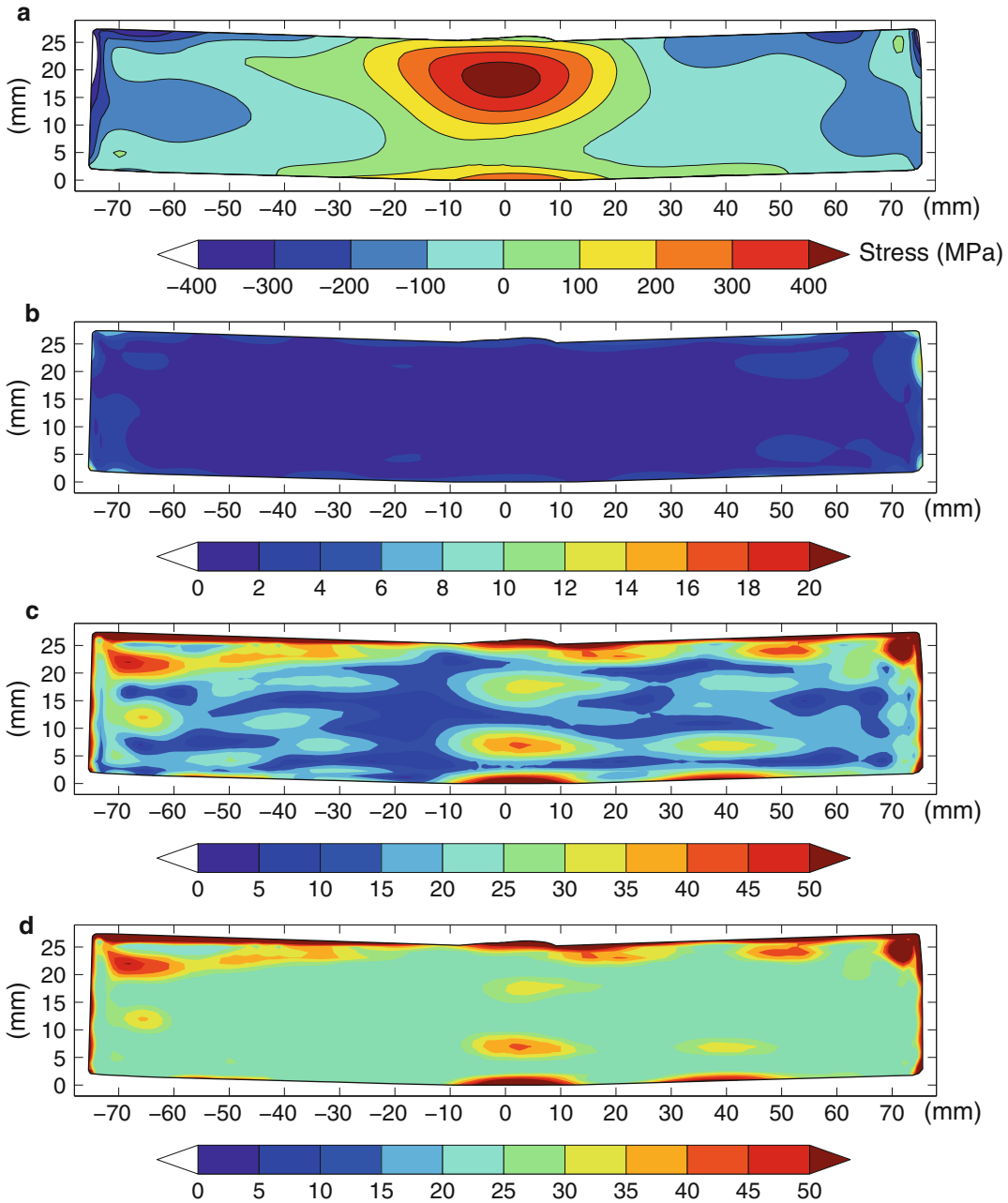

Fig. 37.7 Results from the contour method measurement in a stainless steel welded plate: (**a**) measured residual stress, (**b**) displacement error, (**c**) model error, and (**d**) total uncertainty

37.5 Summary/Conclusions

This paper describes a single measurement uncertainty estimator for the contour method, which accounts for noise in measured displacement field and error associated with smoothing. This represents a significant improvement over available techniques for contour method uncertainty estimation. The error arising from noise in the measured displacement field is estimated using a Monte Carlo approach by finding the standard deviation of the differences in stress resulting from applying normally distributed noise to the measured surface. The error associated with the smoothing model for the displacement field was found by taking the standard deviation of stresses computed using different levels of smoothing.

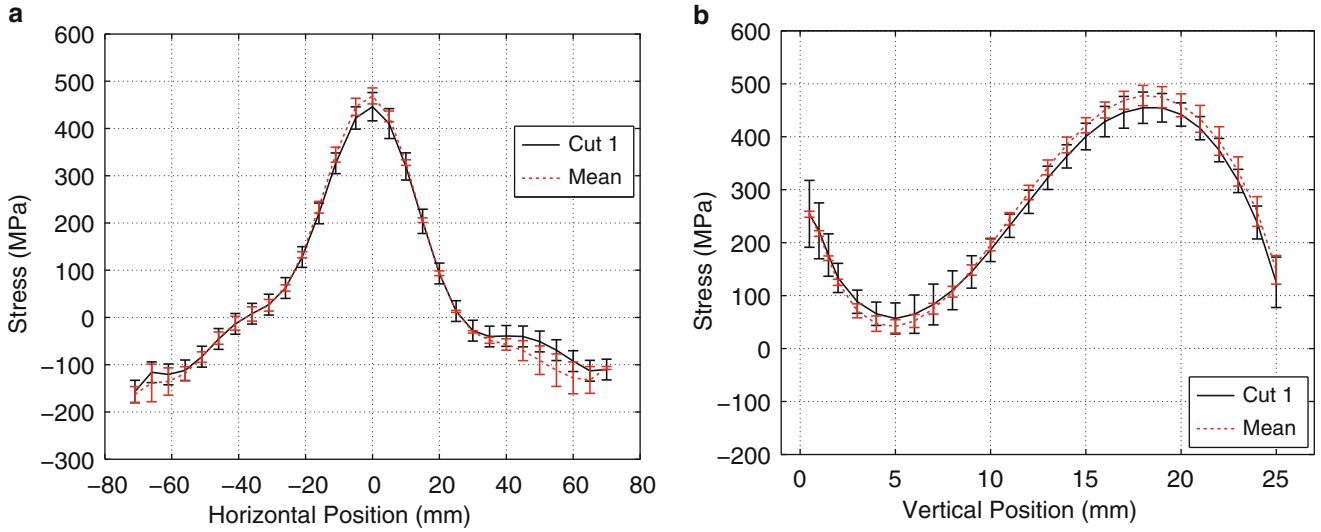

Fig. 37.8 Line plots of the measured residual stress in the stainless steel welded plate with the total uncertainty shown as error bars along the (**a**) horizontal direction at the weld root (y = 17 mm) and (**b**) vertical direction at the mid-width (x = 0)

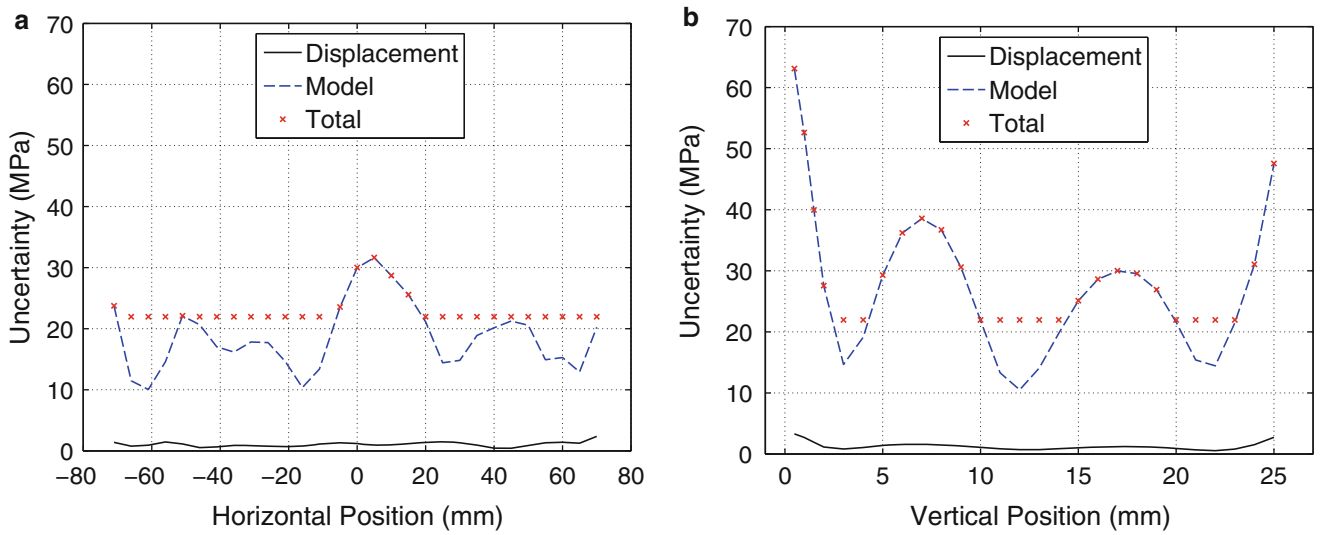

Fig. 37.9 Line plots of the displacement error, model error, and total uncertainty in the stainless steel welded plate along the (**a**) horizontal direction at the weld root (y = 17 mm) and (**b**) vertical direction at the mid-width (x = 0)

The uncertainty estimate was evaluated in two contour method experiments. The uncertainty estimates have similar features for both samples, including: very low displacement error (appears to be negligible in the two cases examined), low model error in the interior, higher model error along the part perimeter, and the total uncertainty distribution is dominated by the model error. The uncertainty in the stainless steel sample is systemically higher than that found in the aluminum sample.

Acknowledgements With gratitude, the authors acknowledge the U.S. Air Force Research Laboratory for providing financial support for this work (contract FA8650-14-C-5026). The authors would also like to acknowledge helpful discussions with David Riha and John McFarland from the Southwest Research Institute related to uncertainty quantification.

References

1. M.B. Prime, Cross-sectional mapping of residual stresses by measuring the surface contour after a cut. J. Eng. Mater. Technol. **123**, 162–168 (2001)
2. J. Kelleher, M.B. Prime, D. Buttle, P.M. Mummery, P.J. Webster, J. Shackleton et al., The measurement of residual stress in railway rails by diffraction and other methods. J Neutron Res **11**, 187–193 (2003)
3. D.W. Brown, T.M. Holden, B. Clausen, M.B. Prime, T.A. Sisneros, H. Swenson et al., Critical comparison of two independent measurements of residual stress in an electron-beam welded uranium cylinder: neutron diffraction and the contour method. Acta Mater. **59**, 864–873 (2011)
4. M.B. Prime, A.T. DeWald, *Practical Residual Stress Measurement Methods (Ch. 5)* (Wiley, West Sussex, 2013)
5. A.T. DeWald, J.E. Rankin, M.R. Hill, M.J. Lee, H.-L. Chen, Assessment of tensile residual stress mitigation in Alloy 22 welds due to laser peening. J. Eng. Mater. Technol. **126**, 465–473 (2004)
6. F. Hosseinzadeh, P. Ledgard, P.J. Bouchard, Controlling the cut in contour residual stress measurements of electron beam welded Ti-6Al-4V alloy plates. Exp. Mech. **53**, 829–839 (2012)
7. M.B. Prime, T. Gnäupel-Herold, J.A. Baumann, R.J. Lederich, D.M. Bowden, R.J. Sebring, Residual stress measurements in a thick, dissimilar aluminum-alloy friction stir weld. Acta Mater. **54**, 4013–4021 (2006)
8. F. Hosseinzadeh, P.J. Bouchard, Mapping multiple components of the residual stress tensor in a large P91 steel pipe girth weld using a single contour cut. Exp. Mech. **53**, 171–181 (2012)
9. M.B. Prime, R.J. Sebring, J.M. Edwards, D.J. Hughes, P.J. Webster, Laser surface-contouring and spline data-smoothing for residual stress measurement. Exp. Mech. **44**, 176–184 (2004)
10. M.D. Olson, A.T. DeWald, M.R. Hill, M.B. Prime, Estimation of uncertainty for contour method residual stress measurements. Exp. Mech. **55**, 577–585 (2014)
11. M.B. Prime, M.R. Hill, Uncertainty, model error, and order selection for series-expanded, residual-stress inverse solutions. J. Eng. Mater. Technol. **128**, 175 (2006)
12. H.W. Coleman, W.G. Steele, *Experimentation, Validation, and Uncertainty Analysis for Engineers (Ch. 2)* (Wiley, Hoboken, 2009)
13. J.M. Hammersley, D.C. Handscomb, *Monte Carlo Methods* (Halsted Press, Sydney, 1964)
14. M.R. Hill, M.D. Olson, Repeatability of the contour method for residual stress measurement. Exp. Mech. **54**, 1269–1277 (2014)
15. SAE Aerospace, Heat Treatment of Wrought Aluminum Alloy Parts, AMS 2770, 2006
16. J.S. Robinson, D.A. Tanner, C.E. Truman, A.M. Paradowska, R.C. Wimpory, The influence of quench sensitivity on residual stresses in the aluminium alloys 7010 and 7075. Mater. Charact. **65**, 73–85 (2012)
17. M.D. Olson, M.R. Hill, E. Willis, A.G. Peterson, V.I. Patel, O. Muránsky, Assessment of weld residual stress measurement precision: mock-up design and results for the contour method. J. Nuclear Eng. Rad. Sci. **1**, 031008 (10 pages) (2015)
18. Abaqus/Standard, Version 6.10, Providence, RI, 2010
19. C. Ohms, R.C. Wimpory, D.E. Katsareas, A.G. Youtsos, NET TG1: residual stress assessment by neutron diffraction and finite element modeling on a single bead weld on a steel plate. Int. J. Press. Vessel. Pip. **86**, 63–72 (2009)
20. M.C. Smith, A.C. Smith, NeT bead-on-plate round robin: comparison of residual stress predictions and measurements. Int. J. Press. Vessel. Pip. **86**, 79–95 (2009)
21. P.J. Bouchard, The NeT bead-on-plate benchmark for weld residual stress simulation. Int. J. Press. Vessel. Pip. **86**, 31–42 (2009)

Chapter 38
On the Separation of Complete Triaxial Strain/Stress Profiles from Diffraction Experiments

H. Wern and E. Jäckel

Abstract The fundamental equation in X-ray diffraction relates the measured strain quantities to a superposition of six independent components, three normal and three shear components which can exist as gradients with depth. However, the linear system of equations to solve for the six components leads to a singular matrix. In such a case of nonunique solution is expected. In the literature then so called regularization methods are recommended. All these methods work only if the determinant of the matrix is close to zero, in diffraction experiments it is definitely zero because of the existence of the normal component ε33. Therefore in the past, assumptions were made such as biaxial stress states and so on. It is shown that by a numerical differentiation the shear components can simply resolved. Once the shear components have been subtracted from the fundamental equation, the three normal components remain. By a Taylor series development of the fundamental equation, it is shown that ε33 and its first derivative at $\psi = 0$ are independent of the rotation angle φ. This requires a special structure of the matrix to analyze the data at different φ rotations. Once these two values are obtained, they serve as the initial conditions of a differential equation of second kind which is solved numerically. The unknown functions in the differential equation are approximated by a Taylor series expansion whose coefficients are determined by a nonlinear optimization procedure. Together with simulated data, first results are presented.

Keywords X-ray diffraction • Triaxial strain/stress profiles • Separation of profiles • Numerical solution of differential equation of second kind • Nonlinear least squares approach

38.1 Introduction

All measuring methods which rely on Bragg's law such as X-ray or neutron diffraction, primarily detect a strain state rather than a stress state. A strain state assigned to any point of the material under investigation is represented by a symmetric second rank tensor containing six different elements, three normal and three shear components. Because the strain state of a polycrystalline material is assumed to be the response of residual stress, the strain tensor does not have to be conform with the crystal symmetry as thermal expansion does. As a consequence, no further restrictions can be made and the full triaxial tensor must always be considered. In this sense, the so called "sine-square-psi" method [1] is a restriction which can be reviewed as a first approach in the early days of X-ray stress analysis.

38.2 Goniometers

In the X-ray diffraction technique, two different types of measuring geometries are established [2]: the Ω and ψ goniometers, which are illustrated in Figs. 38.1 and 38.2:

38.2.1 Fundamental Equations

A typical experimental setup uses the variation of a rotation angle φ and tilt angles ψ with respect to the sample coordinate system. The normal L refers to the measurement direction which is selected by the Miller indices (hkl). Residual strain or

H. Wern (✉) • E. Jäckel
HTW des Saarlandes, Goebenstraße 40, Saarbrücken 66117, Germany
e-mail: harald_wern@t-online.de

S. Bossuyt et al. (eds.), *Residual Stress, Thermomechanics & Infrared Imaging, Hybrid Techniques and Inverse Problems, Volume 9*, Conference Proceedings of the Society for Experimental Mechanics Series, DOI 10.1007/978-3-319-21765-9_38

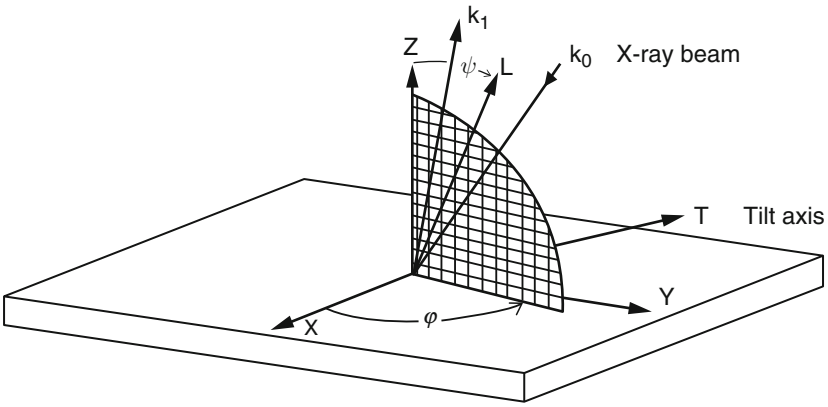

Fig. 38.1 Angular definitions of the Ω-goniometer with respect to the specimen coordinate system. The tilt axis T lies in the specimen surface and in the diffraction plane but is perpendicular to the diffraction vector (hkl), which is parallel to L

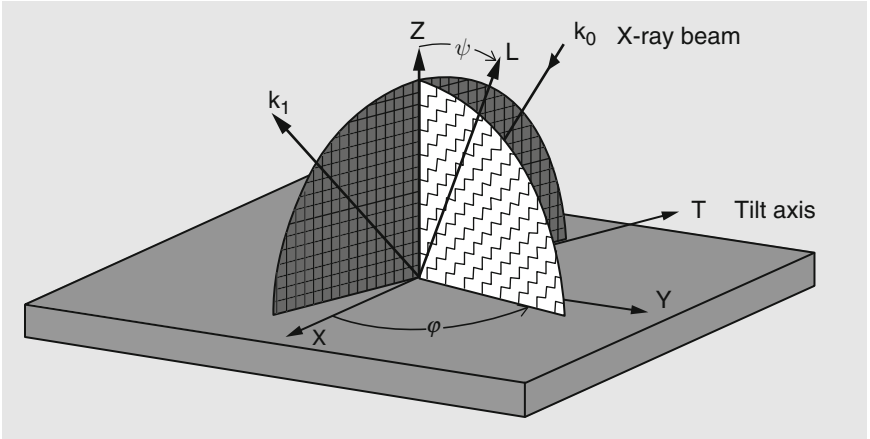

Fig. 38.2 Angular definitions of the ψ-goniometer

stress depth profiles measured with X-rays in the near surface region of polycrystalline materials are always averaged quantities because the counted intensities are averages over the diffracted volume. Therefore, the measured profiles are called τ-profiles where τ is the 1/e penetration depth of the X-rays. The measured profiles can be expressed as

$$\langle \varepsilon \rangle_{\varphi\psi_i}(\tau_i) = \frac{d\varphi\psi_i(\tau_i) - d0}{d0} = \frac{\int_0^D e^{-\frac{z}{\tau_i}} \varepsilon_{\varphi\psi_i}(z)dz}{\int_0^D e^{-\frac{z}{\tau_i}} dz} \tag{38.1}$$

where ε follows from the usual transformation law of a second rank tensor ε from the laboratory system to the specimen system shown in Fig. 38.2.

$$\begin{aligned} \langle \varepsilon_{\varphi\psi}(\tau) \rangle = {} & \varepsilon_{11}(\tau)\cos^2\varphi \sin^2\psi + \varepsilon_{22}(\tau)\sin^2\varphi \sin^2\psi + \varepsilon_{33}(\tau)\cos^2\psi \\ & + \varepsilon_{12}(\tau)\sin 2\varphi \sin^2\psi + \varepsilon_{13}(\tau)\cos\varphi \sin 2\psi + \varepsilon_{23}(\tau)\sin\varphi \sin 2\psi \end{aligned} \tag{38.2}$$

For the ψ-goniometer τ_i is given by (38.3)

$$\tau_i = \frac{\sin\Theta_0 \cos\Psi_i}{2\mu} \tag{38.3}$$

where μ is the absorption coefficient for the particular wavelength and the material under investigation . Θ_0 is the Bragg angle of the stress free lattice spacing d0. Because of the independent existence of the normal component eps33 at all φ-rotations the above system in (38.2) written as a linear system of equations for the six unknowns becomes always singular. Therefore a unique solution cannot be expected. This is well known in literature and the reason why several simplifications have been made such as to consider only biaxial stresses and so on [3–6].

The purpose of this paper is to find a method to separate all six and therefore triaxial components.

In order to achieve this goal, in a first step we have to use simulated data with known conditions. Therefore the left hand side of (38.2) (the measurement side) has been simulated for data in ψ geometry together with typical values for a steel specimen and Cr Kα radiation. The strains are then assumed to be converted to stresses with the corresponding X-ray elastic constants. This has the advantage that we can use a further boundary condition, namely that $\sigma_{33}(z{=}0)$ at a free surface must be zero.

38.2.2 Simulation

With the aid of a random number generator, a total of six different stress gradients have been simulated according to the following formulae:

$$\sigma_{i,\,j}(z) = \left(a_0 + a_1 z + a_2 z^2\right) e^{-az_3} \tag{38.4}$$

The profiles of the three normal components are shown in Fig. 38.3.

These equations are put into (38.1) to produce the τ profiles. In (38.1) and (38.2) simply replace strain by stress. The results are shown in Figs. 38.4 and 38.5 respectively.

Without loss of generalization we restrict the procedure only for the case $\varphi = 0$.

The shear components are not shown because they can be exactly obtained by the following procedure: The fundamental equation (38.2) is differentiated with respect to the rotation angle φ in order to get rid of the third normal component. The left hand side is differentiated by fitting a Fourier series with respect to φ to the experimental or simulated data. In consequence, one obtains a linear system of equations for the three shear components and the difference $\varepsilon_{22}(\tau) - \varepsilon_{11}(\tau)$. The matrix is regular and therefore a unique solution is obtained. Once the shear components are separated they are

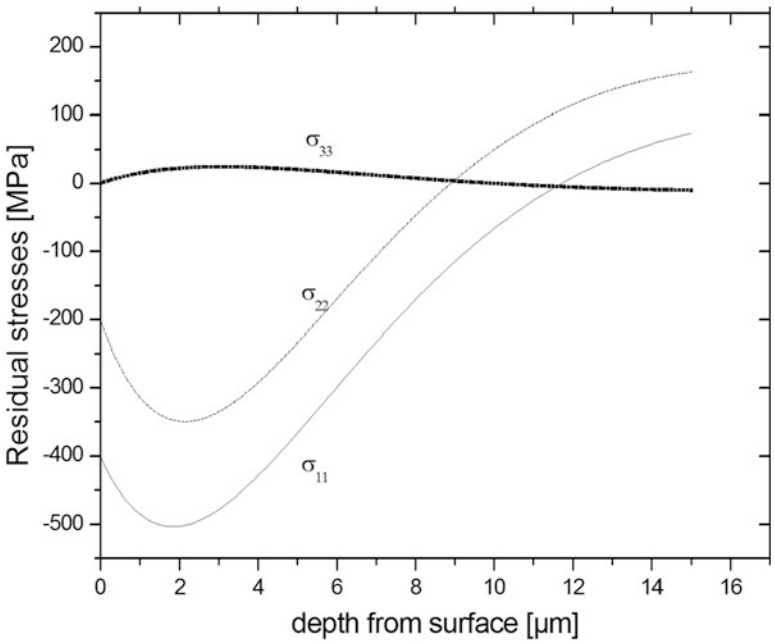

Fig. 38.3 Simulated normal stress gradients versus depth from surface

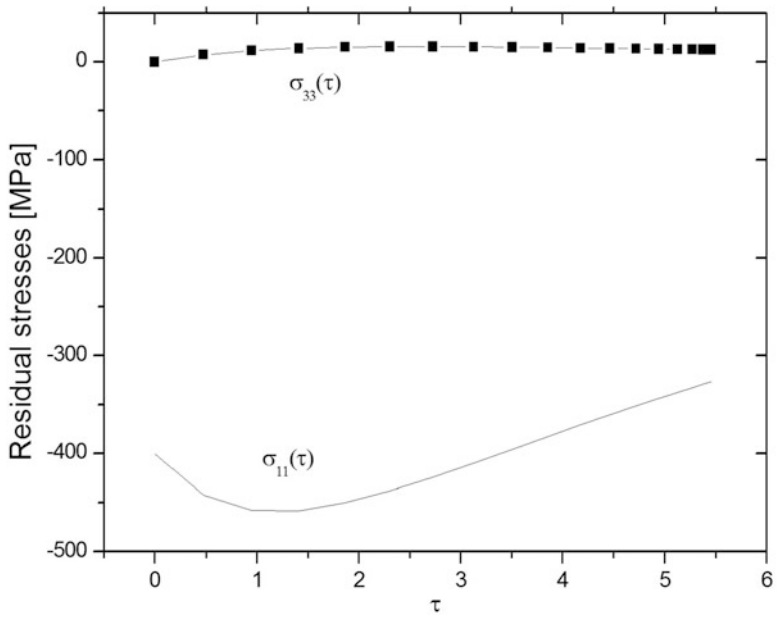

Fig. 38.4 Simulated normal stresses versus τ (μm)

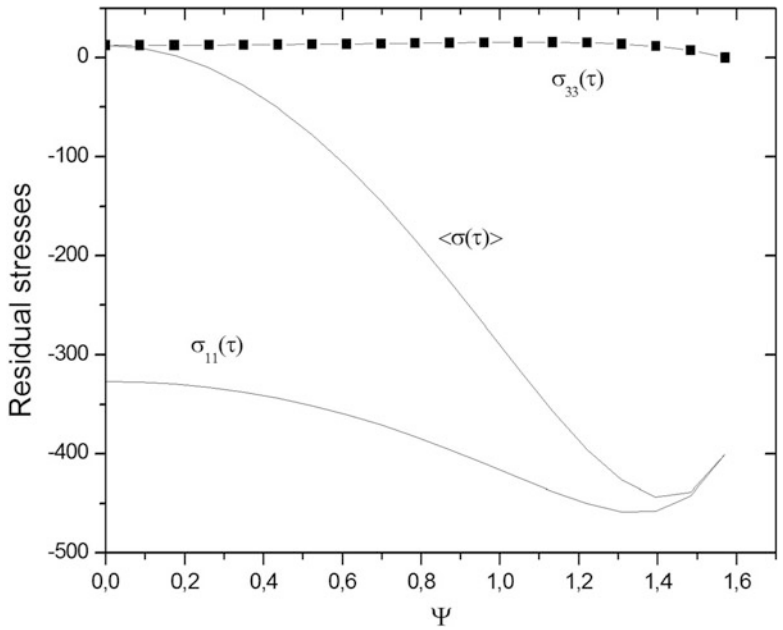

Fig. 38.5 Stress profiles as a function of ψ

subtracted from the fundamental equation with their corresponding weights. It remains the superposition of the three normal components. In order to simplify the procedure we restrict us to $\varphi = 0$. Now we start from behind, that means we plot the τ-profiles as a function of the tilt angle ψ shown in Fig. 38.5.

The curve in the middle is the superposition of both profiles which corresponds to the measuring quantity. A Taylor series expansion of the fundamental equation with respect to ψ at $\psi = 0$, exhibits the following form which reads as

$$\begin{aligned}\langle\sigma(\psi)\rangle = \sigma_{33}(0) + \sigma_{33}{}'(0) + \left(\sigma_{33}{}''(0) - 2\sigma_{33}(0) + 2\sigma_{11}(0)\right)\psi^2/2 \\ + \left(\sigma_{33}{}'''(0) - 6\sigma_{33}{}'(0) + 6\sigma_{11}{}'(0)\right)\psi^3/6 + \cdots\end{aligned} \tag{38.4}$$

A least squares analysis of the measured data yield the corresponding coefficients of the Taylor series.

It is important to note that the first two terms are independent of the orientation angle φ. This knowledge allows us to properly perform a least squares analysis at different ψ rotations. As a result, we know the exact values of σ_{33} and $\sigma_{33}{}'$ at

$\psi = 0$. The idea now was to calculate the profile as the solution of a differential equation of second kind whose initial conditions are known. Under the assumption that σ_{33}'' and σ_{33}''' at $\psi = 0$ are small we can at least obtain approximate initial conditions for σ_{11}. The two differential equations will certainly not have constant coefficients but will be rather functions of ψ. Because we do not know the functions, we again write them as a Taylor series with unknown coefficients. Let us abbreviate the superposition from the measurement as $\langle\sigma(\psi)\rangle^{M}$ and from the solution of the differential equations as $\langle\sigma(\psi)\rangle^{DGL}$. Then we can define an error functional which reads as $\sum_i \left(\sigma(\psi_i) - \sigma(\psi_i)\right)^2 = \mathrm{F}^2$. Now, we minimize the error function with respect to the unknown parameters in the Taylor series of the differential equations. For that reason we need the derivatives of the $\langle\sigma(\psi)\rangle^{DGL}$ with respect to the parameters. Because they are not known analytically, we have to adopted a numerical procedure. We replace the derivatives by a symmetric difference quotient. For that reason, we have to solve the differential equations twice for each parameter. First results will be presented in the oral presentation.

References

1. E. Macherauch, P. Püller, Das $\sin^2\psi$ Verfahren der röntgenographischen Spannungsmessung. Z. Angew. Phys. **13**, 305–312 (1961)
2. U. Wolfstieg, Aufnahmeverfahren. Härterei-Tech. Mitt. **31**, 19–22 (1976)
3. A. Peiter, *Handbuch Spannungsmeßpraxis* (Vieweg Verlag, Braunschweig, 1992)
4. V. Hauk, *Structural and Residual Stress Analysis by Nondestructive Methods* (Elsevier, Amsterdam, 1997)
5. H. Wern, Influence of measurement and evaluation parameters on stress distributions investigated by X-rays. J Strain **27**, 127–136 (1991)
6. I.C. Noyan, J.B. Cohen, *Residual Stress* (Springer, New York, 1987)

Chapter 39
Residual Stress Mapping with Multiple Slitting Measurements

Mitchell D. Olson, Michael R. Hill, Jeremy S. Robinson, Adrian T. DeWald, and Victor Sloan

Abstract This paper describes the use of slitting to form a two-dimensional spatial map of one component of residual stress in the plane of a two-dimensional body. Slitting is a residual stress measurement technique that incrementally cuts a thin slit along a plane across a body, while measuring strain at a remote location as a function of slit depth. Data reduction, based on elastic deformation, provides the residual stress component normal to the plane as a function of position along the slit depth. While a single slitting measurement provides residual stress along a single plane, the new work postulates that multiple measurements on adjacent planes can form a two-dimensional spatial map of residual stress. The paper uses numerical simulations to estimate the quality of a slitting measurement, relative to the proximity of a given measurement plane to a free surface, whether that surface is the edge of the original part or a free surface created by a prior measurement. The results of the numerical simulation lead to a recommended measurement design for mapping residual stress. Finally, the numerical work and recommended measurement strategy are validated with physical experiments using thin aluminum slices containing residual stress induced by quenching. The physical experiments show that two-dimensional residual stress mapping with slitting has precision on the order of 10 MPa.

Keywords Residual stress • Slitting • Crack compliance • Mapping • Uncertainty • Measurement design

39.1 Introduction

The present work is directed at developing a method for determining the two-dimensional distribution of one in-plane component of residual stress in a thin part, that can be idealized as a two-dimensional body. There is a wide range of potential techniques for residual stress measurement, with some providing residual stress at a point (e.g., hole drilling or X-ray diffraction) and others providing a profile of stress along a line (e.g., slitting or deep hole drilling). The contour method, recently invented by Prime [1], provides a two-dimensional distribution of the residual stress component normal to a plane. The contour method results are useful because they illuminate spatial variations of the stress field that may not be recognizable with a point or line measurement, which can be very useful for failure assessment or process model validation. The present work describes a method to determine a two-dimensional residual stress distribution, in x and y, like that provided by the contour method, but where the part is thin (along z), and the stress component of interest lies in the plane of the thin part (i.e., either σ_{xx} or σ_{yy}).

A two-dimensional distribution, commonly called a "map", of one or more residual stress components might be determined in a variety of ways. A map of the near surface stress could be built up by performing a series of point stress measurements using X-ray diffraction or hole drilling. Neutron diffraction could be used in a similar way, but with that method's larger sampling volume providing a thickness-averaged, rather than near surface, measurement. A map of

M.D. Olson (✉) • M.R. Hill
Department of Mechanical and Aerospace Engineering, University of California, One Shields Avenue, Davis, CA 95616, USA
e-mail: molson@ucdavis.edu

J.S. Robinson
Materials and Surface Science Institute, University of Limerick, Limerick, Ireland

A.T. DeWald
Hill Engineering, LLC, 3035 Prospect Park Drive, Rancho Cordova, CA 95670, USA

V. Sloan
Victor Aviation Service, Inc., 2415 Embarcadero Way, Palo Alto, CA 94303, USA

S. Bossuyt et al. (eds.), *Residual Stress, Thermomechanics & Infrared Imaging, Hybrid Techniques and Inverse Problems, Volume 9*, Conference Proceedings of the Society for Experimental Mechanics Series, DOI 10.1007/978-3-319-21765-9_39

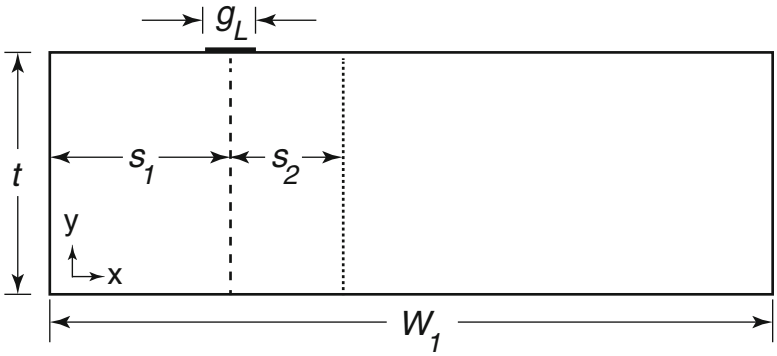

Fig. 39.1 Geometry for the numerical study: t is the part thickness, W_1 the part width (3t), g_L is the gage length (0.02t), and s_1 is the distance from the edge to the gage center, and s_2 is the distance from the first to second measurement plane

the in-plane stress could also be built up by performing a series of line stress measurements. Such a map might be constructed from a series of deep hole drilling measurements [2] in thick parts or a series of slitting measurements [3] in thin parts. Recently, a technique comparison was developed for mapping of in-plane residual stress in a thin slice taken from a dissimilar metal weld, and compared maps made using hole drilling, neutron diffraction, and slitting [4]. The results of that work showed all three methods capable of mapping in-plane residual stress, with slitting having lower experimental complexity and providing the best precision.

This work is directed to develop methods for mapping one in-plane residual stress component in a thin body using a series of slitting measurements, since slitting has excellent measurement precision [5] and utilizes readily available equipment [6]. To fix ideas, consider a single slitting method measurement in a rectangular, two-dimensional part having width W along the x direction and thickness t along the along the y direction. A typical slitting method measurement is performed at the mid-width ($x = W/2$), and determines $\sigma_{xx}(W/2, y)$ (i.e., the residual stress component normal to the mid-width plane, as a function of through thickness position). The measurement consists of cutting a thin slit across the thickness, from $y = 0$ to $y = t$, while measuring part deformation as a function of cut depth (typically using a strain gage placed at $(x, y) = (W/2, t)$). Cutting is typically performed using wire electric discharge machining (EDM) and deformation is typically measured using metallic foil strain gages. Given measured deformation as a function of cut depth, residual stress is computed using an elastic inverse. A map of stress could be formed by making a number of slitting measurements on adjacent planes, but a study is required to determine a means to maintain the quality of the slitting measurements.

The most fundamental issues in using slitting for stress mapping can be framed by considering two adjacent measurements made on a single part. Assuming elastic behavior dominates, which is fundamental to slitting, and all mechanical stress release measurement techniques, superposition allows any number of adjacent measurements to be planned from knowledge gained by studying two adjacent measurements. Consider a first measurement along the dashed line in Fig. 39.1, with the slit cut from $y = 0$ to $y = t$ and deformation measured by a single strain gage at $y = t$. Past work suggests that the quality of this measurement will depend on the distance from the part free edge to the slit plane, s_1, because it affects the response of the strain gage to stress on the cut plane (further discussed below). A second measurement location is indicated with the dotted line in Fig. 39.1, which is a distance s_2 from the prior measurement. The first measurement affects the second measurement in two ways. First, the quality of the measurement will be affected by s_2 in the same way the first measurement was affected by s_1 (the distance from the free edge) and second, s_2 will determine the degree to which stress released during the first measurement will change the stress measured during the second measurement.

The initial goals of this paper are to determine values of s_1 and s_2 that are likely to be useful in slitting mapping. The first goal is to determine the effect of s_1 (and also s_2) on measurement uncertainty. The second goal is to provide experimental confirmation of the numerical work. The physical experiments use a series of thin slices removed from a quenched aluminum bar and demonstrate the effects of various choices made in designing a mapping experiment.

39.2 Methods

A useful summary of the theoretical background for slitting is given in [3], with key details summarized here to support an understanding of an uncertainty analysis that enables achieving the first goal of this work. Considering the orientation of Fig. 39.1, the unknown residual stress perpendicular to the slit plane, as a function of position y, $\sigma_{xx}(y)$, is assumed to be a sum of known basis functions, $P_j(y)$, having a set of unknown amplitudes A_j

$$\sigma_{xx}(y) = \sum_{j=1}^{m} A_j P_j(y). \tag{39.1}$$

The strain that would occur at the strain gage, for a particular cut depth a_i, $\varepsilon_{xx}(a_i)$, is related to the unknown amplitudes through a *compliance matrix*, C_{ij}

$$\varepsilon_{xx}(a_i) = \sum_{j=1}^{m} C_{ij} A_j. \tag{39.2}$$

Each entry of the compliance matrix is the strain that would occur in a body having a slit of depth a_i, when the slit faces are loaded by a traction distribution $P_j(y)$. Given a specific strain gage size and location, the entries of the compliance matrix may be determined using elastic finite element modeling, as was described earlier [7].

The unknown amplitudes, A_j, are determined from measured strain versus slit depth data. Adopting matrix notation, (39.2) becomes

$$\boldsymbol{\varepsilon} = \boldsymbol{CA} \tag{39.3}$$

where $\boldsymbol{\varepsilon}$ is a column vector of strain measured at each slit depth, $\boldsymbol{A}$ is a column vector of amplitudes, and $\boldsymbol{C}$ is the compliance matrix having rows and columns reflecting slit depth and basis functions, respectively. The compliance matrix often has more rows than columns, so that (39.3) is solved in a least squares sense

$$\boldsymbol{A} = \boldsymbol{B\varepsilon} \tag{39.4}$$

where $\boldsymbol{B}$ is the pseudoinverse [8] of $\boldsymbol{C}$

$$\boldsymbol{B} = \left(\boldsymbol{C}^T\boldsymbol{C}\right)^{-1}\boldsymbol{C}^T. \tag{39.5}$$

An uncertainty estimate for residual stress measured by slitting was developed by Prime and Hill [9]. A column vector of stress variance (square of uncertainty), with rows reflecting stress at a series of discrete y values (usually taken to be the cut depths), is given by

$$\boldsymbol{s}^2 = diag\left(\boldsymbol{PB}\left[DIAG\left(\boldsymbol{u}^2{}_{\varepsilon}\right)\right]\boldsymbol{B}^T\boldsymbol{P}^T\right) \tag{39.6}$$

where $\boldsymbol{u}^2{}_{\boldsymbol{\varepsilon}}$ is a column vector of the strain variance with rows reflecting the cut depths, $\boldsymbol{P}$ is a matrix containing the values of $P_j(y_k)$, with rows corresponding to the discrete y values and the columns correspond to the basis functions, *diag* is an operator that forms a vector from the diagonal values of a matrix, and *DIAG* is an operator that forms a diagonal matrix from the values of a vector. Typically, the strain variance is either assumed constant at all depths, or computed as the difference between the measured strain and the strain fit, $\boldsymbol{u}^2{}_{\varepsilon} = \boldsymbol{\varepsilon} - \boldsymbol{CA}$.

With an uncertainty estimate established, the effect of s_1 on measurement quality can be found by determining the uncertainty inherently associated with measurement for a range of values of s_1. This approach follows on the work of Rankin and Hill, who used the numerical quality of the compliance matrix, which correlates with stress uncertainty, as a basis for selecting strain gage configurations in slitting [10].

To understand how measurement uncertainty varies with s_1, a series of compliance matrices were developed with a range of values of s_1. The analysis considered a body with unit thickness, t, and width $W = 3t$, as shown in Fig. 39.1. The distance from the edge of the sample to the cut plane, s_1, was varied from $0.05t$ to $1.5t$. Each compliance matrix was determined using a finite element model with 400 elements evenly spaced along the thickness, and element size increasing with distance from

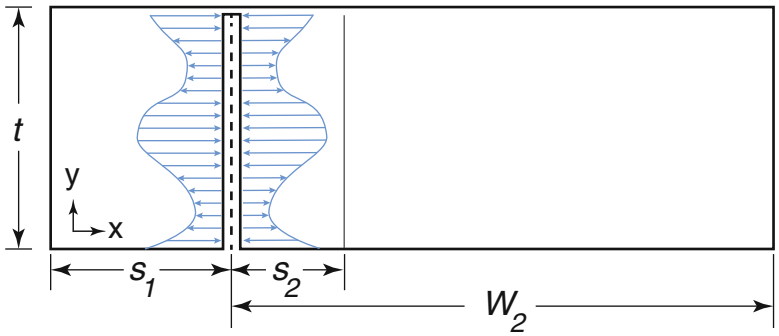

Fig. 39.2 Geometry of the supplemental finite element model used to find the correction for prior measurement: a traction boundary condition is applied to cut faces of the prior measurement at x = s_1, and the resulting stress is extracted at the subsequent measurement plane, which is a distance s_2 from the prior measurement

the cut plane, varying from $t/400$ at the cut plane to $t/40$ at the free edge. Each compliance matrix assumed Legendre polynomial basis functions, orders 2–6, and cut depths evenly spaced by $0.01t$. The stress uncertainty for a given value of s_1 was then found using (39.6), assuming 1 με uncertainty at all cut depths. Comparison of uncertainty for various values of s_1 versus position in the depth, and as a root mean square over all depths, enables an assessment of measurement quality.

The procedure to use slitting to form a map is very similar to the procedure used to make a single measurement. For the second measurement, the compliance matrix could be different, if $s_2 \neq s_1$. If $s_2 = s_1$, the compliance matrix for s_2 may be nearly the same as the compliance matrix for s_1, since the first slitting measurement essentially creates a new free surface (the maximum cut depth is usually about $0.95t$), but would be different since $W_2 \neq W_1$. If the measurements are close enough to one another, the effect of the first slitting measurement on the second may need to be accounted for. The effect of the first slitting measurement on the second should depend on s_2. For small values of s_2, there should be a large effect and for large values of s_2, there should be a negligible effect.

The effect of a prior measurement on a subsequent one will be accounted for using a *correction*, which is determined using a supplemental stress analysis, similar to earlier work by Pagliaro et al. [11] and Wong and Hill [12]. In both of these earlier studies, the supplemental stress analysis used stress determined in the prior measurement as a traction boundary condition input on a model whose geometry reflected the configuration of the subsequent measurement (i.e., the model included the prior cut from contour or from slitting), the measured stress was applied as a traction on the prior cut plane, and stress was determined at the subsequent measurement plane. Here, the correction is used for two *parallel* measurement planes. The analysis is illustrated in Fig. 39.2, and used commercial finite element software [13]. The correction approach comprises a sum of the output of the supplemental stress analysis at the subsequent plane and the stress that will be measured at the subsequent plane to find the original stress present at the subsequent plane. This process is repeated for each subsequent measurement, where the supplemental stress analysis uses the total original stress present at the prior measurement plane.

A series of physical experiments were performed to test conclusions drawn from the numerical results. Measurements were made on 5 mm thick slices removed from a long 7050 aluminum alloy bar that had been quenched to induce high residual stresses indicative of the T74 temper. The slices have a width of 77.8 mm and a height of 50.8 mm. The coordinate system used in this work has the origin at the center of the slice in the horizontal direction (38.9 mm from the edge) and at the bottom of the slice. The x-direction is positive to the right and the y-direction is positive up. All slitting measurements cut from $y = 0$ to 48.9 mm (to a depth of 96 % of the part height). A total of six slices were used in this work and will be called slice 1, slice 2, etc. The first four slices were used to form a map of stress in the slice. Slice 1 had measurements at −20, 0, and 20 mm; slice 2 had measurements at −15, 0, and 15 mm; slice 3 had measurements at −10, 0, and 10 mm; and slice 4 had measurements at −5, 0, and 5 mm, all of which can be seen in Fig. 39.3. The remaining two slices (slices 5 and 6) were used to test if the measurement order would affect the measured result. Slices 5 and 6 used the same measurement locations as slice 3, but altered the order so that the stress at each spatial location could be measured with a different measurement order. The measurement locations and cut order can be seen in Table 39.1 and the choice of s (s_1, s_2, and s_3) for each measurement can be seen in Table 39.2.

The stress in each slice was measured on three planes of constant x. The stress at the third measurement plane is found using the same methodology as is used to calculate the stress at the second measurement plane, except that the traction boundary condition applied in the supplemental stress analysis is the total stress at the second measurement plane (i.e., the measured stress from slitting at the second measurement plus the correction from the first measurement at the second location).

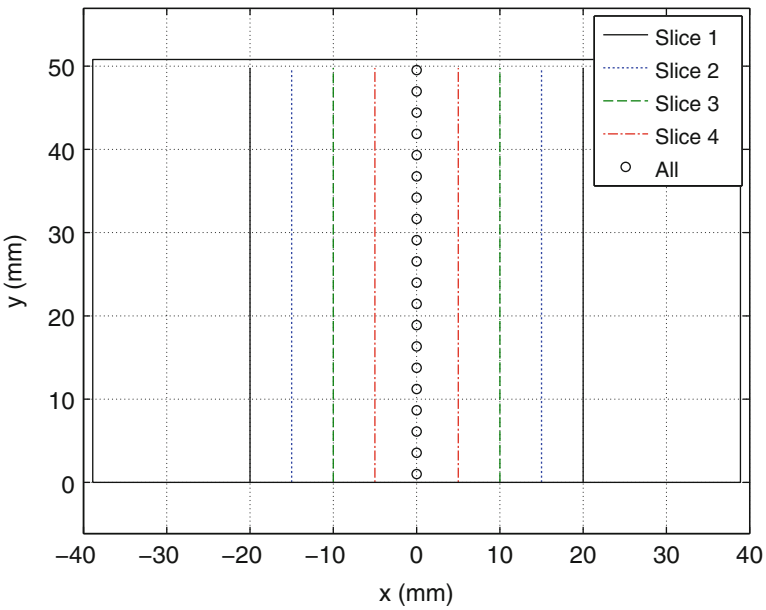

Fig. 39.3 Diagram of slitting locations

Table 39.1 Measurement order and measurement plane locations for all slices

	x-position with corresponding cut order (mm)								
Slice	−20	−15	−10	−5	0	5	10	15	20
1	1				2				3
2		1			2			3	
3			1		2		3		
4				1	2	3			
5			1		3		2		
6			3		1		2		

Table 39.2 Distances between measurement planes, s, normalized distances between measurement planes, s/t, and normalized widths, W/t

Slice	s_1 (mm)	s_2, s_3 (mm)	s_1/t	s_2/t, s_3/t	W_2/t	W_3/t
1	18.9	20	0.372	0.394	1.16	0.77
2	23.9	15	0.470	0.295	1.06	0.77
3	28.9	10	0.569	0.197	0.96	0.77
4	33.9	5	0.667	0.098	0.86	0.77
5	28.9	10	0.569	0.197	0.96	0.39
6	38.9	10	0.766	0.197	0.77	0.77

The experiments followed best practices given by Prime [14] and by Hill [3]. Each measurement used a single strain gage mounted on the back face of the sample ($y = 50.8$ mm) with a 1.57 mm active gage length, and temperature compensated for aluminum. Each slitting measurement consisted of 60 cut increments, ranging in size from 0.25 to 1.5 mm. After each cut increment, the EDM wire was powered off and strain was recorded after allowing the Wheatstone bridge strain indicator to develop a stable readout (~1 min). Cut closure was avoided using visual inspection and cutting toward the initial cut depth as needed to maintain a gap on the cut plane. Elimination of cut closure is required given the linear formulation of (39.2). After the experiment, an instrumented optical microscope was used to determine the location of the slit, the location of the strain gage, the maximum slit depth, and the slit width.

A compliance matrix for each experiment was determined from a 2D, plane strain, finite element model and unit pulse basis functions for residual stress. The model reflected the measured geometry, which assures fidelity of measured residual stress [15], and assumed an elastic modulus of 70 GPa and Poisson's ratio of 0.3, to match aluminum. A typical model had 400,000 eight-node, biquadratic elements, with 1000 elements across the thickness and a bias of element size with distance away from the cut plane, with square elements at the cut plane and element size 10× larger at the free end. Lastly, since the compliance matrix is computed using a plane strain model, it was scaled using the correction scheme developed by Aydiner and Prime [16] to account for the finite thickness of the slice.

The uncertainty in each slitting measurement was calculated with (39.6). The strain uncertainty, u_ε, was taken as the maximum of either the difference between measured strain and fit strain, or a minimum value of 2 με. The uncertainty in the corrections for prior slitting measurements was estimated using a Monte Carlo approach. Each correction was found five times with a "noisy" stress distribution, where the noisy stress is the sum of the known, prior measured stress and normally distributed noise with a magnitude corresponding the uncertainty in the prior measurement. The error in the corrections was then taken as the standard deviation of the five corrections with added noise. The total uncertainty was found using

$$U = \sqrt{U_{slitting}^2 + U_{correction}^2} \tag{39.7}$$

where U is the total uncertainty of the stress in the slice, $U_{slitting}$ is the uncertainty from the slitting measurements, and $U_{correction}$ is the uncertainty in the prior measurement correction.

39.3 Results

Figure 39.4 shows that small values of s_1 result in large uncertainty in stress. The uncertainty as a function of cut depth, in Fig. 39.4a, has a similar distribution for different values of s_1, with uncertainty being largest at the initial cut depths and decreasing as cut depth increases. The similar shape of the uncertainty estimates is a result of the shape of the basis functions used in the stress calculation (i.e., $\boldsymbol{P}$ in (39.6)). The uncertainty is large for small values of $s_1 = 0.05t$ and $0.10t$, but quickly becomes smaller for $s_1 \geq 0.2t$. This is further illustrated in Fig. 39.4b, which shows the RMS of the uncertainty, across all cuts depths, as a function of s_1. The results show the uncertainty is significantly larger for small values of $s_1 = 0.05t$ and $0.10t$, but decreases rapidly and begins to plateau at $s_1 > 0.5t$.

Based on these results, we suggest the optimal selection of s (s_1, s_2, ... etc) is $s = 0.2t$ as a balance between fine measurement spacing (small values of s) and reasonable measurement precision, since the uncertainty increases significantly for $s < 0.2t$. Using this recommendation, a good mapping experiment would consist of having $s \geq 0.2t$. When this criterion is applied to the aluminum slices used in the present experimental work, we would expect good measurement precision for the measurements with spacing of 20 mm ($0.39t$), 15 mm ($0.30t$), and 10 mm ($0.20t$), but poor measurement precision for the measurements with spacing of 5 mm ($0.098t$).

Measured strain data for all three measurements on slice 3 are given in Fig. 39.5a, and residual stresses are given in Fig. 39.5b. The strain and stress magnitudes are largest for the first measurement, which had $s_1 = 0.57t$, and are smaller and similar for the second and third measurements, which had $s_2 = s_3 = 0.2t$. It is expected that the strain signal would be the largest for the first measurement since there were no prior measurements. The corrections for the second and third measurement in slice 3 were very similar, as can be seen in Fig. 39.5c, which suggests that the initial stress was similar at the first and second measurement planes (since the correction at the second measurement is from the total stress at the first measurement location and the correction at the third measurement is from the total stress at the second measurement location).

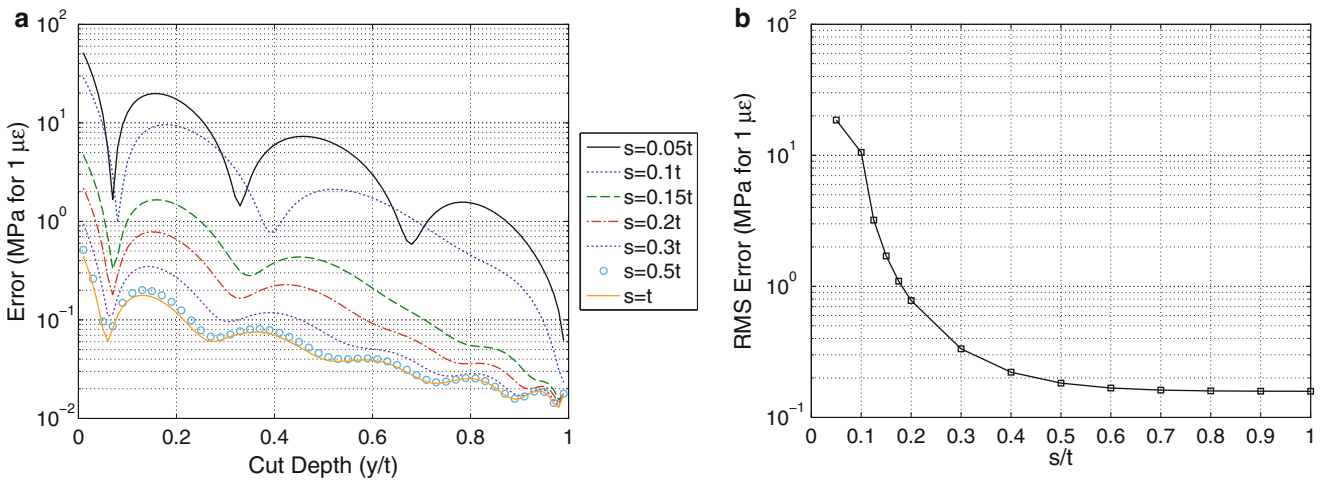

Fig. 39.4 Uncertainty in stress for 1 με strain error as a function of distance from strain gage to edge of coupon (s_1)

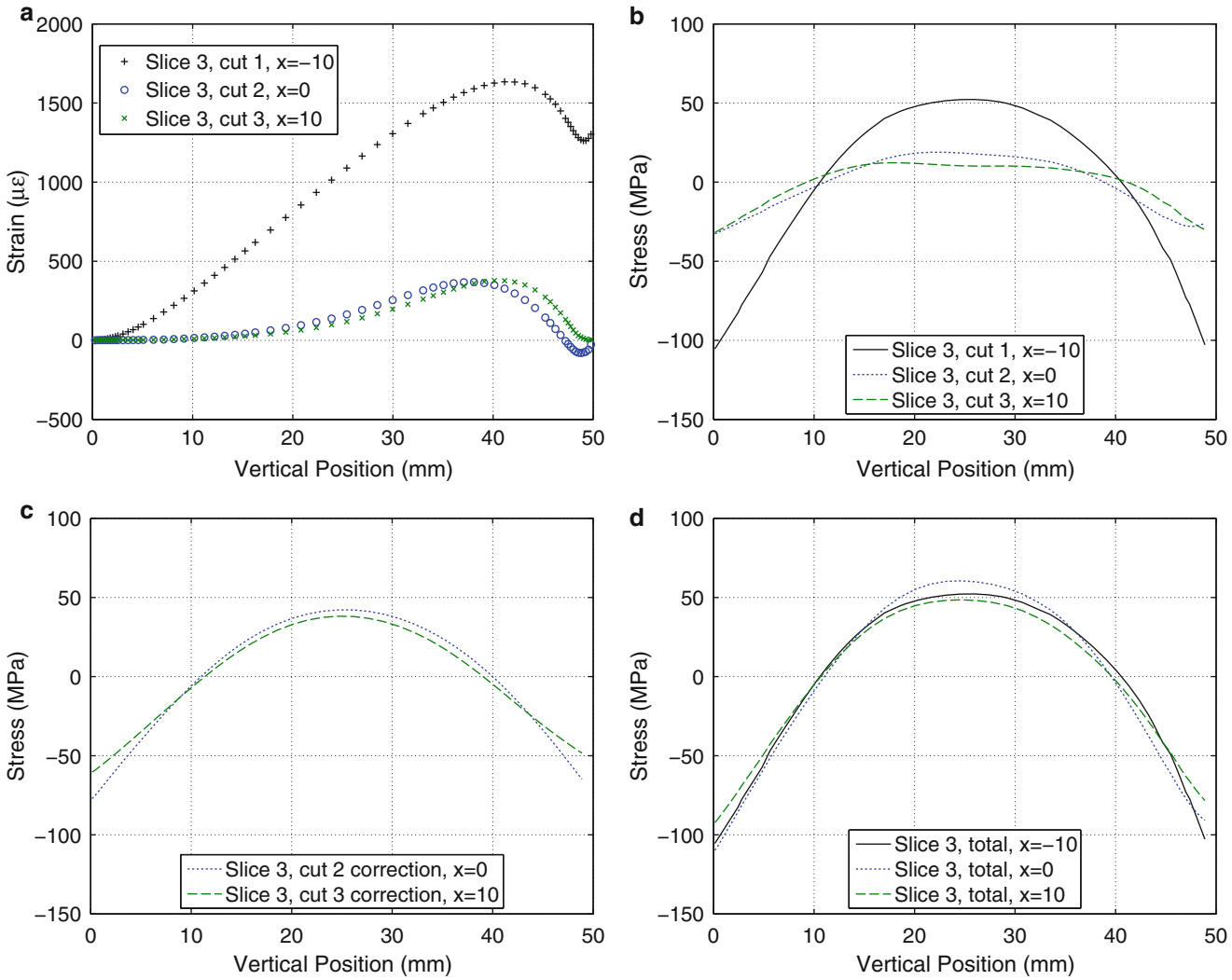

Fig. 39.5 Line plots from slice 3 (10 mm measurement spacing) of (**a**) the measured strain, (**b**) the computed stress, (**c**) corrections, and (**d**) total stress

The total stress for the three measurements on slice 3 is plotted in Fig. 39.5d and shows that the quenching induced stress is roughly parabolic along y, and relatively constant along x, over the 20 mm measurement span between planes 1 and 3 on slice 3.

The total stress at $x = 0$ in all six slices is shown in Fig. 39.6a. The measurements in slice 2, 3, 5, and 6 are nearly identical to one another, while the measurements in slices 1 and 4 differ somewhat. The measured stress for the first and third measurements (measurements at $x = \pm s$ from the mid-plane) in slices 1–4 can be seen in Fig. 39.6b. The measured stresses at ± 20 mm are very similar to one another, showing symmetry that is expected in a part that was uniformly quenched. The same symmetry is evident in the results for measurements at ± 15, ± 10, and ± 5 mm.

The results of the additional measurements intended to test the effects of measurement order using slices 3, 5, and 6 are shown in Fig. 39.7. The results show that although the individual slitting measurements are different due to the order of the measurement, the total stress at the three different locations are nearly identical. Since the results are independent of measurement order, this confirms that superposition holds in the measurements, and that the measurements have good accuracy.

The two-dimensional spatial maps of stress and uncertainty in Fig. 39.8 show tensile residual stress in the center of the slice, maximum near 60 MPa, and compressive stresses along the upper and lower edges, minimum near -100 MPa. (There are six measurements of stress at $x = 0$, but the results from slice 6 are used in the map because they are judged to have the best measurement fidelity.) The uncertainty map shows that the total uncertainty is very low for all measurements, except for the measurement at $x = 5$ mm. To better understand the how the uncertainty is affected by the choice of s, the

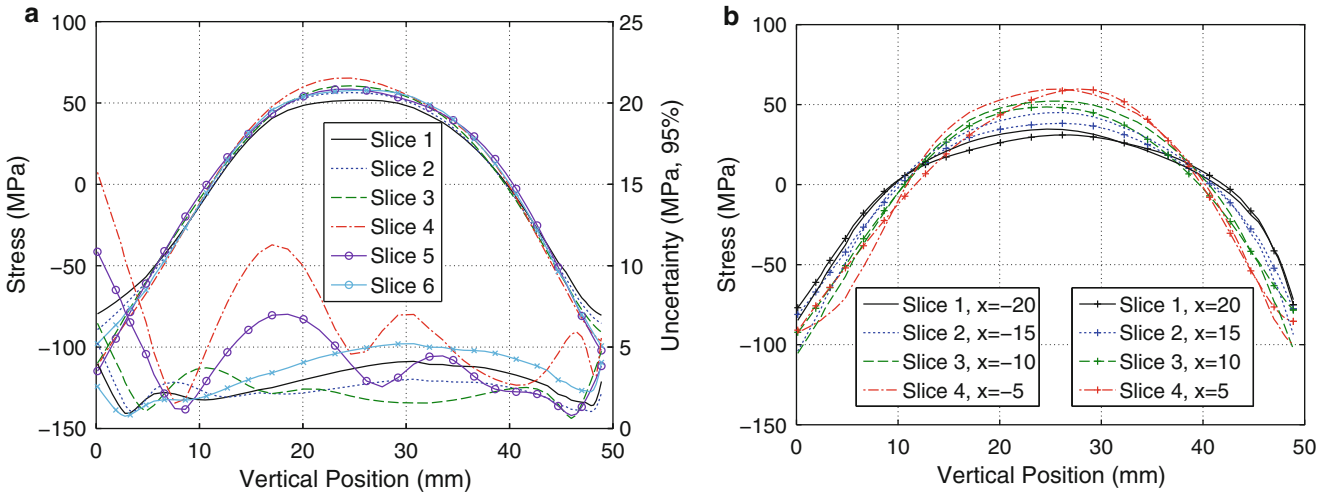

Fig. 39.6 (**a**) Total stress at x = 0 mm and uncertainty (95 % confidence interval, lines toward bottom of chart) and (**b**) total stress at various positions symmetric about x = 0

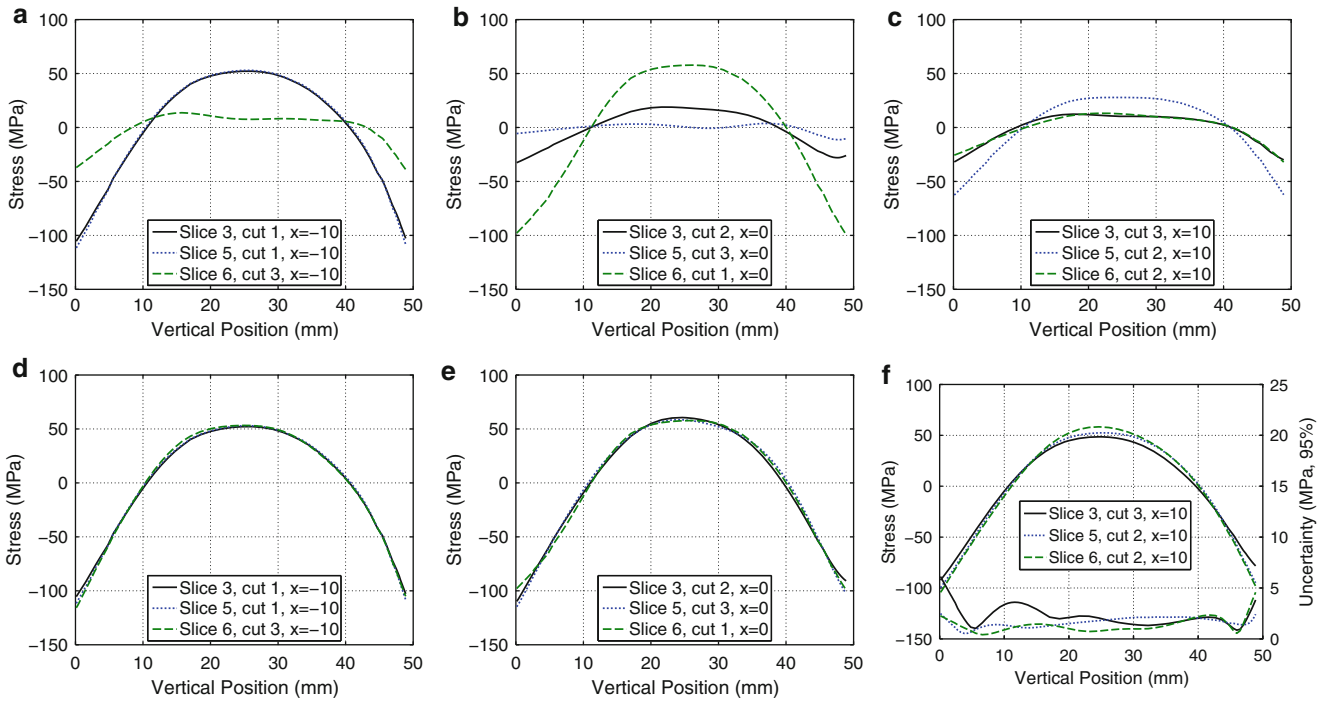

Fig. 39.7 Measured slitting results from slices 3, 5, and 6 at (**a**) x = −10 mm, (**b**) x = 0, (**c**) x = 10 mm, and the total stress at (**d**) x = −10 mm, (**e**) x = 0, (**f**) x = 10 mm

RMS of uncertainty for each slitting measurement, correction, and total have been plotted in Fig. 39.9 as a function of measurement spacing. The results clearly show the uncertainty increases significantly when the measurement spacing is 5 mm (0.01t). Furthermore, the uncertainties for the third measurements in slices 1–4 are shown in Fig. 39.10 for both slitting and the corrections. The uncertainty for the slitting measurements show the uncertainty to increase with decreasing s, with the measurement with $s = 5$ mm having significantly larger uncertainties (15 MPa compared to 7 MPa). The uncertainty in the corrections also has uncertainty increasing for decreasing s, with $s = 10$, 15, and 20 mm having small uncertainty (under 3 MPa), but $s = 5$ mm having a large uncertainty (30 MPa). The reason the uncertainties in the corrections are less severe than the uncertainty in the slitting measurement for a given measurement spacing, is that they are represented by high-frequency noise, whose effect becomes small over a relatively short distance. These uncertainty values confirm what was stated earlier, that using a very small measurement spacing ($s < 0.2t$) can lead to an imprecise measurement.

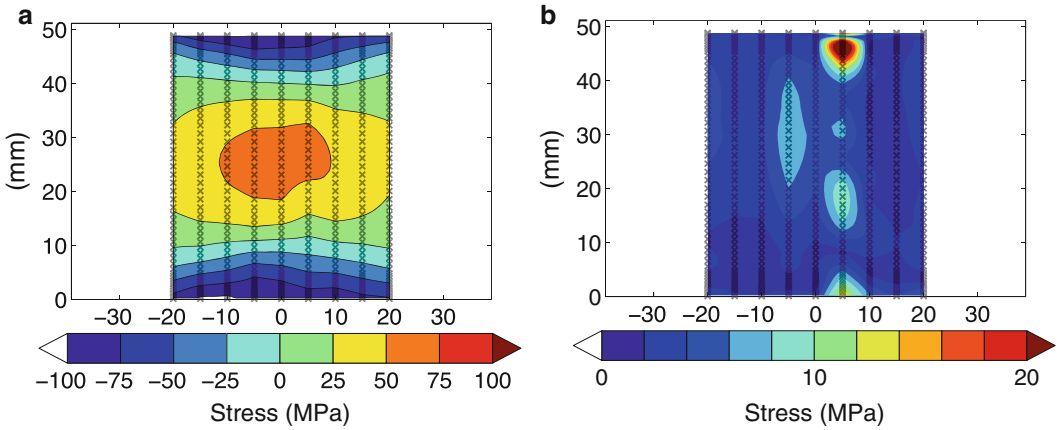

Fig. 39.8 Maps of the total x direction (**a**) stress and (**b**) uncertainty

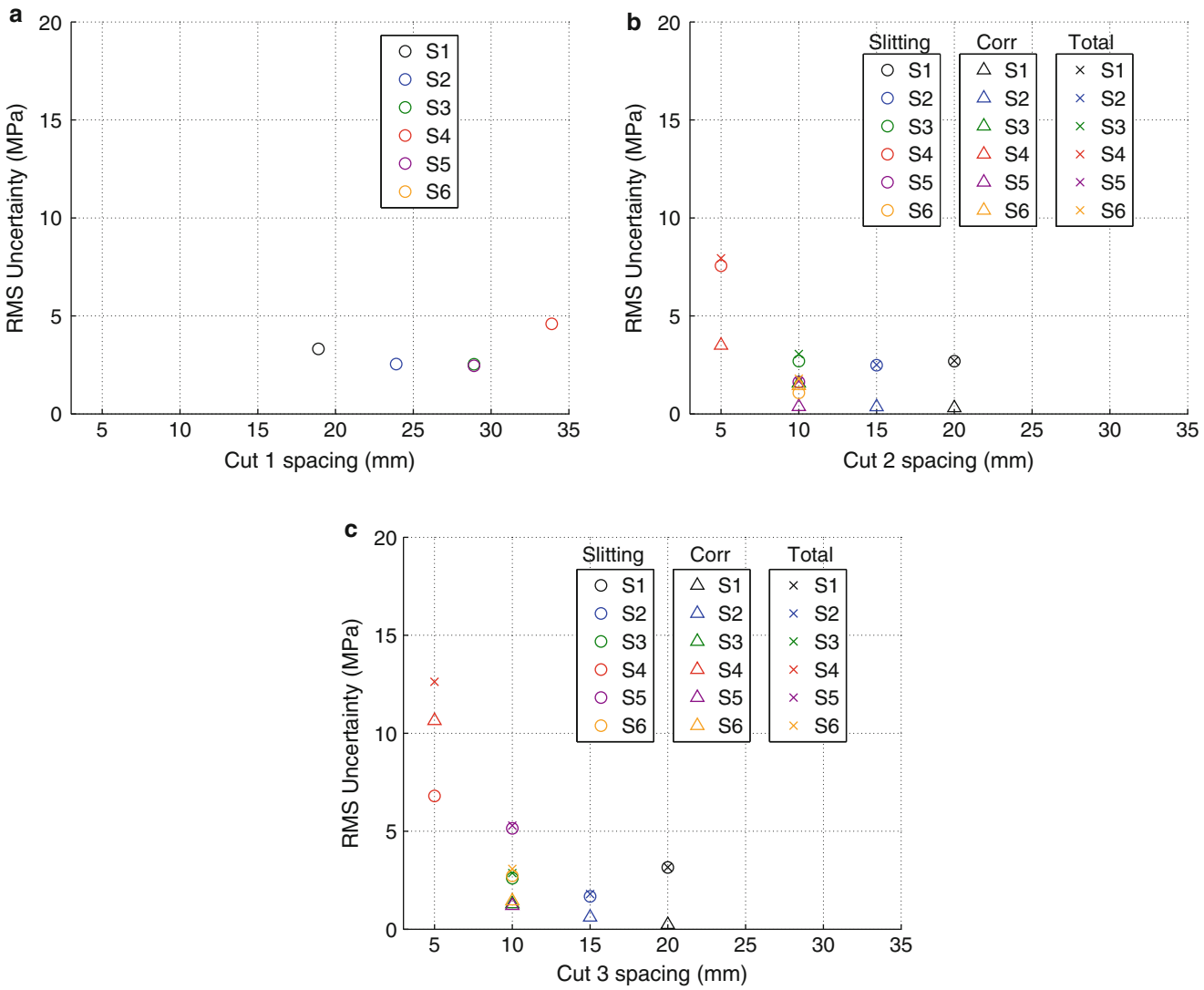

Fig. 39.9 Uncertainty as a function of cut spacing for (**a**) cut 1, (**b**) cut 2, and (**c**) cut 3. Note: for cut 1 there is no correction, thus the total uncertainty is the same as the uncertainty from slitting

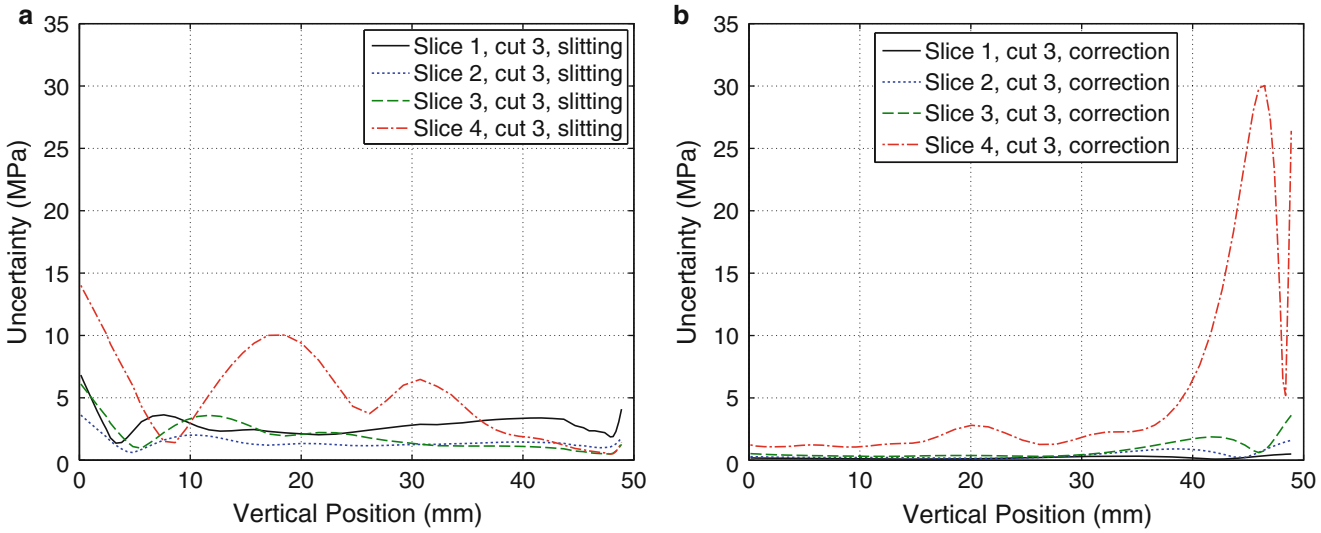

Fig. 39.10 Line plots of the uncertainty (95 % confidence interval) for the third measurement from (**a**) slitting and (**b**) corrections

39.4 Discussion

The results presented above show several significant outcomes regarding mapping with slitting. The most significant outcome is the experimental demonstration of slitting mapping, which provided good precision, except when measurements were too closely spaced. The numerical analysis suggested, and experimental measurements confirmed, that measurement spacing of $s \geq 0.2t$ provides good measurement precision (around 5 MPa in the experiments on slice 3) while the spacing of $s = 0.1t$ results in poor precision (around 30 MPa in the experiments on slice 4). The poor precision for small values of s_1 (or s_2) is due to poor condition of the compliance matrix because stress release does not cause strain change for shallow cut depths when s is small.

The measured stresses at $x = 0$, in Fig. 39.6a enable a comparison of the measurements for various choices of s and it is promising that the measurements in slice 2, 3, 5, and 6 show very good agreement. The measured strain and calculated stress for the second measurement on slice 4, shown in Fig. 39.11, clearly illustrates that the measurement spacing is too small because the measured stress and uncertainty have similar magnitude. Although it is understandable that the measurement in slice 4 is an outlier, it is confounding that the measurement in slice 1 does not agree well with the other results (by around 50 MPa at shallow cut depths and 10 MPa at the mid-thickness), especially since this measurement has low uncertainty (under 5 MPa).

To further explore the fidelity of the two-dimensional stress map made with slitting, confirmatory residual stress measurements were made at the mid-height ($y = 25.4$ mm) of a slice as a function of x using EPSI hole drilling, X-ray diffraction, and a newly developed X-ray diffractometer that measures the full Debye ring with a single measurement (i.e., doesn't require tilting for $\sin^2\Psi$ vs. Ψ). Standard practice was followed, as described in [17] for ESPI hole drilling and [18] for X-ray diffraction. There is limited background publication regarding the new diffractometer (μ-X360 from Pulstec Industrial Co., Ltd) and the results presented here are for illustrative purposes. The measured results from the various techniques can be seen in Fig. 39.12, where the ESPI hole drilling results are consistently higher than the slitting results, by around 10 MPa, the conventional X-ray diffraction results are consistently lower than the slitting results, by 10–20 MPa, and the Debye ring results appear to be systemically lower than the conventional X-ray diffraction results by about 5–10 MPa, with significantly larger uncertainties. All four sets of results show a small degree of asymmetry, which is unexpected given the uniform quenching. Considering that 10 MPa is a significant fraction of the precision typical of any of the four measurement techniques [19]. The degree of agreement in Fig. 39.12 is reasonable.

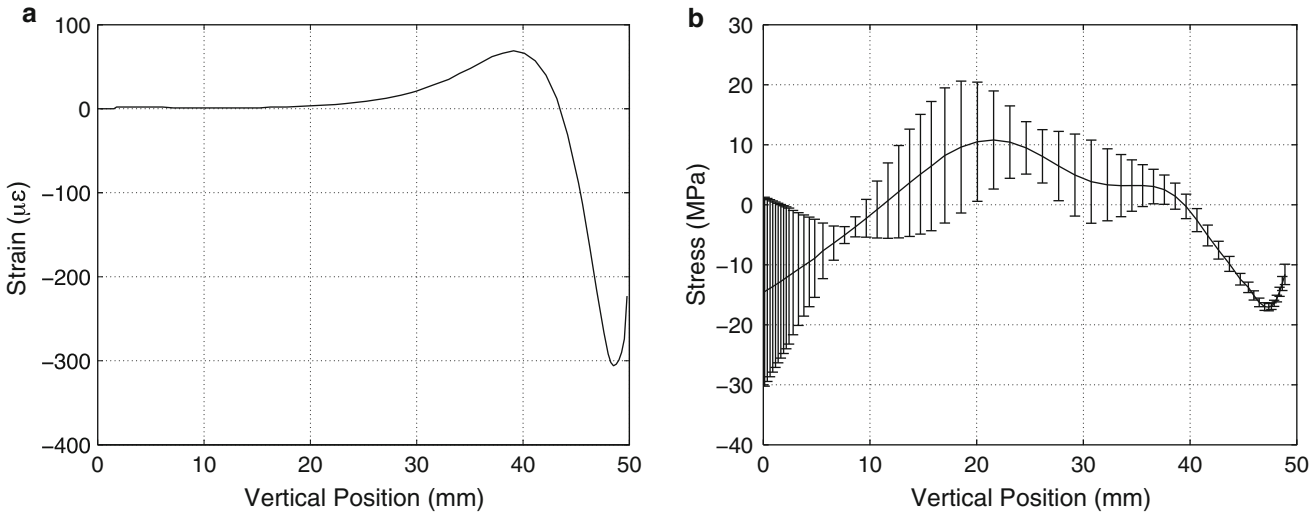

Fig. 39.11 Slice 4, cut 2 at x = 0 (**a**) measured strain and (**b**) calculated stress with uncertainty

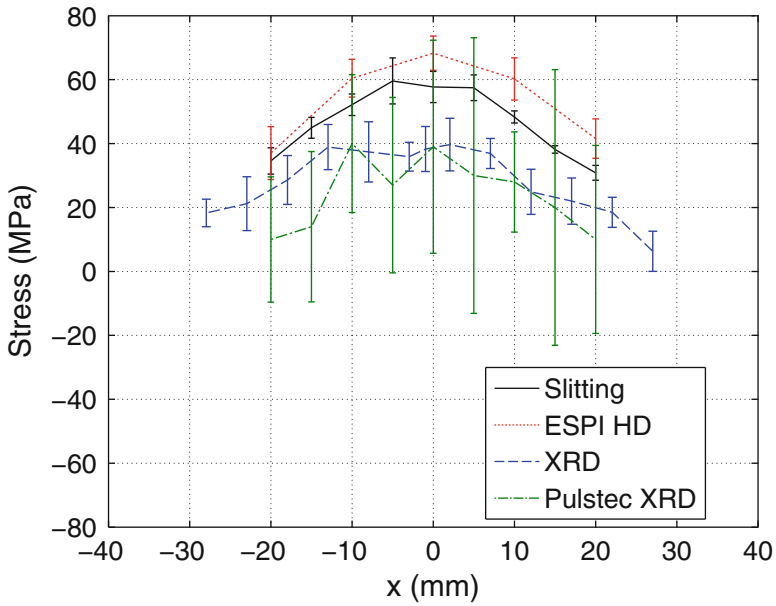

Fig. 39.12 Line plot showing the stress measured at y = 25.4 from slitting, ESPI hole drilling (HD), conventional laboratory X-ray diffraction (XRD), and Pulstec X-ray diffraction (Pulstec XRD)

39.5 Summary/Conclusions

The use of slitting to form a two-dimensional map of one in-plane residual stress component in a two-dimensional body has been considered in detail. A numerical study assessed the fidelity of a slitting measurement as the distance to the part free edge is varied. The results of this numerical study show there would be very large uncertainties when the slitting measurement plane is close to either the part edge or a previous slitting measurement plane, and leads to a recommended minimum measurement spacing of $0.2t$.

The results of the numerical study were confirmed with physical experiments using slices that had residual stresses induced by quenching. The physical experiments showed excellent precision (under 10 MPa) for measurements with spacing greater than $0.2t$. Results from confirmatory measurements made with X-ray diffraction and ESPI hole drilling agree well with the slitting mapping results, giving further confidence in the use of slitting to form a 2D stress map.

Acknowledgements The authors acknowledge financial support from the Electric Power Research Institute, Materials Reliability Program (Paul Crooker, Senior Technical Leader), and technical support from Daniel Goldin and Kyler Steele (undergraduate student researchers at UC Davis).

References

1. M.B. Prime, Cross-sectional mapping of residual stresses by measuring the surface contour after a cut. J. Eng. Mater. Technol. **123**, 162–168 (2001)
2. D.J. Smith, Deep hole drilling, in *Practical Residual Stress Measurement Methods (Chapter 3)*, ed. by G.S. Schajer (Wiley, West Sussex, 2013), pp. 65–87
3. M.R. Hill, The slitting method, in *Practical Residual Stress Measurement Methods (Chapter 4)*, ed. by G.S. Schajer (Wiley, West Sussex, 2013), pp. 89–108
4. M.D. Olson, M.R. Hill, B. Clausen, M. Steinzig, T.M. Holden, Residual stress measurements in dissimilar weld metal. Exp. Mech. **55**, 1093–1103 (2015)
5. M.J. Lee, M.R. Hill, Intralaboratory repeatability of residual stress determined by the slitting method. Exp. Mech. **47**, 745–752 (2007)
6. M.B. Prime, Residual stress measurement by successive extension of a slot: the crack compliance method. Appl. Mech. Rev. **52**, 75–96 (1999)
7. M.J. Lee, M.R. Hill, Effect of strain gage length when determining residual stress by slitting. J. Eng. Mater. Technol. **129**, 143–150 (2007)
8. A. Albert, *Regression and the Moore-Penrose Pseudoinverse* (Elsevier, New York, 1972)
9. M.B. Prime, M.R. Hill, Uncertainty, model error, and order selection for series-expanded, residual-stress inverse solutions. J. Eng. Mater. Technol. **128**, 175 (2006)
10. J.E. Rankin, M.R. Hill, Measurement of thickness-average residual stress near the edge of a thin laser peened strip. J. Eng. Mater. Technol. **125**, 283–293 (2003)
11. P. Pagliaro, M.B. Prime, H. Swenson, B. Zuccarello, Measuring multiple residual stress components using the contour method and multiple cuts. Exp. Mech. **50**(2), 187–294 (2010)
12. W. Wong, M.R. Hill, Superposition and destructive residual stress measurements. Exp. Mech. **53**, 339–344 (2013)
13. Abaqus/Standard, Version 6.10, Providence, RI, USA, 2010
14. M.B. Prime, Experimental procedure for crack compliance (slitting) measurements of residual stress, Los Alamos National Laboratory Report (LA-UR-03-8629), 2003
15. M.R. Hill, W.Y. Lin, Residual stress measurement in a ceramic-metallic graded material. J. Eng. Mater. Technol. **124**, 185 (2002)
16. C.C. Aydɑner, M.B. Prime, Three-dimensional constraint effects on the slitting method for measuring residual stress. J. Eng. Mater. Technol. **135**(3), 031006 (2013)
17. M. Steinzig, E. Ponslet, Residual stress measurement using the hole drilling method and laser speckle interferometry: part I. Exp. Tech. **27**, 43–46 (2003)
18. J.S. Robinson, D.A. Tanner, C.E. Truman, A.M. Paradowska, R.C. Wimpory, The influence of quench sensitivity on residual stresses in the aluminium alloys 7010 and 7075. Mater. Charact. **65**, 73–85 (2012)
19. M.R. Hill, M.D. Olson, Repeatability of the contour method for residual stress measurement. Exp. Mech. **54**, 1269–1277 (2014)

Chapter 40
A Novel Approach for Biaxial Residual Stress Mapping Using the Contour and Slitting Methods

Mitchell D. Olson and Michael R. Hill

Abstract This paper describes a residual stress measurement approach that determines a two-dimensional map of biaxial residual stress. The biaxial measurement is a combination of contour method, slitting method measurements on a thin slices removed adjacent to the contour plane, and a computation to account for the effects of slice removal. The measurement approach uses only mechanical stress release methods, which is advantageous for some measurement articles. The measurement approach is verified with independent confirmation measurements. Biaxial mapping measurements are performed in a long aluminum bar (77.8 mm width, 51.2 mm thickness, and 304.8 mm length) that has residual stresses induced with quenching. The measured stresses are consistent with quench induced residual stress, having peak magnitude of 150 MPa and a distribution that is tensile toward the center of the bar and compressive around the boundary. The validating confirmation measurement results have good agreement with results from the biaxial mapping approach.

Keywords Residual stress measurement • Contour method • Slitting • Validation • Quenching

40.1 Introduction

Residual stress can play a role in many failure mechanisms. Fatigue [1, 2] and stress corrosion cracking [3–6] are particularly sensitive to the presence of tensile residual stresses. Residual stresses can be difficult to predict because they are often the result of complex manufacturing processes, which makes their measurement important for both understanding failure [7, 8] and for validation of computational models of stress inducing processes [9–14].

Many methods exist for measuring residual stress, and each provides a limited portion of the stress tensor and has various limitations. For example, large samples or samples with difficult microstructure (e.g., texture, large grains, etc.) are difficult to measure with diffraction techniques [15]. Conversely, some mechanical stress relief methods are prone to systematic errors for large magnitude residual stresses [16], especially if the stresses concentrate during sectioning [17, 18]. One mechanical stress relief method, the contour method, has been found to be especially useful since it inherently measures a map of residual stress over a cross-section. The contour method measures the *change* in stress when cutting a part in half (at the cut plane). Since the cut has created a free surface, the stress normal to the cut plane must be zero after the cut, so that the contour method completely determines the out-of-plane stress component that existed at the cut plane, prior to cutting. Pagliaro et al. [19] further showed that the contour method also determines the change in stress for the in-plane normal components of residual stress at the cut plane. Therefore, additional measurements of in-plane stresses on the cut surface can be used to determine the original in-plane stresses. The first measurement of this type was performed in [19] and used X-ray diffraction and hole drilling to measure the remaining in-plane stress at the contour cut plane (after the contour measurement). Our recent work has extended this methodology to use only mechanical stress release methods [20, 21], but that extension requires validation.

This paper describes an approach for mechanical biaxial residual stress mapping. The approach is then carried out on a quenched bar, and the residual stresses determined are validated with complementary measurements.

M.D. Olson (✉) • M.R. Hill
Department of Mechanical and Aerospace Engineering, University of California, One Shields Avenue, Davis, CA 95616, USA
e-mail: molson@ucdavis.edu

S. Bossuyt et al. (eds.), *Residual Stress, Thermomechanics & Infrared Imaging, Hybrid Techniques and Inverse Problems, Volume 9*, Conference Proceedings of the Society for Experimental Mechanics Series, DOI 10.1007/978-3-319-21765-9_40

40.2 Methods

40.2.1 Measurement Approach

The new measurement approach comprises multiple mechanical stress release measurements, in conjunction with stress analysis and superposition, to determine multiple stress components at a single plane of interest in a body. Each mechanical stress release measurement will change the part configuration (i.e., change the geometry of the part) and each configuration will be denoted with a capital letter (e.g., A, B, C). The residual stress tensor in each configuration, at the plane of interest, is indicated with a superscripted σ (e.g., σ^{A}). The biaxial stress mapping approach determines the out-of-plane stress, σ_{zz}, and one component of the in-plane stress, either σ_{xx} or σ_{yy}, at the plane of interest; by obvious extension, a triaxial mapping approach could by applied, if three stress components were needed.

The configuration changes comprising the new approach are shown in Fig. 40.1a and include cutting the part in half at the plane of interest (configuration A to B) and removing a thin slice (configuration B to C) adjacent to the plane of interest. The coordinates assumed in work are shown in Fig. 40.1, with x and y lying in the plane of interest, and z along the length. Using superposition, the stress in configuration A can be found with

$$^{A}(x, y, 0) = {}^{i}(x, y, 0) + {}^{B}(x, y, 0) = {}^{i}(x, y, 0) + {}^{ii}(x, y, 0) + {}^{C}(x, y, 0) \tag{40.1}$$

where σ with a superscripted Roman numeral denotes the stress released by a change of configuration, defined as the stress in the current configuration subtracted from the stress in the prior configuration (e.g., $\sigma^{i} = \sigma^{A} - \sigma^{B}$). Although (40.1) applies at all spatial locations, our concern is only the plane of interest, at $z = 0$. The contour method is used to determine σ^{i}, and this measurement completely determines the out of plane component (σ_{zz}) of σ^{A}, since the plane of interest is a free surface in configuration B. The slitting method is used to determine one in-plane component of σ^{C}.

As shown in Fig. 40.1b, σ^{A} can decomposed so that

$$^{A}(x, y, 0) = {}^{A(z)}(x, y, 0) + {}^{C}(x, y, 0) \tag{40.2}$$

where $\sigma^{A(z)}$ is the effect of the out-of-plane stress on the thin slice of configuration C, which can be determined using σ_{zz} found by the contour method. Furthermore, $\sigma^{A(z)}$ is a theoretical construct that gives the change in stress that would occur in a thin slice, if the out-of-plane stress were removed; and it is the sum of σ^{i} and σ^{ii}. Using (40.1) and (40.2), only σ^{i} and σ^{C} need to be measured to find σ^{A}, thus there is no need to directly measure σ^{ii}. A locally smooth stress field is requited so that $\sigma^{C}(x, y, 0)$ can be assumed equal to an average of $\sigma^{C}(x, y, z)$ through the slice thickness. Experimental details are discussed below.

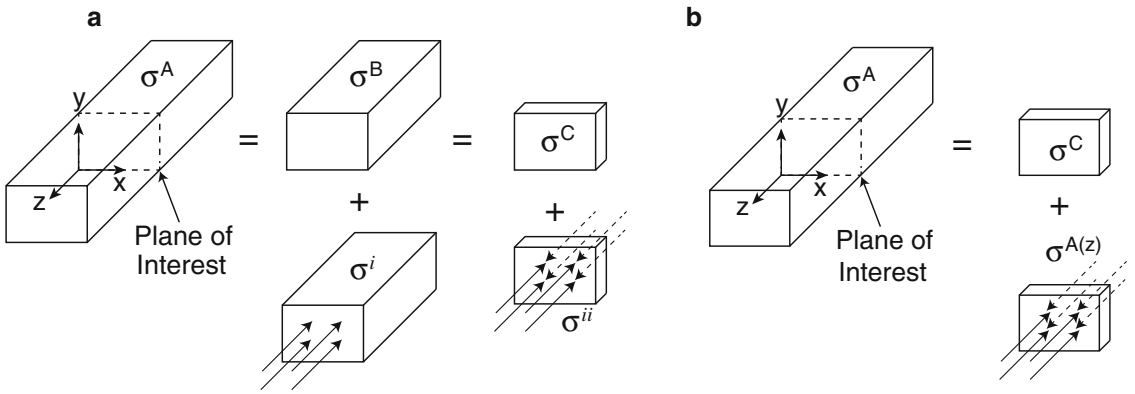

Fig. 40.1 Stress decomposition diagrams. (**a**) The original stresses (σ^{A}, all stress components, at the plane of interest) are equal to the stress release from cutting the part in half (σ^{i}), the stress released when removing a thin slice (σ^{ii}), and the stress remaining in the slice (σ^{C}). (**b**) The original stress (σ^{A}) is equal to the stress remaining in a thin slice (σ^{C}) plus the effect of total longitudinal stress on the thin slice ($\sigma^{A(z)}$)

40.2.2 Biaxial Mapping

The experimental validation requires two sets of measurements: the first set comprises the biaxial mapping approach itself, and the second set provides additional data that confirm the results from biaxial mapping. Measurements were performed on an aluminum bar that was cut from 51.2 mm (2.02 in.) thick, rolled 7050 aluminum plate to form a 305 mm (12 in.) long bar with a cross section 51.2 mm (2.02 in.) thick by 77.8 mm (3.06 in.) wide, as shown in Fig. 40.2. The original bar was in the T7451 condition, being over-aged and stress relieved by stretching. The bar had an additional heat treatment performed to introduce a higher stress, representative of the T74 temper [22]. The heat treatment consisted of solution heat treatment at 477 ˚C for 3 h, immersion quenching in room temperature water with 16 % polyalkylene glycol (Aqua-Quench 260), and a dual artificial age at 121 ˚C for 8 h then 177 ˚C for 8 h.

The biaxial mapping approach consists of a measurement of σ_{zz} with the contour method [23], removing three thin slices, each 5 mm thick, adjacent to contour measurement cutting plane, and measuring σ_{xx} in the slices with the slitting method [24].

The theoretical underpinning of the contour method has been established earlier by Prime [25] and detailed experimental steps have been established by Prime and DeWald [23]; a brief summary of the experimental procedure is given here, which followed the practical advice in [23]. The specimen is cut in two using a wire electric discharge machine (EDM) along the plane of interest, at the mid-length of the bar (Fig. 40.2). Cutting is performed with the specimen rigidly clamped to the EDM frame. Following cutting, the profile of each of the two opposing cut faces is measured with a laser scanning profilometer to determine the surface height normal to the cut plane as a function of in-plane position. The surface height data are taken on a grid of points with spacing of 200 μm 200 μm, so that there are roughly 96,000 data points for each surface. The two surface profiles are then averaged on a common grid, and the average is fit to a smooth bivariate Fourier series [26], where the number of coefficients in the surface is determined by the choice of the maximum fitting parameters (m, n) for the (x, y) spatial dimensions. A level of smoothing is determined by choosing the fitting parameters (m, n) during data reduction.

The residual stress on the contour plane is found with a linear elastic finite element analysis that applies the negative of the smoothed surface profile as a displacement boundary condition on the cut plane. The finite element mesh used eight-node, linear displacement brick elements with node spacing of 1 mm on the cut face, and node spacing normal to the cut face that increased with distance away from the cut, being 1 mm at the cut face and 5 mm at the end of the bar. The mesh was

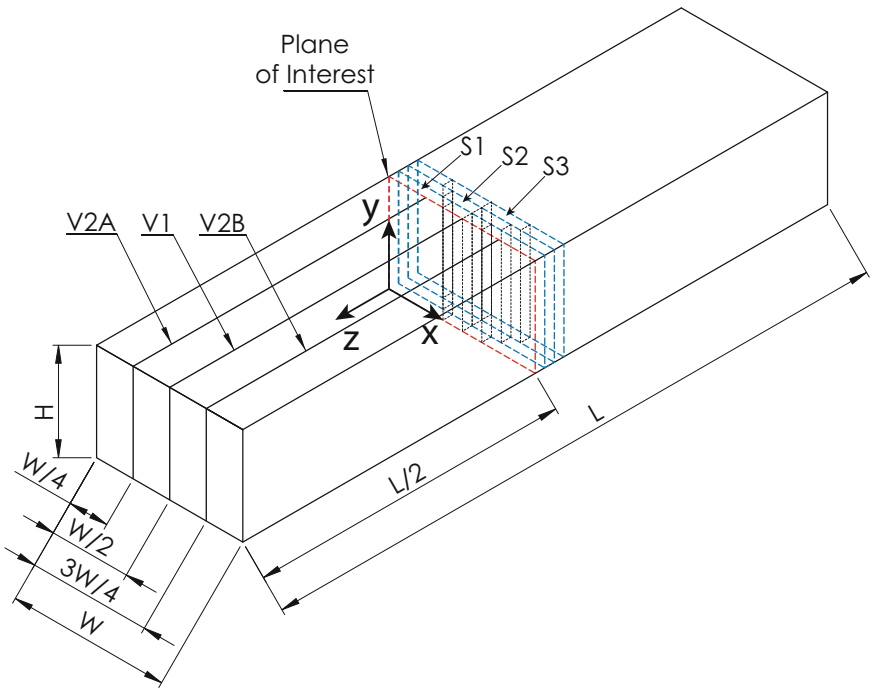

Fig. 40.2 Dimensioned diagram of the measurement article with the location of measurement planes (W = 77.8 mm, H = 51.2 mm, and L = 304.8 mm). The biaxial measurement plane is at z = 0 mm and the three confirmation measurements (V1, V2A and V2B) are at x = 38.9, 19.45, and 58.35 mm. Three slices were removed adjacent to the plane of interest by cutting at z = −5 mm (S1), −10 mm (S2), and −15 mm (S3). Each slice has a slitting measurement at the mid-width of the slice and at ±10 mm (S1), ±15 mm (S2), and ±20 mm (S3) from the mid-width

sufficiently refined such that when the node spacing is halved there is negligible change of stress. The model used an elastic modulus of 71.0 GPa and a Poisson's ratio of 0.33.

To find σ_{xx} in the three removed slices, the slitting method (also known as crack compliance) was used. The theoretical underpinning of the slitting measurements has been given by Prime [27] and best experimental practices have been given by Hill [24]. Slitting measurements consist of incrementally cutting through the sample (along y) using a wire EDM while measuring strain at the back face of the cut plane for each cut increment. The stress normal to the cut plane is then determined from measured strain versus cut depth data using an elastic inverse, with smoothing of the stress profile provided by Tikhonov regularization [28]. The elastic inverse uses a compliance matrix that relates the strain that would be caused by an assumed set of basis functions for each cut depth (for further details, see [29]). The compliance matrix is determined using a plane strain finite element model of the part geometry and a stiffness correction scheme developed by Aydiner and Prime [30] to accurately reflect the finite thickness of the slice.

Since the goal of this work is to determine a map of the stress, multiple slitting measurements are needed, at a set of x positions, and these were made in a set of three slices. The three 5 mm thick slices were removed adjacent to the contour measurement plane by cutting with wire EDM at $z=-5$, -10, and -15 mm. The slitting measurements provided $\sigma_{xx}(y)$ and were made at x locations symmetric about the mid-width, $x_m=38.9$ mm. Measurement locations in the first slice were at x_m and at $x_m \pm 10$ mm; measurement locations in the second slice were at x_m and at $x_m \pm 15$ mm; and, measurement locations in the third slice were at x_m and at $x_m \pm 20$ mm.

We assume that the stress near the plane of interest is invariant of z, so that the stresses determined in different slices can be collapsed onto a single measurement plane. Since we are performing multiple slitting measurements on each slice, the effect of previous slitting measurements on the current measurement is needed and is found with a supplemental stress analysis. A detailed description of the supplemental stress analysis is given in [31] and consists of applying the measured stress from a previous slitting measurement as a traction boundary condition at the prior measurement plane, in a finite element model of the part, and extracting the resulting stress at the current measurement site. The total stress, at a given plane is a superposition of the stress measured from slitting and the effect of any prior measurement, determined with a supplemental stress analysis.

To find $\sigma^{A(z)}$, the longitudinal stress field found with the contour method is applied as a traction boundary condition to both in-plane (x-y) faces of a finite element model of the thin slice used in the slitting measurements. The finite element mesh used eight-node, linear interpolation brick elements with node spacing of 1 mm on the cut face, and five elements through the thickness. The material behavior was elastic, using the properties stated earlier.

40.2.3 Confirmation Measurements

Confirmation measurements are required to validate the biaxial mapping approach. To do so, σ_{xx} is measured at specific planes using the contour method on configuration B, the half-length bar. Three contour measurements are made at planes V1, V2A, and V2B shown in Fig. 40.2. The first validation measurement, at plane V1, is made at $x=38.9$ mm and the second and third measurements are made at $x=19.45$ mm (plane V2A) and 58.35 mm (plane V2B). The first validation measurement aligns with measurements from the biaxial map, but the second and third measurements are not exactly aligned with the measurement locations from the biaxial map (i.e., slitting measurements were offset in x by 0.55 mm). The transverse stress from the biaxial mapping result will be interpolated from nearby data to evaluate stresses at the same positions. Since the stress in the bar was induced with quenching, it is expected that the stress should be constant along the length of the bar, except near the ends.

The confirmation measurements followed the methods for contour measurement described above. The effect of the measurement at plane V1 on stress at planes V2A and V2B was accounted for using superposition. However, it should be noted that the effect of the contour measurement in the biaxial map at $z=0$ has not been accounted for in the validation measurements, since its effect roughly one thickness away from $z=0$ will be negligible. The confirmation contour measurements are cut along the z direction, and determine $\sigma_{xx}(y, z)$ at a set of points with approximately 1 mm in-plane spacing. Since the stress is due to quenching, it is expected to be invariant with z, except near the ends of the half-length bar (at $z=-152$ and 0 mm) where σ_{xx} would be affected by the free surface condition. To compare the results of the confirmation contour measurements with results from the biaxial mapping, we report $\sigma_{xx}(y)$ as an average of results at the set of z-positions farther than one thickness from the free end of the half-length bar (i.e., for $-100\ \text{mm} \le z \le -52$ mm), rather than reporting results for an arbitrarily chosen value of z. At a given value of y, the uncertainty of the confirmation measurement is taken to be the standard deviation of the values from which the average was determined; at nearly all locations, this uncertainty exceeded underlying uncertainty in the contour measurement.

40.3 Results

40.3.1 Biaxial Mapping

The raw surface profiles from the contour measurement at $z=0$ can be seen in Fig. 40.3. The surface profiles from each side of the cut show similar distributions, which indicate good clamping during cutting. The fitting parameters for the contour measurement selected during data processing are $(m, n)=(1, 1)$. The average and fit surface profiles have shapes similar to the measured surface profiles. Line plots of the surface profile data (Fig. 40.4) show that the fit surface appropriately represents the underlying data.

The longitudinal stress and uncertainty can be seen in Fig. 40.5. The stress has a paraboloid distribution with compressive stresses along the exterior (minimum of −153 MPa) and tensile stresses toward the center (maximum of 157 MPa), as would be expected in a quenched bar [32].

The measured strain for the slitting measurement at $x=18.9$ mm ($x=x_m-20$ mm) is shown in Fig. 40.6a, and the calculated stress is shown in Fig. 40.6b. The stress profile is roughly parabolic, as would be expected from a rapid quench. The strain data and stress results at other planes resemble those at $x=18.9$ mm.

The transverse stress from the biaxial map can be seen in Fig. 40.7. The stresses remaining in the slice, σ^{C}, are compressive along the exterior (minimum of −90 MPa) and tensile toward the center (maximum of 55 MPa). The effect of the longitudinal stress, $\sigma^{A(z)}$, has a paraboloid distribution, compressive along the exterior (minimum of −70 MPa) and tensile toward the center (maximum of 33 MPa). The total transverse stress also has a paraboloid distribution, being compressive along the exterior (minimum of −160 MPa) and tensile toward the center (maximum of 90 MPa), which is expected for quenched samples. Line plots of the two contributions to the total transverse stress at a horizontal position of 38.9 mm ($x=x_m$) can be seen in Fig. 40.8. The plot shows that both contributions, σ^{C} and $\sigma^{A(z)}$, are significant parts of the total.

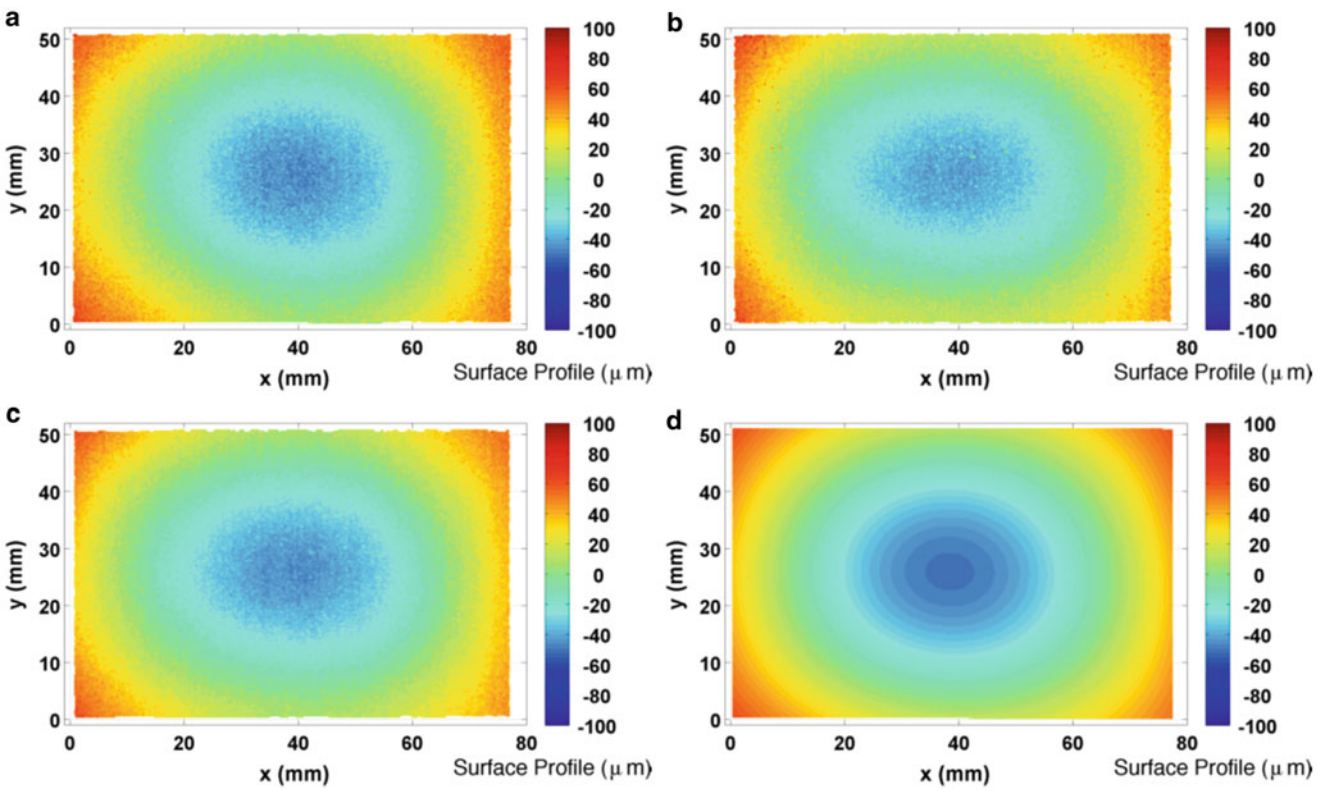

Fig. 40.3 Measured surface displacement from the contour method measurement. (**a**) Surface "1", (**b**) surface "2", (**c**) averaged surface, and (**d**) fitted surface

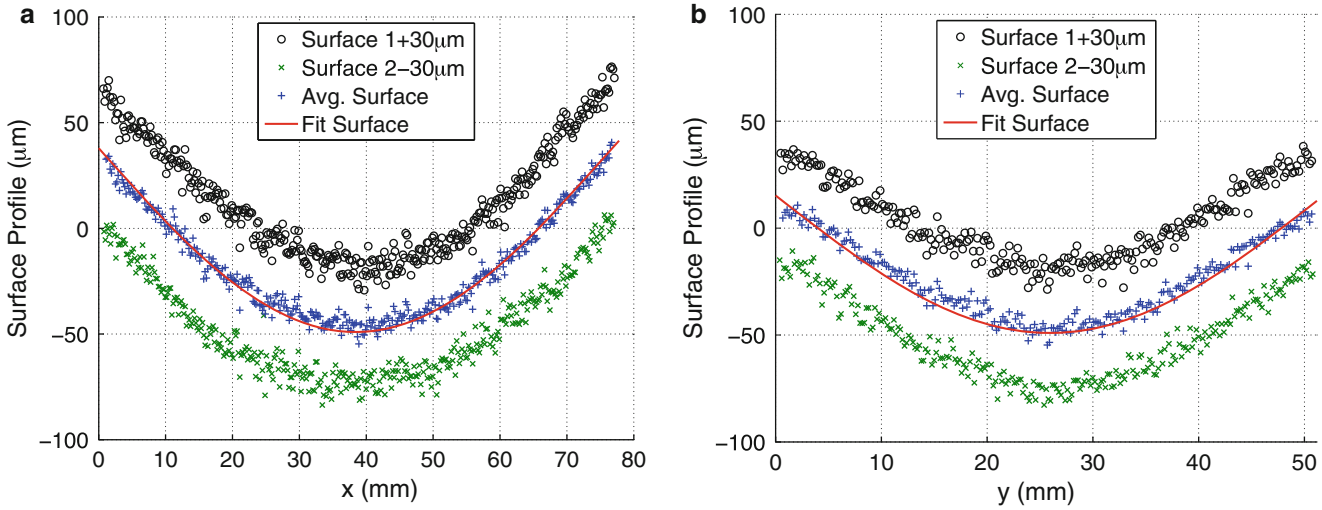

Fig. 40.4 Measured surface displacements along the (**a**) horizontal direction at mid-vertical dimension and (**b**) vertical direction at mid-horizontal dimension. Note: the data from surface 1 is offset by 30 μm and the data from surface 2 is offset by −30 μm, so that the average and fit are also visible on the same plot

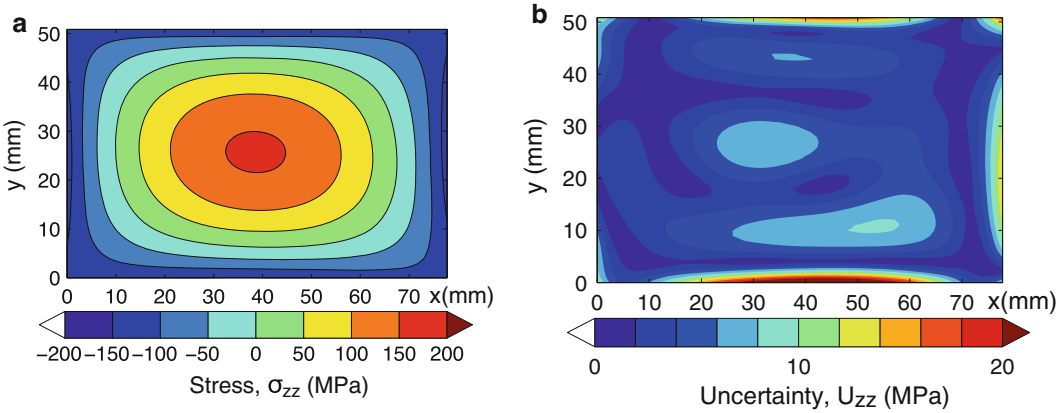

Fig. 40.5 Measured longitudinal (**a**) stress and (**b**) uncertainty (68 % confidence interval)

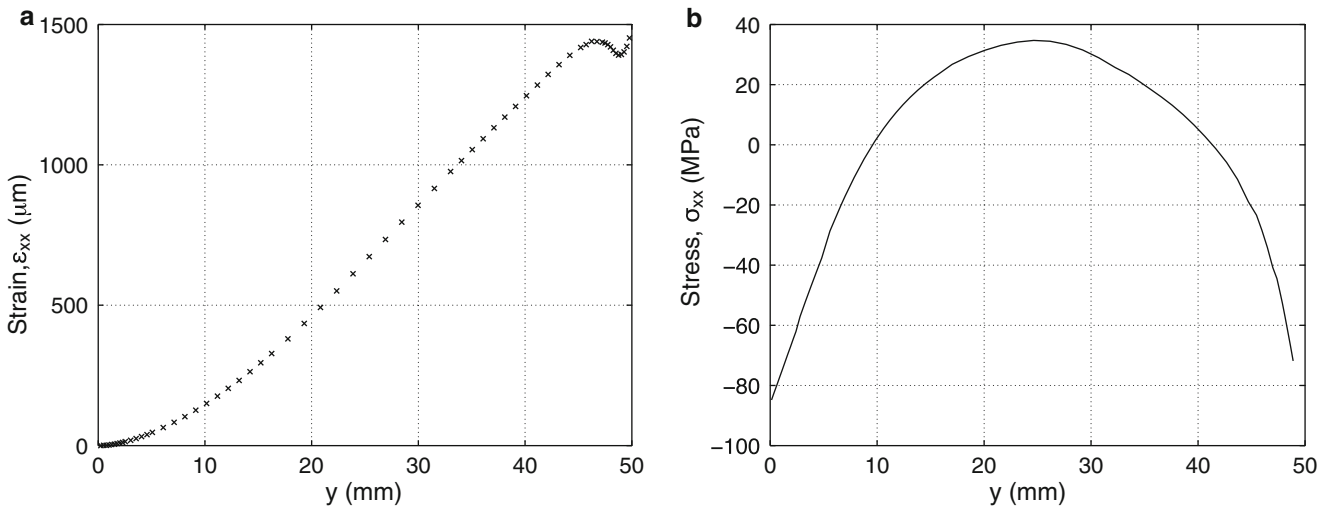

Fig. 40.6 (**a**) Measured strain and (**b**) calculated stress for the slitting measurement at x = 18.9 mm

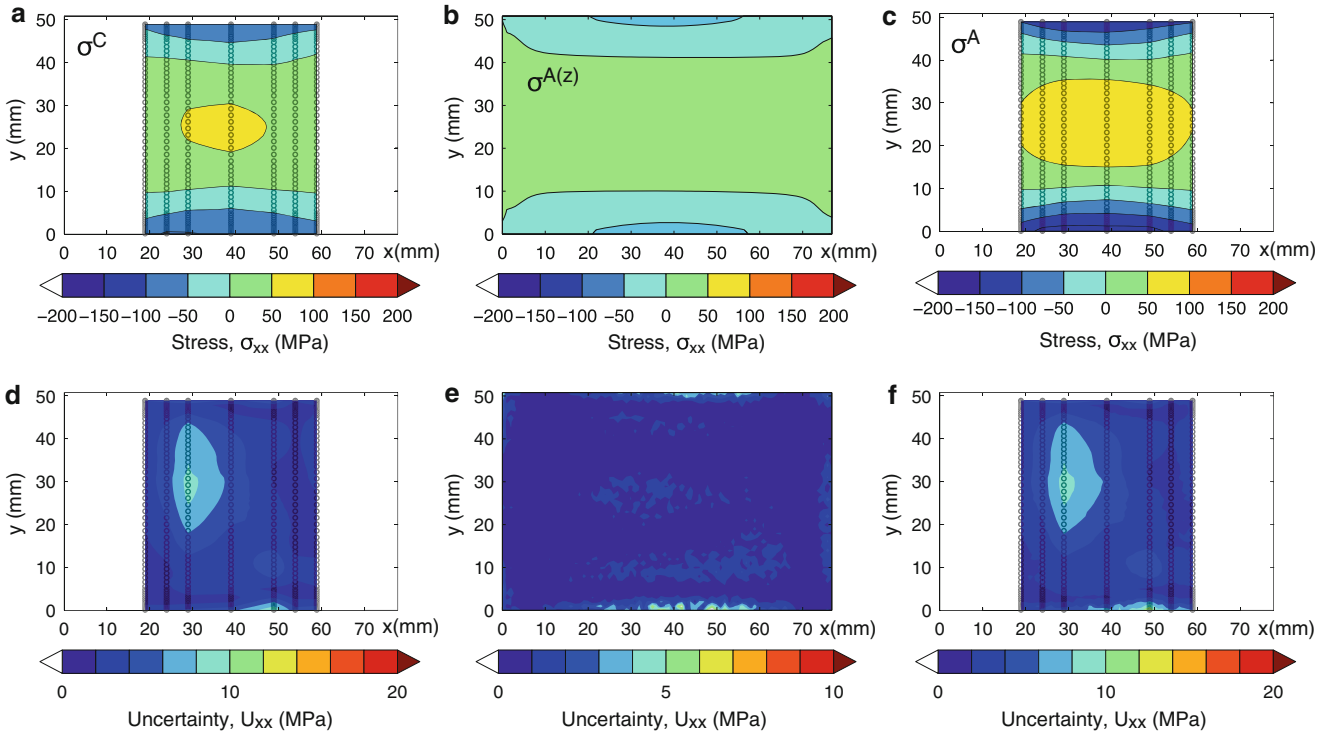

Fig. 40.7 Long transverse stress: (**a**) remaining in slice, (**b**) effect of longitudinal stress on the thin slice, and (**c**) total, with (**d–f**) showing corresponding uncertainty, at a 68 % confidence interval

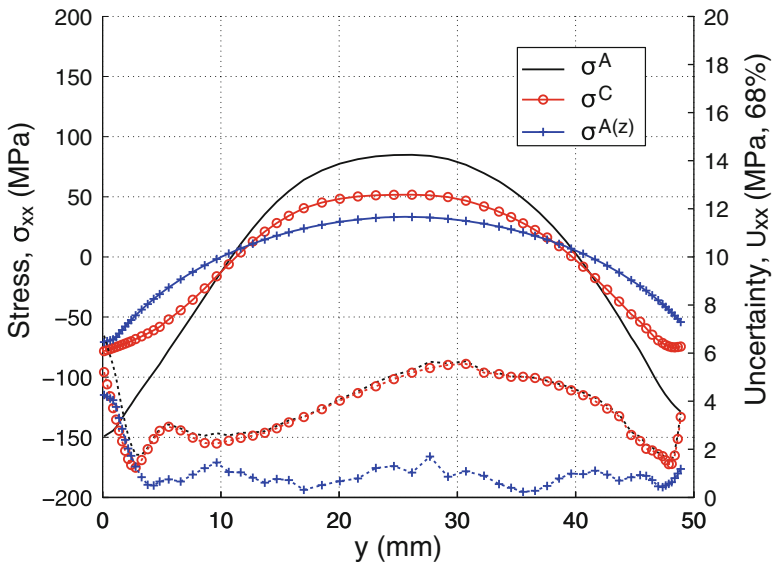

Fig. 40.8 Stress and uncertainty of the two contributions to the transverse stress measurement and the total (σ^A), at a horizontal position of 38.9 mm. Uncertainty is shown as *dotted lines* and is further described in [36]

40.3.2 Confirmation Measurements

The results of the three confirmation measurements can be seen in Fig. 40.9. The fitting parameters for the contour measurement at $x=38.9$ mm ($x=x_m$), 19.45 mm ($x=x_m-19.45$), and 58.35 ($x=x_m+19.45$) have $(m, n)=(2, 1)$, $(3, 1)$, and $(3, 1)$, respectively. The results of the confirmation measurement at $x=38.9$ mm shows a roughly parabolic distribution through thickness (away from the edges), with compressive stresses along the exterior (minimum of −160 MPa) and tensile stresses toward the center (maximum of 75 MPa). Results of the other two confirmation measurements, at $x=x_m\pm19.45$, are

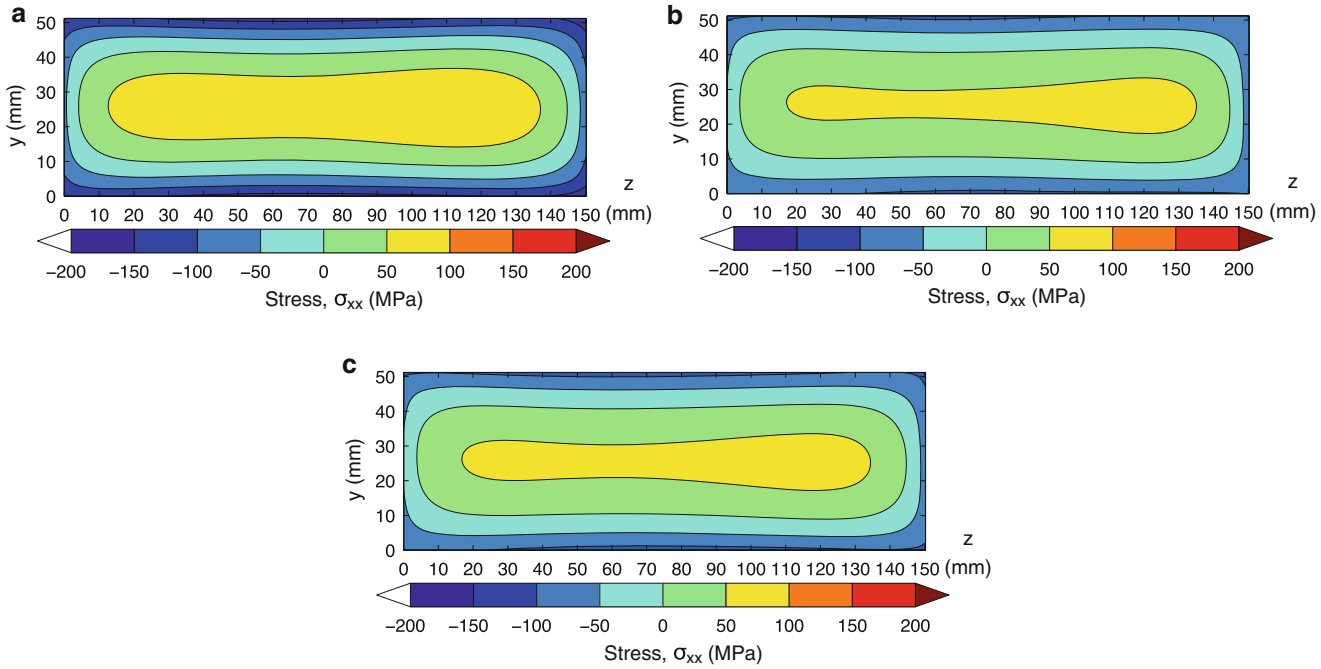

Fig. 40.9 Measured transverse stress at (**a**) x = 38.9 mm, (**b**) x = 18.9 mm, and (**c**) x = 58.9 mm

also parabolic and are self-similar, with lower magnitude than found at $x = 38.9$ mm. These features are consistent with a quench stress field.

The transverse stress σ_{xx} from the biaxial map and from the confirmation measurements are compared in Fig. 40.10. Results from two sets of measurements are in agreement at all locations. The largest difference occurs at $x = 38.9$ mm, being 25 MPa near $y = 50$ mm. However, at most points, the measurements agree well. Overall, the good agreement between the two methods validates the biaxial mapping approach.

40.4 Discussion

The new biaxial mapping method has some advantages over other established residual stress measurement techniques. For example, biaxial mapping measurements in welded components have been shown to be especially useful [20, 33, 34]. In welds, the primary advantage derives from the use of mechanical stress release, which is largely unaffected by the microstructural issues commonly present in welds that very often complicate diffraction based measurements. Furthermore, the use of slitting brings the excellent precision offered by that technique, as compared to somewhat poorer precision of other methods that could be used for mapping stress in the thin slice [35].

One point of concern in developing the biaxial mapping approach is that the superposition of multiple measurements could result in poor precision. However, we have found that not to be the case, as is further discussed in [36]. The uncertainty found in that work shows the transverse stress uncertainty (of the biaxial map) is low, under 10 MPa, in large part because slitting has excellent precision [37, 38]. To contrast, the longitudinal stress, which consisted of a single contour measurement, had somewhat larger uncertainties, up to 20 MPa. The 20 MPa uncertainty found in the contour measurement will affect the uncertainty in $\sigma_{xx}^{A(z)}$, but to smaller degree because the effect of the longitudinal stress on the axial stress in the thin slice is always smaller than the longitudinal stress itself. The uncertainty found here compares favorably with uncertainties typical of other residual stress measurement techniques [39].

Another issue that is relevant for biaxial mapping is the optimal selection of slitting measurement locations. If measurements in the slice are too close to one another, the precision of the measurement decreases. A recent study has addressed this topic [31] and found the minimum distance between slitting planes for good measurement precision is 0.2 times the part thickness.

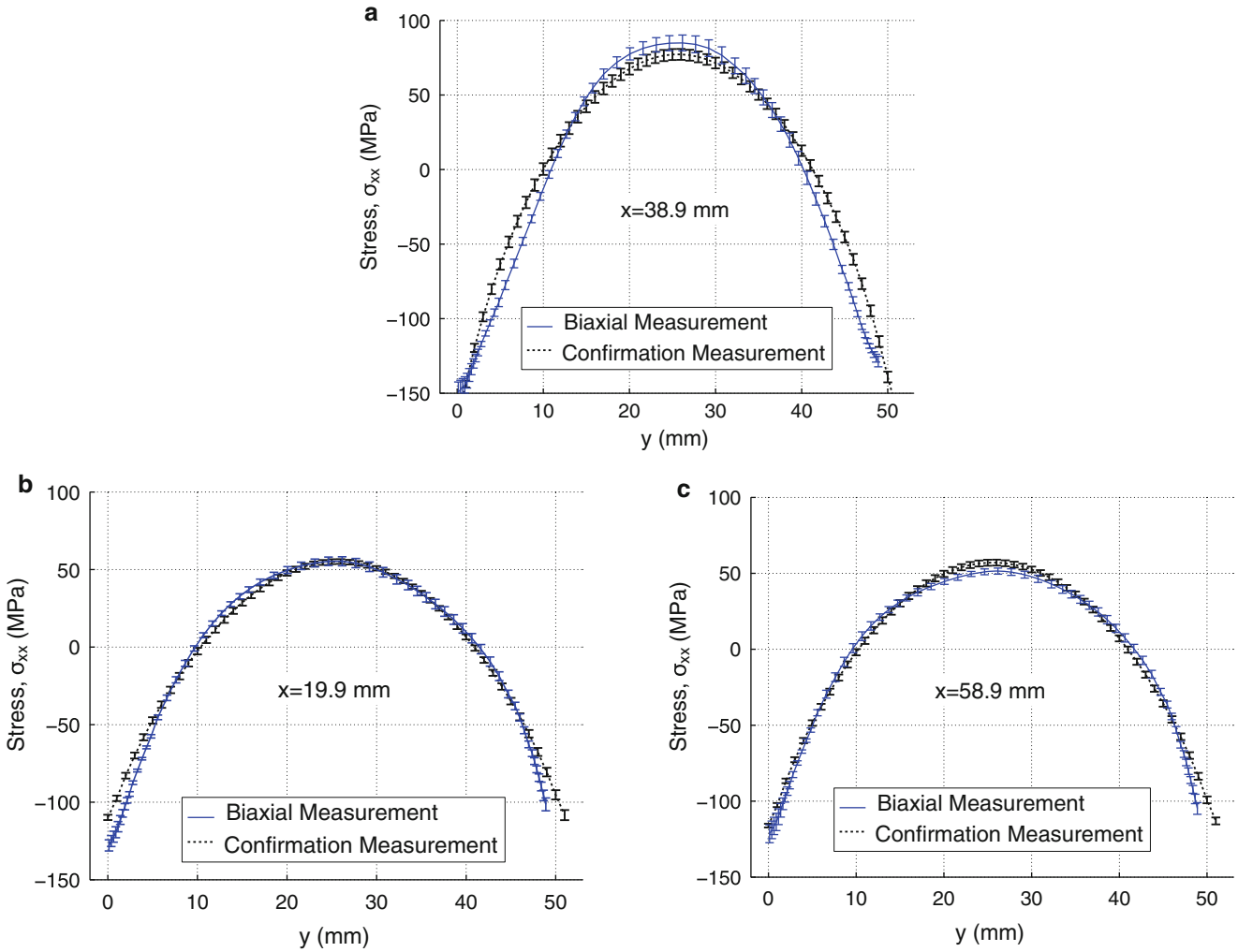

Fig. 40.10 Line plots comparing the biaxial measurement of the transverse stress and the confirmation measurement at x positions (**a**) 38.9 mm, (**b**) 19.9 mm, and (**c**) 58.9 mm

40.5 Summary

A biaxial residual stress mapping approach using mechanical stress release methods was described. The measurement consists of decomposing the initial residual stress into the stress remaining in a thin slice and the effect of the longitudinal stress on that slice. The longitudinal stress is found using the contour method. The effect of the longitudinal stress on a thin slice is found using a finite element computation. The transverse stress remaining in the slice is found using several slitting measurements.

Physical experiments were performed to find a biaxial map of longitudinal and transverse stress in a quenched aluminum bar. Both the longitudinal and transverse stresses were found to have a paraboloid distribution, with tensile stress in the center of the cross-section and compressive stress along the edges, which agrees with the residual stress field typical of quenching. The minimum and maximum of the longitudinal stresses are −153 and 157 MPa and of the transverse stress are −160 and 90 MPa.

The results of the biaxial mapping measurement were compared to confirmation measurements of the transverse stress at three planes. The good agreement with the confirmation measurements validates the biaxial mapping approach.

Acknowledgements The authors acknowledge financial support from the Electric Power Research Institute, Materials Reliability Program (Paul Crooker, Principal Technical Leader). The authors acknowledge helpful discussions with Adrian T. DeWald of Hill Engineering, LLC and Michael B. Prime of Los Alamos National Laboratory.

References

1. M.N. James, D.J. Hughes, Z. Chen, H. Lombard, D.G. Hattingh, D. Asquith et al., Residual stresses and fatigue performance. Eng. Fail. Anal. **14**, 384–395 (2007)
2. H. Luong, M.R. Hill, The effects of laser peening on high-cycle fatigue in 7085-T7651 aluminum alloy. Mater. Sci. Eng. A **477**, 208–216 (2008)
3. M. Mochizuki, Control of welding residual stress for ensuring integrity against fatigue and stress–corrosion cracking. Nucl. Eng. Des. **237**, 107–123 (2007)
4. R. Parrott, H. Pitts, Chloride stress corrosion cracking in austenitic stainless steel, Research Report RR902, Health and Safety Laboratory, 2011
5. J.I. Tani, M. Mayuzumi, T. Arai, N. Hara, Stress corrosion cracking growth rates of candidate canister materials for spent nuclear fuel storage in chloride-containing atmosphere. Mater. Trans. **48**, 1431–1437 (2007)
6. EPRI, Material reliability program crack growth rates for evaluating primary water stress corrosion cracking (PWSCC) of alloy 82, 182, and 132 Welds, MRP-115NP, Electric Power Research Institute, 2004
7. P.J. Withers, Residual stress and its role in failure. Rep. Prog. Phys. **70**, 2211–2264 (2007)
8. S.H. Bush, Failure mechanisms in nuclear power plant piping systems. J. Press. Vessel Technol. **114**, 389–395 (1992)
9. J. Mullins, J. Gunnars, *Validation of Weld Residual Stress Modeling in the NRC International Round Robin Study* (Swedish Radiation Safety Authority, Stockholm, 2013)
10. O. Muránsky, M.C. Smith, P.J. Bendeich, T.M. Holden, V. Luzin, R.V. Martins et al., Comprehensive numerical analysis of a three-pass bead-in-slot weld and its critical validation using neutron and synchrotron diffraction residual stress measurements. Int. J. Solids Struct. **49**, 1045–1062 (2012)
11. H.J. Rathbun, L.F. Fredette, P.M. Scott, A.A. Csontos, D.L. Rudland, NRC welding residual stress validation program international round robin program and findings, in *PVP2011-57642, 2011 ASME Pressure Vessels and Piping Division Conference*, Baltimore, MD, USA, 2011
12. EPRI, *Materials Reliability Program: Finite-Element Model Validation for Dissimilar Metal Butt-Welds (MRP-316)* (Electric Power Research Institute, Palo Alto, 2011)
13. H. Ou, J. Lan, C. Armstrong, M. Price, An FE simulation and optimisation approach for the forging of aeroengine components. J. Mater. Process. Technol. **151**, 208–216 (2004)
14. L. Zhang, X. Feng, Z. Li, C. Liu, FEM simulation and experimental study on the quenching residual stress of aluminum alloy 2024. Proc. Inst. Mech. Eng. B J. Eng. Manuf. **227**, 954–964 (2013)
15. M.T. Hutchings, P.J. Withers, T.M. Holden, T. Lorentzen, *Introduction to the Characterization of Residual Stress by Neutron Diffraction (Chapter 6)* (CRC Press, Boca Raton, 2005)
16. ASTM, *E837, Standard Test Method for Determining Residual Stresses by the Hole-Drilling Strain-Gage Method* (ASTM International, West Conshohocken, 2009)
17. M.B. Prime, Plasticity effects in incremental slitting measurement of residual stresses. Eng. Fract. Mech. **77**, 1552–1566 (2010)
18. A. Mahmoudi, S. Hossain, C. Truman, D. Smith, M. Pavier, A new procedure to measure near yield residual stresses using the deep hole drilling technique. Exp. Mech. **49**, 595–604 (2009)
19. P. Pagliaro, M.B. Prime, J.S. Robinson, B. Clausen, H. Swenson, M. Steinzig et al., Measuring inaccessible residual stresses using multiple methods and superposition. Exp. Mech. **51**, 1123–1134 (2010)
20. M.R. Hill, M.D. Olson, Biaxial residual stress mapping in a PWR dissimilar metal weld, in *PVP2013-97246, ASME 2013 Pressure Vessels and Piping Division Conference*, Paris, France, 2013
21. M.R. Hill, M.D. Olson, A.T. DeWald, Biaxial residual stress mapping for a dissimilar metal welded nozzle, in *PVP2014-28328, ASME 2014 Pressure Vessels and Piping Division Conference*, Anaheim, CA, USA, 2014
22. SAE Aerospace, Heat treatment of wrought aluminum alloy parts, AMS 2770, 2006
23. M.B. Prime, A.T. DeWald, *Practical Residual Stress Measurement Methods (Chapter 5)* (Wiley, West Sussex, 2013)
24. M.R. Hill, *Practical Residual Stress Measurement Methods (Chapter 4)* (Wiley, West Sussex, 2013)
25. M.B. Prime, Cross-sectional mapping of residual stresses by measuring the surface contour after a cut. J. Eng. Mater. Technol. **123**, 162–168 (2001)
26. E.M. Shaw, P.P. Lynn, Areal rainfall evaluation using two surface fitting techniques. Hydrol. Sci. Bull. **17**, 419–433 (1972)
27. M.B. Prime, Residual stress measurement by successive extension of a slot: the crack compliance method. Appl. Mech. Rev. **52**, 75–96 (1999)
28. G.S. Schajer, M.B. Prime, Use of inverse solutions for residual stress measurement. J. Eng. Mater. Technol. **128**, 375–382 (2006)
29. M.J. Lee, M.R. Hill, Effect of strain gage length when determining residual stress by slitting. J. Eng. Mater. Technol. **129**, 143–150 (2007)
30. C.C. Aydıner, M.B. Prime, Three-dimensional constraint effects on the slitting method for measuring residual stress. J. Eng. Mater. Technol. **135**(3), 031006 (2013)
31. M.D. Olson, M.R. Hill, Residual stress mapping with slitting. Exp. Mech. (2014 manuscript in preparation for publication)
32. J.S. Robinson, D.A. Tanner, C.E. Truman, A.M. Paradowska, R.C. Wimpory, The influence of quench sensitivity on residual stresses in the aluminium alloys 7010 and 7075. Mater. Charact. **65**, 73–85 (2012)
33. M.D. Olson, M.R. Hill, V.I. Patel, O. Muránsky, T. Sisneros, Measured biaxial residual stress maps in a stainless steel weld. J. Nucl. Eng. Radiat. Sci. (2015 accepted for publication)
34. M.D. Olson, M.R. Hill, B. Clausen, M. Steinzig, T.M. Holden, Residual stress measurements in dissimilar weld metal. Exp. Mech. **55**(6), 1093–1103 (2015)
35. A.T. DeWald, M.R. Hill, Repeatability of incremental hole drilling and slitting method residual stress measurements. Residual Stress Thermomech. Infrared Imag. Hybrid Tech. Inverse Probl. **8**, 113–118 (2014)
36. M.D. Olson, M.R. Hill, A new mechanical method for biaxial residual stress mapping. Exp. Mech. **55**, 1139–1150 (2015)
37. M.J. Lee, M.R. Hill, Intralaboratory repeatability of residual stress determined by the slitting method. Exp. Mech. **47**, 745–752 (2007)
38. M.B. Prime, M.R. Hill, Uncertainty, model error, and order selection for series-expanded, residual-stress inverse solutions. J. Eng. Mater. Technol. **128**, 175 (2006)
39. M.R. Hill, M.D. Olson, Repeatability of the contour method for residual stress measurement. Exp. Mech. **54**, 1269–1277 (2014)

Chapter 41
Measurement of Residual Stresses in B_4C-SiC-Si Ceramics Using Raman Spectroscopy

Phillip Jannotti and Ghatu Subhash

Abstract Processing-induced residual stresses in reaction bonded B_4C-SiC-Si ceramic composites were investigated using Raman peak shift measurements. The measured stresses in the residual silicon phase were compared with classical formulation which predicts stress development due to thermal mismatch between a particle and the surrounding matrix. It was found that the residual stress does not remain uniform in a given particle as predicted in the classical formulation. The two methods matched at the boundary between the particle and the matrix, but varied drastically both in magnitude and nature in the interior of the particle. This variation became more dramatic when the particle was of irregular shape with high aspect ratio.

Keywords Reaction bonded • B4C • Raman spectroscopy • Thermal mismatch • Residual stress

41.1 Introduction

Boron carbide ceramics are prime candidates for structural applications where strength and weight are desired properties. However, typical methods of processing (e.g., hot pressing or pressureless sintering) are limited in their ability to produce complex, near-net shape components. Reaction bonding is an alternative to traditional sintering methods, which offers a relatively low temperature (1410 °C) means of producing intricate parts with minimal final shaping [1]. For example, one-piece helicopter seats can be made rather than the traditional methods of using mosaic tiles to construct the ceramic seat (see Fig. 41.1).

In reaction bonding, a ceramic powder compact (e.g., B_4C), called a preform, is placed into a vacuum furnace with silicon (Si) lumps. As the temperature is raised above the melting point of Si (1410 °C), the molten Si infiltrates the porous ceramic preform. The Si reacts with a carbon (C) source in the preform (free C or B_4C) to form silicon carbide (SiC) which bonds the microstructure together; hence the name reaction bonding. When the C source is B_4C, both SiC and an Si-doped B_4C phase evolve [3]. The final B_4C ceramic produced is fully-dense and is primarily composed of B_4C, SiC, and some residual Si. Due to differences in thermo-mechanical properties between all of the phases, there is potential for residual stress generation. As Si is the weakest mechanical constituent phase, it is of significant interest to determine whether residual microstresses develop due to processing. More importantly, the spatial distribution is of profound concern.

Little is known regarding the effects of the reaction bonding process on the development of residual stresses due to thermal mismatch [3, 4], especially in the residual Si regions. Jannotti and Subhash [4] used Raman spectroscopic point scans to verify the appearance of peak shifting in the residual Si regions which suggested the development of beneficial residual compressive stresses. However, the influence of Si region shape and size on the resulting residual stress field remains unclear. This information is critically relevant as the development of residual compressive stresses in reaction bonded boron carbides has been proposed to enhance the mechanical performance leading to improved utility for nominally brittle ceramics [5, 6]. In the current study, micro-Raman spectroscopy was utilized to analyze the spatial evolution of thermal microstresses in the residual Si phase of reaction bonded B_4C-SiC-Si ceramics.

P. Jannotti • G. Subhash (✉)
Mechanical and Aerospace Engineering, University of Florida, Gainesville, FL 32611, USA
e-mail: subhash@ufl.edu

S. Bossuyt et al. (eds.), *Residual Stress, Thermomechanics & Infrared Imaging, Hybrid Techniques and Inverse Problems, Volume 9*, Conference Proceedings of the Society for Experimental Mechanics Series, DOI 10.1007/978-3-319-21765-9_41

Fig. 41.1 One-piece ceramic helicopter seat produced by reaction bonding [2]

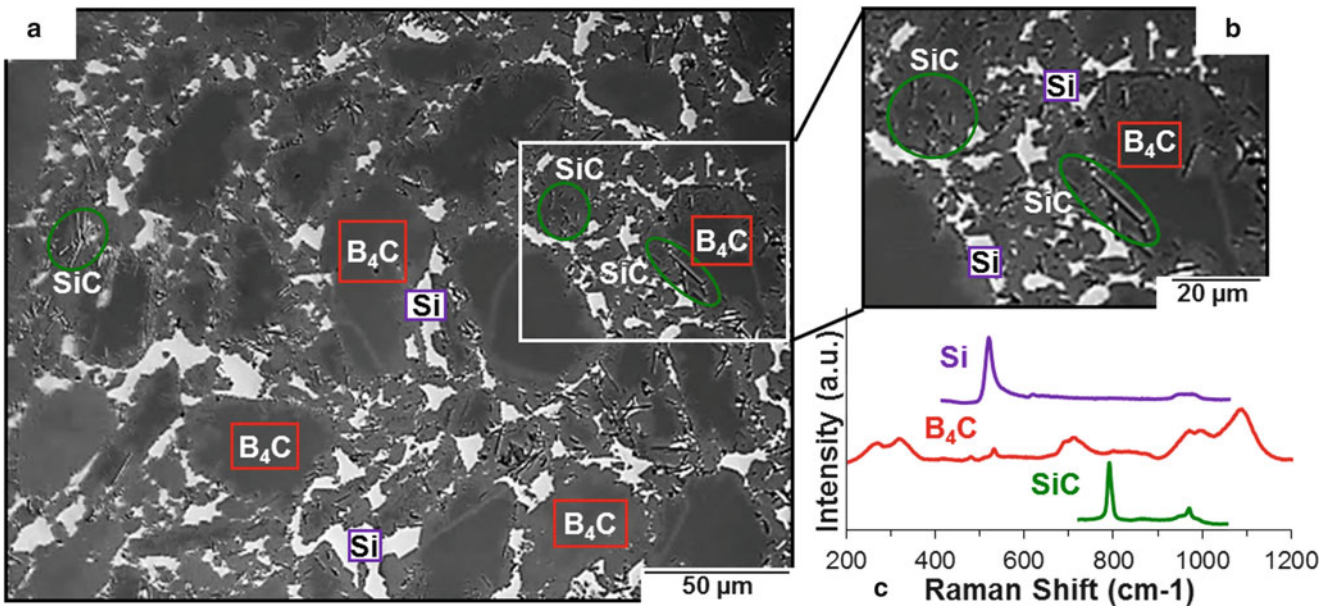

Fig. 41.2 (**a**) A typical microstructure of a reaction bonded B_4C-SiC-Si, (**b**) an enlarged micrograph, and (**c**) characteristic Raman peaks associated with each constituent phase

41.2 Materials

A reaction bonded B_4C-SiC-Si ceramics was provided by M-Cubed Technologies (Trumbull, CT, USA). Exact details of the manufacturing process are proprietary and were not disclosed. The final ceramic composition was determined by the manufacturer using quantitative X-ray diffraction (XRD): 75 % B_4C, 8 % SiC and 17 % residual Si. Sample surfaces were polished using standard ceramographic procedures up to a final polishing step with 1 µm diamond. Figure 41.2a, b shows a representative micrograph of a reaction bonded boron carbide ceramic. The various constituent phases (B_4C, SiC and Si) have been identified by Raman spectroscopy based on their characteristic peaks as shown in Fig. 41.2c.

Due to the differences in thermo-mechanical properties of the various ceramic phases in reaction bonded ceramics, thermal mismatch stresses are expected to develop during cooling from the processing temperature (ΔT). Although

Table 41.1 Selected properties of B_4C, SiC, and Si

Property	B_4C	SiC	Si
Elastic modulus, E (GPa)	450 [1]	450 [13]	160 [13]
Poisson's ratio, ν	0.17 [1]	0.14 [13]	0.22 [13]
CTE, α (10^{-6}/°C)	6.0 [4]	4.8 [4]	3.7 [4]

mismatch stresses are likely present in all of the phases, the residual Si phase is of particular interest given that it is the weakest mechanical phase in the composite. It is also one of the most widely characterized materials by Raman spectroscopy [4, 7–11]. Selected material properties which are used in computing the predicted residual stress magnitude are given in Table 41.1. Most importantly, the coefficients of thermal expansion (α), or CTE, for B_4C, SiC, and Si are approximately 6.0, 4.8, and 3.7 $\times$ 10^{-6}/°C [12], respectively. In the Si phase, the primary mismatch occurs between the B_4C and Si phases. Because the CTE of SiC and Si are much closer, less thermal mismatch effect is expected between these two phases. Additional properties used in determining the residual stress magnitude developed by thermal misfit are the elastic modulus (E) and Poison's ratio (ν).

Assuming a spherical Si region, or particle (p), surrounded by a carbide matrix (m), the level of equibiaxial residual stress (σ) in the Si regions can be approximated using the following equation [14],

$$\sigma = \frac{\Delta\alpha \cdot \Delta T}{\left[\frac{0.5(1+\nu_m)+f_p(1-2\nu_m)}{E_m(1-f_p)} + \frac{1-2\nu_p}{E_p}\right]} \tag{41.1}$$

where the stress (σ) is a function of the elastic properties listed in Table 41.1 and the volume fraction of Si particle phase (f_p). For B_4C-Si and SiC-Si mismatch, the predicted mismatch stresses developed are −589 and −127 MPa (i.e., compression), respectively. Taking a weighted average of the thermal stresses based on relative fraction of the carbide phases, −545 MPa of residual compression is expected to develop uniformly over all Si regions. However, Si particle size and shape characteristics are anticipated to lead to non-uniformities in the stresses developed.

41.3 Experimental

Raman spectroscopy was used to characterize the thermal stress development in the residual Si phase of the reaction bonded ceramic. A Raman spectrometer (Renishaw InVia model, Hoffman Estates, IL, USA) equipped with a 532 nm (green) laser rated at 100 mW total power was used. All scans were acquired at 10 % laser power to maximize signal intensity while minimizing any effects of laser heating of the sample. Prior to each set of scans, the Raman system was calibrated using the Si standard. Scan variability for chosen test parameters has been verified to be as low as 0.02 cm^{-1}.

Raman peak position was used to determine the presence of peak shifts away from the stress-free crystalline Si peak position of 520 cm^{-1}, which is indicative of the induced stress state [15]. Fundamental relationships relating the Raman peak shift in Si to a corresponding value of residual stress have been well-established in literature [7–9]. Assuming an equibiaxial stress state, the observed peak shift can be related to residual stress in Si as follows [9],

$$\sigma_X = \sigma_y = -250\Delta w \tag{41.2}$$

where peak shifts to higher wavenumbers ($+\Delta w$) indicate residual compressive stress, while shifts to lower wavenumbers ($-\Delta w$) are indicative of residual tensile stresses.

41.4 Results and Discussion

The measured residual stresses and spatial distributions in the residual Si phase were compared with classical formulation which utilizes elastic properties and thermal mismatch between a particle and the surrounding matrix. A representative Raman map of a selected Si region is shown in Fig. 41.3, which illustrates the variability in both stress uniformity and magnitude of thermal stresses developed. It was observed that the residual thermal stress does not remain uniform in a given

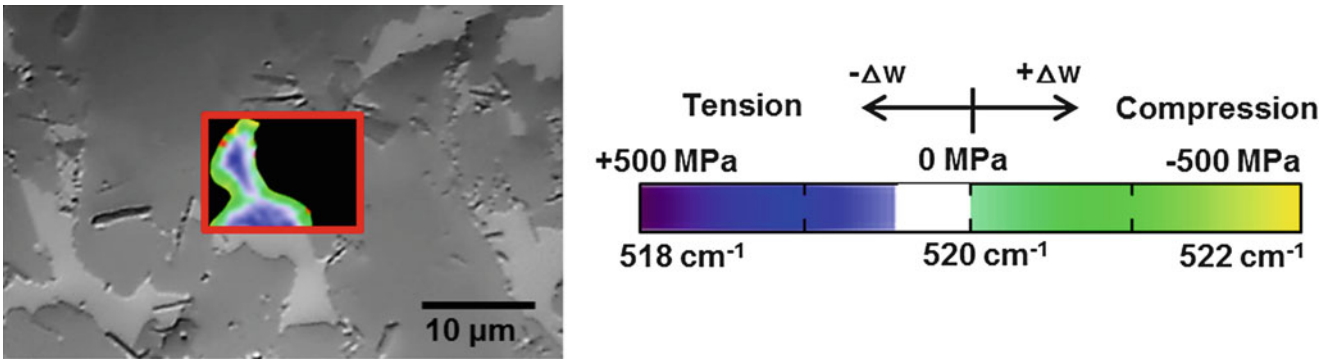

Fig. 41.3 Raman stress map of the residual Si phase of a reaction bonded B_4C-SiC-Si ceramic. The *map legend* denotes the color-coding according to the residual stress state based on peak position of the "silicon" peak

Si particle as predicted by classical formulation. Instead, it varies over the Si region. In fact, the presence of residual tensile stresses in the center of the Si region was observed, which was not predicted by classical formulation. However, the perimeter of the Si region remained in compression (as expected). The level of compression at the Si perimeter reached up to almost −500 MPa, compared to the predicted compression of −545 MPa. Stress non-uniformity was also seen to become more pronounced for high-aspect ratio and irregularly-shaped regions.

The implications of these results on material performance are of paramount importance and are likely to play a vital role in the utility of such ceramics in a particular application. Given that the performance of reaction bonded ceramics has been proposed to exhibit a direct link to the residual compression developed within the Si region, future studies aimed at correlating the residual stresses with the mechanical properties such as strength, hardness, etc. must be performed.

41.5 Conclusion

Based on the predicted and experimental Raman results, the two methods only match at the boundary between the Si region and the carbide matrix, but vary widely in magnitude and stress state in the interior of the particle. Stress non-uniformity becomes even more dramatic when the particle is of irregular shape with high aspect ratio.

Acknowledgements The authors would like to thank M-Cubed Technologies (a II–VI subsidiary) for providing the materials examined and for the insightful discussions during the study. Financial support from the National Defense Science and Engineering Graduate (NDSEG) Fellowship program provided to Phillip Jannotti is also gratefully acknowledged. This research was made with Government support under and awarded by DOD, AirForce Office of Scientific Research, NDSEG, 32 CFR 168a.

References

1. P.G. Karandikar, G. Evans, S. Wong, M.K. Aghajanian, M. Sennett, A review of ceramics for armor applications, in *Advances in Ceramic Armor IV: Ceramic Engineering and Science Proceedings*, vol. 29, issue 6 (Wiley, Hoboken, 2009), pp. 163–175
2. M-Cubed Technologies. http://www.mmmt.com/resources/b4c.html. Accessed 20 Feb 2015
3. P. Jannotti, G. Subhash, J.Q. Zheng et al., Raman spectroscopic characterization of the core-rim structure in reaction bonded boron carbide ceramics. Appl. Phys. Lett. **106**, 041903 (2015)
4. P. Jannotti, G. Subhash, B. Song, D. Casem, Micro-Raman spectroscopic evaluation of residual microstresses in reaction bonded boron carbide ceramics, in *Dynamic Behavior of Materials*, ed. by J. Kimberley, vol. 1 (Springer, New York, 2015), pp. 39–43
5. M.K. Aghajanian, Toughness enhanced silicon-containing composite bodies, and methods for making same, US Patent 6,995,103, 2006
6. M.K. Aghajanian, B.N. Morgan, J.R. Singh, J. Mears, R.A. Wolffe, A new family of reaction bonded ceramics for armor applications, in *Ceramic Materials By Design*, ed. by J.W. McCauley, A. Crowson, W.A. Gooch Jr. et al. (American Ceramic Society, Westerville, 2002), pp. 527–540
7. S. Ganesan, A.A. Maradudin, J. Oitmaa, A lattice theory of morphic effects in crystals of the diamond structure. Ann. Phys. **56**, 556–594 (1970)
8. E. Anastassakis, A. Pinczuk, E. Burstein, F.H. Pollak, M. Cardona, Effect of static uniaxial stress on the Raman spectrum of silicon. Solid State Commun. **8**, 133–138 (1970)

9. I.D. Wolf, Micro-Raman spectroscopy to study local mechanical stress in silicon integrated circuits. Semicond. Sci. Technol. **11**, 139–154 (1996)
10. V. Srikar, A.K. Swan, M.S. Unlu, B.B. Goldberg, S.M. Spearing, Micro-Raman measurement of bending stresses in micromachined silicon flexures. J. Microelectromech. Syst. **12**, 779–787 (2003)
11. S. Ryu, Q. Zhao, M. Hecker et al., Micro-Raman spectroscopy and analysis of near-surface stresses in silicon around through-silicon vias for three-dimensional interconnects. J. Appl. Phys. **111**, 063513 (2012)
12. Purdue University, Thermophysical Properties Research Center. Thermal expansion—non-metallic solids, in *Thermophysical Properties of Matter—The TPRC Data Series*, ed. by Y.S. Touloukian, R.K. Kirby, E.R. Taylor, T.Y.R. Lee (IFI/Plenum, New York, 1977)
13. W.N. Sharpe Jr., W.N. Sharpe, *Springer Handbook of Experimental Solid Mechanics* (Springer, New York, 2008)
14. K.K. Chawla, *Ceramic Matrix Composites* (Kluwer Academic, Boston, 2003)
15. A. Tiberj, J. Camassel, Raman imaging in semiconductor physics: applications to microelectronic materials and devices. Raman Imaging **168**, 39–83 (2012)

Chapter 42
Hole Drilling Determination of Residual Stresses Varying Along a Surface

Alberto Makino and Drew Nelson

Abstract Hole drilling is a widely applied method for determining residual stresses. In numerous cases of practical interest, residual stresses vary significantly along the surface at a location to be drilled. Previous efforts to use strain gages to determine stresses in such cases are briefly reviewed. A computational approach is presented for determining two orthogonal stresses and their surface gradients at a location where stresses can be considered approximately uniform with depth of a drilled hole. The approach is designed for use with optical methods instead of strain gages. Optical interference fringe patterns obtained by holographic interferometry are shown for holes drilled into the side of a beam experiencing elastic bending stresses and associated gradient. Stresses and a gradient determined from fringe patterns are compared with expected values.

Keywords Hole-drilling • Residual stress • Optical • Gradient • Interferometric

42.1 Introduction

The hole drilling method is a well-established method for determining residual stresses [1, 2]. The method is typically applied with the assumption that stresses do not vary significantly along the surface (or planes parallel to the surface) at a location to be drilled. In some cases, residual stresses vary significantly over relatively small distances. Examples include residual stresses near welds or cold-expanded fastener holes, as illustrated in Fig. 42.1.

In 1969 and 1984 respectively, Cordiano and Salerno [5] and Kabiri [6] presented expressions relating stresses in two orthogonal directions and their gradients to radial strains from drilling a single hole at a location of interest. Special rosettes with five or more strain sensing elements were used. Their expressions were based on theoretical relations for stresses in a thin sheet with a through hole. In 1978, Nawwar and Shewchuck [7] investigated how residual stress varied with location from the boundary of an edge-dimpled thin sheet by drilling multiple holes inwards starting near the boundary. In 1991, Nicoletto [8] also used multiple hole drilling to determine how stresses varied along the surface as depicted in Fig. 42.2.

The purpose of this paper is to present an approach for determining the magnitude of two orthogonal stresses and their gradients at a location where the blind hole drilling method is to be applied. The approach relates in-plane and out-of-plane surface displacements from hole drilling to stresses and gradients and is intended for use with interferometric optical approaches or digital image correlation.

Reasons for interest in this capability include the following. (1) When strong surface gradients in stress are expected, the accuracy of hole drilling results may be improved by taking into account the effect of gradients in determining the magnitude of stresses. (2) To find distributions like those in Figs. 42.1 and 42.2, the number of holes needed (and associated time and costs) could potentially be lessened by an approach that makes use of both stress and gradient information from each hole vs. stress alone. (3) At locations where stresses change from compressive to tensile or vice versa, stress magnitudes are minimal, and finding surface stress gradients by hole drilling could provide useful information.

A. Makino
NASA Ames Research Center, Mountain View, CA 94035, USA

Mechanical Engineering Department, Stanford University, Stanford, CA 94305, USA

D. Nelson (✉)
Mechanical Engineering Department, Stanford University, Stanford, CA 94305, USA
e-mail: dnelson@stanford.edu

S. Bossuyt et al. (eds.), *Residual Stress, Thermomechanics & Infrared Imaging, Hybrid Techniques and Inverse Problems, Volume 9*, Conference Proceedings of the Society for Experimental Mechanics Series, DOI 10.1007/978-3-319-21765-9_42

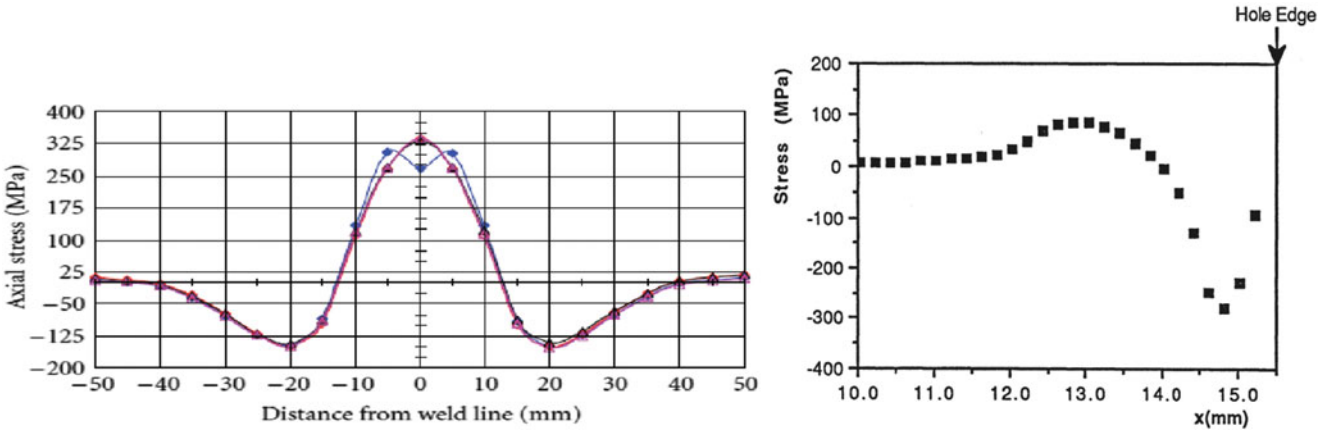

Fig. 42.1 Residual stress gradients near a weld [3] and a cold-worked fastener hole [4]

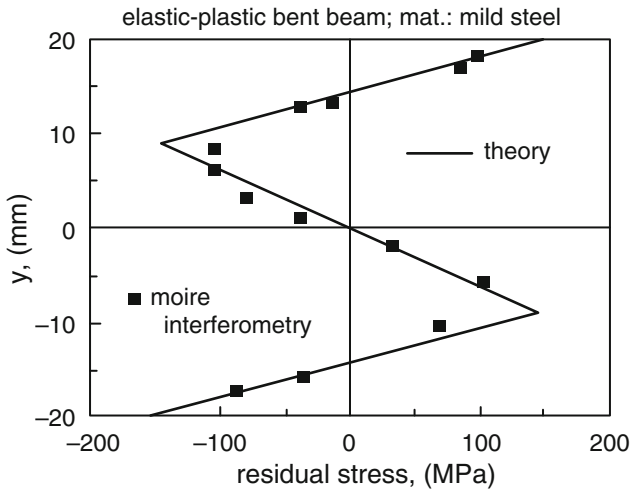

Fig. 42.2 Residual stress variation across a beam from elastic-plastic bending [8]

42.2 Displacements from Hole Drilling

Referring to Fig. 42.3, the surface displacements from drilling a blind hole in the presence of two linear gradients will be approximated by

$$u_r = L_1 \sum u_{rn} \sin n\theta \tag{42.1a}$$

L_1 = stress gradient (MPa/mm)

$$u_\theta = L_1 \sum u_{\theta n} \cos n\theta \tag{42.1b}$$

r, θ, z = cylindrical coordinates

$$u_z = L_1 \sum u_{zn} \sin n\theta \tag{42.1c}$$

u_{rn}, $u_{\theta n}$, u_{zn} = expansion coefficients

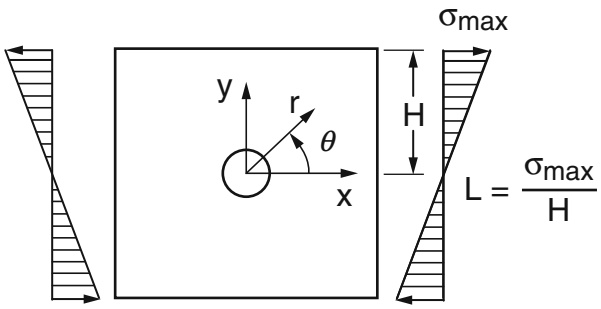

Fig. 42.3 Stress gradients in two orthogonal directions

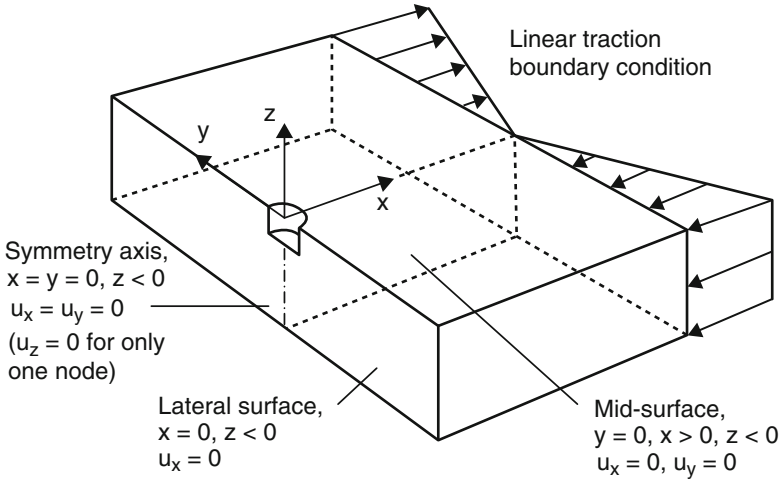

Fig. 42.4 Traction and displacement boundary conditions for finite element model

Based on the form of a plane stress solution (through hole in thin plate) for displacements, (42.1a), (42.1b) and (42.1c) will be applied by taking n = 1 and 3, giving

$$u_r = (A_L \sin\theta + B_L \sin 3\theta)L_1 \tag{42.2a}$$

$$u_\theta = (C_L \cos\theta + D_L \cos 3\theta)L_1 \tag{42.2b}$$

$$u_z = (F_L \sin\theta + G_L \sin 3\theta)L_1 \tag{42.2c}$$

Isotropic, linear elastic material behavior will be assumed. Coefficients A_L to G_L for a given radial position, r, were obtained from a three-dimensional finite element model depicted in Fig. 42.4 by applying a gradient and de-activating elements to represent material removed by hole drilling. Nodal displacements for various constant values of r and three angles (e.g., $\theta = 0°$, 30° and 60°) were used with (42.2a), (42.2b) and (42.2c) to find the coefficients. In general, A_L to G_L will depend on modulus of elasticity E, Poisson's ratio ν, hole radius r_o, radial location r and normalized hole depth (h/D). They can be made independent of hole diameter and the elastic constants by defining the following non-dimensional coefficients:

$$\begin{aligned} a_L &= 8EA_L/(1-\nu)(r_0)^2 \quad b_L = 8EB_L/(r_0)^2 \quad c_L = 8EC_L/(1-\nu)(r_0)^2 \\ d_L &= 8ED_L/(r_0)^2 \qquad\qquad f_L = 8EF_L/(r_0)^2 \quad g_L = 8EG_L/2\nu(r_0)^2 \end{aligned} \tag{42.3}$$

A sample of non-dimensional coefficients is given in Table 42.1 for stresses uniform with depth.

The development of the coefficients assumed a Poisson ratio $\nu = 0.3$. Modeling using values of 0.25 and 0.35 revealed a weak dependence on ν.

Table 42.1 Non-dimensional coefficients as a function of radial location (r/r_0) for a hole drilled to a depth of h/D = 1.2, where D is hole diameter and h is depth

r/r_o	a_L	b_L	c_L	d_L	f_L	g_L
1.0	1.0029	2.4029	−0.9556	2.0138	0.1402	1.4969
2.0	0.2719	1.0412	−0.2573	−0.0035	0.1125	0.4825

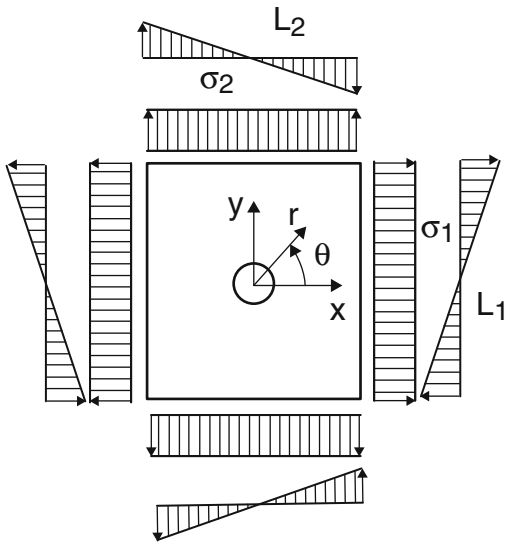

Fig. 42.5 Combined uniform stresses and gradients

By applying the superposition principle, expressions for displacements for two orthogonal gradients L_1 and L_2 in Fig. 42.5 are

$$u_r = (A_L \sin\theta + B_L \sin 3\theta)L_1 + (A_L \cos\theta - B_L \sin 3\theta)L_2 \tag{42.4a}$$

$$u_\theta = (C_L \cos\theta + D_L \cos 3\theta)L_1 + (-C_L \sin\theta + D_L \sin 3\theta)L_2 \tag{42.4b}$$

$$u_z = (F_L \sin\theta + G_L \sin 3\theta)L_1 + (F_L \cos\theta - G_L \cos 3\theta)L_2 \tag{42.4c}$$

Referring to Fig. 42.5, the displacements from the release of uniform principal stress components σ_1 and σ_2 by hole drilling are given by [9, 10]

$$u_r = (A + B\cos 2\theta)\sigma_1 + (A - B\cos 2\theta)\sigma_2 \tag{42.5a}$$

$$u_\theta = C(\sigma_1 - \sigma_2) \tag{42.5b}$$

$$u_z = (F + G\cos 2\theta)\sigma_1 + (F - G\cos 2\theta)\sigma_2 \tag{42.5c}$$

where coefficients A through B are functions of (r/r_o) and can be computed from available non-dimensional coefficients [9, 10] that are similar to but somewhat different in form than A_L to G_L. In Fig. 42.5, stress gradients are assumed to act along principal directions.

Strictly speaking, equilibrium relations are not satisfied unless a non-uniform shear traction distributions are imposed. However, such shear tractions can be neglected as a reasonable first approximation, as also suggested by Kabiri [6].

42.3 Phase-Displacement-Stress Relations

If a hologram is made of a location of interest, and a hole drilled there, the resulting displacements from stress release will generate optical interference fringes in real time that represent optical phase shifts. The shifts $\varphi(r, \theta)$ can be related to surface displacements expressed in Cartesian coordinates by [9, 10]

$$\varphi(r,\theta) = K_x(r,\theta)u_x(r,\theta) + K_y(r,\theta)u_y(r,\theta) + K_z(r,\theta)u_z(r,\theta) \tag{42.6}$$

where $K_x = (2\pi/\lambda)\cos\gamma_1\cos\zeta$, $K_y = (2\pi/\lambda)\cos\gamma_1\sin\zeta$, $K_z = (2\pi/\lambda)(1 + \sin\gamma_1)$, λ = laser light wavelength, γ_1 = angle between illumination direction and surface (x-y) plane and ζ = angle between illumination direction and σ_1. From relations between Cartesian and cylindrical displacements, phase shifts on the right hand side of a hole can be expressed in terms of fringe order n by [9, 10]

$$\pi n = \left(K_x\cos\theta + K_y\sin\theta\right)u_r + \left(-K_x\sin\theta + K_y\cos\theta\right)u_\theta + K_z u_z \tag{42.7}$$

Substitution into (42.7) of displacements from (42.4a), (42.4b) and (42.4c) superposed with those from (42.5a), (42.5b) and (42.5c) provides relations between stresses, gradients and resulting phase shifts.

42.4 Experiments

To explore this approach experimentally, a stress relieved aluminum 7075-T651 beam of 0.762 mm thickness was loaded elastically in four point bending to a maximum bending stress of 412 MPa, giving a gradient of 108 MPa/mm. A hologram was made, then holes were drilled in the side of the beam on the neutral axis as well as at locations offset towards the top or bottom of the beam to produce combinations of stress with a gradient. Hole diameters were 1.58 mm and depths were 1.9 mm. Hole centers were kept at a distance of 1.5 times hole diameter from the top or bottom of the beam to minimize edge effects on displacements, in accordance with a guideline proposed by Nawwar and Shewchuk [7].

A sample of fringe patterns for a hole drilled on the neutral axis and offset from the neutral axis are shown in Fig. 42.6 for $\zeta = 0$ and an illumination angle of $\gamma_1 = 45°$.

Numerous ways could be used to determine stresses and gradients from fringe patterns. One way is to select a value of (r/r_o) such as 2, and determine the angles θ where a circle of that radius intersects different fringes of order n. Knowledge of order n and corresponding θ values for different fringes provides a system of equations resulting from (42.7) along with (42.4a), (42.4b), (42.4c), (42.5a), (42.5b) and (42.5c) that can be solved for unknowns σ_1, σ_2, L_1 and L_2. For instance, consider the right hand side of the pattern in Fig. 42.6a, which is from a stress gradient only. The top fringe has $n = 1$, and the bottom one $n = -1$, as was determined by introducing a temporary phase shift and observing the direction of fringe movement. Using four values of θ, plus coefficients A to G and A_L to G_L for $(r/r_o) = 1$, gives a solution of $L_1 = 118$ MPa/mm, $L_2 = 0.7$ MPa/mm, $\sigma_1 = -6$ MPa, and $\sigma_2 = 12$ MPa. The actual L_1 was 108 MPa/mm with $L_2 = \sigma_1 = \sigma_2 = 0$. The system of equations to be solved can utilize more n and θ values than unknowns to enable a least squares solution.

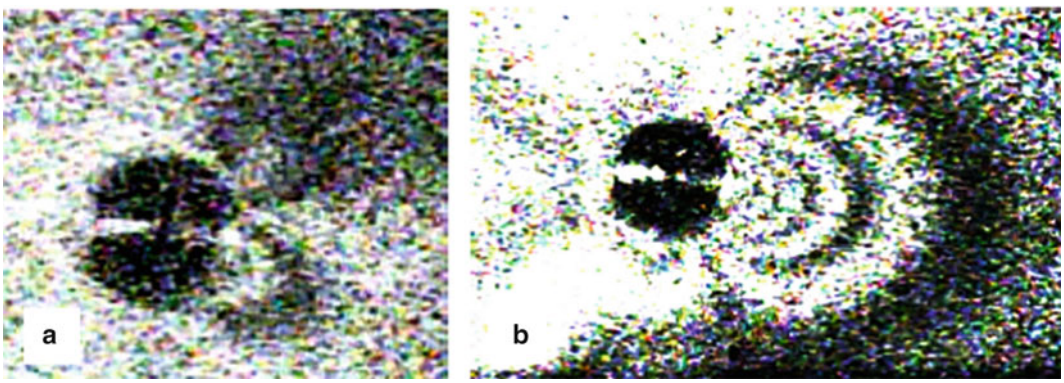

Fig. 42.6 Fringe pattern for (**a**) stress gradient of 108 MPa/mm and (**b**) a stress of 77 MPa and the same gradient

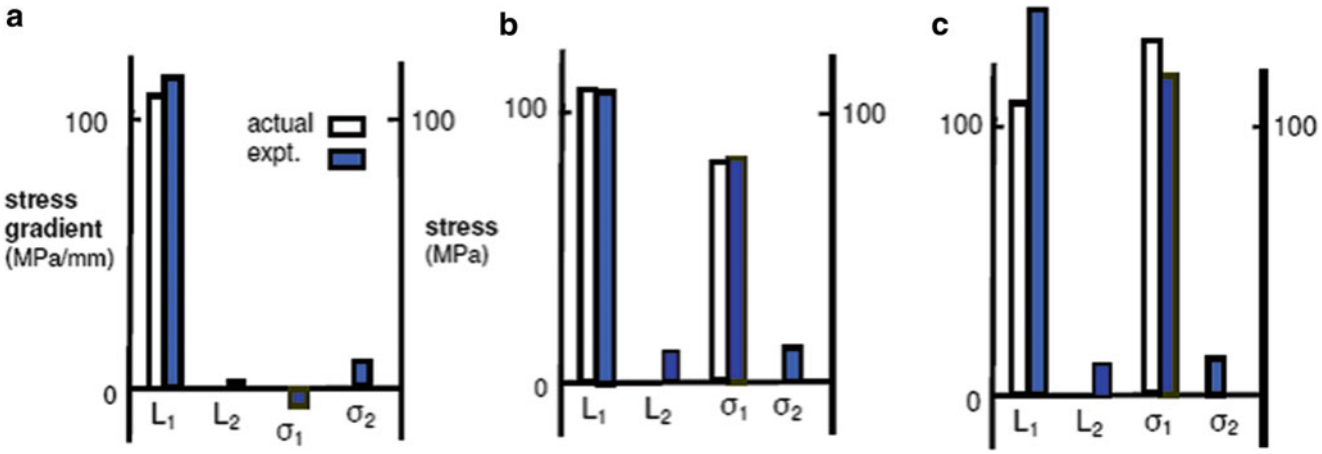

Fig. 42.7 Comparison of experimentally determined stresses and a gradient with actual values for (**a**) a gradient L_1 of 108 MPa/mm only, (**b**) stress $\sigma_1 = 77$ MPa with the same gradient and (**c**) stress $\sigma_1 = 130$ MPa with the same gradient. (Note that actual $\sigma_2 = L_2 = 0$)

The approach for determining stresses and gradients was applied to fringe patterns such as that in Fig. 42.6b resulting from a combination of uniform stress with a stress gradient. Values of stress σ_1 and gradient L_1 determined by this approach are compared with actual values in Fig. 42.7b, c. The results in Fig. 42.7a are those for the gradient alone, as described above. For Fig. 42.7b, (r/r_o) values of 1 and 2 and eight angles θ were used, while for Fig. 42.7c, nine angles were used.

The comparisons shown in Fig. 42.7 are favorable, especially considering that results were obtained with a relatively few number of input data points (i.e., angles θ). Other approaches for making use of the information contained in fringe patterns may well be more suitable.

42.5 Discussion

The magnitude of the stress gradient used in these experiments was in the range of those typically encountered in practice. It would be of interest, of course, to check the methodology presented here using gradients of other magnitudes. It would also be worth checking the accuracy of the method with a specimen and loading that could produce two orthogonal, well-characterized stresses and corresponding gradients. Having mentioned that, it should be noted that stresses acting in one direction with a corresponding gradient are often dominant, as in Figs. 42.1 and 42.2.

The methodology in this paper was explored with experiments in which the illumination direction of laser light was aligned with principal stress σ_1. For situations in which the directions of principal stresses are unknown in advance, the methodology could still be applied by replacing angle θ with $(\theta + \beta)$ in (42.4a), (42.4b), (42.4c), (42.5a), (42.5b) and (42.5c), where β is an angle between σ_1 and the illumination direction (x-direction here) that could be found, in principle, from the data contained in fringe patterns.

Although experimental data in this paper were obtained by holographic interferometry, it should be noted again that the methodology should be applicable with other interferometric methods, or with digital image correlation, which could bypass the need for fringe patterns if its displacement sensitivity is sufficient.

The approach given here is limited to cases where localized elastic-plastic deformation at a hole does not invalidate assumed linear elastic behavior and where material behavior can be considered isotropic.

In many cases, residual stresses will vary both along the surface and in depth simultaneously. A method for determining stress in such situations would certainly be worthwhile, but could be challenging to develop in a generalized form.

The methodology presented here was applied experimentally using a hole depth, h, slightly greater than diameter, D, for stress uniform with depth. Use of coefficients A to G and A_L to G_L in (42.4a), (42.4b), (42.4c), (42.5a), (42.5b) and (42.5c) developed for lower h/D ratios could make the assumption of stress constant with hole depth more likely to be a reasonable approximation in various cases of practical interest.

42.6 Conclusions

For situations in which residual stresses vary significantly along the surface at a location, a displacement-based methodology for determining two orthogonal stresses and their corresponding stress gradients by drilling a single hole has been derived, intended for use with interferometric optical methods or digital image correlation.

Initial experiments applying the methodology to find the magnitude of uniaxial stress, plus a surface stress gradient, have provided encouraging results.

References

1. G. Schajer, P. Whitehead, Hole drilling and ring coring, in *Practical Residual Stress Measurement Methods*, ed. by G. Schajer (Wiley, New York, 2013), pp. 29–64
2. E837-08, Standard test method for determining residual stresses by the hole-drilling strain-gage method (American Society for Testing and Materials, West Conshohocken, 2008)
3. E. Quereshi, A. Malik, N. Dar, Residual stress fields due to varying tack weld orientation in circumferentially welded thin-walled cylinders. Adv. Eng. **2009**, 351369 (2009). doi: 10.1155/2009/351369
4. L. Edwards, T. Ozdemir, Residual stresses at cold expanded fastener holes, in *Measurement of Residual and Applied Stresses Using Neutron Diffraction*, ed. by M.T. Hutchings, A.D. Krawitz (Kluwer Academic Publishers, Dordrecht, 1992), pp. 545–553
5. H. Cordiano, V. Salerno, Study of residual stresses in linearly varying biaxial-stress fields. Exp. Mech. **9**, 17–24 (1969)
6. M. Kabiri, Nonuniform residual-stress measurement by hole-drilling method. Exp. Mech. **24**, 326–336 (1984)
7. A. Nawwar, J. Shewchuk, On the measurement of residual-stress gradients in aluminum-alloy specimens. Exp. Mech. **18**, 269–276 (1978)
8. G. Nicoletto, Moire interferometry determination of residual stresses in the presence of gradients. Exp. Mech. **31**, 252–256 (1991)
9. A. Makino, D. Nelson, Residual-stress determination by single-axis holographic interferometry and hole drilling—part I: theory. Exp. Mech. **34**, 66–78 (1994)
10. A. Makino, D. Nelson, E. Fuchs, D. Williams, Determination of biaxial residual stresses by a holographic-hole drilling technique. J. Eng. Mater. Technol. **118**, 583–588 (1996)

Chapter 43
Sensitivity Analysis of i-DIC Approach for Residual Stress Measurement in Orthotropic Materials

Antonio Baldi

Abstract Measuring residual stress in orthotropic materials is significantly more difficult than in isotropic materials. Indeed, in addition to the usual technical problems, several new points have to be taken into account, e.g. the accurate identification of material principal directions and the thickness of the laminae, (assuming we are dealing with composite materials).

Recently, a new approach to residual stress measurement in orthotropic materials has been proposed: it is based on the use of problem-specific displacement functions in the measuring loop of a Digital Image Correlation code. This is an elegant and effective solution because it allows for direct measurement of residual stress without the intermediate estimation of the displacement field.

This work attempts to analyze the sensitivity of the new methodology to some of its controlling parameters such as the location of the center of the hole, the estimation of its radius and the identification of material parameters. By using synthetic images, all parameters and stress components are exactly known, thus a statistical analysis is possible and allows identification of the most critical ones, together with the required accuracy for reliable estimation of stress levels.

Keywords Residual stress • Orthotropic material • Integrated digital image correlation • Inverse problem

43.1 Introduction

The hole drilling technique is probably the approach most used for residual stress measurement. In its standard implementation [1], a small hole is drilled in the center of a specifically designed strain gauge rosette and, due the material removed, the self-balanced state of internal stresses is broken and a strain field develops. The resulting strains are usually measured by a strain gauge rosette and correlated via numerically calibrated coefficients with the residual stress level of the component under analysis.

The measuring principle (breaking the internal equilibrium state, measuring the developed strains/displacements correlating the acquired data with the residual stress level inside the component) is quite general and does not enforce the use of strain gauges; this point has been noted by several authors [2–5], and nowadays different measuring techniques of the displacement/strain field around the hole have been proposed. In particular, interferometric optical techniques are well suited for residual stress measurement owing to several advantages with respect to the standard approach: high sensitivity (which, depending on the specific technique used, can sometimes also be tuned to the problem), non-contact measurement, very simple or no pre-processing of the surface, ability to work at high temperature, large data redundancy (thus allowing statistical treatment of experimental data) and high reliability of the measurement, are the most often cited advantages of optical methods; however, the use of optical interferometric methods is still confined to research laboratories: indeed, their high sensitivity to vibrations makes their use very difficult in an industrial environment and residual stresses continue to be measured using strain gauges.

Recently, a non-interferometric optical approach based on integrated Digital Image Correlation (iDIC) has been proposed by the author [6, 7]. Even though the standard Digital Image Correlation (DIC) is not well suited to residual stress measurement owing to the relatively low sensitivity and the large standard deviation of displacements, in the works cited above it has been shown that by integrating in the DIC formulation the displacement functions to be expected around the hole after drilling, most of the problems can be overcome and the resulting measuring procedure is simpler than using hole drilling in combination with standard DIC, it is highly reliable and its sensitivity can be compared to what is observed when using interferometric approaches.

A. Baldi (✉)
Dipartimento di Ingegneria Meccanica, Chimica e dei Materiali, Università degli Studi di Cagliari, Via Marengo, 2, Cagliari 09123, Italy
e-mail: antonio.baldi@dimcm.unica.it

S. Bossuyt et al. (eds.), *Residual Stress, Thermomechanics & Infrared Imaging, Hybrid Techniques and Inverse Problems, Volume 9*, Conference Proceedings of the Society for Experimental Mechanics Series, DOI 10.1007/978-3-319-21765-9_43

The proposed algorithms require pre-computation of calibration coefficients, which depends on several geometric and material-related quantities, thus it is not clear how robust the proposed approach is with respect to potential errors of these parameters. This work attempts to fill the gap by performing a sensitivity analysis of the algorithms on the controlling parameters. In particular, it focuses on the orthotropic version of the algorithm and is organized as follows: the next section summarizes the integrated Digital Image Correlation approach for isotropic material. The successive section extends the formulation to orthotropic material, showing the most important parameters. Then the analysis procedure is described and finally some results are presented.

43.2 Integrated Digital Image Correlation for Residual Stress Measurement

The Digital Image Correlation technique works under two main assumptions: (a) the surface of the specimen under analysis contains a texture (either natural or artificial); (b) the intensity of each speckle of the texture remains the same during motion (and eventually deformation) of the body. The former hypothesis allows identification of a given location on the basis of the local pattern; the latter makes it possible to perform the same operation at a successive step, providing strains are not too large (this usually implies that the two frames under comparison are not too far away in the time-scale of the event under study). Combination of the two hypotheses allows correlation of motion and optical flow through the well-known relation:

$$\frac{\partial I}{\partial x}V_x + \frac{\partial I}{\partial y}V_y + \frac{\partial I}{\partial t} = 0 \tag{43.1}$$

where V_x and V_y are the x and y components of velocity, I is the image intensity at point (x, y) and t is the time.

Equation (43.1) depends on two unknowns (the well-known *aperture problem*), thus it cannot be used unless an auxiliary condition is specified. The most common solution to this problem is the Lukas-Kanade approach [8], which overcomes this limitation by assuming that the displacement field can be locally described by a simple function (usually a polynomial expression of local coordinates), thus allowing identification of the solution by a nonlinear least squares approach.[1] Field data can be obtained by sampling the test image at different locations, i.e. by performing a series of separate analyses at locations of nodes of a (usually rectangular) sampling grid.

Owing to the statistical approach, Digital Image Correlation is not well suited for measuring elastic displacements (in general) and in particular it is not well suited for measuring residual stress-induced displacement data: indeed, the standard deviation of displacements depends on the square root of the number of pixels involved in the fit, i.e. on the dimension of the subset of the image used for sampling the displacement field. Thus, in presence of large gradients, we are faced with the dichotomy of either using small subsets to follow the rapidly changing displacements (with a large dispersion of results), or using a larger subset to reduce standard deviation but, de-facto, low-pass filtering results owing to the large moving window. This problem is particularly significant in residual stress analysis, where most of the significant signal is located near the hole and the subsets have to be small; thus the use of DIC for residual stress measuring [9, 10] requires development of a special data processing procedure able to cope with outliers [11].

However, a simpler solution exists: if the displacement-describing functions used in the DIC loop to (locally) map the reference image into the test one are replaced by hole-drilling specific functions, then there is no need to subdivide the domain into subsets; a single, large patch is able to correctly describe the behavior of the specimen and the problem of outliers is completely removed. Indeed, the displacement field around the hole of a residual stress components is very well known:

[1] Without going into details, available in several works, the fit is nonlinear because the Chi-square function (the error function used in the Least-Squares formulation) involves both the starting and end location of each speckle. The latter is one of the unknowns, thus, the known terms of the solution system can be estimated only on the basis of the results of previous iteration. This also implies that a starting procedure (to identify an initial point not too far from the sought location) is required to start the iteration.

$$\begin{aligned} u_r &= A(\sigma_x + \sigma_y) + B\left[(\sigma_x - \sigma_y)\cos(2\theta) + 2\tau_{xy}\sin(2\theta)\right] \\ u_\theta &= C\left[(\sigma_x - \sigma_y)\sin(2\theta) - 2\tau_{xy}\cos(2\theta)\right] \\ u_z &= F(\sigma_x + \sigma_y) + G\left[(\sigma_x - \sigma_y)\cos(2\theta) + 2\tau_{xy}\sin(2\theta)\right] \end{aligned} \tag{43.2}$$

where the $A, B, \ldots, F$ coefficients depend on material properties and on the ratio ρ of hole radius r_0 and distance of the point under inspection from the center of the hole:

$$\begin{aligned} A &= \frac{r_0}{2E}(1+\nu)\rho & B &= \frac{r_0}{2E}\left[4\rho - (1+\nu)\rho^3\right] \\ C &= \frac{r_0}{2E}\left[2(1-\nu)\rho + (1+\nu)\rho^3\right] & F &= 0 \quad G = \frac{\nu t}{2}\rho^2 \end{aligned} \tag{43.3}$$

E and ν being respectively Young's modulus and Poisson's ratio (note that a hole through configuration was assumed when writing (43.3)).

Thus, by projecting (43.2) in the x and y directions and using the resulting displacement components as a replacement for the general-purpose mapping functions, a residual-stress-specific DIC code is obtained. An added advantage of this approach (known as iDIC, i.e. integrated Digital Image Correlation) results from a side effect of the proposed procedure: because the new displacement functions (43.2) are expressed in terms of stress components, these quantities become the fitting parameters. Thus, the iDIC code adjusts stress components to make the reference and test images as similar as possible. The result of the least-square fit is the optimal set of parameters, i.e. the residual stress components. This is completely different from the standard two-steps approach where DIC (or whatever experimental technique) is used to estimate the displacement/strain field and the residual stress components are estimated a-posteriori by solving an inverse problem.

43.3 Orthotropic Material

Describing the displacement field around a hole in orthotropic materials is significantly more complex. Indeed, the theoretically exact solution (owing to Lekhnitsky and Savin [12–15]) requires mapping the hole in the complex plane and is particularly involved. However, Smith [16] showed that a large class of orthotropic materials can be described using a much simpler formulation:

$$\begin{aligned} u_x &= A_x\left[Y_1(1+\beta m)\tau_{xy} - X_1(\sigma_x - \beta m\sigma_y)\right] + B_x\left[Y_2(1+\alpha m)\tau_{xy} - X_2(\sigma_x - \alpha m\sigma_y)\right] \\ u_y &= A_y\left[X_1(1+\beta m)\tau_{xy} - Y_1(\sigma_x - \beta m\sigma_y)\right] + B_y\left[X_2(1+\alpha m)\tau_{xy} - Y_2(\sigma_x - \alpha m\sigma_y)\right] \end{aligned} \tag{43.4}$$

where A_x, A_y, B_x and B_y are material-dependent parameters, X_1, X_2, Y_1 and Y_2 depend on geometry and

$$\begin{aligned} m &= \sqrt[4]{E_{xx}/E_{yy}} \quad \kappa = \frac{1}{2}\sqrt{E_{xx}E_{yy}}\left[1/G_{xy} - (2\nu_{xy})/E_{xx}\right] \\ \alpha &= \sqrt{\kappa + \sqrt{\kappa^2 - 1}} \quad \beta = \sqrt{\kappa - \sqrt{\kappa^2 - 1}} \end{aligned} \tag{43.5}$$

Looking at equation (43.4), it is clear that it can be rearranged as

$$\begin{aligned} u_x &= -(A_xX_1 + B_xX_2)\sigma_x + m(\beta A_xX_1 + \alpha B_xX_2)\sigma_y + \left[(1+m\beta)A_xY_1 + (1+m\alpha)B_xY_2\right]\tau_{xy} \\ u_y &= +(A_yY_1 + B_yY_2)\sigma_x - m(\beta A_yY_1 + \alpha B_yY_2)\sigma_y + \left[(1+m\beta)A_yX_1 + (1+m\alpha)B_yX_2\right]\tau_{xy} \end{aligned} \tag{43.6}$$

thus making explicit the linear dependence on stress components. Thus, the iDIC shape functions for orthotropic materials are formally identical to the isotropic case, provided the coefficients are rearranged opportunely.

It could be objected that the given solution is not completely general because α and β cannot be estimated for all the thermodynamically admissible materials (i.e. when $\kappa < 1$, see (43.5)). However, it is easy to show that the calibration coefficients appearing in (43.6) can be easily estimated either numerically or using Lekhnitskii's formulation: in fact, by rearranging (43.6) as

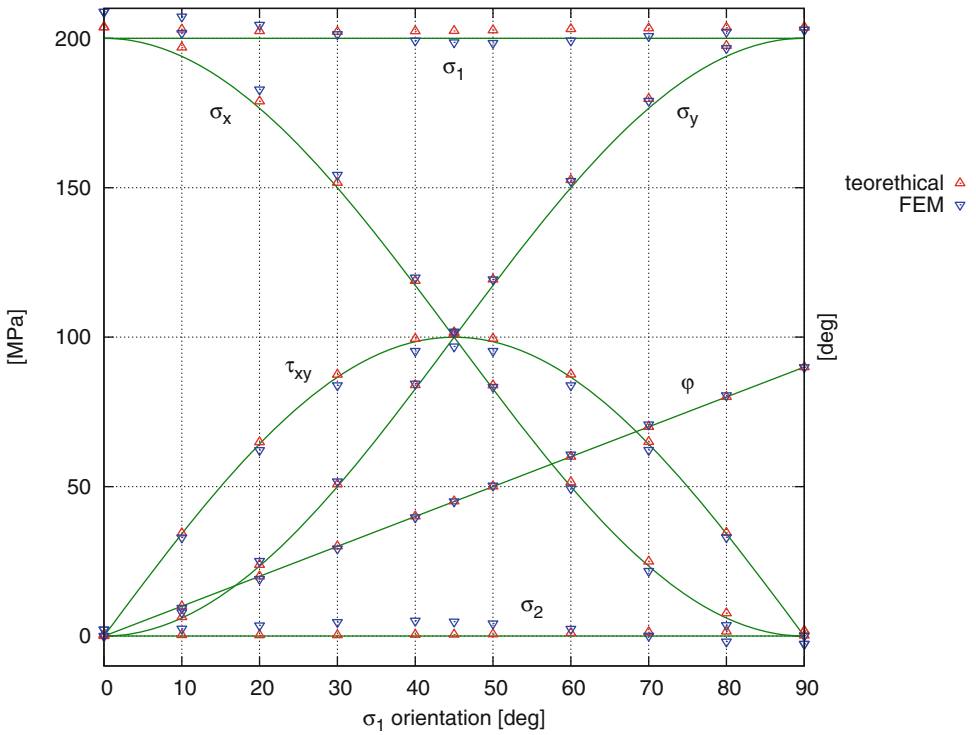

Fig. 43.1 Stress values estimated by the iDIC code vs theoretical values (continuous lines). A single stress component, oriented from 0° to 90° with respect to the principal axis of the material is assumed. Test images were synthesized using a speckle-generator and the iDIC analyses were performed using both theoretical- and FEM-estimated calibration coefficients

$$\begin{aligned} u_x &= c_{11}\sigma_x + c_{12}\sigma_y + c_{13}\tau_{xy} \\ u_y &= c_{21}\sigma_x + c_{22}\sigma_y + c_{23}\tau_{xy} \end{aligned} \tag{43.6a}$$

it is clear that if both the applied stress components and the resulting displacements are known in at least three different configurations, the c_{ij} can be estimated. Thus a FEM code can be used to simulate the hole-drilling problem and the resulting displacements can be employed to calibrate the system; alternatively, it is possible to estimate the displacements at the point by using the general formulation for different (known) loading cases, thus enabling the use of (43.6a) for all materials. Figure 43.1 compares iDIC-estimated residual stresses and the expected value for a set of synthetic images related to a single stress state at different orientations with respect to the principal axis of the material. Looking at the picture, it is apparent that iDIC is able to reliably estimate the correct stress state using both theoretical and FEM-estimated coefficients.

43.4 (A Sort of) Sensitivity Analysis

The iDIC approach allows solving most of the problems related to direct use of Digital Image Correlation, i.e. the relatively low sensitivity and the high probability of having unreliable data near the border of the hole. However, before entering the nonlinear fitting-loop, the c_{ij} coefficients appearing in (43.6a) have to be estimated. Since they depend on the radius of the hole, the coordinate of the center of the hole and material characteristics, an erroneous identification of these parameters is likely to affect the accuracy of results. Although a theoretical analysis of the sensitivity of the algorithm is too complex to be performed, a numerical analysis based on synthetic images is possible: using our in-house developed speckle image generator, it is possible to create couples of images (reference and deformed) related to user-specified residual stress fields. Since all the parameters are exactly known, an error analysis is possible. Figure 43.2 shows an example of a numerically generated speckle image. To avoid any errors due to polynomial interpolation, images are synthesized by superimposing several bell-shaped functions. The known intensity field is then mapped using an analytical function, thus no interpolation is

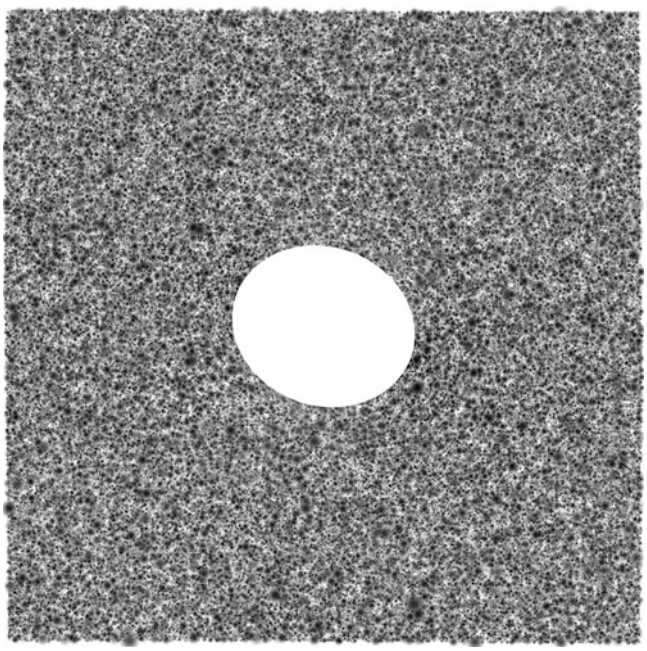

Fig. 43.2 A synthetic image generated using our in-house developed speckle generator. Each speckle corresponds to a known, bell-shaped, function. The displacement field is described using (43.4), thus no interpolation is performed at any stage of the generation process. Note that unrealistic material parameters were used to emphasize the applied load

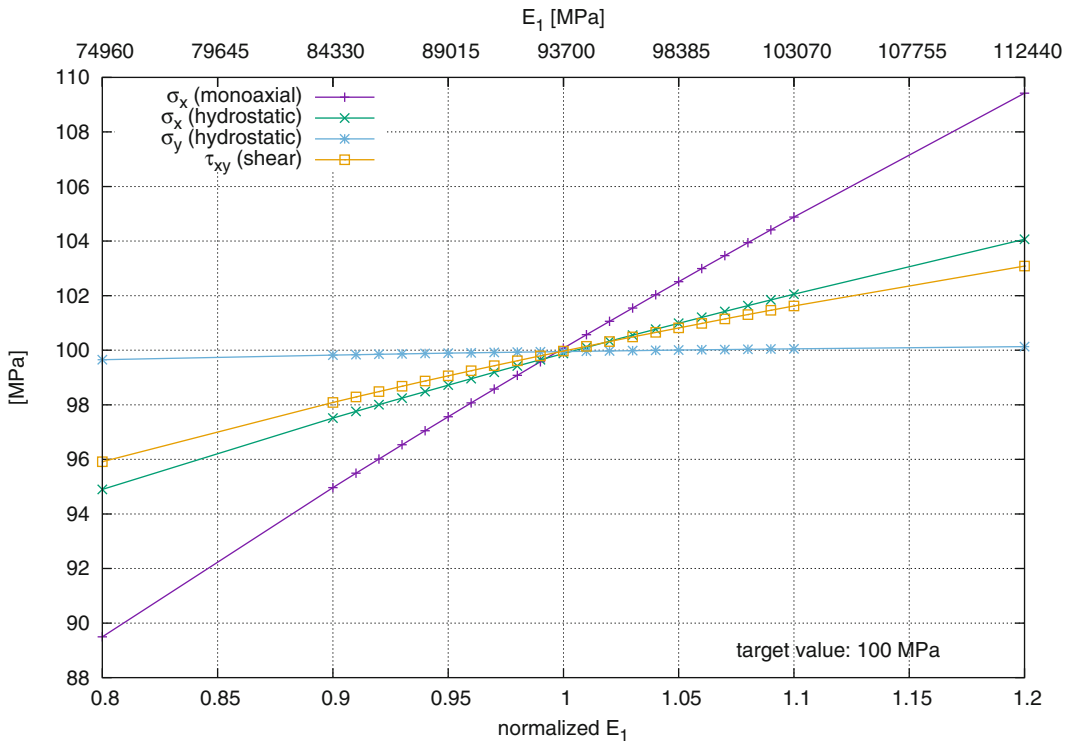

Fig. 43.3 Influence of E_1. The most affected stress state corresponds (as expected) to a mono-axial loading parallel to the first material axis. Note the small deviation from linearity at large errors

performed at any step of the process. Note that to make the displacement field apparent, unrealistic parameters were used as input while generating Fig. 43.2.

Figure 43.3 shows one of the most critical parameters of the set we analyzed: three simulated sets of images, respectively corresponding to a mono-axial stress state ($\sigma_x = 100$ MPa), a hydrostatic state ($\sigma_x = \sigma_y = 100$ MPa) and a pure shear ($\tau_{xy} = 100$ MPa), were generated using a mildly orthotropic material ($E_1 = 93{,}700$ MPa, $E_2 = 7450$ MPa, $G_{12} = 3976$ MPa,

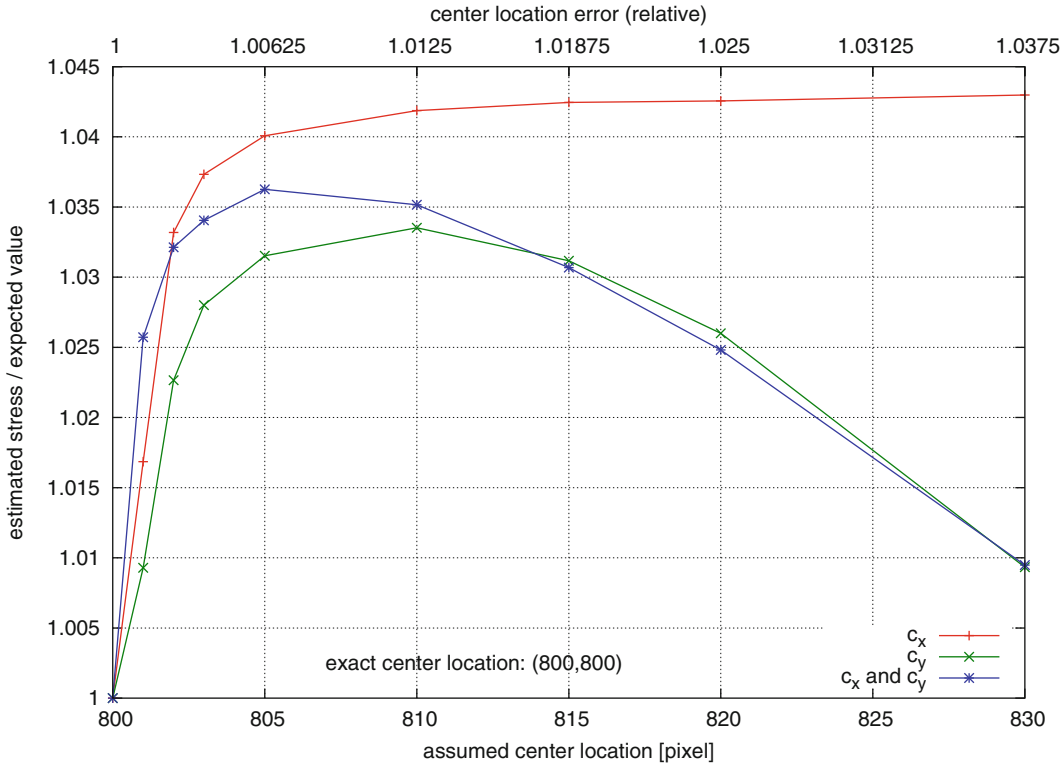

Fig. 43.4 Influence of the errors in the identification of center location. The three curves correspond respectively to errors in the x direction only (c_x), in the y direction only (c_y) or both (c_x and c_y). Behavior is symmetrical with respect to the center, thus only half of the range is shown

$\nu_{12} = 0.261$; thus $\kappa = 3.24$). Then a series of iDIC analyses were performed using different E_1 settings ranging from 80 to 120 % of the target value. As expected, errors in stress estimation increase almost linearly with $\varepsilon(E_1)$, but some points are to be noted:

- Even in the worst case, corresponding to a stress field oriented parallel to the principal axis, the scale factor is less than 0.5, thus a 9 % error in the stress estimate corresponds to 20 % error in the Young modulus estimation.
- Looking at the hydrostatic stress state, the σ_y estimates are almost constant (and correct), thus errors on E_1 do not affect the estimation of stress in the orthogonal direction (i.e. there is little or no cross-talk).
- Maximum error for the shear test case is less than 4 %.

Figure 43.4 shows the iDIC behavior when assuming an erroneous location of the center of the hole. Three different tests were performed, using either an erroneous x-coordinate, or an erroneous y-coordinate or both. Apart from the absolute value of the error (less than 5 %), the behavior of the c_y curve (error direction orthogonal to the principal direction of the material) is quite interesting, because after an initial increase, errors decrease to less than 1 %. Note that the influence of the y-displacement is so large that even when both x and y locations are incorrectly estimated a similar behavior is observed.

Finally, Fig. 43.5 shows the influence of the incorrect estimation of the radius of the hole: it is apparent that an overestimation of the radius induces small or no errors in the final result, whilst underestimating the radius induces large errors. However, there is a clear saturation effect and this parameter does not influence the estimation of the τ_{xy}.

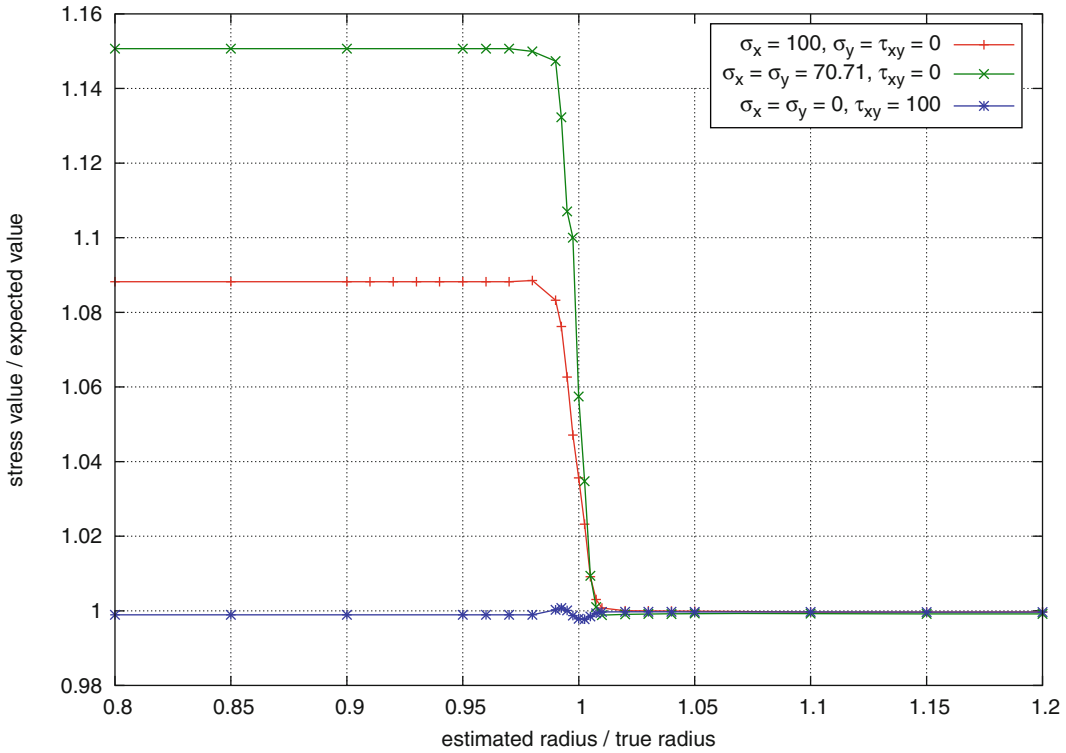

Fig. 43.5 Influence of the radius of the hole. The three curves correspond respectively to different residual stress fields. Note that the τ estimation is not affected by this parameter

43.5 Conclusions

The analysis we performed shows that the proposed iDIC approach to residual-stress estimation is robust and reliable not only in isotropic materials, but also in orthotropic ones. Although the algorithm requires estimation of calibration coefficients based on the material and geometric parameters, the final estimate is usually within 10 % of the expected results. The most influential parameter is the radius of the hole. However, an error is significant only in the case of underestimation of the true value, whilst an overestimation appears to have little or no effect on the accuracy. Material parameters obviously directly affect the final results. However, the estimates in the two principal directions appear to be weakly correlated. Finally, a poorly estimated center location appears to have little influence on the accuracy of the results, with errors being below 5 % in all cases.

References

1. ASTM E837-08e1, Standard test method for determining residual stresses by the hole-drilling strain-gage method (American Society for Testing and Materials, West Conshohocken, 2008). doi:10.1520/E0837-08E01
2. A.J. Albertazzi, C. Kanda, M.R. Borges, F. Hrebabetzky, A radial in-plane interferometer for ESPI measurement, in *Laser Interferometry X. Techniques and Analysis*, ed. by M. Kujawinska, R.J. Pryputniewicz, M. Takeda. Proceedings of SPIE, vol. 4101 (Bellingham, Washington, 2000), pp. 77–88
3. A. Baldi, A new analytical approach for hole drilling residual stress analysis by full field method. J. Eng. Mater. Technol. **127**(2), 165–169 (2005)
4. G.S. Schajer, M. Steinzig, Full-field calculation of hole drilling residual stress from electronic speckle pattern interferometry data. Exp. Mech. **45**(6), 526–532 (2005). doi:10.1177/0014485105059553
5. G.S. Schajer, Advances in hole-drilling residual stress measurements. Exp. Mech. **50**, 159–168 (2010). doi:10.1007/s11340-009-9228-7
6. A. Baldi, Residual stress measurement using hole drilling and integrated digital image correlation techniques. Exp. Mech. **54**, 379–391 (2014). doi:10.1007/s11340-013-9814-6
7. A. Baldi, Residual stress analysis of orthotropic materials using integrated digital image correlation. Exp. Mech. **54**, 1279–1292 (2014). doi:10.1007/s11340-014-9859-1

8. B.D. Lucas, T. Kanade, An iterative image registration technique with an application to stereo vision, in *Proceedings of Imaging Understanding Workshop*, vol. 130 (1981), pp. 121–130
9. J. Gao, H. Shang, Deformation-pattern-based digital image correlation method and its application to residual stress measurement. Appl. Opt. **48**(7), 1371–1381 (2009)
10. K.J. Kang, N. Yao, M. He, A. Evans, A method for in situ measurement of the residual stress in thin films by using the focused ion beam. Thin Solid Films **433**(1), 71–77 (2003)
11. G.S. Schajer, B. Winiarski, P. Withers, Hole-drilling residual stress measurement with artifact correction using full-field DIC. Exp. Mech. **53** (2), 255–265 (2013)
12. S.G. Lekhnitskii, *Theory of Elasticity of an Anisotropic Elastic Body*. Holden-day (translation of 1950 Russian ed.), (1963)
13. S.G. Lekhnitskii, *Anisotropic Plates* (Gordon and Breach Science Publisher, Philadelphia, 1968)
14. G.N. Savin, *Stress Concentration Around Holes* (Pergamon Press, Oxford, 1961)
15. J. Schimke, K. Thomas, J. Garrison, *Approximate Solution of Plane Orthotropic Elasticity Problems* (Management Information Services, Detroit, 1968)
16. C.B. Smith, *Effect of elliptic or circular holes on the stress distribution in plates of wood or plywood considered as orthotropic materials*, Tech. Rep. Mimeo 1510, USDA Forest Products Laboratory, Madison, WI, (1944)
17. A. Baldi, F. Bertolino, F. Ginesu, Sensitivity analysis of integrated digital image correlation approach for residual stress measurement, in *Proceedings of ICEM 16 Conference*, Cambridge, 7–11 July 2014

Chapter 44
Stress Measurement Repeatability in ESPI Hole-Drilling

Theo Rickert

Abstract Repeatability measurements are useful for measuring residual stress by hole-drilling since single holes don't provide a lot of information about measurement quality. Besides measurement procedure and statistics, they also allow assessing microstructural variability. This study uses Electronic Speckle Pattern Interferometry (ESPI) for making multiple stress measurements in samples made from aluminum and polycarbonate. Under bending, the aluminum samples show large variability in the stress depth profiles while the general trends fit the expected linear stress curves. The experiments suggest that the variability is primarily due to the microstructure rather than measurement errors. Deviations from the linear bending curves originate in residual stresses in the undeformed bar, which can change from location to location. In the polycarbonate sample, the measured stresses are reasonably close to those calculated when the holes were small. Larger holes produced stress depth profiles with significant shifts towards higher stresses. This effect is attributed to frictional heating during drilling and therefore, inappropriate drilling parameters.

Keywords Stress measurement • ESPI • Incremental hole-drilling • Measurement repeatability • Polycarbonate

44.1 Background

Hole-drilling in combination with strain-gages has been used successfully for stress measurements for many decades and is now one of the most commonly used methods. A significant draw-back is that the measurements do not provide much information about the magnitude of measurement errors. Since multiple strain-gage applications are inconvenient and time-consuming, confirmation measurements are less common. This might mean that poor sampling statistics and measurement problems may not be discovered.

Optical methods for measuring the stress relief due to hole-drilling avoid much of the hassle the strain-gage method has with repeat measurements. Only complex sample positioning will be a significant hindrance. But many samples have relatively large, roughly flat, surfaces where the stress distribution can be assumed to be comparable. Such samples allow multiple measurements by ESPI hole-drilling in relatively short time spans.

44.2 Experimental

Stress measurements were made on two aluminum samples, which were mounted in a 4-point bending device. The device has a 10″ outer support span and a 5″ inner span. Care was taken to minimize any friction counteracting the bending movement. The deflections were measured at center-width of the device using a dial gage when relieving the pressure. The maximum deflection used, 3.5 mm, should produce stresses far below 50 % of the yield strength of the material (on the order of 380 MPa). Both samples were made from Al7075 and cut to length from the same original bar, which shows obvious visual characteristics of extruded bars. The bars are 1″ wide, ~12″ long and ¼″ (~6.3 mm) thick. The material parameters used for the stress calculation are a Young's modulus of 71.7 GPa and a Poisson's ratio of 0.33.

Further measurements were made on a polycarbonate sample. Plastic materials may exhibit creep at room temperature at relatively low strains. The 4-point bending device could not hold the sample in place at the low strains necessary to avoid creep. Thus, a fixed curvature bending device with a large radius was used. The clear polycarbonate sample was clamped to an aluminum block with curved surface of a radius of ~507 mm, producing a strain of near 0.3 % (calculated) in the surfaces

T. Rickert (✉)
American Stress Technologies, Inc., 540 Alpha Drive, Pittsburgh, PA 15238, USA
e-mail: Theo.Rickert@astresstech.com

S. Bossuyt et al. (eds.), *Residual Stress, Thermomechanics & Infrared Imaging, Hybrid Techniques and Inverse Problems, Volume 9*, Conference Proceedings of the Society for Experimental Mechanics Series, DOI 10.1007/978-3-319-21765-9_44

of the nearly 3 mm thick bar. The bar width is also 1″. The material parameters used are a Young's modulus of 2.37 GPa and a Poisson's ratio of 0.38.

All measurements on the polycarbonate sample show very low stresses for the first two depth increments. This seems to be characteristic for the sample or the experimental design. The issue is not further investigated here and the first two data points are omitted in all results shown to allow better focus on the issues discussed.

All measurements were made with a Prism[1] residual stress measurement system, which combines incremental hole-drilling with ESPI (Electronic Speckle Pattern Interferometry) [1]. To obtain favorable optical properties of the surfaces, all samples were lightly spray-painted matte white or light-gray. The measurements on the first aluminum sample were made including in-plane and out-of-plane displacements. All others were solely of in-plane displacements. The holes were made using square-end end mills of various diameters. Those made with a 1/32″ tool are in the following referred to as 0.8 mm holes, those with a 1/16″ tool as 1.6 mm. All end mills were TiN coated. The drilling increments were adjusted for the different hole diameters. Twenty or more increments were used for each depth profile. Each measurement within each series used the same list of depths so that arithmetic averages could be calculated from equivalent data sets. The instrument measures surface displacements and correlates these directly with stresses. The stress calculation followed the Integral Method [2, 3]. All depth profiles shown were calculated using modest regularization, a form of smoothing.

44.3 Results

The first aluminum bar, Al1, was bent to five deflections from about 0.5 to 2.5 mm in the first measurement series and measured using a 2 mm diameter end mill. While the stress depth profiles generally follow the trends of the predicted curves, each shows large deviations from it (Fig. 44.1). All have a relative low in the depth range between 0.1 and 0.3 mm.

The 2.5 mm deflected part was measured five more times in a second measurement series to investigate measurement statistics. The line of holes was made parallel to sample length. Some data points from each measurement deviate 20 % or more from the calculated bending curve. A stress depth profile generated from the averages of the five measurements produces a much flatter curve with close to the expected slope (Fig. 44.2, blue line, to >1 mm). Significantly lower than expected stresses are found in a depth range of around 0.2–0.3 mm. Two residual stress measurements made later without any bending show significant compressive stresses at depths similar to the lows of the measured bending curves (Fig. 44.2, green line, bottom). Unfortunately, these were made several inches away from the bending stress measurements, towards one sample end, and no consideration was given to the exact position in sample width direction.

A third measurement series on the first aluminum sample was made with a 0.8 mm diameter tool in-between the other two series of 2 mm holes. The five depth profiles show even more variation than the ones from 2 mm holes. The curve of the

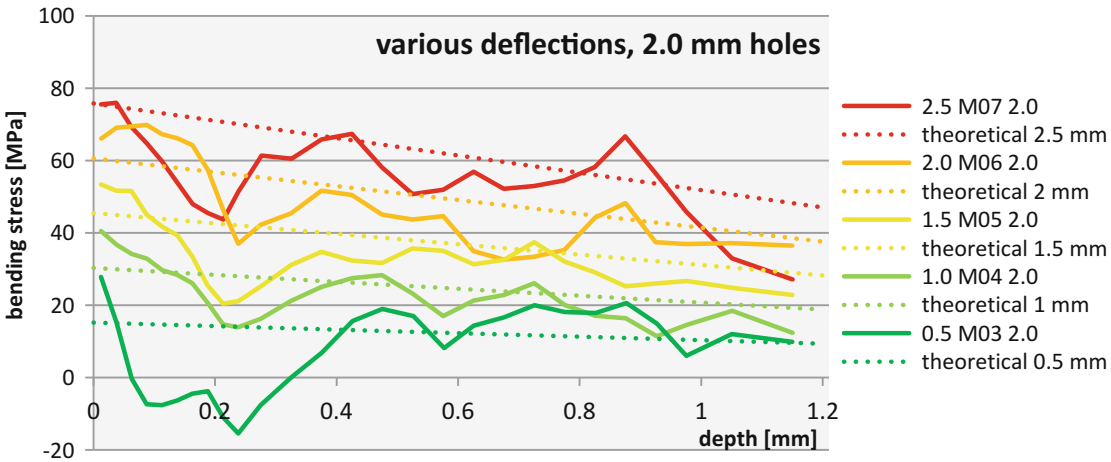

Fig. 44.1 Aluminum Al1, stress profiles as function of bending amount

[1] Prism® is a registered trade mark of American Stress Technology, Pittsburgh, PA.

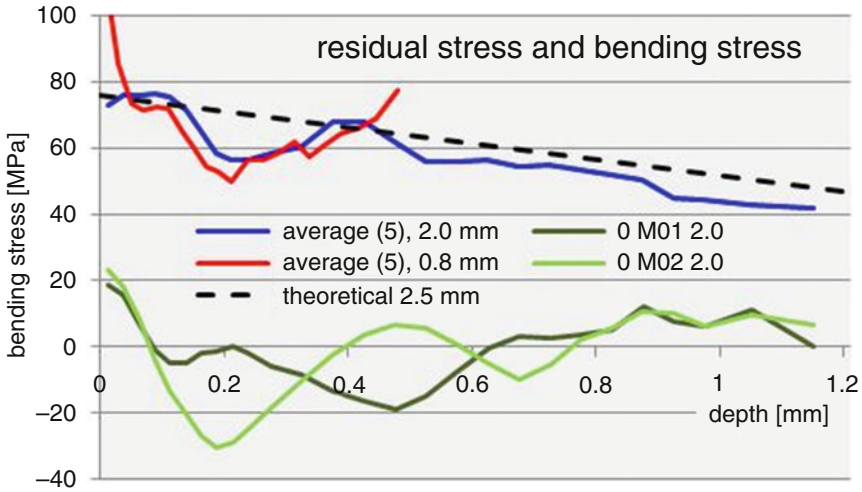

Fig. 44.2 Aluminum Al1, averages from five measurements, each, for two hole sizes and two residual stress measurements

averages for 0.8 mm (Fig. 44.2, red line, to ~0.5 mm) is very close to that for 2 mm and shows the same low stress region at lower depths.

The second aluminum bar, Al2, was bent to a deflection of 3.5 mm and three measurement series were made. There are five measurements, each, with 0.8, 1.6 and 2.5 mm diameter holes and each series was drilled in a line parallel to sample length. Measurement variation clearly increases with decreasing hole size (Fig. 44.3). The curves of the averages show surprisingly large differences. While the general trends of all follow the calculated bending stress curve, there seem to be characteristic differences, which is particularly obvious for the 2.5 mm measurements where all five measurements are clearly higher for much of the depth range. Subsequent measurements in line with the three series show that the residual stresses are different in the different locations (Fig. 44.6b). The measurements in line with the 0.8 and 1.6 mm bending stress series were made with a 1.6 mm tool, those for the 2.5 mm series also used 2.5 mm holes. One of the data sets for the latter ends at 1.1 mm depth due to a measurement problem. The other is shown separately in Fig. 44.6b to indicate the continuation of tensile stresses at higher depths.

The first measurement series on the polycarbonate bar was made with a 1.6 mm diameter end mill. Four of the five first measurements have very similar results; the fifth is somewhat different. Since the hole from the latter is closest to the sample edge, an influence of the measurement location was suspected and five additional measurements were made. Again, the one hole closest to the sample edge is different. The difference becomes quite obvious in the curves of the averages for the "regular" and near-edge measurements (Fig. 44.4b). This prompted a second measurement series with 0.8 mm diameter holes mostly near the edge of the sample. But all five measurements of this series are very similar, independent of their distance to the sample edge (Figs. 44.4a and 44.5b). Also, all 0.8 mm measurements are close to the calculated bending stress curve while the 1.6 mm stresses are higher. That suggests a hole size effect on the stress results. Three measurements made with 2.0 mm holes immediately before the current measurements seem to support this. Their average curve matches the one for the 1.6 mm edge measurements and is farthest away from the calculated bending curve (Fig. 44.7). All average curves have slopes very similar to the calculated bending stress curve. But the larger the hole the more are the measured stress curves shifted to greater depths and higher stresses.

44.4 Discussion

The stress depth profiles of the two aluminum samples measured all deviate substantially from the expected linear bending curves. They are also different from each other even though they originate from the same extruded piece. The first sample is characterized by a low-stress zone near the surface, which all measurements show except for one of the residual stress measurements (Fig. 44.2). Unfortunately, the locations of the residual stress measurements were not close to the others. That this can be critical is seen in the results from the second sample. Residual stresses are clearly different as function of the position in the sample width direction (Fig. 44.6b). On first view, the second sample suggests stress differences as function of hole size (Figs. 44.3 and 44.6a). However, the differences between the measurement series match those of the residual stresses made in line with them—even though not all were made with the corresponding hole size. The correlation with hole

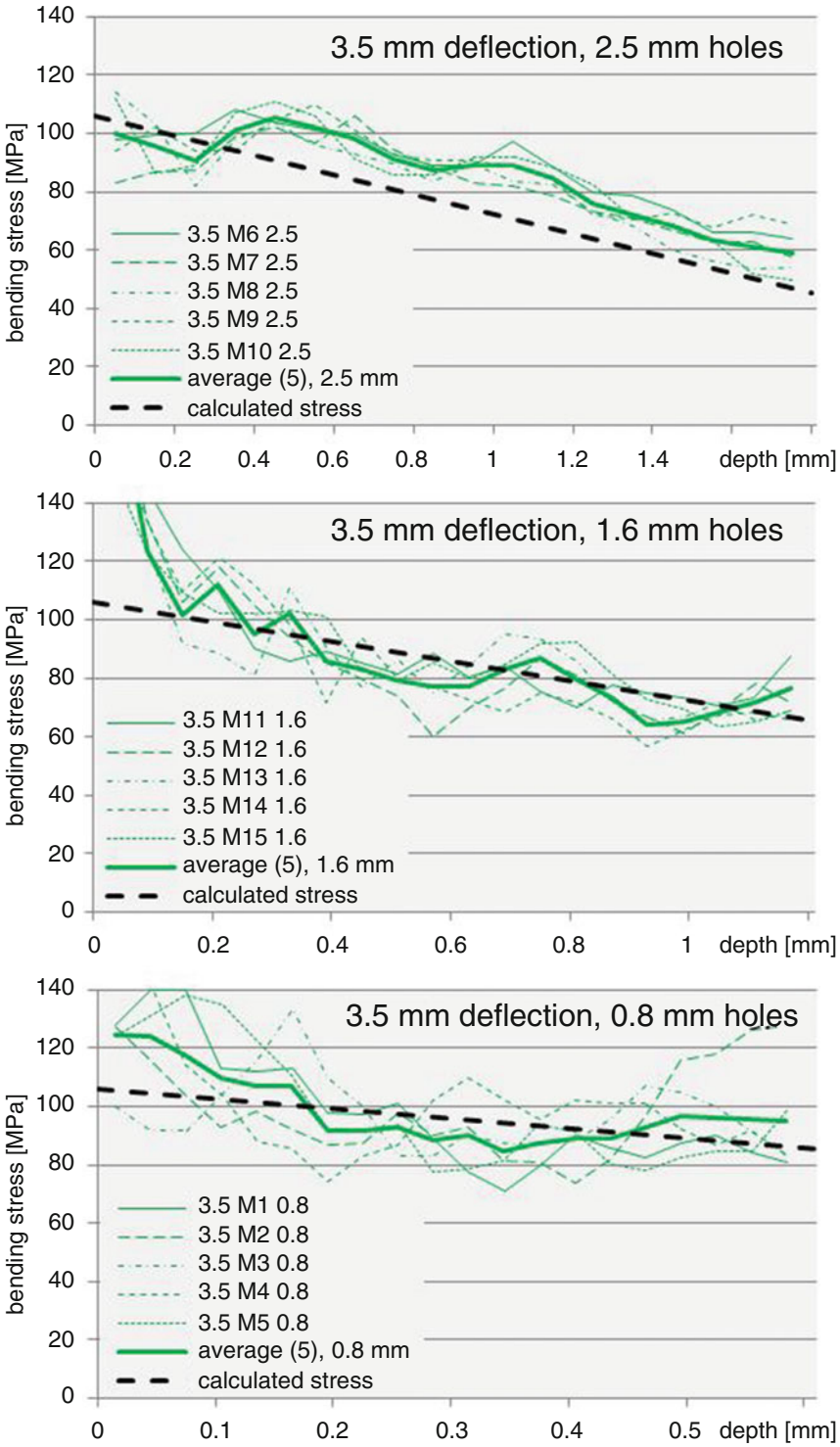

Fig. 44.3 Aluminum Al2, averaging the results for different hole sizes, showing differences in variability

size in the bending stress measurements is therefore caused by the measurement arrangement and under-lying banded microstructure parallel to the extrusion direction.

The repeat measurements show that measurement variability is clearly dependent on hole size in the measurements on these aluminum samples (Fig. 44.3). Certainly, the magnitude of the displacements increases with the measurement volume. Therefore, measurement statistics should improve with larger holes. It is also suspected that microstructural factors contribute to this hole size effect in these samples since they show microstructural variability in their stresses.

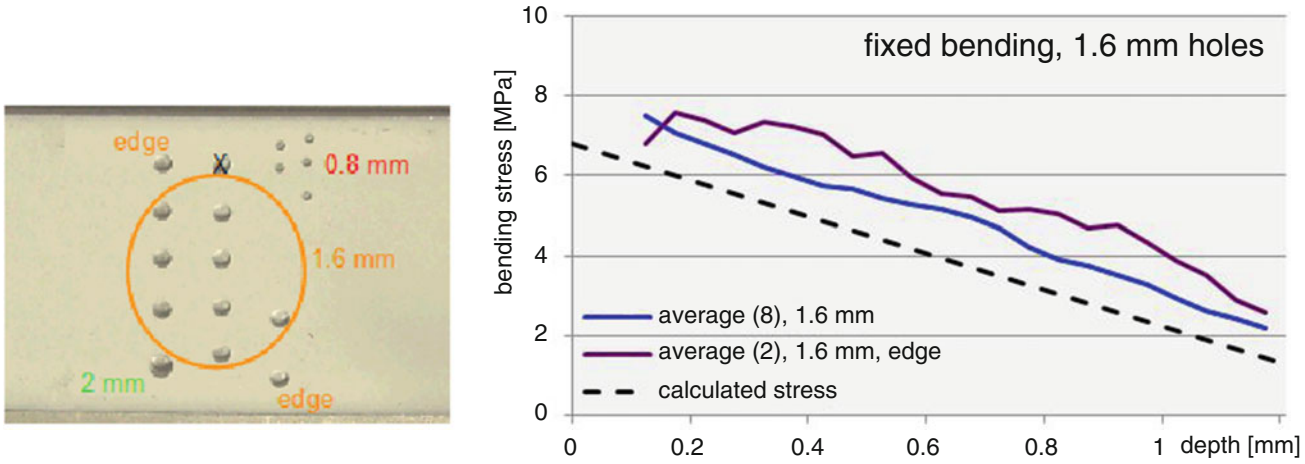

Fig. 44.4 Polycarbonate, hole positions (**a**, *left*) and averages of the "regular" results and the two outliers (**b**, *right*)

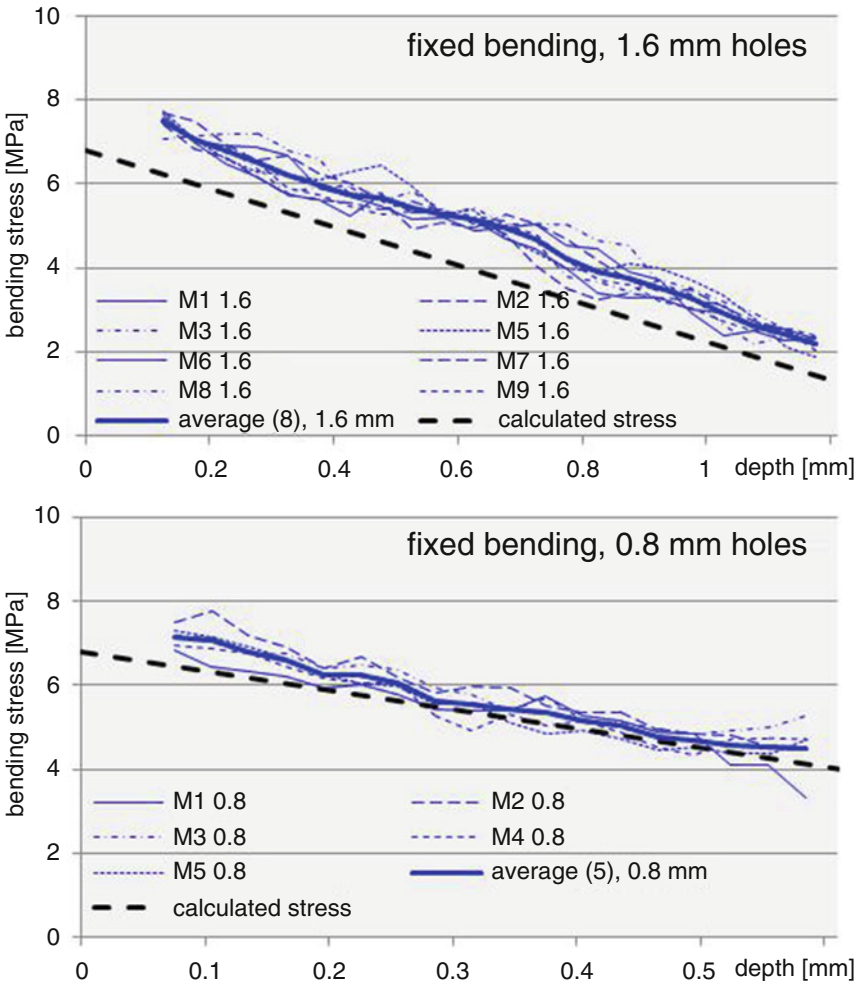

Fig. 44.5 Polycarbonate, averaging the results from 1.6 mm (regular, **a**, *top*) and 0.8 mm holes (**b**, *bottom*)

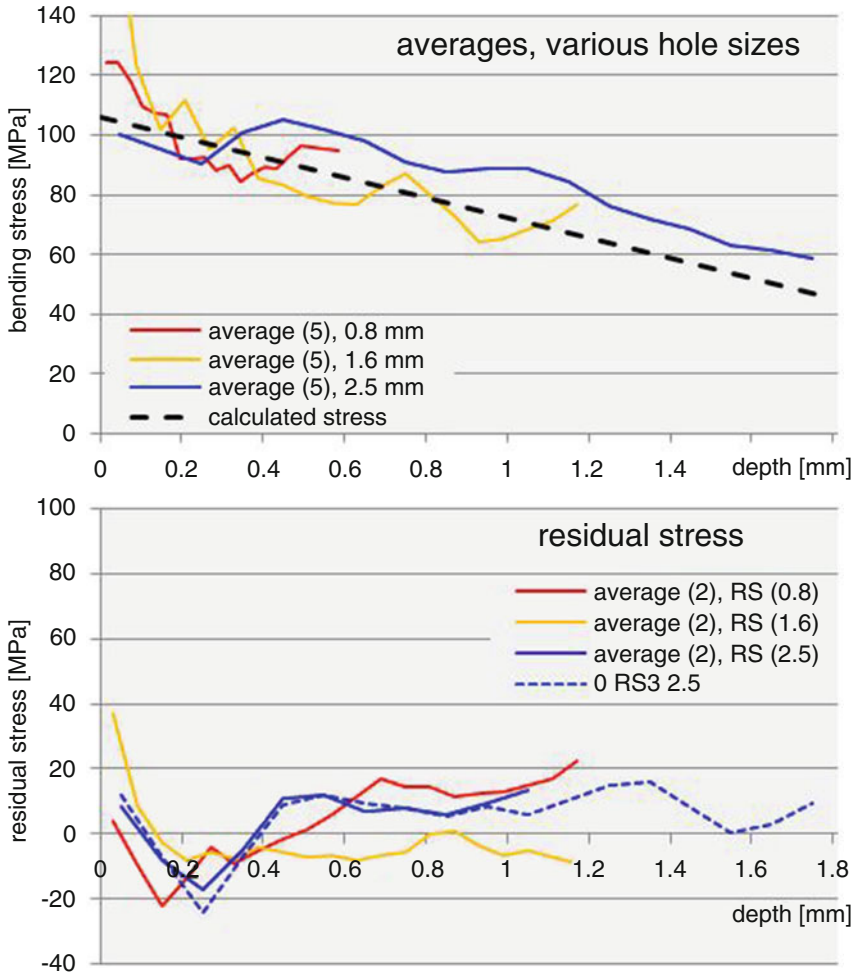

Fig. 44.6 Aluminum Al2, comparison of averages of bending (**a**, *top*) and residual stresses (**b**, *bottom*)

The polycarbonate measurements show much lower variability than those on the aluminum samples and the slopes of the stress depth profiles follow closely that of the calculated stress curve (Fig. 44.5). This indicates that the measurement series were conducted with high consistency. Unfortunately, the average stress curves are shifted against each other and against the predicted curve (Fig. 44.7). The shift generally increases with hole size. This is very likely a heating effect.

Hole-drilling of samples made from plastic faces a special problem. The low thermal conductivity of the material means that heat generated at the hole edges during drilling dissipates very slowly. It has been reported that measurement quality improves with reduced rotational speed [4]. Thus, all measurements on the polycarbonate sample were made with the minimum speed possible. To further reduce local heating, only very small volumes of material were removed at a time. But an increase in tool diameter causes the speed at the hole edge to increase by the square, making it more and more difficult to avoid heating effects. Drilling parameters were adjusted for each hole size, yet apparently not sufficiently. The problem is that the total measurement time for the larger holes, which were also drilled deeper, increases very substantially.

A strong argument that the measurements were affected by local heating is that not only the stresses in bending direction but also perpendicular to that show the hole size effect (Fig. 44.7). Frictional heating should be non-directional within planes parallel to the surface and thus one should expect very similar effects for all surface directions. The results from the smallest hole deviate the least from the linear bending stress curve. The 1.6 mm outliers from closer to the sample edge (Fig. 44.4) may have been caused by special drilling conditions. It is believed that the bending device used doesn't necessarily hold the sample perfectly tight against the bending block in all locations. Vibrations from the drill together with some degree of freedom of the sample may have exacerbated frictional heating in measurements closer to the edge. A smaller tool would not necessarily cause the same situation.

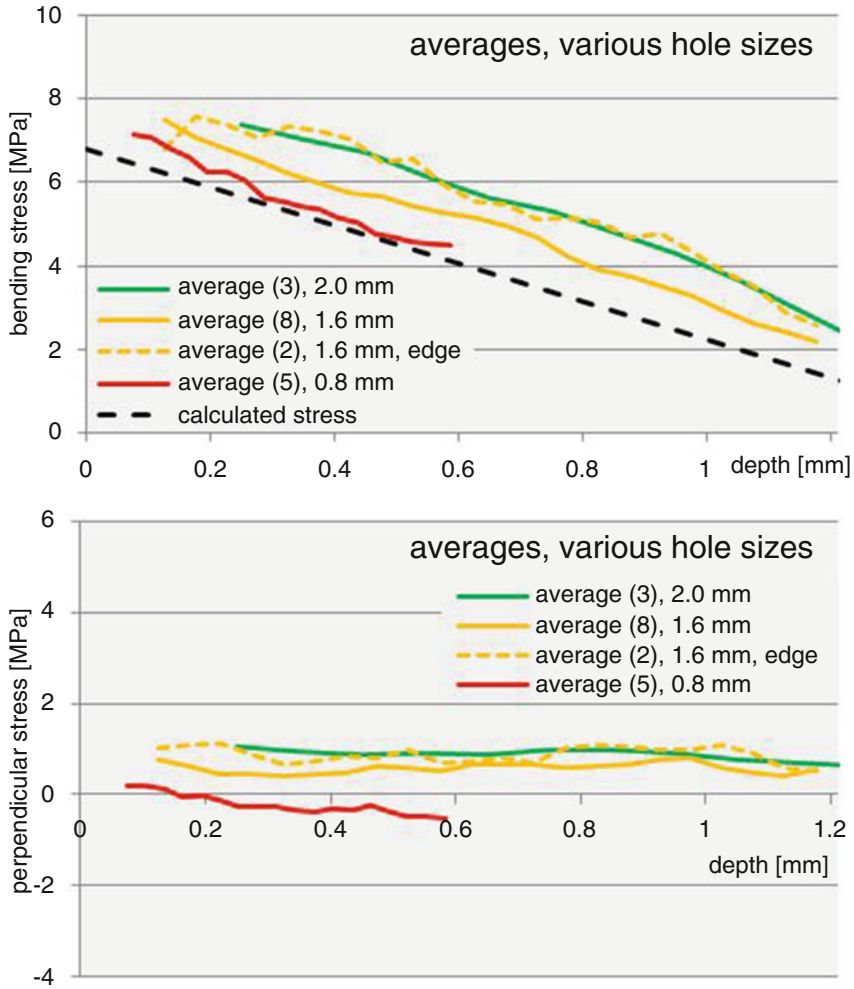

Fig. 44.7 Polycarbonate, comparison of averages of bending (**a**, *top*) and perpendicular stresses (**b**, *bottom*)

References

1. M. Steinzig, E. Ponslet, Residual stress measurement using the hole drilling method and laser speckle interferometry, parts I-IV. Exp. Tech. **27**(3–6), 59–63 (2003)
2. G.S. Schajer, M. Steinzig, Full-field calculation of hole drilling residual stresses from electronic speckle pattern interferometry data. Exp. Mech. **44**(6), 526–532 (2005)
3. G.S. Schajer, T.J. Rickert, Incremental computation technique for residual stress calculations using the integral method. Exp. Mech. **51**(7), 1217–1222 (2011)
4. A. Nau, B. Scholtes, M. Rohleder, J. Nobre, Application of the hole drilling method for residual stress analyses in components made of polycarbonate. J. Plast. Technol. **7**(3), 66–85 (2011)

Chapter 45
Some Aspects of the Application of the Hole Drilling Method on Plastic Materials

Arnaud Magnier, Andreas Nau, and Berthold Scholtes

Abstract Residual stresses are always present in nearly every component as a consequence of the manufacturing process. If the material exhibits a crystalline structure, diffraction methods are undoubtedly a method of choice for residual stress analysis. However such a method is not always applicable on plastics. As they undergo complex manufacturing processes, they also have to be evaluated in terms of introduced residual stresses. Here, mechanical methods like the incremental hole drilling method might be more suitable. However, for a reliable residual stress analysis in plastic materials, the hole drilling method usually applied for isotropic metallic materials has to be adapted. A critical point comes from the required strain gauge rosette technique. It involves a stiffening effect due to its assembly and its bonding. Further issues are the stressless introduction of a geometrically defined hole, temperature effects and the viscoelastic behavior of plastic materials. Those critical points were investigated numerically and experimentally on different types of plastic materials in order to improve the hole drilling method and to provide an opportunity to estimate more precisely residual stresses.

Keywords Residual stress • Plastic • Polypropylene • Hole drilling • Viscoelastic

45.1 Introduction

There is a great interest in residual stress analyses in components made of plastic but this exhibits also a considerable challenge for existing measurement techniques. Among mechanical methods hole drilling is widely used, and guidelines exist [1, 2] when working on metals. The adaptation of this method to plastic materials is the subject of this publication using an extruded polypropylene sheet (PP) as example. Indeed plastic materials compared with metals require different approaches concerning the preparation of the sample, the drilling process, or when choosing the feed voltage of the strain gauges [3]. Critical points considered in this paper are temperature effects, stiffness effects and the viscoelastic behavior of materials. These effects are of minor importance for metal but they shouldn't be overlooked when working with plastic materials.

45.2 Thermal Effects

Industrial strain gauge rosettes (SGR) are usually temperature compensated for metallic materials. The rolling process of the metallic grids of the SGR enables to change their thermal property, so that they can self-compensate the thermal expansion of the material under investigation at room temperature. SGR are usually adapted for steel and aluminum, e.g. SGR EA-06-062RE-120 (steel) and EA-13-062RE-120 (aluminum) by Vishay. As plastics have a much higher thermal expansion coefficient than metals, it is mandatory that thermal effects are quantified during a measurement. The following measurement was made on an extruded polypropylene (PP) sheet, which has a ten times higher thermal expansion coefficient than steel: 120 µm/(m °C). Figure 45.1 depicts how very sensible a measurement can be.

During this experiment two samples of PP were used. On each sample a SGR was applied: one to be drilled, the other one to analyze and to compensate the temperature influence during the experiment. The strain vs. time curve corresponds to this temperature compensation SGR. Here, only one of the three strain signals is shown. A continuous increase of the signal can

A. Magnier (✉) • A. Nau • B. Scholtes
Institute of Materials Engineering—Metallic Materials, Kassel University, Moenchebergstr. 3, Kassel 34125, Germany
e-mail: magnier@uni-kassel.de; nau@uni-kassel.de; scholtes@uni-kassel.de

S. Bossuyt et al. (eds.), *Residual Stress, Thermomechanics & Infrared Imaging, Hybrid Techniques and Inverse Problems, Volume 9*, Conference Proceedings of the Society for Experimental Mechanics Series, DOI 10.1007/978-3-319-21765-9_45

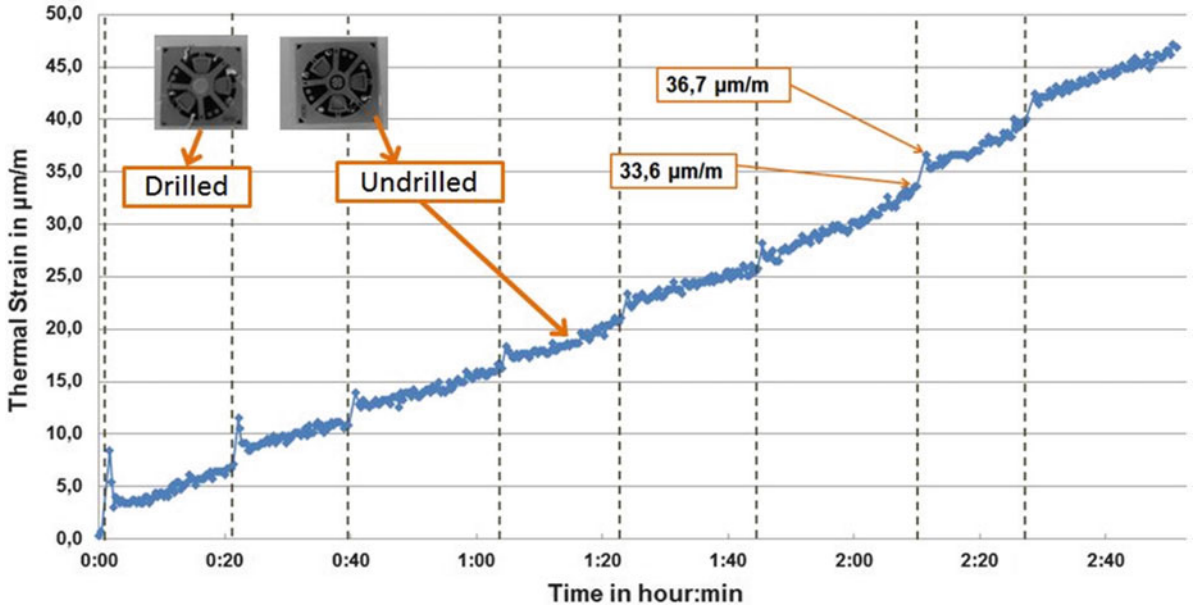

Fig. 45.1 Thermal strain output of a strain gauge rosette applied on an extruded polypropylene sheet

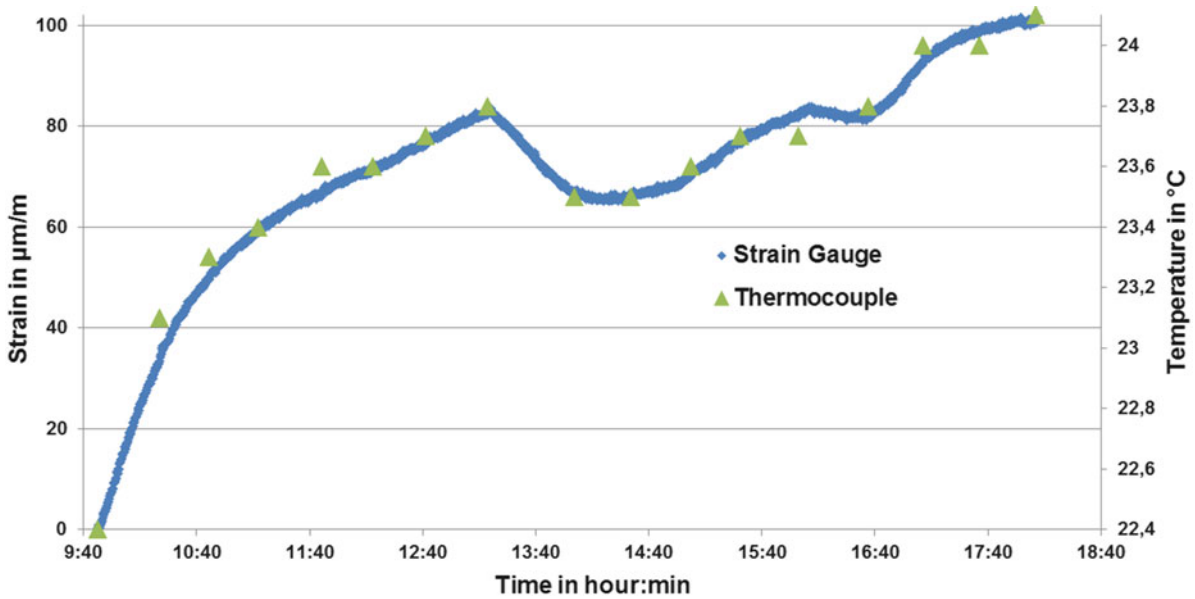

Fig. 45.2 Correlation between room temperature variation measured with a thermocouple and strain measured on a polypropylene sample

be observed, which can be related to a global room heating. Each dotted vertical line was drawn to indicate the time when an increment was drilled on the "drilled" SGR. A sharp strain increase of about 3 µm/m can be observed at those times on the temperature compensation SGR. A possible explanation is that this SGR reacted to the generation of heat by the person who came close (about 30 cm) to both samples, when drilling a new increment. This is an evidence about the extreme sensibility of SGR to local temperature changes when working on PP. The effect of global room temperature variation can also be seen in Fig. 45.2. Here, a SGR was applied on a PP sheet and a strain measurement was carried out without any mechanical impact or drilling operation (curve in Fig. 45.2). At the same time the room temperature near the SGR was measured with a

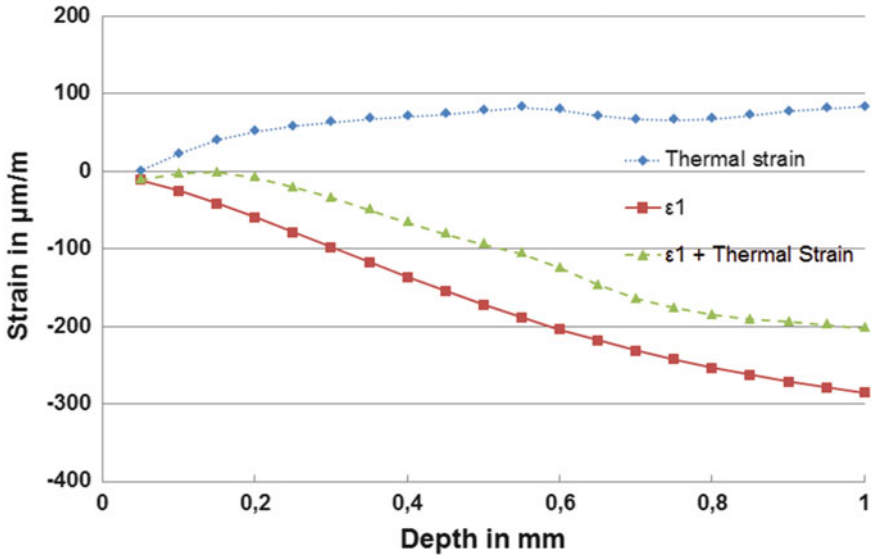

Fig. 45.3 Simulated strain with and without compensation of thermal strain on a polypropylene sample

thermocouple (triangular measuring points). In fact, a quite good correlation between the SGR's strain and temperature variation can be stated and the influence of even small temperature variations on measured strains is not negligible.

It should be mentioned that the experiment took place within a laboratory without an air-conditioning system. However, this experiment also reveals that the measured strain values do not exactly correspond to the thermal expansion coefficient of the sample. Indeed, the gauge compensates a part of it. Here, 2 °C have a 100 µm/m impact. The question is now how to quantify and how to consider this effect for a reliable residual stress measurement. As the elastic modulus of plastics is around a hundred times lower than that of steel, much higher strains can be expected when measuring residual stresses on plastics. However residual stress amounts on plastics are much smaller, and roughly around a hundred times lower than on steel [4]. Therefore the accuracy of strain analysis needed for plastics is in the same order as the one for metals. The norm specifies a value of about 1 µm/m [1]. Here this order of magnitude will be used to assess the importance of errors. Errors can be simulated considering an ideal stress field together with the consequences of thermal strain. In Fig. 45.3 an ideal strain course (solid line) was calculated using coefficients from [1] for a type A rosette. A biaxial homogeneous stress field with $\sigma = 2$ MPa was assumed. The elastic properties of the specimen are described by a Young's modulus of $E = 1.7$ GPa and a Poisson's ratio of $\nu = 0.4$. With those parameters the solid line in Fig. 45.3 represents the released strain ε_1 obtained when drilling a 2 mm diameter hole up to a depth of 1 mm, using twenty 50 µm increments. A time interval for each of the drilling steps of 20 min is assumed. If the thermal strain based on the temperature effect measured before (Fig. 45.2) is superimposed, a "false" strain curve is calculated (dashed curve ε_1 + thermal strain in Fig. 45.3). This "false" strain curve is what would be measured if the thermal strain due to temperature variation is not compensated and taken into account during an experiment.

With this strain curve containing strain due to the release of residual stress as well as thermal effects, a comparison can be made between a recalculated stress profile and the assumed ideal one (Fig. 45.4). As the strain was chosen for an axisymmetric stress profile and thermal expansion is assumed to be axisymmetric, the resulting stress curve is also axisymmetric and does not depend on the chosen stress direction. Therefore only one curve for the principal stress is represented. In Fig. 45.4 it can be noticed that adding a thermal effect moves the residual stress profile near the surface to compressive residual stresses. This means that due to heating, small tensile residual stress near the surface could be misinterpreted as being compressive. Of course if compressive stresses are already present on the surface of a material, still higher compressive stress will be assumed from the measured strain. The opposite is the case when drilling is stopped at a depth of approximately 0.6 mm and when the laboratory is left empty. It results in a decrease of the temperature (Fig. 45.2) and residual stresses move to tensile residual stresses when the measurement is resumed. Altogether it is clearly to be seen that temperature effects need special attention during hole drilling strain measurements in plastics.

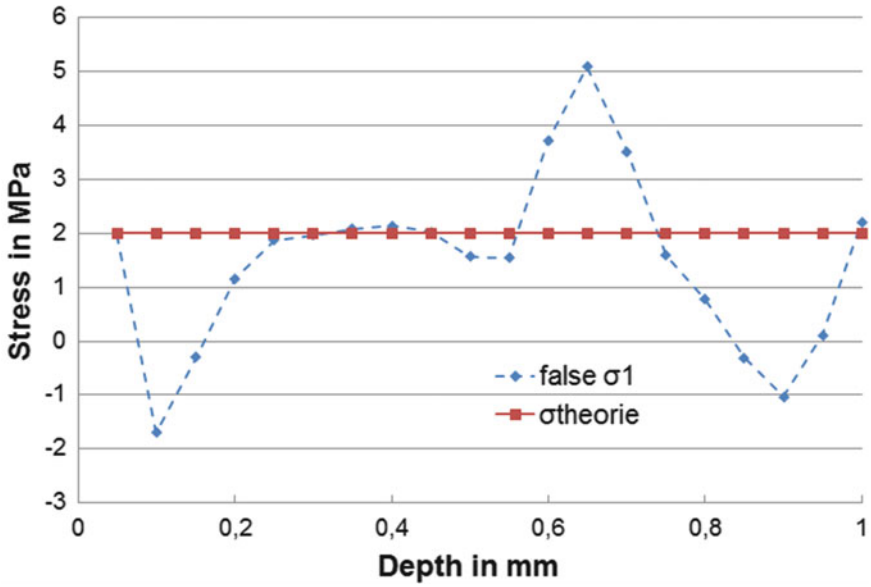

Fig. 45.4 Principal stresses with and without temperature compensation

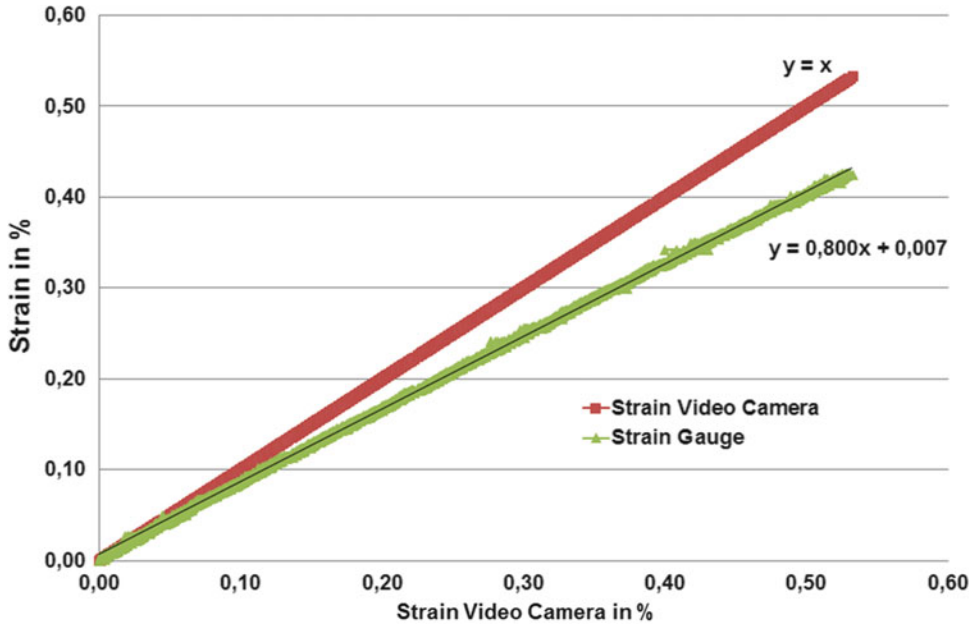

Fig. 45.5 Strain from a strain gauge versus strain from a video camera (Digital Image Correlation)

45.3 Stiffening Effects

It is well known that due to stiffening effects the strain measured by a SGR is lower than the real one of the specimen if there is a low specimen-SGR stiffness ratio. In this context the influence of other parameters like sample thickness, grid length of the strain gauge or type of the carrier material of the strain gauge are of importance [5, 6]. Experimentally the stiffening effect can be quantified by a tensile test. The result of such an experiment using a PP-specimen is shown in Fig. 45.5. Here, strains given by a strain gauge and by a video camera (Digital Image Correlation) were measured simultaneously. The result reveals a constant difference of 20 % between the two signals.

The same type of experiment was carried out for different types of SGRs usually used for residual stress analyses (gauge types 1, 2, 3 in Fig. 45.6): an eight grids rosette [7, 8], a rosette type A from Vishay MM (EA-06-062RE-120) and a rosette for

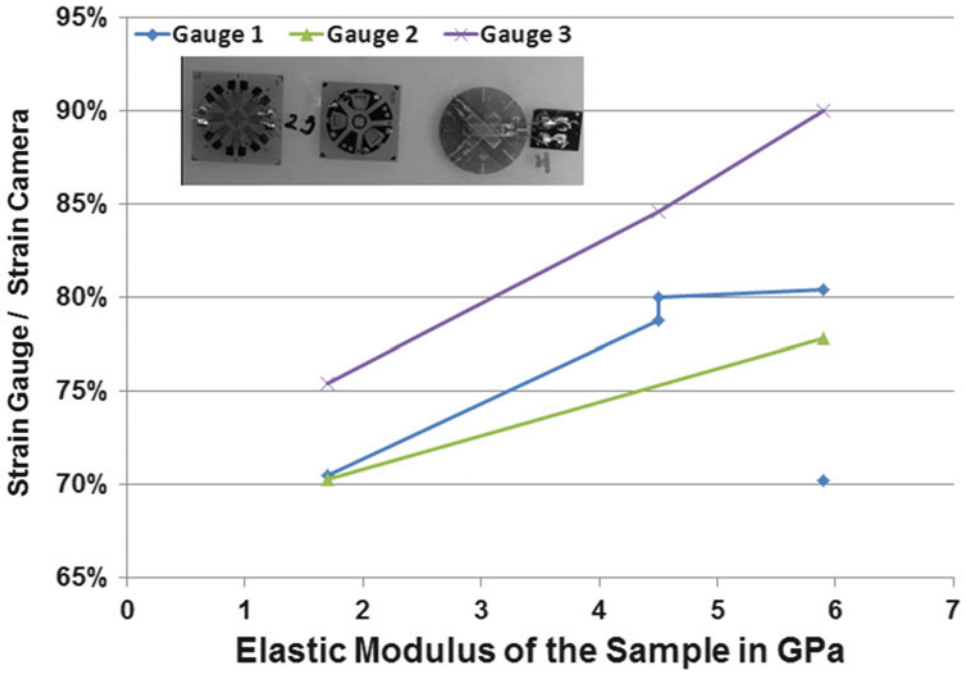

Fig. 45.6 Reduction of strain using different kinds of strain gauges on three materials

the ring-core method type FR-5 by Preusser Messtechnik GmbH. Three materials were investigated: an extruded PP sheet and two self-reinforced PP materials [9] with clearly different elastic moduli of 1.7, 4.5 and 6 GPa. In all cases, considerable differences between strains measured with an optical method and by the strain gauges were observed. Differences are significantly higher for materials with smaller elastic moduli. The best agreement was obtained for the third type SGR (Fig. 45.6). The measured strain is about 90 % of the strain measured by the video camera. This seems coherent as the SGR was applied on a "stiff" material (E = 6 GPa). Moreover the carrier of the third SGR is made of epoxide (E = 2.5 GPa) the stiffness of which is lower than that of the polyimide carrier (E = 3.6 GPa) of the two other gauges [10]. Finally the grid length of the third strain gauge (5 mm) is three times higher than the one of the two other strain gauges. Note that one of the values seems invalid (SGR 1 on the 6 GPa stiff material), which can be related to the woven shape of this self-reinforced material. The worst case observed is about 30 % strain reduction when using a common rosette on a low modulus material.

Figure 45.7 shows results of a numerical study which considers the ratio Yr between the Young's moduli of the component and the strain gauge rosette. The component was uniaxially stressed with 100 MPa. The foil of the SGR at the position of the hole was removed on the modelisation. It can be seen that the lower Yr the more the stress state at the point of measurement differs from the applied stress. Moreover, additional stresses are introduced due to the notch effect as a consequence of the local stiffness difference between the material and the SGR. If the Yr-value is nearly one, the notch effect still exists but is much lower. With increasing of Yr, its value tends to the ratio between the stress state of the component and the SGR. In addition, the value of the stress state at the measurement position tends to the applied one, except for a small stress increase due to the notch effect.

Table 45.1 gives an overview about the effect of different stiffness ratios Yr between the material and the SGR for various stress states (uniaxial, equi-biaxial, pure shear stress). The results ζ represent the percentage difference between the calculated stress state at the position of the hole and the applied stress. For the uniaxial stress state, the value of the second principal stress should be zero. The deviation ζ of the second principal stress represents in this only case a percentage of the applied principal stress ($\sigma_I = 100$ MPa) and not of the second applied principal stress compared with the biaxial and pure shear stress state.

It can be concluded that a pure shear stress is the worst case near the surface. Here, the calculated stress is higher than the applied stress. However this tendency is the opposite deeper in the material. For a 1 GPa stiff material, residual stresses 40 % lower than the applied one are calculated deep in the material and up to 22 % higher stress is measured near the surface. When working on a 6 GPa stiff material, this difference decreases and it amounts up to 15 % near the surface for the worst calculated state. Whereas the first principal stress differs remarkably from the applied stress, the second principal stress is influenced in the case of pure shear stress state and equi-biaxial stress state.

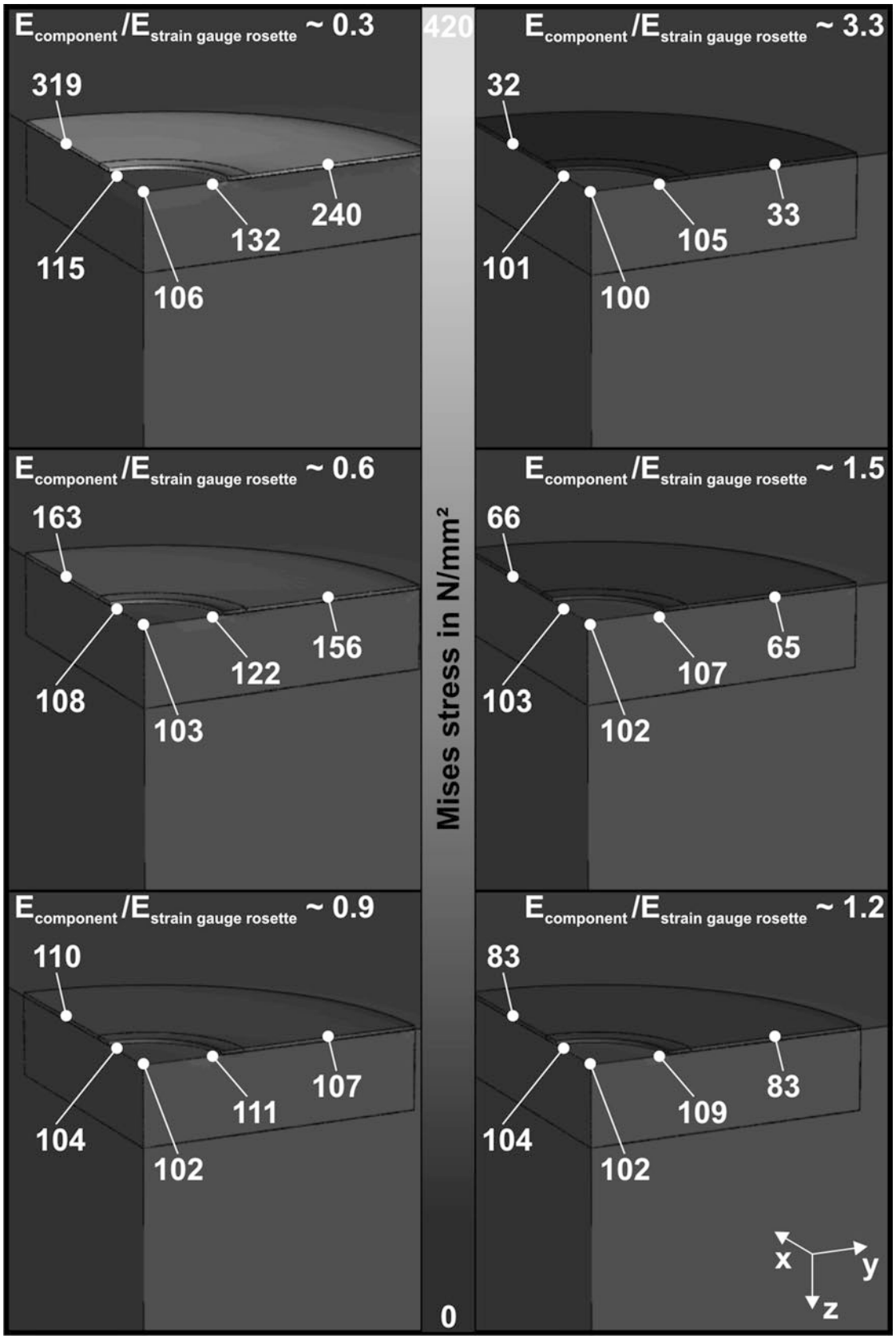

Fig. 45.7 Influence of the stiffness ratio component/strain gauge rosette on the residual stress state. Figures indicate the local Mises stresses

Table 45.1 Percentage difference ζ between the calculated and the applied calibration stress as a consequence of the stiffness effect of the adhesive layer and the strain gauge rosette carrier (E = 3.4 GPa) depending on the specimen's Young's modulus E_S, the stress state

	Uniaxially loaded $\sigma_I = 100$ N/mm^2, $\sigma_{II} = 0$ N/mm^2											
	$E_s = 1$ GPa		$E_s = 2$ GPa		$E_s = 3$ GPa		$E_s = 4$ GPa		$E_s = 5$ GPa		$E_s = 6$ GPa	
t in mm	ζ_{σ_I} in %	$\zeta_{\sigma_{II}}$ in %	ζ_{σ_I} in %	$\zeta_{\sigma_{II}}$ in %	ζ_{σ_I} in %	$\zeta_{\sigma_{II}}$ in %	ζ_{σ_I} in %	$\zeta_{\sigma_{II}}$ in %	ζ_{σ_I} in %	$\zeta_{\sigma_{II}}$ in %	ζ_{σ_I} in %	$\zeta_{\sigma_{II}}$ in %
0.00	57	3	43	5	33	4	27	4	23	3	20	3
0.05	22	−2	21	0	17	1	15	1	13	1	12	1
0.10	4	−4	9	−1	9	0	8	0	7	0	7	0
0.15	−7	−5	1	−2	3	−1	3	−1	4	0	4	0
0.20	−14	−5	−4	−2	−1	−1	0	−1	1	−1	1	−1
0.25	−19	−5	−8	−3	−4	−2	−2	−1	−1	−1	−1	−1
0.30	−23	−6	−11	−3	−6	−2	−4	−1	−3	−1	−2	−1
0.35	−26	−6	−13	−3	−8	−2	−6	−1	−4	−1	−3	−1
0.40	−29	−6	−15	−3	−10	−2	−7	−2	−5	−1	−4	−1
0.45	−31	−6	−17	−3	−11	−2	−8	−2	−6	−1	−5	−1
0.50	−32	−6	−18	−3	−12	−2	−9	−2	−7	−1	−6	−1
0.55	−34	−6	−19	−3	−13	−2	−10	−2	−8	−1	−7	−1
0.60	−35	−6	−20	−3	−14	−2	−11	−2	−9	−1	−7	−1
0.65	−36	−6	−21	−4	−15	−2	−11	−2	−9	−1	−8	−1
0.70	−36	−6	−22	−4	−15	−3	−12	−2	−9	−2	−8	−1
0.75	−37	−6	−22	−4	−16	−3	−12	−2	−10	−2	−8	−1
0.80	−38	−6	−23	−4	−16	−3	−12	−2	−10	−2	−8	−1
0.85	−38	−6	−23	−4	−16	−3	−13	−2	−10	−2	−9	−1
0.90	−39	−7	−23	−4	−17	−3	−13	−2	−11	−2	−9	−2
0.95	−40	−7	−24	−4	−17	−3	−13	−2	−11	−2	−9	−2
	Equi-biaxially loaded $\sigma_I = 100$ N/mm^2, $\sigma_{II} = 100$ N/mm^2											
0.00	69	69	52	52	40	40	33	33	28	28	24	24
0.05	26	26	24	24	20	20	17	17	15	15	14	13
0.10	5	5	10	10	10	10	9	9	9	8	8	8
0.15	−7	−7	2	2	4	4	4	4	4	4	4	4
0.20	−15	−15	−4	−4	−1	−1	1	1	1	1	2	2
0.25	−20	−20	−8	−8	−4	−4	−2	−2	−1	−1	0	0
0.30	−25	−25	−11	−11	−7	−7	−4	−4	−3	−3	−2	−2
0.35	−28	−28	−14	−14	−9	−9	−6	−6	−4	−4	−3	−3
0.40	−30	−30	−16	−16	−10	−10	−7	−7	−6	−6	−4	−4
0.45	−33	−33	−18	−18	−12	−12	−9	−9	−7	−7	−5	−5
0.50	−34	−34	−19	−19	−13	−13	−10	−10	−8	−8	−6	−6
0.55	−36	−36	−21	−21	−14	−14	−11	−11	−8	−8	−7	−7
0.60	−37	−37	−22	−22	−15	−15	−11	−11	−9	−9	−7	−7
0.65	−38	−38	−22	−22	−16	−16	−12	−12	−10	−10	−8	−8
0.70	−39	−39	−23	−23	−16	−16	−13	−13	−10	−10	−8	−8
0.75	−40	−40	−24	−24	−17	−17	−13	−13	−10	−10	−9	−9
0.80	−40	−41	−24	−24	−17	−17	−13	−13	−11	−11	−9	−9
0.85	−41	−41	−25	−25	−18	−18	−14	−14	−11	−11	−9	−9
0.90	−42	−42	−25	−26	−18	−18	−14	−14	−11	−11	−10	−10
0.95	−43	−43	−26	−26	−19	−19	−15	−15	−12	−12	−10	−10
	Biaxially loaded with $\sigma_I = 100$ N/mm^2, $\sigma_{II} = -100$ N/mm^2											
0.00	96	39	57	31	41	24	32	20	27	17	23	15
0.05	55	13	35	14	26	13	21	11	18	10	15	9
0.10	33	−1	23	5	18	6	15	5	13	5	11	5
0.15	20	−10	15	−1	12	1	10	2	9	2	8	2
0.20	11	−16	10	−6	8	−3	7	−1	6	0	6	0
0.25	4	−21	5	−9	5	−5	5	−3	4	−2	4	−1
0.30	−2	−25	2	−12	2	−7	2	−5	2	−4	2	−3

(continued)

Table 45.1 (continued)

	Uniaxially loaded $\sigma_I = 100$ N/mm^2, $\sigma_{II} = 0$ N/mm^2											
	$E_s = 1$ GPa		$E_s = 2$ GPa		$E_s = 3$ GPa		$E_s = 4$ GPa		$E_s = 5$ GPa		$E_s = 6$ GPa	
t in mm	ζ_{σ_I} in %	$\zeta_{\sigma_{II}}$ in %	ζ_{σ_I} in %	$\zeta_{\sigma_{II}}$ in %	ζ_{σ_I} in %	$\zeta_{\sigma_{II}}$ in %	ζ_{σ_I} in %	$\zeta_{\sigma_{II}}$ in %	ζ_{σ_I} in %	$\zeta_{\sigma_{II}}$ in %	ζ_{σ_I} in %	$\zeta_{\sigma_{II}}$ in %
0.35	−6	−27	−1	−14	0	−9	1	−7	1	−5	1	−4
0.40	−9	−30	−4	−16	−2	−11	−1	−8	0	−6	0	−5
0.45	−12	−31	−6	−18	−3	−12	−2	−9	−2	−7	−1	−6
0.50	−15	−33	−7	−19	−5	−13	−3	−10	−2	−8	−2	−6
0.55	−17	−34	−9	−20	−6	−14	−4	−11	−3	−8	−3	−7
0.60	−18	−35	−10	−21	−7	−15	−5	−11	−4	−9	−3	−7
0.65	−19	−36	−11	−21	−7	−15	−6	−12	−4	−9	−4	−8
0.70	−20	−37	−12	−22	−8	−16	−6	−12	−5	−10	−4	−8
0.75	−21	−37	−12	−22	−9	−16	−7	−12	−5	−10	−4	−8
0.80	−22	−38	−13	−23	−9	−16	−7	−13	−6	−10	−5	−9
0.85	−23	−38	−13	−23	−9	−16	−7	−13	−6	−10	−5	−9
0.90	−23	−39	−14	−23	−10	−17	−7	−13	−6	−11	−5	−9
0.95	−23	−39	−14	−24	−10	−17	−8	−13	−6	−11	−5	−9

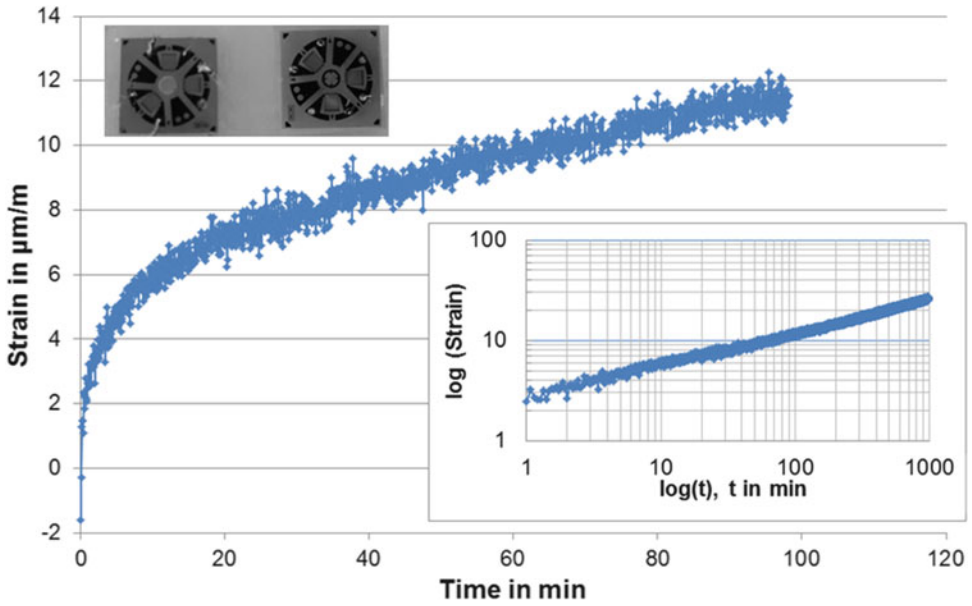

Fig. 45.8 Strain vs. time curve after drilling a hole increment in an extruded polypropylene sheet

45.4 Effects of Viscoelastic Behavior

A special characteristic of plastics is their strong viscoelastic behavior. Consequently PP samples are highly sensitive to creep and relaxation processes. In order to avoid errors due to additional time-dependent thermal strain in this part of the investigation, it was decided to compensate global thermal effects, and to drill manually with a very small rotational speed. This is possible due to the low strength of PP and avoids local heating of the material in the surrounding of the hole [11, 12]. As a consequence the influence of viscoelasticity could directly be quantified, avoiding disturbing thermal noise. In Fig. 45.8 the strain vs. time curve after drilling a hole step from 460 to 500 µm in a PP sample is shown.

A zero balance in terms of the strain signal was made before drilling. The reference time 0 min corresponds to the first value "directly" measured after drilling. As there is no thermal strain, the obtained strain profile corresponds to the "relaxation" of the material. It can be realized that the signal is not all constant within the time interval of the measurement. Moreover we see a relaxation of around 4 µm/m after 5 min, 10 µm/m after 1 h and 25 µm/m after 16 h. The logarithmic

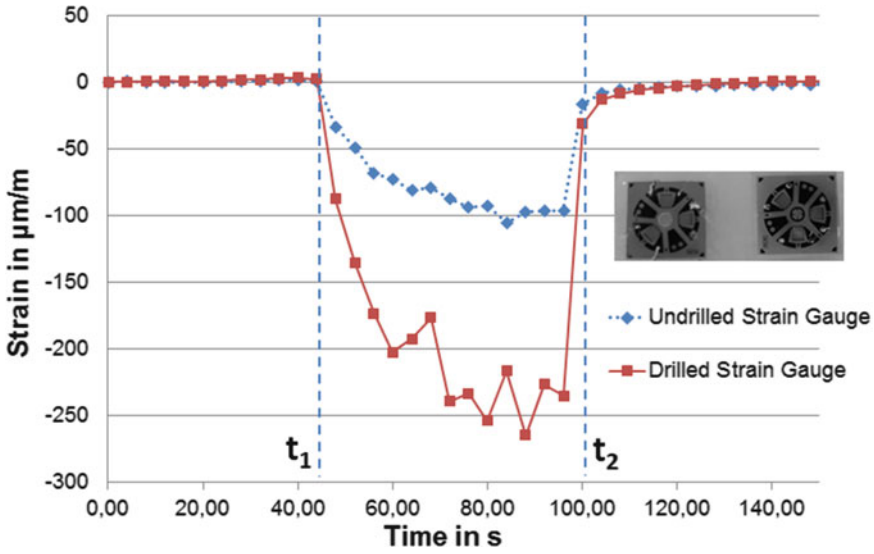

Fig. 45.9 Strain measured on two strain gauge rosettes during the drilling process

representation of the strain vs. time curve (Fig. 45.8) suggests that a creep effect occurs. It comes out that waiting until the signal is stabilized would not achieve reasonable strain values for a residual stress calculation. If one represents the measured relaxed strain '$\boldsymbol{\varepsilon_R}$' due to the release of residual stresses as the sum of a time dependent component '$\boldsymbol{\varepsilon_{Rt}}$' and a "spontaneous" constant component '$\boldsymbol{\varepsilon_{R0}}$', it would mean that we need this last elastic and time independent component '$\boldsymbol{\varepsilon_{R0}}$' to calculate the underlying residual stress. In Fig. 45.8 it should correspond to the first measured value at the time 0. But there is still another aspect which has to be taken into account. Figure 45.9 represents the strain measured during the same experiment, especially during the drilling process. Two SGRs spaced around 2 cm apart were bonded on the same specimen. Only one SGR was drilled. The solid line represents the result obtained while drilling the first gauge (drilled gauge), the dotted curve represents what was measured by the second gauge (undrilled gauge). The drilling process started at $t = t_1$. It can be noticed that although only one SGR was drilled, a qualitatively similar signal could be measured on both of them. The observed strain gradient is too significant to be attributed to a local thermal effect. It is rather a purely mechanical effect due to the compression induced by the drilling tool while drilling. Indeed polypropylene has a strong viscoelastic behavior and, hence, the material creeps while being mechanically loaded.

Based on this assumption the following model is used to obtain the component 'ε_{R0}' required to calculate residual stress. If the strain due to the compression effect of the drilling tool is called '$\boldsymbol{\varepsilon_c}$', then this strain can be decomposed as mentioned above in two strains: a time independent elastic component '$\boldsymbol{\varepsilon_{c0}}$' and a time dependent component '$\boldsymbol{\varepsilon_{ct}}$'. To explain the following point, it is considered that residual stresses are only released at the time t_2 (end of the drilling process in Fig. 45.9), and not step by step while drilling. Based on the above mentioned assumptions it follows:

$$\varepsilon(t) = \varepsilon_{c0}, \quad t = t_1 \tag{45.1}$$

While drilling, a viscoelastic effect is obtained because of the compressing effect of the drilling tool:

$$\varepsilon(t) = \varepsilon_{c0} + \varepsilon_{ct}(t - t_1), \quad t_1 < t < t_2 \tag{45.2}$$

Finally just after drilling, strain release occurs caused by the release of residual stresses and due to elastic unloading, because the drilling tool is no more compressing the sample. Using the Boltzmann superposition principle (theory for linear viscoelasticity), the material keeps in memory the previous deformation, i.e. the viscoelastic part from the previous drilling tool compression (45.2):

$$\varepsilon(t) = \varepsilon_{c0} + \varepsilon_{ct}(t_2 - t_1) + \varepsilon_{R0} - \varepsilon_{c0}, \quad t = t_2 \tag{45.3}$$

$$\Rightarrow\gg \varepsilon(t) = \varepsilon_{ct}(t_2 - t_1) + \varepsilon_{R0}, \quad t = t_2 \tag{45.4}$$

$$\varepsilon(\mathrm{t}) = \varepsilon_{ct}(\mathrm{t} - t_1) - \varepsilon_{ct}(\mathrm{t} - t_2) + \varepsilon_{R0} + \varepsilon_{Rt}(\mathrm{t} - t_2), \quad \mathrm{t} > t_2 \tag{45.5}$$

$$\varepsilon(\mathrm{t}) = \varepsilon_{R0} + \varepsilon_{Rt}(\mathrm{t} - t_2), \quad \mathrm{t} \gg t_2 \tag{45.6}$$

Based on (45.4), it is clearly to be seen that measuring the strain directly after drilling would produce an incorrect result. Because of the creep effect while drilling the material, the released strain directly after drilling at the time t_2 in Fig. 45.9 does not only correspond to the relaxation of residual stress. It also corresponds to the viscoelastic part caused by compression during the drilling process: $\varepsilon_{ct}(t_2 - t_1)$ in (45.4). During an experiment, strains were measured directly after drilling and an average variation of strain of about 8 µm/m was observed during a time interval of 8 s. This demonstrates the challenge connected with correct strains to be taken for the calculation of a residual stress profile. Using (45.5) one can formulate an assumption about a possible method. Under the assumption that the two components caused by the compression effect of the drilling tool 'ε_{ct}' will compensate themselves after a sufficient period of time (45.5), the strain will only depend on the release of residual stress: $\varepsilon_{R0} + \varepsilon_{Rt}(\mathrm{t} - t_2)$, which leads to (45.6). Assuming a creep law for the strain which depends on the relaxation of residual stresses (Fig. 45.8), we may extrapolate to get the time independent component 'ε_{R0}' and finally calculate residual stresses. This will be the purpose of further work.

45.5 Conclusion

The results demonstrated in this publication reveal the influence of different parameters when measuring residual stresses on plastics with the hole drilling method. Neglect of temperature compensation will generally result in measuring compressive stresses near the surface of the material. Depending on the thermal expansion of the plastics, errors may be more or less important. In addition there is a stiffening effect, which reduces the strain measured by the strain gauge rosette when working on low-stiffness materials. Finally, the influence of viscoelasticity on the measured strain has to be taken into account. An assumption is proposed to determine the valid strain and therefore to compensate viscoelastic effects. The creeping behavior of the released strain may be extrapolated after each increment to get the required strain to calculate a residual stress profile.

Acknowledgement The work presented is supported by the German Science Foundation DFG in the frame of SFB/TRR 30 which is gratefully acknowledged.

Reference

1. ASTM E837-13, Standard test method for determining residual stresses by the hole-drilling strain-gage method, ASTM International, 2013
2. Working Group on Residual Stresses, "AIAS – TR 01:2010", The hole-drilling strain gauge method for the measurement of uniform or non-uniform residual stresses (2010)
3. A. Nau, B. Scholtes, M. Rohleder, J.P. Nobre, Application of the hole drilling method for residual stress analyses in components made of polycarbonate. J. Plast. Technol. **7**(3), 66–85 (2011)
4. A.I. Isayev, D.L. Crouthamel, Residual stress development in the injection molding of polymers. Polym.-Plast. Technol. Eng. **22**(2), 177–232 (1984)
5. S. Zike, L.P. Mikkelsen, Correction of gauge factor for strain gauges used in polymer composite testing. Exp. Mech. **54**(3), 393–403 (2013)
6. A. Ajovalasit, L. D'Acquisto, S. Fragapane, B. Zuccarello, Stiffness and reinforcement effect of electrical resistance strain gauges. Exp. Mech. **43**(4), 299–305 (2007)
7. P.J. McGrath, D.G. Hattingh, M.N. James, I.N. Wedderburn, A novel 8-element gauge for residual stress assessment using the high-speed centre hole-drilling method. SAIMechE Res. Dev. J. **18**(1), 1–6 (2002)
8. A. Nau, G. Feldmann, J. Nobre, W. Zinn, B. Scholtes, An almost user-independent evaluation formalism to determine arbitrary residual stress depth distributions with the hole-drilling method. Mater. Sci. Forum **768–769**, 120 (2013)
9. H.-P. Heim, A. Ries, A.K. Bledzki, Challenge of functional gradation of self-reinforced polypropylene composites, in *SAMPE Europe SEICO 11–32nd* (2011), pp. 148–155
10. Carrier data taken from the firm Preusser Messtechnik GmbH, https://dms-technik.de/, German
11. E. Valentini, A. Benincasa, L. Bertelli, Experimental residual stress analysis by the hole-drilling method on plastic materials, in *Conference Paper, AIAS 2009-123* (2009)
12. J.P. Nobre, J.-H. Stiffel, A. Nau, J.C. Outeiro, A.C. Batista, W. Van Paepegem, B. Scholtes, Induced drilling strains in glass fibre reinforced epoxy composites. CIRP Ann. Manuf. Technol. **62**(1), 87–90 (2013)